

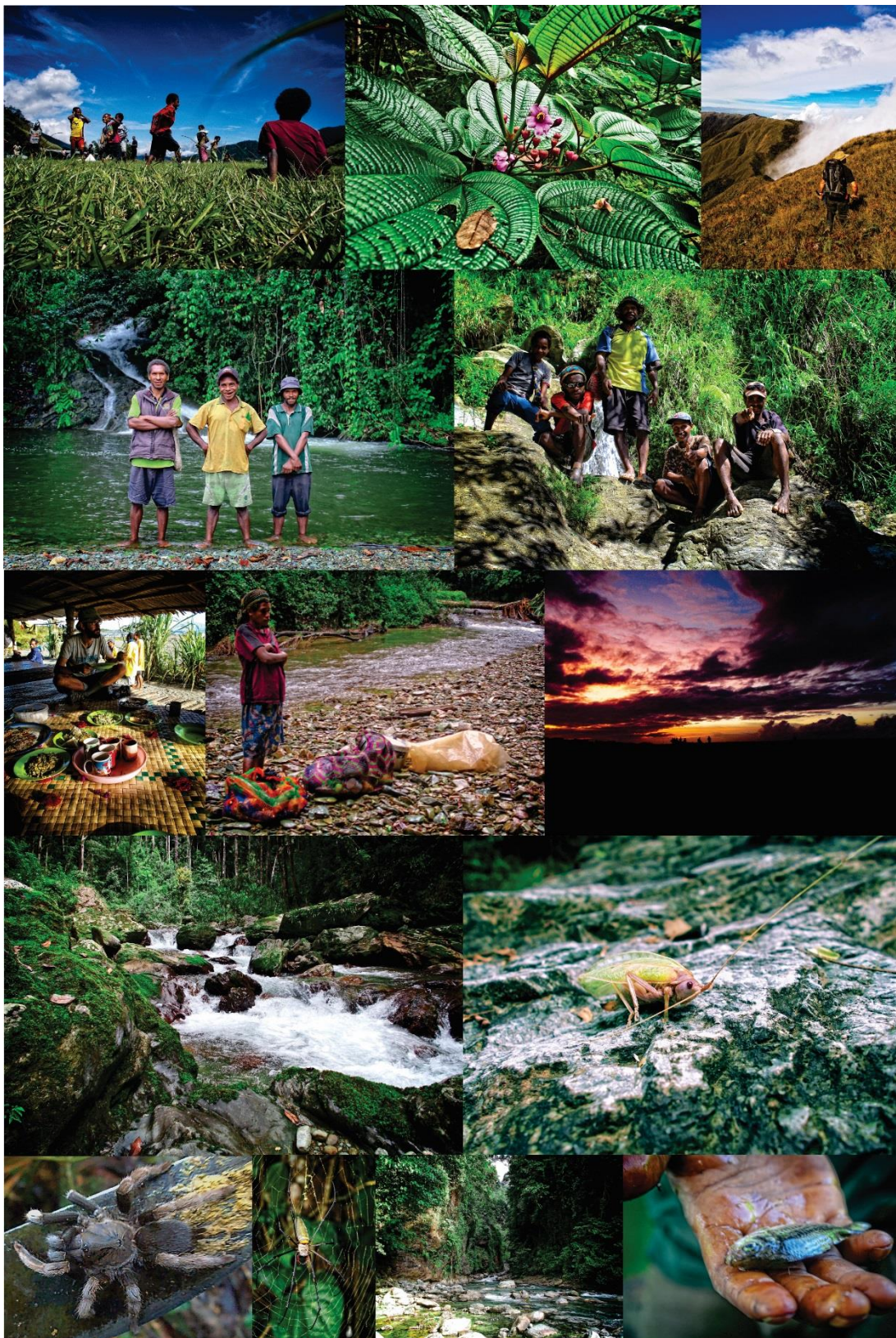
**DEFORMATIONAL PROCESSES ACCOMMODATING
SLIP ON AN ACTIVE LOW-ANGLE NORMAL
FAULT, SUCKLING-DAYMAN METAMORPHIC
CORE COMPLEX, PAPUA NEW GUINEA**

Marcel Mizera

A thesis
submitted to the Victoria University of Wellington
in fulfilment of the requirements for the degree of
Doctor of Philosophy

Victoria University of Wellington
December 2019

Frontispiece



Abstract

Detachment faults that can be shown to have slipped at dips $<30^\circ$ in highly extended continental crust are referred to as “Low-Angle Normal Faults” (LANFs). Their apparent low-dip angle exposed at the Earth’s surface contradicts Anderson-Byerlee frictional fault mechanics theory, which predicts that normal faults initiate at dips of $\sim 60\text{--}70^\circ$ and frictionally “lock-up” at dips $<30\text{--}45^\circ$. LANFs also lack significant associated seismicity; yet, a small number of normal faults are demonstrably active today at low angles ($<30^\circ$). To address the longstanding paradox of LANFs, this thesis focuses on one of the few known, and probably best-preserved, active LANFs on Earth: the Mai’iu fault in SE Papua New Guinea—a structure that bounds the topographic massif of the Suckling-Dayman Metamorphic Core Complex (SDM). In particular, three fundamental questions are investigated regarding LANFs by studying the deformational processes accommodating slip on the Mai’iu fault: (1) “How do continental detachment faults achieve low dips at the Earth’s surface: do they originate as low-angle normal faults, or does the footwall of an originally steeper fault deform in response to a ‘rolling-hinge’ unloading process?”; (2) “What micro-scale deformation mechanisms accommodate slip on LANFs in a metabasaltic protolith, and how do they vary with depth—are LANFs prone to aseismic creep, or earthquakes, or both?”; and (3) “What stresses (principal stress orientations, differential stresses, stress ratios) drive slip on an active LANF, and how do they vary with depth?”.

Structural field data and geomorphic data interpreted from GeoSAR-derived digital terrain models (gridded at 5–30 m spacing) and aerial photographs show that dip-slip on the active Mai’iu fault has exhumed a little-eroded, strongly corrugated, continuous fault surface on its footwall that is >28 km wide. The Mai’iu fault emerges from the ground at the range front near sea level with a northward dip of $\sim 21^\circ\text{N}$ (locally as low as $\sim 15^\circ$) and flattens southwards over the ~ 3 km-high crest of the domal SDM. The southernmost mapped portion dips $\sim 12^\circ\text{S}$. Uplift and exhumation of the footwall was accompanied by progressive back-warping of both the exhumed fault surface and an underlying foliation through $>26^\circ$ about an axis parallel to the fault strike. Antithetic-sense (i.e., northside-up) dip-slip motion on a widespread set of faults that cut the exposed footwall of the Mai’iu fault, and strike parallel to it, accommodated

some of the inelastic footwall bending that caused the Mai'iu fault to develop a domal shape. In agreement with this rolling hinge-style bending, bedding-fault cutoff angles in a stranded rider block of former hangingwall rocks indicate that the Mai'iu fault had an initial surface dip of $\geq 40^\circ$. Today, aligned microseismicity 12–25 km downdip of the Mai'iu fault trace delineates a convex upward fault zone that steepens downward to a 30–40° dip.

Detailed microstructural, textural and geochemical data combined with chlorite-based geothermometry of fault rocks rapidly exhumed from 20–25 km depth ($T \sim 425^\circ\text{C}$) reveal the processes operating inside the Mai'iu fault zone. Deformation in mylonitic rocks in the footwall of the Mai'iu fault is controlled by sliding and rotation of a pre-existing fine-grained (6–33 μm diameter) mafic assemblage together with syn-tectonic chlorite precipitation. This diffusion-accommodated grain-boundary sliding in the mylonites took place at $>270\text{--}370^\circ\text{C}$. At shallower levels ($T \geq 150\text{--}270^\circ\text{C}$), the mylonites are overprinted by an overlying <3 m thick zone of foliated cataclasite. Fluid-assisted mass transfer and metasomatic reactions created the foliated cataclasite fabric during inferred periods of aseismic creep. Pseudotachylites and ultracataclasites mutually cross-cut both the foliations and one another, recording repeated episodes of seismic slip. In these fault rocks, paleopiezometry based on calcite twinning yields peak differential stresses of $\sim 140\text{--}185$ MPa at inferred depths of 8–12 km. These differential stresses were high enough to drive continued slip on a $\sim 35^\circ$ dipping segment of the Mai'iu fault, and to cause new brittle yielding of strong mafic rocks in the exhuming footwall of that fault. In the uppermost crust (<8 km; $T < 150^\circ\text{C}$), where the Mai'iu fault dips shallowly and is most misoriented for slip, active fault rocks are clay-rich gouges containing abundant saponite, a frictionally weak mineral ($\mu < 0.28$).

In summary, the Mai'iu fault evolves by the "rolling-hinge" mechanism involving progressive flexural back-tilting during exhumation of an originally moderate dipping fault. The Mai'iu fault is frictionally weak near the surface, where the fault is poorly oriented; the fault is strongest at 8–12 km depth, where it both creeps and nucleates earthquakes. Locally high differential stresses drive this slip on a part of the fault that is not particularly misoriented. **This research elucidates the mechanics of low-angle normal faulting in the best-exposed and fastest-slipping LANF on Earth.**

Table of Contents

Abstract.....	i
Table of Contents.....	iii
List of Figures.....	vii
List of Tables.....	x
List of Abbreviations.....	xi
List of Mineral Abbreviations.....	xii
Acknowledgements.....	xiii
Chapter 1: Introduction	1
1.1 Background: Low-Angle Normal Faults—A Mechanical Paradox.....	1
1.1.1 Low-Angle Normal Faults and Metamorphic Core Complexes.....	4
1.1.2 Models of Low-Angle Normal Fault Evolution.....	7
1.1.3 Slip-parallel Fault Surface Corrugations.....	15
1.1.4 Mechanisms of Brittle and Ductile Deformation in Extensional Tectonic Settings.....	15
1.2 The Research Project and the Structure of this Thesis.....	19
1.2.1 Thesis Format.....	22
1.2.2 Contributors.....	26
1.2.3 Related Publications.....	27
1.2.4 Manuscripts in preparation.....	27
1.3 The Mai'iu Fault—A Natural Laboratory.....	28
1.3.1 Tectonic Setting of the Woodlark Rift.....	28
1.3.2 Seismicity in the Woodlark Rift.....	32
1.3.3 Dip-slip rate of the Mai'iu fault.....	34
1.3.4 Suckling-Dayman Metamorphic Core Complex.....	35
1.3.5 Major Faults in the Suckling-Dayman Metamorphic Core Complex Region.....	40
1.4 Methodology.....	40
1.4.1 Geomorphic Analysis (Chapter 2).....	41
1.4.2 Optical Microscopy, Imaging and Textural Analysis (Chapter 3 and Chapter 4).....	42
Chapter 2: Structural and Geomorphic Evidence for Rolling-Hinge Style Deformation of an Active Continental Low-Angle Normal Fault, SE Papua New Guinea	45
2.1 Introduction.....	46
2.2 Tectonic and Geological Setting of the Mai'iu Fault.....	50
2.2.1 Tectonic Setting of the Woodlark Rift.....	50
2.2.2 Geology of the Mai'iu Fault.....	52
2.2.3 Previous Geomorphic Work on the Mai'iu Fault.....	54
2.3 Methodology.....	55
2.3.1 Tectonic-Geomorphic Analysis.....	55
2.3.2 Fault Surface Modeling.....	56
2.4 Morphology of the Exhumed Mai'iu Fault Surface.....	57

2.5	Drainage Network and Fluvial Geomorphology	67
2.6	Late-Stage Footwall Deformation Structures.....	71
2.6.1	Footwall Faults Cutting the Exhumed Mai'iu Fault Surface	71
2.6.2	Folding of Sedimentary Beds in the Gwoira Rider Block	74
2.6.3	Microfolding of Foliation in the Goropu Metabasalt.....	76
2.7	Discussion	77
2.7.1	“Rolling-hinge” Style Deformation of the Footwall.....	77
2.7.2	Kinematics of the “Rolling-Hinge” Mechanism.....	80
2.7.3	Geodynamic Modeling	84
2.7.4	Summary of the “Rolling-Hinge” Processes.....	87
2.8	Conclusions	89
 Chapter 3: Slow-to-Fast Slip Deformation of Mafic Rocks on an Actively Exhuming Low-Angle Normal Fault, Woodlark Rift, SE Papua New Guinea .. 91		
3.1	Introduction.....	92
3.2	Tectonic Setting of the Woodlark Rift.....	96
3.2.1	Geology of the Mai'iu Fault	100
3.2.2	Fault Rock Sequence of the Active and Inactive Mai'iu Fault	101
	Non-mylonitic schist (Protolith)	103
	Mafic mylonite	103
	Foliated cataclasite.....	104
	Ultracataclasite	105
	Gouges and Principal Displacement Surface	106
3.3	Methods.....	106
3.3.1	Thin Section Preparation and Analytical Methods	106
3.3.2	Chlorite-based Geothermometry.....	107
3.4	Results: Microstructural Observations of Mai'iu Fault Rocks.....	108
3.4.1	Geochemical and Microstructural Analysis	108
	Mylonites	108
	Foliated Cataclasites	112
	Ultracataclasite	116
	Gouges	119
3.4.2	Hangingwall Conglomerate	121
3.4.3	Crystallographic Preferred Orientations of Mafic Minerals in the Fault Rocks	123
	Actinolite, Epidote, Titanite, Albite.....	124
	Quartz-rich Veins.....	126
3.4.4	Chlorite Geothermometry	129
3.5	Discussion	132
3.5.1	Mai'iu Fault Structure and Fault Rock Assemblage.....	132
3.5.2	Evolution of Deformation Mechanisms during Shearing of a Metabasaltic Footwall	135
	Prior to exhumation and peak metamorphism in the mylonites	135
	Late Neogene and Younger Mylonites	136
	Foliated cataclasite.....	137
	Ultracataclasite	139
	Gouge and Principal Displacement Surface.....	141
3.5.3	Strain Rates during Exhumational Shearing of the Mai'iu Fault.....	142
3.5.4	Seismic Slip and High Stress Ramp along the Mai'iu Fault.....	144
3.6	Conclusions.....	145

Chapter 4: Strength and Stress Evolution of an Actively Exhuming Low-Angle Normal Fault, Woodlark Rift, SE Papua New Guinea.....	147
4.1 Introduction	148
4.2 Tectonic Setting of the Suckling-Dayman Metamorphic Core Complex	153
4.2.1 Fault Rock Sequence of the Mai'iu Fault.....	156
4.2.2 Calcite Veins and Late Brittle Faulting in the Footwall and Hangingwall of the Mai'iu Fault.....	160
4.3 Methods	163
4.3.1 Structural Measurements, Sample Locations and Thin Section Preparation.....	163
4.3.2 Paleostress Analysis	164
Recrystallized Grain-Size Paleopiezometry.....	164
Calcite Twinning Paleopiezometry	166
Principal Stress Orientations.....	166
4.4 Results: Paleostress Analysis.....	168
4.4.1 Paleostress Reconstruction and Deformation Temperatures Based on Calcite Veins	168
Field and microstructural description of the calcite veins.....	168
Estimated differential stresses and deformation temperatures	176
Paleo-principal stress orientations and stress ratios based on calcite-twin slip data..	179
4.4.2 Paleo-Principal Stress Orientations and Stress Ratios based on Fault-slip Data for Late Brittle Faults.....	183
4.5 Discussion.....	187
4.5.1 Uncertainties in Calcite Paleopiezometry and its Applicability to Fault Rocks	187
4.5.2 Peak Metamorphic Conditions of Mylonites, Calcite Deformation Temperatures and Temperature-Depth Distribution.....	189
4.5.3 Strength-Depth Profile of the Mai'iu fault	191
4.5.4 Disposition of Principal Stress Axes	195
4.5.5 Mohr Construction for Slip on the Mai'iu Fault.....	199
4.6 Conclusion	201
Chapter 5: Conclusion—A Synthesis of Detachment Fault Evolution	203
5.1 Questions and Conclusions.....	203
5.2 The Low-Angle Normal Fault Mechanical Paradox.....	209
5.3 Future Research: Unanswered Questions and Directions	210
Appendix A	213
A.1 Stream Modelling, Fault Surface Model and Fault Surface Roughness Analysis	213
A.2 Unpublished Structural Data.....	222
A.3 Tilted Terraces	223
A.4 Strike-Distribution of Crenulation Foliation.....	225
A.5 Rotation of the Mai'iu Fault Accommodated by Vertical Footwall Faults	227
A.6 Flexing Mechanisms Accommodating Flexural Failure.....	229
A.7 Geodynamic Model	233
A.8 The effect of topographic stresses and density contrasts on the stress field	238

Appendix B.....	241
B.1 EDS-based Elemental Compositions of Mafic Fault Rocks	242
B.2 Additional SEM Back-Scatter Images and EDS Maps of Mafic Fault Rocks	246
B.3 EBSD Data Processing.....	250
B.4 EBSD-based Fabric Strength and Grain-Size Estimates of Mafic Fault Rocks.....	251
B.5 Recrystallized Quartz Grain Size Paleopiezometry	286
B.6 Temperature-Dependent Magnetic Susceptibility Experiment on Ultracataclasite ...	289
B.7 TEM Analysis of a Mirror-like Facet on Gabbroic Clast.....	294
B.8 Raman spectroscopy	295
B.9 XRD analysis on Mai'iu Fault Rocks	297
B.10 XRF Chemical Data of Bulk Mafic Fault Rocks	307
B.11 EPMA	309
Appendix C	311
C.1 Estimated Recrystallized Calcite Grain Sizes and Differential Stresses.....	311
C.2 Estimated Mean Twin Width, Mean Twin Density and Differential Stress of Twinned Calcite Grains.....	312
C.3 Paleo-principal Stress Axes Based on Calcite Twin-Pairs.....	313
C.4 Temperature Constraints On Calcite Veins.....	316
C.5 Calcite E-twin Boundary Removal for Grain-Size Analysis in MTEX.....	317
C.6 Differential Stress Limited by Coulomb Failure.....	318
Bibliography	320

List of Figures

Figure 1.1. Dip distribution of normal fault earthquake ruptures ($M > 5.5$).	2
Figure 1.2. Google Earth Satellite image of the Mai'iu fault.	4
Figure 1.3. World map of continental, continental margin and oceanic core complexes.	7
Figure 1.4. Rolling-hinge model for metamorphic core complex formation.	10
Figure 1.5. Domino-block rotation model for metamorphic core complex formation.	12
Figure 1.6. Schematic section of continental detachment faults cutting isotropic quartzofeldspathic basement.	19
Figure 1.7. Plate tectonic setting of the Woodlark Rift and present-day pole of rotation.	31
Figure 1.8. Tectonic map of the Woodlark Rift.	32
Figure 1.9. Microseismicity map of the Woodlark-D'Entrecasteaux Rift.	34
Figure 1.10. Geological and structural map of the Suckling-Dayman Metamorphic Core Complex.	39
Figure 2.1. Two prominent models for the evolution of large-displacement normal faults with present-day low-angle dips at the surface.	49
Figure 2.2. Plate tectonic setting of the Woodlark Rift.	52
Figure 2.3. Field photographs of the Mai'iu fault trace and the abandoned, exhumed fault surface up-dip of that trace.	58
Figure 2.4. Map showing remnants of the Mai'iu fault and Cross-section of the exhumed fault surface.	60
Figure 2.5. Fault surface model.	63
Figure 2.6. Fault Surface Roughness Analysis.	66
Figure 2.7. Drainage pattern, windgaps and tilted-terraces.	69
Figure 2.8. Late structures deforming the exhumed footwall of the Mai'iu fault.	73
Figure 2.9. Synclinally folded Gwoira Conglomerate.	75
Figure 2.10. Cross-section and subsurface continuation of the Mai'iu fault.	81
Figure 2.11. Thermomechanical model of LANF evolution.	85
Figure 2.12. Summary of footwall deformation in the exhuming slab of the Mai'iu fault with superimposed stress trajectories.	89
Figure 3.1. Schematic spatial changes of the rheology within the crust cut by an extensional detachment.	93
Figure 3.2. Simplified tectonic map of the Woodlark Rift.	99
Figure 3.3. Schematic section through the fault rock sequence of the Mai'iu fault.	102
Figure 3.4. Optical photomicrographs with crossed polarizers and layered elemental EDS map of mafic mylonites.	111
Figure 3.5. Field photograph, optical photomicrographs, CL image and layered elemental EDS maps of the foliated cataclasite unit.	115
Figure 3.6. Feldspar composition in mylonites and foliated cataclasites.	115
Figure 3.7. Optical photomicrographs and SEM back-scatter images of the ultracataclasite unit.	117
Figure 3.8. Curves of temperature dependant magnetic susceptibility for ultracataclasite sample.	118
Figure 3.9. SEM images and optical photomicrograph of gouge samples.	121
Figure 3.10. Dolerite cobble from the hangingwall with nanograin coating	123
Figure 3.11. EBSD phase maps of representative samples from the mylonite, cataclasite, ultracataclasite and gouge unit.	125
Figure 3.12. Grain size versus M-index plot for actinolite.	126
Figure 3.13. Quartz microstructural data for quartz-rich veins in mafic mylonites.	129
Figure 3.14. Binary plot of chlorite formation temperatures.	131
Figure 3.15. Profile across the Mai'iu fault and schematic interpreted spatiotemporal changes of deformation mechanisms in the different fault rock units.	135
Figure 4.1. A conceptual model of a crustal-strength profile in the footwall of an exhumed detachment fault.	153
Figure 4.2. Simplified tectonic map of the Woodlark Rift.	156
Figure 4.3. Lower-hemisphere, equal-area stereograms of fault kinematic data collected in the exposed footwall of the Mai'iu fault.	159

Figure 4.4. Outcrop photographs of the fault rock units exposed in the footwall of the Mai'iu fault and photomicrographs of calcite-filled veins that cross-cut them.	163
Figure 4.5. EBSD-based microstructural images of calcite veins in a non-mylonitic schist.	171
Figure 4.6. Microstructural observations of calcite veins in the foliated cataclasite unit.	175
Figure 4.7. Estimated deformation temperatures and differential stresses based on deformation twinning in calcite.	178
Figure 4.8. Reconstructed principal stress directions based on observed calcite-twin pairs as analysed by the MIM-method.	181
Figure 4.9. Paleo-principal stress axis solutions based on MIM analysis of fault-slip data for all brittle faults that cross-cut the exhumed footwall of the Mai'iu fault.	187
Figure 4.10. Depth versus temperature plot of the Mai'iu fault.	191
Figure 4.11. Strength profile of the Mai'iu fault.	195
Figure 4.12. Evolution of paleo-principal stress axes in the footwall and hangingwall of the Mai'iu fault.	197
Figure 4.13. Mohr construction for peak differential stress conditions as observed in the foliated cataclasites and ultracataclasites of the SDM.	201
Figure 5.1. Schematic profiles and strength profile across the Mai'iu fault.	208
Figure A.1. Three-dimensional Fault-surface model of the Mai'iu fault.	218
Figure A.2. Fault-roughness analysis.	221
Figure A.3. Map of Agaun Valley hosting several fluvial terraces.	223
Figure A.4. Schematic evolution of the strike orientation of measured crenulation foliation.	227
Figure A.5. Sketch of an array of vertical faults causing rotation of the main fault.	228
Figure A.6. Critical beam thickness that allows distributed crunching or localized snapping flexural failure.	231
Figure A.7. Snapshots for the thermomechanical model shown in Figure 2.11.	237
Figure A.8A. Differential stress magnitude and maximum principal compressive stress direction for a close-up of the thermomechanical model.	238
Figure B.1. Layered elemental images of polyphase clasts embedded in fault gouge.	243
Figure B.2. Layered elemental image and SEM back-scatter images of polyphase clasts embedded in fault gouge.	245
Figure B.3. EDS maps of mafic mylonite.	246
Figure B.4. Pseudotachylite vein in mylonite sample.	247
Figure B.5. EDS maps of foliated cataclasite.	248
Figure B.6. SEM back-scatter images of ultracataclasite and EDS spectra of albite and K-feldspar grains.	249
Figure B.7. SEM back-scatter images and EDS maps of ultracataclasite.	250
Figure B.8. EBSD analysis of mylonite sample PNG16-142C (active Mai'iu fault trace).	261
Figure B.9. EBSD analysis of mylonite sample PNG15-43.	262
Figure B.10. EBSD analysis of mylonite sample PNG15-73 (close to active Mai'iu fault trace).	263
Figure B.11. EBSD analysis of an epidote-rich domain of mylonite sample PNG15-59A (close to active fault trace).	264
Figure B.12. EBSD analysis of mylonite sample PNG15-59A-2 (close to active fault trace).	265
Figure B.13. EBSD analysis of albitic boudin in mylonite sample PNG15-59A (albite only; close to active fault trace).	266
Figure B.14. EBSD analysis of (ultra?)mylonite sample PNG16-17E (close to the inactive Mai'iu fault trace).	267
Figure B.15. EBSD analysis of mylonite sample PNG15-52 (just south of active Mai'iu fault trace).	268
Figure B.16. Microstructural analysis of an albite porphyroclast in the mafic mylonite sample PNG15-73.	269
Figure B.17. EBSD analysis of foliated cataclasite sample PNG16-142E (at active Mai'iu fault trace).	270
Figure B.18. EBSD analysis of foliated cataclasite sample PNG16-151E-1 (just south of active Mai'iu fault trace).	271
Figure B.19. EBSD analysis of foliated cataclasite sample PNG16-151E-2 (just south of active Mai'iu fault trace).	272
Figure B.20. EBSD analysis of foliated cataclasite sample PNG15-50D-Redux (active Mai'iu fault trace).	273

Figure B.21. EBSD analysis of foliated cataclasite sample PNG15-50E (active Mai'iu fault trace).....	274
Figure B.22. EBSD analysis of cataclasite sample PNG16-125B (just south of active(?) Mai'iu fault trace, close to Gwoira fault).	275
Figure B.23. EBSD analysis of ultracataclasite sample PNG16-125A.	276
Figure B.24. EBSD analysis of ultracataclasite sample PNG16-142D2.	277
Figure B.25. EBSD analysis of gouge sample PNG16-142A (active Mai'iu fault trace).....	278
Figure B.26. EBSD analysis of gouge sample PNG16-142B (active Mai'iu fault trace).	279
Figure B.27. EBSD analysis of a non-mylonitic schist (PNG15-72A).	280
Figure B.28. EBSD analysis of a non-mylonitic schist (~5.7 km south of the active Mai'iu fault trace; PNG16-169).	281
Figure B.29. EBSD analysis of a non-mylonitic schist (~4.5 km south of the active Mai'iu fault trace; PNG16-176).	282
Figure B.30. EBSD analysis of a non-mylonitic schist (~1.8 km south of the active Mai'iu fault trace; PNG16-182).	283
Figure B.31. EBSD analysis of a non-mylonitic schist (just south of active(?) Mai'iu fault trace, close to Gwoira fault; PNG16-126A).	284
Figure B.32. EBSD analysis of a non-mylonitic schist (just south of active(?) Mai'iu fault trace, close to Gwoira fault; PNG16-126B).	285
Figure B.33. Shape preferred orientation (SPO) analysis of recrystallized and relict quartz grains using MTEX.....	288
Figure B.34. Curves of temperature dependant magnetic susceptibility for sample PNG16-142D ..	290
Figure B.35. Back-scatter images of magnetite-bearing veins and clasts in ultracataclasite (PNG16-142D).	291
Figure B.36. EDS-spectra of magnetite-bearing veins.....	292
Figure B.37. EDS-spectra of a magnetite-bearing clast.....	293
Figure B.38. EDS analysis of a single magnetite grain in the ultracataclasite matrix (PNG16-142D).	294
Figure B.39. Raman spectra of silica-rich domain embedded in fault gouge..	296
Figure B.40. Whole rock, Ca-saturated X-ray diffraction patterns.....	299
Figure C.1. Mean principal axes distribution in lower hemisphere, equal area stereonet from all calcite veins and the mean distribution of all samples derived from different stress inversion techniques.	315
Figure C.2. Mohr diagram in which Coulomb failure limits differential stress	319

List of Tables

Table 1.1. List of key structural and geomorphic features that are diagnostic of the rolling-hinge or domino-block rotation process sorted by priority.....	14
Table A.1. Unpublished structural field data.	222
Table A.2. Surface slope information of tilted fluvial terraces (Figure A.3) from a 5-meter DTM.	224
Table A.3. Overview of variables used for equations in Appendix A.6.	232
Table A.4A. Frictional and thermal properties of modeled materials (thermomechanical model). ...	237
Table A.5B. Ductile rheological properties of modeled materials (thermomechanical model).	237
Table B.1. EDS-based elemental compositions of the different fault rock units.	242
Table B.2. EDS-based elemental composition of polyphase clasts in a gouge sample (PNG16-142A).	243
Table B.3. EDS-based elemental compositions (wt%) of polyphase clasts in a gouge sample (PNG16-142B)	244
Table B.4. Grain-size statistics, J-index, S-index and M-index for actinolite based on EBSD analysis..	253
Table B.5. Grain-size statistics, J-index, S-index and M-index for epidote based on EBSD analysis. ...	255
Table B.6. Grain-size statistics, J-index, S-index and M-index for albite based on EBSD analysis.	257
Table B.7. Grain-size statistics, J-index, S-index and M-index for titanite based on EBSD analysis....	259
Table B.8. Calculated differential stresses based on the recrystallized grain-size of quartz using the paleopiezometer equation Eq. B.2..	287
Table B.9. Mineral Phases in Mai'iu fault rocks determined by X-Ray Diffraction.	298
Table B.10. Chemical analyses of Mai'iu fault rock samples.	308
Table C.1. Calculated differential stresses based on the recrystallized grain-size of calcite using the paleopiezometer equations by Valcke et al. (2015) and Platt and De Bresser (2017).	311
Table C.2. Calculated differential stresses based on the twin density of calcite grains using the paleopiezometer equations by Rybacki et al. (2013), Rowe and Rutter (1990), and Ferrill (1998)..	312
Table C.3. Results of the calcite strain-gage technique based on Groshong (1972, 1974).....	313
Table C.4. Reconstructed orientations of paleo-principal stress axes based on the Multiple Inverse Method by Yamaji (2000), P-, B- and T-axes calculations after Turner (1953) and dihedral calculation after Angelier & Mechler (1977).	314
Table C.5. Temperature constrains on the formation and deformation of calcite veins.	316
Table C.6. Material parameters and variables to calculate differential stresses limited by a linear Coulomb failure criterion as described above.....	319

List of Abbreviations

BDT	Brittle-ductile transition
CAT	Cataclasite
CCA	Clast cortex aggregates
CPO	Crystallographic preferred orientation
EBSD	Electron backscatter diffraction
EBSP	Electron backscatter diffraction pattern
EDS	Energy dispersive spectroscopy
FEG-SEM	Field emission gun scanning electron microscope
FIB	Focused ion beam
GBS	Grain Boundary Sliding
GOS	Grain orientation spread
GSI	Grain size insensitive
GSS	Grain size sensitive
LANF	Low-angle normal fault
MCC	Metamorphic core complex
MUD	Multiples of uniform distribution
ODF	Orientation Density Function
PDS	Principal displacement surface
PUB	Papuan Ultramafic Belt
RMS	Root-mean-square
SDM	Suckling-Dayman Metamorphic Core Complex
SPO	Shape preferred orientation
SRTM	Shuttle Radar Topography Mission
TEM	Transmission electron microscopy
UCAT	Ultracataclasite
XPOL	Crossed polarizers
XRD	X-Ray powder diffraction
XRF	X-ray fluorescence

List of Mineral Abbreviations

Ab	Albite
Am	Amorphous material
Amp	Amphibole
An	Anorthite
Act	Actinolite
Ap	Apatite
Cc	Calcite
Cpx	Clinopyroxene
Dol	Dolomite
Ep	Epidote
Kfs	K-feldspar
Kln	Kaolinite
Qtz	Quartz
Or	Orthoclase
Pmp	Pumpellyite
Prh	Prehnite
Px	Pyroxene
Py	Pyrite
Sap	Saponite
Sme	Smectite
Ttn	Titanite

Acknowledgements

First and foremost, I would like to thank my supervisor, Tim Little, for his invaluable guidance, enthusiasm, continuous support, seemingly endless revisions and patience. Tim's office door was always open for advice and fundamental discussions. He sacrificed many hours to provide me with useful ideas, insights in the interpretation of the collected data and detailed critique that substantially improved original drafts of this thesis. His endless passion and dedication to this project was always exemplary and a driving force to me. I am deeply grateful for the opportunity that he gave me to be part of this project to study in such an amazing place and among a team of such great researchers. Thank you, Tim.

I would like to thank my co-supervisor Kevin Norton for opening my eyes towards tectonic geomorphology—an epiphany moment in my career as a structural geologist. His guidance, help and advice on geomorphological matters was essential to finalize Chapter 2 in this thesis and that ultimately led to its publication in 2019. Kevin and I spent countless hours in front of my computer interpreting and wading through all the geomorphic data collected in ArcGIS. Most importantly, Kevin is also thanked for his cheese fondue—one of the best I have ever had.

I also thank Dave Prior from the University of Otago, who taught me everything about electron backscatter diffraction. His help and advice were integral to the results and interpretation of the collected microstructural data. I would also like to thank Dave for his never-ending positive attitude during my time in Dunedin and the countless coffee breaks accompanied by scientific discussions.

My sincere thanks also go to Carolyn Boulton for her input, guidance, discussion and review on fault rock and grain-scale deformation mechanism related matters. Her infinite knowledge and curiosity on fault rocks majorly improved early drafts of Chapter 3. Thank you, Carolyn—you are not only a great researcher I deeply admire, but also a great friend, who helped me through the more difficult times of my Ph. D.

Susan Ellis, thank you for all your support and advice. Your geodynamic models and our long discussions together with James Biemiller were essential for this thesis. Your amazing skills as a field geologist has also helped to understand and interpret all

the structural data we collected during the field campaign in 2015. Are you sure you are not a structural geologist?

I would like to thank Sam Webber for endless debates on low-angle normal faults in the kitchen of Croydon Street; but also for his input, insights and for being a seemingly infinite source of ideas. Sam's positive attitude even at times of frustrations was always an inspiration. Thanks for being not only a great colleague, but also an awesome friend.

Jürgen Österle—my colleague, my officemate, my friend. During all the hours we have spent in office CO418 I couldn't have wished for a better colleague. We went together through moments of deep anxiety, but also of big excitement. Thanks for your presence, patience and friendly ear. Your work discipline and your skills as a researcher were always a great inspiration and a driving force.

Many thanks go to James Biemiller at the University of Texas, Austin, for providing geodynamic models together with Susan Ellis that were essential for this thesis. I also want to thank James for all the great discussions we had that go far beyond dynamic modelling.

Thanks to Diane and Terry Seward—I am grateful for your cakes, cookies, encouragement, scientific discussions and endless support. Diane, thank you very much for proofreading parts of this thesis.

A special thankyou goes to some colleagues at the Victoria University of Wellington: Euan Smith, thank you for providing MATLAB codes that were essential for the paleostress analysis in Chapter 4. Julie Vry, thank you for all the petrology-related discussions and advice. Colin Wilson, thank you for the coffee and cake supply, and always having a sympathetic ear. A huge thanks to coffee place CO418 with coffee brewmaster Tom (T-chem) Womack—his coffee kept me going during the course of my studies. Mike Hannah, thank you for helping me taking high-resolution scans of my thin sections. Many thanks go to Stewart Bush who prepared all polished thin sections for my studies. Ian Schipper is thanked for his guidance during the microprobe analysis. I am thankful to Bruce Charlier for some geochemistry (TIMS) work on calcite vein samples. A huge thanks to Monika Hanson for sorting all financial matters.

I want to thank all my Wellington friends, colleagues, former PhD students, and flatmates—the people who kept me sane, believed in me, supported and tolerated me:

Leo Pure, Cam Watson, Jane Chewings, Elliot Swallow, Valeria van den Bos, Kosta Tashkoff, Esther van Dijk, Clarisse Lamarque, William Ivan Henriquez Gonzalez, Luisa Ashworth, Nabil Allaf, Annika Greve, Celine Mandon, Eva Sutter, Eliza Piispa, Dez Tessler, Ben Hines, Danielle Salmon, Ashok Gunawardene, Enock Rotich, Berit Mohr, Bird, Miranda Voke, Elena Kondrateva, Lisa Dowling, Jesse Kearse, Claudie McCarthy, David Uhrig, Rubianca Benavidez, Sandra Cortes-Acosta, LiWen Choy, Chriselle Braganza, Thomas Teunissen, all the geophysicists from the fifth floor especially Konstantinos Michailos, the “Shut up and Write” group especially Sara Cotterall and so many more! I want to thank my friends and former PhD students in Dunedin especially Kat Sauer for her friendship, accommodation and the opportunity to travel to the Australian Synchrotron in Melbourne to work on fault rocks from the Alpine fault, but also Luke Easterbrook, Jack Williams, Grace Duke, Martina Kirilova, Adrienne Lukacs, Rosie Cole, Jasper Hofmann, Meike Seideman, Arran Murch, Matthew Tarling, Christine McLachlan, Rachael Baxter, Jeremy Rooney, and many more!

I want to thank all our friends in Papua New Guinea, who supported our work and helped us during this adventure. I want to thank all the ward councillors and their families who provided local help, accommodation, food and advice: Ernest Duba (Bibitan); Colin Egairo, his many wives (far too many to list here) and his parents Samuel and Caroline (Biniguni), Evertius Maiao (Bonenau); James Benson Aniton (Pumani); Theopolis and his wife Delfi (Wapon); and Kingsley (Amon). Many thanks go to all the landowners, oral chiefs, and other elders who listened to our requests and who granted us permission to study their land and sample the Mai’iu fault; also to the many other citizens who allowed us to stay in their village or house. Special thanks go to Evertius Maiao, Edmund Kamut, Ernest Duba, Wellington Oyabu, Gabriel Yoba, and Mickland Waiyan for expressing an enthusiasm for our research, and for explaining the goals of our research to their communities in their local languages. Paul and Ethel Gardebo (in Rako) for accommodation and logistics at Rakau. And most importantly, I am thankful to all the strong men and women who were employed by us as guides and carriers—carrying our heavy packs, building shelters, fetching water and firewood, and helping us to communicate with others:



(Field Team 2015, from left to right, top row to bottom row) Reginald, Andrew, Marcel, Mark, Jürgen, Ernest, Lassma, Genum, Tim, Oxton, Susan, Luke, Dixon, Mark



(Field Team 2016, from left to right, top row to bottom row) Jürgen, Harold, Andrew, Ernest, Sam, Derek, Amos, Steven, Jerome(?), Marcel, Tim, Tennyson(?), Phineas, Mark, Danziel, Winston

Most importantly I want to thank my family:

Vielen Dank Mama und Papa für eure Liebe und kontinuierliche Unterstützung. Vielen Dank auch an meine großen Brüder Mirco und Malte, die immer zu mir gehalten haben, sowie ihre Familien Imke, Soja, Janna, Felix und Nils.

Chapter 1: Introduction

1.1 BACKGROUND: LOW-ANGLE NORMAL FAULTS—A MECHANICAL PARADOX

Continental and oceanic detachment faults are key features accommodating lithospheric extension and have slip magnitudes sufficient to exhume rocks from the middle to lower crust (e.g., Platt et al., 2015). Detachment faults that can be shown to have slipped at dips $<30^\circ$ are referred to as “Low-Angle Normal Faults” (LANFs; Axen, 2004; Whitney et al., 2013; Platt et al., 2015). Initiation and active slip of these faults at such low dip angles cannot be simply explained by basic rock mechanical principals (e.g., Anderson, 1951; Sibson, 1985). For an extensional tectonic setting, Andersonian theory predicts a vertical maximum principal stress orientation (σ_1), while the intermediate (σ_2) and minimum (σ_3) principal stresses are horizontal (Anderson, 1951). Fault slip can occur if stress tractions resolved on a fault plane meet a failure criterion. For this stress system, the Mohr-Coulomb failure criterion predicts that normal faults will typically initiate at an ideal dip of $\sim 60^\circ$ in a brittle crust with “Byerlee” coefficient of static friction ($\mu=0.6\text{--}0.85$; Byerlee, 1978; Sibson, 1990) and may frictionally lock up at dips $<30\text{--}45^\circ$ (e.g., Collettini & Sibson, 2001; Axen, 2004). The rarity of moderate to large magnitude historic earthquakes on demonstrably shallow-dipping normal faults supports this conventional idea that most normal faults are predicted to dip steeply (**Figure 1.1**; e.g., Jackson, 1987; Jackson & White, 1989, Abers et al., 2016; Collettini et al., 2019). Initiation of a primary LANF in isotropic crust can only be explained if the maximum principal stress direction σ_1 is non-vertical to satisfy the Coulomb criterion (e.g., Axen, 2004); otherwise a fault initiating in formerly intact, homogeneous crust will most likely dip steeply.

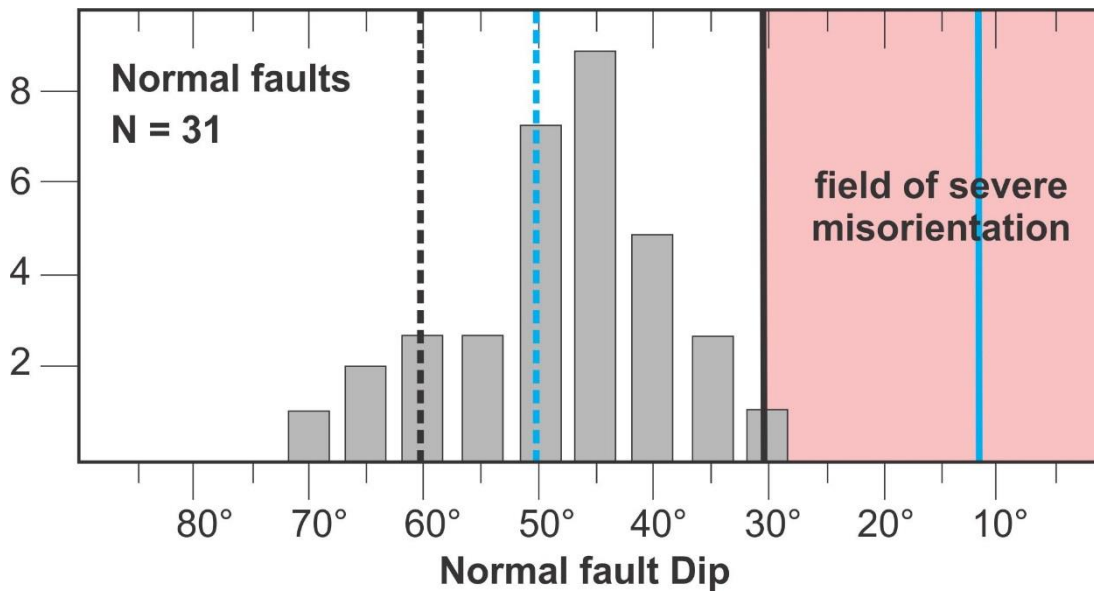


Figure 1.1. Dip distribution of normal fault earthquake ruptures ($M > 5.5$) obtained from focal mechanisms of intracontinental, shallow earthquakes where rupture planes are unambiguously identified (compilations of Jackson & White, 1989; Collettini & Sibson, 2001; Sibson, 2009; Collettini et al., 2019). Vertical lines indicate the optimal orientation (dashed lines) and frictional lock-up dip angle (solid lines) of normal faults for a static coefficient of friction of $\mu_s = 0.6$ (black) and $\mu_s = 0.2$ (blue).

A small number of normal faults are demonstrably active today at low angles ($< 30^\circ$; e.g., Rigo et al., 1996; Sorel, 2000; Chiaraluce et al., 2007). Geological evidence for slip on active and inactive normal faults at low dips includes field-based structural studies (e.g., Lister & Davis, 1989; Kirby et al., 2003; Isik et al., 2003; Collettini & Holdsworth, 2004; Hayman, 2006; Smith et al., 2007), distribution of microseismicity to depths of up to ~ 16 km near active faults (e.g., Rigo et al., 1996; Chiaraluce et al., 2007), and continuous global positioning system (GPS) data for active faults (e.g., Hreinsdóttir & Bennett, 2009; Wallace et al., 2014). Microseismic and geodetic evidence from the Alto Tiberina fault in the northern Apennines, Italy, shows that this normal fault is active today at a dip of $\sim 15^\circ$ in the upper crust from 4 km to ~ 14 – 16 km depth (Chiaraluce et al., 2007; Hreinsdóttir & Bennett, 2009). Based on focal mechanisms and borehole break outs, the Alto Tiberina fault is active in an Andersonian stress field, with a subvertical σ_1 and subhorizontal σ_3 (Montone et al., 2004). This modern example of an LANF accords with structural field-based studies of ancient detachment faults; for example the Whipple Mountain or Black Mountains detachment faults, Nevada and California, where the faults dip at 10 – 36° relative to syntectonic bedding in their hangingwalls, and where Andersonian stresses have been inferred from brittle faults in the hangingwall and footwall of these detachments (Axen

& Selverstone, 1994; Hayman et al., 2003; Axen, 2004 and references therein). In these examples, σ_1 is inferred to have been subvertical and thus disposed at a high angle (54° – 80°) to the highly misoriented detachment faults (e.g., Axen & Selverstone, 1994; Hayman et al., 2003). The observed activity of such normal faults at dips $<30^\circ$ in an Andersonian stress regime therefore raises questions about Mohr-Coulomb mechanics.

Active slip on misoriented faults might be assessed through consideration of fault reactivation from pre-existing low-angle structures, such as thrust faults (e.g., Singleton et al., 2018). Reactivation of a misoriented “Byerlee” fault in an Andersonian stress regime would require: (1) high pore fluid pressures within the fault zone ($P_f > \sigma_3$); and/or (2) frictionally weak fault materials such as a phyllosilicate-rich (talc, montmorillonite or saponite) gouge (e.g., Floyd et al., 2001; Collettini et al., 2009a; Collettini, 2011 and references therein). Due to the rarity of active LANFs that are well exposed at the Earth’s surface, and that can be examined in situ, these hypotheses are still mostly untested. Most well-studied continental LANFs are ancient and inactive; thus, the processes that affected them as active structures have been overprinted and obscured by postformational tilting and erosion (Axen & Bartley, 1997; Axen, 2004; Collettini, 2011; Whitney et al., 2013). The mechanical paradox of LANFs is therefore still debated today. Fundamental questions that remain include: how (and at what angles) did present-day LANFs in continental crust originally form?; do LANFs initiate at steep angles then back rotate as “dominos” before being cross-cut by younger and steeper generations of faults?; or do they form at originally steep angles, then back-warp by a “rolling-hinge” mechanism as a single large structure—convex upward in shape—that accumulates slip (as has been demonstrated for oceanic detachment faults) to achieve low dips at the surface?; are LANFs intrinsically weak, containing frictionally weak fault rocks?; do LANFs generate large earthquakes albeit infrequently or do they generally creep aseismically?

The Mai’iu fault in SE Papua New Guinea is an ideal “natural laboratory” in which to address such questions using direct observations and field data (**Figure 1.2**). It is one of the fastest slipping (Holocene dip-slip rate of 11.7 ± 3.5 mm/yr, Webber et al., 2018) and probably the best preserved of only a handful of known active LANFs on Earth (e.g., Spencer, 2010; Little et al., 2019). More than 25 km wide and barren of any cover rocks, the upper, self-exhumed part of the Mai’iu fault surface, together with

local outcrops of its deep- to shallow-formed fault rocks, provide a valuable window into deformational processes that accommodate slip on an active LANF.

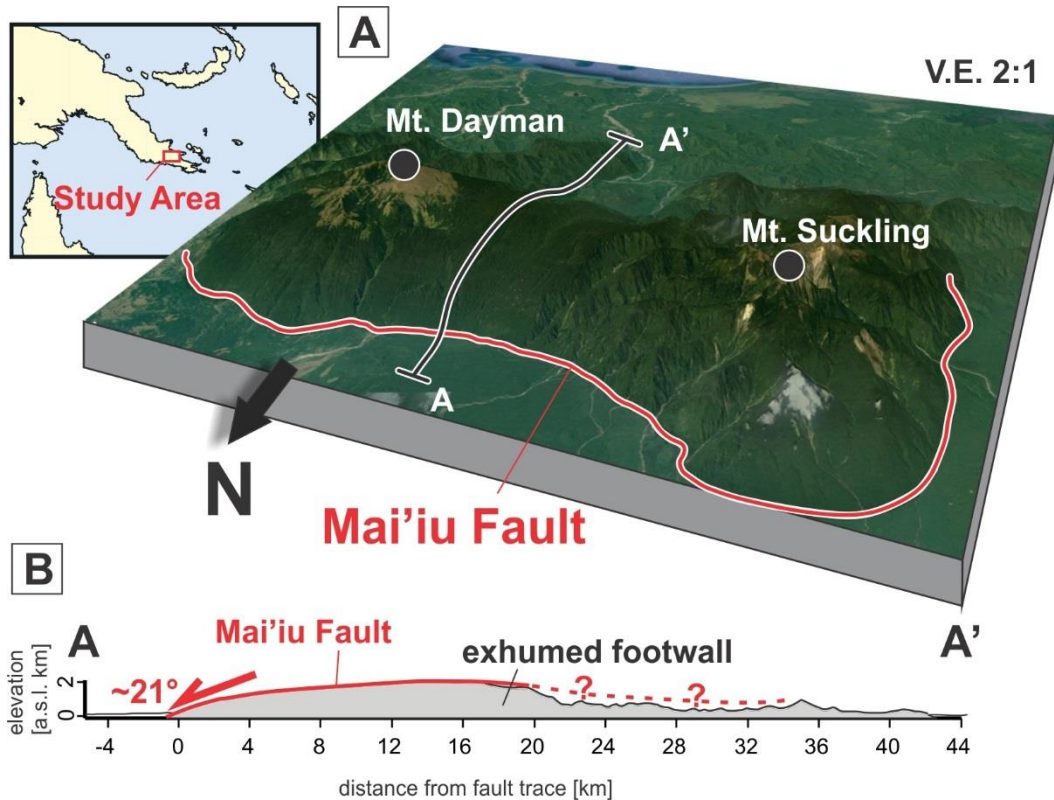


Figure 1.2. A) Google Earth Satellite image of the Mai'iu fault bounding the smooth and corrugated dome of the Suckling-Dayman Metamorphic Core Complex (SDM). B) Cross-section of the well-preserved Mai'iu fault.

1.1.1 Low-Angle Normal Faults and Metamorphic Core Complexes

Detachment faults that have formed and/or slipped at low-angles ($<30^\circ$) are called “low-angle normal faults” (LANFs; e.g., Axen, 2004). These are typically domal in shape and have large slip magnitudes (10's of km's; Whitney et al., 2013). They commonly separate tilted and faulted upper crustal unmetamorphosed rocks in the hangingwall from middle to lower crustal metamorphic rocks in the footwall (e.g., Coney, 1980; Armstrong, 1982; Tucholke et al., 1998; Whitney et al., 2013; Platt et al., 2015). The structurally highest part of the footwall typically includes a zone of mylonitic rocks that formed as a result of extensional ductile shearing at depth (e.g., Davis, 1983; Lister & Davis, 1989; Singleton & Mosher, 2012; Platt et al., 2015). The ductile extensional fabrics define a shear zone that is overprinted across older pre-extensional fabrics that may be preserved at greater structural depth in the footwall (e.g., Cooper et al., 2017). Slip on the detachment fault ultimately carries the mylonites

across the brittle-ductile transition (BDT), causing them to be overprinted by later brittle deformation (Lister & Davis, 1989; Axen, 2004; Platt et al., 2015; Cooper et al., 2017). Shear sense indicators in both the mylonites and brittle fault rocks preserve a record of continuing normal-sense slip (e.g., John & Cheadle, 2010).

At the Earth's surface, the metamorphic footwall is juxtaposed against highly extended, unmetamorphosed hangingwall rocks (e.g., Whitney et al., 2013). This contrast occurs abruptly across a gently dipping ($<30^\circ$) detachment fault that is antiformal or domal in shape (e.g., Platt et al., 2015). This domal assemblage of rocks is called a Metamorphic Core Complex (MCC). MCCs are usually >20 km in diameter and up to 1–2 km in height (Whitney et al., 2013). Syn-exhumational magmatic intrusions in the footwall of MCCs are common, but not always present (e.g., Parsons & Thompson, 1993; Smith et al., 2011a; Whitney et al., 2013). Crustal conditions during extension conducive to formation of MCCs include a thick and mechanically weak middle to lower crust, a thin layer of elastic-brittle upper crust, and a fault zone that strain-weakens during slip (e.g., Lavier et al., 1999; Platt et al., 2015; Cooper et al., 2017). MCCs occur near oceanic spreading centres in oceanic lithosphere, and also in rifts, hyper-extended margins, and collision zones in continental crust (e.g., Baldwin et al., 2012; Whitney et al., 2013; Platt et al., 2015; Brun et al., 2018). Globally, MCCs exhibit a remarkable diversity of setting and expression that can be attributed, in part, to varying petrological and rheological characteristics of the rocks; different pre-extensional crustal structures, thicknesses, and geothermal gradients; and to the wide range of extensional boundary conditions (**Figure 1.3**; e.g., John & Cheadle, 2010; Whitney et al., 2013; Platt et al., 2015).

Continental MCCs were first identified in the late 1970's and early 1980's in the Cenozoic Basin and Range Province in the North American Cordillera (**Figure 1.3A, 1.3B**; e.g., Anderson, 1972; Coney, 1974; Proffett, 1977; Coney, 1980). These ancient "Cordilleran-style metamorphic core complexes" can be traced throughout a semi-continuous >3000 -km-long belt extending from southern Canada to northwestern Mexico (Armstrong, 1982), but were also identified in a number of other continental locations worldwide (e.g., Cycladic Archipelago, Aegean Sea, Lister et al., 1984; Norwegian Caledonides, Steltenpohl et al., 2004; Paparoa Ranges, New Zealand, Tulloch & Kimbrough, 1989; and West Antarctica, Richard et al., 1994). The D'Entrecasteaux Islands and the Suckling-Dayman Metamorphic Core Complex at the

tip of the Woodlark Rift in Papua New Guinea have been described as rare examples of continental MCCs on Earth that are demonstrably active today (e.g., Wallace et al., 2014; Eilon et al., 2015; Abers et al., 2016). Rapid continental extension in this region has led to the surficial exposure of the world’s youngest known (Pliocene age) eclogites in extensional gneiss domes (MCCs cored by high-grade migmatitic rocks) in the D’Entrecasteaux Islands (Hill et al., 1992; Baldwin et al., 2004, 2008; Little et al., 2007, 2011; Gordon et al., 2012; Little et al., 2019). The majority of continental MCCs seem to occur in regions of initially thickened crust which have undergone subsequent extension, suggesting that gravitational collapse can be an important driving force for MCCs on the continents (Whitney et al., 2013 and references therein).

Oceanic MCCs or “megamullions” have been identified in seafloor bathymetric images at dominantly slow and ultra-slow spreading mid-ocean ridges such as the Mid-Atlantic ridge and the Southwest Indian ridge (**Figure 1.3A, C**; Cann et al., 1997; Blackman et al., 1998; Tucholke et al., 1998; Ranero & Reston, 1999; Dick et al., 2000; Tucholke et al., 2001). The existence and activity of low-angle detachments bounding these structures have been confirmed through marine geophysical observations (bathymetry, seismic reflection, microseismicity), by sea-floor sampling and photography using deep-diving submersibles and unmanned vehicles, and by scientific ocean drilling (Escartín et al., 2003; Schroeder & John, 2004; Ildefonse et al., 2007). These studies indicate that deformation in oceanic MCCs is influenced by plagioclase, pyroxene and olivine in dominantly gabbroic rocks that are reaction-softened due to partial hydrothermal alteration to form talc, chlorite and serpentine (Schroeder & John, 2004; Miranda & John, 2010; John & Cheadle, 2010). By contrast, continental MCCs are mostly dominated by quartzofeldspathic rock types. In these, rheology is controlled by feldspar and quartz and/or calcite—minerals may be hydrothermally altered to form assemblages that are rich in chlorite and white mica or—at lower temperatures—clay minerals. Whereas oceanic MCCs form in mechanically thin lithosphere that is subject to high geothermal gradients and juvenile basaltic magmatism, including sea-floor spreading; continental MCCs generally form in typical-thickness lithosphere, are subject to lower geothermal gradients, and are commonly devoid of syn-extensional magmatic rocks (e.g., John & Cheadle, 2010).

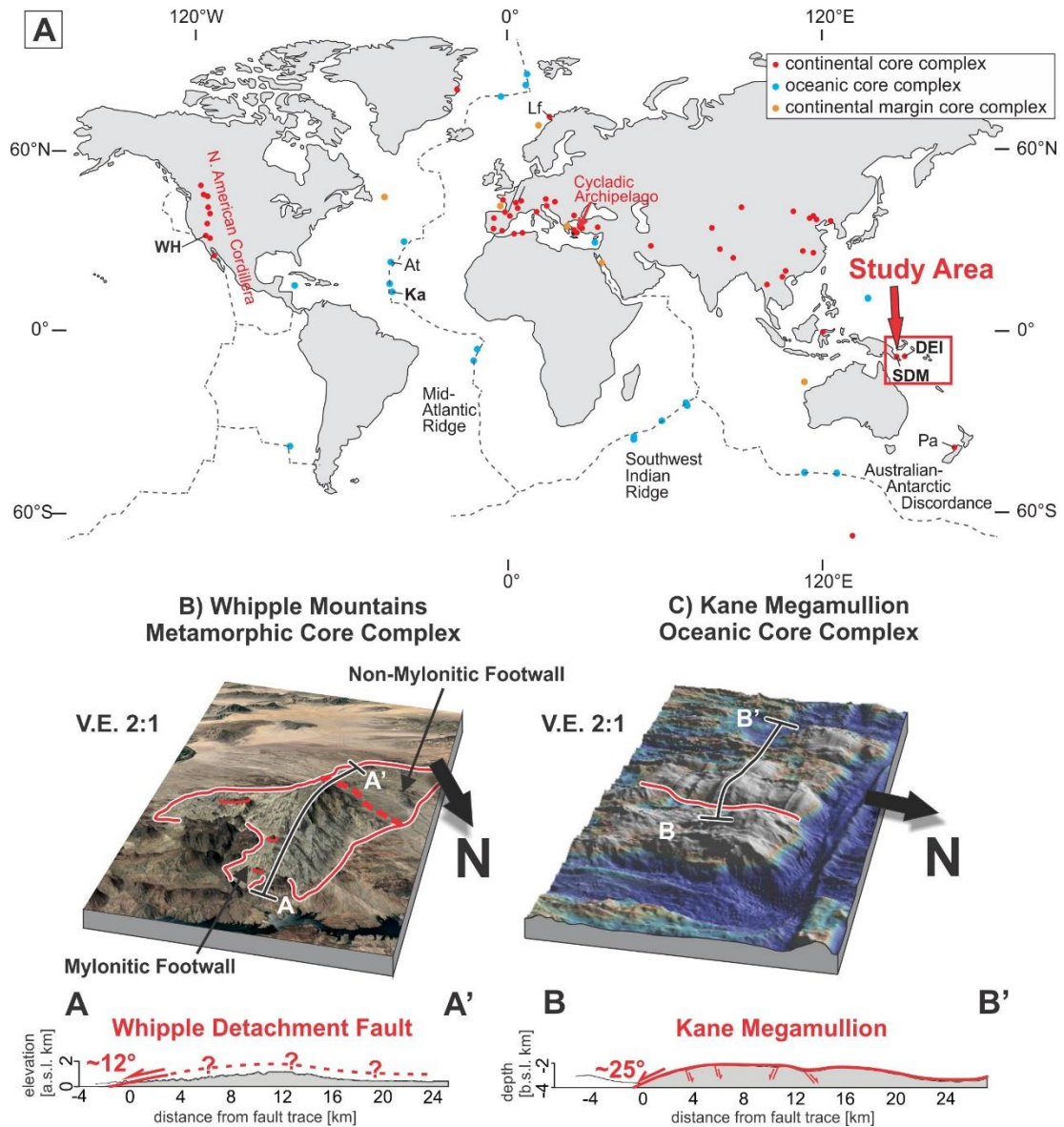


Figure 1.3. A) World map of continental, continental margin and oceanic core complexes (after Whitney et al., 2013). At—Atlantic Massif; DEI—D’Entrecasteaux Islands; Ka—Kane Megamullion; Lf—Lofoten, Norwegian Caledonides; Pa—Paparoa metamorphic core complex, South Island, New Zealand; SDM—Suckling-Dayman Metamorphic Core Complex; WH—Whipple Mountains. B) Google Earth Satellite image of the Whipple Mountains, SE California, showing the oxidized tilted hangingwall rocks and the lighter coloured footwall rocks separated by the Whipple Detachment Fault (e.g., Gans & Gentry, 2016). C) Shipboard multibeam bathymetry image from the GeoMapApp© (www.geomapp.org) of the Kane “Megamullion”, Mid-Atlantic Ridge, illustrating the smooth and slip-parallel corrugated exhumed detachment surface crosscut by high-angle normal faults (e.g., Tucholke et al., 1998).

1.1.2 Models of Low-Angle Normal Fault Evolution

Despite lithological, tectonic and maybe physical differences both continental and oceanic MCCs are similar in geometry and dimension and share similar

fundamental questions concerning the evolution of LANFs (e.g., Whitney et al., 2013). Several models have been proposed to explain the widespread occurrence of gently dipping large-offset normal faults at the surface (e.g., Spencer, 1984; Buck, 1988; Wernicke & Axen, 1988; Gans & Gentry, 2016). The main differences between these models are the initial fault dip angle and whether extension is accommodated by slip on a single deformable fault or by an array of nearly rigid fault blocks. The large width of LANFs is seemingly best explained by slip along a shallow or moderately-dipping single fault (e.g., Spencer, 1984; Buck, 1988; Wernicke & Axen, 1988); however, field observations of some continental MCCs are also compatible with fault rotation caused by sequential activation of “domino”-like normal faults (e.g., Gans & Gentry, 2016).

The above obstacles have recently been overcome in the case of oceanic MCCs. Using paleomagnetic techniques, several studies demonstrate that oceanic detachment faults originally dipped steeply, and that their upper parts back-warped into a shallow-dipping, convex upward shape as a result of tens of kilometres of slip on the fault (e.g., Garcés & Gee, 2007; Zhao & Tominaga, 2009; Morris et al., 2009). This so-called “rolling-hinge” behaviour (**Figure 1.4**) has been suggested for some continental LANFs (e.g., Fletcher & Spelz, 2009; Spencer, 2010), but has been persistently difficult to demonstrate convincingly (Jackson, 1987; Buck, 1988; Scott & Lister, 1992; Axen, 2007; Gans & Gentry, 2016). Part of the uncertainties in continental MCCs arise from the lack of paleohorizontal markers in the footwall, the difficulty in applying paleomagnetic techniques on typical quartzofeldspathic metamorphosed footwall rocks and structural overprinting in ancient MCCs including subsequent fault tilting, erosion and activity of other faults that postdate MCC formation (e.g., Axen & Wernicke, 1991). The exhumed middle to lower crust of some continental MCCs is plastered with hangingwall imbricates bounded by faults on the main detachment surface (**Figure 1.4B1**), whereas many oceanic MCCs exhumate a single, continuous fault surface that is barren of imbricates (**Figure 1.4B2**). Here, I distinguish between two essential models that have been proposed for continental MCC formation—(a) the rolling-hinge model (**Figure 1.4**; e.g., Spencer, 1984; Buck, 1988; Hamilton, 1988; Wernicke & Axen, 1988) and (b) the domino-block rotation model (**Figure 1.5**; e.g., Proffett, 1977; Gans & Miller, 1983; Gans & Gentry, 2016):

“Rolling-hinge” model. This model involves progressive flexural back-tilting during exhumation of an originally moderate to steeply dipping fault that back-warps

into an abandoned, domal structure while remaining active at depth (**Figure 1.4**; Spencer, 1984; Wernicke & Axen, 1988). Isostatic rebound of the tectonically unloaded footwall forms an antiformal hinge that migrates through the footwall in the direction of upper plate tectonic transport. As the footwall passes through the hinge and rotates to shallower dip angles, the uppermost part of the fault becomes progressively abandoned (Spencer, 1984; Axen & Bartley, 1997). Surficial parts of the fault may be abandoned when the hangingwall is cross-cut by a new, steeply dipping fault that merges downdip into the deeper, still active part of the original fault. This process can result in the capture of a so-called rider block of original hangingwall rocks into the footwall (**Figure 1.4B1**; e.g., Reston & Ranero, 2011; Webber, 2017). The Kane “megamullion” is an oceanic MCC where a rolling hinge has been demonstrated (**Figure 1.3C**). Secondary high-angle faults cross-cutting the fault surface in the footwall of these oceanic “megamullion” structures have been attributed to flexure of a single beam due to footwall rollover (**Figure 1.4B2**; Tucholke et al., 1998 and 2008; Karson et al., 2006; Schouten et al., 2010; Hayman et al., 2011).

“Rolling-hinge” model:

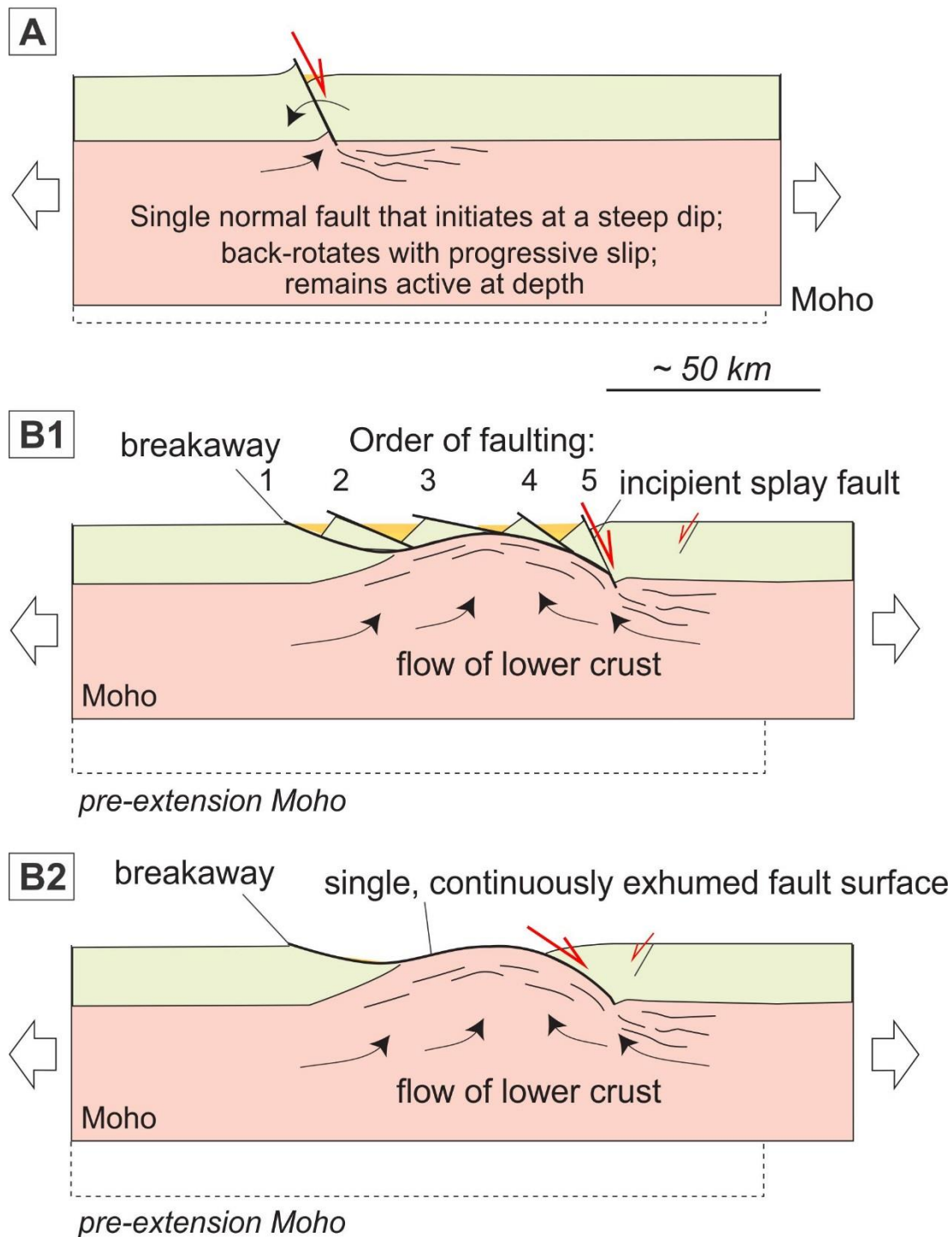


Figure 1.4. Rolling-hinge model for metamorphic core complex formation. A) Single normal fault initiates at a moderate to steep dip rooting into the middle to lower crust and back-rotates with progressive slip, while remaining active at depth. B1) Sequential splay faulting in the upper plate causes rider block formation. Rider blocks might be sequentially tilted and abandoned with progressive slip. B2) The detachment fault exhumes a single continuous fault plane without any upper-plate rider block formation.

“Domino-block rotation” model. This model involves slip on an array of high-angle normal faults that systematically rotate to shallower dip angles with progressive extension, and which may ultimately allow a particular “domino” fault to acquire a larger offset (**Figure 1.5**; Proffett, 1977; Miller et al., 1983; Wong & Gans, 2008). At very low dip angles ($<30^\circ$) the normal faults become less viable for slip as the resolved shear stress is diminished (Collettini & Sibson, 2001), leading to them being cross-cut by a younger set of better oriented, high-angle normal faults (Proffett, 1977; Miller et al., 1983). An apparent large-displacement detachment fault evolving by this model may in fact be a composite surface, comprising multiple generations of faults which were active at different times (cf. the Whipple Detachment Fault, **Figure 1.3B**; see Gans & Gentry, 2016).

“Domino-block rotation” model:

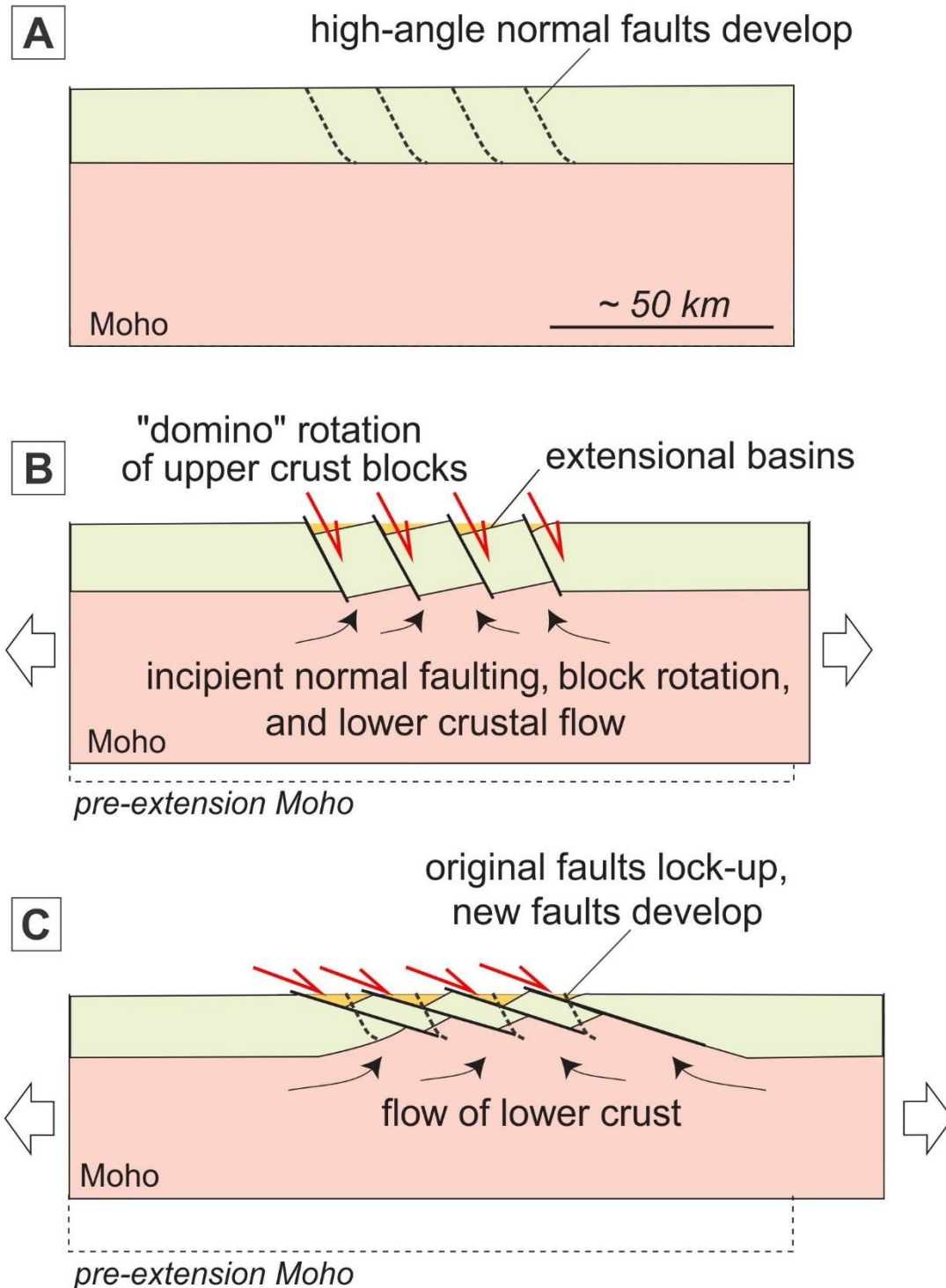


Figure 1.5. Domino-block rotation model for metamorphic core complex formation. A) Prior to extension. Dashed lines indicate an array of initially moderate to steep normal faults that will develop during extension in this model. B) Rigid-body rotation of normal faults and fault blocks to gentle dips with progressive slip in a “domino” or “bookshelf” style. C) At shallow dip angles, the original faults will lock up and may be cross-cut by younger high-angle normal faults that themselves tilt to shallower dips.

Bartley et al., (1990) emphasizes that footwall deformation accommodating internal bending of a continuously active large-slip fault is essential to demonstrate a rolling-hinge evolution; however, depending on its magnitude, such warping deformation may also contribute to the geometric evolution of a composite surface that is largely the result of a “domino” process (Gans & Gentry, 2016). So telling these cases apart—which are not mutually exclusive—is non-trivial. Despite some geometrical similarities, the main processes forming them are quite different. **Table 1.1** summarizes key structural and geomorphic features that are diagnostic of the rolling-hinge or domino-block rotation process. The Mai’iu fault in SE Papua New Guinea has been described as the clearest continental example of a detachment fault that might undergo a rolling-hinge style deformation (Spencer, 2010). The well-exposed and well-preserved detachment surface of the Mai’iu fault (**Figure 1.2**) is ideal to delineate near surface deformation patterns of tectonic activity using structural and geomorphic features that are diagnostic of a fault that potentially has evolved through the rolling-hinge process (e.g., Spencer, 2010; Daczko et al., 2011).

Table 1.1. List of key structural and geomorphic features that are diagnostic of the rolling-hinge or domino-block rotation process sorted by priority (1 – highest; 5 – lowest).

#	Structural and Geomorphic Features	"Rolling-hinge" style rotation		"Domino-block" style rotation	
1	Single fault surface vs. multiple normal faults	Single, continuously exhumed fault surface	The rolling-hinge mechanism involves continued slip on a single, large offset fault, with tilting of the shallower part of the fault to lower dips achieved by isostatic rebound and flexure of its unloaded footwall.	Multiple, crosscutting normal faults	Crustal-scale domino-style block rotation involves multiple normal faults that tilt synchronously to shallower dip angles accommodating the extensional offset. At very low dip angles (<30°), the normal faults become less viable for slip, leading to them being cross-cut by a younger set of high-angle normal faults.
2	Tilting patterns of structural markers	Continuously back-tilted and warped markers in footwall	Flexure of the footwall of a once steeply dipping fault surface may be recorded by gradual warping and back-rotation of structural markers (e.g., paleomagnetic vectors) attached to the footwall of the fault.	Synchronously back-tilted markers within the domino-style fault array	Domino-style rotation of fault blocks may be recorded by synchronous tilting of structural markers together with normal faults showing a systematic pattern within the domino-style fault array.
3	Strain histories of footwall rocks	Late-stage slip-parallel footwall contraction	Because of the unbending strains in the outer arc of a once steeper but now unflexed beam, contractional structures accommodating shortening might be expected in the abandoned, surficial part of the exhumed fault subparallel to the regional extension direction.	Slip-parallel footwall extension	Footwall deformation within the crustal fault blocks is purely extensional; however, tilted blocks may not record internal deformation.
4	Footwall flexure vs. rigid-body rotation	Flexure of the footwall and fault surface.	If fault rotation is achieved by gradual warping of the footwall, then the footwall may behave as a flexed elastic beam that partially fails in response to bending stresses. Inelastic bending might be accommodated by secondary high-angle faults that are largely irrotational as documented in several oceanic core complexes and rarely in continental MCCs.	Domino-like nearly rigid back-tilting of a set of faults	Fault back-tilting is achieved by synchronous slip on a set of rotational normal faults. Faults and fault-blocks rotate simultaneously about an axis parallel to the strike of the faults. A particular "domino" fault may acquire a larger offset. Depending on its magnitude, warping deformation (or rolling-hinge style deformation) may also contribute to the geometric evolution of this particular fault and is therefore less of a diagnostic criterion.
5	Fault geometries	Convex up fault geometry	Starting from moderate to steep dips, continuous uplift and warping of a single fault leads to a convex up shape of the fault surface. For an active fault, the continuation of the fault as a moderate or steeply dipping structure downdip in the subsurface might, in theory, be resolved by seismicity.	Multiple, convex-down fault geometries	Domino-block normal faults sole listrically in the middle crust leading to convex-down fault geometries. The array of faults is cross-cut by younger high-angle normal faults that themselves tilt to shallower dips. The final geometry might be a composite detachment fault that is similar in shape to a fault that evolves by the rolling-hinge mechanism.

1.1.3 Slip-parallel Fault Surface Corrugations

Besides the first order domal form of MCCs, exhumed detachment surfaces are typically corrugated at the several meter to kilometre wavelength. Slip-parallel corrugations form antiformal and synformal grooves that have amplitudes of tens of hundreds of meters (e.g., Whitney et al., 2013; Singleton, 2013; Parnell-Turner et al., 2018). These structural features are conspicuous in many oceanic MCCs where they are called “megamullions” (e.g., Tucholke et al., 1998). Because of their cusplate or scalloped geometries, corrugations have been interpreted to represent an initially cusplate-shaped fault (Jackson & White, 1989; Wong & Gans, 2008) or a segmented normal fault that became linked (Ferrill et al., 1999; Duebendorfer et al., 2010). Other authors suggest that corrugations are primary detachment fault grooves that were influenced by pre-existing foliation structures or have formed by continuous casting of a plastically deforming footwall under the corrugated basement of the rigid hangingwall during exhumation (John, 1987; Davis & Lister, 1988; Spencer, 1999). Corrugations and megacorrugations have also been described as secondary folds produced by extension-perpendicular shortening during exhumation of the footwall (e.g., Yin, 1991; Fletcher & Bartley, 1994; Chauvet & Séranne, 1994; Mancktelow & Pavlis, 1994; Holm et al., 1994; Oldow et al., 2009). The exact mechanisms and timing by which corrugations are formed are not well-understood; however, it has been suggested that they may be at least partially inherited (original features of a sinuous or segmented fault) and that during continuing slip they grow or amplify as folds (e.g., Seiler et al., 2010; Singleton, 2013). In this thesis, understanding the origin of the corrugated morphology of the Mai’iu fault is not a chief target of study.

1.1.4 Mechanisms of Brittle and Ductile Deformation in Extensional Tectonic Settings

Fast slip of detachment faults in both oceanic and continental settings allows the preservation of early formed microstructures in the rapidly exhumed footwall rocks. These potentially provide an archive of past physical conditions and deformation mechanisms along the fault in the subsurface (Behr & Platt, 2011; Smith et al., 2011b; Platt et al., 2015; Cooper et al., 2017). The progressive upward localisation of slip in the fault rock sequence means that older, more deeply deformed fault rocks are carried upward passively with the footwall, thus preserving them from later overprints. This

situation archives originally deeper parts of the fault zone in the lower part of the fault rock sequence (e.g., mylonites); and originally shallower parts of it in the upper part (e.g., gouges). An incremental, ductile-to-brittle deformation sequence (though not necessarily a complete one) can thus be reconstructed by evaluating each fault rock unit separately. Exhumation of the footwall from the middle crust through the BDT and upward to the surface may preserve a sequence of fault zone microstructures that provide information about the changing mechanics of fault-slip as a function of depth (Gueydan et al., 2005; Behr & Platt, 2011, 2013; Platt et al., 2015). Previous studies of continental and oceanic MCCs and their detachment fault zones describe a zone of anastomosing faults, most commonly 1- to 200 m thick, that contain mylonites, cataclasites and gouges that were formed diachronously as part of a down-temperature, ductile-to-brittle progression (**Figure 1.6**; e.g., Smith et al., 2011b; John & Cheadle, 2010). In general, fault rock formation in MCCs can be divided into the brittle regime, BDT and ductile regime that are explained below.

A ductile shear zone may be characterised, at the simplest level, by one of two dominant modes: grain-size insensitive (GSI) and grain-size sensitive creep (GSS; Mehl & Hirth, 2008; Behr & Platt, 2011, 2013; Platt et al., 2015; Miranda et al., 2016). These creep mechanisms are more commonly discussed using the terms dislocation creep and diffusion creep (including grain-boundary sliding mechanisms), respectively. The former deformation mechanism typically results in formation of a crystallographic preferred orientation (CPO), where crystals deform internally and also rotate in response to deformation (e.g., Wenk, 1985). Introduction and propagation of dislocations (i.e., line defects) through the crystal lattice under an applied differential stress causes grain deformation (e.g., Passchier & Trouw, 2005). The accumulation of dislocations is a driving force for grain-boundary production and grain-size reduction by dynamic recrystallization (e.g., Urai et al., 1986; Stipp et al., 2002). In grain-boundary diffusion creep (Coble creep), atoms are removed from grain boundary segments that face a direction of high normal stress, and diffuse towards adjacent segments facing directions of lower normal stress (e.g., Poirier, 1985; Knipe, 1989). The deformation is grain-size sensitive because finer-grains require a shorter diffusion path (e.g., Herwegh et al., 2011 and references therein). This is accomplished by movement of vacancies in a crystal lattice towards high stress regions and the movement of atoms towards low stress regions resulting in net diffusive mass transfer

of atoms to cause a change in shape of the grain (e.g., Passchier & Trouw, 2005). The rate of grain-boundary diffusive mass transfer is increased by the presence of an intergranular pore fluid (e.g., Rutter & Mainprice, 1979). The fluid acts as a medium into which material is dissolved at high stress regions, within which it is transported along the grain-boundary film by diffusion, and from which it precipitates at the adjacent low-stress deposition site—a composite process known as dissolution-precipitation creep (e.g., Rutter & Mainprice, 1979; Rutter, 1983). Another deformational process, Grain-Boundary Sliding (GBS) accommodates deformation through inter-particle displacements along grain boundaries, and does not involve intracrystalline plastic deformation (e.g., Karato, 2012). GBS usually leads to space opening up along grain boundaries, or to grain overlaps or impingements (Raj & Ashby, 1971). These misfits may be accommodated through removal of local asperities by dissolution-precipitation creep, or by some other deformational process. Dissolution-precipitation creep and/or GBS creep typically do not create a CPO (Jiasheng et al., 1994; Jiang et al., 2000; Lapworth et al., 2002).

In most MCCs where the detachment fault cuts quartzofeldspathic rocks exhumed from the middle crust, the mylonite deformation is chiefly accommodated by recrystallization-assisted dislocation creep (Hirth et al., 2001; Stipp et al., 2002) in rocks that are quartz-rich (Behr & Platt, 2011 and 2013). Extreme grain-size reduction by dynamic recrystallization takes place close to the BDT, where the deformation is most localized (e.g., in a thin zone of ultramylonites), and where the strain-rate and differential stress are highest. Because of the extreme grain-size reduction in this region, there may be an upward switching from dislocation creep to GSS deformation mechanisms (grain-boundary sliding and diffusion creep). Near the BDT, deformation may be localized into a network of cm-to-m thick shear zones, and may switch between brittle- and ductile processes during the seismic cycle (e.g., Platt et al., 2015; Cooper et al., 2017). These narrow shear zones may experience strain rates as high as $\sim 10^{-11} \text{ s}^{-1}$ (e.g., Platt et al., 2015 and references therein). By comparison, rheologic studies of mafic composition (gabbroic) mylonites from oceanic detachment faults document dislocation creep and grain boundary sliding accommodated diffusion creep in pyroxene and plagioclase at $\sim 900\text{--}850^\circ\text{C}$ and $\sim 750\text{--}670^\circ\text{C}$ at strain rates of 10^{-12} to 10^{-11} s^{-1} (Miranda, 2006; Mehl & Hirth, 2008; Miranda et al., 2016). At lower temperatures and shallower domains, fault rocks from oceanic detachment faults

usually undergo extensive hydration reactions resulting in foliated cataclasites (Schroeder & John 2004; Boschi et al., 2006; Dick et al., 2008; McCaig et al., 2010).

Frictional sliding and microfracturing in the brittle regime lead to the formation of fault gouge, cataclasites, breccia and pseudotachylites. The brittle fault rocks are commonly localized in a zone of <1 to ~10 m thickness. Fault rocks that form near and above the BDT in MCCs commonly include (micro)breccia and (ultra-)cataclasites (e.g., Smith et al., 2011b; Platt et al., 2015; Cooper et al., 2017). Continental detachment faults that deform quartzofeldspathic protoliths in their footwall are commonly underlain by a tabular zone, 1–10 m thick, of coherent cataclasites composed of milled-down wallrock fragments or clasts, such as quartz, plagioclase and K-feldspar, that are cemented by retrograde chlorite, epidote, albite, actinolite, clinozoisite, sericite, and/or calcite (Davis et al., 1980; Reynolds & Lister, 1987; Lister & Davis, 1989; John & Cheadle, 2010 and references therein). Dissolution and precipitation processes within the cataclasites and/or the breakdown of feldspar may lead to a passive concentration of phyllosilicates in fault-parallel seams, which may weaken the fault (Bos & Spiers, 2002; Collettini & Holdsworth, 2004). It has been suggested that these rocks typically have a friction coefficient of $\mu \approx 0.4$ allowing slip on normal faults at dips as shallow as 30° (Platt et al., 2015 and references therein). In oceanic cataclasites, the ultramafic wallrocks undergo extensive hydration reactions at temperature <500°C forming new actinolite-tremolite, chlorite and/or serpentine with remnant clasts of feldspar, olivine and clinopyroxene (e.g., Schroeder & John, 2004; Boschi et al., 2006; Dick et al., 2008; McCaig et al., 2010). Serpentinites are common in ultramafic shear zones, wherein serpentine, tremolite and magnetite have replaced olivine and pyroxene (e.g., Hirose & Hayman, 2008).

In cases of seismogenic slip, pseudotachylites may form as a result of frictionally induced melting (e.g., Di Toro et al., 2005; Prante et al., 2014), and these have been recognized as veins cutting the cataclastic fault rocks of several MCCs (e.g., John, 1987; Davis & Lister, 1988; Goodwin, 1999; John & Cheadle, 2010; Prante et al., 2014). Pseudotachylite veins are commonly retrogressed and/or broken-up by cataclastic deformation on the way to the Earth's surface and may not be preserved or easily recognizable (e.g., Kirkpatrick & Rowe, 2013). Fault gouge develops at shallow depth (low pressures and low temperatures, <200°C) as a product of cataclasis and may be rich in authigenic (newly formed) clay minerals such as montmorillonite,

saponite and talc reducing the coefficient of friction $\mu < 0.2$ (Collettini et al., 2009b; Holdsworth et al., 2011). These frictional weak fault gouges produce a profound rheological contrast to the clay-free wallrocks and, as they are velocity-strengthening, may promote aseismic slip on LANFs with dips $< 20^\circ$ (e.g., John & Cheadle, 2010; Platt et al., 2015); however, most weak clay minerals become unstable with depth and higher temperatures (Haines & van der Pluijm, 2012).

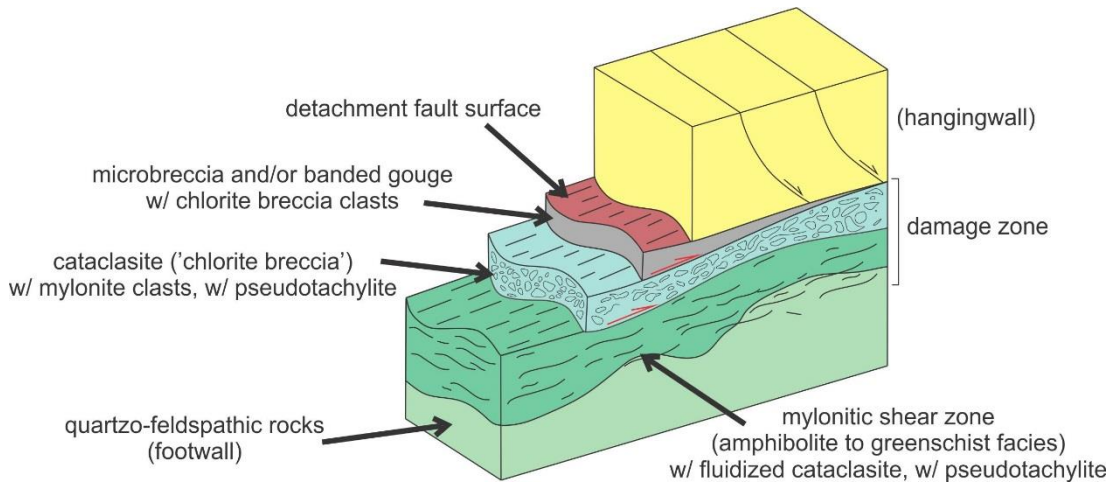


Figure 1.6. Schematic section of continental detachment faults cutting isotropic quartzofeldspathic basement (after John & Cheadle, 2010). Strain localization in the anastomosing low-angle normal faults/shear zones is indicated by overprinting relations. Hydrothermal alteration may occur in the footwall within the damage zone.

Rapid slip on the active Mai'iu low-angle fault has exhumed a layer of fault rocks that are locally fully exposed in outcrop. They constitute an archive of ductile to brittle fault rocks that formed as the footwall cooled, and the fault zone evolved, between the middle crust ($\sim 400^\circ\text{C}$) and the Earth's surface. Microstructures in the fault rocks can be used to document the sequential activity of different deformation mechanisms along a detachment fault that deforms a basaltic protolith, including (I will argue) both earthquake slip and aseismic creep.

1.2 THE RESEARCH PROJECT AND THE STRUCTURE OF THIS THESIS

Located in the remote Owen-Stanley Mountains of SE Papua New Guinea, the active Mai'iu fault has self-exhumed a smooth and corrugated fault surface footwall bounding the Suckling-Dayman Metamorphic Core Complex (SDM; **Figure 1.2**). The

geology of the SDM was mapped in reconnaissance in the late 1960s and early 1970s (e.g., Davies & Smith, 1971; Smith & Davies, 1976). The geomorphology of the exhumed detachment surface of the Mai'iu fault has been studied remotely using aerial photography (Ollier & Pain, 1980) and more recently Shuttle Radar Topography Mission (SRTM) data gridded at 90 m (Caffi, 2008; Spencer, 2010; Daczko et al., 2011). A petrological study of the mafic mylonites exhumed in the footwall of the Mai'iu fault near sea-level was undertaken by Daczko et al. (2009). Mantled in rainforest, the majority of the SDM is inaccessible except by foot and has not been the target of field studies since the early reconnaissance work was done with the aid of a helicopter over 50 years ago. As part of a Marsden Project, a team of researchers from New Zealand and overseas carried out field work on the SDM during 2014–2016 and 2018 in order to tackle longstanding questions on the mechanics of low-angle normal faults based on direct examination of an active, “natural laboratory” example. My Ph. D. thesis field work was undertaken during the field campaigns of 2015 and 2016, when I focused on collecting structural data on the Mai'iu fault and collecting oriented samples of the exposed fault rocks for subsequent laboratory and microstructural analysis.

In my thesis, I address several questions concerning the evolution and mechanics of LANFs. Each of the three main chapters of this thesis are devoted to one of these questions:

- (1) "How do continental detachment faults achieve low dips at the Earth's surface: do they originate as low-angle normal faults, or does the footwall of an originally steeper fault deform in response to a ‘rolling-hinge’ unloading process?” (Chapter 2);
- (2) "What micro-scale deformation mechanisms accommodate slip on LANFs in a metabasaltic protolith, and how do they vary with depth; are low-angle normal faults prone to aseismic creep, or earthquakes, or both?" (Chapter 3);
- (3) "What stresses (principal stress orientations, differential stresses, stress ratios) drive slip on an active LANF, and how do they vary with depth?" (Chapter 4).

Targeting the Mai'iu fault, I address these questions using diverse data: structural, geomorphological, microstructural, geochemical and mineralogical. In more detail, than stated above, I aim to:

- Delineate near-surface patterns of translation and tilting affecting the exhumed plane of the now-domal Mai'iu fault using structural field data together with geomorphic data interpreted from GeoSAR-derived digital terrain models (DTMs) and aerial photography in order to infer the style of deformation and morphological evolution of that LANF (Chapter 2).
- Constrain deformation mechanisms and strain rates accommodating slip on the Mai'iu fault at different structural levels by characterizing the exhumed sequence of fault rocks in the field, and by applying a range of microanalytical techniques on the collected fault rocks. Furthermore, identify any processes contributing to weakening (or strengthening) of the fault rocks during their exhumation. Using chlorite-based paleotemperature estimates, assign deformational temperatures to these fault rocks (Chapter 3).
- Estimate differential stresses, principal stress orientations, and stress ratios in the above-studied fault rocks, and construct a depth-stress profile for the Mai'iu fault using paleopiezometric and stress inversion techniques, and by converting paleotemperature estimates to depths based on constraints regarding (and modelling of) the crustal temperature structure near the Mai'iu fault (Chapter 4).

The research of our team, including this Ph. D. project, has benefited from collaboration with experts in such fields as: geodynamic modelling (Susan Ellis, GNS Science; James Biemiller, University of Texas at Austin), rock deformation and fault mechanics (Carolyn Boulton, Victoria University of Wellington), and microstructural analysis (Dave Prior, University of Otago). Their particular contributions to my thesis are identified below. A small amount of field data for several sites that we did not visit during our own field work was derived from the unpublished field notebooks by Ian Smith and Hugh Davies from their work in the 60s and 70s, and Nathan Daczko and Peter Caffi in 2008 and 2009. These researchers not only provided their field books,

but also aerial photographs, rock samples and advice regarding their structural data and field observations.

1.2.1 Thesis Format

This thesis consists of five chapters, three appendices and a CD-Rom with additional digital supplementary data (or available online from the ResearchArchive of the Victoria University of Wellington). The first and last chapters are the Introduction and Conclusions of this Ph. D. thesis, respectively. Chapters 2, 3 and 4 were designed as stand-alone journal articles, and were written in a manuscript format. For this reason, there is some unavoidable repetition between them, in particular in their “Introduction” and “Tectonic Setting” sections; however, for brevity I have sequestered all the bibliographical references cited in this thesis into a single reference section that is placed at the end of this thesis (after the Appendices). All work presented herein was conducted by myself unless otherwise specified, below.

Chapter 1: Introduction

The chapter introduces the paradox of low-angle normal faults, outlines previous work on basic fault mechanics and metamorphic core complexes, lists the main questions and objectives of this thesis, and its structure, and summarises the tectonic setting of the Mai’iu fault in the Woodlark Rift of SE Papua New Guinea. Finally, it provides with a summary of the analytical methods used in this thesis, and identifies the specific contributions of collaborators who are listed as co-authors on the several intended manuscripts (Chapters 2, 3, and 4).

Chapter 2: Structural and Geomorphic Evidence for Rolling-Hinge Style Deformation of an Active Continental Low-Angle Normal Fault, SE Papua New Guinea

This chapter addresses the question, “*How do continental detachment faults achieve low dips at the Earth's surface: do they originate as low-angle normal faults, or does the footwall of an originally steeper fault deform in response to a ‘rolling-hinge’ unloading process?*” Structural field data together with geomorphic data interpreted from GeoSAR-derived digital terrain models and aerial photography are combined to interpret the evolution of the Mai’iu fault and to argue that it is a well-constrained example of a rolling-hinge type low-angle normal fault. I present a detailed three-dimensional fault surface model of the Mai’iu fault that is studied to delineate fault

surface information such as changes in its curvature and aspect (dip-direction dip), scales of corrugation, and fractal dimension of roughness. Structural field-based and geomorphic observations are compared with predictions of a finite element thermomechanical model to highlight first-order geodynamic processes involved in the evolution of finite dip-slip on a single normal fault to magnitudes of up to several tens of kilometres. The manuscript was peer-reviewed by Jon Spencer and Gary Axen and has been published in the AGU journal “Tectonics” (Mizera et al., 2019). Material from this study is also partially published in two other manuscripts I co-authored (Little et al., 2019; Biemiller et al., 2019). The co-authors of this paper are Tim Little, James Biemiller, Susan Ellis, Sam Webber, and Kevin Norton. As first author, I participated in the fieldwork, undertook the geomorphic and structural analyses, and am responsible for all the interpretations that are presented. I drafted all the figures and wrote the first (and all later) drafts of the paper, while receiving editorial feedback from my co-authors, especially my supervisors Tim Little and Kevin Norton. Thermomechanical modelling was contributed by Susan Ellis and James Biemiller. Sam Webber provided additional field data of the Gwoira rider block and a three-dimensional model of the inactive Mai’iu fault.

Chapter 3: Slow-to-Fast Slip Deformation of Mafic Rocks on an Actively Exhuming Low-Angle Normal Fault, Woodlark Rift, SE Papua New Guinea

This chapter addresses the question: “*What micro-scale deformation mechanisms accommodate slip on LANFs in a metabasaltic protolith, and how do they vary with depth; are low-angle normal faults prone to aseismic creep, or earthquakes, or both?*”

The composition, texture, and microstructure, of exhumed rocks along the Mai’iu fault (mylonites, cataclasites, ultracataclasites and gouges) are analysed in detail to interpret the progression of deformation mechanisms that have accommodate slip on this fault at different structural levels. For microscopic and textural analyses of the fault rocks, I mainly used a field emission gun scanning electron microscope (FEG-SEM) equipped with energy dispersive spectroscopy (EDS) and electron backscatter diffraction (EBSD) detectors, and a cold-cathode cathodoluminescence (CL) microscope—all housed at the University of Otago under the guidance of David Prior. Compositional data on chlorite and albite were acquired with an electron probe microanalyser (EPMA) at the Victoria University of Wellington. Some physiochemical (mineral and chemical compositional) analyses of the fault rocks were

analysed by X-Ray fluorescence (XRF) under contract to the analytical facility at the University of Waikato. X-Ray Diffraction (XRD) analysis of fine-grained mineral phases present in selected fault rocks was undertaken under contract at the Centre for Australian Forensic Soil Science in Urrbrae, South Australia. Temperature-dependent magnetic susceptibility experiments on an ultracataclasite sample are provided by Emma Watson (M. Sc. student) at the Victoria University of Wellington. Transmission electron microscopy (TEM) analysis on a “mirror”-like surface of a fault-truncated cobble is provided by Joseph White at the University of New Brunswick.

Chapter 4: Strength and Stress Evolution of an Actively Exhuming Low-Angle Normal Fault, Woodlark Rift, SE Papua New Guinea

Chapter 4 addresses the question, *"What stresses (principal stress orientations, differential stresses, stress ratios) drive slip on an active LANF, and how do they vary with depth?"* The exhumed fault rocks of the Mai'iu fault are cross-cut by multiple generations of calcite veins and late brittle faults. By sampling the incrementally deformed sequence of fault rocks at the surface, and applying paleopiezometric and geothermometric methods to them, I attempt to reconstruct the stress-temperature distribution on the Mai'iu fault. By reference to an inferred temperature-depth profile for the fault constructed from geological constraints and geodynamical modelling by Biemiller et al. (2019), these data are reformulated into a stress-depth profile to which the fault rocks were subject during the history of their exhumation. Calcite veins and brittle faults that cross-cut these fault rocks are used in this chapter to reconstruct differential stresses and principal stress orientations. The stress–depth profile along the Mai'iu fault is used to determine the peak strength of this fault and integrated strength of the brittle crust in this region during extension.

Chapter 5: Conclusion—A Synthesis of Detachment Fault Evolution

Chapters 2, 3 and 4 contain their own “Discussion” and “Conclusion” sections. This final chapter presents a summary of the results and a synthesis of the data obtained. Finally, I give an overview of the research on the Mai'iu fault I have started but was beyond the scope of this thesis and give recommendations for future work.

Appendix A—Structural and Geomorphic data of Chapter 2

This appendix supports Chapter 2. It contains further explanations and descriptions regarding stream channel and fault surface modelling, fault-surface roughness

analyses together with a Python code to calculate the fourier transformation of topographic profiles, unpublished structural data from previous workers, surface information of tilted fluvial terraces, equations by Buck (1997) used to assess the mechanisms accommodating flexural failure of a footwall beam of stated dimensions and properties, and a description of numerical methods and model setups used for the thermomechanical modelling. Parts of the latter description were written by James Biemiller and Susan Ellis, as edited (with their permission) by myself.

Appendix B—Compositional and Microstructural Data on Mafic Fault Rocks Exhumed by the Mai'iu Fault (Chapter 3)

This appendix contains compositional and microstructural data on metabasaltic fault rocks that support Chapter 3. The data was acquired by several analytical techniques, including: (1) FEG-SEM equipped with EDS and EBSD detectors; (2) temperature-dependent magnetic susceptibility experiments; (3) Raman spectroscopy analysis; (3) TEM; (4) XRF; (5) XRD; and (6) EPMA. The appendix contains a collection of photomicrographs, element and phase maps, compositional data on the mafic fault rocks, grain size statistics, and pole figures of the main mineral assemblage in the fault rocks.

Appendix C—Paleostress Dataset

This appendix contains the dataset for the paleostress analysis (Chapter 4) including tables of calculated differential stresses from calcite veins and the estimations of paleo-principal stress orientations. I also provide equations and explanation to calculate brittle failure curves presented in strength-depth profiles in Chapter 4.

Digital Appendix

The Digital Appendix (CD-Rom or ResearchArchive by the Victoria University of Wellington) contains: (1) a digital version of this thesis ('Mizera_thesis.pdf'); (2) calcite orientation data from the analysed fault rocks ('Calcite Paleopiezometry' → 'Calcite E-Twin Analysis'); (3) a MATLAB code by Euan Smith (Victoria University of Wellington) to calculate slip plane (e-plane) and glide direction from calcite host-twin pairs and to transform EBSD acquired orientation data from a sample reference frame into a geographic system ('Calcite Paleopiezometry' → 'Euler Conversion'); (4) relict and recrystallized grain size maps of calcite veins together with grain-size statistics ('Calcite Paleopiezometry' → 'Calcite Grain-Size Piezometer'); (5) EPMA

data on albite and chlorite ('EPMA Data'); (6) exported reports (from Oxford Aztec software) from all EDS and EBSD analysis presented in this thesis ('FEG-SEM EDS EBSD'); (7) An excel spreadsheet to calculate the grind limit for particles ('Grind Limit for Particles'); (8) all structural field and sample data with locations collected during the field campaigns in 2014, 2015, and 2016 ('Mai'iu Fault Structural Data and Samples'); and (9) MTEX scripts used for the EBSD data processing ('MTEx').

1.2.2 Contributors

Tim Little, Victoria University of Wellington: Primary advisor, structural data and sample collection during field campaigns in 2014, 2015 and 2016, general guidance, discussion of results and manuscript review.

Kevin Norton, Victoria University of Wellington: Secondary advisor, geomorphic data collection, assistance with ArcGIS techniques, discussion of results, guidance and manuscript review.

David J. Prior, University of Otago: Assistance with SEM techniques, discussion of results and guidance.

Carolyn Boulton, Victoria University of Wellington: Help with analysis and interpretation of fault rocks, and interpretation of XRD-data, and discussion of results and manuscript review of Chapter 3.

James Biemiller, University of Texas, Austin: Together with Susan Ellis, undertook the thermomechanical models that are referenced in Chapters 2 and 4, and contributed manuscript review of Chapter 2.

Susan Ellis, GNS Science: Co-developer of the SULEC finite element package that was used in above-mentioned thermomechanical modelling with which she assisted James Biemiller. She also helped the team with structural data collection in the field, and with manuscript review of Chapter 2.

Euan Smith, Victoria University of Wellington: Provided a MATLAB code for Chapter 4 to: a) convert EBSD acquired crystallographic orientation data from Euler angles into a sample reference frame (after Britton et al., 2016); b) calculate for every calcite host-twin pair the orientation of the twin plane and glide direction (required for stress inversion techniques); and c) convert the crystallographic orientation data from a sample reference frame into geographic coordinates.

Emma Watson, Victoria University of Wellington: Conducted a temperature dependent magnetic susceptibility test on an ultracataclasite sample shown in Chapter 3.

Joseph White, University of New Brunswick: Undertook TEM analysis of a "mirror"-like, fault-truncated surface of a cobble in the hangingwall of the Mai'iu fault presented in Chapter 3, Figure 3.10D-J.

Norio Shigematsu, National Institute of Advanced Industrial Science and Technology, Tsukuba, Japan: Provided photomicrographs of faceted cobble in Chapter 3, Figure 3.10A-C.

1.2.3 Related Publications

Mizera, M., Little, T. A., Biemiller, J., Ellis, S., Webber, S., & Norton, K. P. (2019). *Structural and Geomorphic Evidence for Rolling-Hinge Style Deformation of an Active Continental Low-Angle Normal Fault, SE Papua New Guinea*. Tectonics.

Biemiller, J., Ellis, S., **Mizera, M.,** Little, T., Wallace, L., & Lavier, L. (2019). *Tectonic inheritance following failed continental subduction: a model for core complex formation in cold, strong lithosphere*. Tectonics.

Little, L., Webber, S., **Mizera, M.,** Boulton, C., Oesterle, J., Ellis, S., Boles, A., van der Pluijm, B., Norton, K., Seward, D., Biemiller, J. & Wallace, L. (2019): *Evolution of a rapidly slipping, active low-angle normal fault, Suckling-Dayman Metamorphic Core Complex, SE Papua New Guinea*. Geological Society of America Bulletin.

1.2.4 Manuscripts in preparation

Mizera, M., Little, T. A., Boulton, C., Prior, D., White, J., Watson, E. & Shigematsu, N (in prep). *Slow-to-Fast Slip Deformation of Mafic Rocks on an Actively Exhuming Low-Angle Normal Fault, Woodlark Rift, SE Papua New Guinea* (This is based on Chapter 3 of this thesis)

Mizera, M., Little, T. A., Prior, D., Biemiller, J., Smith, E. & Boulton, C. (in prep). *Strength and Stress Evolution of an Actively Exhuming Low-Angle Normal Fault, Woodlark Rift, SE Papua New Guinea* (This is based on Chapter 4 of this thesis)

Mizera, M., Little, T.A., Webber, S., Biemiller, J. & Ellis, S (in prep.). *Continuous Corrugation Growth Accommodates Slip on an Active Low-Angle Normal Fault, Mai'iu Fault, Woodlark Rift, SE Papua New Guinea*.

1.3 THE MAI'IU FAULT—A NATURAL LABORATORY

1.3.1 Tectonic Setting of the Woodlark Rift

SE Papua New Guinea is an active tectonic regime governed by the oblique convergent motion of the Pacific plate (PAC) moving west-southwest at ~100–110 mm/yr relative to the Australian plate (**Figure 1.7**; AUS; Wallace et al., 2004). Interaction between the two plates has driven orogenic events in Papua New Guinea since at least the late Oligocene (Pigram & Symonds, 1993). Tectonics in the intervening collision zone are complicated by a complex array of microplates (South Bismarck, Woodlark-Solomon Sea, North Bismarck and New Guinea highlands microplates) rapidly rotating with respect to one another about nearby poles of rotation (Wallace et al., 2004, 2014 and references therein). The Woodlark-Solomon Sea microplate and the Trobriand block rotate counterclockwise at 2–2.7°/Myr relative to the Australian plate about a nearby Euler pole resulting in a north-south-opening basin with maximum extension to the east (**Figure 1.7**; Wallace et al., 2004; Eilon et al., 2015).

In the eastern Woodlark Basin seafloor spreading has occurred at rates >20–60 mm/yr since ~6 Ma, as indicated by magnetic anomalies there (Taylor et al., 1999). Farther west of this spreading centre, continental rifting (Woodlark Rift) is thought to have initiated by 8.4 Ma, with current extension rates of up to 20 mm/yr (Taylor & Huchon, 2002; Wallace et al., 2014). V_P and V_S velocity models derived from inverted P- and S-wave velocities from depth between 50 and 250 km reveal a low-velocity zone in the mantle parallel to the E-W axis of the Woodlark Rift in accordance with the thinnest crust, high heat flow (~150 mW/m²), and a linear trend of volcanoes (Eilon et al., 2015). This slow velocity region extends 250 km along strike from the spreading ridge merging into a zone of continental rifting (Eilon et al., 2015). The Woodlark Rift is elsewhere characterized by a low geothermal gradient of ~18.2 °C/km (Tjhin, 1976; Martinez et al., 2001) and low heat flow (50–73 mW/m²), which may reflect the very young age of the oceanic Woodlark Basin relative to the thermal time constant of the crust (e.g., Weissel et al., 1982).

Continental Rifting in SE Papua New Guinea is accommodated by slip on a relatively small number of normal faults with some of them bounding the flanks of the exhumed D'Entrecasteaux Islands gneiss domes (**Figure 1.8**; Little et al., 2007, 2011; Fitz & Mann, 2013; Wallace et al., 2014). On the nearby mainland, the Mai'iu fault

bounds the western margin of the Woodlark rift and is a key component of the Owen Stanley Fault Zone (OSFZ) between the Woodlark-Solomon Sea and Australian plates (Smith & Davies, 1976). The active OSFZ separates the Australian plate derived Owen-Stanley metamorphics and ophiolitic rocks in the SW from the Cretaceous-Paleogene ophiolitic and basement rocks of the Woodlark plate as well as their sedimentary and volcanic cover to the NE (Wallace et al., 2014). The OSFZ formed during the obduction of an oceanic and island arc upper plate (the Late-Cretaceous Papuan Ultramafic Belt; PUB) over an oceanic marginal basin and continental margin rocks (Davies, 1978; Webb et al., 2008; Daczko et al., 2011). Previous workers have suggested that the Mai'iu fault may represent an extensionally reactivated part of the OSFZ (Davies, 1978; Webb et al., 2008; Daczko et al., 2011; Little et al., 2019). Today, to the NW of the western tip of the Woodlark Rift, a northern part of the OSFZ slips as a left-lateral strike slip fault, whereas at its far north-western end it is a contractional plate boundary structure, with these changes being controlled by its relative position along strike to the nearby Euler pole (Wallace et al., 2014).

Figure 1.7 (previous page). Plate tectonic setting of the Woodlark Rift and present-day pole of rotation (modified after Fitz & Mann, 2013; Wallace et al., 2014). The tectonic regime in PNG is governed by the oblique convergent motion of the Pacific plate (PAC) moving west-southwest at ~10-11 cm/yr relative to the Australian plate (AUS). The Woodlark-Solomon microplate and the Trobriand Block rotate counter-clockwise relative to AUS about a nearby Euler pole resulting in a north-south-opening basin with maximum extension to the east. To the west most of the continental rifting is accommodated by slip on the Mai'iu fault which bounds the western margin of the Woodlark rift. DEI—D'Entrecasteaux Islands; GB—Goodenough Bay; MS—Moresby Seamount.

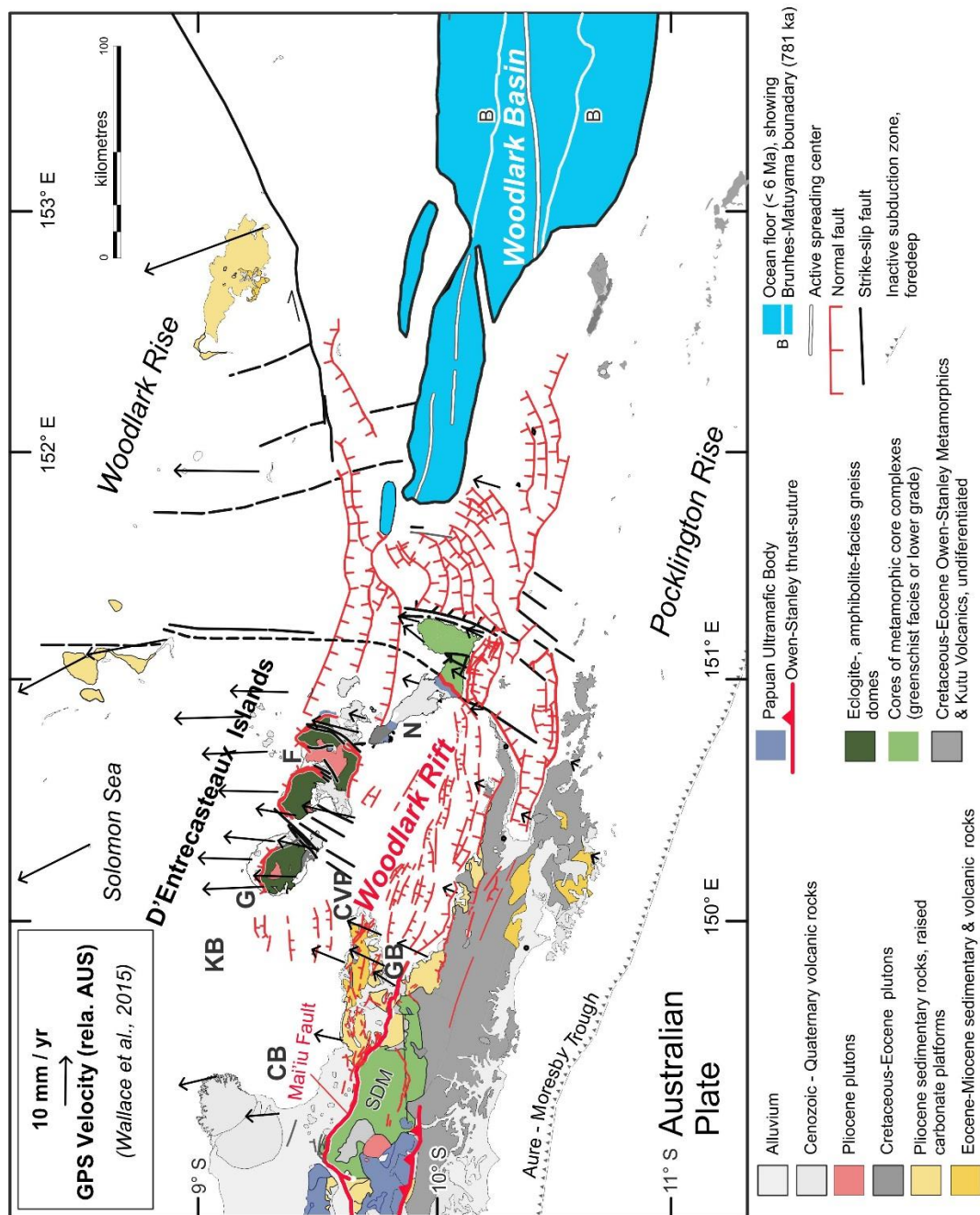


Figure 1.8. Tectonic map of the Woodlark Rift (after Little et al., 2011, 2019, and Abers et al., 2016). CB—Collingwood Bay; CVP—Cape Vogel Peninsula; F—Fergusson Island; G—Goodenough Island; KB—Kiribisi Basin; MS—Moresby Seamount; SDM—Suckling-Dayman Metamorphic Core Complex; WHSFZ— Ward Hunt Strait Fault Zone.

1.3.2 Seismicity in the Woodlark Rift

Seismicity data including microearthquakes and large earthquakes (795 earthquakes, $M_L > 1.5$) collected at the Woodlark Rift from the CDPapua and WOODSEIS regional arrays outline crustal deformation that extends from the oceanic rift axis at 151.7°E westwards (**Figure 1.9**; e.g., Eilon et al., 2015; Abers et al., 2016).

The most active microearthquake zone that also includes the largest ($M > 6$) earthquakes extends west from the oceanic rift tip and north of the Moresby Seamount detachment fault (Taylor & Huchon, 2002) to the north of Fergusson Island (e.g., Abers et al., 2016). Most shallow hypocentres surround the D'Entrecasteaux Islands (Eilon et al., 2015; Abers et al., 2016) following inferred and mapped faults of the Goodenough and Fergusson Islands (Davies & Warren, 1988; Little et al., 2011). The seismicity data indicate ongoing exhumation of these metamorphic core complexes on the southern and northern side of these islands in agreement with campaign GPS data (Wallace et al., 2014). Besides some diffuse hypocentres along the Papuan Peninsula at various crustal depths, intense seismicity occurs between the south-eastern corner of Goodenough Island and Cape Vogel Peninsula at $\sim 149.9^\circ\text{E}$. This seismicity is inferred to be on at least two connected faults. Seismic data to the east of 149.9°E form a swath of microearthquakes crossing the Ward Hunt Strait. Together with a bathymetric high in this strait, the data show evidence for a northeast striking fault zone with an oblique transtensional slip inferred from aftershocks of a $M_W=5.4$ earthquake (Abers et al., 2016). This seismic region is known as the Ward Hunt Strait Fault Zone. The western portion of the earthquakes at 149.9°E lies beneath the Kiribisi Basin (KB in **Figure 1.9**). The hypocentres here define a surface between ~ 12 – 25 km depth that dips gently to the north at ~ 30 – 40° (Eilon et al., 2015; Abers et al., 2016). This alignment of hypocentres projects southward updip to coincide with the surface trace of the Mai'iu fault (inset in **Figure 1.9**). This seismic corridor has been interpreted as the downdip extension of the active fault surface of the Mai'iu fault (Abers et al., 2016; Little et al., 2019). At the surface, the exposed Mai'iu fault surface dips $\sim 21^\circ\text{N}$. Inferred right-lateral slip in the Ward Hunt Strait Fault Zone and NNE movement of the Kiribisi Basin relative to Goodenough Basin are consistent with normal faulting on the Mai'iu fault.

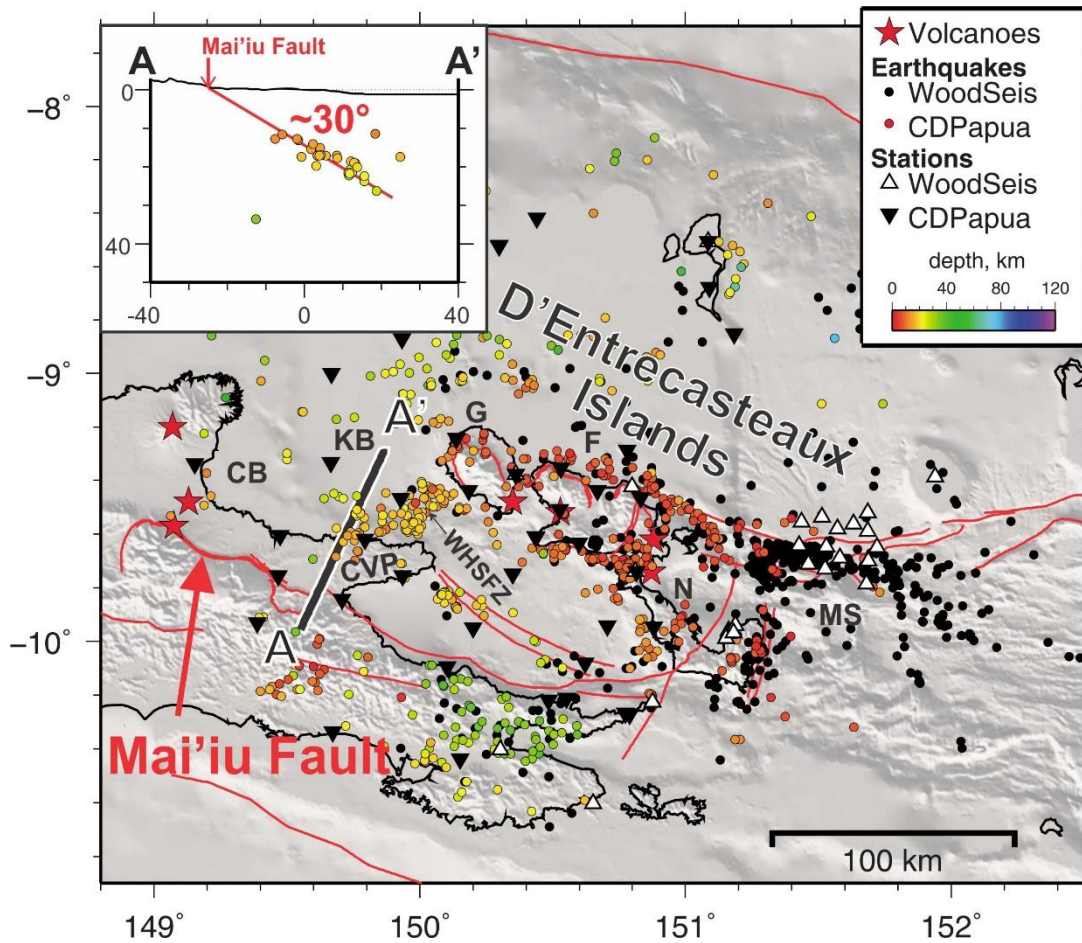


Figure 1.9. Microseismicity map of the Woodlark-D'Entrecasteaux Rift from regional arrays from CDPapua (seismograph stations are indicated by black triangles) and WOODSEIS (stations are indicated by open triangles; modified after Abers et al., 2016). The recorded hypocentres based on CDPapua are colour coded (upper right scalebar). 3-D location uncertainties of plotted events are less than 2.5 km (Eilon et al., 2015). Cross-section A-A' is shown in the upper left inset. Cross-section shows microearthquake foci scattered at ~12–25 km depth (mid to lower crust). These define a deformation zone dipping ~30–40°. This zone is colinear with the surface trace of the Mai'iu fault. Note, lack of observed seismicity at shallow (<15 km) depths. The apparent earthquake gap and low rates of seismic moment release in the Woodlark Rift (Abers, 2001) suggests that the upper part of Mai'iu fault may be creeping aseismically. CB—Collingwood Bay; CVP—Cape Vogel Peninsula; F—Fergusson Island; G—Goodenough Island; KB—Kiribisi Basin; MS—Moresby Seamount; WHSFZ—Ward Hunt Strait Fault Zone.

1.3.3 Dip-slip rate of the Mai'iu fault

The Mai'iu fault takes up almost all of the extension at the western tip of the Woodlark Rift and is arguably the fastest slipping terrestrial normal fault known globally (Webber et al., 2018; Little et al., 2019). Cosmogenic nuclide exposure dating of ^{10}Be in quartz veins on the lowermost 130 m of the bedrock-exhumed fault scarp of

the Mai'iu fault near the central part of its trace indicates a late Holocene dip-slip rate of 11.7 ± 3.5 mm/yr (1σ ; Webber et al., 2018). Geodetic velocities from three years GPS campaign measurements within the Woodlark Rift suggest a present-day N–S horizontal extension of ~ 7 – 9 mm/yr across the centre of the Mai'iu fault (Wallace et al., 2014). Using an observed surface dip of the Mai'iu fault surface of $\sim 21^\circ$ (Little et al., 2019) this corresponds to a geodetically measured dip-slip rate of 7.5 – 9.6 mm/yr assuming that the Mai'iu fault is the only structure that accommodates extension in this area. This dip-slip rate is within the uncertainties of the longer-term dip-slip rate inferred from cosmogenic nuclide-based exposure dating (Webber et al., 2018; Little et al., 2019). The modelled geodetic velocities do not require significant interseismic coupling of the Mai'iu fault, nor were major earthquakes recorded in relation of this fault in the past fifty years, and it is therefore suggested that a large component of slip on the Mai'iu fault may be accommodated by aseismic creep (Wallace et al., 2014; Biemiller et al., 2018). This is currently tested using a dense network of campaign GPS sites (3–4 km station spacing) across the Mai'iu fault (Biemiller et al., 2018).

1.3.4 Suckling-Dayman Metamorphic Core Complex

The Mai'iu fault bounds the Suckling-Dayman Metamorphic Core Complex (SDM), the exhumed lower plate of which includes three antiformal culminations (**Figure 1.10**): Mt Suckling (3,576) to the west; Mt Dayman (2,950) in the center; and Mt Masasoru ($\sim 1,700$ m) in the east. Based on fault surface outcrops the Mai'iu fault dips $\sim 21 \pm 3^\circ$ to the NNE where it emerges from the Holocene alluvial gravel of its hangingwall near sea level (Spencer, 2010) and locally dips as little as ~ 15 – 17° at the surface near its trace (Little et al., 2019). Wear striae preserved on the Mai'iu fault surface trend 009 – 015° (Little et al., 2019). These are subparallel to the velocity of the Trobriand (Solomon Sea) block relative to Australia as derived from elastic block modelling of campaign GPS data by Wallace et al. (2014; **Figure 1.8**), and to the trend of numerous corrugations in the footwall of the SDM (Spencer, 2010; Daczko et al., 2011; Little et al., 2019).

The footwall of the SDM mainly consists of a metamorphosed basalt of >3 – 4 km thickness with minor interbedded phyllitic metasediments, limestone, and chert, known as the Goropu Metabasalt (Smith & Davies, 1976). Planktonic foraminifera in the interlayered pelagic limestones reveal a late Cretaceous age (Smith & Davies, 1976). Chemically, the metabasalt resembles typical mid-ocean ridge basalt (MORB;

Smith & Davies, 1976; Davies, 1978). Most of the SDM footwall comprises schistose (non-mylonitic) mafic rocks that decrease in metamorphic grade southward. Greenschist-facies mafic schists are exposed in the northern part of the SDM. A pumpellyite-out isograd has been mapped approximately mid-way up the north flank of the SDM representing peak temperatures of 350–375°C (Little et al., 2019). Pumpellyite-actinolite facies rocks are exposed on more southern parts of the SDM. Ultramafic rocks, the so called Papuan Ultramafic Belt, were obducted southwardly onto the metabasalt during a Paleogene arc-continent collision (e.g., Davies & Jaques, 1984; Lus et al., 2004; Smith, 2013). Granitoid stocks (Mai'iu Monzonite and Suckling Granite; Davies & Smith, 1974) intrude the lower plate of the SDM near Mt Suckling (**Figure 1.10**) and are decapitated beneath the Mai'iu fault. These syn-extensional intrusions have U-Pb crystallisation ages on zircon of 1.9–3.7 Ma (Oesterle et al., 2018; Little et al., 2019). The granitoids record melting of continental crust at depth, and geophysical data (based on seismic travel-times) confirms that the Goropu Metabasalt is underlain by continental crust of felsic to intermediate composition that reaches a thickness of ~32 km near the SDM (e.g., Finlayson et al., 1977; Ferris et al., 2006; Eilon et al., 2015; Abers et al., 2016).

The hangingwall of the Mai'iu fault at the northern range front consists chiefly of Pliocene and younger alluvial conglomerates including the Gwoira conglomerate, which forms a strongly south tilted rider block in a synformal embayment between Mt Dayman and Mt Masasoru (**Figure 1.10**; Smith & Davies, 1976; Caffi, 2008; Daczko et al., 2009 and 2011). The so-called Gwoira rider block was transferred to the footwall of the Mai'iu fault, when the Gwoira fault initiated to the north of what is now an inactive strand of the Mai'iu fault. The Gwoira fault dips 37-47° to the NE at the surface and is inferred to link up with the active Mai'iu fault in the subsurface based on: (1) a corridor of microseismicity that extends downdip of the Mai'iu fault to the north of its intersection with the Gwoira splay fault; (2) a lack of microseismicity directly downdip of the active Gwoira fault (**Figure 1.9**; Abers et al., 2016; Webber, 2017); and (3) the absence of a ~45° dipping scarp or fault plane anywhere along the Mai'iu fault to the east or west of the Gwoira fault.

The lowest, northernmost and most recently exhumed part of the scarp of the Mai'iu fault consists of mafic mylonite that has a shallowly-dipping mylonitic foliation and a NNE plunging mineral elongation (Little et al., 2019). The stretching lineation

is parallel to the wear striae on the fault surface. The mylonitic fabrics are inferred to be Neogene or younger in age. Actinolite-chlorite-epidote-albite-quartz-calcite-titanite (greenschist facies) assemblages in these mylonites indicate peak-metamorphic conditions of 5.9–7.2 kbar and temperatures of ~425°C based on pseudosection modelling (Daczko et al., 2009). This implies an exhumation of the basal footwall from depths of ~25±5 km. Several microstructures crosscut the mylonite zone and record early ductile deformation supplanted by a progressive embrittlement during exhumation through the BDT. The active slip surface of the Mai'iu fault overprints the mylonites. It includes an up to ~50 cm thick core consisting of ultracataclasites and fault gouge. Pseudotachylite veins have been documented in a 1.5–3 m thick foliated cataclasite structurally above the mylonites.

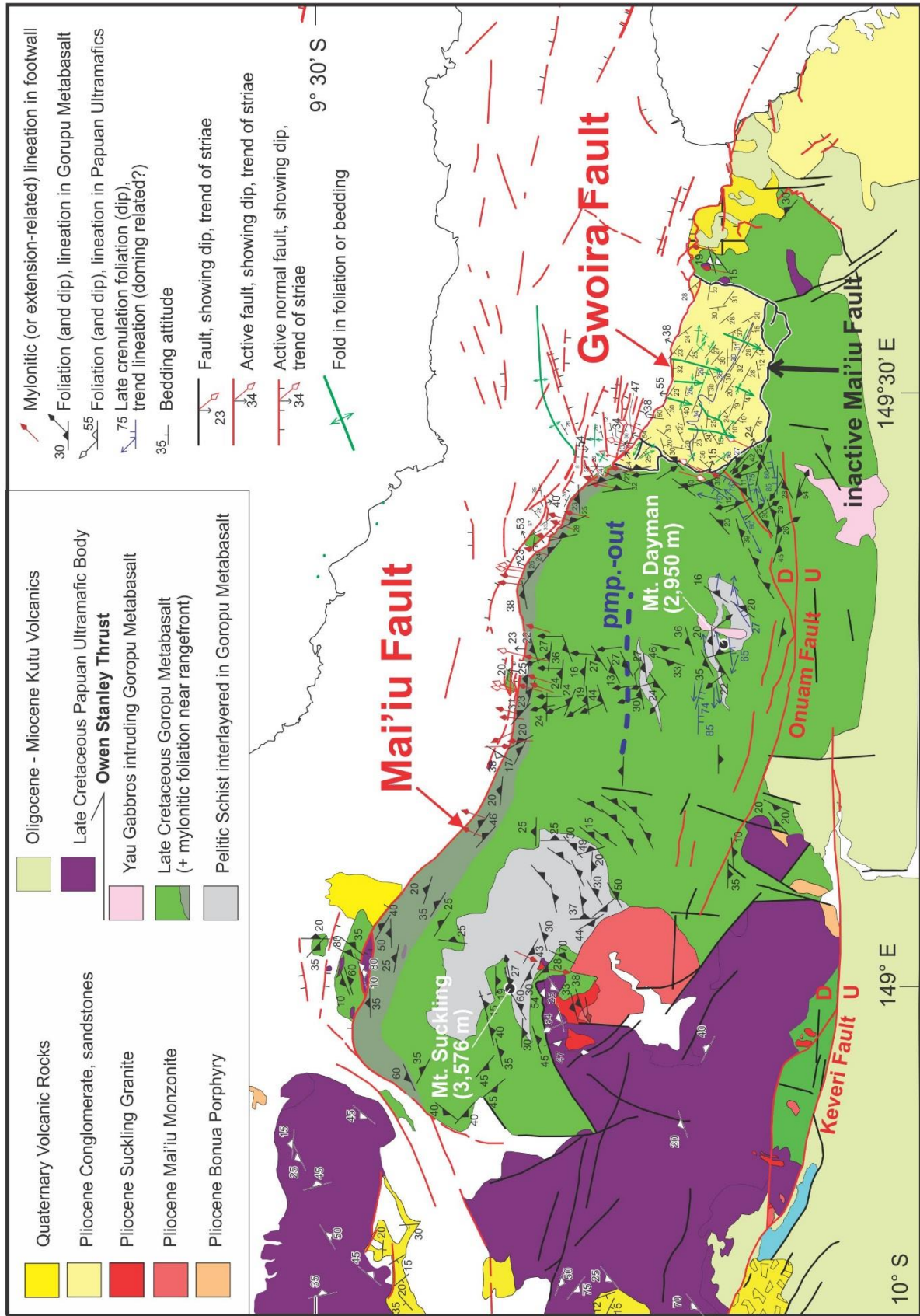


Figure 1.10 (previous page). Geological and structural map of the Suckling-Dayman Metamorphic Core Complex (modified after Davies & Smith, 1974; Little et al., 2019). The footwall mainly consists of a metamorphosed basalt (Goropu Metabasalt). Ultramafic rocks (Papuan Ultramafic Belt) were obducted southwardly onto this metabasalt during a Paleogene arc-continent collision (Davies & Jaques, 1984). The hangingwall of the Mai'iu fault consists chiefly of Pliocene and younger alluvial conglomerates. These include the Gwoira conglomerate, which forms a strongly south-tilted rider block in the east of the study area. This block was transferred from the hangingwall to the footwall of the Mai'iu Fault, when the Gwoira Fault formed to the north of what is now an inactive strand of the Mai'iu fault. The lowest, northernmost and most recently exhumed part of the footwall of the Mai'iu fault consists of mafic mylonite that has a shallowly-dipping mylonitic foliation and a NNE plunging stretching lineation.

1.3.5 Major Faults in the Suckling-Dayman Metamorphic Core Complex Region

The footwall of the SDM is also cross cut by two apparently active, high-angle normal faults on its deeply eroded southern flank: the Keveri and Onuam faults (**Figure 1.10**). Understanding these faults informs the question of whether some back-tilting in the footwall of the Mai'iu fault might be attributed to fault-block rotations (or “domino” rotation) related to slip on these faults. According to Davies and Smith (1974) the Keveri fault has a throw of ~3 km and down-drops rocks of the PUB to the north against uplifted Kutu Volcanics and related sedimentary rocks to the south. Pliocene fluvial conglomerates (Domara River Conglomerate) within the Keveri valley occur on both sides of the Keveri fault where they are tilted to the SW by 10–40° (Davies & Smith, 1974; Lindley, 2014). Based on aeromagnetic data, Lindley (2014) argues that the Keveri fault is steeply dipping. A possible late Quaternary strike-slip component of movement on this fault was argued on the basis of: 1) a single horizontal striation observation at one locality on the subparallel-striking Wavera valley fault south of the main Keveri fault; and 2) up-to ~300 m right-stepping deviation of several streams that cross the Keveri fault (Lindley, 2014). The Onuam fault farther to the east is inferred to be up-to-the-south based on up to 180 m high uphill-facing scarps as evident in digital terrain models (Little et al., 2019). This fault seems to divert southward draining streams laterally by up to 1 km to the right. Based on map patterns (e.g., Davies & Smith, 1974), geological offsets, and the post-Pliocene sense of stratal tilting, it is inferred (in agreement with Daczko et al., 2011) that the Keveri and Onuam faults are steep, north-dipping faults that have normal dip-slips of maybe up to 3–4 km; and that any strike-slip component is minor relative to dip-slip. These two faults must contribute some SW-tilting to the footwall of the SDM; however, their steep dips and modest offsets indicate that this contribution must be small.

1.4 METHODOLOGY

Fieldwork was an important component of my thesis. Structural measurements of the exhumed footwall, hangingwall and the Mai'iu fault were collected during the 2015 and 2016 field campaigns at more than 570 outcrops on the SDM, from which more than 458 samples were taken. These traverses covered the high summits, dome flanks, and northern fault margin of the exhumed Mai'iu fault surface, with the fault

rocks of the Mai'iu fault being a particular target. All orientation data of collected rock samples and structural measurements can be found in the digital supplementary data. Samples are cut perpendicular to the foliation and parallel to the lineation (kinematic XZ plane). Fragile specimens were impregnated with epoxy and dried for approximately 24 h at 50°C. Thin sections were prepared and polished by our in house petrology lab technician Steward Bush. For ultrapolishing he used a diamond paste before a final stage of SYTON-polishing, in order to have a scratch-free, highly reflective surface of the thin section.

1.4.1 Geomorphic Analysis (Chapter 2)

For the tectonic-geomorphic analysis presented in Chapter 2, I examined high-resolution aerial photography stereopairs (air surveys in 1954 and 1973) using a Wild Heerbrugg stereoscope to place the collected field data into a larger, dome-wide context and to identify faults and fault scarps that offset the abandoned part of the exhumed Mai'iu fault surface. Complementary to this analysis, I also used 30 meter-spaced, and locally 5 meter-spaced, digital topographic datasets processed by FUGRO, Ltd. This GeoSAR data employs the interferometric synthetic aperture radar system (IFSAR) operating at two frequencies simultaneously that penetrates vegetation and cloud cover to generate high-quality Digital Terrain Models (DTMs). These commercial DTMs do not cover the whole study area. The rest of the study area is covered by a DTM obtained from Shuttle Radar Topography Mission (SRTM) data with a resolution of the unprocessed raw data of one arcsecond (~30 m). This SRTM data is freely available since 2016 on the USGS website. Chapter 2 also involves an examination of stream patterns, which are tectonic gauges that are sensitive to uplift, tilting and faulting in this active tectonic regime. More precisely, I identified and mapped deflected streams, stream piracy, wind gaps, and tilted fluvial terraces to establish directions of recent landscape tilting related to slip on the Mai'iu fault. Maps with constructed stream channels are shown in Chapter 2. An explanation of how these streams were constructed in ArcGIS 10.1 can be found in Appendix A.1. Furthermore, I constructed a three-dimensional, preerosional fault surface model of the Mai'iu fault from the GeoSAR derived DTM in ArcGIS 10.1. The well-preserved part of the SDM that is only slightly dissected by streams (e.g., Ollier & Pain, 1980; Caffi, 2008; Spencer, 2010; Daczko et al., 2011) is ideal for this reconstruction. This three-dimensional fault surface model is used to delineate fault surface information such as

corrugations, change in curvature and aspect (dip-direction dip) of the surface. The fault surface was constructed from the ridges of the SDM topography. A step-by-step explanation of the fault-modelling process can be found in the Appendix A.1.

1.4.2 Optical Microscopy, Imaging and Textural Analysis (Chapter 3 and Chapter 4)

In a first stage of optical analysis, I used a petrographic microscope to assess the mineralogy and microstructures of ~250 oriented samples. The overall change in mineralogy, metamorphism and occurrence of different fault rocks and their characteristic microstructures, also investigated by Tim Little and Jürgen Österle are summarized by us in Little et al. (2019), but in much less detail than I have undertaken in my thesis. In a second stage, I selected a suite of ~30 representative fault rock samples comprising protolith rock, mylonite, foliated cataclasite, ultracataclasite and fault gouge samples for further textural and chemical analysis. One of the main purposes of the textural analysis was to collect orientation data of the mineral assemblage in the fault rocks to see if a crystallographic preferred orientation is present (Chapter 3). Furthermore, orientation data from calcite grains and deformation twins in calcite veins were collected for the paleostress analysis (Chapter 4). The data was acquired using a field emission gun scanning electron microscope (FEG-SEM) equipped with energy dispersive spectroscopy (EDS) and electron backscatter diffraction (EBSD) detectors at the University of Otago. Many of my analyses presented in Chapter 3 and 4 are based on EBSD data. The paleostress analyses based on calcite are explained in detail in Chapter 4.

EBSD mapping was carried out on a Zeiss SIGMA-VP FEG-SEM equipped with an Oxford Instruments Nordlys EBSD camera. The FEG-SEM was operated at 30 kV accelerating voltage and 90 nA beam current, at a working distance of 20–30 mm. This technique can be used for examining crystallographic preferred orientation, phase determination, and grain, phase and twin boundary identification. The polished samples were placed on a brass sample holder in the SEM chamber that was oriented at a tilted angle of ~70° to the incident electron beam. The phosphor screen of the EBSD camera is tilted 90° relative to the horizontal and detects backscattered electrons diffracted from the sample. The backscattered electrons have a certain distribution distinct to the crystal lattice of an individual mineral. This causes a statistical pattern of diffracted electrons usually accumulating along bands—Kikuchi bands or electron

backscatter diffraction pattern (EBSP). The EBSD-camera detects these patterns for low light imaging. Minerals and their orientations within a thin section are determined by the orientation, relative position, strength and spacing of the Kikuchi bands. Maps are recorded and generated by the Oxford Aztec software. The data was acquired by automatic beam rastering over a selected area. Different step sizes ranging from 0.2 to 2.0 μm were applied depending on the particular research objective (i.e., grain size analyses, orientation maps, calcite twins etc.). The software provided phase and orientations maps. Band contrast maps are related to the quality of the indexed patterns in these maps. These grey-scale maps indicate the quality of the indexing—light contrast, areas of good indexing; dark areas, poor or no indexing (Maitland & Sitzman, 2006). The collected EBSD data from the different fault rocks (Chapter 3) and calcite veins (Chapter 4) were processed with the MTEX toolbox for MATLAB written by Bachmann et al. (2010). In MTEX, raw EBSD data of indexed pixels is converted to grains based on a Voronoi decomposition method (Bachmann et al., 2011). The script is populating the whole map with grains, whereas non-indexed phases are removed in a later step. With this approach well-indexed grains will maintain a realistic geometry in areas of poorly indexed pixels. The grain sizes of different minerals are calculated as the diameter of an area-equivalent circle. Calcite twin width and twin densities within the calcite grains used for the calcite twin stress analysis presented in Chapter 4 were measured manually using the software Channel 5 by Oxford Instruments. Detailed explanation of the EBSD data processing can be found in Appendix B.3; MTEX scripts used for EBSD data processing can be found in the Digital Appendix in the folder ‘MTEX’.

Chapter 2: Structural and Geomorphic Evidence for Rolling-Hinge Style Deformation of an Active Continental Low-Angle Normal Fault, SE Papua New Guinea

Abstract

To what degree Low-Angle Normal Faults (LANFs) deform by a “rolling-hinge” mechanism is still debated for continental Metamorphic Core Complexes (MCCs). The Mai’iu fault in SE Papua New Guinea is one of the best preserved and fastest slipping active continental LANFs on Earth, providing an ideal setting in which to evaluate footwall deformation and doming in MCCs. We analyzed structural field data from the exhumed slip surface and subjacent footwall of the Mai’iu fault, together with geomorphic data interpreted from aerial photographs and GeoSAR-derived digital terrain models. The exhumed part of the Mai’iu fault forms a smooth, continuous surface, traced at least 28 km in the slip direction. The fault emerges from the ground near sea level with a northward dip of $\sim 15\text{--}22^\circ\text{N}$ and flattens southward over the crest of the Suckling-Dayman Dome. Its most southern mapped portion dips $\sim 12^\circ\text{S}$. Geomorphic and structural evidence indicates up dip tectonic transport of the footwall and progressive back-tilting of the exposed part of the fault and the underlying foliation through $>26^\circ$. We infer that antithetic (northside up) dip slip on an array of steep-dipping faults striking parallel to the Mai’iu fault accommodated some of the exhumation-related inelastic bending of the footwall. The exhuming footwall was subject to late-stage slip-parallel contractional strain as recorded by a postmetamorphic crenulation foliation that strikes parallel to the curved Mai’iu fault trace, by folds of bedding in a large rider block that is stranded on the current footwall and by strike-parallel warps in the exhumed fault surface. Geodynamic modeling predicts the observed footwall strain.

2.1 INTRODUCTION

Metamorphic Core Complexes (MCCs) are common in highly extended domains of both continental and oceanic lithosphere (e.g., Coney, 1980; Whitney et al., 2013). Continental MCCs are bounded by normal faults with slip magnitudes of tens of kilometres that can be shown to have slipped at dips $<30^\circ$. These so called low-angle normal faults (LANFs) or detachment faults are typically domal in shape, and commonly separate tilted and faulted upper crustal unmetamorphosed rocks in the hangingwall from middle-to-lower crustal metamorphic rocks in the footwall (e.g., Coney, 1980; Armstrong, 1982; Tucholke et al., 1998; Platt et al., 2015). Activity and especially initiation of normal faults at such low dips contradicts the predictions of Coulomb failure (e.g., Anderson, 1951) and is not consistent with the observed seismicity in active rifts, which is dominated by slip on moderate to steeply dipping normal faults (Jackson, 1987; Jackson & White, 1989; Collettini & Sibson, 2001; Abers et al., 2016).

Using paleomagnetic techniques, oceanic LANFs with slip magnitudes of tens of kilometers have been shown to have originated at dips of $45\text{--}60^\circ$ (Garcés & Gee, 2007; Morris et al., 2009). The progressive flexural-isostatic shallowing of an initially steep single fault during unloading of the footwall is called “rolling-hinge” evolution (e.g., Spencer, 1984; Buck, 1988; Wernicke & Axen, 1988). In continental lithosphere, a “rolling-hinge” evolution of LANFs is often assumed or inferred but not demonstrated. This is because observational data rarely require a presently shallowly dipping fault to have formed at an originally steep dip, nor do they provide evidence of footwall rotations about a horizontal axis, or require a progressive shallowing of the fault dip through a “rolling-hinge” bending process in the footwall (e.g., Axen & Bartley, 1997). Paleohorizontal markers in metamorphic footwall rocks are rare. Compounding this problem, most well-studied continental LANFs are ancient and inactive; thus the processes that affected them as active structures have since been overprinted and obscured by postformational tilting and erosion (Axen & Bartley, 1997; Axen, 2004; Collettini, 2011; Whitney et al., 2013). Therefore, the question of whether most continental LANFs initiated as moderately to steeply dipping faults that later were deformed to shallower dips in the near surface as part of a “rolling-hinge” bending process is not straightforward, and is still debated.

The Mai'iu fault is an exceptionally well-exposed active LANF that has not suffered postformational overprints. Located in SE Papua New Guinea, it is one of the fastest slipping and probably the best preserved of only a handful known active continental LANFs (e.g., Webber et al., 2018), and has been described as a prime example of a LANF that evolved through a “rolling-hinge” process (Spencer, 2010; Little et al., 2019).

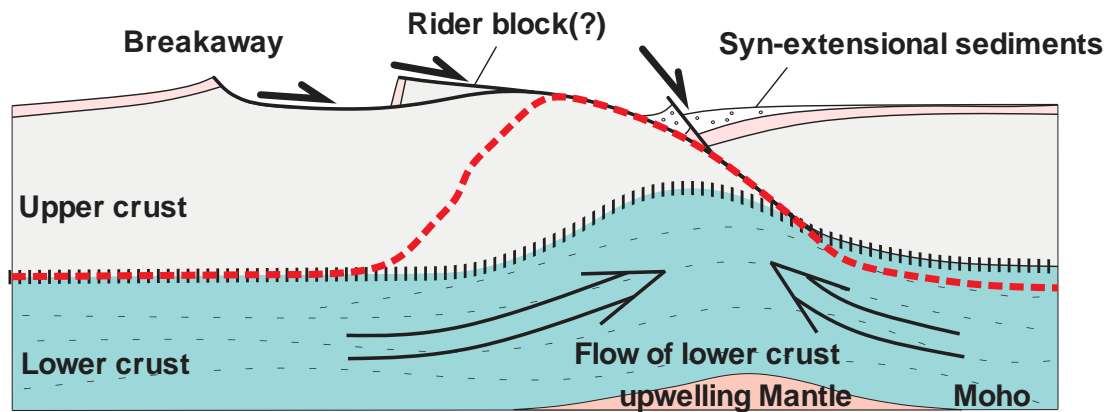
The “rolling-hinge” model involves progressive back-tilting during exhumation of an originally moderate to steeply dipping fault that back-warps the footwall into an abandoned, domal structure while the fault remains active at depth (**Figure 2.1A**; Spencer, 1984; Wernicke & Axen, 1988). Isostatic rebound of the tectonically unloaded footwall forms an antiformal hinge that migrates through the footwall in the direction of upper plate tectonic transport. As the footwall passes through the hinge and tilts to shallower dip angles, the uppermost part of the fault becomes progressively abandoned—this process overall is known as the “rolling-hinge” mechanism (Spencer, 1984; Axen & Bartley, 1997). During “rolling-hinge” activity, the hangingwall may be cross-cut by new, steeply dipping splay faults that merge downdip into deeper and still active part of the original fault resulting in the capture of original hangingwall rocks into the footwall (rider block; e.g., Reston & Ranero, 2011). The shallow dip of some detachment faults might have also resulted from “domino”-like tilting of more nearly rigid fault blocks, followed by their intersection by younger faults, leading to a composite detachment fault of different-aged faults (**Figure 2.1B**, “domino block rotation” model, e.g., Proffett, 1977; Lister & Davis, 1989; Gans & Gentry, 2016). Differentiating between these processes—which are not mutually exclusive—is non trivial (see Gans & Gentry, 2016). Despite some geometrical similarities between these two models, the main processes forming them are quite different. The following list identifies the key structural and geomorphic features that we believe are diagnostic of a fault that has evolved through a “rolling-hinge” process (**Figure 2.1A**):

- (a) **Single, continuously exhumed fault surface.** The “rolling-hinge” mechanism involves continued slip on a single, large offset fault, with tilting of the shallower part of the fault to lower dips achieved by isostatic rebound and flexure of its unloaded footwall.
- (b) **Convex up fault geometry.** Starting from moderate to steep dips, continuous uplift and warping of a single fault leads to a convex up shape

of the fault surface. For an active fault, the continuation of the fault as a moderate or steeply dipping structure downdip in the subsurface might, in theory, be resolved by seismicity.

- (c) **Continuously back-tilted and warped markers in footwall.** Flexure of the footwall of a once steeply dipping fault surface may be recorded by warping and back-rotation of structural markers attached to the footwall of the fault. These might include fluvial terraces, sedimentary beds, foliation, stream channels, or paleomagnetic vectors (Axen & Bartley, 1997; Morris et al., 2009).
- (d) **Flexure of the footwall and fault surface.** If fault rotation is achieved by gradual warping of the footwall, then the footwall may behave as a flexed elastic beam that partially fails in response to bending stresses. Inelastic bending might be accommodated by secondary high-angle faults as documented in several oceanic core complexes (Tucholke et al., 1998, 2008; Karson et al., 2006; Schouten et al., 2010; Hayman et al., 2011) and rarely in continental MCCs (e.g., Spencer, 1985; Axen et al., 1995; Spencer, 2011).
- (e) **Slip-parallel footwall contraction.** Because of the unbending strains in the outer arc of a once steeper but now unflexed beam, contractional structures accommodating shortening might be expected in the abandoned, surficial part of the exhumed fault subparallel to the regional extension direction (Manning & Bartley, 1994; Axen et al., 1995). If the fault surface is strongly corrugated or indented, then such contraction might be expected to act at right angles to the geometrically imposed gradients in the magnitude of footwall denudation caused by slip on the three-dimensional fault. Near a deep reentrant, the direction of contraction would be expected to deviate away from the fault slip direction and toward the interior of the reentrant.

“Rolling-hinge” model: back-tilted high-angle normal fault



B “Domino-block rotation” model: systematically rotated high-angle faults

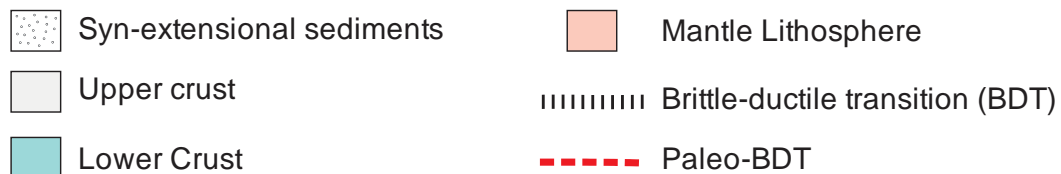
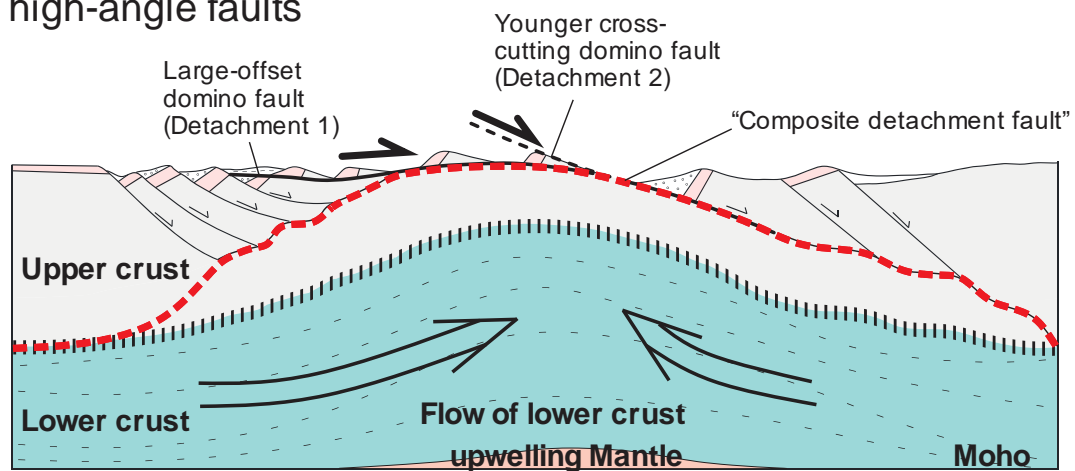


Figure 2.1. Two prominent models for the evolution of large-displacement normal faults with present-day low-angle dips at the surface. A) Normal fault initiates at steep dip and progressively flattens with slip as a result of unloading-related back-tilting of the exhumed fault, while remaining active at depth (“rolling-hinge” model; after Wernicke & Axen, 1988). B) An array of initially steep normal faults tilt to gentle dips with progressive slip in a domino-style. At low dips, faults may be cross-cut by younger high-angle normal faults that themselves eventually tilt to shallower dips. The final geometry may include a composite of different-aged fault segments (the older “Detachment 1” and the younger “Detachment 2”) that resemble a single detachment fault (“composite detachment fault”; Gans & Gentry, 2016).

The rapidly slipping Mai’iu fault in SE Papua New Guinea exposes a well-preserved, continuous and corrugated detachment surface that is >20-km wide in the slip direction. It is an ideal setting to study deformation and tilting in the exhumed

footwall of an active MCC, and to document and evaluate a likely example of a “rolling-hinge” normal fault in the context of the key structural and geomorphic features presented above. In this paper we analyze a detailed terrain model of the topography and a three-dimensional model of the Mai’iu fault constructed from that topography, in order to describe the morphology and distribution of roughness and curvature in the exhumed fault surface. We evaluate late-stage deformational processes and patterns of near-surface back-tilting in the footwall accommodating slip on this active LANF by combining field structural geology and tectonic geomorphology. The geomorphological analysis is chiefly based on field observations and GIS-based analysis of GeoSAR-derived digital terrain models (DTMs) resolved mostly at 30-m grid spacing. Finally, we compare our field and geomorphic observations to the predictions of a finite element thermomechanical model constrained by boundary conditions tuned to the Mai’iu fault, which highlights first-order geodynamic processes of MCC formation, including an expected pattern of stress trajectories in the near surface. Our study provides a systematic, multidisciplinary demonstration of “rolling-hinge” behavior of an active and rapidly slipping LANF in a continental rift.

2.2 TECTONIC AND GEOLOGICAL SETTING OF THE MAI’IU FAULT

2.2.1 Tectonic Setting of the Woodlark Rift

The tectonic regime in SE Papua New Guinea is governed by the oblique-convergent motion of the Pacific Plate (PAC) relative to the Australian Plate (AUS) creating a complex array of microplates in the collision zone (**Figure 2.2**; Tregoning et al., 1998; Wallace et al., 2004, 2014). The Woodlark-Solomon Sea microplate rotates counterclockwise relative to the Australian plate about a nearby Euler pole resulting in a north-south opening of the Woodlark Basin with extension rates increasing to the east (Taylor et al., 1999; Wallace et al., 2004; Eilon et al., 2015). In the east, seafloor spreading has occurred at rates >20–60 mm/year since ~6 Ma, as recorded by magnetic anomalies in the Woodlark Basin (Taylor et al., 1999). The Woodlark Rift cuts continental crust and is thought to have initiated by 3.6–8.4 Ma (Taylor & Huchon, 2002; Petersen & Buck, 2015) with current geodetically measured extension rates there of up to 20 mm/year (Wallace et al., 2014). Extension in the western, continental part of this extensional zone is accommodated by slip on a relatively small number of predominantly north dipping normal faults, some of which

bound the flanks of the subaerially exhumed D'Entrecasteaux Islands gneiss domes (Little et al., 2007, 2011; Fitz & Mann, 2013; Wallace et al., 2014). West of Goodenough Island, most of the Woodlark Rift extension is accommodated by the Mai'iu fault, a normal fault that has geologically and geodetically determined dip-slip rates of ~12 mm/year (Wallace et al., 2014; Webber et al., 2018). Downdip of its surface trace, microearthquake foci scattered between 12 and 25 km depth (middle to lower crust) define a deformation zone that dips north at 30–40° (**Figure 2.2B**; Abers et al., 2016). Abers et al. (2016) interpreted this deformation zone as the subsurface continuation of the Mai'iu fault. Previous workers have suggested that the Mai'iu fault formed by extensional reactivation of the older Owen-Stanley Fault Zone (OSFZ), a Late Cretaceous-Paleocene subduction thrust with an ophiolite in its hangingwall (Davies, 1978; Webb et al., 2008; Daczko et al., 2011; Little et al., 2019). Today, to the NW of the Woodlark rift, a northern part of the OSFZ slips as a left-lateral strike-slip fault, whereas at its far northwestern end it is a contractional plate boundary structure, with these changes being controlled by its location along-strike relative to the Euler pole (Wallace et al., 2014).

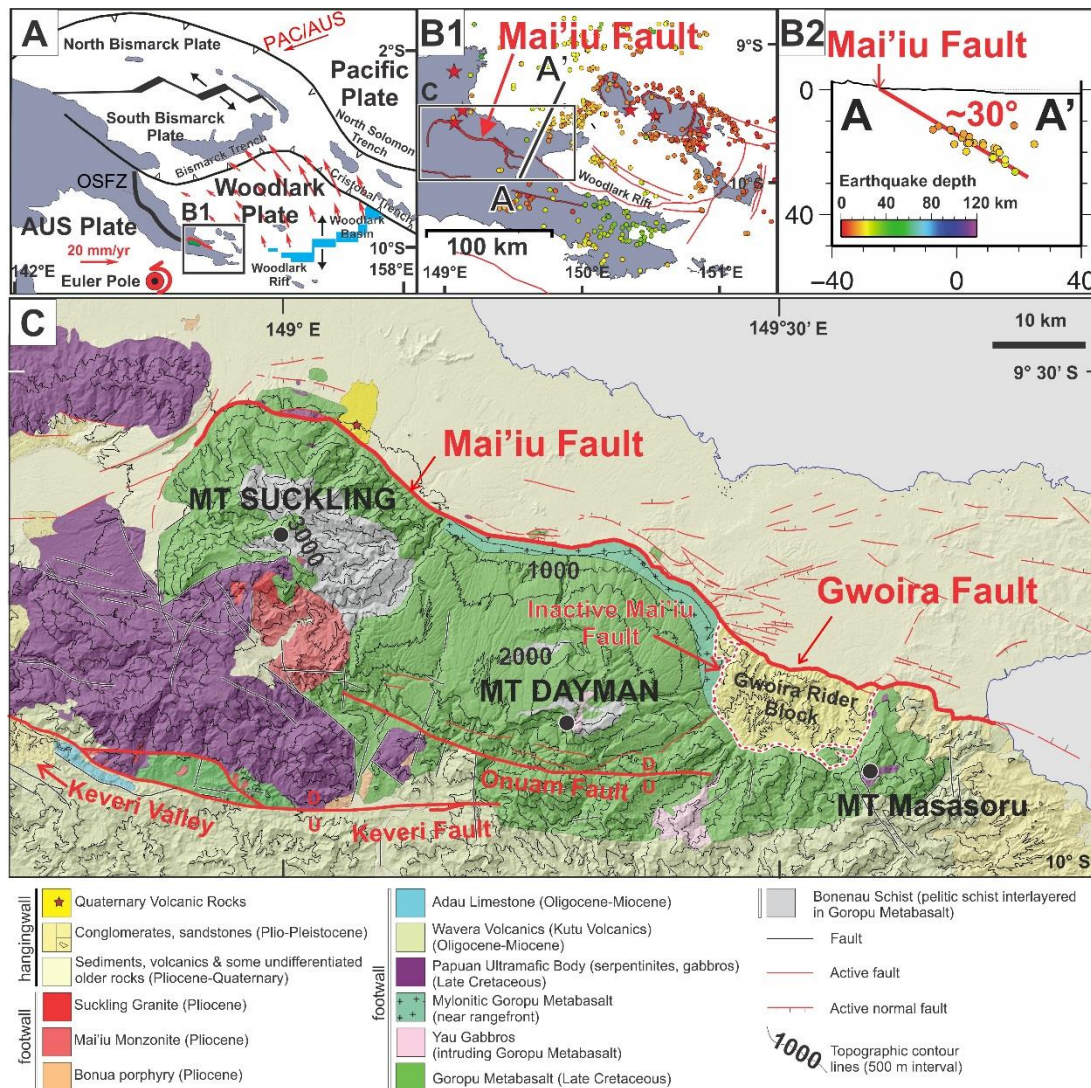


Figure 2.2. A) Plate tectonic setting of the Woodlark Rift and present-day GPS-derived pole of rotation with the SDM highlighted in green (modified after Fitz & Mann, 2013; Wallace et al., 2014). B1) Microseismicity map for part of the Woodlark Rift (acquired for the period March 2010 to January 2011 and modified after Abers et al., 2016). Dots: Color-coded hypocenters of microearthquakes (depth scale bar in B2); red stars: Volcanoes. B2) Cross-section A-A' from B1 with microearthquake foci defining a 30–40° dipping deformation zone colinear with the surface trace of the Mai'iu fault. C) Simplified geologic and structural map of the SDM in SE Papua New Guinea (modified after Smith & Davies, 1976; Lindley, 2014; Little et al., 2019). At the surface, the topographically defined SDM consists chiefly of smooth, little eroded dip slopes of the exhumed Mai'iu fault. The Gwoira rider block is bounded by an inactive segment of the Mai'iu fault to the south and the active Gwoira fault splay to the north. SDM=Suckling-Dayman Metamorphic Core Complex.

2.2.2 Geology of the Mai'iu Fault

The Mai'iu fault bounds the northern side of the Suckling-Dayman MCC (SDM) and has a surface dip of ~22° where it emerges from Holocene gravel at its surface trace (Spencer, 2010; Little et al., 2019). The MCC hosts three NNE-trending

culminations and intervening synformal corrugations (**Figure 2.2C**)—(a) Mt Suckling (3,576 m) in the west, (b) Mt Dayman (2,950 m) in the center, and (c) Mt Masasoru (~1,700 m) to the east. The exposed footwall of the MCC consists mainly of metabasaltic rocks—the Goropu Metabasalt, which varies in grade from greenschist-facies at the base of the scarp near the Mai'iu fault trace, to pumpellyite-actinolite-facies farther up the scarp, to prehnite-pumpellyite-facies south of the main divide of the Owen Stanley Ranges (Davies, 1978). The ~3–4 km-thick Goropu Metabasalt is a Late Cretaceous sequence of MORB lavas with minor interbedded calcareous to pelitic metasedimentary rocks and chert that grades southward into an unmetamorphosed equivalent called the Kutu Volcanics (Smith & Davies, 1976; Davies & Warren, 1988; Daczko et al., 2011). Ultramafic rocks of the Papuan Ultramafic Belt (PUB) were obducted southward over the Goropu Metabasalt during a Paleocene-Eocene arc-continent collision—the Papuan Orogeny (Davies & Jaques, 1984; Smith, 2013). The observed dominant foliation in the Goropu Metabasalt probably formed during this obduction (Little et al., 2019). A flap of PUB overlies the Goropu Metabasalt on a southern part of the footwall of the Mai'iu fault. Mostly undeformed Pleisto-Pliocene (~2.0–3.3 Ma; Little et al., 2019) granitoid intrusives (**Figure 2.2C**: Mai'iu Monzonite and Suckling Granite; Davies & Smith, 1974) intrude the basal contact of the PUB near the summit of Mt Suckling but are absent at the surface farther east near the Mt Dayman and Mt Masasoru culminations. The granitoids imply the presence of thick continental crust (>18 km) beneath the PUB ophiolitic suite, as confirmed by geophysical surveys (e.g., Finlayson et al., 1977; Abers et al., 2002; Ferris et al., 2006; Jin et al., 2015; Abers et al., 2016).

At the base of the Mai'iu fault scarp at the northern range front, the schistose Goropu Metabasalt transitions northward into Neogene-age extensional mylonites reaching locally a thickness of at least 60 m (**Figure 2.2C**; Daczko et al., 2009; Little et al., 2019). The transition is marked by a rotation of the dominant lineation trend in the footwall from NNW to NNE, and a change in the sense of shear from top-to-the-SE (thrust sense) to top-to-the-NE (normal sense) shear fabrics, respectively (Little et al., 2019). The mylonites have been exhumed from an inferred depth of 20–25 km (400–450°C) based on pseudosection modeling of the mafic mineral assemblage (Daczko et al., 2009, 2011). A <3-meter-thick zone of Mai'iu fault rocks is exposed at several locations along its trace (see Little et al., 2019, for locations). These fault rocks

structurally overlie the mylonite zone. From bottom to top, the fault rocks consist of (1) foliated cataclasite (and breccia) locally cut by pseudotachylite veins (~1.5 m thick); (2) massive ultracataclasite (<0.4 m); and (3) saponite- and corrensite-rich gouges (<0.2 m). The upwardly narrowing arrangement of fault rocks are interpreted as a strain-localizing time sequence, where the higher units are more shallow-derived and have cannibalized the underlying ones. The upper units contain progressively lower temperature alteration products than the lower ones (Little et al., 2019).

The hangingwall at the northern range front consists chiefly of Pliocene and younger alluvial conglomerates, the Gwoira Conglomerate, which rests on a basement of PUB (e.g., Daczko et al., 2011). Inception of the ~38–47° dipping Gwoira fault, a hangingwall splay, transferred a slice of the Gwoira Conglomerate to the footwall of the Mai'iu fault, and formed the Gwoira rider block, which has a minimum stratigraphic thickness of ~2,600 m (Webber, 2017; Little et al., 2019). This slice (rider block) is underlain and surrounded by synformal dip slopes of an inactive segment of the Mai'iu fault (inactive Mai'iu fault, **Figure 2.2C**). The Gwoira fault is inferred to root into (rather than cross-cut) the active Mai'iu fault in the subsurface at ~800-m depth. This merging inference is based on: 1) the aforementioned corridor of microseismicity that extends downdip of the Mai'iu fault to the north of its intersection with the Gwoira splay fault; 2) a lack of microseismicity directly downdip of the active Gwoira fault (Abers et al., 2016; Webber, 2017); and 3) the absence of a ~45° dipping scarp or fault plane anywhere along the Mai'iu fault to the east or west of the Gwoira fault. The footwall of the SDM is also cross-cut by two apparently active, high-angle normal faults on its deeply eroded southern flank: the Keveri and Onuam faults (**Figure 2.2C**). These two faults must contribute some SW-tilting to the footwall of the SDM; however, their steep dips and modest offsets indicate that this contribution must be small (Little et al., 2019).

2.2.3 Previous Geomorphic Work on the Mai'iu Fault

The geomorphology of the SDM has been studied remotely using aerial photography and DTMs, the latter derived from Shuttle Radar Topography Mission (SRTM) data gridded at 90 m (Spencer, 2010; Daczko et al., 2011; Miller et al., 2012; Webber, 2017). These data reveal that the exhumed fault surface is more deeply fluvially dissected near Mt Suckling than it is near Mt Dayman to the east and that

footwall dip slopes—attributed to slip on the Mai’iu fault—are best preserved between Mt Masasoru and an area to the west of Mt. Dayman (Daczko et al., 2011).

Most previous geomorphic analysis of the fault focused on the smooth and little eroded surface in the central and eastern SDM. These authors noted (1) that the exhumed surface has a convex upward shape, with dip and curvature decreasing southward away from the fault trace (Spencer, 2010); (2) that it contains numerous linear stream channels and ridge crests, (“lineaments” of Daczko et al., 2011) demarking channels and corrugations on the surface that are parallel to the slip direction (Spencer, 2010; Daczko et al., 2011); (3) that many stream profiles have prominent upward convexities at the upstream ends of inner gorges draining the fault surface (Miller et al., 2012); and (4) that many fluvial canyons traverse the main divide of the SDM, across which they split into north and south draining segments separated by a crestal windgap (Spencer, 2010). The latter author suggested that these geomorphic features record southward displacement and down-flexure of the exhuming footwall at high elevation as are consistent with a “rolling-hinge” style bending.

2.3 METHODOLOGY

2.3.1 Tectonic-Geomorphic Analysis

Structural data were collected during field campaigns in 2014, 2015, and 2016 by traversing the exhumed surface of the fault plane in order to infer the deformational history of the footwall and the Mai’iu fault zone (**Figure 2.3**). In addition, we examined (1) high-resolution aerial photography stereopairs (air surveys in 1954 and 1973); and (2) a DTM based on 30-meter and locally 5-meter gridded GeoSAR topographic data (flown and processed in 2006 by Fugro Spatial, Ltd., Australia). All maps are projected in the UTM coordinate system of the Australian Map Grid (Zone 55) and reference the Australian Geodetic Datum (AGD) 1966. Elevations are relative to Mean Sea Level. The chief aims of this geomorphic analysis were: (a) to map remnants of the Mai’iu fault surface; (b) to evaluate the drainage network and fluvial geomorphology on the uplifted and exhumed fault plane; and (c) to identify any active or inactive structures, such as faults, that cut the exhumed footwall of the Mai’iu fault surface and that have contributed to its deformation. These results are presented in Sections 2.4–2.6 of this chapter.

2.3.2 Fault Surface Modeling

GeoSAR topographic data penetrate clouds and vegetation cover and reveal the shape of the exhumed footwall of the SDM. Based on the distribution of fault surface remnants (map in **Figure 2.4**) a preerosion, three-dimensional model of the Mai'iu fault surface ($\text{Surf}_{\text{Model}}$) was constructed as follows: (1) most slopes $>24^\circ$ were excluded from the model because these are clearly the result of channel incision. Exceptions to this along the range front were the steep scarp of the Gwoira fault and (farther south) dip slopes of the inactive Mai'iu fault, which we infer to have been tilted; and (2) all points at the bottom of channels and river valleys were excluded. The residual of this subtractive process selects the generally smooth interfluvies on the exhumed footwall. The fault surface model was built from the nondeleted point set by using a natural-neighbor interpolator algorithm in ArcGIS 10.1 (**Figure 2.5**). As shown in profile B of **Figure 2.5B**, the interpolated surface is unnaturally smooth in areas of deeply incised and wide stream channels. These are artifacts and have resulted in loss of some fault-surface topographic information at the tens- to hundreds-of-meters scale. The most comprehensive restoration of the original fault surface was accomplished directly up dip of the fault trace where the footwall is exposed most continuously and where it is least incised. There, small-scale corrugations are especially well preserved (profile A of **Figure 2.5B**). The fault surface model is presented in Section 2.4 (**Figure 2.5**).

We also quantified the roughness of Mai'iu fault's corrugated surface using a Fourier-based power spectral analysis of profiles across it. This was done to evaluate the geometry of the corrugations across different spatial scales and especially to document systematic variations of the roughness spectra—if any—with distance up the fault scarp (e.g., Candela et al., 2012; Brodsky et al., 2016; Parnell-Turner et al., 2018). To undertake this analysis required us to first remove the broad, domal (i.e., ~30-km wide) shape of the SDM before evaluating the roughness caused by smaller-wavelength corrugations that lie upon the fault surface. To this end, we calculated a 4th-order polynomial surface from the fault surface model (called the “reference surface”, Surf_{Ref}). This smoothed, average surface of the fault was subtracted from the fault surface model ($\text{Surf}_{\text{Model}}$) to measure local “fault surface relief” ($\Delta = \text{Surf}_{\text{Model}} - \text{Surf}_{\text{Ref}}$; **Figure 2.5G**; see also Appendix A.1, **Figure A.1**; e.g., Bistacchi et al., 2011; Parnell-Turner et al., 2018). We extracted several profiles on the “fault surface relief”

model in the direction perpendicular to slip (**Figure 2.6A**), from which we calculated power spectral density (PSD) curves (PSD plot, **Figure 2.6B**). If the fault had been exhumed continuously as part of a single evolving, “rolling-hinge” structure, then one might expect a similar roughness scaling-behavior (i.e., Hurst-exponent ζ , Candela et al. 2009) for cross-slip profiles up and down the scarp. Finally, Appendix A.1 (**Figure A.2**) presents PSD curves for profiles that are parallel to slip and compares these to other reported global examples across a range of spatial scales.

2.4 MORPHOLOGY OF THE EXHUMED MAI’IU FAULT SURFACE

Despite being covered in rainforest, the convex up antiformal geometry of the central and eastern SDM is remarkably smooth and well defined (**Figure 2.3A**). The Mai’iu and Gwoira faults are exposed in outcrops where streams cut across their trace at the range front. The active part of the Mai’iu fault dips $\sim 22^\circ$ where it emerges from Holocene gravels along the range front (**Figure 2.3B**). Smooth, planar dip slopes adjacent to the active trace indicate minimum fault dips of $15\text{--}16^\circ$. The exhumed fault surface updip from the trace is marked by a slip-parallel, linear drainage pattern (**Figure 2.3C**). Individual stream channels can be traced southward across the dome’s crestal divide where they drain in opposite direction. Atop the main divide the abandoned stream channels form numerous windgaps (**Figure 2.3D**). The exhumed slip surface is also cross-cut by linear steps that we interpret as fault scarps. These scarps mostly face south, and typically have 3- to 15-m northside up relief on them. The inferred faults strike subparallel to the Mai’iu fault and commonly divert otherwise NNE draining streams laterally either to the right or to the left around the south facing, topographic fault scarp (**Figure 2.3E, F**).

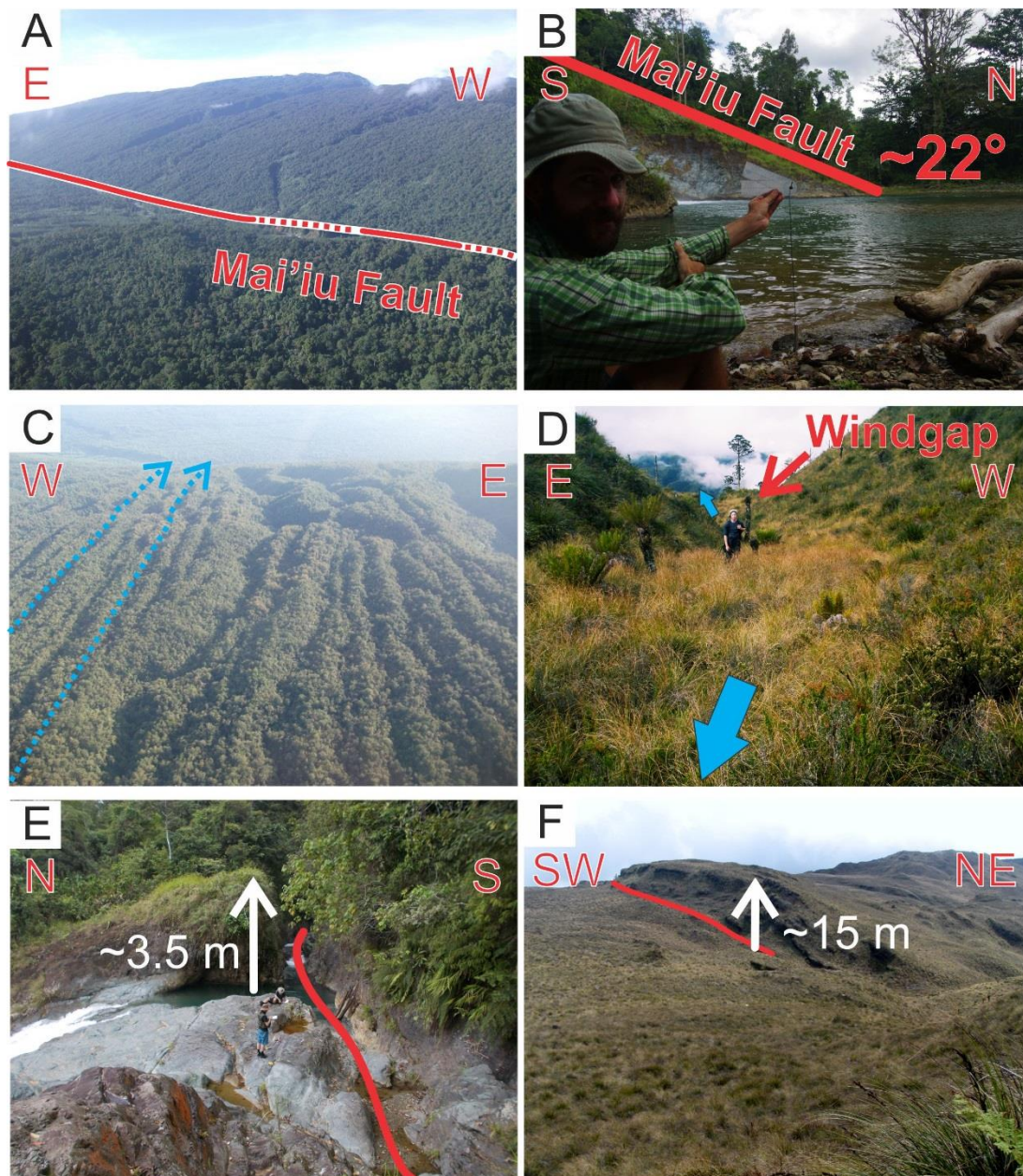


Figure 2.3. Field photographs of the Mai'iu fault trace and the abandoned, exhumed fault surface updip of that trace. A) View toward the southeast shows the smooth, convex up morphology of the central SDM; B) View toward the west shows a bedrock exposure of the exhumed Mai'iu fault surface dipping $\sim 22^\circ$ to the north at the range front; C) View to the north and downdip of the exhumed fault surface showing a parallel network of stream channels in the slip direction; D) Abandoned stream channel (windgap) perched on the main divide of the SDM to the west of Mt Dayman; E) Bedrock exposure of a steeply dipping, up-to-the-north fault (red line) cross-cutting the exhumed bedrock footwall of the Mai'iu fault. A deeply incised stream (Biniguni River) is diverted westward by the south facing scarp of this fault before breaching through the uplifted block as a waterfall and flowing northward down the dip of the fault; (F) Scarp formed by a steep-dipping antithetic fault (red line) cutting the remnant Mai'iu fault surface to the west of Mt Dayman. SDM = Suckling-Dayman Metamorphic Core Complex.

The Mai'iu fault surface north of the main divide is little eroded and well preserved, with several gorges deeply incising the central and eastern SDM (**Figure 2.4A**). Fault surface remnants on the interfluves are trending toward $017\pm4.0^\circ$ (95% conf.), subparallel to the inferred slip direction (see also Daczko et al., 2011); however, some ridges are arranged perpendicular to this dominant trend (**Figure 2.5B**). The exhumed fault surface can be traced continuously ~22 km (pink shading) in the updip direction near Mt Dayman, whereas eroded, south-dipping remnants of the surface can be traced beyond the main divide to a distance of ~28 km (blue shading). We view this last distance as a minimum estimate of the finite slip magnitude on the Mai'iu fault (**Figure 2.4, Figure 2.5**). Still farther south, the remnants become deeply eroded and are difficult to trace. The synformal dip slopes that surround the Gwoira rider block on three sides were formed by the inactive Mai'iu fault. These slopes are smooth and well expressed over a 1- to 6-km-width updip from the fault trace, beyond which they become much incised.

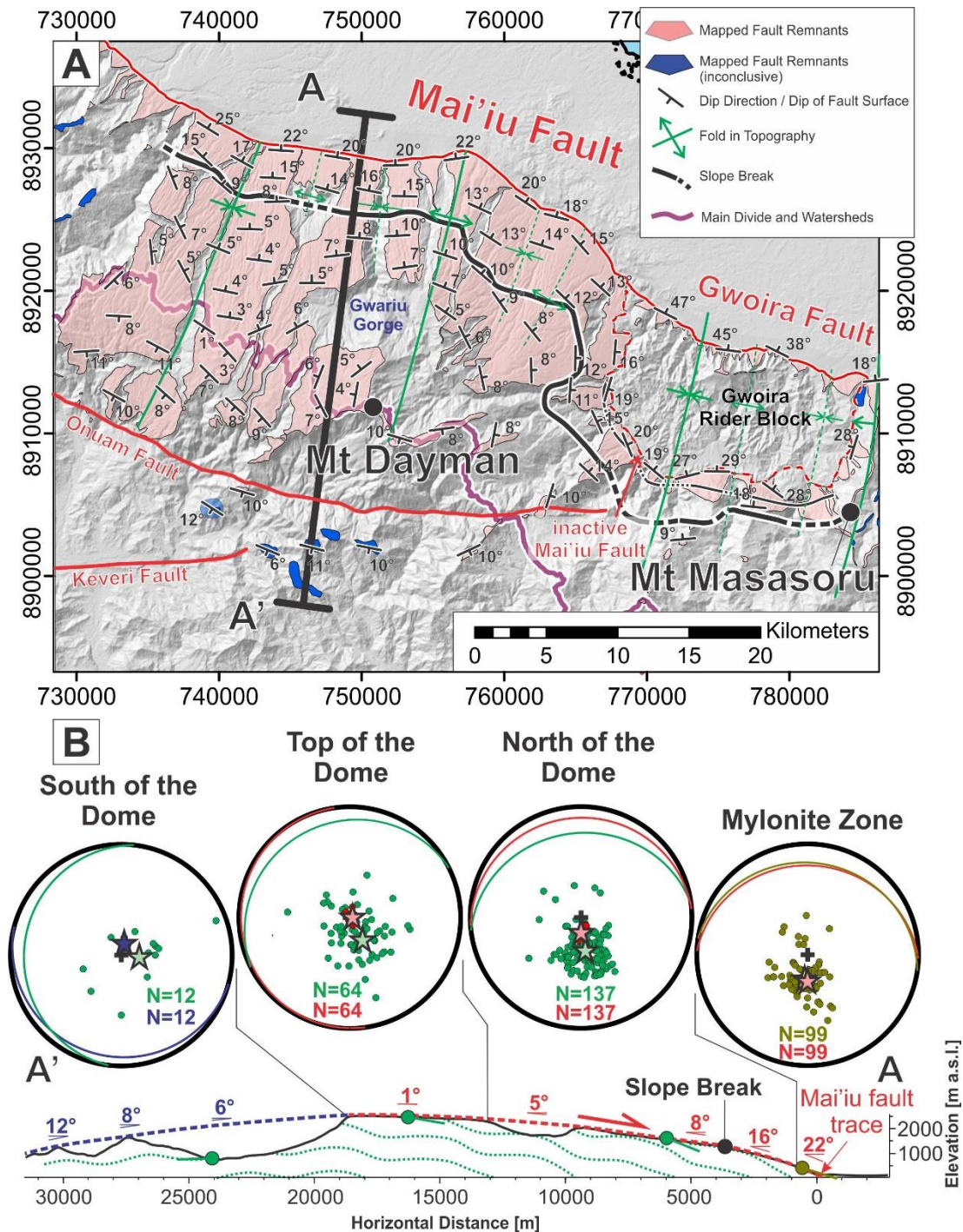


Figure 2.4. A) Map showing remnants of the Mai'iu fault. Shaded relief based on a 30-meter digital terrain model. Pink, mapped fault surface remnants; Blue, possible fault remnants. B) Cross-section of the exhumed fault surface. This includes lower-hemisphere, equal-area stereograms of poles to the dominant (non-mylonitic) foliation in the Goropu Metabasalt (green dots), Neogene mylonitic foliation (gold dots), and the exhumed Mai'iu fault surface (red and blue dots) for four domains at varying distances up the scarp. Great circles and stars represent average dip-direction/dip of measured data (mean plane). Dip-tick “tadpoles” shown on cross-section are average apparent dips of the foliation in the domain represented by the stereogram above.

Based on an analysis of near-trace dip slopes and direct measurements of the outcropping fault surface, the active Mai'iu fault has an average dip of $\sim 21 \pm 4^\circ \text{N}$ ($\pm 2\text{SD}$) in the near-surface, while locally dipping at as low as $\sim 15^\circ$. Farther south, the fault is warped to shallower dips, cresting subhorizontally across the main divide of the SDM, beyond which it reverses dip direction to dip at $12 \pm 6^\circ \text{S}$ ($\pm 2\text{SD}$, **Figure 2.4**). The eastward continuation of the Mai'iu fault, bounding Mt Masasoru, has a near-trace dip as low as 12°N . In contrast to the convex up antiformal geometry of most of the SDM, smooth dip slopes surrounding the Gwoira rider block define a synformal embayment and megacorrugation (**Figure 2.5A** and **5C**). The inactive segment of the Mai'iu fault beneath the rider block plane has a concave-up morphology, dipping 14°E , 29°N , and 28°W on its western, southern, and eastern flanks, respectively. Based on outcrop data, the active Gwoira fault, bounding the rider block to the north, dips $\sim 42 \pm 7^\circ \text{N}$ (Little et al., 2019).

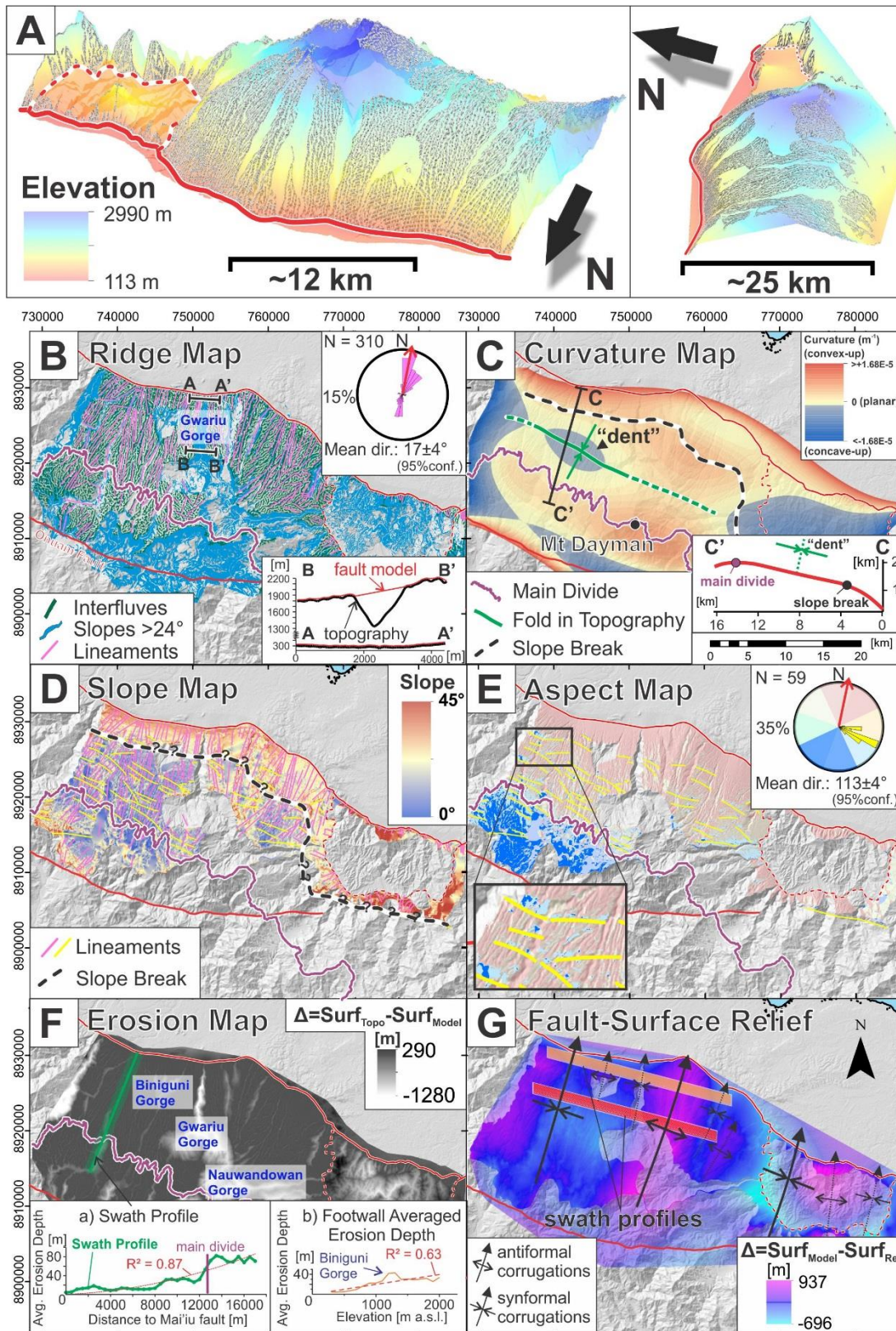


Figure 2.5 (previous page). Fault surface modeling. Scale bar for maps B-G in 5C. A) Fault surface model showing the remnant points used for the natural neighbor interpolation as viewed from the NW (left) and W (right). B) Ridge map showing the remnants of the fault surface on the interfluvies bounded by slopes inclined at $>24^\circ$. Pink lines highlight the dominant trend of ridges. Inset shows a rose diagram with the orientation of the ridge-parallel lineaments. The two strike-parallel profiles show the relationship between modeled fault surface and incisional topography: Profile A-A': cross-section close to the fault trace; Profile B-B': cross-section across the Gwariu River gorge farther up the scarp. C) Curvature map of the fault surface. Here, a positive curvature value (red) indicates a convex up surface; a negative value (blue) indicates a concave-up surface. Green line highlights fold in topography defined by change in curvature. Inset: Topographic profile of the fault surface model (exaggerated in elevation). D) Slope map representing the dip of the fault surface indicating a break in slope at ~ 3.8 km from the fault trace. Lineaments from the ridge (pink) and aspect map (yellow) are superimposed on this map. E) Aspect map representing the local dip-direction of the modeled fault surface. Red colors represent dips to the north; blue colors dips to the south; yellow lines highlight areas (especially south facing scarps north of the main divide) that dip in the opposite direction to the general NNE fault surface dip; inset shows a rose diagram with the trend of these lines of slope-aspect reversal. F) Erosion map represented by the subtraction of the fault surface model from the topography ($\Delta = \text{Surf}_{\text{Topo}} - \text{Surf}_{\text{Model}}$). Darker color indicates less erosion. Inset a) demonstrates averaged erosion depth as a function of distance to the Mai'iu fault along the green swath profile. Inset b) shows footwall averaged erosion depth as a function of elevation north of the main divide. G) "Fault surface relief" map derived from subtracting the 4th-order polynomial reference surface from the fault surface model. Black arrows—trend of megacorrugations; orange swath—slip-perpendicular profiles below slope break (N=20); red swath—slip-perpendicular profiles above slope break (N=20).

By comparing the dip of the foliation as measured in outcrop in the exhumed footwall, with the dip and dip-direction of the overlying exhumed fault surface as modeled in **Figure 2.5** on a slip-parallel profile (**Figure 2.4B**), we show that the progressive shallowing of the fault is matched by a corresponding progressive tilting of the mylonitic to non-mylonitic foliation of the Goropu Metabasalt in the subjacent footwall (Little et al., 2019). Foliation data on the southern flank of the eroded dome are derived from unpublished field books (1968) and field sheets (Australian Geological Survey Organization; orientation data are partially published in Smith & Davies, 1976; see Appendix A.2, **Table A.1** for locations). The Neogene mylonitic foliation near the fault trace is subparallel to the smooth exhumed fault surface and has an average dip of $18 \pm 3^\circ$ (95% conf., N=99) to the NNE. Farther up the scarp, the average dip of the pre-existing, non-mylonitic foliation is $25 \pm 3^\circ$ (95% conf., N=137). The foliation is consistently $\sim 14^\circ$ more steeply north dipping than the fault surface above it, but both dip in the same direction to the NNW. On top of the SDM the fault

surface is essentially horizontal (dips $\sim 2^\circ$ to the west). At the same location, the non-mylonitic foliation dips to the NW at $14^\circ \pm 5^\circ$ (95% conf., N=64). The southern remnants of the fault surface dip $\sim 9^\circ$ to the SSW, whereas the foliation in that region dips to the west at $13^\circ \pm 19^\circ$ (95% conf., N=12). We attribute most statistical scatter in the foliation dip data to postmetamorphic folding associated with a pervasive crenulation foliation that deforms it (see Section 2.6). Despite the angular discordance of $\sim 14^\circ$ between the Mai'iu fault plane and the steeper non-mylonitic foliation beneath it, both surfaces are bent in tandem up the dip of the SDM through an angle of $26\text{--}28^\circ$ showing that both surfaces have been equally affected by the footwall back-warping.

A fault-strike parallel locus of high curvature in the exhumed fault surface occurs 3.8 ± 1.1 km (± 1 SD) south from the Mai'iu fault's frontal trace (**Figure 2.4, Figure 2.5C, 5D**). This curvilinear zone of enhanced convex upward curvature accommodates northward-steepening of the exhumed surface of $\Delta 8 \pm 3^\circ$ (± 1 SD) over a zone width of ~ 0.5 km. West of the Gwariu River gorge, the exhumed fault surface abruptly transitions southward from a convex upward curvature (at the above-mentioned slope break) to a concave-up one (**Figure 2.5C**). The curvature anomalies trend subparallel to fault strike. Still farther south, the concave-up fault curvature, transitions back to convex up. These curved features resemble folds. The zone of concave-up curvature is expressed as synformal “dent” in the fault surface, whereas the slope break to the north appears antiformal in morphology (see also topographic profile derived from the fault surface model in **Figure 2.5C**). East of the Gwariu Gorge, fault curvature changes from nearly planar to convex up in geometry in the updip direction, and the northern, upwardly convex slope-break becomes less pronounced and higher in elevation. This dome-wide curvature pattern is superimposed by many shorter-wavelength reversals in curvature polarity and slope aspect on the exhumed fault surface (**Figure 2.5E**). We interpret these smaller, more discontinuous (i.e., ~ 100 s of m-long) curvature anomalies as south facing fault scarps that cut the fault surface. This interpretation was verified in the field at six localities (see Section 2.6 and **Figure 2.8**). These scarps on average strike $113 \pm 4^\circ$ (95% conf.) subparallel to the strike of the Mai'iu fault, and they correspond to steep faults in the bedrock of the footwall (e.g., **Figure 2.3E, F**). Note, the aspect map captures only some of the most conspicuous examples of the steep faults cutting the footwall that are observed in this study (see Section 2.6.1, below).

Figure 2.4 plots the trace of several conspicuous slip-parallel megacorrugations (both antiformal and synformal) in the exhumed surface of the Mai'iu fault. Little et al. (2019) showed that some of these corrugations affect not only the topography of the Mai'iu fault surface but also the underlying footwall foliation. They inferred this to be an expression of constrictional deformation. The largest megacorrugations are laterally continuous and can be mapped updip from the fault trace for 13–23 km horizontally. They span the entire width of the exhumed fault surface, affirming that the Mai'iu fault represents a single, continuously exhumed structure. Slip-perpendicular profiles (N=40) across the “fault surface relief” map (**Figure 2.5G**) show that most large corrugations have amplitudes of 220 ± 50 m and wavelengths 11.9 ± 1.0 km ($\pm 2SD$), downdip of the slope break. The same values are 290 ± 40 m and 11.5 ± 1.4 km ($\pm 2SD$), respectively, updip of the major slope break (**Figure 2.6A**). The slightly higher amplitude of corrugations in the updip area is largely influenced by the aforementioned concave-upward curvature anomaly (so-called, fault plane “dent”) in that region (**Figure 2.5C**). Slip-parallel profiles across this are presented in Appendix A.1 (**Figure A.2**). The very largest corrugations on the SDM have wavelengths of 20–40 km and amplitudes of between 300 and 800 m. Additionally, former NNE-trending stream channels on the eastern flank of the antiformal megacorrugation near Mt Dayman now drain eastward, and Pliocene strata in the rider block are synclinally folded—relationships that Little et al. (2019) attributed to landscape tilting during near-surface amplification of the corrugations as fold-like structures. In the PSD-plot of **Figure 2.6B**, the averaged power spectra of the below-slope-break (orange) and above-slope-break (red) slip-perpendicular profiles line up at a wavelength of ~ 300 m, which coincides with the overall stream-spacing attributed to synformal corrugations (Spencer, 2010; Daczko et al., 2011). At higher wavelength, the averaged power spectra show an identical scaling behavior expressed by the same Hurst exponent of $\zeta=0.68\pm0.04$ ($\pm 2SD$, **Figure 2.6B**). The obvious lateral continuity of the megacorrugations in the DTM and the fault model and the similar scaling behavior across the SDM affirm that the Mai'iu fault is a single continuously exhumed surface.

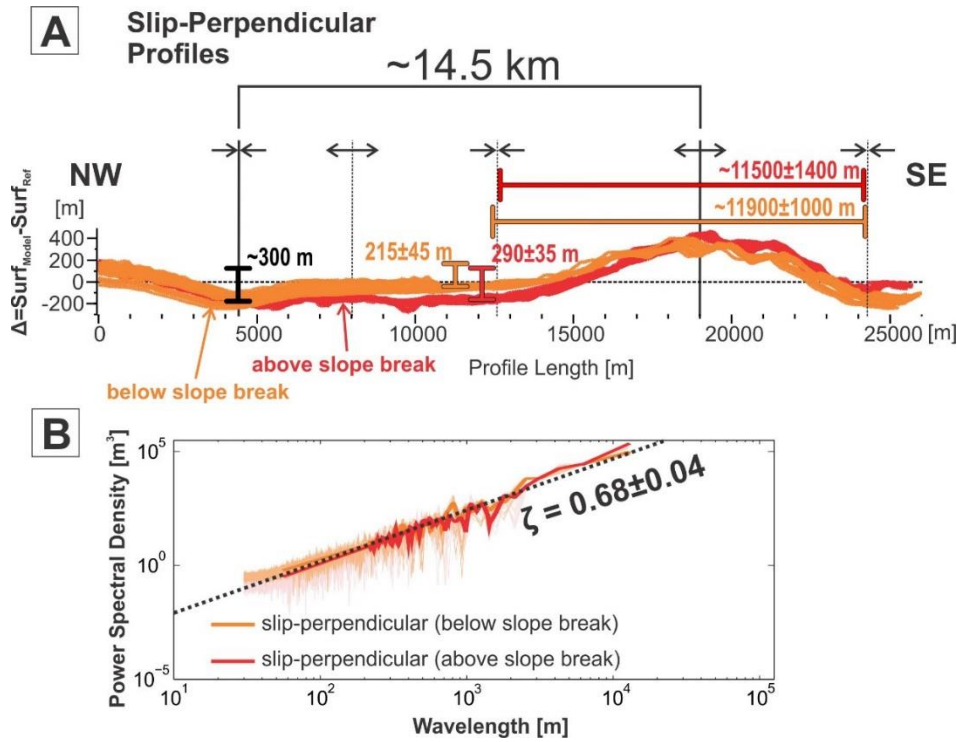
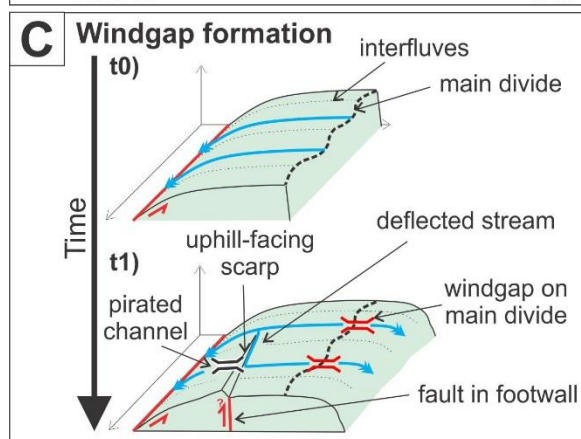
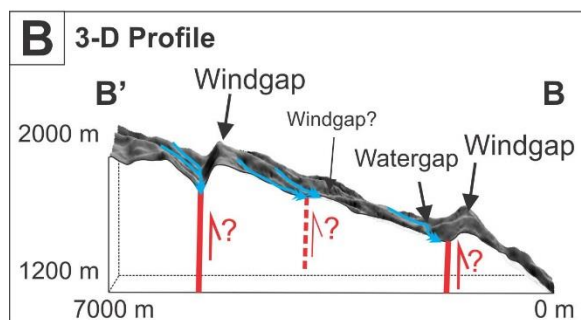
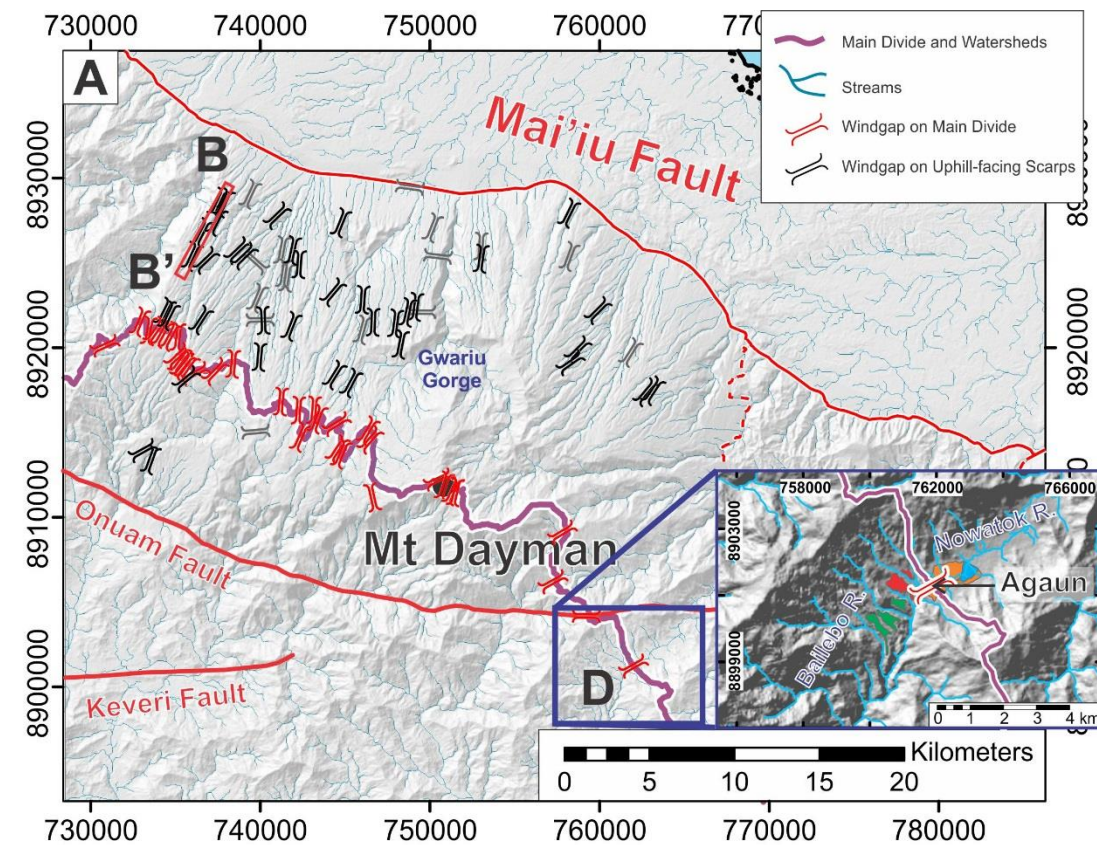


Figure 2.6. A) Slip-perpendicular profiles derived from the “fault surface relief” map in Figure 2.5G. Note, profiles are exaggerated in elevation relative to profile length. B) Power spectra density (PSD)-plot with a compilation of slip-perpendicular roughness data: ζ —Hurst exponent; Light colored lines—stacked roughness spectra; Dark colored lines—averaged spectra.

We constructed an erosion map of the SDM by subtracting the modeled fault surface from the modern topography ($\Delta = \text{Surf}_{\text{Topo}} - \text{Surf}_{\text{Model}}$; **Figure 2.5F**). The erosion map shows that there is little erosion of central and eastern parts of the Mai’iu fault surface, except in the deeply incised Biniguni, Gwariu, and Nauwandowan river gorges, and on the southernmost flank of the SDM. The graph to the left in the inset of **Figure 2.5F(a)** shows calculated averaged erosion depth as a function of horizontal distance to the trace of the Mai’iu fault along a slip-parallel swath profile of 2-km width. It shows a nonlinear trend of increasing erosion along the typically convex up shaped stream profiles relative with distance from the fault trace. This nonlinear increase in erosion continues across the main divide ($R^2=0.87$). **Figure 2.5F(b)** shows overall averaged erosion depth of this part of the SDM to the north of the main divide as a function of elevation. Mean erosion depth at elevations $>2,000$ m is mainly controlled by localized incision in the deep Gwariu and Nauwandowan gorges. This gorge contribution is excluded in the graph of 5F(b). Compared to the left-hand swath profile, the footwall averaged erosion depth increases with elevation in an approximately linear trend ($R^2=0.63$).

2.5 DRAINAGE NETWORK AND FLUVIAL GEOMORPHOLOGY

Uplift, tilting, and fault scarp development in the footwall of the Mai'iu fault are recorded by the deflection and local piracy of stream channels, and by deformation of fluvial terraces. In order to characterize the drainage network on the exhumed surface of the Mai'iu fault, streams were constructed from the 30-meter DTM using hydrology tools in ArcGIS 10.1 and compared with conventional topographic maps (AMS, 1:50000 topographic survey, 1989) and aerial photography (**Figure 2.7**). The remarkably linear stream pattern of the SDM, dominated by slip-parallel channels regularly spaced at 150–300 m (**Figure 2.3C**, **Figure 2.7**), has been inferred to be controlled by synformal corrugations in the fault surface that are occupied by the streams (Spencer et al., 2010; Daczko et al., 2011). Some streams are locally jogged in approximate perpendicularity to the dominant NNE flow direction before deflecting back to that dominant trend. Where such stream deflections were observed by us in the field, the stream channels are bounded by south facing scarps. The south facing scarps and their associated stream deviations are clearly evident in aerial photographs and DTMs, one example of which is shown in **Figure 2.7B**.



D Tilted Fluvial Terraces (Agaun)

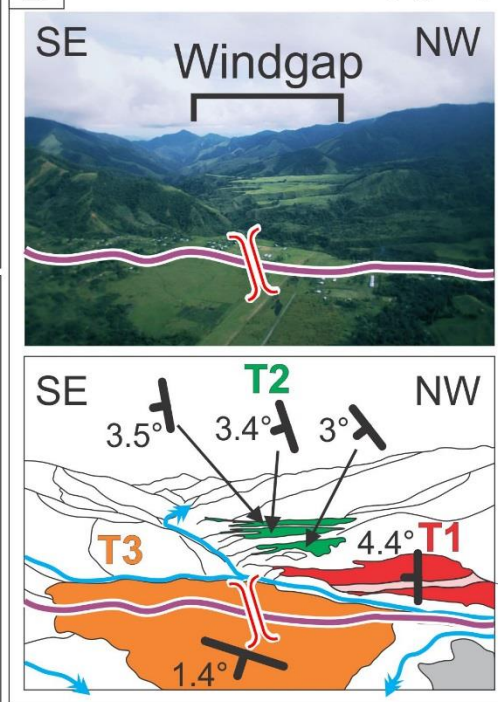


Figure 2.7 (previous page). A) Hillslope shaded DTM showing drainage pattern and plotting location of the main divide (thick purple line) of the SDM. The map shows the location of windgaps: some on the main divide, others on the south facing scarps of northside up faults that cut the generally NNE-draining, exhumed fault surface. Inset shows the location of Agaun Village and its fluvial terraces. B) A slightly oblique 5-meter DTM derived 3-D profile showing south facing scarps (northside up) and associated windgaps. Location of the 3-D profile is indicated in A. C) Model for windgap formation; t0: representative point in time during progressive footwall uplift and warping; t1: Advection of slip-parallel drainages over the dome crest and drainage reorganization related to south facing scarps (faults?) formed during subaerial exposure. D) Upper photo looking SW shows the village of Agaun and fluvial terraces; below, an interpretation of the studied terraces and their attitudes (dip-direction/dip).

Many stream channels are continuous across the crest of the SDM (main divide; purple line in **Figure 2.7A**), across which their flow direction reverses (**Figure 2.3D**). The abandoned parts of the stream channels perched atop the main divide of the SDM are windgaps (red symbols in **Figure 2.7**). Following Spencer (2010), we infer that the windgaps formed during the updip southward tectonic advection of the footwall as a result of fault slip, together with southward back-tilting of the landscape leading to a reversal in slope direction over the crest of the SDM (**Figure 2.7C**). Other windgaps to the north of the crestal divide formed as a result of stream piracy resulting from uplift of the south facing scarps that cut the exhumed fault surface (black windgap symbols in **Figure 2.7A**). The three-dimensional profile in **Figure 2.7B** shows that the streams, bounded by these scarps, abandon their former uplifted, downstream channel and deflect either to the right or left to follow a new channel that drains laterally along the south facing scarp. Channel abandonment creates a windgap that is perched above the scarp on the northern, uplifted block. Such a trellis drainage pattern conceivably might form by differential erosion along the boundary between more resistant and less resistant formations, but our field observations affirm that these deflections, and the nearby windgaps, occur along south facing fault scarps. Because the fault scarps deflect pre-existing streams that had already been established on the otherwise mostly NNE draining, exhumed fault surface, we infer that the antithetic-sense faults are active or late Quaternary in age (**Figure 2.7C**).

The village of Agaun, located SE of Mt Dayman within the Agaun Valley at about 980-m elevation above sea level, hosts the largest and deepest windgap on the crestal divide of the SDM. Here, the Nowatok River drains to the NE and the Bailebo River to the SW (**Figure 2.7A, D**). The ridges on either side of the streams rise to

~1,800 m above sea level. Within the Agaun Valley, the Goropu Metabasalt is unconformably overlain by ~100 m of unconsolidated alluvial sediments (conglomerate, sandstone, and siltstone) that Smith and Davies (1976) called the Agaun Conglomerate (inferred Pleistocene age). The Agaun Conglomerate forms a series of well-developed, gently north dipping alluvial terraces in Agaun Valley that also extend south of the main divide for about 2 km south into the upper reaches of the Bailebo River. There, the gently inclined terraces are perched on the flank of a deeply incised and steeply SW-draining river gorge (Smith & Davies, 1976).

We extracted surface slope information from a 5-meter DTM of the terrace flight to measure tilt (dip-direction/dip) on five terraces, namely (from the oldest to the youngest): T1, T2_A, T2_B, T2_C, and T3 (**Figure 2.7D**, see Appendix A.3 for methodology, error calculation and additional cross-section). T1 is the highest and presumably the oldest terrace with an elevation of 1,027 m. It dips SE at 4.4°. The local morphology and slope aspect of T1 is controlled in part by an apron of colluvial deposits, sourced from the NW wall of the valley that partially buries the original alluvial terrace. The A, B and C terraces of T2 form a younging flight of terraces that are arranged (respectively) from the SW to NE. The gentle terraces are incised by the steeply SW-draining Bailebo River. They lie at average elevations of 1,014, 1,012 and 1,004 m. Their treads dip SE at slopes of 3.5°, 3.4° and 3.1°, respectively. By contrast, the upper reaches of the Bailebo River slopes downward to the SW at 4.4–6.1°. Just south of the terraces, the river is inclined to the SSW at 17.3–19.4°. The youngest of the Nowatok river terraces are located in the bottom of Agaun Valley. The tread of T3, located directly on the main divide at Agaun village, has a mean elevation of ~982 m and dips ENE (i.e., toward the Nowatok River) at 1.4°. NE of Agaun village, other terrace remnants of the Nowatok River dip NE at 0.4°. The nearby Nowatok River below them slopes NE at 1.1–1.7°.

We interpret the above described differential tilting in the terrace flight to record a history of progressive southward tilting of an originally NE dipping set of Pleistocene fluvial terraces of the Nowatok River. This rotation took place about a subhorizontal rotation axis that is approximately E-W trending. Without paleocurrent data we cannot rule out that terraces on the SW side of the main divide may have formed by the Bailebo River. However, given the steep SW gradient and incisional character of the modern Bailebo River in contrast to the thick and aggradational character of the gently

inclined Agaun terrace, the apparent continuity of the Agaun terraces with others on the Nowatok River and the temporal progression in the dip directions of the Agaun terraces parallel to the Nowatok River in the youngest terrace but becoming more southerly in dip with increasing age (and distance south), we believe that our interpretation is the simplest. Indeed, such south-tilting must be what caused the deep windgap to exist at Agaun in the first place. The Nowatok River was advected and warped southwardly across the main divide.

2.6 LATE-STAGE FOOTWALL DEFORMATION STRUCTURES

2.6.1 Footwall Faults Cutting the Exhumed Mai'iu Fault Surface

We mapped steep faults cutting the exhumed footwall using field observations of bedrock and tectonic landforms, interpretation of aerial photography, and analysis of the 5-meter and 30-meter gridded DTMs. The following lines of evidence were used to identify faults cutting the exhumed fault surface: (1) stream deflection; (2) topographically defined slope convexities and anomalously steep slopes; (3) stream piracy; and (4) anomalous slope aspect (i.e., south facing). Our field observations confirmed the existence of south facing scarps at six different localities on the footwall. Uncertainties are related to limitations in resolution of the DTM, poor exposure, rainforest cover in aerial photography and postformational erosion.

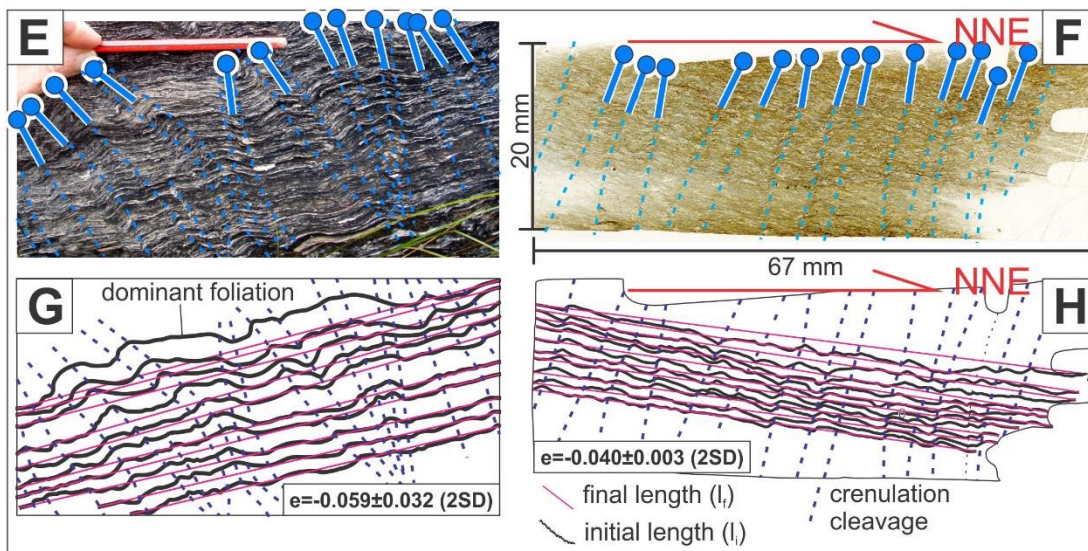
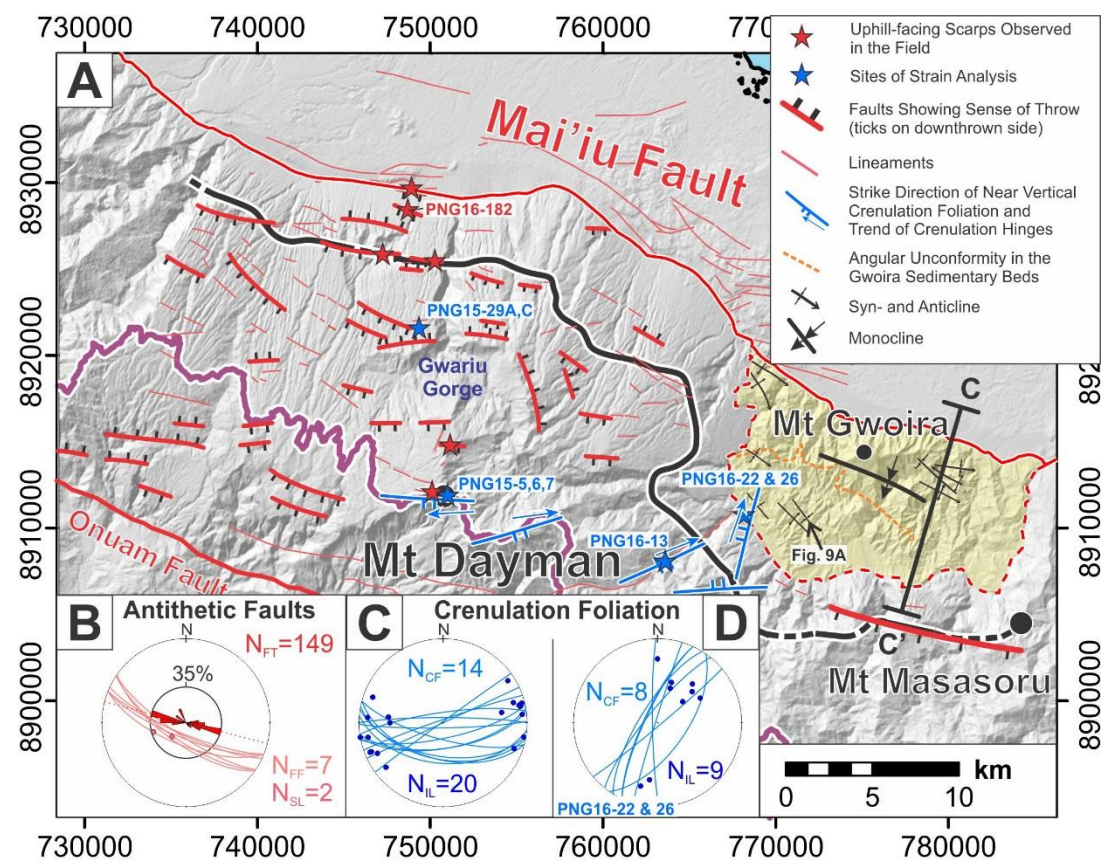


Figure 2.8 (previous page). Late structures deforming the exhumed footwall of the Mai'iu fault. A) Map showing the trace of faults that cut the abandoned footwall of the Mai'iu fault surface, the attitude of post-mylonitic crenulation foliations observed in the Goropu Metabasalt, and the trend of fold hinges deforming Pliocene strata in the Gwoira rider block (yellow shading). B) Stereogram (lower-hemisphere, equal area) showing the orientation of an antithetic-sense footwall fault (N_{FF}) and its slickenlines (N_{SL}) as observed in a bedrock outcrop at site PNG16-182. The rose diagram inset inside of the stereogram shows the angular distribution of strike directions of all the fault traces (N_{FT}) mapped by us in the exhumed footwall ($N_{FT}=149$; mean strike of $107\pm 7.2^\circ$; 95% conf.). Parts C and D): stereograms (equal area, lower hemisphere) showing orientations of the late crenulation foliation (N_{CF}) and its associated intersection/crenulation lineation (N_{IL}), across the central part of the SDM (part C) (for a more detailed map see Little et al., 2019), and along the western flank of the Gwoira embayment (Part D, corresponding to locations PNG16-22 and PNG16-26). E) Photograph of crenulation foliation in outcrop (PNG15-5, view direction is to the ENE), the enveloping surface (dominant foliation) has a mean orientation of $275^\circ N/14^\circ$. F) Scan of thin section (PNG15-29C) with a mean dominant foliation orientation of $351^\circ N/20^\circ$. G and H) Interpretation of the samples used for analysis of shortening strain accommodated by late-stage crenulation microfolding.

In the central and eastern part of the SDM, including near Mt Dayman, footwall faults have strike length of >200 m, reaching a maximum of 5.5 km (**Figure 2.8**). Based on their topographic expression, the faults are (a) chiefly northside up in dip slip sense and have a mean throw of 18.1 ± 15.6 m ($\pm SD$, $N=46$); and (b) subordinate to these antithetics are northside down (synthetic) faults. These have a mean apparent throw of 38.9 ± 21.6 m ($\pm SD$, $N=22$). The antithetic-sense faults are marked by south facing scarps and cause E-W deflections in the otherwise linear, NNE flowing streams (as described above). We confirmed this relationship at several fault outcrops in bedrock. At one locality (**Figure 2.8**; PNG16-182) a fault plane causing a 10-m northside up throw of the landscape is exposed in bedrock. The fault has a dip of $\sim 78^\circ$ to the SSW and slip striae that plunge nearly downdip (**Figure 2.8B**). The Mai'iu fault slip surface here dips $16\text{--}20^\circ$ to the NNE, whereas the foliation dips $\sim 30^\circ$ to the NE. The foliation is subject to a contractional heave across the steeper-dipping antithetic fault. Farther up the scarp the foliation is only gently dipping to the north (**Figure 2.4**). If the fault-foliation cutoff angle remains the same ($\sim 72^\circ$), antithetic faults cutting the upper part of the SDM may have been back-tilted through the vertical to become reverse in sense. Both the synthetic- and antithetic-sense faults are widely distributed on the SDM and both strike subparallel to the Mai'iu fault at $107\pm 7.2^\circ$ (or 287° ; 95% conf.; **Figure 2.8B**). Taken together, they have an apparent mean cross-strike spacing of ~ 1.5 km. This is likely to be a significant overestimate of the real spacing because

of undersampling of these poorly exposed faults as discerned in aerial photographs and DTMs. Faults with a throw of <5 m, for example, (e.g., **Figure 2.3E**) would be difficult to resolve.

Windgaps are not present on the upthronside of all the south facing scarps, a relationship that may indicate that some faults formed in the subsurface prior to exhumation of the Mai'iu fault surface and the establishment of a drainage network or that postfaulting erosion has removed the windgaps. The thin red lines in **Figure 2.8** are topographic lineaments that are not marked by an obvious scarp on the DTM but that commonly are associated with sharp stream deflections, windgaps, or other geomorphic evidence that we have used to infer their origin as faults.

2.6.2 Folding of Sedimentary Beds in the Gwoira Rider Block

Uplifted Pliocene(?) aged sedimentary rocks in the Gwoira rider block dip consistently to the south. This has been attributed to back-tilting of these sedimentary beds during slip on both the Mai'iu and Gwoira faults (Smith & Davies, 1976; Webber, 2017). An E-W trending monoclinial antiform deforms the older strata in the rider block. Beds on the southern limb of this fold dip more steeply to the south ($\sim 22^\circ$, and locally up to 54°) than those on the northern limb ($\sim 17^\circ$; Webber, 2017). The fold is best expressed in the central-northern part of the rider block (i.e., south of Mt Gwoira; **Figure 2.8A**). Several other smaller folds in the rider block have similarly E-W trending hingelines that are oriented perpendicular to the inferred slip direction (**Figure 2.8A**, **Figure 2.9B**). Where well exposed, the folds have a half wavelength of ~ 500 m (**Figure 2.9B**). The mean axial trace of these folds strikes subparallel to the Gwoira fault at $105 \pm 6^\circ$ (95% conf.). The mean axial planes dip subvertically as inferred by bisecting mean limb dips on either side of each fold. Such folds were observed at all structural levels within the rider block, including the uppermost (dip fanning) strata (**Figure 2.9A**). The young beds are nearly horizontal (Smith & Davies, 1976). In the uppermost part of the rider block, stratal horizons onlap northward against steeper dipping, older strata near Mt Gwoira. Webber (2017) inferred from this relationship that the uppermost strata were deposited after capture of the Gwoira rider block by the Gwoira fault, an event marked by uplift of that fault's footwall. Therefore, the E-W trending folds that deform these beds must have also formed following initiation of the Gwoira fault. We believe that the E-W trending folds in the rider block document late-stage N-S compression in the footwall of the Gwoira fault.

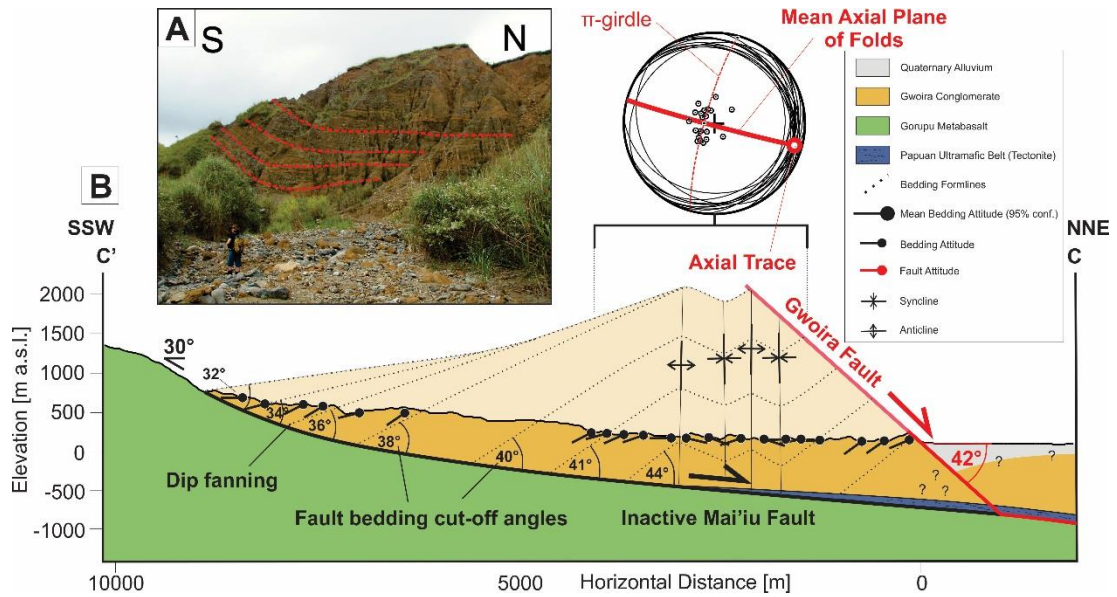


Figure 2.9. A) Photograph of synclinally folded Gwoira Conglomerate in the upper, most nearly flat-lying part of the Gwoira rider block (location is shown in Figure 2.8A). The fold hinge is E-W trending. B) Cross-section C-C' across the Gwoira rider block. For location of the section, see Figure 2.8. Bedding data are compiled from detailed maps in Little et al. (2019) and Webber (2017). Stereograms (lower-hemisphere, equal-area) showing bedding orientations (great circles and poles) within a 2 km wide swath of the cross-section line.

The rider block is also important for allowing estimates of bedding-fault cutoff angle as constraints on paleofault dip. Beneath the Gwoira rider block, the subsurface shape of the inactive Mai'iu fault has been modeled in 3-D using the program Leapfrog Geo (Webber, 2017). This model, a cross-section of which is presented here in **Figure 2.9B**, is underpinned by a rich dataset—the smooth dip slopes that surround the Gwoira rider block, like an amphitheater, on three sides (**Figure 2.4A**). North of **Figure 2.9B**, further constraints on fault shape are provided by the distribution of microseismicity (Abers et al., 2016); however, the deeper, downdip geometry of the Mai'iu fault is not important here. **Figure 2.9B** shows (1) that within the Gwoira rider block, the inactive Mai'iu fault is concave-up and dips shallowly ($\sim 5^\circ$) at a depth of ~ 800 m; and (2) that north of the Gwoira fault, the Mai'iu fault—still active at depth—becomes convex up to link with the microseismically active part of the Mai'iu fault at 12- to 25-km depth (Abers et al., 2016). In **Figure 2.9B** we graphically estimate bedding-fault cutoff angles based on a downward projection of observed stratal surface dips to meet the fault model underneath. There are, of course, uncertainties associated with this estimation. We point out, however, that relative to fault dip slopes observed at the southern end of the rider block—which dip north at $>15^\circ$ (**Figure 2.4A**)—the

modeled fault surface dips more gently ($\sim 5^\circ$). The effect of using the model, therefore, has been to reduce any estimate of cutoff angle. In our opinion, our estimates of cutoff angles are realistic and conservative. The estimated cutoff angles of the deeper sedimentary strata range from $40\text{--}44^\circ$, implying that the Mai'iu fault had this dip at the surface during early deposition of the coarse-grained Gwoira Conglomerate derived from the erosion of its mafic footwall.

2.6.3 Microfolding of Foliation in the Goropu Metabasalt

Postmetamorphic microfolding is widespread in the exhumed footwall of the Mai'iu fault where it shortens the dominant foliation in the Goropu Metabasalt. An upright crenulation foliation is pervasively developed in both non-mylonitic and mylonitic footwall rocks. In the non-mylonitic footwall, good outcrops of microfolded foliation occur near Mt Dayman in Goropu Metabasalt, and also farther to the SE in areas of dominantly pelitic schist (**Figure 2.8E**). In metabasalt, an upright crenulation foliation is evident in most thin sections that are cut subparallel to the dip-direction of the Mai'iu fault (**Figure 2.8F**). In the west, the crenulation foliation strikes subparallel to the Mai'iu fault, having a mean attitude of $282^\circ/\text{S}/56^\circ$ ($N=14$), while crenulation hinges on average plunge gently toward 077° or 257° ($N=20$; see stereogram inset in **Figure 2.8C**). On the eastern flank of the SDM at locations PNG16-22 and PNG16-26 the crenulation foliation strikes $205^\circ/\text{W}/76^\circ$ ($N=8$) while crenulation hinges generally plunge toward 047° or 227° (**Figure 2.8D**). Thus, the strike of the crenulation foliation deflects anticlockwise on approaching the reentrant of the Gwoira depression from the west (**Figure 2.8A**). In other words, the crenulation microfolds record N-S shortening in the center of the SDM where the Mai'iu fault strikes E-W; whereas farther east on the margin of the southward indented Gwoira embayment, they record a more nearly E-W direction of shortening. At all locations the crenulation fabric deforms the preexisting metamorphic foliation. Infilling of local dilation sites by calcite is the only evidence for new mineral growth during this deformation. Although the crenulations are not yet dated radiometrically, the fabric clearly postdates the mylonitic fabric, which it overprints near the range front. The mylonitic fabric is extensional in origin and is of likely Plio-Quaternary age (Little et al., 2019). Thus, like the aforementioned folds of bedding in the Gwoira rider block, the structures record a post-Pliocene increment of horizontal contraction in the footwall of the central Mai'iu fault that is subparallel to the regional extension direction.

By measuring the length of a crenulated foliation surface (the initial length, l_i) and the final length (l_f) perpendicular to the trace of the crenulation cleavage, a minimum estimate of shortening strain (relative to the foliation) can be made (Johnson & Williams, 1998). We measured contractional strain in two outcrop photos and four thin sections assuming constant volume and plane strain deformation. The cut surfaces of the thin sections are 5×7.5 cm and approximately perpendicular ($70\text{--}90^\circ$) to the intersection lineation between the crenulation cleavage and dominant foliation. We did 10 measurements per sample and calculated the average shortening using the standard expression for change in length of a line. Sample locations are highlighted in the map of **Figure 2.8**. The estimated shortening strain in the analyzed samples vary between -4.0% and $-4.9 \pm 1.6\%$ ($\pm 2\text{SD}$). A weak crenulation foliation could also be identified in most other thin sections of footwall mafic schist; however, these samples were less suitable for strain analysis, because their orientation was not exactly parallel to local fault dip. Measurements of crenulation foliation shortening strains were also undertaken at an outcrop-scale near Mt Dayman from digitized photographs. The estimated strain in those outcrops are $-5.9 \pm 3.2\%$ ($\pm 2\text{SD}$) close to the dome's summit (PNG15-5), and $-9.6 \pm 4.8\%$ ($\pm 2\text{SD}$) in a river valley southeast of it (PNG16-13).

2.7 DISCUSSION

2.7.1 “Rolling-Hinge” Style Deformation of the Footwall

Our field and geomorphic observations show that the SDM exposes a single, continuous exhumed fault surface that is smoothly curved. Megacorrugations on this surface can be traced across the entire width of the exhumed fault, and there are no significant differences in the Fourier-based power spectra density curves at different distances along the slip direction (**Figure 2.4**, **Figure 2.5**, and **Figure 2.6**). We interpret the approximately linear increase in the mean depth of erosion with distance in the updip slip direction as an age-related relationship that pertains to a single, continuously exhumed fault surface; that is, the higher slopes are progressively older and more deeply eroded than the lower slopes (**Figure 2.5F**). One possible interpretation (not favored by us) for the slope break about ~ 3.8 km south of the Mai'iu fault trace (**Figure 2.4A**, **Figure 2.5C** and **5D**) is that it might represent an intersection between two different low-angle fault surfaces that differ in a dip by only $\sim 8^\circ$ (e.g., Lister & Davis, 1989; Gans & Gentry, 2016). Our data are incompatible with this interpretation: 1) the megacorrugations are continuous across the slope break; 2) the

scaling behavior of the fault roughness does not change across the slope break; and 3) the depth of erosion progressively increases in updip slip direction. Finally, 4) there is no down-faulted wedge of upper plate material (e.g., conglomerate) emplaced between two faults. These observations confirm that the smooth, dome-shaped landscape surface in the SDM represents a single, continuously exhumed fault plane. Our preferred interpretation is that the $\sim 8^\circ$ break in slope near the range front represents a line of sharp flexure in the footwall, across which the sense of curvature in the deformed fault surface changes from convex up to concave-up in a southward direction. The curvature reversal is fold-like, and we suggest that it may record N-S contraction and associated flexure in the exhumed footwall (**Figure 2.5C**).

The overall convex up shape of the exhumed, upper part of the Mai'iu fault is obvious from the topographic and structural shape of the SDM (**Figure 2.3A**, **Figure 2.4A**, and **Figure 2.5A**). Further evidence for this shape is provided by the distribution of inferred on-fault microseismicity on the downdip and still-active part of the Mai'iu fault. Abers et al. (2016) documented a corridor of microseismicity that dips $30\text{--}40^\circ$ at depths of 12–25 km, and that this zone of activity is colinear with the Mai'iu fault trace (**Figure 2.2B**). The estimated maximum burial depth of the mylonites is 20–25 km, based on pseudosection calculations of the mafic mineral assemblage (Daczko et al., 2009). If the fault is planar, and dips at 20° throughout the upper crust, then this amount of exhumation would require a finite dip-slip of ~ 59 km. For a convex up shaped fault that matches the corridor of microseismicity, the required dip-slip is less, $\sim 37\text{--}45$ km. The latter estimate more nearly matches the preserved width of the exhumed fault surface (~ 30 km), and thus seems more likely. The overall convex upward fault shape, steepening downward to a dip of $30\text{--}40^\circ$ at depth provides strong evidence for “rolling-hinge” behavior. By implication, the footwall of the SDM has been bent through $40\text{--}50^\circ$ in the process of being exhumed through its flat crest and continuing to a reverse dip of $>10^\circ$ on its southern side.

The expected magnitude of flexural back-rotation in the footwall of the SDM is confirmed by the progressive change in dip (southward shallowing) of foliation in that footwall (**Figure 2.4B**). Moreover, active back-rotation in the footwall is recorded by windgap formation and by tilting of Quaternary fluvial terraces near Agaun Village (**Figure 2.7A**, **7D**). As noted by Spencer (2010) the formation of windgaps on the crest of the MCC indicates tectonic advection of stream channels over the main divide and

a reversal in their dip direction caused by progressive back-warping of the exhumed fault surface (**Figure 2.3D** and **Figure 2.7C**). We have identified structures accommodating strain in the fault footwall that we believe are related to “rolling-hinge” style bending. These are an array of high-angle faults that strike subparallel to the Mai’iu fault. The faults cross-cut the exhumed surface with throws locally >10 m, and with a dominantly northside up (antithetic) sense of dip-slip (**Figure 2.3E, 3F** and **Figure 2.8A**). The youthfulness of these faults is attested by their offset of the modern drainage on the exhumed fault surface and by the stream piracy related to this (**Figure 2.7B, 7C**). The MCC-wide distribution of the steep footwall faults, and especially their northside up sense of dip-slip might be explained either as (1) a response to far-field extensional stresses (e.g., Manning & Bartley, 1994) or (2) a response to near-surface, hinge-related stresses due to bending/unbending of the footwall or (3) a combination (this is our favored interpretation; see Section 2.7.3). Secondary high-angle faults in oceanic MCCs have been observed cross-cutting the exhumed fault surface in both a synthetic and antithetic sense; these have been attributed to single-beam flexure of the footwall due to its unloading and rollover (Tucholke et al., 1998 and 2008; Karson et al., 2006; Schouten et al., 2010; Haymann et al., 2011). Similar-looking faults have previously been described in some continental MCCs (Spencer, 1985, 2010 and 2011; Axen et al., 1995) and may be of similar origin.

Evidence for late-stage contraction in the footwall of the SDM subparallel to the NNE slip direction of the Mai’iu fault includes ESE-WNW folding of Pliocene strata in the footwall of the Gwoira splay fault (**Figure 2.9**); widespread upright microfolding of foliation, including the extensional mylonitic foliation, about axes subparallel to the local strike of the Mai’iu fault (**Figure 2.8**); and fold-like, ESE-WNW undulations in the abandoned fault surface along a central part of the Mai’iu fault (“dent”, **Figure 2.5C**). We note that the “dent” in **Figure 2.5C** may appear as an almost flat spot suggesting late-stage extension, perhaps due to the spreading weight of the topographic massif, rather than contraction; however, the folding of the fault surface is well-expressed by two corrugations in slip-parallel profiles from the “fault surface relief” map in Appendix A.1 (**Figure A.2C**). Thus, we interpret that the folds with hinges trending ESE-WNW accommodate some N-S shortening in the slip direction. In the Gwoira rider block, such folding might be attributed to adjustments in an extensional critical wedge (Spencer et al., 2016). Little et al. (2019) argue that

this scenario is unlikely and instead attribute shortening strain to footwall unloading and flexure in response to inception of the Gwoira splay fault. The crenulation fabric is pervasive throughout the SDM footwall, overprinting all metamorphic fabrics, including the mylonitic one, which is of Pliocene or younger age. Like the folding of Pliocene strata in the Gwoira rider block, the upright crenulation structures accommodated a NNE shortening across the central SDM. We attribute this late-stage, extension-direction parallel contractional strain to “rolling-hinge” flexure that accompanied the uplift and unloading of the footwall (e.g., Manning & Bartley, 1994). Supporting evidence for that interpretation includes the change in strike of the crenulation foliation in proximity to the Gwoira reentrant of the Mai’iu fault, where the strike of the crenulation foliation deflects to become more northerly (**Figure 2.8A, 8D**). This transition might be expected if the shortening direction tracks the direction of maximum exhumation gradient in the footwall, because this will vary spatially in azimuth if the fault is curved (see Appendix A.4, **Figure A.4**). Close to the southward indented Gwoira depression, where the (inactive) Mai’iu fault is nearly N-S striking, that direction would have been roughly E-W before initiation of the Gwoira fault. To summarize, we attribute a reversal from NNE extension to (dominantly) NNE shortening in the footwall of the SDM during the Pliocene and younger activity of the Mai’iu fault to unloading-related strains that attended “rolling-hinge” style isostatic back-flexure, a process that was presaged by Wernicke & Axen (1988) and Axen & Bartley (1997). We attempt to model this process in Section 2.7.3.

2.7.2 Kinematics of the “Rolling-Hinge” Mechanism

The exposed antiformal shape of the Mai’iu fault can be used to determine the radius and center of curvature of the domal-shaped fault surface (Manning & Bartley, 1994). **Figure 2.10** shows a cross-section of the Dayman Dome with its inferred fault surface and subsurface continuation based on the projected hypocenters of microearthquakes (Abers et al., 2016) from farther east of this cross-section (see **Figure 2.2B**). We drew perpendicular lines to the reconstructed fault surface at every 2.5° change in fault dip. According to this reconstruction the main radius of the antiformal dome, R_{MIN} , is 59.6 km and its curvature, w''_{MIN} , is $1.68\text{E-}5 \text{ m}^{-1}$. Locally higher curvatures (shorter radii) can be measured near the slope break, where the radius, R_{MAX} , is locally as short as 26.4 km, and the curvature, w''_{MAX} , as high as $3.79\text{E-}5 \text{ m}^{-1}$. Radii of other real and modeled footwall antiforms range from 10–60 km with

an average of ~30 km (Spencer, 1984; Block & Royden, 1990; Buck, 1988; Hamilton, 1988; Manning & Bartley, 1994).

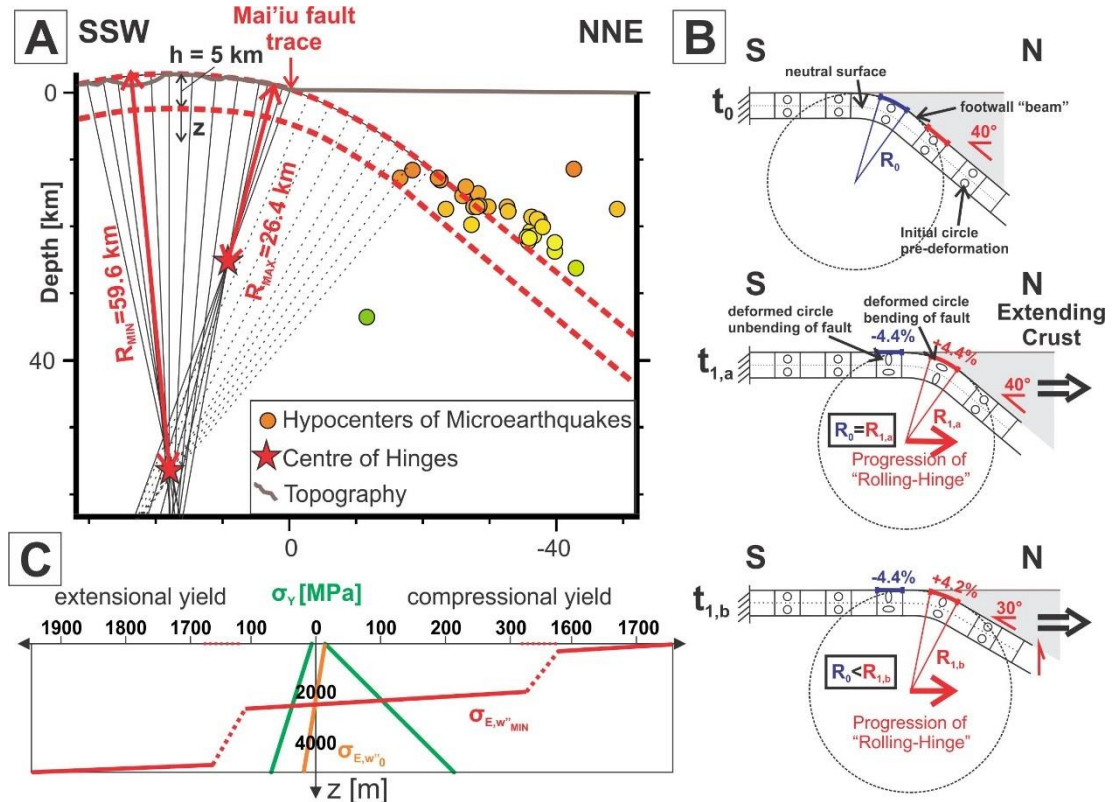


Figure 2.10. A) Cross-section (A-A' in Figure 2.4) and subsurface continuation of the Mai'iu fault. Perpendicular lines to the deformed fault surface define two different radii of curvature; Red stars plot the corresponding centers of curvature ("center of hinges"). B) Flexural hinge model (modified after Manning & Bartley, 1994); t_0 : fault geometry after hinge formation that has been active long enough to flatten the detachment and the top of the exhumed footwall. $t_{1,a}$: Northward advance of the "rolling-hinge" (relative to the exhuming footwall rocks) during fault slip. Blue line on the fault surface exits the hinge and shortens. Red line enters the hinge and stretches. $t_{1,b}$: same as in $t_{1,a}$ but footwall beam shallows in dip relative to earlier. Hinge-related contraction is greater than the incoming extension. Note, unbending of the slab to a shallower fault dip (between $t_{1,a}$ and $t_{1,b}$) causes an increment of footwall contractional strain at the surface—unrelated to passage of rocks through the "rolling-hinge"—that is not depicted in the figure. C) Predicted change of yield stress (σ_Y) and elastic fiber bending stress (σ_E) with depth (z) in a 5 km-thick beam that represents unbending of the SDM footwall (see text and Appendix A.6). The red curve assumes a curvature that is equal to the observed w''_{MIN} of $1.68E-5$ m^{-1} (equivalent to R_{MIN} , see part A). Note, the dotted parts of the red curve indicate a "jump" in the scale; the fiber bending stresses remain continuous across this "jump". For comparison, the orange line assumes a curvature, w''_0 , of $1.69E-7$ m^{-1} . This is the theoretical limiting curvature at the top of an otherwise fully elastic footwall beam.

According to the flexural failure kinematic model of "rolling-hinges" by Manning and Bartley (1994), a flexed fault-parallel line element in the footwall close

to the detachment surface is first elongated as it enters the hinge from below, and later shortened as it exits the hinge above. This steady state concept is shown in **Figure 2.10B**: A line element close to the detachment surface shortens with progressive regional extension when it exits the hinge as shown by the blue line element from time step t_0 to $t_{1,a}$; the red line element that is about to enter the hinge in t_0 extends in time step $t_{1,a}$. If the position and shape of the hinge is fixed, and there is no change in the fault profile as a function of time nor a deflection of the neutral surface, then a line element which has already entered the hinge would be shortened while exiting the hinge by the same amount as it was extended upon entering.

The predicted amount of finite stretching and shortening of 4.4% in **Figure 2.10B** can be calculated from the observed radius of curvature of the fault and the thickness of the flexed beam (**Figure 2.10A**). For the Mai'iu fault, we assume that the thickness of the Goropu Metabasalt, ~5 km, is the beam thickness and that the neutral surface is in the middle of this layer. Using R_{MIN} , these values lead to an estimated longitudinal strain value (on exiting the hinge) of -4% to -9.6%. If the fault profile is not steady state, but changes in shape over time; for example, evolving toward shallower dips together with a net unbending of the slab, as depicted in time step $t_{1,b}$, then the shortening of the line element upon exiting the hinge would increase and be larger than any stretching increment. Cooling of the footwall during exhumation may deflect the neutral surface to deeper depth (e.g., Bodine et al., 1981). This would also result in an increase in shortening of the line element as it exits the hinge relative to an earlier stretching. Far-field extensional stresses would displace the neutral surface to deeper depth where rocks enter the hinge and to shallower depth where rocks exit the hinge meaning that earlier stretching of the line element may exceed later shortening (see Manning & Bartley, 1994). We call the stretching and shortening of these line elements bending and unbending, respectively. Such a deformational sequence might be expected first to cause conjugate extensional faults to form in the footwall that strike perpendicular to the regional extension direction. Of course, such faults may also form in response to the regional extensional stresses (or both). After formation, the faults might be back-rotated on the exhuming footwall, with the antithetic subset of those normal faults being steepened in dip and later reactivated as contractional faults during the “unbending”.

We infer that the steep antithetic faults in the footwall of the SDM played a role in accommodating the “rolling hinge” process—perhaps being reactivated as contractional structures during unbending of the exhuming footwall, as described above. Even without flexure, slip on steep antithetic-sense faults will contribute kinematically to bending and uplift of the exhumed footwall (Spencer, 1984; Wernicke & Axen, 1988; Wdowinski & Axen, 1992). While taking into account that the mean spacing of these faults is likely shorter than what we were able to map, simple strain calculations show that it is unlikely that the full footwall rotation in the SDM was achieved by dip-slip on the array of antithetic faults (see Appendix A.5, **Figure A.5**).

Whether a flexed piece of thin lithosphere (<10 km) will bend in a purely elastic way, break in a distributed manner over a broad area (“crunching”), or break in one place and cut through its entire thickness (“snapping”) depends on the maximum bending moment that can be maintained by horizontal forces (Buck, 1997). When the local elastic bending stress (σ_E) exceeds the respective yield stress (σ_Y) of a bended beam, it will fail plastically or fracture (Buck, 1997; Burov & Guillou-Frottier, 1999). Using the equations in Buck (1997) with a coefficient of friction of 0.6 and a cohesion of 5 MPa, we evaluated the predicted flexing mechanism of the Mai’iu fault. Here, we assume that the thickness of the bended beam is equal the thickness of the Goropu Metabasalt (~5 km) and that this beam of mafic rocks is decoupled from the underlying Kagi metamorphics, which consist of felsic continental crust (see Appendix A.6 for all variables and calculations). Based on this beam thickness, the distribution of plastic yielding in the fault beam can be predicted from the known curvature (e.g., w''_{MIN}). Except near the neutral surface, the observed curvature of the fault surface is such that elastic fiber bending stresses exceed the predicted yield stress ($\sigma_E \gg \sigma_Y$; **Figure 2.10C**). If no average horizontal stress (σ_P) is applied (Buck, 1997), the beam should “snap” at a beam thickness of ≤ 685 m and “crunch” at greater thickness; however, the critical layer thickness increases with increasing σ_P and cohesion. According to our calculations for the unbending, the 5 km thick Goropu Metabasalt beam (applying an effective density of $1,860 \text{ kg/m}^3$) should snap if σ_P exceeds ~110 MPa or ~60 MPa for cohesions of 5 MPa or 20 MPa, respectively. The Goropu Metabasalt represents a minimum thickness and the average horizontal stress might not exceed these limiting values predicting that the footwall should deform in a distributed manner (“crunching” mode). We note that flexural rigidity or the effective elastic thickness of the footwall

beam is likely to change over space and time by cooling of the exhuming rocks, coupling or decoupling with the structurally underlying rocks, far-field extensional stresses, and nonlinear flexure of the beam resulting in a deflection of the neutral surface vertically in the bent footwall beam either upward or downward (Manning & Bartley, 1994; Burov & Diamant, 1995). Thus, we do not exclude the possibility that the Goropu Metabasalt beam in the upper crust has “snapped” at some point in time maybe at an early stage of exhumation; however, if this speculative exercise is correct it accords with our field observations of widely distributed spaced faults with small offsets.

2.7.3 Geodynamic Modeling

We expand upon the analytical model from the previous section by using a thermomechanical finite-element code to model the development of a LANF following tectonic inversion of a previous subduction thrust (Biemiller et al., 2017) and the stress evolution during footwall exhumation. The model uses a two-dimensional plane-strain approximation, which is supplemented by and compared to an approximation of the out-of-plane third-dimensional stress. We use the code SULEC (Ellis et al., 2011; Buiter & Ellis, 2012) with kinematic boundary conditions based on the current tectonic setting of the active Mai'iu fault (**Figure 2.11A**). The modelled Goropu Metabasaltic footwall slab uses a composite flow law which selects the lower yield stress of the calculated diffusion and dislocation creep stresses of synthetic wet anorthite-diopside aggregates (An₇₅Di₃₅W) by Dimanov & Dresen (2005) and incorporates grain-size dependence using the grain-size piezometer for experimentally deformed plagioclase aggregates by Post & Tullis (1999) (see Appendix A.7 for model details). The model we show here is inherently non-unique, owing to the complex inferred initial pre-extensional lithospheric conditions; nonetheless, the pattern of stresses seen in **Figure 2.11B** is representative of a suite of models that activate and rotate a LANF (Biemiller et al., 2017). We use the geodynamic model to help determine mechanisms by which the syn-exhumational principal stress direction might rotate or flip (NNE extension, then compression), as inferred from structural and geomorphological observations.

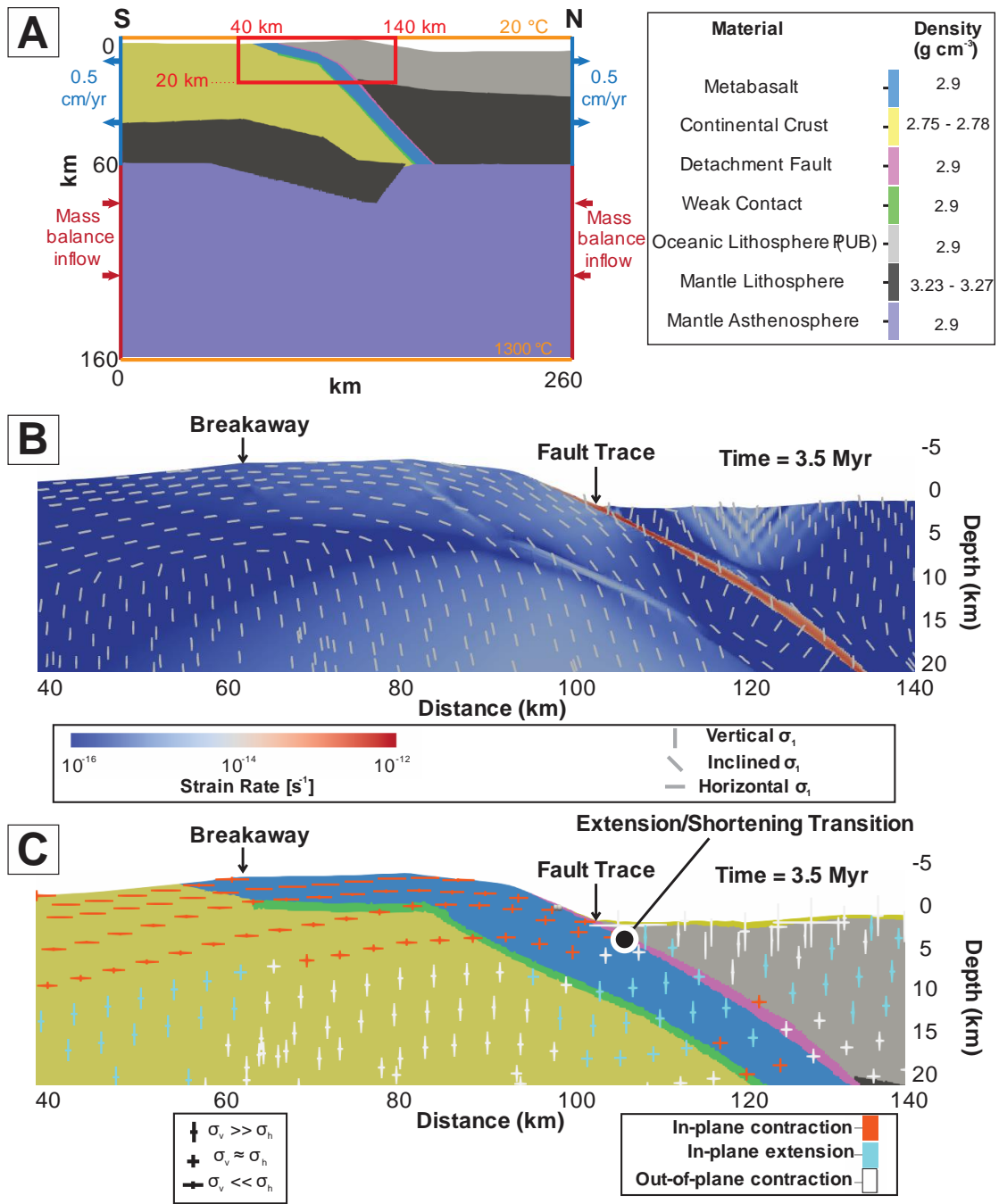


Figure 2.11. A) Model setup. For materials with nonzero thermal expansivity, the full range of initial density is listed. Red box shows the pre-extension location of B and C. B) Strain rate magnitude (second invariant) after 3.5 Myr. White glyphs indicate the direction of the maximum in-plane stress, σ_1 . C) Material properties after 3.5 Myr. Crosses show the relative magnitude of the vertical and horizontal in-plane stresses, normalized by the mean in-plane stress σ_m . Crosses are colored by the deformation state predicted by the parameter A_ϕ from Simpson (1997), where white represents regions where lithostatic overburden stress exceeds the maximum calculated in-plane stress, suggesting out-of-plane contraction (see Appendix A.7 for description).

Figure 2.11 (B, C) shows model results after 3.5 Myr of extension and exhumation, at which point ~30 km of LANF offset has exhumed a >30-km-wide and ~4-km-tall dome. The maximum in-plane compressive stress (σ_1) direction is plotted in **Figure 2.11B**, showing an upward transition from near-vertical orientations in the metabasalt slab and continental crust at depths greater than 10 km to shallowly north dipping, near-horizontal orientations in the shallower footwall metabasalt near and in the exhumed dome. Hangingwall σ_1 directions are near vertical, corresponding to an Andersonian state of horizontal extensional stress. By contrast, in the upper 5 km of the exhumed metabasaltic footwall, the near-horizontal σ_1 orientations imply local in-plane contraction. The near-vertical compressive principal stress directions in the deeper footwall are consistent with in-plane horizontal extensional stress, suggesting footwall rocks undergo a stress transition from extensional to contractional stress states with progressive exhumation—a phenomenon that has also been documented in an oceanic MCC based on a local microearthquake study, including focal mechanisms (Parnell-Turner et al., 2017). We attribute the rotation of the principal stress direction during footwall exhumation to outer-surface contractional unbending stresses in the exhumed footwall that largely arise during early stages of the “rolling-hinge” evolution, in combination with the topographic and flexural stresses that develop in the exhumed dome. These oppose subsequent extensional offset on the main detachment (see also Appendix A.8). Note, this is different to the flexural failure steady state model by Manning and Bartley (1994) shown in **Figure 2.11B**, which describes the effects on a volume of rocks passing through a static hinge.

Although the plane-strain model is two dimensional, insight into the three-dimensional state of stress can be gained by modifying the assumed out-of-plane stress, which is implicitly assumed to be the intermediate principal stress in a plane-strain formulation. If we instead approximate the out-of-plane stress as the lithostatic overburden pressure, we can highlight regions most likely to undergo out-of-plane deformation. Our approximation (detailed in the Appendix A.7) certainly does not capture the full three-dimensional kinematic complexity of the region, but it serves as a useful reference case where out-of-plane stresses are equal to the overburden stress. With estimates of all three principal stresses, the attitude and style of faulting can be predicted, and one can identify regions where out-of-plane deformation may be expected to dominate over in-plane deformation. We use all three principal stresses to

identify regions where in-plane extension or contraction is predicted as the dominant deformation mechanism, shown as red and blue glyphs in **Figure 2.11C**, respectively, where the transition between extension and contraction is indicated by the black dot. All other regimes predicted by the Simpson (1997) classification are shown by white glyphs and are interpreted as regions where out-of-plane (i.e., E-W) contractional deformation is predicted. This final category includes all styles of out-of-plane deformation including strike-slip faulting, reverse faulting, or folding which are not differentiated well by our simple out-of-plane stress approximation. Nonetheless, this quantification of predicted faulting styles further reveals the transition from in-plane extension in the deeper footwall to in-plane contraction in the exhumed metabasaltic footwall dome. The method also highlights two regions where out-of-plane deformation is expected to dominate: (1) in the continental crust underlying the metabasaltic slab in the footwall, and (2) in the shallowest portion of the hangingwall.

2.7.4 Summary of the “Rolling-Hinge” Processes

In several places of this contribution we compare oceanic MCCs with the SDM, which might not be justified given the differences of these settings. These include (a) a high heat flow at mid-ocean ridges versus a low geothermal gradient in the Woodlark Rift (~ 18.5 °C/km; Garside, 1973; Martinez et al., 2001); (b) a juvenile, largely magmatically formed footwall in the case of oceanic MCCs; and (c) a mechanically thin lithosphere at mid-ocean ridges versus a thick continental crust at the SDM. On the other hand, similarities between the oceanic MCCs and the SDM are striking, including (1) the bareness of the exhumed Mai’iu fault, which has only one ride block on it in a structural depression; (2) the 100 m to several-km wavelength of corrugations on the SDM (cf., Karson & Dick, 1983; Tucholke et al., 1998; Parnell-Turner et al., 2018); (3) the large amount of inferred back rotation that has warped the footwall (~ 40 – 50° in the SDM; cf., Morris et al., 2009); (4) steep faults cutting the footwall (e.g., Tucholke et al., 1998); (5) the mafic composition of the footwall rock; and (6) an inferred updip transition from horizontal extension to horizontal compression in the footwall (Parnell-Turner et al., 2017). These similarities imply some overlap in the mechanics of the detachment faulting process in both settings.

A summary of the deformation in the upper part of the footwall and observed geometric features accommodating the bending and unbending of this layer is given in **Figure 2.12**. Here, we use the mechanics investigated in our numerical model to help

interpret the geological cross-section of **Figure 2.10**. The deepest northern, downdip part of the footwall in the subsurface is predicted to undergo extension, leading to the formation of normal faults in the footwall as a result of regional extensional strain and as a result of bending farther updip. At some depths in the footwall beam, σ_1 and σ_2 may be approximately equal in magnitude and temporally switch with respect to one another to lead to a transition from NS-extension to EW-(strike-parallel) contraction as shown in the geodynamic model (**Figure 2.11C** and see Appendix A.7). This transition is also documented for several MCCs and is particularly apparent in the SDM where corrugations and other folds with fold hinges trending parallel to the slip direction are common (e.g., Singleton, 2013; Little et al., 2019). The footwall faults formed at the deeper parts of the convex upward shaped fault may have been later back-tilted at shallower levels. In the footwall, synthetic normal faults dipping in the transport direction are rotated to shallower dips and become inactive; whereas antithetic ones steepen in dip, perhaps through the vertical. Continued slip on the detachment fault warps its exhumed, upper part, which is abandoned and now defines a dome. This bending is also expressed by a progressive back-tilting of foliation in the footwall, by the formation of windgaps on the crest of the dome, and by back-tilting of fluvial terraces. After passing through the stress transition point (black dot; see also **Figure 2.11C**), the footwall undergoes slip-parallel shortening, as documented by the formation of crenulation foliation and strike-parallel fold hinges in the Gwoira rider block in response to what is now a subhorizontal σ_1 in the near surface. Some of the now strongly back-tilted footwall faults that formed as normal faults at depth may eventually become reactivated as reverse faults in the exhumed part of the footwall due to the subhorizontal σ_1 orientation there, which is related to flexure of the Mai'iu fault. As a result of exhumation and associated cooling of the exhuming Goropu Metabasalt, the flexural rigidity of the footwall beam and its unbending stresses may increase. For this reason, the increment of late-stage contraction may exceed any earlier extensional strain in the footwall. Thus, it is possible that the late reverse faults in the SDM may have formed anew during the exhumation without necessarily reactivating earlier normal faults, although this is not our favoured interpretation. In short, footwall faults may experience extensional and then contractional heave during their lifetime, with the latter being a response to unbending caused by the “rolling-hinge” exhumation.

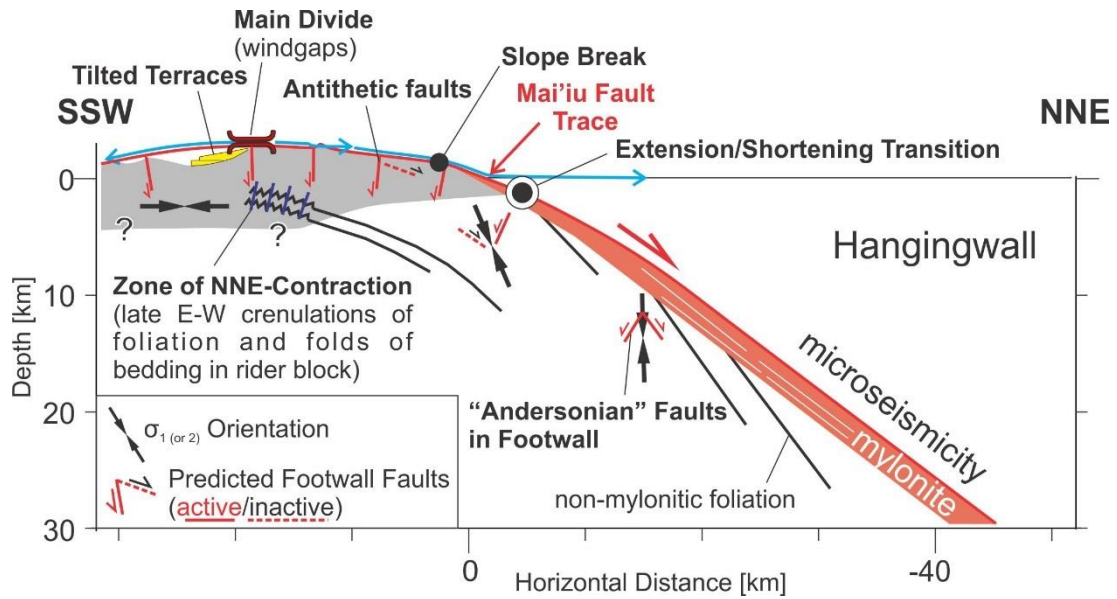


Figure 2.12. Summary of footwall deformation in the exhuming slab of the Mai'iu fault with superimposed stress trajectories from Figure 2.11. Note, according to the geodynamic model σ_1 and σ_2 are locally equal in magnitude and temporally switch with respect to one another. See text for explanations.

2.8 CONCLUSIONS

Structural and geomorphic data presented here indicate that the Mai'iu fault evolved by the “rolling-hinge” mechanism from a fault having an original surface dip of at least 40°N to one that is highly exhumed and domal in shape. On the strongly back-warped, southern flank of the MCC, the exhumed fault surface dips south at $\sim 12^\circ$, requiring a total angular rotation in the footwall of $42\text{--}52^\circ$.

Supporting evidence includes the following:

1. Microseismicity suggests that today deeper parts of the Mai'iu fault dip at $30\text{--}40^\circ$ at depths of >20 km (Abers et al., 2016).
2. Windgaps perched on the crest of the dome, and nearby south tilted fluvial terraces that were deposited by north flowing streams provide direct evidence of updip tectonic advection of the exhumed footwall together with progressive back-tilting of the fault surface.
3. The observed magnitude of arching of the footwall foliation agrees with the domal shape of the exhumed fault surface.

4. Bedding-fault cutoff angles in an uplifted rider block (now part of the footwall) indicate former fault dips at the surface of at least 40°.

We infer that antithetic slip on an array of steeply dipping faults accommodated some of syn-exhumational, inelastic unbending of the footwall (Axen & Bartley, 1997); these faults also reveal that the footwall plastically yields in a distributed type of flexural failure (i.e., “crunching” mode; Buck, 1997).

Finally, we interpret structures in the footwall as recording a late-stage, exhumation-related increment of shortening that was subparallel to the regional extension direction. We interpret the phenomenon as an expectable response to footwall unbending at the “rolling-hinge”, as explored by us in a numerical model.

Chapter 3: Slow-to-Fast Slip Deformation of Mafic Rocks on an Actively Exhuming Low-Angle Normal Fault, Woodlark Rift, SE Papua New Guinea

Abstract

Rapid slip on the active Mai'iu low-angle normal fault in SE Papua New Guinea has exhumed a single fault surface across a >25 km-wide dome. Field work reveals that the fault has a <3 m-thick fault core, consisting of gouges and cataclasites. These overprint a structurally underlying carapace of mylonitic rocks that are locally >60 m-thick. Detailed study of these fault rocks with a EBSD/EDS equipped FEG-SEM reveal that mylonitic deformation was controlled by sliding and rotation of a pre-existing fine-grained (6–33 μm in diameter) mafic assemblage together with syn-tectonic chlorite precipitation. Chlorite geothermometry reveals that this diffusion-accommodated grain-boundary sliding in the mylonites took place at >270–370°C. At shallower levels on the fault ($T \approx 150$ –270°C), fluid-assisted mass transfer and metasomatic reactions created a foliated cataclasite fabric during dissolution-precipitation creep. In this unit, pseudotachylites and ultracataclasites mutually cross-cut both the foliated cataclasite and one another, recording repeated episodes of seismic slip. At the shallowest crustal levels ($T < 150^\circ\text{C}$), clay-rich gouges contain abundant saponite, promoting creep on the most poorly oriented part of the Mai'iu fault (dipping ~ 15 –22°). Our field and microstructural data support geodetic, seismological, and geomorphic evidence for mixed-mode, seismic-to-aseismic slip behavior on the Mai'iu fault.

3.1 INTRODUCTION

Domal normal faults (or detachments) that today dip $<30^\circ$ are key structures accommodating lithospheric extension. Bounding a metamorphic core complex, these faults typically have slip magnitudes of tens of kilometres, sufficient to exhume rocks in their footwall from below the brittle-ductile transition (BDT, **Figure 3.1A**; e.g., Whitney et al., 2013; Platt et al., 2015). The apparent low dip of these faults, exposed at the Earth's surface, is at odds with fault mechanical theory: Andersonian normal faults should initiate and slip at dips of $60\text{--}75^\circ$ and frictionally lock-up at dips $<30\text{--}45^\circ$ (e.g., Anderson, 1951; Sibson, 1985; Lister & Davis, 1989; Collettini & Sibson, 2001; Axen, 2004, 2007; Collettini, 2011). This expectation is supported by the rarity of moderate-to-large magnitude earthquakes attributable to normal faults with dips $<30^\circ$ (Jackson, 1987; Jackson & White, 1989; Abers et al., 1997; Collettini & Sibson, 2001; Abers et al., 2016). Yet, a small number of normal faults are demonstrably active at low angles (dips $<30^\circ$) near the Earth's surface today (e.g., Chiaraluce et al., 2007 and references therein). A possible explanation for such low-angle normal faults (LANFs) is that they have a weaker-than-“Byerlee” frictional strength ($\mu=0.6\text{--}0.85$; Byerlee, 1978).

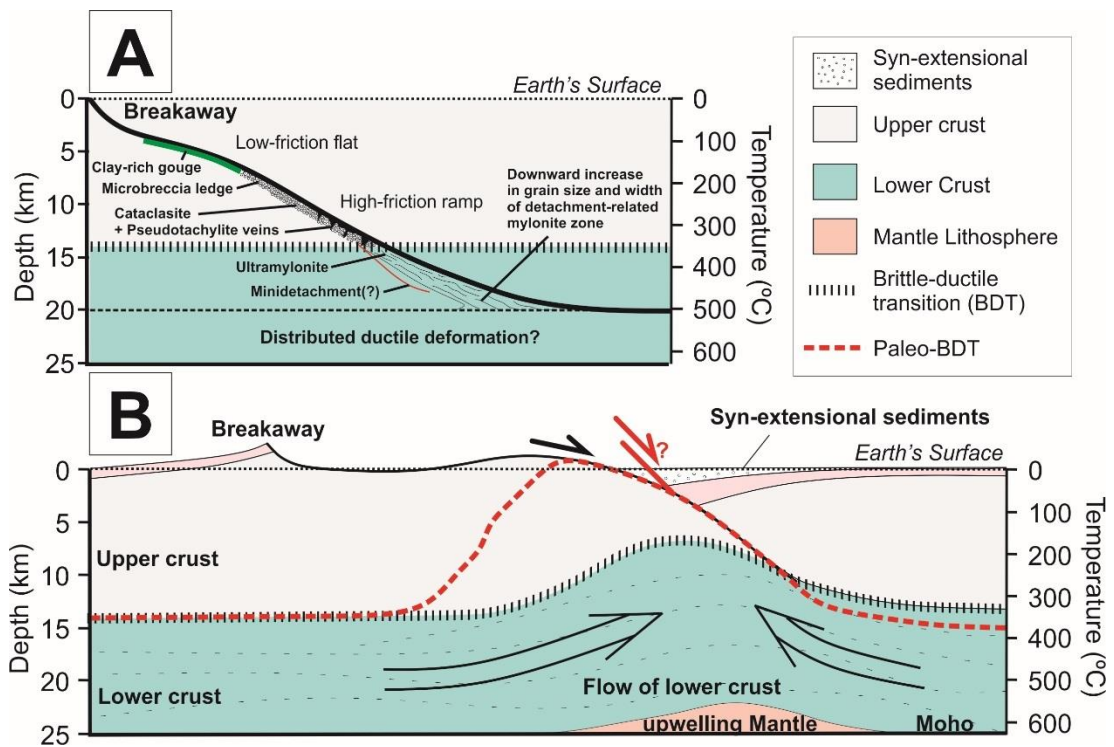


Figure 3.1. A) Schematic spatial changes in the fault rock sequences within the crust cut by an extensional detachment (modified after Cooper et al., 2017). B) Sketch of the “rolling-hinge model” in which a normal fault initiates at a moderate to steep dip-angle and isostatic unloading of the lower crust causes uplift and warping of the upper inactive part of the fault surface (Wernicke & Axen, 1988; Mizera et al., 2019).

Deformational processes at different crustal levels that might lead to severe weakening of a fault, allowing it to slip at low angles, are not well understood (e.g., Collettini, 2011). Most active continental LANFs are concealed beneath a cover of upper plate rocks (Rigo et al., 1996; Chiaraluce et al., 2014), while ancient ones have been overprinted by combinations of post-slip tectonic tilting, chemical alteration, and erosion (e.g., Axen & Bartley, 1997; Axen, 2004; Collettini, 2011; Whitney et al., 2013). The Mai’iu fault in SE Papua New Guinea is a rare exception. It is one of the best preserved of only a handful of known active LANFs on Earth (e.g., Spencer, 2010). Cosmogenic nuclide studies on the fault scarp indicate that the fault has a Holocene to present-day dip-slip rate of 11.7 ± 3.5 mm/yr (Webber et al., 2018), whereas geodetic data indicate a slip-rate of 7.5–9.6 mm/yr (Wallace et al., 2014). Over the last 3–4 Myrs, this rapid slip has exhumed a >25 km width of footwall fault surface beneath which a sequence of overprinting microstructures are well preserved. The sequence of fault rocks exhumed along this fault provides snapshots of processes

and deformation mechanisms active from the middle to uppermost crust in a protolith of predominantly basaltic composition (Little et al., 2019).

Detachment faults, including demonstrable LANFs, commonly juxtapose unmetamorphosed hangingwall rocks against metamorphosed, and typically in part mylonitic, middle- to lower-crustal footwall rocks (e.g., Whitney et al., 2013; Platt et al., 2015). This tectonic assemblage is known as a Metamorphic Core Complex (MCC) and is common in both continental and oceanic extensional settings. Based on microseismicity, the Mai'iu fault has been shown to dip at 30–40° at depths of ~12–20 km (Abers et al., 2016), whereas the exposed (abandoned) part of this convex upward shaped fault surface dips at ~15–24° (Spencer, 2010; Little et al., 2019; Mizera et al., 2019). The flexural-isostatic back-rotation and shallowing of an initially moderate- to steeply-dipping normal fault during progressive unloading of its footwall caused by slip is called “rolling-hinge” evolution (**Figure 3.1B**; e.g., Spencer, 1984; Buck, 1988; Wernicke & Axen, 1988). Such rotation of the footwall has been verified by paleomagnetic studies of young, oceanic MCCs (e.g., Garcés & Gee, 2007; Morris et al., 2009), but it has been difficult to demonstrate unequivocally for ancient examples in continental crust (Wernicke, 1981; Jackson, 1987; Buck, 1988; Scott & Lister, 1992; Axen, 2007; Gans & Gentry, 2016). As the footwall passes through the hinge and tilts to shallower dip angles, the uppermost part of the fault back-warps to form a domal-shaped, abandoned fault surface, with the steeper dipping part of the fault remaining active at depth (Spencer, 1984; Wernicke & Axen, 1988). During this process, the hangingwall may be cross-cut by relatively steeply dipping splay faults that merge into the deeper, still active part of the fault downdip (e.g., Choi & Buck, 2012). Such splaying can result in the capture of a rider block of original hangingwall rocks into the uplifting footwall (**Figure 3.1B**; e.g., Reston & Ranero, 2011).

More deeply exhumed parts of the footwall of a MCC commonly contain mylonitic fabrics acquired as a result of ductile shearing at depth (**Figure 3.1A**; e.g., Singleton & Mosher, 2012; Platt et al., 2015). Rocks in the middle to lower crust typically show evidence for crystal-plastic deformation accomplished by viscous deformation mechanisms such as dislocation or solid-state diffusion creep (e.g., John & Cheadle, 2010). Mylonitic microstructures are later overprinted by brittle deformation due to their passage through the BDT as a result of their continuing fault motion and cooling during uplift through the crust (e.g., Whitney et al., 2013 and

references therein). The timing and location of this shift from crystal-plastic to frictional-cataclastic deformational processes depends on numerous variables, including: geothermal gradient, mineralogy, grain size, texture, strain rate, fault orientation, fluid pressure, and pore fluid composition (e.g., Wintsch & Yeh, 2013 and references therein). Deformation near the BDT is commonly quite localized, with slip focused into cm- to m-thick shear zones of very fine-grained rock, including ultramylonites (e.g., Behr & Platt, 2014). These sheared rocks may show evidence for both brittle and ductile processes (e.g., Platt et al., 2015 and references therein). For example, pseudotachylites caused by frictional melting during seismic events may be ductilely deformed or interleaved with mylonitic rocks (e.g., Sibson, 1977; Goodwin, 1999; Sibson et al., 2006). Updip from the BDT, abundant microfracturing, frictional sliding and cataclasis in the fault zone may yield brittle fault rocks such as gouge, cataclasite and (micro-)breccia (**Figure 3.1A**; e.g., Cowan et al., 2003; Collettini & Holdsworth, 2004; Hayman, 2006; John & Cheadle, 2010).

One way to explain slip on a highly misoriented fault such as a LANF is that as fault rocks and their fabrics evolve in the brittle crust, they acquire a very low frictional resistance (e.g., Collettini, 2011; Richard et al., 2014 and references therein). Two main hypotheses allowing sliding at low resolved shear stresses have been suggested: (1) fluid overpressure greatly reduces the effective normal stress (Etheridge et al., 1984; Rice, 1992; Sleep & Blanpied, 1992); or (2) weak minerals such as talc, montmorillonite, saponite and other phyllosilicates significantly lower the coefficient of friction to well below “Byerlee” values (Collettini et al., 2009b; Collettini, 2011; Richard et al., 2014). At the onset of grain-scale brittle deformation near the BDT, fluid influx may cause alteration reactions in the protolith rock and form new phyllosilicates or other minerals that are weaker than the original reactant phases (reaction softening; e.g., Wintsch & Yeh, 2013). These metasomatic reactions together with fluid-assisted diffusive mass transfer (e.g., Rutter & Mainprice, 1979; Rutter, 1983) may promote the development of interconnected networks of weak phases that can reduce the long-term frictional strength of the fault rock to sub-“Byerlee” friction values (textural softening; e.g., Jefferies et al., 2006). Alternatively, rotation of the principal stress axes to “non-Andersonian” orientations may promote slip on an otherwise seemingly misoriented fault; such rotations can arise through a local stress refraction across an interface into a weak fault zone layer (Faulkner et al., 2006; Healy,

2008); or as a result of topographic loads, lateral density variations, and/or horizontal or vertical shear tractions caused by lower crustal flow (e.g., Spencer & Chase, 1989; Yin, 1989 and related comments by Buck, 1990; Westaway, 2005).

The exposure and preservation of mylonites, cataclasites and gouges that have only recently been exhumed in the footwall of a rapidly slipping, high finite slip active LANF makes the Mai'iu fault an ideal natural laboratory in which to study the spatiotemporal evolution of microstructures in a major fault zone (Daczko et al., 2009; Little et al., 2019). Here, we document microstructures in fault rocks to infer the progression of deformation mechanisms and strain rates accommodating slip in the mafic footwall of the Mai'iu fault at different structural levels, and to identify processes leading to weakening (or strengthening) of the fault rocks during their exhumation. Our investigations incorporate field observations, microstructural and fabric analyses, mineral and elemental compositions, and chlorite-based estimates of paleotemperature. We show that fluid-assisted alteration of the fine-grained mafic protolith led to a reduction of long-term (steady state) strength of the Mai'iu fault allowing it to slip at dips of only $\sim 15\text{--}22^\circ$ in the near surface; however, at deeper levels of the crust, where it dips $>30^\circ$, we document a mixed-mode, variably seismic-to-aseismic slip behavior on the Mai'iu fault.

3.2 TECTONIC SETTING OF THE WOODLARK RIFT

The Oligocene to recent tectonic regime in SE Papua New Guinea is governed by the oblique-convergent motion of the Pacific and Australian plates creating a complex array of microplates in the collision zone (**Figure 3.2A**; Tregoning et al., 1998; Wallace et al., 2004, 2014). The Woodlark-Solomon Sea-Trobriand microplate today rotates counterclockwise at $2\text{--}2.7^\circ/\text{Myr}$ relative to the more southern Australian plate about a nearby Euler pole (Wallace et al., 2014). In the east, this has resulted in a north-south seafloor spreading in the active Woodlark Basin (Wallace et al., 2004; Eilon et al., 2015). Farther west, the spreading center transitions into a zone of active continental rifting (Woodlark Rift), which is thought to have initiated at 3.6–8.4 Ma (**Figure 3.2A**; Taylor & Huchon, 2002; Wallace et al., 2014; Cairns et al., 2015). Extension in the Woodlark Rift is accommodated by slip on a relatively small number of mostly north-dipping normal faults, some of which bound the flanks of the subaerially exhumed D'Entrecasteaux Islands gneiss domes (Little et al., 2007, 2011; Fitz & Mann, 2013; Wallace et al., 2014). The Mai'iu fault occurs at the SW margin

of the Woodlark Rift (**Figure 3.2A, 2B**), where it takes up most of the extension at dip-slip rates of ~1 cm/yr (Wallace et al., 2014; Webber et al., 2018). Previous workers have suggested that the Mai'iu fault represents an extensionally reactivated part of the Owen-Stanley Fault Zone (OSFZ), a Paleogene subduction thrust (**Figure 3.2A**; Davies, 1978; Webb et al., 2008; Daczko et al., 2011; Little et al., 2019). The OSFZ accommodated the southwest-directed obduction of an oceanic and island arc in its upper plate (the Late-Cretaceous Papuan Ultramafic Belt; PUB) over a partially subducted assemblage of oceanic marginal basin and accreted continental margin rocks (Davies, 1978; Webb et al., 2008; Daczko et al., 2009).

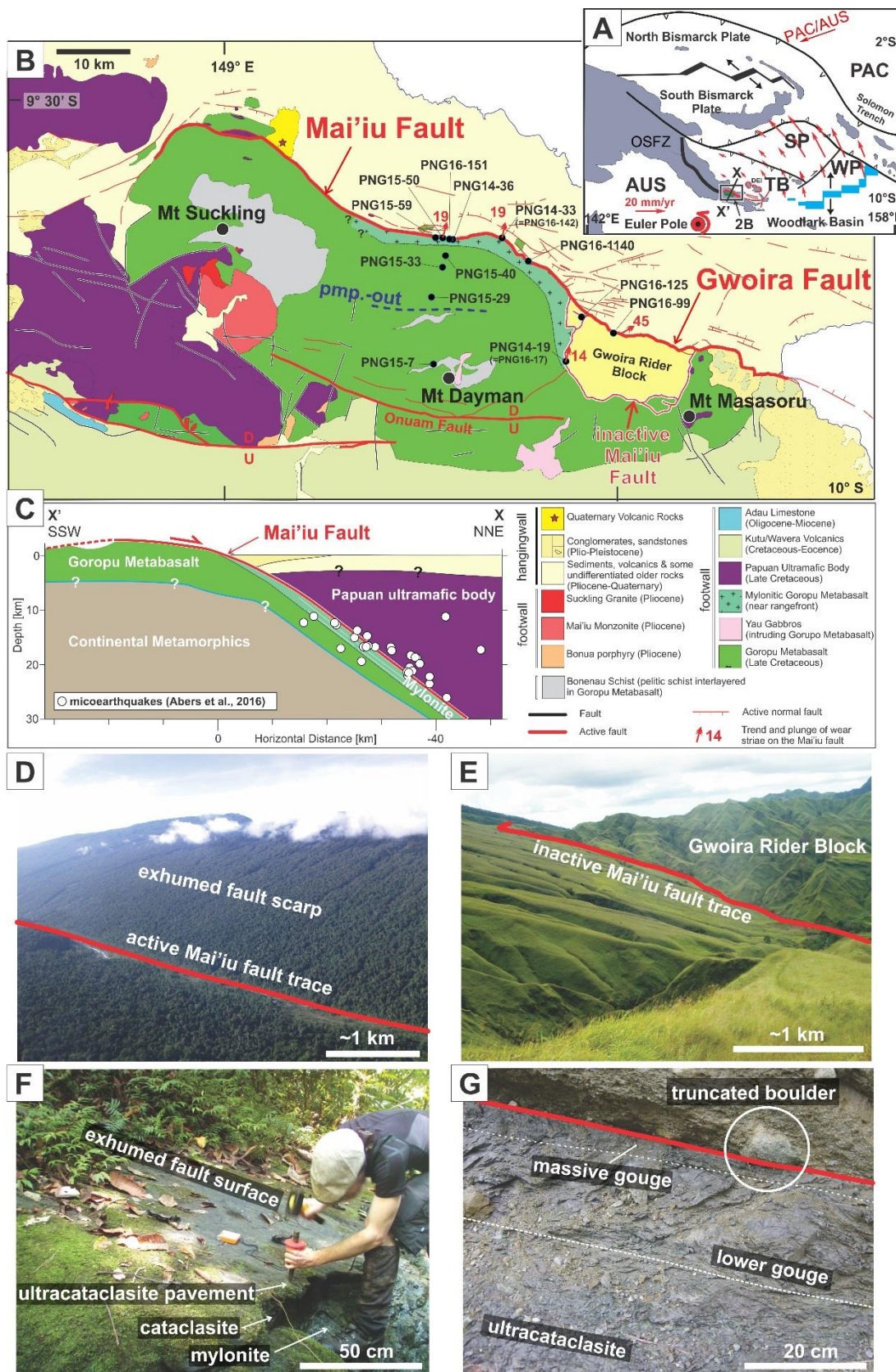


Figure 3.2 (previous page). A) Simplified tectonic map of the Woodlark Rift (after Wallace et al., 2004). PAC=Pacific plate; AUS=Australian plate; WP=Woodlark plate; SP=Solomon-Sea plate; TB=Trobriand block; DEI=D'Entrecasteaux Islands; OSFZ=Owen-Stanley Fault Zone. Locations of **Figure 3.2B** and cross-section X-X' of **Figure 3.2C** are shown. B) Geological and structural map of the Suckling-Dayman Metamorphic Core Complex (SDM) (after Smith & Davies, 1976; Lindley et al., 2014; Little et al., 2019). C) Tectonic cross-section of the Mai'iu fault (after Daczko et al., 2011; Little et al., 2019). Microearthquake foci are based on Abers et al. (2016). D) Oblique aerial photograph of the active Mai'iu fault range front scarp covered in rainforest looking SE. E) Exhumed grassy dip slopes along the Mai'iu fault where it is inactive and structurally overlain by a rider block of Gwoira Conglomerate looking SE. F) Youngest, most recently exhumed surface of the active Mai'iu fault at the base of its scarp. Here, the surface is covered by a dark ~5 cm thick ultracataclasite layer, whereas a soft gouge layer has probably been eroded away from that harder pavement (Location PNG15-50). G) Fault rock sequence of an inactive segment of the Mai'iu fault preserved beneath the Gwoira rider block at site PNG14-19. Note, hanging wall conglomerates (upper right) including a fault-truncated cobble. Beneath the fault are two gouge units (massive and lower) and ultracataclasite.

3.2.1 Geology of the Mai'iu Fault

The Mai'iu fault bounds the Suckling-Dayman Metamorphic Core Complex (SDM), the exhumed lower plate of which includes three antiformal culminations that coincide with peaks on the main divide (**Figure 3.2B**): Mt Suckling (3,576 m), Mt Dayman (2,950 m) and Mt Masasoru (~1,700 m). The fault trace that bounds the northern flank of the MCC is near sea level. The footwall of the SDM consists chiefly of MORB-derived metabasaltic rocks of >3–4 km thickness together with minor interbedded phyllitic metasediments, limestone, and chert, known as the Goropu Metabasalt (Smith & Davies, 1976). The Late Cretaceous metabasalt grades southward into unmetamorphosed equivalents and younger Eocene basaltic rocks called the Kutu Volcanics (Smith & Davies, 1976). Mafic mylonites are exposed near the fault trace at the northern edge of the Mai'iu fault scarp (**Figure 3.2B**). Undeformed granitoid stocks (Mai'iu Monzonite, Suckling Granite, and Bonua Porphyry; Davies & Smith, 1974) intrude the lower plate of the SDM near Mt Suckling and have U-Pb-based zircon crystallisation ages of 1.9–3.7 Ma (Oesterle et al., 2018; Little et al., 2019). The granitoids record melting of continental crust at depth, and geophysical surveys (based on seismic travel-times) confirm that the Goropu Metabasalt is underlain by continental crust of felsic to intermediate composition that reaches depths of up to ~32 km near the SDM (**Figure 3.2C**; e.g., Finlayson et al., 1977; Ferris et al., 2006; Eilon et al., 2015; Abers et al., 2016). A flap of Papuan Ultramafic Belt overlies the Goropu Metabasalt on a southern part of the footwall of the Mai'iu fault, but these ultramafic rocks otherwise form the basement of the hangingwall. Above the PUB, the hangingwall of the Mai'iu fault includes Pliocene alluvial conglomerates of the Gwoira Conglomerate. These are best exposed in a single rider block that occurs to the south of the active Gwoira splay fault which merges westward and downdip into the Mai'iu fault (**Figure 3.2B**). The rider block is floored by an inactive strand of the Mai'iu fault (inactive Mai'iu fault) that preserves a full thickness of fault rocks (**Figure 3.2E, 2G**). The rider block (cf. **Figure 3.1B**) consists of a >2,600 m-thick sequence of southwardly back-tilted hangingwall strata (Webber, 2017; Little et al., 2019).

Outcrops and dip slope geomorphic data indicate that the Mai'iu fault dips from 15 to 24° (mostly 20–22°) to the NNE along its trace near the range front (**Figure 3.2D, 2F**; Little et al., 2019; Mizera et al., 2019). A linear alignment of microseismicity that is co-planar with the surface trace of the Mai'iu fault indicates that the fault steepens

to a 30–40° dip in the subsurface (**Figure 3.2C**; Abers et al., 2016). Wear striae on the exposed fault surface and decorating fault-truncated cobbles in the hangingwall trend ~012–015° (Little et al., 2019). They are subparallel to the velocity direction derived from block modelling of campaign GPS data by Wallace et al. (2014) for the Trobriand block relative to Australia (**Figure 3.2A**) and subparallel to the trend of numerous corrugations in the footwall of SDM (Spencer, 2010; Daczko et al., 2011; Mizera et al., 2019).

3.2.2 Fault Rock Sequence of the Active and Inactive Mai'iu Fault

Figure 3.3 shows a schematic section of the Mai'iu fault rock sequence that is partially eroded on exhumed parts of the active fault (**Figure 3.2D, 2F**), but fully preserved in outcrops along the inactive fault that is beneath the rider block (**Figure 3.2E, 2G**). The fault sequence includes five units: a) non-mylonitic schist (protolith); b) mylonite; c) foliated cataclasite; d) ultracataclasite; e) gouge and principal displacement surface (PDS). The fault rocks that occur structurally above the locally up to 60 m-thick mylonite unit are asymmetrically arranged across a zone that is 1.5–3 m thick, in which higher units cannibalize underlying ones. Each unit was described in brief previously by Little et al. (2019), and expanded descriptions are provided in the following paragraphs.

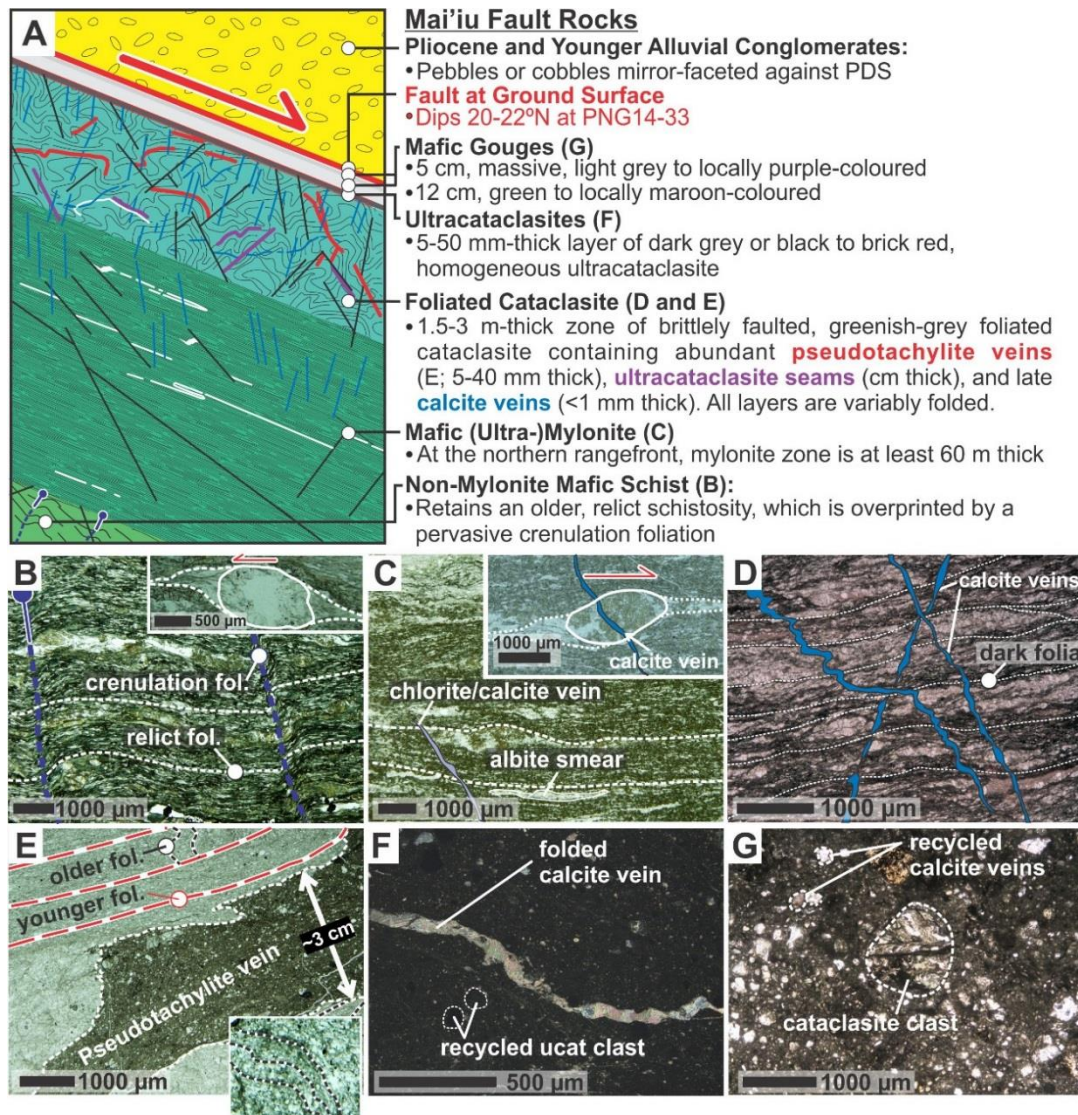


Figure 3.3. A) Schematic section through the fault rock sequence based on the Mai'iu fault outcrop at site PNG14-33 (modified from Little et al., 2019). B-G) Representative optical photomicrographs. All thin sections are cut parallel to the kinematic XZ-direction—perpendicular to foliation (fol.) and parallel to the slip direction or mineral lineation—with downdip direction to the right. B) Non-mylonitic mafic schist: A relict, non-mylonitic schistosity (white lines) is overprinted by a spaced crenulation foliation (blue lines; PNG15-7). Inset, asymmetry of strain shadow around epidote porphyroclast indicates top-to-the-SSW sense of shear. C) Mafic mylonite: the greenschist facies mineral assemblage defines a LS-tectonite cross-cut by several chlorite and calcite veins at a high angle to the foliation. Inset, top-to-the-north sense of shear indicated by strain shadow around epidote porphyroclast (PNG14-36). D) Foliated cataclasite: dark and light folia are cross-cut by variably deformed calcite veins. Note, backward inclined calcite veins (relative to the slip direction) are folded while forward inclined are necked (PNG16-125B). E) Glassy pseudotachylite vein (~3 cm thick) in a cataclasite sample from site PNG14-19. F) Ultracataclasite with folded calcite vein (XPOL; PNG15-50B). Note, recycled ultracataclasite (ucat) clasts can be found in the ultrafine-grained matrix. G) Green gouge: Note, the cataclasite clast in which differentiated foliation of the foliated cataclasite unit is visible in the centre. Clasts consisting of calcite vein fragments are also present (PNG16-142A).

Non-mylonitic schist (Protolith)

Most of the SDM footwall comprises schistose (non-mylonitic) mafic rocks (Goropu Metabasalt; **Figure 3.3B**) that decrease in metamorphic grade southward. Greenschist-facies mafic schists are widely exposed in the northern flank of the SDM. These schists consist of a fine-grained assemblage of epidote, actinolite, chlorite, albite, titanite, relict clinopyroxene, \pm quartz, \pm calcite, \pm stilpnomelane, \pm (chalcopyrite), \pm mica, \pm apatite and \pm opaque minerals (Smith & Davies, 1976; Daczko et al., 2009; Little et al., 2019). The foliation is defined by: a) shape preferred orientation (SPO) of actinolite and chlorite; and 2) foliation-parallel compositional layers (including deformed veins), 2–5 mm thick, that are variably enriched in epidote or albite (Daczko et al., 2009; Little et al., 2019). A NNW-trending stretching lineation is defined by elongated strain shadows containing predominantly chlorite, and the SPO of actinolite grains. A top-to-the-SSW (thrust) sense of shear is indicated by: (1) the asymmetry of strain fringes filled with fibrous quartz \pm actinolite or of strain shadows filled with blocky chlorite (**Figure 3.3B**, inset); (2) extensional (C') shear bands; and (3) actinolite porphyroclasts having fine-grained, sigmoidal tails. Little et al. (2019) infer that these fabrics were developed during the Paleogene Papuan Orogeny when the Goropu Metabasalt was underthrust northward beneath the Papuan Ultramafic Belt along the OSFZ. A pumpellyite-out isograd has been mapped approximately mid-way up the north flank of the SDM representing peak temperatures of 350–375°C (**Figure 3.2B**; Beiersdorfer & Day, 1995; Daczko et al., 2009; Little et al., 2019). Pumpellyite-actinolite facies rocks are exposed on more southern parts of the SDM as far south as the Onuam fault (**Figure 3.2B**), beyond which a zone of prehnite-pumpellyite facies rocks occurs (Davies, 1978).

Mafic mylonite

Within a ~2 km width that is updip from the fault trace along the range front, mylonitic fabrics are exposed in the exhumed metabasaltic footwall of the active Mai'iu fault. Along the fault trace, partial exposures of the mylonite zone are at least 60 m thick, whereas farther south and updip (beneath the rider block) the zone narrows to as little as 1.5 m width. The mylonitic rocks are LS-tectonites that have a strong NNE-trending stretching lineation (**Figure 3.3C**). Pseudosection modelling of the greenschist-facies mineral assemblage in the mafic mylonites indicates peak metamorphic conditions of ~425°C and 5.9–7.2 kbar (Daczko et al., 2009). These

authors attribute the growth of newly formed Fe³⁺-rich sodic-calcic amphiboles (winchite, ferrowinchite and ferrobarroisite) in the mylonites to an elevated oxidation state at 350–400°C and <~4.5 kbar during a post-peak part of their exhumation path. Stretching lineations in these rocks are defined by: a) chlorite strain shadows around epidote porphyroclasts; b) a strong SPO of actinolite and chlorite; and c) smears of albite grains disaggregated from strongly deformed albite-rich veins. The NNE-trending lineation is sub-parallel to the brittle slip direction of the Mai'iu fault and to GPS-derived velocities of the Trobriand Plate relative to Australia. Top-to-the-NNE (normal) sense of shear is everywhere indicated by extensional C'-shear bands deforming the mylonitic foliation and by the asymmetry of chlorite strain shadows (**Figure 3.3C**, inset). Little et al. (2019) inferred these extensional ductile fabrics to be late Neogene or younger in age. The mylonites are cross-cut by multiple generations of mm-thick chlorite and calcite veins that are mostly oriented sub-perpendicular to the foliation (**Figure 3.3C**). Some veins have been deflected away from the foliation-orthogonal attitude as a result of post emplacement normal-sense ductile shearing, and are variably cross-cut by younger generations of veins that remain a more nearly foliation-orthogonal attitude.

Foliated cataclasite

In the footwall, there is an upward transition from mylonite into a layer of mylonite-derived foliated cataclasite that is 1.5–3 m thick. The contact is typically gradational across a zone of: a) decreasing mean grain size that also features mm- to cm-thick, anastomosing bands of ultramylonite near the top contact; b) increasing intensity of microfaulting and brecciation; and c) increasing degree of apparent bleaching of the parent basaltic protolith (Little et al., 2019). A coarsely spaced and differentiated foliation characterizes the cataclasite (**Figure 3.3D**). This fabric is distinct from the much finer and more continuous foliation in the mylonites. Folia in the cataclasite unit alternately consist of: (1) light-coloured albite ± quartz-rich domains that include abundant veining and cementation by calcite; and (2) darker phyllosilicate (predominantly chlorite)-rich folia that anastomose around less deformed domains and lenticular clasts of the albite-rich material (**Figure 3.3D**). The foliation is complexly folded and crenulated in an irregular to chaotic way (**Figure 3.3E**). Locally, younger foliation seams truncate older, more folded ones. Microscale transgranular faults disrupt the foliation and shatter the rock. Multiple generations of

calcite veins (μm - to <1 mm thick) cross-cut the cataclasites. These veins are typically oriented sub-perpendicular to the foliation (**Figure 3.3D**). Backward-inclined gash veins (with respect to the sense of shear) are shortened and folded, while forward-inclined ones have been stretched and show necking structures—a change in strain type that is expected for the known normal shear sense (**Figure 3.3D**). Pseudotachylite veins (5–40 mm thick) are widespread in the unit. These have intrusive, discordant contacts against the surrounding host rock, or are aligned sub-parallel to remnants of the precursor mylonitic foliation (**Figure 3.3E**). The veins contain angular to rounded clasts of albite, quartz, epidote and other material that is inferred to be wall rock-derived. The pseudotachylite matrix is glassy, amorphous for at least some of the veins as verified by quantitative X-ray powder diffraction (see Little et al., 2019). More commonly, the matrix has been devitrified. Five pseudotachylite veins with glassy matrices at site PNG14-19 (location in **Figure 3.2B**, see Little et al., 2019, for detailed description) were dated by $^{40}\text{Ar}/^{39}\text{Ar}$ geochronology at the Noble Gas Laboratory of the University of Michigan; the derived ages (interpreted as minimum ages for friction melting) range from 2.24 ± 0.29 Ma to 3 ± 0.43 Ma (Little et al., 2019).

Ultracataclasite

The foliated cataclasites are structurally overlain by a 5–40 cm thick layer of dark grey to black (and locally brick-red) ultracataclasite. **Figure 3.2F** shows the smooth top surface of the ultracataclasite layer where it has been exhumed—and probably stripped of an original gouge cover—just above the active fault trace. The fault surface is marked by fine wear striae trending NNE. In thin section, the ultracataclasites contain remnant mylonite-derived mafic minerals and older (recycled) ultracataclasite fragments that are embedded in a clay-rich matrix that consists predominantly of corrensite (mixed-layer chlorite-trioctahedral smectite) and/or saponite (trioctahedral smectite; **Figure 3.3F**; based on X-ray powder diffraction data, Little et al., 2019). K-feldspar is common in samples of the ultracataclasite unit that were collected along the active Mai'iu fault at the range front (Little et al., 2019). Calcite veinlets of <100 μm thickness cut across the ultracataclasite and are mostly unfractured, but may be ductilely deformed (**Figure 3.3F**). For the latter, these veinlets that are backwards-inclined are folded (**Figure 3.3F**), whereas those which are forward-inclined are planar (not shown here; see Little et al., 2019).

Gouges and Principal Displacement Surface

The ultracataclasite unit is sharply overlain by one or more layers of incohesive clay-rich gouge as best exposed in outcrops of the fault rock sequence beneath the rider block (**Figure 3.2G**; Little et al., 2019). At site PNG14-19, a 17 cm-thick layer of medium grey gouge is overlain by a 1–2 cm-thick, light grey gouge (location in **Figure 3.2B**; **Figure 3.2G**). A sharp, planar slip surface (principal displacement surface, PDS) places the unmetamorphosed, hangingwall Gwoira Conglomerate against the gouge. Gabbroic, doleritic, phyllitic and metabasaltic sedimentary cobbles in the Gwoira Conglomerate are sharply truncated against the PDS (**Figure 3.2G**). The cobbles have acquired a smooth, mirror-like coating on the faulted facets of the cobbles that bear fine striae. Adjacent, higher parts of the Gwoira Conglomerate are mostly both unfaulted and unbrecciated.

At site PNG14-33, which sits along the active segment of the Mai'iu fault (location in **Figure 3.2B**), a lower layer of green gouge is 12 cm-thick. This layer is overlain by ≥ 5 cm layer of light-grey to purple gouge. The gouges contain various angular fragments of the underlying fault rocks and are texturally coarser-grained than the structurally underlying ultracataclasites (**Figure 3.3G**). There are no cross-cutting calcite veins in the gouges, only porphyroclastic fragments of calcite and quartz veins, probably derived by reworking of the underlying ultracataclasite and foliated cataclasite units. Based on optical microscopy and X-Ray Diffraction (XRD)-analysis, gouges from both localities PNG14-19 and PNG14-33 contain abundant saponite (Little et al., 2019).

3.3 METHODS

3.3.1 Thin Section Preparation and Analytical Methods

The rock samples were collected in 2014, 2015 and 2016 (**Figure 3.2B**; Little et al., 2019). Thin sections were cut parallel to lineation and perpendicular to foliation (kinematic XZ plane; X—parallel to lineation; Y—parallel to foliation and normal to lineation; Z—normal to foliation). Fragile fault rocks (e.g., ultracataclasites and gouges) were impregnated with epoxy resin. An optical microscope was used initially to describe the mineral assemblage, microstructures, and grain size of 157 samples. From these, we selected a suite of 47 representative samples to be prepared into polished sections for analysis by a field emission gun scanning electron microscope

(FEG-SEM) equipped with energy dispersive spectroscopy (EDS) and electron backscatter diffraction (EBSD) detectors, and a cold-cathode cathodoluminescence (CL) microscope at the University of Otago. In addition, one sample of the collected fault-truncated cobbles was subjected to analysis by transmission electron microscope (TEM) at the University of New Brunswick; one silica-rich gouge sample was investigated by Raman spectroscopy at University of Otago, Department of Chemistry; and 12 mylonite and foliated cataclasite samples for analysis by an electron probe microanalyser (EPMA) at the Victoria University of Wellington. Additional whole rock major element concentrations of 4 mafic fault rocks including mylonite and gouge were determined based on X-ray fluorescence (XRF) analysis at the University of Waikato. The methods used in these techniques are detailed in Appendix B. All fault rock images on the figures are arranged with the normal slip sense of the Mai'iu fault shown top-to-the-right.

3.3.2 Chlorite-based Geothermometry

Various empirical geothermometers exploit the relationships between the composition and formation temperature of chlorite (see Bourdelle & Cathelineau, 2015). In this study, the geothermometer by Cathelineau (1988) was chosen as being the most appropriate to use for low-grade rocks of basaltic bulk composition (e.g., Bevins et al., 1991). This geothermometer is based on the occupancy of $\text{Al}^{(\text{IV})}$ content in tetrahedral sites of the chlorite structure and was calibrated for mafic rocks from 150–300°C by using combined microthermometric data, especially fluid inclusion studies on quartz coexisting with clays (Cathelineau & Nieva, 1985; Cathelineau, 1988). We collected chlorite compositions with EPMA from 12 samples (296 measurements; see ‘Chlorite_EPMA_data.xlsx’ in the Digital Appendix). The Windows© program WinCcac by Yavuz et al. (2015) was utilized for chlorite classification based on 14 oxygens and calculation of formation temperatures applying the geothermometer by Cathelineau (1988). Because chlorite shows considerable variation in structure at low temperatures, including the possibility of swelling varieties of trioctahedral character (mixed-layer clays such as smectite-chlorite), we applied the method by W. Wise presented in Bettison and Schiffman (1988) to calculate the relative fraction of chlorite to “swelling” component (X), where X=1 represents pure chlorite and X=0 is representative for saponite. Bevins et al. (1991) showed that the above thermometer is applicable for X values >0.55.

3.4 RESULTS: MICROSTRUCTURAL OBSERVATIONS OF MAI'IU FAULT ROCKS

3.4.1 Geochemical and Microstructural Analysis

In this section, we used optical microscopy and EDS analysis to describe microstructures and elemental compositions of the several fault rock units and to document any spatiotemporal changes in these. In this section, we also present EBSD-based estimates of mean grain size (diameter of a circle with the equivalent area of a given grain) for the phases actinolite, epidote, titanite and albite as observed in the kinematic XZ plane (two dimensional) for the various fault rock units. The data were collected with step sizes varying between 0.5–2 μm and processed by using the MTEX toolbox for MATLAB after the method proposed by Cross (2015; see Appendix B.3 and B.4 for detailed method description and **Table B.4** to **Table B.7** for estimated grain sizes of all samples). Qualitative XRD and XRF analyses were performed on very fine-grained ultracataclasite and gouge samples (see Appendix B.9 and B.10). Additional detailed EDS data and descriptions of the analysed fault rocks can be found in Appendix B.1, B.2 and the Digital Appendix under the folder 'FEG-SEM EDS EBSD'.

Mylonites

Most metabasaltic mylonites contain two distinct compositional domains (**Figure 3.4A**): 1) a dominant fine-grained matrix containing a well-dispersed mafic mineral assemblage consisting predominantly of epidote, actinolite, albite, chlorite and titanite; and 2) less common, mm- to cm-thick veins of albite- and/or quartz that are boudinaged and/or folded within the matrix. In the mylonitic matrix, fine-grained epidote grains (mean grain size: $21 \pm 7 \mu\text{m}$, 1σ) are subhedral, variably fragmented and/or microboudinaged (**Figure 3.4B**). Rims and fractures of epidote are commonly Fe^{+3} -rich (see Appendix B.2, **Figure B.3C**), in accordance with an elevated oxidation state during postmetamorphic peak deformation (Daczko et al., 2009). Fractures and microboudin necks in this mineral are filled with chlorite, \pm albite, \pm calcite, and \pm quartz. The latter minerals also occur in other grain-scale dilation sites including asymmetrical strain shadows of epidote that indicate top-to-the-NNE (normal) sense of shear (**Figure 3.4C**, inset). Dimensional alignment of acicular actinolite grains (mean grain size: $17 \pm 7 \mu\text{m}$, 1σ) define a strong SPO in the mafic matrix that is parallel to the foliation. Epidote and actinolite grains have straight phase boundaries against

another as well as against the other mafic minerals that are sub-parallel to the mylonitic stretching lineation and can be traced along several grain widths (**Figure 3.4B**). Some larger actinolite grains ($\sim 100\ \mu\text{m}$) are fractured along their long axis, in part displaying fracture-parallel dilational offset in the direction of the mylonitic lineation (**Figure 3.4B**), and/or at an high-angle to it in areas where the mylonitic foliation is folded at μm - to mm-scale (**Figure 3.4A**, inset). Albite and chlorite fill the dilational hinge zones of these folded crystals. Albite grains (mean grain size: $15\pm 7\ \mu\text{m}$, 1σ) are commonly irregularly curved or bulged and rarely polygonal. Aggregates of albite grains form “smears” of grains in the mafic matrix that are aligned in the mylonitic foliation in a direction that is sub-parallel to the stretching lineation. Chlorite grains intrude actinolite and epidote grains indicating growth of chlorite at the expense of epidote and actinolite (**Figure 3.4B**). Titanite (mean grain size: $12\pm 4\ \mu\text{m}$, 1σ) is usually fractured, and the long axes of these grains are aligned sub-parallel to the mylonitic foliation. Larger epidote, albite and actinolite grains ($\sim 100\ \mu\text{m}$ up to 2 mm in diameter), here referred to as porphyroclasts, are variably fractured with the fragments being sealed by chlorite. Indentation of porphyroclast rims is accommodated by inward bulging of chlorite (\pm iron oxides) into the interior of the porphyroclasts and/or by mantling of the porphyroclasts by dark seams containing chlorite, stilpnomelane and iron oxides (**Figure 3.4C**).

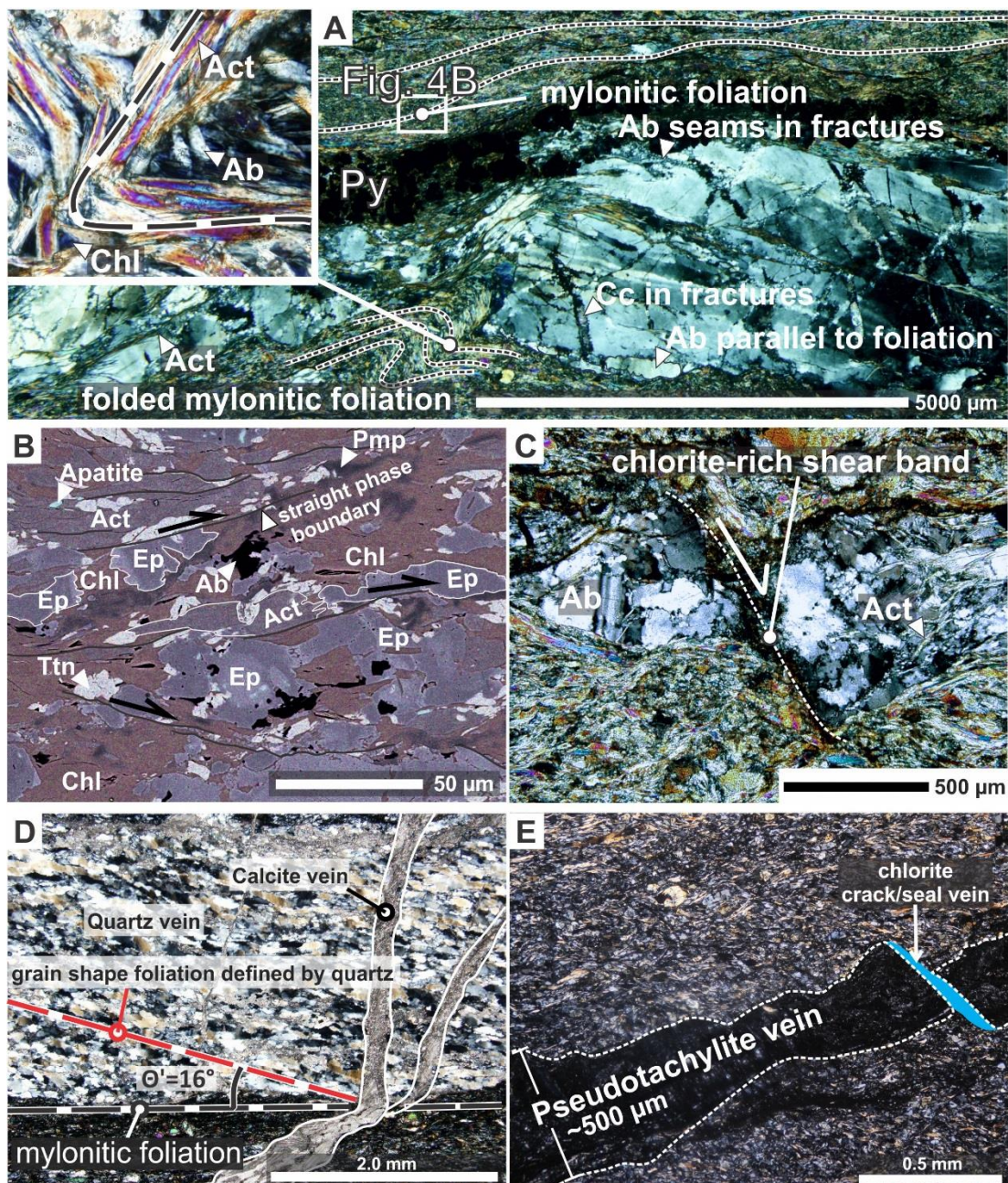


Figure 3.4 (previous page). Optical photomicrographs with crossed polarizers (XPOL; A, C, D, E) and layered elemental EDS map (B) of the mafic mylonites. A) Mylonitic sample (PNG15-59A) with a fine-grained mafic matrix and fragmented and boudinaged albite porphyroclasts. The albite porphyroclast shows strong internal deformation including fractures filled with μm -sized albite and/or calcite grains; albite twins; and foliation-parallel albite grains at the rim of the porphyroclast. Inset, folded mylonitic foliation defined by rotated and fractured actinolite grains. The dilational hinge zones in the folded domain are filled with chlorite and albite. B) Layered elemental and back-scatter image of the fine-grained mafic mylonitic matrix (PNG16-59A) based on EDS analysis on the area highlighted in 5A. Dark, brick red colours denote chlorite, which we infer to have grown together with the consumption of epidote (purple colour) and actinolite (light purple colour). Albite grains (black spots) have bulged and irregularly shaped phase boundaries against the other mafic minerals and locally occur as inclusions in epidote. Thin black lines indicate straight, planar phase boundaries between epidote and actinolite, or other minerals. Black arrows indicate grain offsets along straight phase boundaries. C) Albite porphyroclast showing strong intracrystalline deformation. Matrix and porphyroclast are crosscut by a chlorite-rich shear band. D) Quartz-rich vein in a mafic mylonite (PNG16-1BW-E) with elongated quartz grains defining a grain-shape foliation that is oblique ($\sim 16^\circ$) to the mylonitic foliation indicating a top-to-the-S (thrust) shear sense. The quartz-rich vein is cross-cut by several calcite veins that are emplaced sub-perpendicular to the mylonitic foliation. E) Optical photomicrograph of the mafic mylonite cross-cut by a pseudotachylite vein (PNG16-142C). The pseudotachylite vein is in turn cross cut by chlorite-filled crack/seal veins (highlighted in blue). Ab–albite; Act–actinolite; Chl–chlorite; Ep–epidote; Pmp–pumpellyite; Py–pyrite; Ttn–titanite.

Brittle fragmentation of albitic boudins within the metabasaltic mylonites has formed σ -porphyroclasts that are up to 2 cm in diameter (**Figure 3.4A**). These may show undulose extinction, deformation twins, bent twin lamellae, and microfractures indicating internal lattice distortion. Some albitic boudins are intergrown with actinolite fibres that are oriented sub-parallel to the mylonitic foliation. Finer-grained aggregates of polygonal albite grains (“seams” in **Figure 3.4A**) commonly occur at the rims of albite boudins and along fractures and/or veins that cross-cut the highly deformed albite porphyroclasts (**Figure 3.4A**). The fine grains of albite in these aggregates are typically elongate in shape. Fine-grained calcite grains of similar size are also commonly present. Grain boundaries between albite grains are usually bulged or sawtooth-shaped, while phase boundaries between the albite porphyroclasts and mafic matrix are variably straight to indented. Monophase quartz veins are usually arranged sub-parallel to the mylonitic foliation (**Figure 3.4D**). Elongated quartz grains within these veins define a grain shape fabric that is oblique to the mylonitic foliation ($\sim 16^\circ$) and consistently indicate a top-to-the-south (thrust) sense of shear. The elongated quartz grains are usually surrounded by finely recrystallized quartz grains

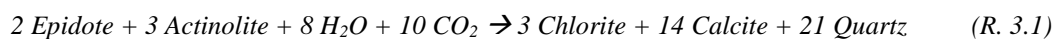
(~6–15 μm in diameter). Quartz grain boundaries in these veins are interlobate and bulged at a wavelength similar to the recrystallized grain size. Quartz porphyroclasts that are up to 2 cm in diameter may show deformation lamellae and subgrain boundaries, and are transected by bands of recrystallized grains (see Little et al., 2019).

The mafic matrix of the mylonites is locally cross-cut by ~0.5–1 mm thick seams of ultrafine-grained (optically irresolvable) rock containing epidote, albite, quartz, titanite, abundant pyrite and wall-rock (mylonite) fragments. The seams are typically discordant to the mylonitic foliation and have strongly indented, intrusive contacts indicating injection (**Figure 3.4E**). We interpret these to be pseudotachylite veins similar to the aforementioned ones that are found in the foliated cataclasite. The pseudotachylite vein shown in **Figure 3.4E** includes two domains: (1) a cryptocrystalline domain inferred to be devitrified friction-melt; and (2) an optically isotropic domain inferred to consist of predominantly amorphous material together with host rock survivor clasts and disseminated abundant pyrite grains. The pseudotachylite vein is also cross-cut by several chlorite-filled crack/seal veins recording subsequent brittle deformation (**Figure 3.4E**).

Foliated Cataclasites

The dominant foliation in the cataclasites is spaced at mm- to cm-scale and is defined by alternating dark and light folia. These are cross-cut by multiple generations of pseudotachylite veins (**Figure 3.5A, 5C**). Ultracataclasite bands within the foliated cataclasites may also overprint domains of relict mafic mylonite and/or calcite veins (**Figure 3.5B**). Most of the dark folia consist of phyllosilicates <2 μm in size, epidote (mean grain size: 17 ± 6 μm , 1σ), actinolite (mean grain size: 12 ± 4 μm , 1σ) and titanite (mean grain size: 9 ± 2 μm , 1σ ; **Figure 3.5C, 5E**). The phyllosilicates are dominated by chlorite and lesser 1Md and 2M1 illites as indicated by EDS data (see Appendix B.2, **Figure B.5**) and verified by XRD analyses (see Little et al., 2019). Actinolite and epidote grains typically have indented or truncated phase boundaries in contact with chlorite. Bulging of chlorite inwardly into epidote and actinolite grains suggests growth of chlorite together with dissolution and removal of these other phases. Albite, calcite and quartz are rare in the dark-coloured folia. Where preserved in these folia, albite grains are anhedral and have interlobate or sutured phase boundaries in contact with the other mafic minerals; or are preserved as inclusions inside epidote together with calcite, quartz and/or chlorite inclusions (**Figure 3.5E**). Hashimoto (1972) and

Skelton et al. (2000, and references therein) proposed a possible mineral reaction for the transformation of epidote and actinolite to chlorite in (sub)greenschist-facies metabasalt:



If this fluid-driven metasomatic reaction was operative, we would expect calcite and quartz to be formed at the expense of consumed actinolite and epidote. In the foliated cataclasite, abundant neorecrystallisation of calcite and quartz occurs in grain-scale dilation sites in the mm-thick albitic domains (light domains; **Figure 3.5C, 5F**). Optical CL microphotographs reveal pervasive cementation of these lighter domains by calcite (highlighted as orange colours in **Figure 3.5D**). Albite grains within the light-coloured domains are usually anhedral, untwinned and fragmented by cross-cutting calcite veins or the dark-coloured folia. EPMA analyses of albite porphyroclasts in the mylonite unit and of albite in the light-coloured layers in the foliated cataclasite unit indicate an average composition of An₀₅ in both settings, but with the albite in the cataclasite showing a wider compositional spread (**Figure 3.6**).

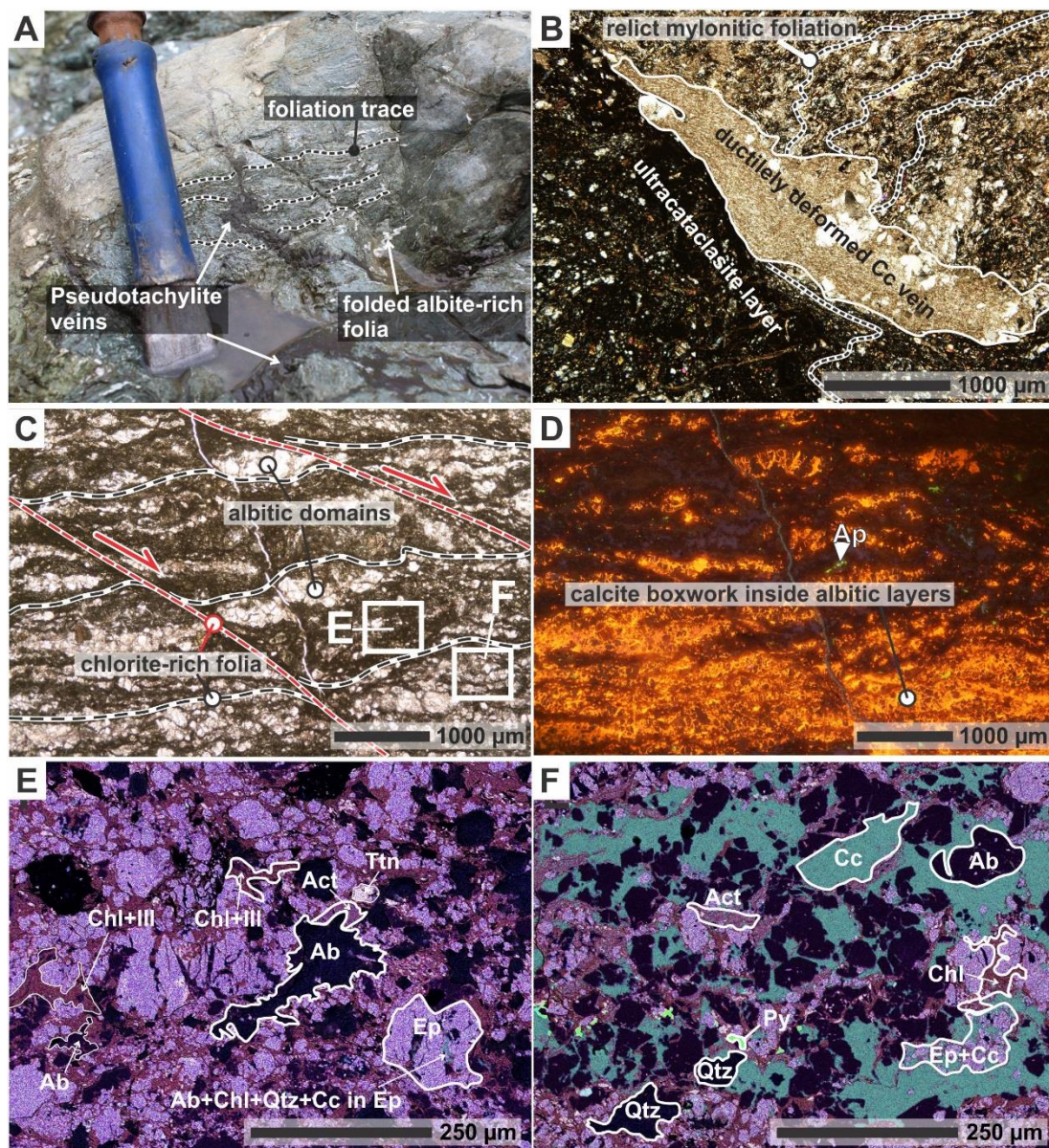


Figure 3.5 (previous page). Field photograph, optical photomicrographs, CL image and layered elemental EDS maps of the foliated cataclasite unit. A) Field photograph of the foliated cataclasite cross-cut by several pseudotachylite veins (dark seams; PNG14-19). Dashed lines indicate foliation trace in the cataclasites. B) Optical photomicrograph (XPOL) of a domain in the cataclasites preserving folded relicts of the mylonitic foliation (upper right) and ductilely deformed calcite (Cc) vein (center) cross-cut by an ultracataclasite layer (PNG16-50B). C) Optical photomicrograph of foliated cataclasite. Light layers contain albite, calcite and quartz (Figure 3.5F); dark folia contain predominantly chlorite \pm illite, plus minor epidote and actinolite (Figure 3.5E). Note, an S-C' fabric is defined by two dark seams consisting of predominantly chlorite. D) Optical cathodoluminescence of (C) highlights calcite box-work (orange) inside albite clasts (light layers in C). E) Layered elemental and back-scatter image based on EDS analysis of the chlorite-rich folia in Figure 3.5C. Dark, brick red colours indicate chlorite. We infer that chlorite grew and was passively concentrated during a reaction that consumed epidote (purple colour) and actinolite (purple-red colour). Epidote is highly fractured and filled with albite, quartz, calcite or chlorite. Relict albite and quartz grains (dark grains) have bulged or irregularly shaped grain boundaries against the other phases. F) Layered elemental and back-scatter image based on EDS analysis of an albitic layer in Figure 3.5C. This light layer is dominated by calcite (light green grains) and albite (dark grains). Minor amounts of mafic minerals (epidote, actinolite and chlorite) are also present. Ab–albite; Act–actinolite; Ap–apatite; Cc–calcite; Chl–chlorite; Ep–epidote; Ill–illite; Py–pyrite; Qtz–quartz; Ttn–titanite.

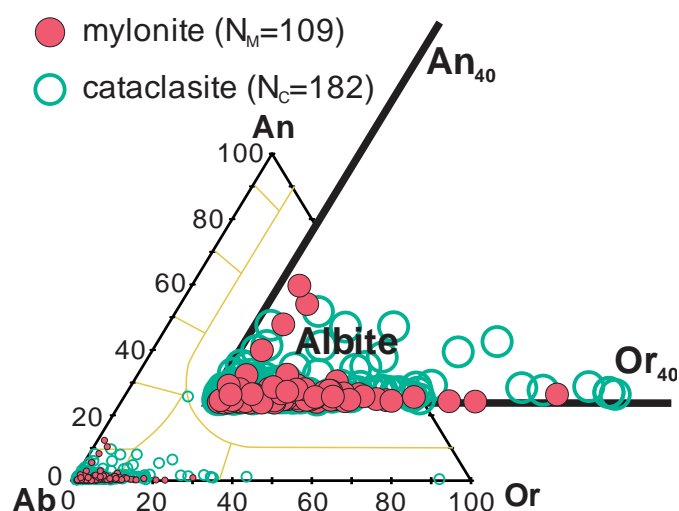
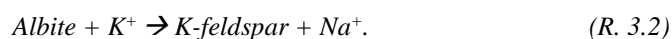


Figure 3.6. Feldspar composition in mylonites and foliated cataclasites indicate ~95% of albite (see also Daczko et al., 2009; see ‘Albite_EPMA_data.xlsx’ in the Digital Appendix for analysed samples). Ab–albite; An–anorthite; Or–orthoclase.

Ultracataclasite

The dark-coloured unfoliated matrix of the ultracataclasites is too fine-grained ($<2\ \mu\text{m}$) to be optically resolved (**Figure 3.7A**). Both XRD and EDS analyses indicate that the matrix contains relict mafic clasts (e.g., actinolite, epidote, titanite, albite) plus K-feldspar and abundant neoformed clays corrensite and saponite. EDS analyses of ultracataclasite samples show an increase in potassium (K) by ~5% in the elemental totals and a drop in sodium (Na) by ~2% relative to the foliated cataclasites and mylonites (Appendix B.1, **Table B.1**). CL microscopy indicates intensive calcite veining in some of the ultracataclasite (compare **Figure 3.7A** and **Figure 3.7B**). Remnant epidote and actinolite clasts in the ultracataclasite matrix are up to $50\ \mu\text{m}$ in diameter, fractured and show ragged boundaries in the contact with the surrounding matrix, dissolution pits and indented rims of albite (**Figure 3.7C**). We infer that these clasts have been reworked from the foliated cataclasite unit that lies structurally below the ultracataclasite layer. Based on our EDS analysis, K-feldspar grains are $>0.5\ \mu\text{m}$ and up to $\sim 12\ \mu\text{m}$ in diameter, both subhedral and unfractured, and in part replace albite (**Figure 3.7A**). The observed increase of K and reduction in Na relative to the underlying fault rocks, and growth of K-feldspar might be related to consumption of albite by the reaction:



We infer that the K-feldspar grains grew authigenically in the ultrafine-grained corrensite and saponite-rich matrix. Ultracataclasite fragments within this matrix are up to $100\ \mu\text{m}$ in size, rounded and rarely fractured (**Figure 3.7C**), and are occasionally coated with an outer cortex (or swirled into the clast) of smectite or magnetite (**Figure 3.7D** and **Figure 3.7E**). These fragments are generally more K-rich than the surrounding ultracataclasite matrix.

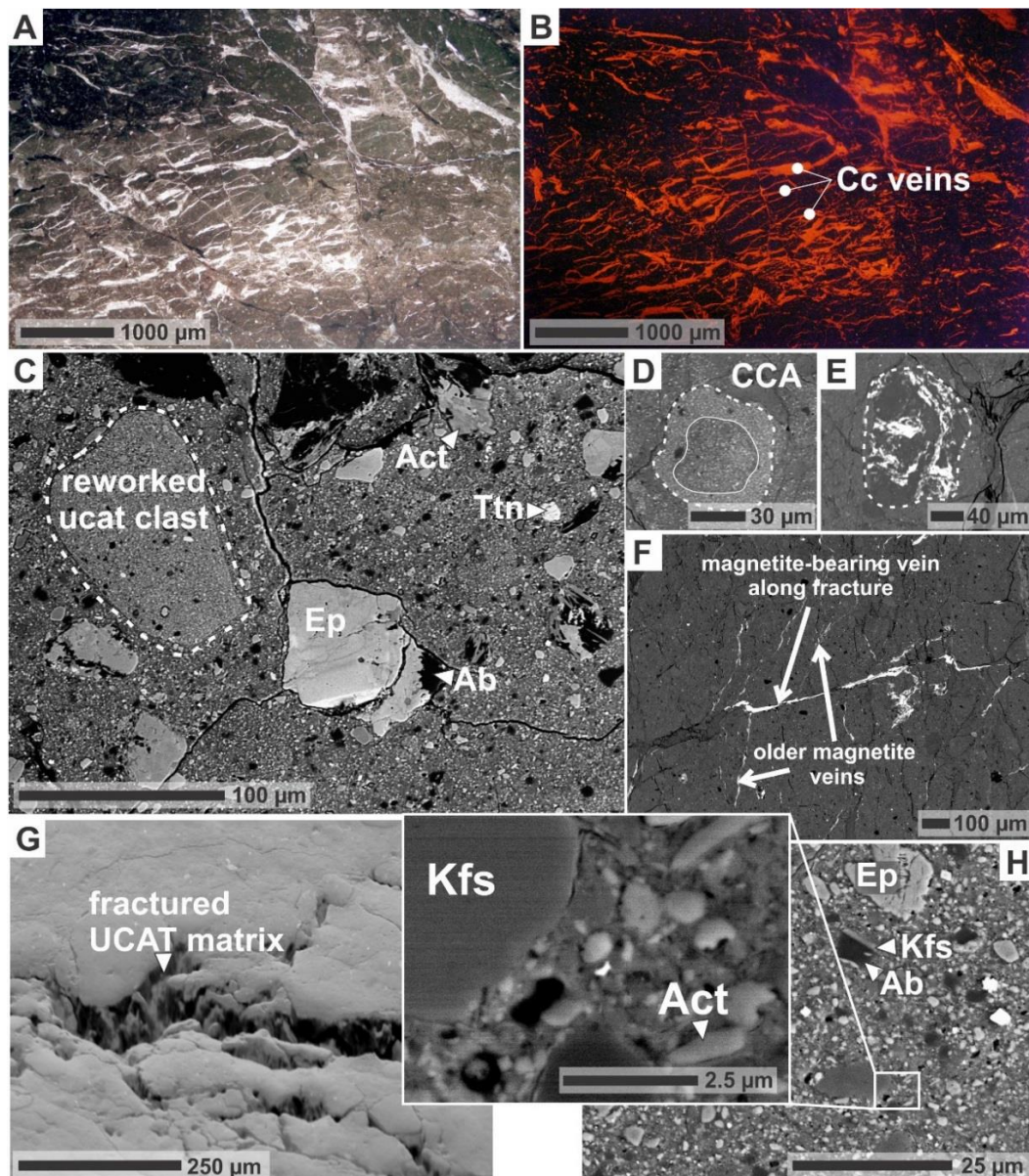


Figure 3.7. Optical photomicrographs and SEM back-scatter images of the ultracataclasite (=ucat) unit. A) Optical photomicrograph (plain light) of an ultracataclasite sample (PNG16-142D). The dark coloured, ultrafine-grained mafic matrix is cross-cut by numerous calcite veins (white colour) highlighted further in Figure 3.7B. B) Optical cathodoluminescence highlights calcite veinlets (orange) that cross-cut the ultracataclasite matrix (dark colour). C) Back-scatter image of ultracataclasite matrix. Older ultracataclasite clasts are reworked in the matrix and show a higher concentration of K relative to the surrounding matrix. Remnant mafic minerals are up to 50 µm in diameter. D) Back-scatter image of a clast cortex aggregate (CCA) that occurs locally in ultracataclasite samples. E) Back-scatter image of porphyroclastic ultracataclasite fragment reworked into a younger ultracataclasite matrix. The fragment contains magnetite-bearing veins (white) swirled into the clast. F) Back-scatter image of mutually cross-cutting magnetite-bearing veins in the ultracataclasite matrix. G) Back-scatter image of a fractured ultracataclasite matrix in part filled with calcite. H) Back-scatter image showing the ultrafine-grained ultracataclasite matrix. Note, grain of authigenic K-feldspar (inset) and rim of K-feldspar on a core of albite (PNG15-50B). Ab–albite, Act–actinolite; Cc–calcite; Ep–epidote; Kfs–K-feldspar; Ttn–titanite.

Some ultracataclasite samples contain magnetite-bearing clasts and multiple generations of ~20–60 μm -thick, magnetite-bearing veins (**Figure 3.7E, 7F**). SEM-EDS analysis show that the magnetite-bearing veins cross-cut each other and may contain magnetite \pm maghemite grains that are $<1\ \mu\text{m}$ in size (**Figure 3.7F**). Temperature-dependent magnetic susceptibility experiments on one of these samples (PNG16-142D; see Appendix B.6, **Figure B.34**, for method and results) show high magnetic susceptibility of $\sim 13 \times 10^{-6}\ \text{m}^3\ \text{kg}^{-1}$ and Curie temperatures between 580°C and 645°C for the magnetic fraction in this ultracataclasite (**Figure 3.8**). These results suggest the presence of cation deficient magnetite (i.e. magnetite slightly oxidized to maghemite), an inference that is also in accordance with our EDS data (Özdemir & Banerjee, 1984; Dunlop & Özdemir, 1997). We infer that the principal magnetic mineral in the ultracataclasite is a stable (reversible), single domain (fine grained) magnetite. Such magnetite particles may have formed by: 1) retrogression of actinolite, titanite and/or epidote, perhaps as a result of hydrothermal fluid-rock interaction (e.g., Putnis et al., 2007); and/or by 2) breakdown of smectite by frictional heating (e.g., Hirono et al., 2006; Mishima et al., 2006).

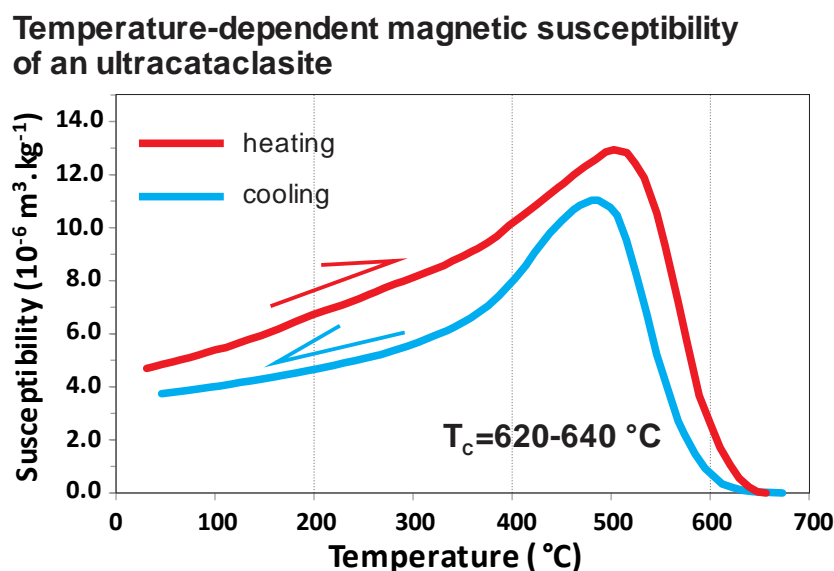
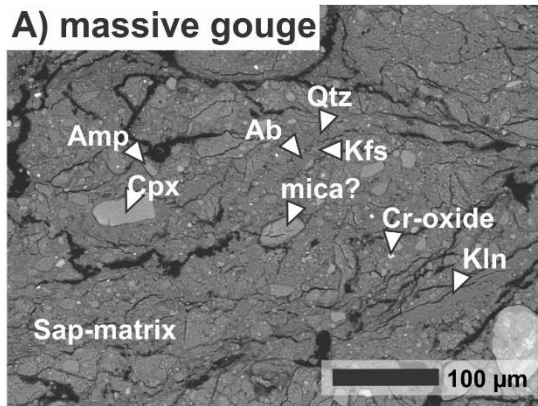


Figure 3.8. Curves of temperature dependant magnetic susceptibility for sample PNG16-142D. The red and blue lines denote heating and cooling, respectively, from 40°C to 700°C and vice versa. T_c refers to the Curie temperature. A detailed explanation of the data curves can be found in Appendix B.6.

Gouges

In contrast to the underlying fault rock units, all 4 analysed gouge samples are devoid of calcite veins, although they do contain clasts of calcite or dolomite that are inferred to have been reworked from older veins. The gouge samples contain angular to sub-rounded mono- and polyphase clasts of plagioclase, clinopyroxene, epidote, titanite, actinolite, quartz and calcite embedded in a phyllosilicate matrix. Based on our XRD and EDS data, the 2 μm fraction of this matrix consists mainly of saponite (**Figure 3.9A, 9B, 9E**). Monophase clasts (mostly albite and clinopyroxene) in gouge samples from the inactive segment of the Mai'iu fault are in general more well-rounded and ellipsoidal (**Figure 3.9A**), than those along the active fault trace (**Figure 3.9E**). Grain sizes of the monophase clasts vary between $<2\ \mu\text{m}$ up to $35\ \mu\text{m}$, distinctly coarser than any clast in the ultracataclasite. Polyphase clasts are up to 1 cm in diameter and include fragments of mafic schist and/or mylonite, foliated cataclasite, and fine-grained K-rich fault rocks that resemble the ultracataclasite in texture and composition (see **Table B.2** and **Table B.3** in Appendix B.1 for EDS analysis of the fragments in the gouges). Some of the K-rich clasts show an enhanced porosity that is not seen in the ultracataclasites (**Figure 3.9H**). The gouges contain trace amounts of dolomite and chromite—two minerals that are strongly associated with ultramafic rocks. Furthermore, XRF-analyses show that the gouges contain elevated concentrations of Cr and Ni compared to the mafic schists or mylonites in the footwall of the SDM (see **Table B.10** in Appendix B.10).

A) massive gouge



B) foliated gouge

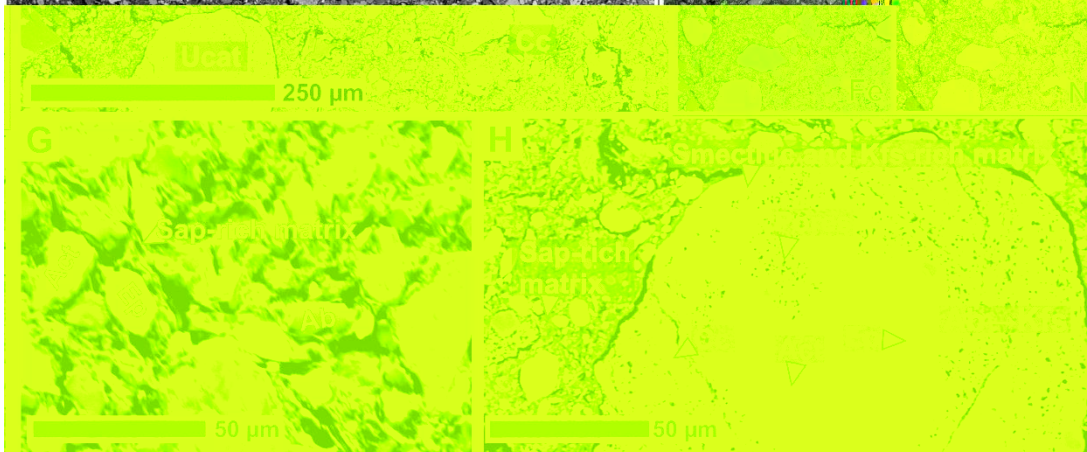
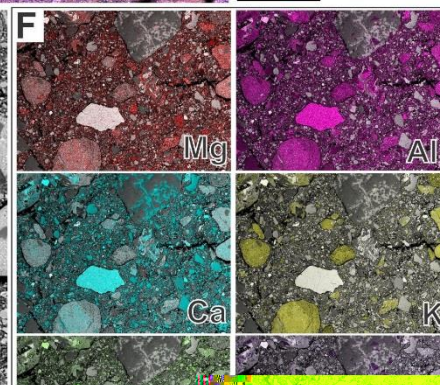
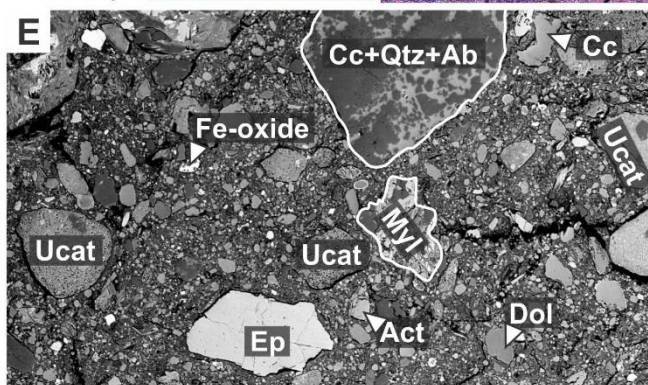
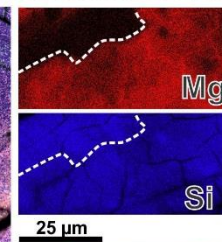
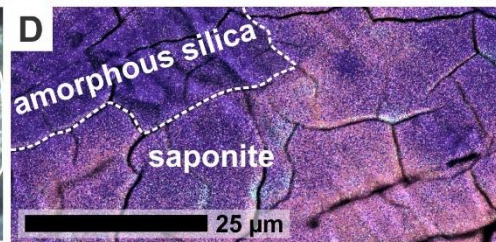
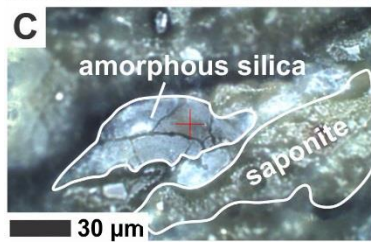
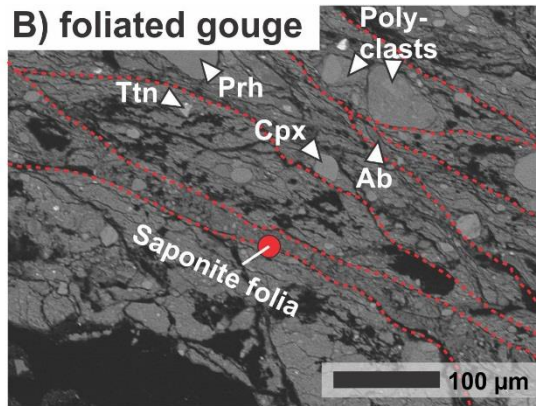


Figure 3.9 (previous page). SEM images and optical photomicrograph of gouge samples. A) SEM image of massive-textured gouge matrix in sample PNG14-19. B) Back-scatter image of a local, ~500 μm -thick foliated domain in the same sample as (A). Foliation is defined by 10–20 μm thick saponite seams. C) Optical photomicrograph of bleb of amorphous silica adjacent to saponite in the gouge sample PNG16-17C. Beam damage in amorphous silica is indicated by dark spot (red crosshairs). D) EDS layered elemental map (Si and Mg) highlighting the transition from saponite to amorphous silica in the same sample as (C). E) Back-scatter image of the gray gouge at location PNG14-33. This gouge contains reworked fragments of the structurally underlying fault rocks including ultracataclasites (ucat), mylonites (or mafic schists) and albitic domains (light coloured folia) of the foliated cataclasites. F) Element maps of (E) at reduced scale. The potassium (K) map highlights the K-rich ultracataclasite fragments. The magnesium (Mg) map highlights the saponite-rich gouge matrix. G) Forescatter diode (FSD) image of the gouge microstructure with mono- and polyphase clasts “floating” in a porous clay-rich matrix. H) Close-up of K-rich, porous ultracataclasite clast. The matrix is dominated by fine-grained mafic minerals and/or K-feldspar, while the gouge matrix is dominated by saponite. An albite grain that shows K-feldspathization is also apparent. Myl–mylonite; Ucat–ultracataclasite; Ab–albite; Act–actinolite; Amp–amphibole; Cc–calcite; Cpx–clinopyroxene; Dol–dolomite; Ep–epidote; Kfs–K-feldspar; Kln–kaolinite; Prh–prehnite; Qtz–quartz; Sap–saponite; Ttn–titanite.

A foliation is not optically visible in the gouges; however, SEM images of the gouge sample PNG16-17A show a ~500 μm thick domain that is oriented sub-parallel to the PDS. The domain contains ~10–20 μm -thick planar seams of saponite that surround lens-shaped bodies consisting of clay-particles and clasts of pyroxene or prehnite (**Figure 3.9B**). In addition, the gouge contains optically isotropic, tens of μm -thick silica-rich domains or patches (**Figure 3.9C**). Raman spectra indicate that the silica-bearing patches are amorphous (see Appendix B.8, **Figure B.39**). **Figure 3.9D** shows the diffuse nature of the transition from saponite to the amorphous silica. These relationships and the proximity of the silica phase to cracks and fractures in the samples suggest that the silica is an alteration product of saponite and/or it has precipitated together with saponite from hydrothermal fluids.

3.4.2 Hangingwall Conglomerate

On the inactive segment of the Mai’iu fault, the PDS of the Mai’iu fault forms the top contact of the fault rock sequence. This planar, mm-thick contact places unmetamorphosed Gwoira Conglomerate in the hangingwall against the gouges in the footwall. The PDS truncates cm- to dm-sized pebbles and cobbles in the Gwoira Conglomerate, forming mirror-like facets on those mostly gabbroic clasts. One faceted cobble of dolerite was analyzed by TEM (**Figure 3.10**). The goal was to describe the

composition, thickness and grain-size of the mirror-like surface and its fine striae. The analyzed TEM foil was cut perpendicular to the shiny surface (**Figure 3.10D**; see Appendix B.7).

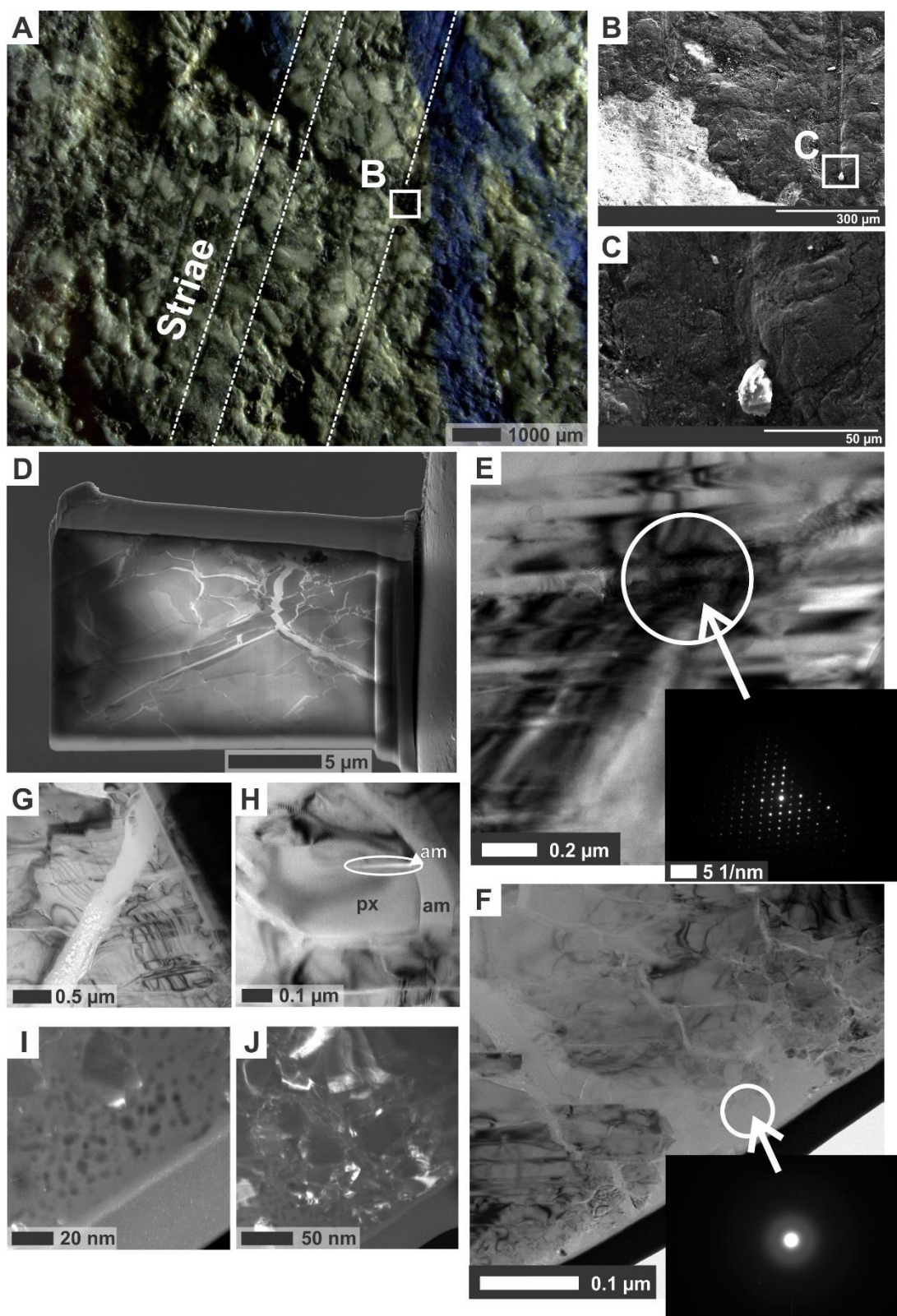


Figure 3.10 (previous page). Dolerite cobble with nanograin coating. A) Optical photomicrograph (reflected light) of the cobble surface that was truncated by the fault. Note, the surface is abraded by NNE-trending striae. B) Close-up of the striae. C) Another close-up, highlights groove lineation behind a quartz asperity on a pyroxene grain. D) Focused ion beam (FIB) sample cut perpendicular to the fault (nanograin) surface. Vein material of diverse thicknesses can be seen cutting across host material from the fault surface. E) TEM brightfield image of host material (pyroxene) comprising lamellae of clino- and orthopyroxene. F) TEM brightfield image of the shiny surface. Vein material and the surface are amorphous (inferred from diffraction pattern, inset). G) Cross-cutting amorphous veins in host pyroxene. Beam damage can be seen as holes. H) Veinlet network and amorphous material surrounding pyroxene grain with injection of amorphous material into grain. I-J) Darkfield TEM images. I) Polished surface of the truncated cobble. Dark spots in the amorphous surface are due to beam damage. J) Low magnification of (I) demonstrating continuity of the amorphous surface. Am—amorphous material; Px—pyroxene

Striations on facet surfaces trend subparallel to the inferred NNE slip direction of the fault (Little et al., 2019). **Figure 3.10A–C** show the striated surface of the analyzed dolerite showing a groove lineation etched into a clinopyroxene-grain by a quartz fragment. The TEM analysis reveals that the mirror surface on the facets is a 2 μm -thick layer of amorphous material mainly consisting of Al and Si (**Figure 3.10I–F**). The TEM images show multiple veins of this amorphous material emanating from the fault-parallel layer and injecting discordantly across host pyroxene grains in the truncated clast (**Figure 3.10G, Figure 3.10H**). Dark spots in the TEM image are holes due to beam damage, suggesting that the amorphous material coating of the mirror surface volatilized under the high voltage current and is hydrous.

3.4.3 Crystallographic Preferred Orientations of Mafic Minerals in the Fault Rocks

We applied EBSD to help us constrain deformation mechanisms accommodating slip in the different fault rocks; for example, CPOs may indicate activity of dislocation creep (e.g., Wenk, 1985). Crystal orientation data were collected in 21 samples for actinolite, titanite, epidote and albite in the mafic matrices of the different fault rock units (mylonite, foliated cataclasite, ultracataclasite and gouge) and also quartz-rich veins in the mylonitic rocks. The fabric strength was quantified using the misorientation-index (M-index). This parameter measures the difference between the observed distribution of uncorrelated misorientation angles and the distribution of uncorrelated misorientation angles for a random fabric—the stronger the fabric, the greater the M-index ranging from 0 (random fabric) to 1 (single crystal; Skemer et al.,

2005; Mainprice et al., 2015). Paleopiezometric studies on recrystallized grain size of quartz have been performed on six quartz-rich veins in 3 mylonitic samples. Relict and recrystallized grains were distinguished from one another in the collected EBSD maps based on the degree of intracrystalline lattice distortion, which can be quantified by the misorientation angle between each pixel in a grain and the mean orientation of that grain (Cross et al., 2017). The two-dimensional recrystallized grain size (diameter of a circle with equivalent area) was calculated for every grain by applying the MTEX script ‘RexRelict.m’ in the contribution by Cross et al. (2017). A detailed explanation of the EBSD method and data processing as well as additional EBSD-derived phase maps and orientation data of the mafic mineral assemblage in the fault rocks can be found in the Appendix B.4.

Actinolite, Epidote, Titanite, Albite

Figure 3.11 shows representative EBSD scans (phase maps) of a mylonite, cataclasite, ultracataclasite and gouge sample as well as lower-hemisphere equal area projections (pole figures) of actinolite (parentheses indicate planes (hkl) and square brackets indicate axes [uvw]). Actinolite in the fine-grained mafic mylonites has a strong CPO (**Figure 3.11A** and **Table B.4** in Appendix B.4); however, there is no microstructural evidence that indicates crystal-plastic deformation of actinolite grains (i.e., undulose extinction or dynamic recrystallization), nor of the other mafic phases. Actinolite in mylonitic samples has a mean M-index of 0.2 ± 0.1 (1σ). The long axes of actinolite grains [001] lie sub-parallel to the slip direction, whereas poles to (010) and (100) planes concentrate sub-parallel to Y and Z, respectively. This lattice preferred orientation becomes weaker in epidote-rich layers (M-index of ~ 0.09), where fine-grained actinolite grains anastomose around epidote porphyroclasts (PNG15-59A; **Figure B.11**, Appendix B.4). The strongest actinolite CPOs occur in the layers that are richest in that mineral (M-index of ~ 0.35 ; **Figure B.10** in Appendix B.4). The transition from mylonite (**Figure 3.11A**) to the foliated cataclasites (**Figure 3.11B**) is accompanied by a weakening in the CPO strength of actinolite. The mean CPO of actinolite in foliated cataclasites has an M-index of 0.12 ± 0.07 (1σ ; **Figure 3.11B**). Some cataclasite samples (e.g., PNG16-151E) have actinolite CPOs similar in strength to mylonites; but most are weaker and girdled with diffuse concentrations of (010) poles and [001] axes that may be oblique to the kinematic axes (**Figure 3.11B**). The pole figures of actinolite derived from the ultracataclasites (**Figure 3.11C**) and gouges

(**Figure 3.11D**) indicate a random distribution (M-index of <0.03). Both fault-rock types are characterized by drastic grain-size reduction and compositional changes (i.e., growth of phyllosilicates) relative to the structurally underlying foliated cataclasites and mylonites (**Figure 3.12**).

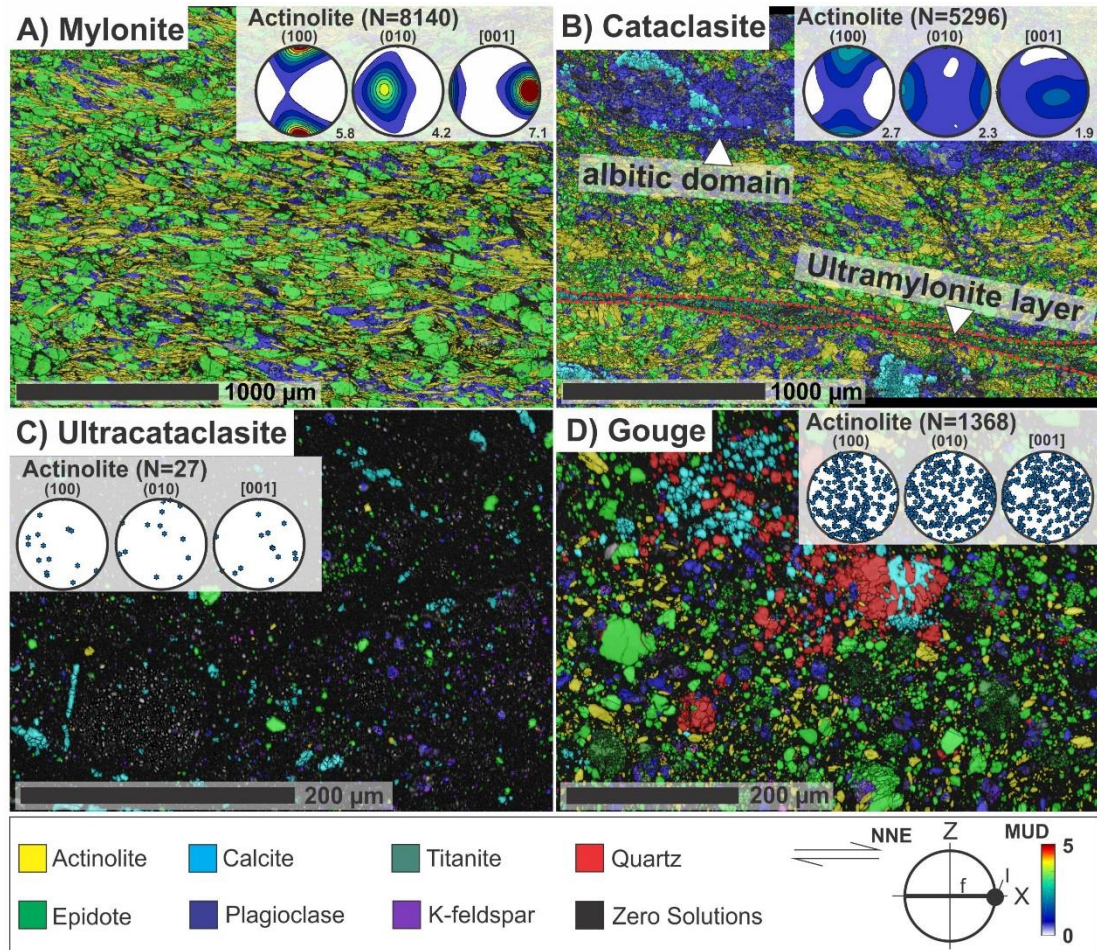


Figure 3.11. EBSD phase maps of representative samples from the mylonite, cataclasite, ultracataclasite and gouge unit at location PNG16-142 and lower-hemisphere, equal-area pole plots (Schmidt projection) of actinolite based on one point per grain. Small numbers next to the pole plots indicate maxima of multiples of uniform distribution (M.U.D.). A) Mylonite sample containing a fine-grained, well-dispersed mafic mineral assemblage (step size: 2 µm). Pole figures of (100), (010) and [001] of actinolite indicate a strong CPO. B) Cataclasite sample containing albite-rich domain and a discrete ultramylonitic layer (step size: 2 µm). The CPO of actinolite grains in the cataclasite is weaker than in mylonites as indicated by the M.U.D. and M-index (Figure 3.12). C) Ultracataclasite sample showing remnant mafic minerals in its fine-grained matrix (step size: 0.5 µm). Detected actinolite grains do not show any preferred orientation. D) Gouge sample showing remnant mafic minerals of various grain sizes (step size: 0.5 µm). Most grains in this sample have a sub-angular grain shape. Actinolite grains do not show any preferred orientation.

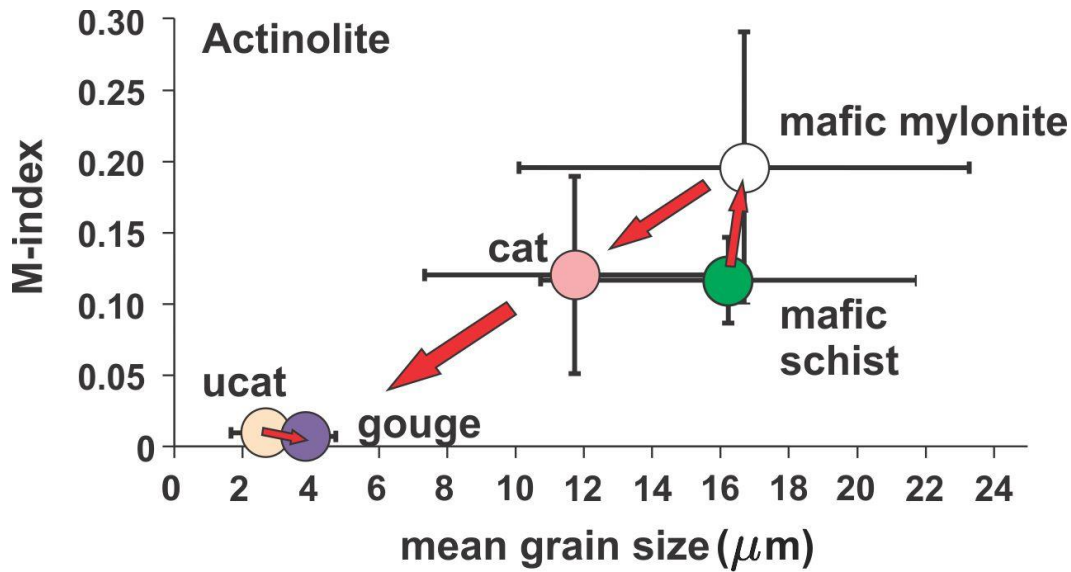


Figure 3.12. Grain size versus M-index plot of actinolite (averaged values; N=number of samples analysed) indicating a strong grain-size reduction and weakening of the fabric strength in the ultracataclasites and gouges relative to the other fault rocks. Mylonite (N=10); Cat=Cataclasite (N=8); Ucat=Ultracataclasite (N=2); Gouge (N=2); Non-mylonitic schist=mafic schist (N=5).

Epidote and titanite in mylonitic samples have random to weak CPOs with M-indices ranging from 0.05 to 0.06. The weak fabrics in these minerals are defined by a tendency for the poles to (010)-planes to be aligned sub-parallel to the slip direction, and [001]-axes sub-perpendicular to it. These minerals do not show a CPO in the foliated cataclasites, nor in the other overlying fault rocks (M-index of <0.03). Albite has a random to weak CPO in the matrices of all analyzed fault rocks (M-index of <0.04; see **Table B.6** in Appendix B.4). Exceptions are newly formed albite aggregates in albite porphyroclast that inherit a weak CPO from their parent grain (see **Figure B.16** in Appendix B.4).

Quartz-rich Veins

In the mylonite unit, we analyzed five monophase quartz veins that are variably folded on mm-scale (PNG16-140C-JS and PNG16-1BW-E), and one albite-quartz vein (PNG15-76C). SPO of the analyzed samples was quantified by using the angular relationship between the two-dimensional long axes of quartz grains and the mylonitic foliation. The angle between the grain shape foliation and mylonitic foliation is given as red and black lines, respectively, in the lower hemisphere, equal-area pole plots of **Figure 3.13**. The SPOs of all samples suggest a grain shape foliation that is oblique to the mylonitic foliation and indicate top-to-the-south (thrust) sense of shear. The CPO of this sample (**Figure 3.13A–C** and **Figure 3.13G–I**) is characterized by a well-

developed c-axis maximum in the center (Y) of the [0001] pole figure, mainly controlled by large relict grains. The recrystallized grains show weaker c-axis maxima in the center (Y) and submaxima close to the Z-axis that are rotated anti-clockwise with respect to the XZ-plane. The fabrics are ascribed to a dominant prismatic $\langle a \rangle \pm \text{rhom}$ $\langle a \rangle$ slip of the relict grains indicative for high and middle deformation temperatures (~400–500°C; e.g., Schmid & Casey, 1986), and a basal $\langle a \rangle$ slip of the recrystallized grains that may have developed during a later lower-temperature deformation. The c-axis CPO of sample PNG16-1BW-E (**Figure 3.13D–E** and **Figure 3.13J–K**) is characterized by a crossed to almost single, Type 1 girdle pattern passing through the center of the Y axis and weaker maxima close to Z. C-axis maxima of the recrystallized quartz grains lie on a great circle in the XZ-plane between the Z and Y-axis. This CPO suggests a dominance of rhomb $\langle a \rangle$ slip at middle (~350–500°C) temperatures (e.g., Mainprice et al., 1986). In sample PNG15-76C, both relict and recrystallized quartz grains show c-axis maxima close to the Z-axis that are rotated anti-clockwise with respect to the XZ plane (**Figure 3.13F**, **Figure 3.13L**). The pattern suggests dominant activation of basal $\langle a \rangle$ slip during deformation at lower to medium (~300–400°C; Okudaira et al., 1995) temperatures. The SPO of quartz grains and the asymmetry of anti-clockwise inclined c-axis girdles with respect to the XZ-plane in all analyzed samples both indicate top-to-the-south (thrust) sense of shear.

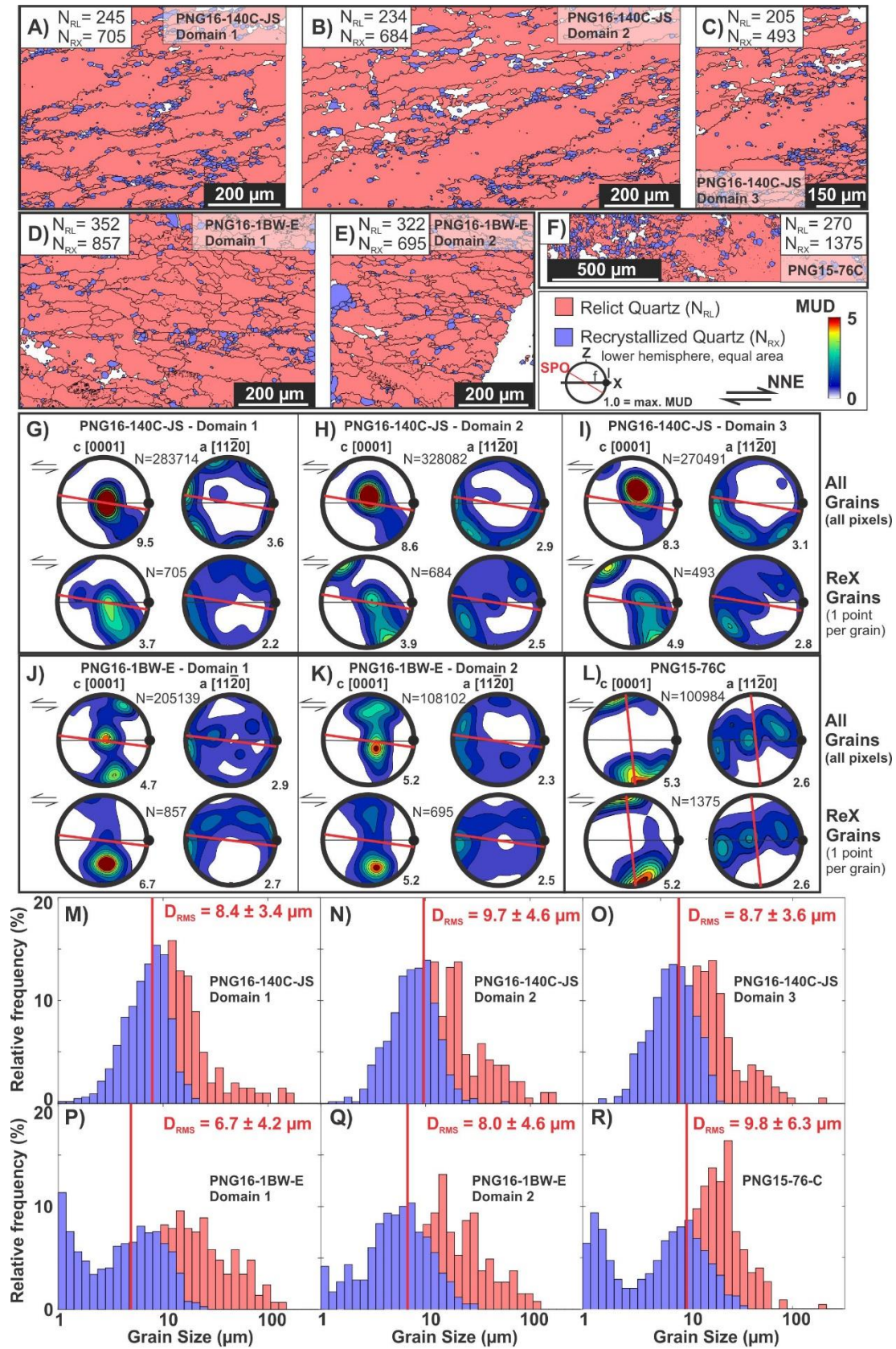


Figure 3.13 (previous page). Quartz microstructural data for quartz-rich veins in mafic mylonites. A–F) EBSD maps of relict and recrystallized (=ReX) quartz grains separated from each other based on the degree of intracrystalline lattice distortion (step size: 0.5 μm ; see Appendix B.5 for a detailed explanation). G–L) Lower-hemisphere, equal-area pole plots (Schmidt projection) of quartz c- and a-axes for all collected points (dominated by relict grains) and one point per grain (dominated by recrystallized grains). Horizontal black line (f) – orientation of mylonitic foliation; Black dot (l) – downdip direction of lineation; red, inclined line (SPO) – grain shape fabric (foliation) defined by both relict and recrystallized grains. M–R) Histograms of grain-size distribution. Red bars – relict grains; Blue bars – recrystallized grains. The average grain size (root mean square; D_{RMS}) is given for the recrystallized grains.

The grain size of dynamically recrystallized quartz (**Figure 3.13M–R**) can be used to estimate differential stresses in the nearly pure quartz-rich veins. Cross et al. (2017) calibrated the “original” quartz recrystallized grain size piezometer by Stipp and Tullis (2003) for EBSD data acquisition. We estimated differential stresses (σ_{Diff}) with the EBSD-based “sliding resolution” piezometer relationship that combines 1 μm step-size data at coarser grain sizes with 200 nm step-size data at finer grain sizes (Cross et al., 2017):

$$D_{\text{RMS}} = 10^{4.22 \pm 0.51} \cdot \sigma_{\text{Diff}}^{-1.59 \pm 0.26}, \quad (\text{Eq. 3.1})$$

where D_{RMS} is the root-mean-square (RMS) mean diameter of recrystallized grains. Based on the recrystallized quartz grain sizes in **Figure 3.13**, the estimated mean differential stresses range between $\sigma_{\text{Diff}}=108\text{--}136$ MPa (see also **Table B.8** in Appendix B.5). Recrystallized grain sizes of samples PNG16-1BW-E (**Figure 3.13P**) and PNG15-76C (**Figure 3.13R**) show a bimodal distribution in the histograms indicating that mean grain size values will be overestimated, and thus underestimate differential stresses in these samples (Cross et al., 2017). If we take into account the smallest fraction of observed recrystallized grains (~ 2.5 μm), differential stresses would be as high as 251 MPa.

3.4.4 Chlorite Geothermometry

We analysed more than 100 chlorite grains (270 microprobe measurements) in 12 samples from 8 localities comprising mylonites and foliated cataclasites in the Mai’iu fault zone. Chlorite grains were targeted in microstructural sites that were infilled syntectonically, including: (a) asymmetrical (normal sense) strain shadows and shear bands as well as pulled-apart necks between boudins of epidote and albite in mafic mylonites; (b) the dark chlorite-rich folia, top-to-the-north shear bands and

ultracataclasite bands in the foliated cataclasites; and (c) little deformed chlorite veins that cross-cut the mylonitic foliation, the spaced foliation in the foliated cataclasite and pseudotachylite veins in the mylonite and foliated cataclasite units. The results of estimated chlorite formation temperatures versus the fraction of chlorite ($X=1$ is pure chlorite) to “swelling” component ($X=0$ is saponite) are shown in **Figure 3.14**. Chlorite geothermometry yields temperatures from: (a) 226°C to 366°C with an average of $310\pm31^\circ\text{C}$ (1σ) in syntectonic sites in mylonites; (b) 158°C to 356°C with an average of $273\pm46^\circ\text{C}$ (1σ) in syntectonic sites in foliated cataclasites; and (c) 140°C to 329°C with an average of $270\pm34^\circ\text{C}$ (1σ) in chlorite-filled veins cross-cutting the mylonite and foliated cataclasite units. The results indicate a linear increase in “swelling” component (X decreases) with decreasing temperatures, whereas pure chlorite (clinochlore) is observed in all mylonite samples ($X>0.85$), and mixed-layer smectite-chlorite to saponite ($X<0.50$) mainly in the dark folia of foliated cataclasites. Following the recommendation by Bevens et al. (1991), we discarded 12 chlorite compositional measurements with $X<0.55$ from the calculated average chlorite formation temperatures. The shaded area in **Figure 3.14** (labelled “BDT”) indicates the overlap between the estimated temperatures in the mylonite samples and the late chlorite veins.

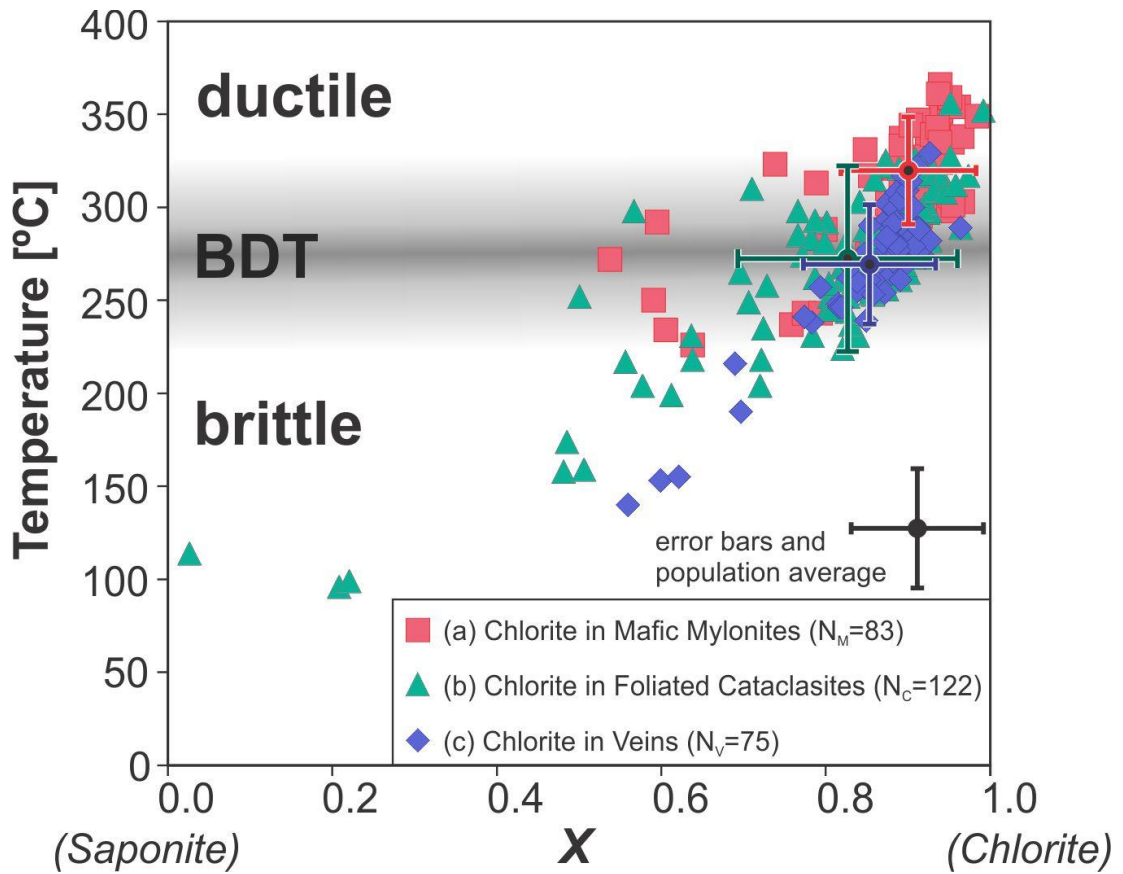


Figure 3.14. Binary plot of chlorite formation temperatures (calculated using the geothermometer by Cathelineau, 1988) versus X (the proportion of chlorite to swelling component after the method by Wise; see Bettison & Schiffman, 1988) for syntectonic microstructures in mylonites and foliated cataclasites and chlorite veins cross-cutting these units in the Mai'iu fault zone (see text for explanations). The crosses indicate average values with 1 σ error for estimated temperatures and chlorite proportion (X). The BDT is indicated, where estimated temperatures in chlorite veins and mafic mylonites overlap.

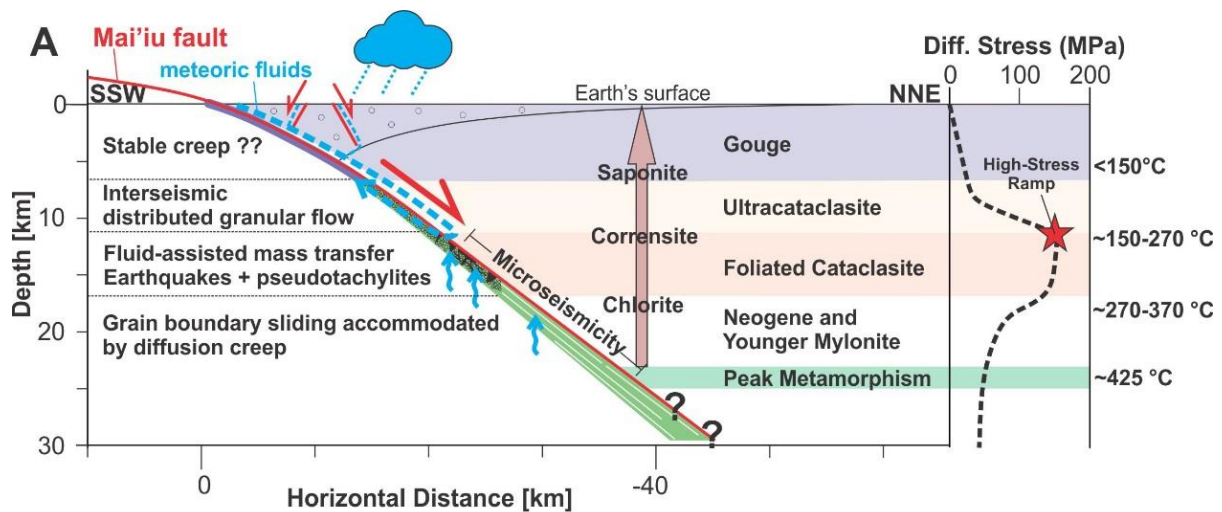
3.5 DISCUSSION

3.5.1 Mai'iu Fault Structure and Fault Rock Assemblage

The Mai'iu fault exposes mafic mylonitic rocks that have been exhumed from $\sim 25 \pm 5$ km depth at peak metamorphic conditions of $\sim 425 \pm 50^\circ\text{C}$ and 5.9–7.2 kbar (based on pseudosection modelling; Daczko et al., 2009). The late Neogene and younger fabrics in the mylonitic unit were later overprinted in the narrower and structurally overlying < 3 m thick fault rock sequence composed of (from bottom to top) foliated cataclasite, ultracataclasite and gouge. The upper mylonite and adjacent foliated cataclasite units are cross-cut by several generations of chlorite, calcite and pseudotachylite veins, some of them ductilely deformed after their emplacement (**Figure 3.3**). The brittle fault rocks (ultracataclasites and gouges) have a NNE-trending striation and a normal shear sense that is parallel to the ductile stretching lineation and shear sense in the mylonitic rocks. The fault rock units become thinner structurally upward and overprint the underlying zones indicating a progressive slip localization in time. The estimated chlorite formation temperatures (**Figure 3.14**) decrease from the mylonite ($226\text{--}366^\circ\text{C}$) to the foliated cataclasite unit ($158\text{--}356^\circ\text{C}$). We relate the wide temperature range of the foliated cataclasite, especially the very high estimated temperatures, to reflect the largely inherited nature of the mylonitic protolith that was reworked into this younger, in part brittle fault rock (**Figure 3.5B**). We interpret the overlap in estimated temperatures between the mylonites and late-stage chlorite veins to indicate a temperature range of 226°C to 329°C for the onset of brittle fracturing as indicated in **Figure 3.14**. The mineral transformation of chlorite to mixed-layer smectite-chlorite (**Figure 3.14**) and the neoformed corrensite in the ultracataclasite unit indicate sub-greenschist-facies temperatures of perhaps $150\text{--}225^\circ\text{C}$ in this fault unit (e.g., Robinson et al., 2002; Surace et al., 2011; Moore et al., 2016). Furthermore, we suggest that saponite, largely observed in the gouges (XRD data, **Table B.9** in the Appendix B.9), was stable at temperatures $< 150^\circ\text{C}$ (e.g., Lockner et al., 2011; Richard et al., 2014; Boulton et al., 2018). We infer from the described fault rock sequence and estimated temperatures a temporal evolution of cooling and embrittlement of the footwall together with a progressive localization of brittle slip during its exhumation through the BDT and to the Earth's surface.

The Mai'iu fault dips $15\text{--}22^\circ$ at its northern trace and continues to dip at $30\text{--}40^\circ\text{N}$ at $12\text{--}25$ km depth as indicated by a corridor of microseismicity downdip of it

(Abers et al., 2016). From that, we infer that the Mai'iu fault has a convex up geometry in the subsurface (Mizera et al., 2019). This structure and fault rock assemblage of the Mai'iu fault is summarized in the conceptual model of **Figure 3.15A**. The model is consistent with crustal models for MCCs that invoke a convex upward detachment fault (**Figure 3.1A**; e.g., Platt et al., 2015; Cooper et al., 2017). In the proposed model by Cooper et al. (2017; **Figure 3.1A**), the evolution of deformation mechanisms, shear resistance, and the degree of slip localization assumes a continental crust of quartzofeldspathic composition, whereas the Mai'iu fault footwall is metabasaltic. Based on our observations, the next section outlines a set of deformation mechanisms, both seismic and aseismic that were variously activated in the different (sequentially formed) metabasaltic fault rock units (**Figure 3.15A**).



B - Evolution of the Foliated Cataclasite Unit

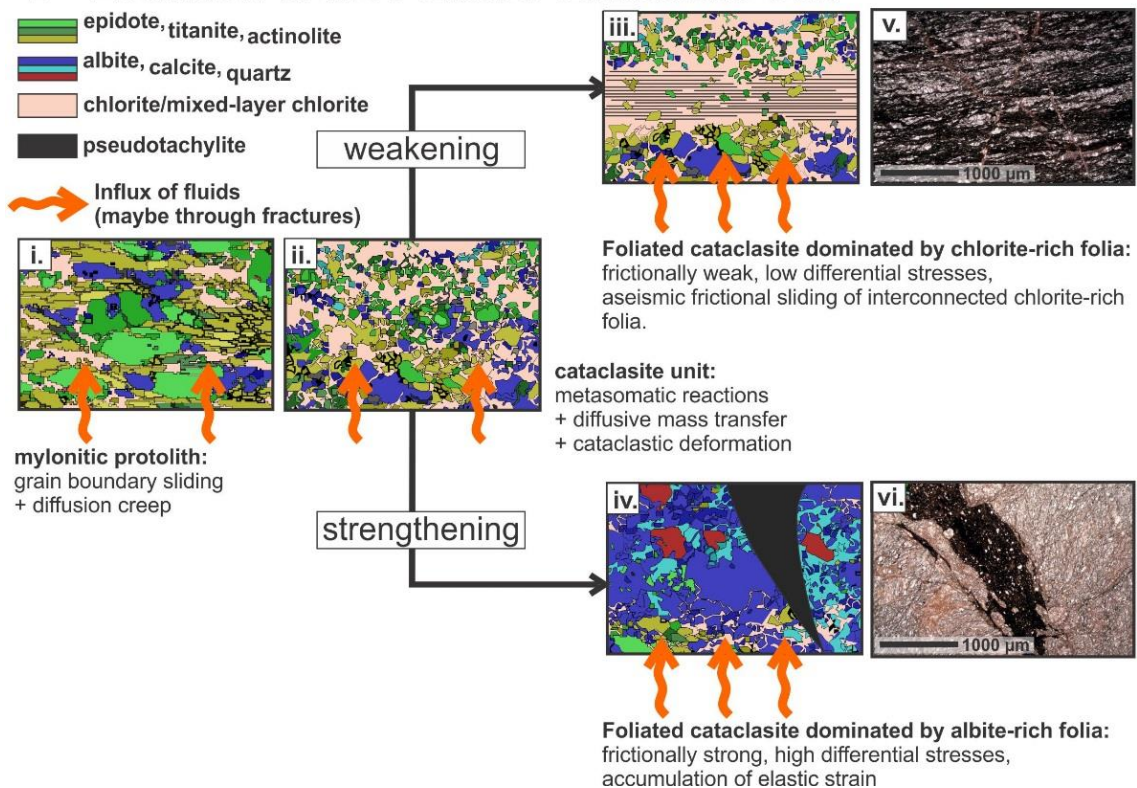


Figure 3.15 (previous page). A) Profile across the Mai'iu fault and schematic interpreted spatiotemporal changes of deformation mechanisms in the different fault rock units. Blue arrows: influx of a chemically active fluid phase (H₂O + CO₂ rich). Rain cloud and blue dashed arrows: infiltration of meteoric fluids. Arrow with Chlorite, Corrensite, Saponite: Stability and change of these minerals as a function of depth. Microseismicity range is based on Abers et al. (2016). Schematic curve of maximum (static) differential stress versus depth for the Mai'iu fault is based on the paleopiezometric data in this contribution and on inferences by Little et al. (2019). Red star on this strength-curve indicates the depth of dated pseudotachylite veins assuming a slip rate of ~10 mm/yr and a convex upward shaped fault dipping at up to 30–40° at depth. B) Schematic evolution of the foliated cataclasite unit (i.–vi.). i) relict mylonite/cataclasite and onset of the influx of H₂O and CO₂. ii) metasomatic reaction (R. 1) leads to consumption of actinolite and epidote, and growth and passive concentration of chlorite. iii) Growth of chlorite leads to the development of an interconnected chlorite-rich folia promoting aseismic frictional sliding. iv.) Precipitation of albite, calcite and quartz from an intergranular fluid phase in fractures and pores strengthen the foliated cataclasites locally and may allow strain accumulation and brittle deformation to occur. v.) Optical photomicrograph of a foliated cataclasite that has developed a strong chlorite-rich folia. vi.) pseudotachylite vein that cross-cut the foliated cataclasite dominated by albite, quartz and calcite.

3.5.2 Evolution of Deformation Mechanisms during Shearing of a Metabasaltic Footwall

Prior to exhumation and peak metamorphism in the mylonites

Deformation mechanisms in the mylonites are herein interpreted and discussed for the fine-grained mafic matrix and the less-common albite and/or quartz-rich veins. Microstructures preserved in the latter domains (SPO and CPO of relict and recrystallized quartz grains, intergrown actinolite fibres) indicate top-to-the-south (thrust) sense of shear at close to peak metamorphic conditions, which we interpret to have pre-dated the onset of normal slip on the Mai'iu fault. Albite-rich veins show evidence for both intracrystalline plasticity (undulose extinction, deformation twins and bent twin lamellae) and fracture (**Figure 3.4A, 4C**). Microstructures observed in quartz-rich veins (finely bulged grain boundaries, subgrains, undulose extinction, recrystallized grains with a strong CPO) suggest deformation by dislocation creep (e.g., Stipp et al., 2002). On the basis of a deformation temperature of ~400°C (as indicated by the activation of certain quartz slip systems close to peak-metamorphic temperatures) and differential stresses of 108–136 MPa (based on grain-size paleopiezometry), the Hirth et al. (2001) dislocation creep flow law for quartz would suggest that the strain rate in the quartz-bearing veins during thrusting was in the range of 1.1×10^{-10} to $2.8 \times 10^{-10} \text{ s}^{-1}$. This is likely to be a minimum strain rate, because we

have argued that differential stresses determined from grain-size paleopiezometry for the samples PNG16-1BW-1E and PNG15-76C are underestimated as the mean grain sizes in these samples are overestimated. Formation of the late Neogene and younger mylonitic fabric during extension imply that flow stresses in the fine-grained mafic matrix were weaker than that required to deform the recrystallized quartz-rich veins which behaved as rigid enclaves.

Late Neogene and Younger Mylonites

We do not observe any evidence for dislocation creep in the primary mineral assemblage (epidote, actinolite, titanite, and albite) of the metabasaltic mylonites. Instead, we infer from the described microstructures in the fine-grained mylonites that deformation in these rocks was accompanied by grain boundary sliding (GBS) accommodated by diffusion creep. The evidence for this interpretation includes: (1) a small average grain size of 6–33 μm of the mafic assemblage (see **Table B.4** to **Table B.7** in Appendix B.4); (2) straight phase boundaries between actinolite and epidote grains and of these minerals against the other phases along distances spanning several grain widths (**Figure 3.4B**); (3) evidence for phase-boundary parallel grain displacement (predominantly titanite, epidote and actinolite) along these straight phase boundaries; and (4) a strong CPO of non-plastically deformed actinolite grains (**Figure 3.11A**). The latter observation is consistent with interpretations regarding deformation mechanisms of clinoamphiboles in other shear zones of greenschist- to amphibolite-facies metabasites (Aspiroz et al., 2007; Getsinger et al., 2013; Getsinger & Hirth, 2014). These authors attribute strong preferred orientations in amphiboles to rigid-body rotation accommodated by diffusion creep in an otherwise weak (plagioclase-rich), fine-grained matrix. Rigid-body rotation of actinolite in our rocks is indicated by folding and fracturing of these acicular grains into albite boudin necks (**Figure 3.4A**, inset). Diffusion creep accommodated by anisotropic dissolution and precipitation of amphibole may also contribute to the development of strong CPOs in amphibole (Pearce et al., 2011), and both processes are not mutually exclusive.

We suggest that the fine grain size of the mafic minerals, the strong CPO and SPO of actinolite, and the syntectonic growth of chlorite (secondary phase admixture) were important weakening mechanisms in the mylonites. The fine grain size and preferred orientation of actinolite increases the cumulative surface area of the grains and decreases mean interparticle distances (e.g., Herwegh et al., 2011 and references

therein), both of which would promote rates of diffusion creep. Newly grown interstitial chlorite can help to overcome local strain incompatibilities between grains (cf. Behrmann, 1985; Stünitz & Tullis, 2001; Speckbacher et al., 2013). This is supported by our observation of chlorite-rich shear bands cross-cutting relatively strong albite-quartz-rich veins to interconnect weaker domains of finer-grained mafic matrix (**Figure 3.4C**).

Foliated cataclasite

The transition from mylonites to the foliated cataclasite unit is marked by: a) bleaching of the greenschist-facies derived metabasalt (lighter in colour and less mafic than the mylonitic protolith); b) development of a mm- to cm-scale spaced foliation defined by alternating albite-rich light and chlorite-rich dark coloured folia (**Figure 3.3D, Figure 3.5A, 5C**); c) strong embayment and truncation of epidote and actinolite against chlorite (**Figure 3.5E**); d) passive concentration and growth of chlorite and subordinate clays in interconnected dark folia; e) abundant calcite veining and cementation of albite in light-coloured folia (**Figure 3.5D**); f) CPO weakening and randomization in actinolite (indicated by decreasing M-index; **Figure 3.11, Figure 3.12**); and g) increasing occurrence and thickness of pseudotachylite veins (**Figure 3.3E, Figure 3.5A**). These microstructures lead us to infer that the spaced foliation in the cataclasite unit formed during deformation by the coupled fluid-assisted dissolution of epidote and actinolite, mostly in the dark-coloured seams, where it was associated with growth and concentration of chlorite and subordinate clays; and precipitation of albite, calcite and quartz, mostly in the light coloured domains. An effect of the dissolution of epidote and actinolite was to bleach the foliated cataclasite relative to the mafic protolith from which it was derived. Although this is a fluid-assisted reaction, we did not observe any evidence for sustained high pore-fluid pressures in the foliated cataclasites. Emplacement of calcite veins indicate that at times fluid pressures were high enough to induce hydrofracturing (i.e., $P_f > \sigma_3$); however, fluid influx was not high enough to completely retrogress the metabasaltic mineral assemblage as observed in other MCCs such as the Moresby Seamount Detachment in the eastern Woodlark Rift (Speckbacher et al., 2012, 2013). Fluid-assisted diffusive mass transfer led to the formation of a foliated cataclasite as shown in **Figure 3.15B** and explained below:

Influx of a chemically active fluid phase ($\text{H}_2\text{O}+\text{CO}_2$) into the cataclasite unit promoted the dissolution of mafic minerals (**Figure 3.15B-i**). In metasomatic reaction (**R. 3.1**), actinolite and epidote react to form abundant chlorite \pm illite residua in the dark colored folia (**Figure 3.15B-ii**); calcite and quartz were largely precipitated in dilation sites. Part of the reaction also involved dissolution of albite into a highly diffusible intergranular fluid and re-precipitation of this mineral in dilation sites, especially in the light colored folia together with calcite and quartz. Compositional changes of albite after dissolution and re-precipitation were insignificant (**Figure 3.6**). This process (mineral transformation, diffusive mass transfer, and re-precipitation) ultimately led to the development of an interconnected chlorite-rich folia in the cataclasites; a case of paired reaction and textural softening (**Figure 3.15B-iii**; e.g., Stewart et al., 2000; Imber et al., 2001; Moore & Lockner, 2004; Collettini & Holdsworth, 2004; Behnsen & Faulkner, 2012; Richard et al., 2014), and—at least temporally—may have promoted aseismic creep by stable frictional sliding in the chlorite-rich folia (e.g., Collettini et al., 2009a). This is in some ways similar to the pressure solution-accommodated sliding model (frictional-viscous flow) of Bos and Spiers (2002), where minerals are dissolved at sites of stress concentration and re-precipitated in pressure shadows. On the other hand, precipitation of albite, calcite and quartz in fractures and pores strengthened the rock locally, especially in the light-coloured folia (**Figure 3.15B-iv**; e.g., Richard et al., 2014). Such healing would slow down rates of dissolution–precipitation creep by increasing the mass transfer distance (e.g., Rutter, 1983). Furthermore, natural and experimental observations indicate that the kinetics of diffusive mass transfer is maximized along boundaries between phyllosilicates and more soluble phases (Niemeijer & Spiers, 2005; Gratier, 2011; Richard et al., 2014 and references therein). An explanation for the mm-scale differentiated foliation (**Figure 3.15B-v**) might be that the fluid activity of the precipitating minerals (albite, quartz and calcite) is limited, and not sufficient to transport mobile elements in the intergranular fluid large distances. Thus, deposition occurred in nearby precipitation sites (**Figure 3.15B-vi**; Gratier et al., 2013).

The foliation in the cataclasites is pervasively and chaotically folded on the mm- to cm-scale and dissected by multiple generations of (less folded) calcite and pseudotachylite veins (**Figure 3.3D, 3E**; **Figure 3.5A**). From this, we interpret that periods of slow viscous shearing were accommodated as distributed slip in the

cataclasite unit (to form the foliation, and later to fold it; and also to ductilely deform pre-existing calcite veins). This creep process was punctuated by localized seismic-slip (to cause renewed fracturing, grain-size reduction, and renewed veining, and to form the ultracataclasite bands and pseudotachylite veins). In other words, the rock experienced a mixed-mode style of slip that was variably seismic to aseismic (e.g., Collettini et al., 2011; Little et al., 2019). The spatial pattern of weakening (chlorite-rich, in the dark folia) and strengthening (calcite cementation and veining, in the light folia) caused the rock to be layered and mechanically anisotropic, a situation that contributed to development of fold instabilities in the spaced foliation fabric. Episodic periods of fluid inflow may have influenced the activity and distribution of the different deformation mechanisms.

Ultracataclasite

The transition from the foliated cataclasite to the ultracataclasite unit is marked by: a) extreme grain-size reduction (e.g., **Figure 3.12**); b) bulk chemical changes (e.g., loss of Na, Ca and gain of K, Mg; **Table B.1** in the Appendix B.1); c) mineral transformation from chlorite to trioctahedral mixed-layer smectite-chlorite \pm corrensite to saponite and the K-feldspathization of albite (**R. 3.2**); d) randomization of all CPOs in actinolite, epidote and titanite (**Figure 3.11**, **Figure 3.12**); and e) formation of K-feldspar and magnetite \pm maghemite (**Figure 3.7**, **Figure 3.8**). We infer that the dark-coloured, homogenous, unfoliated, and clay-rich ultracataclasite unit with its sub-angular to rounded remnant mafic clasts was derived from brittle fragmentation of the footwall. Bulk chemical changes, K-feldspathization of albite and the neoformation of corrensite and K-feldspar indicate hydrous alteration of the basaltic footwall (XRD data of bulk mafic fault rocks **Table B.9** in Appendix B.9 and **Figure 3.7**). The well-rounded ultracataclasite clasts within the ultracataclasite matrix, and especially the observed coated clasts (or clast-cortex aggregates, CCA; **Figure 3.7C–E**) suggest clast rotation during granular flow and accretion of clay material possibly facilitated by electrostatic forces (e.g., Boutareaud et al., 2008; Han & Hirose, 2012; Rempe et al., 2014). Granular flow is also suggested by attitude-dependant stretching versus folding of calcite veins embedded in the ultracataclasite matrix that are inclined towards or against the slip direction, respectively—a relationship that indicates distributed shearing in that matrix (Little et al., 2019).

We interpret the high magnetic susceptibility of ultracataclasite samples from the Mai'iu fault and occurrence of abundant, nm-sized magnetite \pm maghemite in ultracataclasite samples (in veins, as coating and swirled into reworked ultracataclasite clasts) to have formed by the breakdown of predominantly Fe-bearing mixed-layer smectite-chlorite during frictional shearing (thermomechanical decomposition). This interpretation is supported by changes in rock magnetic properties in other fault zones associated with recent earthquakes (e.g., 1999 Taiwan Chi-Chi earthquake, e.g., Mishima et al., 2009; Wenchuan earthquake in Sichuan Province, China, e.g., Cai et al., 2019) and high-velocity frictional experiments on crushed siltstones (containing quartz with a matrix of clay minerals, such as illite, kaolinite, smectite, and chlorite; e.g., Tanikawa et al., 2007). The cited high-velocity frictional experiment showed that the bulk magnetic susceptibility is proportional to the frictional work applied and increases with displacement due to thermal decomposition of paramagnetic clays in the powdered siltstone. Both thermally and mechanically driven mineral transformation reactions contribute to an anomalously high magnetic susceptibility, similar to that observed in our ultracataclasite unit (**Figure 3.8**; e.g., Tanikawa et al., 2008). Frictional devolatilization of Fe-bearing smectite clay is expected at temperatures $>400^{\circ}\text{C}$ (Rowe & Griffith, 2015 and references therein). We did not observe the breakdown of mixed-layer smectite-chlorite during the time-dependent magnetic susceptibility test; however, the test was performed under 1 atm and without any frictional work. Another possibility is that the magnetite was derived from external supersaturated hydrothermal fluids (i.e., magnetite supersaturation; Rowe et al., 2012 and references therein; Malvoisin et al., 2012). This might be supported by the occurrence of magnetite along fractures in the ultracataclasites, but does not explain the precipitation of single magnetite grains scattered within the fault rock (**Figure B.38** in Appendix B.6) or the nanograin coating around older ultracataclasite clasts (**Figure B.35** in Appendix B.6). In addition, we have not identified a possible source for an external Fe-saturated fluid.

We infer that deformation of ultracataclasite occurred at strain rates that varied with time. The observed microstructures in the ultracataclasite unit (mutually cross-cutting magnetite-bearing veins, formation of CCAs, ductilely deformed calcite) indicate a cycle of multiple fast (potentially seismic) slip events, accompanied by thermal decomposition of Fe-bearing minerals such as smectite, alternating with slow

(probably aseismic) creep. The magnetite coating around some CCAs may suggest co-seismic clast rotation. CCAs similar to ones observed in our fault rocks were reproduced in rotary shear experiments by Boutareaud et al. (2010) on smectite-rich granular material at seismic velocities. These authors concluded that a critical temperature is needed to induce pore fluid expansion and fluidization of the granular material for the CCAs to form (see also Han & Hirose, 2012). Hydrous alteration of the ultracataclasite matrix indicates fluid inflow led to weakening of the ultramylonitic matrix by retrogression of chlorite to saponite and corrensite, and strengthening of this fault rock by local calcite cementation.

Gouge and Principal Displacement Surface

The gouges contain recycled clasts from the underlying mafic footwall (ultracataclasite, cataclasite and mylonite fragments) and, in part, from ultramafic rocks in the overlying hangingwall (dolomite and spinel-group minerals). This recycling process is responsible for an increase in grain-size of mono- and polyphase clasts in the gouge matrix relative to the ultracataclasite matrix. The recycled clasts in the gouges “float” in a fine-grained saponite-dominated matrix (**Figure 3.9G**). Single monophase grains are not fractured and have random particle paths. Incorporation of ultramafic components into the gouge potentially promoted saponite-forming reactions (e.g., Moore & Rymer, 2012; Moore, 2014). Saponite is typically derived from the breakdown of chlorite and/or corrensite under declining temperatures. In mafic rocks, its formation requires fluid influx, and it consumes Mg, Fe, Al and (Ca + Na + K) derived from epidote, actinolite, albite (and, in our case potentially also the ultramafic hangingwall; e.g., Moore, 2014). Multiple phases of fluid flow might be recorded by our observation of saponite transitioning into amorphous silica (**Figure 3.9C, 9D**). The Pliocene alluvial conglomerates of the Gwoira Conglomerate (>2.6 km thick; Webber, 2016) and Quaternary deposits in the hangingwall, form permeable pathways for the flow of meteoric fluids that may have significantly altered and weakened this contact in the shallowest part of the Mai’iu fault zone (**Figure 3.15A**; Little et al., 2019). Experimental data on saponite-rich gouges (Carpenter et al., 2012; Moore et al., 2016; Boulton et al., 2018) indicate that they exhibit a weak coefficient of friction ($\mu < 0.2$) and velocity-strengthening behaviour (subject to aseismic stable sliding) across a wide range of sub-seismic sliding velocities, temperatures, and effective normal stresses. Velocity-strengthening minerals such as saponite do not

necessarily prevent large earthquakes ruptures propagating through the gouge, especially at high velocity (e.g., Di Toro et al., 2011; Faulkner et al., 2011; Boulton et al., 2017).

Evidence for seismic slip at shallow depths (<3 km depth as inferred from the thickness of the Gwoira Conglomerate; Webber 2017) might be indicated by the occurrence of mirror-like surfaces (nanograin coating) on hangingwall cobbles truncated by the fault, though this interpretation is not iron-clad (e.g., Verberne et al., 2014; De Paola et al., 2015 and references therein; **Figure 3.2G**; **Figure 3.10**). In some laboratory experiments, a nanograin coating was produced by extreme grain comminution at seismic to subseismic creep velocities (e.g., Verberne et al., 2014). To assess whether the nanograins may have formed by comminution or shear heating, we calculated the minimum grain size that can be achieved by grinding (the grinding limit) for a basaltic rock, plagioclase and quartz based on fracture toughness (K_{IC}) and flow stresses at zero °K ($\hat{\tau}_0$; equation 13 in Sammis & Ben-Zion, 2008; see folder ‘Grind Limit for Particles’ in the Digital Appendix for variables). The estimated minimum grain sizes are $>d_{\min\text{Basalt}}=268$ nm, $>d_{\min\text{Plag}}=53$ nm and $>d_{\min\text{Quartz}}=86$ nm, respectively ($d_{\min\text{Quartz}}$ was calculated by Sammis & Ben-Zion, 2008). This calculation is imprecise due to the uncertainties in material properties (Sammis & Ben-Zion, 2008), but if accurate it means that the interpreted amorphous mirror-like coating on the cobble-surfaces (**Figure 3.10F, 10I, 10J**) cannot be achieved by comminution. For this reason, we interpret this nano-coating of amorphous material (Si and Al rich) and injection veins (**Figure 3.10D, 10G, 10H**) to have been generated by frictional shearing during extreme slip localization at high velocity (e.g., Ohashi et al., 2011; Smith et al., 2013; Rowe & Griffith, 2015 and references therein).

3.5.3 Strain Rates during Exhumational Shearing of the Mai’iu Fault

A maximum strain rate in the mafic mylonites that accommodated slip on the Mai’iu fault can be calculated by the relation $\epsilon=\dot{u}/h$, where ϵ is the strain rate, \dot{u} the slip rate and h the thickness of the deforming zone (e.g., Rowe et al., 2011). By using the known fault slip rate of ~10 mm/yr (Webber et al., 2018) and the width of the mylonites thinning upwards from ~60 m to as low as 1.5 m, implied shear strain rates are in the range of 5.3×10^{-12} to $2.1 \times 10^{-10} \text{ s}^{-1}$. Getsinger and Hirth (2014) showed that flow laws for wet plagioclase can be applied to the rheology of a fine-grained amphibole. Applying experimentally derived diffusion creep flow laws for wet Ab_{100}

(H₂O 0.2 wt.%) by Offerhaus et al. (2001), pure albite with an average grain size diameter of 15 μm at temperature of $\sim 400^\circ\text{C}$ and differential stresses of 60–100 MPa (lower than the estimated flow stresses in the extensionally undeformed, quasi-rigid quartz veins) is predicted to deform at strain rates of 1.5×10^{-13} to $\sim 2.5 \times 10^{-13} \text{ s}^{-1}$. This estimated strain rate is somewhat lower than that required to accommodate the full slip rate. This shortfall may indicate that a natural polyphase mafic aggregate at greenschist facies conditions with its neoformed, interstitial chlorite (and with strong CPO and SPO) is weaker in diffusion creep than that predicted by extrapolations of laboratory experiments on wet albite (see also Little et al., 2019). By comparison, mafic (gabbroic) mylonites exhumed by a convex up oceanic detachment fault at Atlantis Bank (Southwest Indian Ridge) are inferred to have deformed by dislocation creep and grain boundary sliding accommodated diffusion creep in plagioclase and pyroxene at $\sim 900\text{--}850^\circ\text{C}$ and $\sim 750\text{--}670^\circ\text{C}$ at strain rates of 10^{-12} to 10^{-11} s^{-1} (Miranda, 2006; Mehl & Hirth, 2008). The estimated strain rates by these authors are based on microstructural analysis and extrapolation of experimental flow law parameters for plagioclase to geologic strain rates, and are consistent with half-spreading rates at Atlantis Bank accommodated on a $<100 \text{ m}$ wide shear zone of the main detachment fault (Baines et al., 2008; Miranda & John, 2010). We suggest that the strain rates of fine-grained mafic mylonites along the Mai'iu fault and in oceanic detachment faults deforming under grain boundary sliding accommodated by diffusion creep may be similar, even though the deformation temperatures are greatly different.

To accommodate the Mai'iu fault's slip rate in the $\sim 1.5\text{--}3.0 \text{ m}$ -wide foliated cataclasites, aseismic frictional sliding of the interconnected chlorite-rich folia would need to attain a bulk strain rate of 1.1×10^{-10} to $2.1 \times 10^{-10} \text{ s}^{-1}$. Aseismic frictional sliding may be impeded in the foliated cataclasites, where the chlorite-rich folia become locked against relatively strong albitic domains, perhaps causing them to deform cataclastically (e.g., Richard et al., 2014). Loading of albite-rich layers allows elastic strain to accumulate and may result in partial locking where aseismic frictional sliding on chlorite-rich folia has been impeded. This leads to a shortfall in creep rates and the accumulation of stored elastic strain energy. In practice, the bulk slip rate accommodated by dissolution-precipitation creep must be lower than the measured Holocene slip rate of Webber et al. (2018), if some of the slip takes places during

earthquakes as indicated by pseudotachylite veins that cross-cut the foliated cataclasite unit.

3.5.4 Seismic Slip and High Stress Ramp along the Mai'iu Fault

We have cited several lines of evidence that slip on the Mai'iu fault was in part seismic. These include: (1) pseudotachylite veins in mylonites and foliated cataclasites (**Figure 3.3E, Figure 3.4E, Figure 3.5A**); (2) nm-sized magnetite±maghemite grains in veins cross-cutting the ultracataclasite matrix, and in (or around) older ultracataclasite clasts (**Figure 3.7E, 7F**); and (3) mirror-like surfaces on hangingwall cobbles truncated by the fault (**Figure 3.10**). The numerous exposed, 5–40 mm thick pseudotachylite veins as well as brittle faults cross-cutting the foliated fabrics in the cataclasite indicate that aseismic fluid-assisted mass transfer was in part interrupted by earthquakes. During earthquakes, the propagating rupture front may have led to the thermomechanical breakdown of Fe-bearing minerals by frictional shearing (predominantly mixed-layer smectite-chlorite in the ultracataclasites presented here) forming magnetite-bearing veins (e.g., Cai et al., 2019). Nano-coatings of amorphous material (rich in Al and Si) on fault-truncated pebbles and cobbles with multiple veins of amorphous material injecting discordantly from these mirror-like surfaces into the cobbles may have resulted from flash heating at asperities on the slip surface during earthquakes rather than extreme grain comminution (Kuo et al., 2016). The exposed pseudotachylite veins are as young as ca. 2.2 Ma (Little et al., 2019). At a slip rate of 10 mm/yr on a 30–40° dipping fault, the estimated ages by Little et al. (2019) imply pseudotachylite generation at 10–12 km depth. We infer that these veins have formed at a high-stress ramp in a zone of seismic/aseismic slip on the Mai'iu fault at this depth (**Figure 3.15A**). We interpret the corridor of microseismicity at 12–25 km depth (Abers et al., 2016) as reflecting aseismic creep accompanied by microearthquakes in the downdip equivalents of the exhumed mylonites and foliated cataclasites described herein (e.g., Chiaraluce et al., 2007, 2014; Vadacca et al., 2016; see also Little et al., 2019).

3.6 CONCLUSIONS

Our microstructural observations of fault rocks in the Mai'iu fault zone document the space-time evolution of fault rock development in a fine-grained mafic protolith and the changing deformation mechanisms accommodating slip on a rapidly slipping, active low-angle normal fault as its footwall is exhumed towards the Earth's surface.

- Mylonitic deformation was mainly controlled by rotation and sliding of the pre-existing fine-grained (6–33 μm in diameter) mafic mineral assemblage consisting of epidote, titanite, actinolite, chlorite, albite and quartz.
- Slip within the mylonites was accomplished by grain-boundary sliding accommodated by diffusion-creep at temperatures $>270\text{--}370^\circ\text{C}$ and strain-rates of 5.3×10^{-12} to $2.1 \times 10^{-10} \text{ s}^{-1}$.
- At shallower levels on the fault ($T \geq 150\text{--}300^\circ\text{C}$) in the mafic foliated cataclasites, fluid-assisted mass transfer of albite, quartz and calcite during dissolution-precipitation creep led to mineral transformation reactions with continuous chlorite growth, creating a 1.5–3 m thick zone of foliated cataclasite that deformed in part aseismically at a maximum strain rate of 1.1×10^{-10} to $2.1 \times 10^{-10} \text{ s}^{-1}$.
- During the above creep process, precipitation of albite, calcite, chlorite and quartz caused sealing of fractures and pores in the cataclasite. This caused increases in cohesion and mean diffusion distance, reducing creep rates, while also hardening the rock and promoting an increase in frictional strength and differential stress. Build-up of elastic-strain in albite-rich folia may have led to the nucleation of earthquakes as evidenced by multiple generations of pseudotachylite veins that cross-cut the foliated cataclasites within a frictionally strong, high stress ramp at 10–12 km.
- Slip in the ultracataclasite unit ($\sim 150\text{--}225^\circ\text{C}$) was at least in part accomplished by distributed granular flow of the ultrafine-grained mafic minerals as inferred by the formation clast cortex aggregates and

from plastically deformed calcite veinlets embedded in the ultracataclasites.

- At the shallowest crustal levels ($T < 150^{\circ}\text{C}$), clay-rich gouges contain abundant saponite, a velocity-strengthening, weak mineral. Given sufficient areal distribution on the fault plane, saponite gouges would promote aseismic slip on the shallowest dipping most poorly oriented part of the Mai'iu fault (dipping $\sim 15\text{--}22^{\circ}$).
- The fault rocks experienced a mixed-mode style of slip at strain rates that varied spatiotemporally from high (seismic) to low (aseismic).

Chapter 4: Strength and Stress Evolution of an Actively Exhuming Low-Angle Normal Fault, Woodlark Rift, SE Papua New Guinea

Abstract

We estimate differential stresses and principal stress orientations driving rapid dip-slip (~10 mm/yr) on a normal fault—the Mai'iu fault in SE Papua New Guinea that dips ~20° at the surface. The fault's mafic footwall hosts a well-preserved sequence of mylonite, foliated cataclasite, ultracataclasite and gouge. In these fault rocks, we combine stress inversion of fault-slip data and paleostress analysis of syntectonically emplaced calcite veins (mechanical twinning, recrystallized grain-size) with microstructural geothermometry to constrain stress orientations and differential stresses, and to construct a stress profile through the middle crust from which the footwall has been exhumed. We infer from this reconstructed strength profile: 1) mylonites at ~20–12 km depth accommodate slip on the Mai'iu fault at low differential stresses (>25–135 MPa) and are progressively overprinted by localized brittle deformation with decreasing temperatures; 2) differential stresses in the foliated cataclasites and ultracataclasites at ~8–12 km depth are high enough (140–185 MPa) to drive slip on a 30–40° dipping, strong part of the fault and cause new brittle yielding of mafic footwall rocks in a zone of mixed-mode seismic/aseismic slip; and 3) at the shallowest crustal levels on the most poorly oriented part of the Mai'iu fault (dipping ≤22°), clay-rich gouges are inferred to be frictionally weak (~0.15–0.28) and promote active slip. High stress ratios ($\sigma_1 \approx \sigma_2$) with subvertical σ_1 and subhorizontal σ_3 parallel to the extension direction are attributed to vertical unloading and 3-D bending stresses consistent with rolling-hinge style flexure of the footwall (also corrugation growth).

4.1 INTRODUCTION

Studies of the lithospheric strength are essential to the understanding of a range of tectonic processes, such as mountain building and seismicity in continental regions (e.g., Behr & Platt, 2014). Lithospheric or crustal strength is often expressed as the maximum differential stress that a rock can sustain before it fractures (brittle deformation) or flows (ductile deformation). The magnitude and distribution of frictional resistance on gently dipping detachment faults that may have formed and/or slipped as “low-angle normal faults” ($<30^\circ$, LANFs) in highly extended continental crust is a topic that remains controversial: Andersonian normal faults with “Byerlee” frictional strength ($\mu=0.6\text{--}0.85$; Byerlee, 1978) should initiate and slip at dips of $60\text{--}75^\circ$ and frictionally lock-up at dips $<30\text{--}45^\circ$ (e.g., Anderson, 1951; Sibson, 1985; Lister & Davis, 1989; Collettini & Sibson, 2001; Axen, 2004, 2007; Collettini, 2011); and yet, a small number of normal faults are demonstrably active today at low angles (dip $<30^\circ$; e.g., Chiaraluce et al., 2007 and references therein).

How crustal strength changes as a function of depth and whether LANFs are weak relative to their surroundings, to other faults, and to laboratory friction values remain fundamental questions in geodynamics (e.g., Axen, 2004; Behr & Platt, 2011 and references therein). Bounding a metamorphic core complex (MCC), detachment faults typically have slip magnitudes of tens of kilometres, sufficient to exhume rocks in their footwall from below the brittle-ductile transition (BDT; e.g., Whitney et al., 2013; Platt et al., 2015), thus providing a window into the physical conditions of the middle crust (**Figure 4.1A**). Most previously studied examples of MCCs are ancient, such that processes driving slip on detachments have been widely obscured by combinations of post-slip tectonic tilting, erosion, and other postformational overprints; while most known active examples are concealed beneath a cover of brittlely faulted upper-plate rocks (Chiaraluce et al., 2014).

The active Mai’iu fault in SE Papua New Guinea is not covered by upper plate rocks. This fault exhumes a little-eroded, >25 km-wide fault surface in its footwall and provides a rare “natural laboratory” into extensional detachment faults (Spencer, 2010; Mizera et al., 2019). Importantly, the fault also self-exhumes a full sequence of its fault rocks (mylonites, foliated cataclasites, ultracataclasites and gouges; Little et al., 2019). The fault is known to be slipping rapidly—at $\sim 8\text{--}12$ mm/yr (Webber et al., 2018; Wallace et al., 2013). The fault rock sequence records increasing embrittlement and

strain localization during uplift and cooling of the footwall that accommodates progressive slip on the fault (Little et al., 2019). Microstructures in the fault rocks preserve information about changes in temperature and differential stress as they were carried to the Earth's surface. For this reason, the Mai'iu fault is an ideal target from which to reconstruct a strength-profile of this fault through the middle to upper crust and to study the stress regime associated with, and driving slip on, extensional detachment faults.

Most knowledge of brittle rock strength comes from laboratory experiments (e.g., Byerlee, 1978) and deep boreholes (e.g., Zoback & Harjes, 1997; Hickman & Zoback, 2004). These studies typically infer Coulomb frictional failure in the upper crust, in which the differential stress or shear stress (τ) is linearly related to the effective normal stress (σ_e) via a "Byerlee" coefficient of friction (**Figure 4.1A**). The ductile regime of the middle and lower crust is predicted by laboratory experiments to deform plastically. There, differential stresses depend on strain rate, temperature and grain size as a function of the operative (dominant) deformation mechanism (e.g., Brace & Kohlstedt, 1980; Walker et al., 1990). Differential stress in the ductile regime is predicted to increase with decreasing temperature leading to a peak in crustal strength near the brittle-ductile transition (BDT; **Figure 4.1A**). The simplified "Christmas tree" view of static crustal strength variation assumes a fixed strain-rate and geothermal gradient that is controlled by Coulomb frictional failure in the upper crust and laboratory-derived flow laws in the middle and lower crust, and an ideally oriented fault plane dip.

Based on microseismicity, the Mai'iu fault has been shown to dip at 30–40° at depths of ~12–20 km (Abers et al., 2016). The exposed (abandoned) part of this convex upward shaped fault surface dips at ~15–22° (Spencer, 2010; Little et al., 2019; Mizera et al., 2019). The flexural-isostatic back-rotation and shallowing of an initially moderate- to steeply-dipping normal fault during progressive unloading of its footwall caused by slip is called "rolling-hinge" evolution (**Figure 4.1B**; e.g., Spencer, 1984; Buck, 1988; Wernicke & Axen, 1988). For the case of shallow (i.e., <30° dipping) detachment faults, "Byerlee" friction coefficients in the upper crust cannot explain slip on such misoriented faults by applying the Coulomb failure criterion to an assumed case of Andersonian stresses (Anderson, 1951; **Figure 4.1A**, red shaded area). The apparent mechanical paradox is further reinforced by a near absence of low-angle

normal faulting earthquakes and focal mechanisms observed historically in active rifts (Jackson, 1987; Jackson & White, 1989; Collettini & Sibson, 2001; Abers et al., 2016), where most seismic moment release can be attributed to slip on moderate to steeply dipping normal faults as predicted by Anderson (1951).

Slip on a seemingly misoriented, shallow normal fault in an Andersonian stress regime might be achieved by: (1) high pore fluid pressures within the fault zone (e.g., Rice, 1992); and/or (2) frictionally weak fault materials such as a phyllosilicate-rich (i.e., talc, saponite) gouge (e.g., Floyd et al., 2001; Collettini et al., 2009a; Collettini et al., 2009b; Collettini, 2011; Lockner et al., 2011). **Figure 4.1A** indicates the permissible coefficient of friction values for the range 0.15–0.6 (i.e., saponite to “Byerlee” friction; Lockner et al., 2011; Byerlee, 1978) to allow slip on a 30° dipping, cohesionless fault rather than forming new, well-oriented faults in the surrounding mafic crust (CF; Coulomb failure limits differential stress). Another possible way to account for slip on a misoriented fault is by rotation of the principal stress axes away from horizontal and vertical (i.e., “Andersonian”) attitudes towards a more favourably inclined orientation in proximity to the fault; for example, due to damage-induced change in elastic properties in the fault damage zone, earthquake rupture dynamics, topographic loads, lateral density variations, and/or horizontal or vertical shear tractions caused by lower crustal flow (e.g., Yin, 1989 and related comments by Buck, 1990; Axen, 2004; Westaway, 2005; Faulkner et al., 2006).

Behr and Platt (2011) show that microstructural, paleopiezometric, and geothermometric data can be combined to produce a naturally constrained depth-strength profile of exhumed crustal rocks. They argue that detachment faults are particularly appropriate for such an analysis, because progressive strain localization that is typical of such faults preserves spatial snapshots of that history in different fault rocks and microstructural domains. **Figure 4.1A** schematically shows several sites on a normal fault where calcite veins might be emplaced (blue arrows) into fault rock units across certain depths and temperature conditions for which particular elements of the fault rock sequence were (temporarily) active. Deformation of calcite usually produces twin-lamellae (e-twins) that, depending on formation temperatures and differential stress conditions, express characteristic twin morphologies (**Figure 4.1C** C; Burkhard, 1993; Ferrill et al., 2004) and twin densities (**Figure 4.1D**; Rowe & Rutter, 1990; Ferrill, 1998; Rybacki et al., 2011, 2013). At high temperatures, for

example in the mylonite zone, calcite grains within the veins may deform mostly by dynamic recrystallization rather than twinning (e.g., Walker et al., 1990; De Bresser, 2002; Renner et al., 2002). At shallower depths, calcite veins might be emplaced into fault rock units (e.g., foliated cataclasite) that formed in a seismogenically active, lower temperature part of the fault zone where pseudotachylite veins are present and where differential stresses were higher. Nearer to the surface, calcite veins may be emplaced into the upper crustal fault rocks, such as weak, phyllosilicate-bearing ultracataclasite or fault gouge, where they may record lower differential stresses.

The metabasaltic footwall of the Mai'iu fault contains multiple generations of deformed calcite veins and outcrop-scale brittle faults that cross-cut the sequentially formed fault rock units (Little et al., 2019). Our goal is to compile these stress-depth snapshots by taking advantage of space-for-time relationships provided by progressive slip localization on the cooling and exhuming fault zone. By sampling the incrementally deformed sequence of fault rocks at the surface, and applying paleopiezometric and geothermometric methods to them, we attempt to reconstruct the stress-temperature distribution along the fault, and by inference, the stress-depth profile through which the fault rocks were exhumed. Estimated differential stresses are based on the mechanical twinning and/or recrystallized grain-size of deformed calcite veins. Deformation temperatures are based on calcite-twin morphology and chlorite-composition geothermometry. Principal stress orientations in the fault zone and in the surrounding crust were estimated using stress-inversion techniques on crystallographic data for calcite-twins collected by electron backscatter diffraction (EBSD) and on fault-slip data of late brittle faults. Finally, we collected sufficient stress–depth points to construct a stress profile along the Mai'iu fault (<20 km depth), from which we derive the peak strength of this fault and integrated strength of the brittle crust in this region during extension.

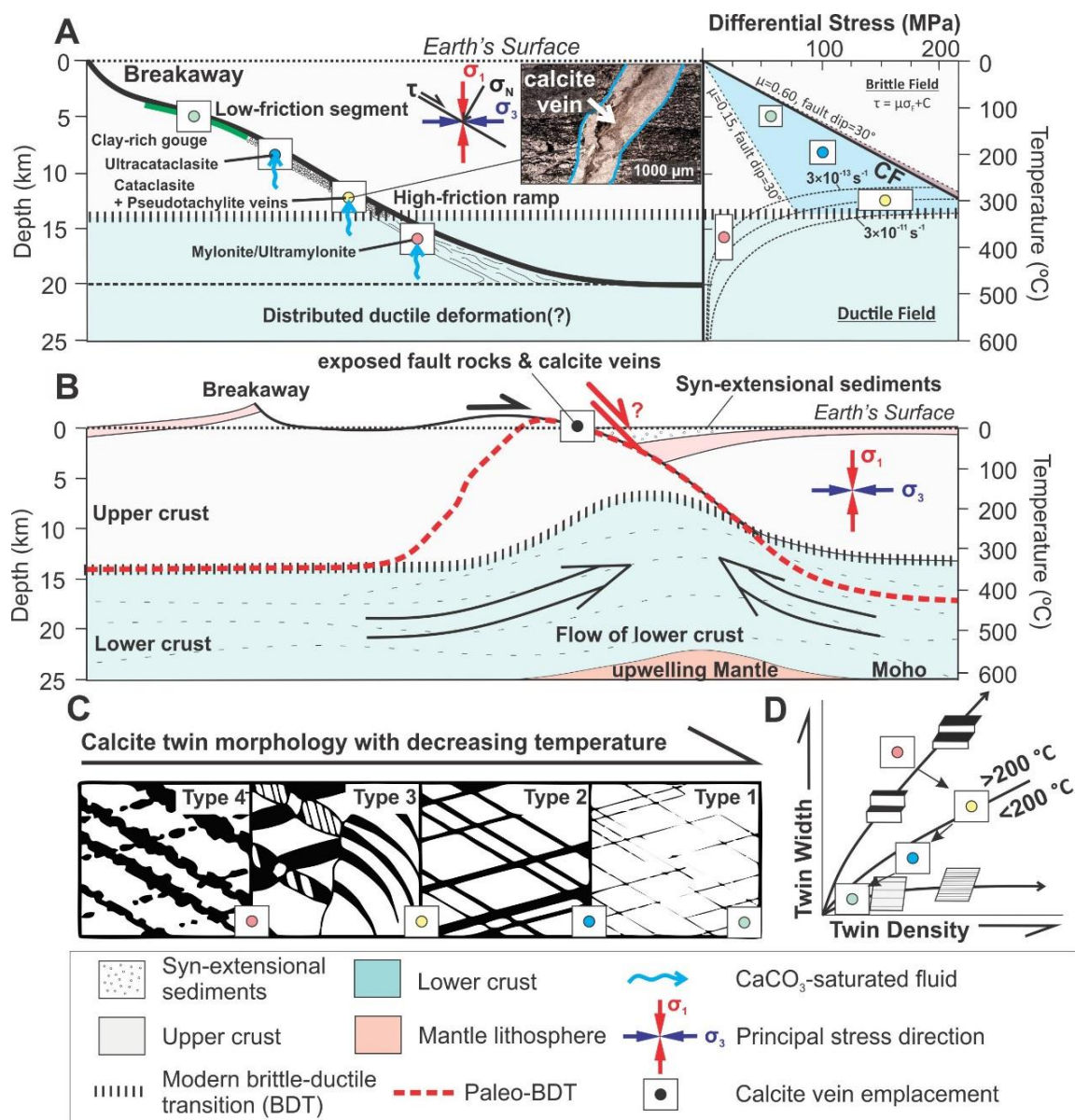


Figure 4.1 (previous page). A conceptual model of a crustal-strength profile in the footwall of an exhumed detachment fault (concept after Behr & Platt, 2011). A) Left: Schematic spatial changes of fault rock units (mylonite, cataclasite, ultracataclasite and gouge) within a continental crust cut by an extensional detachment in an Andersonian stress regime (after Cooper et al., 2017). Red, yellow, blue and green circles: Calcite gash veins may cross-cut the different fault rock units (inset) during exhumation that can be utilised to determine (static) differential stresses (e.g., Rowe & Rutter, 1990) and principal stress axes (e.g., Turner, 1953) at the depth of emplacement. Right: Differential stress versus depth (temperature) plot. Brittle failure curves calculated for an intact basaltic crust (CF, for ideal oriented faults $\sim 60^\circ$ with “Byerlee” friction) and a cohesionless detachment fault dipping $\sim 30^\circ$ with coefficient of friction ranging from 0.15 to 0.6. Red-shaded area—“forbidden” coefficient of friction for slip on this detachment; Blue-shaded area—“permissible” coefficient of friction allowing slip on the detachment fault. Flow laws for calcite plastic deformation for strain rates of 3×10^{-13} to 3×10^{-11} (after Walker et al., 1990). B) Sketch of a normal fault that initiates at a moderate to steep dip-angle and back-rotates in its upper part as a result of “rolling-hinge” unloading and flexure. Isostatic unloading of the lower crust causes uplift and warping of the upper inactive part of the fault surface (Wernicke & Axen, 1988; Mizera et al., 2019). The lower, steeper dipping segment of the detachment fault remains active. C) Calcite twin morphology dependence on temperature (after Burkard, 1993). Coloured circles represent expected twin morphology of calcite grains at the referred depths (temperature and depth of circles are indicated in Figure 4.1A). D) Calcite twin width versus twin density diagram (after Ferrill, 1991; Burkhard, 1993)—the higher the differential stress, the higher the twin density. Coloured circles represent expected twin width and recorded differential stresses in calcite veins at different depths of emplacement (see Figure 4.1A).

4.2 TECTONIC SETTING OF THE SUCKLING-DAYMAN METAMORPHIC CORE COMPLEX

The tectonic regime in SE Papua New Guinea is governed by the oblique-convergent motion of the Pacific (PAC) and Australian plates (AUS) at ~ 100 – 110 mm/yr creating a mosaic of microplates in the collision zone (**Figure 4.2A**; Tregoning et al., 1998; Wallace et al., 2004, 2014). Present-day counterclockwise rotation of the Woodlark-Solomon Sea microplate at 2 – 2.7° /Myr relative to Australia is accompanied by 20 – 40 mm/yr of seafloor spreading in the oceanic Woodlark Basin and, farther west, by 10 – 15 mm/yr of extension across the continental Woodlark rift (e.g., Wallace et al., 2004). Extension in the Woodlark Rift is thought to have initiated somewhere in the interval 3.6 – 8.4 Ma, and has been accommodated by slip on predominantly north-dipping normal faults, some of which bound the eclogite-bearing, migmatitic gneiss domes in the D’Entrecasteaux Islands (**Figure 4.2A**; Taylor & Huchon, 2002; Little et al., 2007, 2011; Fitz & Mann, 2013; Wallace et al., 2014). Near the NW end of the rift, slip on the Mai’iu fault takes up almost all of the extension. There, cosmogenic nuclide

studies on the exposed fault scarp of the Mai'iu fault indicate a late Holocene dip-slip rate of 11.7 ± 3.5 mm/yr (Webber et al., 2018); geodetic data suggest that the fault has a present-day dip-slip rate of 7.5–9.6 mm/yr (Wallace et al., 2014).

The Mai'iu fault bounds the Suckling-Dayman Metamorphic Core Complex (SDM, **Figure 4.2B**). The lower plate of the SDM includes several antiformal culminations: Mt Suckling (3,576 m) in the west; Mt Dayman (2,950 m) in the centre; and Mt Masasoru (~1,700 m) in the east. Wear striae preserved on the Mai'iu fault surface trend $009\text{--}015^\circ$ (**Figure 4.2B** and **Figure 4.3A**; Little et al., 2019). These are subparallel to the velocity of the Trobriand (Solomon Sea) block relative to Australia as derived from elastic block modelling of campaign GPS data by Wallace et al. (2014; **Figure 4.2A**), and to the trend of numerous corrugations in the footwall of the SDM (**Figure 4.2B**; Spencer, 2010; Daczko et al., 2011; Little et al., 2019; Mizera et al., 2019). On average, the Mai'iu fault dips $\sim 21 \pm 3^\circ$ to the NNE where it emerges from the Holocene alluvial gravel of its hangingwall, and locally it dips as little as $\sim 16^\circ$ at the surface (**Figure 4.3A**; Little et al., 2018; Mizera et al., 2019). Downdip of the surface trace, and aligned with it, microearthquake foci are scattered between 12 and 25 km depth to define an actively slipping deformation zone dipping north at $30\text{--}40^\circ$ (**Figure 4.2C**; Abers et al., 2016). Abers et al. (2016) interpret this deformation zone as the subsurface continuation of the Mai'iu fault.

Previous workers have suggested that the Mai'iu fault represents an extensionally reactivated part of the Owen-Stanley fault zone (OSFZ)—a Late Cretaceous-Paleocene subduction thrust (**Figure 4.2A**; Davies, 1978; Webb et al., 2008; Daczko et al., 2011; Little et al., 2019). The OSFZ formed during the obduction of an oceanic and island arc upper plate (the Late-Cretaceous Papuan Ultramafic Belt; PUB) over an oceanic marginal basin and Australian Plate-allied continental margin rocks (Davies, 1978; Webb et al., 2008; Daczko et al., 2009). The footwall of the Mai'iu fault chiefly consists of MORB-derived metabasaltic rocks of $>3\text{--}4$ km thickness with minor interbedded phyllitic metasediments, limestone and chert, known as the Goropu Metabasalt (Smith & Davies, 1976). Mafic mylonites are exposed near the base of the Mai'iu fault scarp (**Figure 4.2B**). Granitoid stocks (Mai'iu Monzonite and Suckling Granite; Davies & Smith, 1974) intrude the lower plate of the SDM near Mount Suckling and are decapitated beneath the Mai'iu fault. These syn-extensional intrusions have U-Pb crystallisation ages on zircon of 1.9–3.7 Ma (Oesterle et al.,

2018; Little et al., 2019). The granitoids record melting of continental crust at depth and geophysical data (based on seismic travel-times) confirms that the Goropu Metabasalt is underlain by continental crust of felsic to intermediate composition that reaches a thickness of ~32 km near the SDM (**Figure 4.2C**; e.g., Finlayson et al., 1977; Ferris et al., 2006; Eilon et al., 2015; Abers et al., 2016).

To the east of the SDM, an inferred inactive part of the Mai'iu fault is overlain by a fault slice of Plio-Pleistocene alluvial conglomerates of the Gwoira conglomerate (**Figure 4.2B**). This slice is a “rider block” (e.g., Choi & Buck, 2012) that formed inside a large synformal megacorrugation when the hangingwall of the Mai'iu fault was cut by a younger and more steeply dipping splay of the Mai'iu fault called the Gwoira fault, that cut across the synformal trough. As a result, part of the Mai'iu fault became inactive, and former hangingwall alluvium was captured into the footwall of the Gwoira fault. Beneath the rider block, the Mai'iu fault is inactive, shallow-dipping and synformally folded. On the western limb of the synform (at site PNG16-17, **Figure 4.2B**), the deformed Mai'iu fault dips $16\pm3^\circ$ to the SE (**Figure 4.3B**). The dips of sedimentary growth strata in the rider block and tilting of younger, later Quaternary fluvial terraces record progressive southward back-tilting (also folding) of the rider block, some of which continues today (Little et al., 2019; Webber et al., 2019).

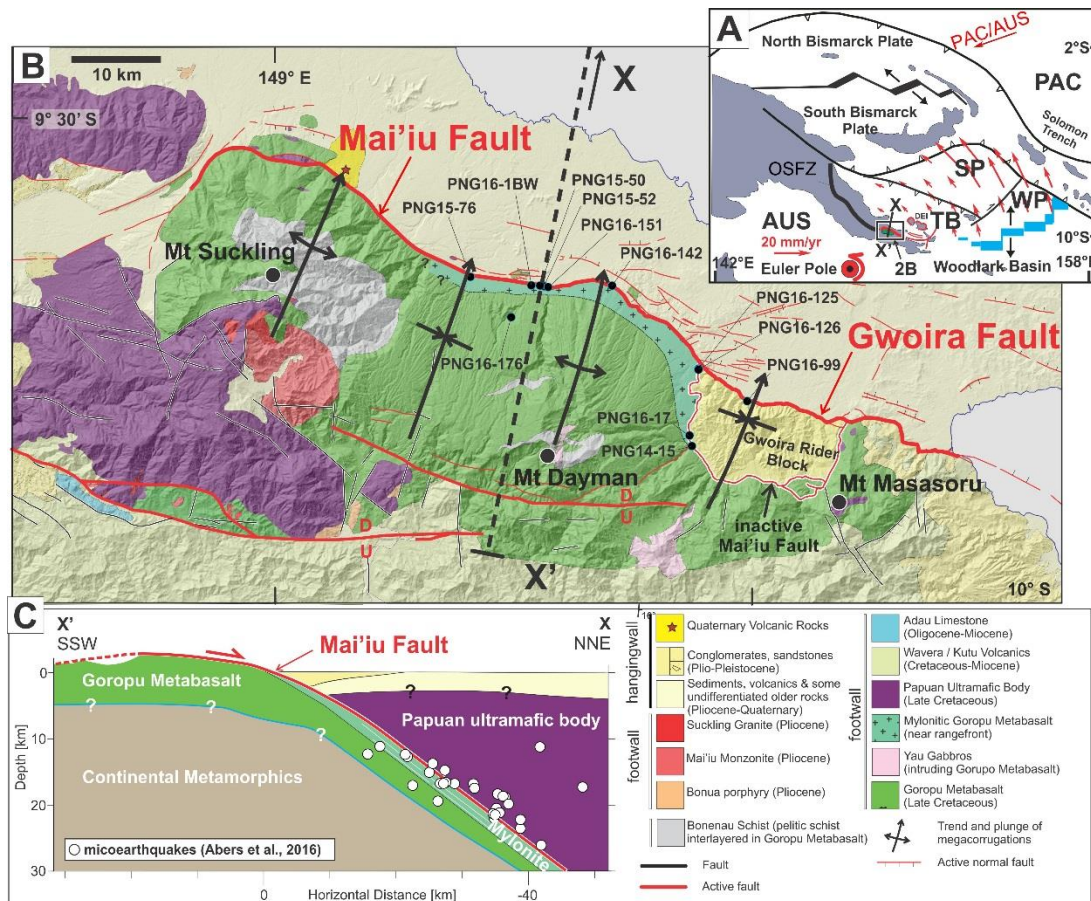


Figure 4.2. A) Simplified tectonic map of the Woodlark Rift (after Wallace et al., 2004). Locations of Figure 4.2B and cross-section X-X' of Figure 4.2C are highlighted in this map. B) Geological and structural map of the SDM (after Smith & Davies, 1976; Lindley et al., 2014; Little et al., 2019). Sample locations are highlighted in this map. C) Tectonic cross-section of the Mai'iu fault (modified after Little et al., 2019). Microearthquake foci are based on Abers et al. (2016). PAC=Pacific plate; AUS=Australian plate; WP=Woodlark plate; SP=Solomon-Sea plate; TB=Trobriand block; DEI=D'Entrecasteaux Islands; OSFZ=Owen-Stanley Fault Zone.

4.2.1 Fault Rock Sequence of the Mai'iu Fault

The footwall of the Mai'iu fault has self-exhumed a sequence of mostly mafic-composition fault rocks. This sequence is well preserved in outcrops of the inactive Mai'iu fault that lie beneath the rider block. From bottom to top, the sequence includes: a) non-mylonitic mafic greenschist (protolith); b) mylonite; c) foliated cataclasite; d) massive ultracataclasite; and e) saponite-rich gouge (Little et al., 2019). The mylonite unit is at least 60 m thick along the northern active range front, whereas farther south and updip of the frontal trace, it narrows to as little as 1.5 m. The mylonitic rocks are LS-tectonites with a well-defined NNE-trending stretching lineation (**Figure 4.3A**). Late Neogene age, normal-sense shear fabrics are pervasive (Little et al., 2019). Based

on pseudosection modelling of the mineral assemblage (epidote, actinolite, chlorite, albite, titanite, \pm quartz, \pm calcite), the mylonites are inferred to have been exhumed from $\sim 25 \pm 5$ km depth at peak metamorphic temperatures of $\sim 425 \pm 50^\circ\text{C}$ and pressures of 5.9–7.2 kbar (Daczko et al., 2009). This unit was overprinted and reworked into the structurally overlying, ~ 3 –1.5 m thick foliated cataclasites. The cm- to mm-spaced foliation in these rocks is defined by light-coloured albite \pm calcite-rich domains and darker phyllosilicate (predominantly chlorite)-rich folia. Locally, younger foliation seams truncate older, more folded ones. Microscale transgranular faults disrupt the foliation and shatter the rock. The foliated cataclasite unit is overlain by a ~ 5 –50 mm thick layer of dark grey to black (and locally brick-red) ultracataclasite. The ultracataclasites contain remnant mafic minerals and older (recycled) ultracataclasite fragments embedded in a clay-rich matrix, predominantly corrensite and/or saponite (Little et al., 2019). The ultracataclasite unit is sharply overlain by one or more layers of up to 12 cm-thick, incohesive, saponite-rich gouge in complete exposures of the fault rock sequence (Little et al., 2019). The gouges contain subangular to rounded fragments derived from the underlying fault rocks and in part from the hangingwall, and are texturally coarser grained than the ultracataclasites. The upwardly narrowing arrangement of progressively lower-temperature fault rocks is interpreted as a strain-localizing time sequence, where the higher units are more shallowly-derived and have cannibalized those underlying (Little et al., 2019). The upper units contain progressively lower temperature alteration products (derived from the protolith metabasalt) than the lower.

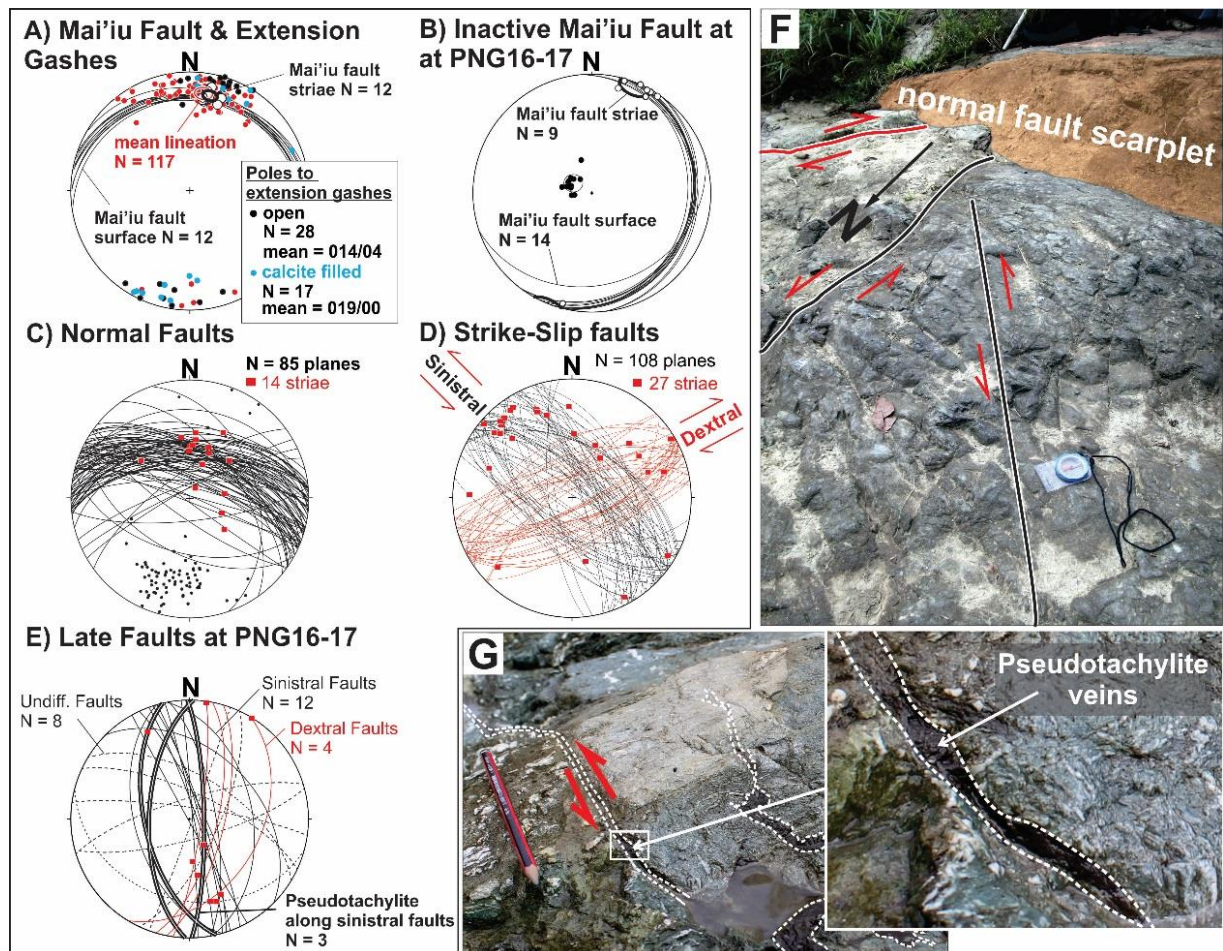


Figure 4.3 (previous page). Lower-hemisphere, equal-area stereograms of fault kinematic data collected in the exposed footwall of the Mai'iu fault. A) Attitudes of the Mai'iu fault surface (black great circles; mean attitude: 283/22/NNE, $\pm 2^\circ$ dip at 95%, N=12), trend and plunge of wear striae on the Mai'iu fault surface (white dots; mean: 012/21, $\pm 3^\circ$ at 95%, N=12) and mylonitic lineation (red dots; mean: 008/16, $\pm 2-4^\circ$ at 95%, N=117), poles of extension gashes that are either open (black dots, N=28) or filled with calcite (light blue dots, N=17). B) Attitudes of the Mai'iu fault surface where tilted eastward on the synformal limb beneath the rider block at location PNG16-17 (black great circles; mean attitude: 024/16/ESE, $\pm 3^\circ$ dip at 95%, N=14); and trend and plunge of wear striae on the Mai'iu fault surface at this location (white dots; mean: 022/04, $\pm 8^\circ$ at 95%, N=9). C) Orientation of mesoscopic normal faults (poles and great circles) that cross-cut mylonites or foliated cataclasites in the footwall of the Mai'iu fault surface (black great circles; mean attitude: 282/63/NNE, $\pm 7^\circ$ dip at 95%, N=85). Black dots—poles to the normal fault planes; Red squares—trend and plunge of striations on these normal faults (N=14). D) Orientation data of strike-slip faults that cross-cut mylonites or foliated cataclasites in the footwall of the Mai'iu fault surface. Black great circles—sinistral faults; red great circles—dextral faults; Red squares—trend and plunge of striations on these faults. E) Orientation data of strike-slip faults (black and red great circles, N=16; thick, black great circles—pseudotachylite coated strike-slip faults, N=3), and several undifferentiated faults (dashed, black great circles, N=8) that cross-cut the footwall of the inactive part of the Mai'iu fault beneath the rider block at PNG16-17. Red squares—trend and plunge of striae on these faults (N=9). F) Outcrop photograph (PNG16-1BW) showing the exhumed footwall of the Mai'iu fault cross-cut by a dip-slip normal fault (orange shading) and dextral and sinistral strike-slip faults. G) Outcrop photograph of the foliated cataclasite exposed in the footwall of the inactive Mai'iu fault trace (PNG16-17). Inset shows a sinistral strike slip fault with pseudotachylite on the slip surface.

4.2.2 Calcite Veins and Late Brittle Faulting in the Footwall and Hangingwall of the Mai'iu Fault

Late-stage extension (to mixed shear-extension) gashes cross-cut the mylonitic rocks at a high angle to the foliation (**Figure 4.3A** and **Figure 4.4A**; Little et al., 2019). Most of these veins are 1–5 mm thick, steeply dipping and infilled with calcite; they are arranged nearly orthogonally to the direction of fault slip and the mean trend of the mylonitic lineation (**Figure 4.3A**, **Figure 4.4A**, and **Figure 4.4B**). Sparse pseudotachylite veins, many of them deformed, are widely distributed in the uppermost 1–2 m of the mylonite zone (Little et al., 2019). Near the base of the scarp, mylonites that form the immediate footwall of the exhumed Mai'iu fault surface are cross-cut by numerous small-offset (slip <1.5 m), brittle faults (**Figure 4.3G**, **3H**)—some coated with calcite. On every exposure, the faults include a) steep, 50°–75° down-to-the-north dipping, synthetic normal faults (**Figure 4.3C**, **3G**); and b) near-vertical strike-slip faults. The latter occur as a conjugate set of ENE-striking dextral and NW-striking sinistral faults that mutually cross-cut one another (**Figure 4.3D**, **3G**; Little et al., 2019). The steep normal faults seem to be at least in part younger than the strike-slip faults (**Figure 4.3G**). Meter-scale to microscale brittle faults, both normal and strike-slip, are more densely developed—but less systematically oriented—in the foliated cataclasite unit that overlies the mylonite unit (**Figure 4.3E**, **3H**). **Figure 4.3H** shows a sinistral strike-slip fault in the foliated cataclasite unit that is coated with an inferred pseudotachylite vein. Multiple generations of up to 40 mm-thick pseudotachylite veins injected into the foliated cataclasites have mutually cross-cutting relationships with steep or foliation subparallel calcite veins (**Figure 4.3H**, **Figure 4.4C**, and **4D**; Little et al., 2019). Five pseudotachylite samples with glassy matrices at site PNG16-17 (location in **Figure 4.2B**; **Figure 4.3H**) were dated by $^{40}\text{Ar}/^{39}\text{Ar}$ geochronology; the ages (interpreted as minimum ages for friction melting) range from 2.24 ± 0.29 Ma to 3 ± 0.43 Ma (Little et al., 2019). Calcite veinlets cut across the ultracataclasite unit and are oriented either subvertical or subparallel to the Mai'iu fault surface (**Figure 4.4E**, **4F**). No intact calcite veins occur in the gouge, but only reworked fragments of former calcite and dolomite veins.

The Gwoira conglomerates exposed in the Gwoira rider block (**Figure 4.2B**) are typically cemented by calcite. In the rider block, these former hangingwall conglomerates are cross-cut by normal faults that dip variably to both the north and south. Some of the faults are coated with calcite. Successive slip on the Mai'iu and

Gwoira faults has caused back-tilting and folding of the Gwoira beds, some of which dip up to 30° (typically to the SSW; Webber et al., 2019). This tilting has likely changed the attitude of these normal faults away from the original dip they had when active.

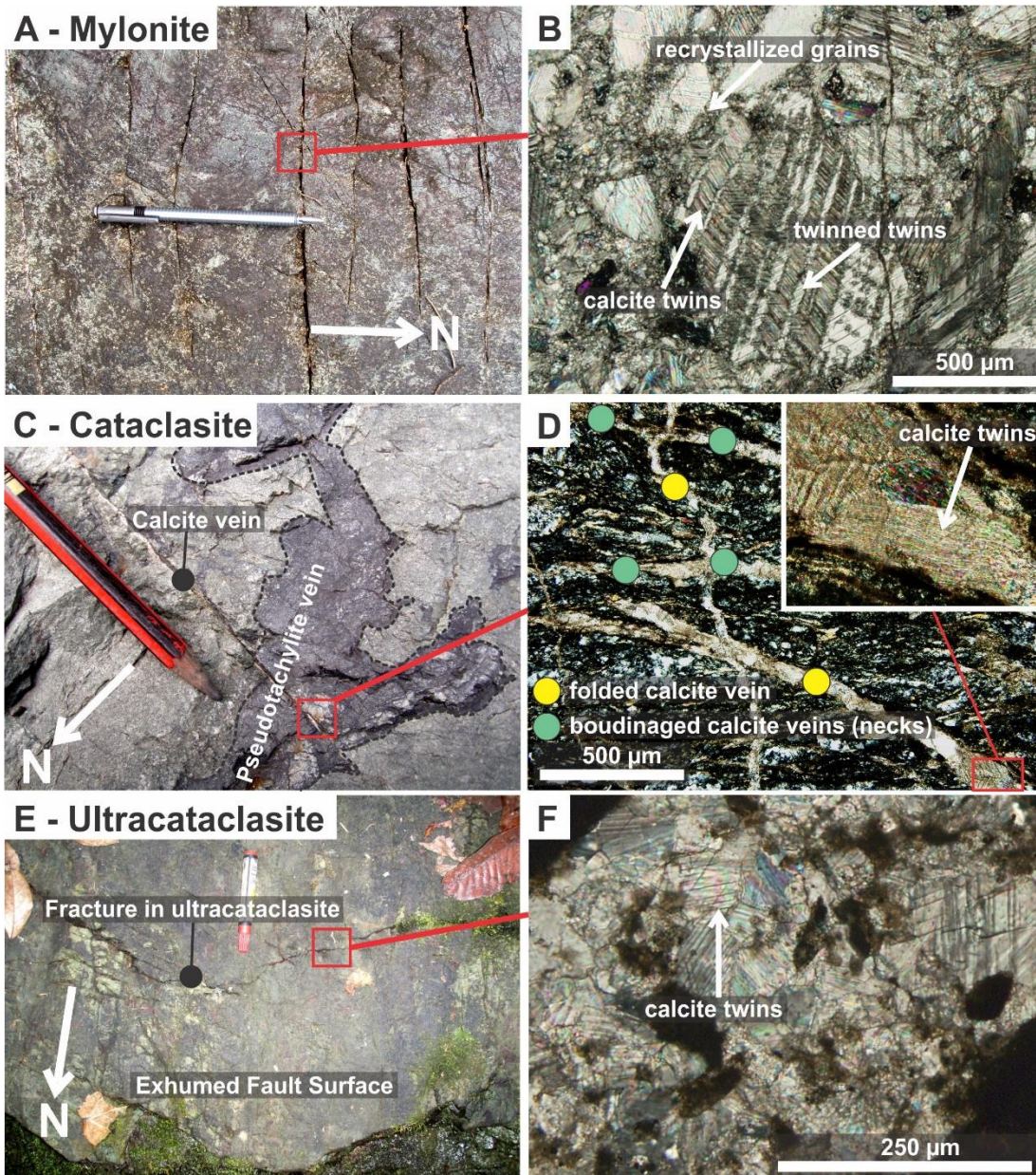


Figure 4.4 (previous page). Outcrop photographs of the fault rock units exposed in the footwall of the Mai'iu fault and photomicrographs of calcite-filled veins that cross-cut them. Sample locations are shown in Figure 4.2B. A) Mylonite outcrop (location, PNG16-1BW, the surface is dipping 21° toward the north). The mylonite is cross-cut by 6 subvertical calcite gash veins. B) Optical photomicrograph of a calcite vein in mylonite (PNG16-1BW). Large, up to 1 mm-sized (long axis of grain), twinned calcite grains are surrounded by fine, 5–20 µm-sized (diameter), untwinned calcite grains. Calcite twins are thick and patchy, and have sutured twin boundaries (Type IV and Type III twins of Burkhard, 1993; see Figure 4.1C). Note multiple twinning. C) Outcrop photograph of foliated cataclasite unit hosting multiple generations of both pseudotachylite and calcite veins (location, PNG16-151). D) Optical photomicrograph of foliated cataclasite containing multiple calcite veins (location, PNG16-125B). Calcite veins contain 50 to 100 µm-sized calcite grains that are almost fully twinned (Type II and Type I of Burkard, 1993; Figure 4.1C). Note, backward-inclined gash veins (with respect to the normal sense of shear) are shortened and folded (yellow dot), while ones that are subparallel to the foliation (green dots) have been stretched and show necking structures. E) Outcrop photograph showing the smooth, fault-bounded top surface of the ultracataclasite unit exposed less than 1 m above the active trace of the Mai'iu fault (location, PNG15-50). F) Optical photomicrograph of calcite vein in the ultracataclasite unit (location, PNG15-50). Calcite grains are ~50 to 100 µm-thick, strongly twinned, and dominantly Type I of Burkhard (1993; **Figure 4.1C**).

4.3 METHODS

4.3.1 Structural Measurements, Sample Locations and Thin Section Preparation

Structural measurements of the Mai'iu fault footwall and samples from the different fault rock units exposed at the SDM were collected. Sample locations are shown in **Figure 4.2B**. Samples were cut parallel to lineation and perpendicular to foliation (kinematic XZ plane). An optical microscope was used to identify calcite veins in over 100 thin sections. We selected a representative suite of 15 samples spanning the several fault rock units to be prepared into ultrapolished sections for further textural analysis. All thin sections were mechanically polished with a diamond paste before a final stage of SYTON (silica suspension) to create a scratch free, highly reflective surface (see Fynn & Powell, 1979). Fragile specimens, especially ultracataclasite and gouge samples, were dried for 24 hours at 50°C and impregnated with epoxy prior to polishing. Fault rock and calcite vein images on the following figures are arranged with the normal (top-to-the-north) slip sense of the Mai'iu fault shown as top-to-the-right.

4.3.2 Paleostress Analysis

In this study we attempted to constrain both differential stress magnitudes (σ_{Diff}) and principal stress orientations. Differential stress estimates were derived from microstructural observation of deformed, monophase calcite veins, including the morphology and density of mechanical twinning and the mean grain-size of dynamically recrystallized grains. Principal stress orientations were determined from the kinematic analysis of multiple twinned versus untwinned crystallographic orientation pairs in e-twinned calcite grains that were observed by EBSD, and the kinematic analysis of mesoscopic fault-slip data that were measured in the field. For this analysis, we assume (1) that microstructures in calcite veins preserve a snapshot of stress conditions that prevailed at the time and P-T conditions when the hosting fault rock was active (e.g., Behr & Platt, 2011); (2) that differential stress estimates based on calcite twin-densities record peak values experienced in the rock (e.g., Rutter et al., 2007; Rybacki et al., 2013); (3) that temperature-dependent twin morphologies (e.g., Burkhard, 1993; Ferrill et al., 2004; **Figure 4.1C**) are accurate at lower deformation temperatures ($<250^{\circ}\text{C}$) where rates of twin widening are reduced (e.g., Rybacki et al., 2013); and (4) that twin densities depend on the differential stress, but are independent of grain size (e.g., Rowe & Rutter, 1990; Rybacki et al., 2013). Consequently, any samples that may have experienced transiently high dynamic stresses, as during earthquake rupture, will yield differential stress estimates or stress orientations that may not be representative of a longer-term (interseismic) time window. Microstructures in polished sections were analysed with a SIGMA-VP field emission gun scanning electron microscope (FEG-SEM) equipped with an electron backscatter diffraction (EBSD) detector at the University of Otago, using 30 kV acceleration voltage, 50–100 nA beam current, 20–30 mm working distance and $70\text{--}71^{\circ}$ sample tilt. Electron backscatter patterns (EBSP) were collected by an HKL Nordlys camera and processed and indexed with the AZTEC software by Oxford Instruments. To resolve the microstructures, we used step sizes between $0.2\text{ }\mu\text{m}$ and $1.5\text{ }\mu\text{m}$.

Recrystallized Grain-Size Paleopiezometry

The mean recrystallized grain size of a mineral such as quartz or calcite is a function of differential stress and can be measured from EBSD maps (e.g., Halfpenny et al., 2006; Valcke et al. 2015; Cross et al., 2017). We followed the procedure of Cross et al. (2017) to measure calcite grain sizes and identify the subset of recrystallized

grains in EBSD maps. This involves: (1) choosing a step-size that is less than one fifth the diameter of the smallest recrystallized grains; and (2) measuring the average grain orientation spread (GOS) inside each grain. The GOS is an index of the average degree of intracrystalline lattice distortion in the grain and is proportional to dislocation density. Recrystallized grains are characterized by a low GOS. In addition, we (3) determined a threshold GOS value to distinguish relict from recrystallized grains by reference to a cumulative number of grains versus GOS plot (“trade-off curve”) for each EBSD map; and (4) calculated a two-dimensional recrystallized grain size (diameter of a circle with equivalent area) for each grain by applying the MTEX script “RexRelict.m” (Cross et al., 2017). The latter script was modified in order to remove twin boundaries and merge calcite grains separated by twins prior to step (4). The modifications of the MTEX-code can be found in Appendix C.5 (and in the ‘MTEX’ folder in the Digital Appendix). Differential stresses were then calculated from the average grain size of recrystallized calcite using the paleopiezometer calibrations by Valcke et al. (2015; $K_{\text{EBSD}}=10^{1.9\pm0.2}$; $p_{\text{EBSD}}=-0.6\pm0.1$), and Platt and De Bresser (2017; $K_{\text{OPT}}=10^{3.1\pm0.3}$; $p_{\text{OPT}}=-1.09(+0.14; -0.18)$):

$$D_X = K_X \cdot \sigma_{\text{Diff}}^{-p_X}, \quad (\text{Eq. 4.1})$$

where D_X is the average grain size, K_X and p_X are constants. The paleopiezometers by Valcke et al. (2015) and Platt and De Bresser (2017) were calibrated by applying different approaches of grain-size acquisition on the same suite of experimentally deformed Carrara marble samples (confining pressure: 300 MPa; natural strains of 0.15–0.90 at strain rates of $3.0 \text{ by } 3.0 \times 10^{-6}$ – $4.9 \times 10^{-4} \text{ s}^{-1}$; temperatures of 700–990°C; differential stresses from 15 to 90 MPa; Ter Heege et al., 2002; De Bresser et al., 2005). Valcke et al. (2015) applied EBSD to measure recrystallized calcite grains. These authors used the paucity of internal lattice distortion in calcite grains with $<1^\circ$ average internal misorientation to discriminate between recrystallized and relict grains (average grain size is based on grain number weighing, D_{AVG}). Platt and De Bresser (2017) applied optical microscopy to identify and measure grain size (root-mean-square mean diameter values; D_{RMS}) of recrystallized calcite grains. Calculated differential stresses with both paleopiezometers by Valcke et al. (2015) and Platt and De Bresser (2017) are shown in the result section. Estimated mean grain sizes and standard deviations with the aforementioned MTEX script are given in **Table C.1** in Appendix C.1.

Calcite Twinning Paleopiezometry

Mechanical e-twinning in calcite accommodates crystal-plastic deformation at temperatures <400°C (e.g., Groshong, 1988), and is commonly used for paleostress analysis (e.g., Ferrill et al., 2004; Rutter et al., 2007; Kanai & Takagi, 2016; Brandstätter et al., 2017). Deformation twinning on e-planes $\{01\bar{1}8\}$ (using hexagonal structural cell indices) in calcite, for which the shear displacement is in the direction $\langle 0\bar{2}21 \rangle^+$ (positive sense; Barber & Wenk, 1979; De Bresser & Spiers, 1997), depends on the orientation of stress and the ability to exceed the critical resolved shear stress (CRSS; 2–12 MPa) on any of the three symmetrically equivalent lattice e-planes (e.g., Jamison & Spang, 1976; Tullis, 1980; Burkhard, 1993; Lacombe & Laurent, 1996; Yamaji, 2015). The CRSS depends on grain size, temperature and strain, ranging from ~12 MPa to ~2 MPa (e.g., De Bresser & Spiers, 1997; Laurent et al., 2000). Experimentally calibrated relations between twinning and stress magnitude found that the twin density in a calcite grain varies directly with differential stress, but is less dependent on temperature, strain, or strain rate; with the latter two also depending on grain size (Rowe & Rutter, 1990; Rybacki et al., 2013). In these experiments the width of a calcite twin increases with temperature and strain, and thus, the twin width provides a rough estimation of peak deformation temperature (Ferrill et al., 2004; Rybacki et al., 2013). In this contribution, microstructural information on calcite-twin pairs in calcite veins were collected from EBSD maps. In each calcite grain, we measured: a) the average e-twin width; b) number of e-twins; c) grain width normal to the e-twins; and d) the crystallographic orientation of the host calcite-crystal and adjacent e-twin lamellae. Differential stresses were estimated using the experimentally calibrated twin-density paleopiezometer of Rybacki et al. (2013):

$$\sigma_{Diff} = (19.5 \pm 9.8)\sqrt{N_L}, \quad (\text{Eq. 4.2})$$

where N_L is the number of e-twins per mm. Results from this and other twin-density paleopiezometers are shown in **Table C.2** in Appendix C.2 and discussed below.

Principal Stress Orientations

Fault slip data (fault attitude, striation direction, sense of slip) for 54 brittle faults cutting the exhumed plane of the Mai'iu fault within the mylonites and foliated cataclasites were collected in the field at 15 locations. These sites are all near the base of the fault scarp, no more than several hundred meters updip of the trace, where

waterfalls are common and outcrop is excellent (**Figure 4.3**). Markers indicating sense of offset included the exhumed bedrock fault surface (best for normal-sense faults), and quartz veins and fractures in the metabasaltic footwall (best for strike-slip faults). Slip directions were inferred from wear striae or calcite fibres (fault surface veins). Combined together, the fault kinematic data were inverted to determine best-fit orientations of the principal stress axes (specifically, σ_1 and σ_3) and the stress ratio (Φ):

$$\Phi = \frac{(\sigma_2 - \sigma_3)}{(\sigma_1 - \sigma_3)}. \quad (\text{Eq. 4.3})$$

Calcite e-twins have been widely used in structural studies to determine paleo-principal stress axes by using a combination of the attitudes of the e-planes and glide directions. Calcite-twin data (a pair of adjacent twinned vs untwinned c-axis crystallographic orientation measurements from EBSD or U-stage analysis) can be made analogous to fault-slip data by the following steps (e.g., Turner, 1962; Groshong, 1975; Engelder, 1979; Kilsdonk & Wiltschko, 1988; Craddock & Magloughlin, 2005; Jaya & Nishikawa, 2013; Kanai & Takagi, 2016): 1) we extracted crystallographic orientation data from calcite grains (N=912) and their e-twins (N=3937) by EBSD; 2) the crystallographic orientations from the e-twin and the host calcite grains were used to determine the e-twin plane pole and glide direction for every twinset based on the known angular relationships (e.g., see Burkhard, 1993); and 3) the orientation data was converted from a sample coordinate system to a geographical one (N–S, E–W, and top–bottom; a MATLAB-code for the conversion can be found in the sub-folder ‘Euler Conversion’ of ‘Calcite Paleopiezometry’ of the Digital Appendix).

To analyse both of the above data sets, we used the multiple inverse method (MIM) by Yamaji (2000) to invert the kinematic observations into best-fit stress orientations and determine the stress ratio parameter, Φ . In addition, we compare the results of the Yamaji (2000) algorithm for the calcite-twin dataset with those of other paleostress-inversion techniques applied to the same data (P-, B- and T-axes calculations after Turner, 1953; strain-gage technique after Groshong 1972, 1974; dihedral calculation after Angelier & Mechler, 1977; see **Table C.3**, **Table C.4**, and **Figure C.1** in Appendix C.3). These recursive methods estimate the deviatoric stresses from fault-slip data based on the Wallace-Bott hypothesis that the fault-slip direction is parallel to the shear stress on the fault plane (Angelier, 1979; Etchecopar et al., 1981;

Yamaji, 2000); however, not all faults (or e-twin planes) slip in response to the same stress field, which is likely to be heterogeneous in both time and space. The advantage of the MIM is that it utilizes a sort of self-correlation of fault-slip data by dividing a set of faults (N_F) into subsets, the number of which equals the binomial coefficient ${}_NC_k = N!/k!(N-k)!$, that might represent component stress field activating that subset of the data. The number of elements (k) that comprise a subset is recommended to be 4 or 5 (Yamaji, 2000). The reliability of this method depends on the number of collected data, the spatial or temporal heterogeneity of the stress state and the number of subsets that can be correlated to one another (Yamaji, 2000; Otsubo & Yamaji, 2006; Otsubo et al., 2008). The spread (or noise) around an average solution for stress for a particular data set is given by the Mean Angular Stress Distance (MASD)—that is, the mean angle between the average stress state and the i th (subset-derived) stress state (Yamaji & Sato, 2006).

4.4 RESULTS: PALEOSTRESS ANALYSIS

In the first part of the results, we present microstructural observations of calcite veins that cross-cut the several fault rock units (non-mylonitic schists, mylonite zone, foliated cataclasite zone, and ultracataclasite unit) based on optical microscopy and EBSD-analysis. Microstructural analyses of deformed calcite veins include observations of grain size, grain shape, twin morphology, twin width, shape preferred orientations (SPO) and crystallographic preferred orientations (CPO). Based on recrystallized grain size of calcite and the mean twin density of calcite-twin pairs, we calculate differential stress magnitudes (σ_{Diff}) and deformation temperatures for 35 calcite veins from 15 samples. In the last part of the section, we continue with the reconstructed orientations of paleo-principal stress axes and estimated values of the stress ratios (Φ ; Eq. 4.3) based on the stress inversion of calcite-twin pairs and fault slip data.

4.4.1 Paleostress Reconstruction and Deformation Temperatures Based on Calcite Veins

Field and microstructural description of the calcite veins

Calcite veins that cross-cut the structurally lower non-mylonitic and mylonitic units are mostly oriented subperpendicular to the foliation (**Figure 4.5A**). Many veins appear to have been deflected away from that originally steep attitude as the result of ductile shearing in a top-down-to-the north (normal) sense (Little et al., 2019). These

ductilely deformed veins are commonly cross-cut by younger veins that are more nearly foliation-orthogonal. Calcite veins in the mylonite zone usually contain large, up to 1 mm-sized (long axis of grain), twinned grains that are surrounded by fine, 5–20 μm -sized, untwinned calcite grains (“core and mantle” microstructure; **Figure 4.5B–5E**). Grain boundaries of the larger grains are usually interlobate and bulged at a wavelength that is similar to the size of the finer calcite grains (**Figure 4.5C**) suggesting dynamic recrystallization by subgrain rotation recrystallization within these samples. A weak shape preferred orientation (SPO) of recrystallized grains may indicate top-to-the-north (normal) sense of shear (**Figure 4.5E**, inset). A preferred orientation of c-axes ([0001]) of relict and recrystallized calcite grains normal to the vein wall is indicated in the lower hemisphere stereograms of **Figure 4.5G** and **5H**. These crystallographic preferred orientations (CPOs) are likely to have formed during oriented growth of calcite within veins (e.g., Rutter et al., 2007). Calcite twins in the larger calcite grains are thick and patchy, bent, twinned (twinned twins), have sutured twin boundaries and form in part trails of tiny grains (**Figure 4.4B**, **Figure 4.5B** and **5C**). The veins also contain single twin boundaries that bulge into the untwinned crystal and merge with other twins within the same calcite grain. These twin morphologies resemble Type IV and Type III twins of Burkhard (1993; see Fig. 1C) consistent with deformation at temperatures $>250\text{--}400^\circ\text{C}$ (e.g., Evans & Dunne, 1991; Ferrill et al., 2004; Passchier & Trouw, 2005). Other calcite veins observed in non-mylonitic to mylonitic schists contain $\sim 200\text{ }\mu\text{m}$ -sized calcite grains with up to $\sim 3\text{ }\mu\text{m}$ -thick, in part bent twins (**Figure 4.5A**, inset), resembling Type III and Type II twins of Burkhard (1993; see **Figure 4.1C**) and may indicate lower temperature ($200\text{--}300^\circ\text{C}$) deformation conditions (Groshong et al., 1984; Evans & Dunne, 1991; Ferrill et al., 2004). These calcite veins with Type III and Type II twins are lacking a core and mantle structure.

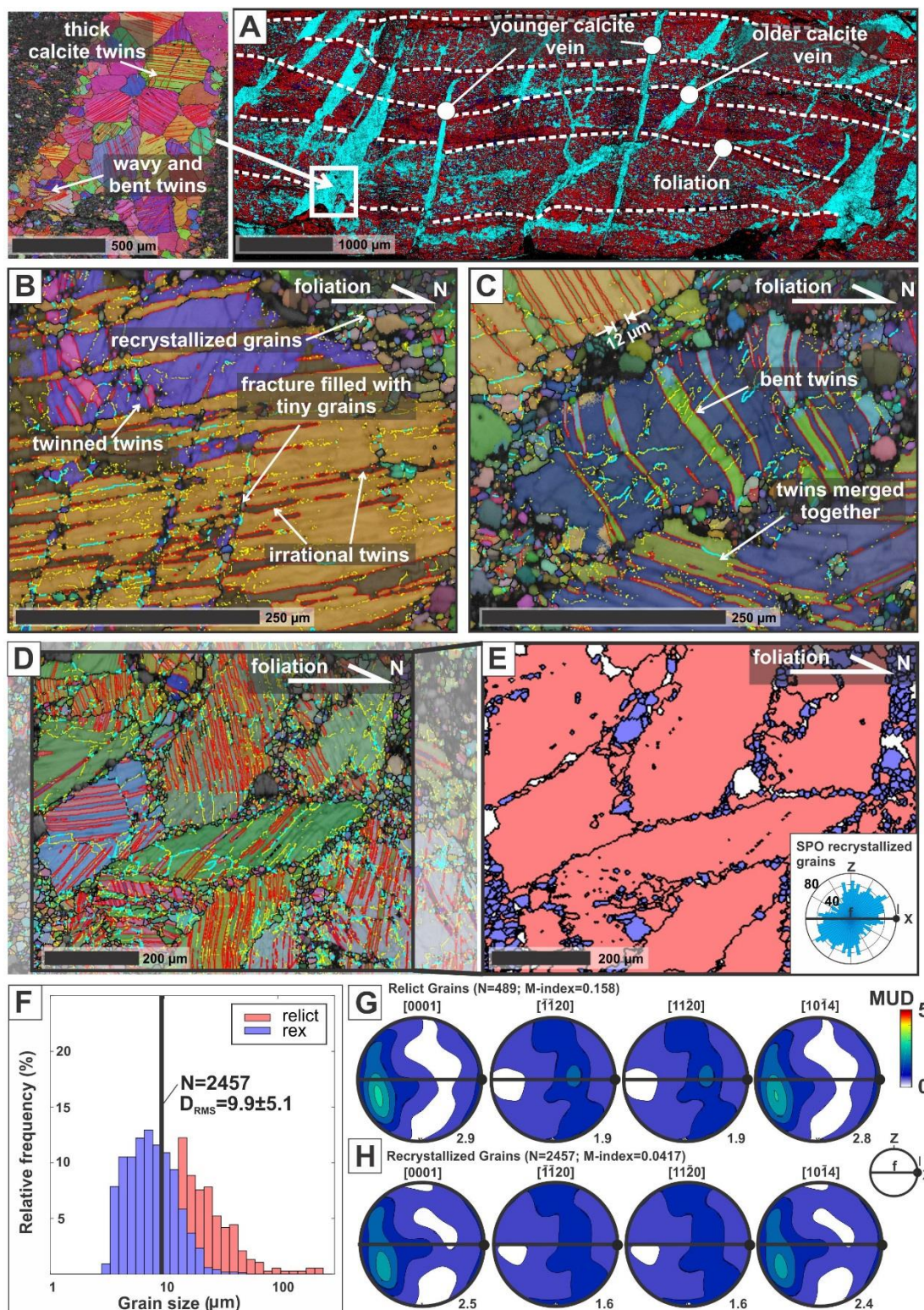


Figure 4.5 (previous page). EBSD-based microstructural images of calcite veins in a non-mylonitic schist (A; location, PNG14-15, inactive fault trace, Figure 4.2B) and mylonite unit (B–E; location, PNG16-1BW, active fault trace, Figure 4.2B). Calcite vein images are arranged with the normal (top-to-the-north) slip sense of the Mai'iu fault shown as top-to-the-right. Code for crystallographic misorientation of boundaries in inset of A and in parts B, C and D are: yellow 2–5°, light blue 5–10°, black >10° (grain boundaries), red $77\pm5^\circ$ (twins). A) Phase map of a metapelitic schist containing multiple generations of calcite veins. Light blue—calcite; red—quartz; white dashed lines—foliation. Inset, close up of a calcite vein containing twinned grains. The colouring is related to the crystallographic orientation of calcite (all Euler map). B) All Euler colour map of a large (~1 mm) calcite grain surrounded by finer recrystallized calcite grains. Fracture in large calcite grain contains 5–10 µm-diameter calcite grains. Note that several large twins (twin width ~25 µm) are internally twinned. C) All Euler colour map of large (~300 µm) calcite grains surrounded by recrystallized calcite grains. Large calcite grains show bent twins and twin boundaries that are merged with other twins in the same host grain. D) All Euler colour map showing several large calcite grains with thick twins and recrystallized calcite at the grain boundaries of the larger grains. E) Map of relict (red) and recrystallized (blue) calcite grains (area investigated shown in D). Inset is a rose diagram with a weak shape-preferred orientation of recrystallized calcite grains. F) Grain size histogram of relict (red) and recrystallized (blue) grains of map shown in E. D_{RMS} —mean (root mean square) recrystallized grain size. G and H) Lower hemisphere, equal-area stereonet (pole plots) of relict (G) and recrystallized (H) grains. MUD—multiples of uniform distribution; f—foliation; l—lineation.

Calcite veins that cross-cut the foliated cataclasite unit are (μm - to $<1\text{ mm}$ thick) and occur in multiple generations. Mostly, they are subvertical or subparallel to the foliation (**Figure 4.4D**, **Figure 4.6A**). Backward-inclined gash veins with respect to the normal sense of shear are folded, whereas forward-inclined ones have been stretched and show necking structures, a relationship that we attribute to normal-sense ductile shearing. The calcite veins have mutually cross-cutting relationships with respect to ultracataclasite and inferred pseudotachylite veins (see also Little et al., 2019). Calcite veins that cross-cut the foliated cataclasite unit typically consist of ~ 30 – $100\text{ }\mu\text{m}$ -sized, almost fully-twinned calcite grains containing predominantly ~ 0.5 – $2\text{ }\mu\text{m}$ wide, straight twins (**Figure 4.4D**). These resemble Type II and Type I twins of Burkhard (1993; **Figure 4.1C**), and suggest deformation at temperatures of ~ 150 – 300°C (e.g., Evans & Dunne, 1991; Ferrill et al., 2004). Some calcite veins contain very fine-grained calcite with a grain size of ~ 3 – $15\text{ }\mu\text{m}$ (**Figure 4.6B**, **6C**). Larger calcite grains with a grain size of (~ 20 – $50\text{ }\mu\text{m}$) have bulged grain boundaries at a wavelength of ~ 4 – $12\text{ }\mu\text{m}$ and usually contain more twins (thick and thin twins, ~ 0.5 – $3\text{ }\mu\text{m}$) than the surrounding finer grains. The finer calcite grains are inferred to be recrystallized and typically form quadruple grain boundary junctions as well as straight grain-boundaries with neighbouring calcite grains (**Figure 4.6B**). Some straight grain boundaries can be traced along several grain widths. The SPO of the recrystallized grains is consistent with a top-to-the-north (normal) sense of shear (**Figure 4.6C**). The c-axes [0001]-orientations of relict and recrystallized grains are forming a weak CPO that is at an angle to the vein wall (**Figure 4.6D**, **6E**). The CPO of recrystallized grains are in general weaker than the relict grains and both are weaker compared to the mylonitic samples. **Figure 4.6F–6I** show an example of a calcite vein that contains shattered or “pulverized” calcite grains with ultrafine grain sizes $\ll 4\text{ }\mu\text{m}$. Unfractured calcite grains (relict) show type II and type I-twinning. Twinning of the shattered calcite grains mostly occurs locally along their grain boundaries and may indicate that these grains were fractured along the e-twin planes or new e-twins were formed at the contact to other calcite grains. Pseudotachylite veins in close contact to pulverized calcite veins may indicate that some calcite grains have experienced dynamic stress conditions during propagation of earthquake ruptures.

The ultracataclasite unit is cross-cut by $\sim 100\text{ }\mu\text{m}$ -thick calcite veinlets that are mostly unfractured (**Figure 4.4F**). Backwards-inclined veinlets with respect to the

shear sense of the Mai'iu fault are folded, whereas those which are forward-inclined are planar, similar to the ones described in the foliated cataclasite unit (see also Little et al., 2019). The latter authors interpret this as evidence for plastic deformation of the calcite veins during normal-sense shearing of the surrounding ultrafine-grained matrix by a distributed granular-flow process. The calcite veins consists of ~50–100 μm -sized calcite grains that usually contain predominantly $<1\ \mu\text{m}$ -thin twins suggesting that plastic deformation was mainly accommodated by twinning. The twin morphologies resemble Type I twins of Burkhard (1993; **Figure 4.1C**) and indicate deformation temperatures of $\leq 170^\circ\text{C}$ (e.g., Groshong et al., 1984; Ferrill et al., 2004).

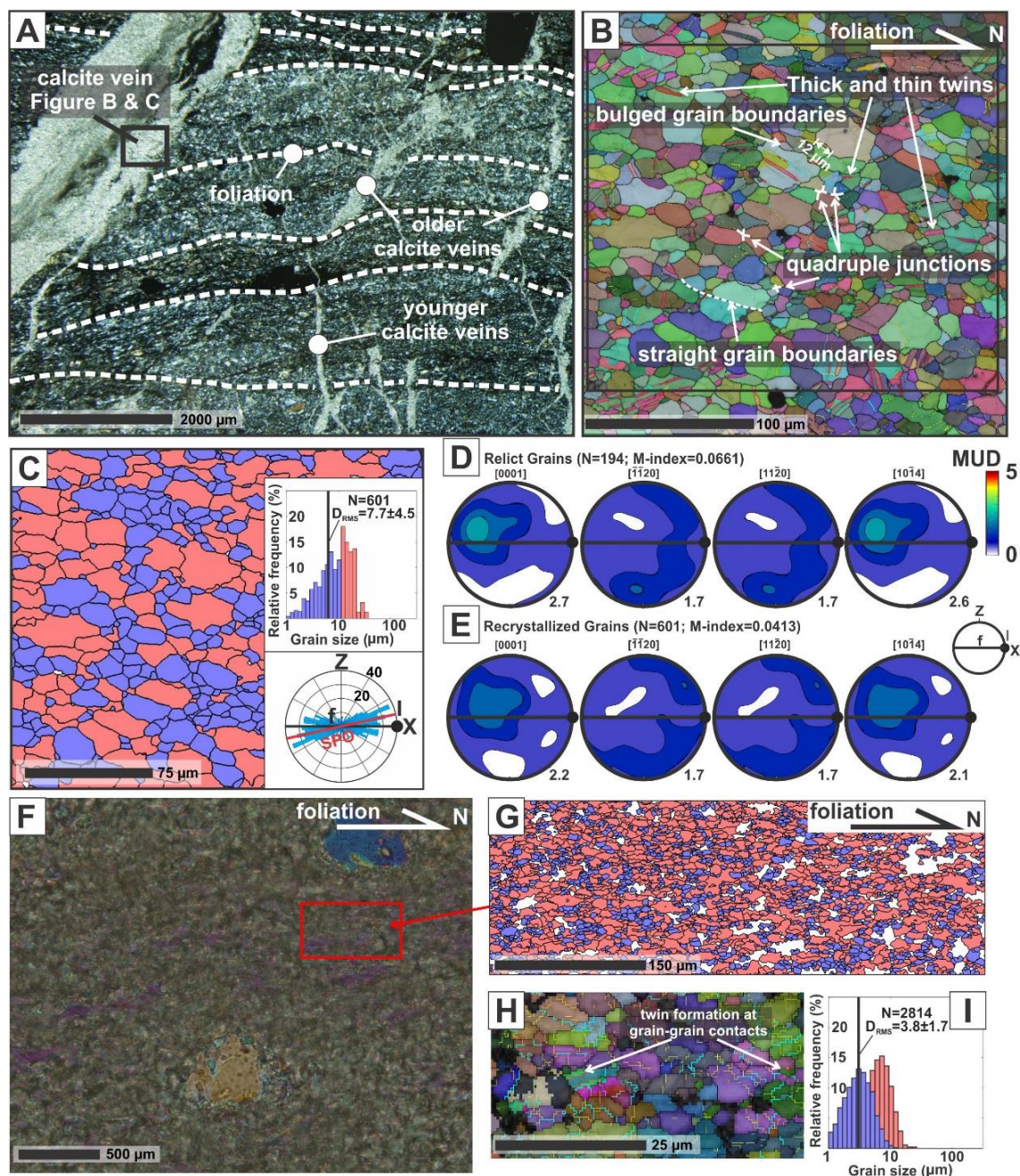


Figure 4.6 (previous page). Microstructural observations of calcite veins in the foliated cataclasite unit (A–E; sample PNG16-151E, active Mai’iu fault trace; and F–I; sample PNG15-50RD, active Mai’iu fault trace; locations in Figure 4.2B). Calcite vein images are arranged with the normal (top-to-the-north) slip sense of the Mai’iu fault shown as top-to-the-right. A) Optical photomicrograph with crossed polarizers showing the fine-grained mafic matrix of a foliated cataclasite cross-cut by multiple generations of calcite veins. White dashed lines are traces of the foliation. Older calcite veins are more deformed and forward-inclined than the thinner, younger veins. B) All Euler angle colouring map of a calcite vein segment (area shown in A). Larger calcite grains in this map are mostly twinned and have bulged grain boundaries. Smaller calcite grains are rarely twinned and typically have quadruple junctions with neighbouring grains. Some calcite grains have straight grain boundaries. Boundary misorientations are coded as follows: black $>10^\circ$ (grain boundaries), red $77^\circ \pm 5^\circ$ (twins). C) Map of relict (red) and recrystallized (blue) calcite grains. Insets, top: grain size histogram of relict (red) and recrystallized (rex; blue) grains of map B. Average grain size (root mean square; D_{RMS}) is given for the recrystallized grains; bottom: rose diagram showing a shape-preferred orientation (SPO) of recrystallized calcite grains. D and E) Lower hemisphere, equal-area pole diagrams of crystallographic directions in calcite for relict (D) and recrystallized (E) grains. F) Optical photomicrograph with crossed polarizers and additional gypsum plate of an ultrafine-grained calcite vein. G) Grain map distinguishing relict (red) and fragmented (blue) calcite grains. The white areas contain calcite grains that were too fine to construct at a step size of $0.5\ \mu\text{m}$ (i.e. contain <5 pixels). H) All Euler angle colouring map of fragmented calcite grains (black boundaries). Note, twinning (red boundaries) of calcite grains mostly occurs at the contact between neighbouring grains in this particular sample. Misorientations are the same as in (B). I) Grain size histogram of relict (red) and fragmented (rex; blue) grains of map (G). Note, the average fragmented grain size (D_{RMS}) is likely to be overestimated as many grains were not detected with a step size of $0.5\ \mu\text{m}$. MUD—multiples of uniform distribution; f—foliation; l—lineation.

Based on these observations, we can summarize and categorize the calcite veins into four groups: **Group 1)** Porphyroclastic calcite grains with Type IV and Type III twins indicating deformation temperatures of $\sim 250\text{--}400^\circ\text{C}$ and that are surrounded by recrystallized calcite grains (“core and mantle” microstructure; **Figure 4.4B**, **Figure 4.5B–5E**). This group appears mostly in the mylonite unit; **Group 2)** Calcite grains that show variably straight or bent twins of Type III and Type II (twinned twins are rare) indicating deformation temperatures of $\sim 200\text{--}300^\circ\text{C}$ (**Figure 4.5A**). This group appears mostly in the mylonite unit and also the underlying non-mylonitic schists; **Group 3)** Porphyroclastic calcite grains with Type II and Type I twins that are surrounded by very fine recrystallized grains—microstructures that suggest high differential stress together with low deformation temperature ($\sim 150\text{--}300^\circ\text{C}$; e.g., Kennedy & White, 2001). This group appears in the foliated cataclasite unit (**Figure 4.6A–6E**) and in one mylonite sample at location PNG16-17; **Group 4)** Calcite grains

that have Type I and Type II twins and that lack any recrystallized grains (e.g., **Figure 4.4D, 4F**). This group of calcite veins is restricted to the foliated cataclasite and ultracataclasite unit. We note that only Group 1 and Group 3 type calcite veins are suitable for application of recrystallized grain-size paleopiezometry. The twin-density paleopiezometer might be not suitable for calcite grains in Group 1 veins as twin widening and twin migration make it difficult to distinguish between host grain and twin, and may also lead to overestimations of the twin width and underestimations of the twin density.

Estimated differential stresses and deformation temperatures

To apply the recrystallized grain size paleopiezometers (Valcke et al. 2015; Platt & De Bresser, 2017), we determined the mean recrystallized grain sizes of the Group 1 and Group 3 veins as outlined above. The estimated mean grain sizes (root mean square, RMS) are $12.8 \pm 7.1 \mu\text{m}$ (1σ ; $N=8$) for Group 1 veins (mylonites) and 8.2 ± 4.2 (1σ ; $N=8$) for Group 3 veins (mylonites and foliated cataclasites). We note that the grain sizes are almost within an error of each other. Based on these estimations, the average differential stresses range from ~ 25 MPa up to ~ 110 MPa, with higher differential stresses in Group 3 veins ($\sim 80 \pm 14$ MPa, 1σ), which are mostly in the foliated cataclasite unit, and lower differential stresses in Group 1 veins ($\sim 54 \pm 15$ MPa, 1σ ; **Figure 4.7C**), which are in the mylonite unit. The highest differential stresses based on the recrystallized grain size of calcite were recorded in a foliated cataclasite sample just structurally below the active Mai'iu fault (PNG16-151E; **Figure 4.4C, Figure 4.6**) and in a mylonite sample just structurally below a minidetachment close to the inactive Mai'iu fault trace (PNG16-17E). These range from >70 – 110 MPa. The lowest differential stresses (~ 28 MPa) were recorded in sample PNG16-125D of Group 1. This sample was collected at the boundary between the mylonite unit and underlying non-mylonitic schists.

Both the mean twin width and mean twin density were used to constrain the deformation temperature of the calcite veins (**Figure 4.7A**). Our results show a decrease in mean twin width and an increase in the mean twin density from the non-mylonitic schists and mylonites (Group 2 veins: $3.1 \pm 1.9 \mu\text{m}$ twin width, 1σ ; $\sim 38 \pm 22$ twins/mm, 1σ) to the foliated cataclasite and ultracataclasite unit (Group 3 and 4: $1.7 \pm 1.1 \mu\text{m}$ twin width, 1σ ; $\sim 71 \pm 33$ twins/mm, 1σ). The estimated twin densities and the twin widths are consistent with a decrease in deformation temperature from

>200°C (non-mylonitic schists and mylonites) to ~170°C (foliated cataclasites and ultracataclasites; **Figure 4.7A**). Differential stresses based on mean twin densities (**Figure 4.7B**) range between 80–135 MPa (mean 114.0 ± 33.8 MPa) in Group 2 veins, and 140–185 MPa (mean 164.3 ± 37.8 MPa) in Group 3 and 4 veins. Sample PNG15-50RD in the foliated cataclasite unit has recorded the highest differential stresses with 229 ± 47.4 MPa; however, the measured calcite twins were difficult to distinguish from host calcite. Compounding this problem, most of the calcite grains in this particular sample are shattered or fractured as described above (**Figure 4.6F–6I**). This sample was excluded in **Figure 4.7**.

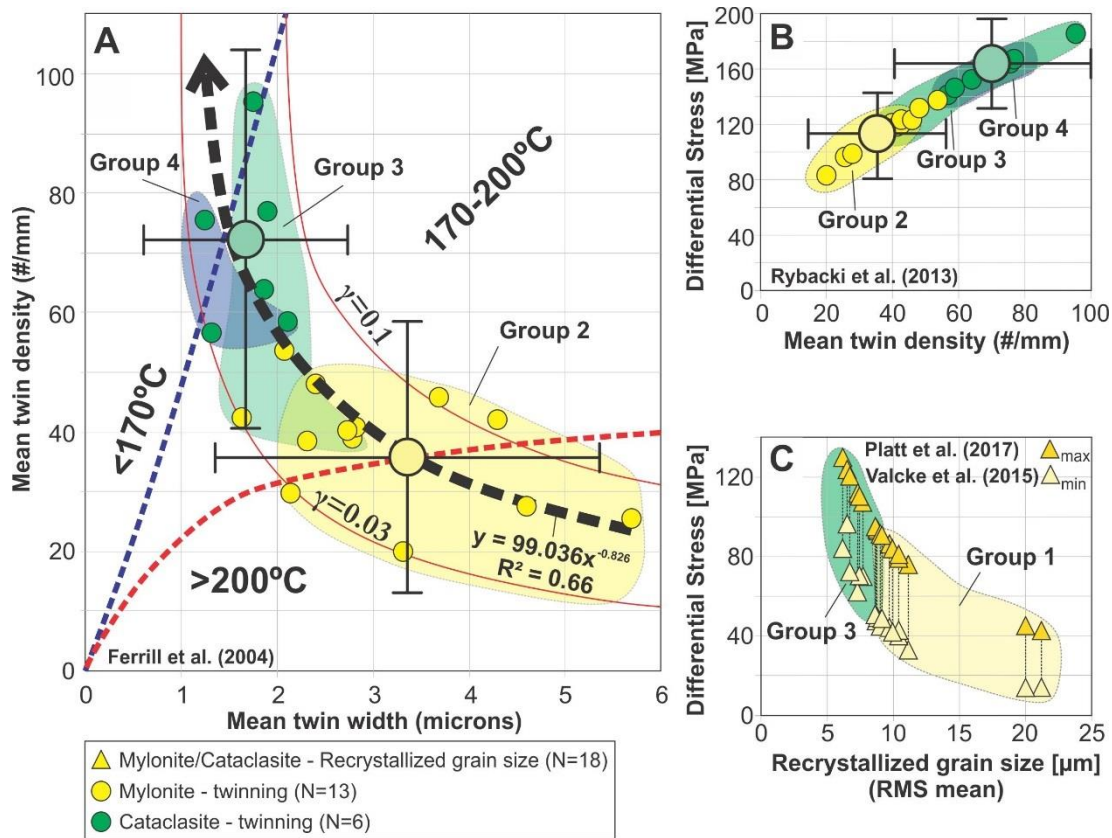


Figure 4.7. Estimated deformation temperatures and differential stresses based on deformation twinning in calcite. A) Graph of mean twin density versus mean twin width (Ferrill et al., 2004). Dashed lines separate deformation temperature domains (after Ferrill et al., 2004). Curved red lines are isostrain magnitude contours (similar to Ferrill et al., 2004; γ —shear strain). Black arrow indicates decreasing deformation temperatures in the observed samples when transitioning from the mylonite zone (structurally lowest fault rock unit) to the ultracataclasite (structurally highest). Big coloured circles indicate average mean twin widths and mean twin densities of mylonites and non-mylonitic schists (yellow), and foliated cataclasites and ultracataclasites (green). The group average standard deviations (1σ) for Group 1-2 and Group 3-4 veins are indicated as black error bars. B) Graph of differential stress versus mean twin density. Differential stresses are based on the paleopiezometer by Rybacki et al. (2013). Big circles indicate average differential stresses and mean twin densities of mylonites and non-mylonitic schists (yellow), and foliated cataclasites and ultracataclasites (green). Group average standard deviations (1σ) are indicated as black bars. C) Differential stress versus recrystallized grain size plot based on the paleopiezometers by Platt and De Bresser (2017) and Valcke et al. (2015).

Paleo-principal stress orientations and stress ratios based on calcite-twin slip data

Figure 4.8 shows lower hemisphere, equal area stereograms of principal stress axes calculated from calcite twin orientation data by the MIM method for 10 calcite-vein bearing fault rock samples. Each stress-state solution (tadpole) for a random subset of five calcite-twin pairs ($k=5$) is represented by a σ_1 (red square) and σ_3 (blue square) pair. The tadpole tail of each solution indicates the azimuth and plunge of the opposing principal stress axis (i.e., the σ_1 -tadpole tail points in the direction of σ_3 and vice versa). Clusters of stress states (tadpole symbols) for σ_1 and σ_3 represent significant stresses with similar attitude and stress ratios (Φ) and were manually shaded in their respective colours. The percentage of all calcite-twin pairs (with an angular misfit threshold of $<30^\circ$) activated by a particular solution cluster and stress ratio are indicated in text below the stereoplot, as is the stress ratio (Φ) calculated for that cluster. The overall mean orientation of σ_1 and σ_3 axes (global average) for each sample based on evaluation of all of its twins (i.e., averaging of all of the calcite-twin pair subsets; see Yamaji & Sato, 2006) is indicated by large white circles (σ_1) and white triangles (σ_3) in the stereonets and in text on the right-hand side of the stereograms. The mean angular dispersion of the individual, subset-calculated stress directions (tadpoles) from the global average is given by an MASD-value (for explanation see Methods 3.2.3). Stress directions calculated from a pooled data set that includes all of the Group 1 and Group 2 veins in the mylonite zone and adjacent non-mylonitic schists (i.e., data sets A+B+C+D+E in **Figure 4.8**) are summarized in **Figure 4.8F**. In a similar way, stress solutions for Group 3 and Group 4 veins in the foliated cataclasite and ultracataclasite units are summarized in **Figure 4.8L**.

Figure 4.8 (previous page). Reconstructed principal stress directions (lower hemisphere, equal-area stereograms) based on observed calcite-twin pairs as analysed by the MIM-method. Solutions for σ_1 (red) and σ_3 (blue) are indicated by filled squares. Red and blue shaded areas identify clusters of stress axis directions (σ_1 and σ_3 , respectively) that are labelled “a”, “b” and “c”. The white circles and triangles depict global average stress directions based on averaging of all the constituent data subsets. Black great circles—orientation of the Mai’iu fault surface at the respective sample location. MASD—mean angular stress distance (see Method section for explanation); N—Number of calcite-twin pairs; N_p —Number of stress states plotted. Sample locations mentioned below are all shown on Figure 4.2B. All samples are from the footwall close to the active fault trace except C and G, which are from the footwall close to the inactive trace. A) PNG16-176 (non-mylonitic mafic schist). B) Sample PNG16-126A (non-mylonitic mafic schist). C) PNG14-15 (phyllitic mylonite/schist beneath east-tilted, inactive part of Mai’iu fault; Figure 4.5A). D) PNG15-76C (mylonite). E) PNG16-1BW-B (mylonite, Figure 4.4B). F) Stress states calculated for all Group 1 and Group 2 veins from the mylonite zone \pm underlying schist except PNG14-15 (see text for explanations). G) PNG16-17E (mylonite) below minidetachment along east-tilted, inactive part of Mai’iu fault (see Little et al. 2019 for photographs of the minidetachment). H) PNG16-151E (foliated cataclasite; Figure 4.4C). I) PNG16-151C (foliated cataclasite). J) PNG15-50RD (foliated cataclasite; Figure 4.4E). K) Samples PNG16-125A and B (foliated cataclasite/ultracataclasite). L) Stress states calculated for all Group 3 and Group 4 veins in the foliated cataclasite and ultracataclasite units, except PNG16-17 (see text).

Based on this analysis, most twin-based estimates for σ_1 orientations follow one of two patterns: 1) the σ_1 axes lie on a \sim E–W striking great circle on which there are several clusters featuring calculated stress ratios of ~ 0.80 (i.e., $\sigma_1 \approx \sigma_2$; Group 1 and 2 veins, **Figure 4.8A, 8B, 8D, 8E and 8H**); or 2) the σ_1 axes populate subvertical clusters carrying stress ratios of < 0.60 (Group 3 and 4 veins, **Figure 4.8G, 8I, 8J and 8K**). Most solutions for σ_3 follow one of the following two patterns: 1) σ_3 axes plunge subhorizontally toward the north to NNE or south to SSW (Group 1 and 2 veins, **Figure 4.8A, 8B, 8C, 8D and 8E**); or 2) σ_3 axes plunge at angles of $\sim 12^\circ$ – 47° with trends that are highly scattered (Group 3 and 4 veins, **Figure 4.8G**). These two patterns for the calculated σ_1 and σ_3 directions correspond well to: pattern 1) Group 1 and 2 veins; and pattern 2) Group 3 and 4 veins, as is summarized in **Figure 4.8F and 8L**, respectively. Note, that the pooled stereograms of **Figure 4.8F and 8L** exclude data from sample PNG16-17E and PNG14-15. The reason for this exclusion is that the inactive Mai’iu fault at these localities, and presumably the fault rocks and veins beneath it, have been tilted east by up to 16° as a result of the synformal deformation on the western limb of the rider block (**Figure 4.2B**). We point out that in the aggregation process leading to the summary stereograms in **Figure 4.8F and 8L**, all

observed twins were weighted equally; that is, samples with a large number of observed calcite-twin sets have a larger impact on the summary stereoplot than do those with fewer twins.

In summary, Group 1–2 calcite veins (mylonites and non-mylonitic schists) produce estimates for σ_1 that chiefly plunge subhorizontally in an ~E–W (250/15) direction (i.e., subparallel to the strike of the Mai’iu fault) and have a calculated stress ratio (Φ) of ~0.8 (implying constrictional stress). The corresponding σ_3 axes plunge subhorizontally in a ~N–S (347/24) direction, which is subparallel to the regional extension direction and to the slip vector trend on the Mai’iu fault. **Figure 4.8A** through **8E** depict a σ_3 that is either dipping shallower than the Mai’iu fault surface, slightly steeper than it, or (less commonly) trending gently to the south. One possible reason that many of the calculated σ_3 axes tend to plunge north is that many of the analysed veins have been ductilely sheared in a down-to-the-north sense (e.g., PNG16-1BW; **Figure 4.8E**). Such deformation, if it is at least in part post-twinning, might rotate twin-based stress solutions in the same sense. The high stress ratio and the E–W spread in solutions for σ_1 suggest a constrictional state of stress, and a tendency for “flipping” between σ_1 and σ_2 axes of subequal magnitude—and between the vertical and horizontal E–W directions. Group 3–4 calcite veins (found in the more shallow-formed foliated cataclasite and ultracataclasite units) mostly record a mean subvertical σ_1 direction and have σ_3 axes that lie on a ~N–S striking great circle with gentle to moderate eastward dip. Estimated stress ratios for the Group 3–4 veins are low (mean Φ of ~0.12) which indicates $\sigma_2 \approx \sigma_3$. The latter global average value for Φ was derived from the amalgamation of data from samples that individually yielded a wide range of stress ratios between 0.25–0.82. Overall, the mixed and complex results imply heterogeneous stresses within the foliated cataclasites and ultracataclasites.

Figure 4.9A presents a global average of all calcite-twin pairs (N=540) spanning Groups 1, 2, 3, and 4 and as taken from all the fault rock units (except the east-tilted samples PNG14-15 and PNG16-17). According to this global average, the paleo-principal stress axes are approximately in accordance with Andersonian normal faulting, that is: σ_1 is subvertical and slightly inclined towards the west; σ_3 is subhorizontal and trends ~N–S. The mean σ_1 is steeply plunging at an angle of ~80 to 75° to the Mai’iu fault surface, whereas the mean σ_3 is subparallel to the inferred extension direction of the Mai’iu fault. The average value for Φ is as low as 0.29.

4.4.2 Paleo-Principal Stress Orientations and Stress Ratios based on Fault-slip Data for Late Brittle Faults

Here, we infer paleo-principal stress orientations based on fault-slip data measured on mesoscopic (slip <1.5 m) faults cutting the footwall of the Mai'iu fault where it has been exhumed at the base of the scarp. As described above, this assemblage embraces small normal faults and also strike-slip faults (both dextral and sinistral). We included one attitude and striae measurement of the Mai'iu fault surface itself for each fault-slip data set as part of the stress inversion. The fault slip kinematic data are presented in **Figure 4.3A–3E**. The fault-slip data have been aggregated from the following locations: a) at several outcrops just south of the active fault trace (N=18, **Figure 4.9B**: PNG15-52, PNG15-76, PNG16-142, PNG16-118, PNG16-50, PNG16-151; N=26, **Figure 4.9D**: PNG16-1BW); and b) just west of the inactive Mai'iu fault segment beneath the rider block (N=10, **Figure 4.9C**: PNG16-17).

Based on the fault-slip data along the active range front (a), the calculated stress orientations include two main populations of σ_1 axes: 1) σ_1 is subvertical (**Figure 4.9B**); and 2) σ_1 is plunging subhorizontally to the ENE or WNW, subparallel to the strike of the Mai'iu fault (**Figure 4.9D**). In both cases, mean σ_3 is plunging subhorizontally to the NNE. The estimated stress ratios (Φ) range from 0.83 to 0.92, indicating that σ_1 and σ_2 are of subequal magnitude ($\sigma_1 \approx \sigma_2$) and thus a constrictional stress state. These principal stress orientations and stress ratios, based on fault-slip data, are similar to those inferred for Group 1 and Group 2 calcite veins, based on calcite twins (**Figure 4.8A–8F**). Based on the fault slip-data along the inactive range front (b), σ_1 is plunging subhorizontally to the ENE and the mean σ_3 axis to the SSW. The estimated stress ratio (Φ) is 0.64. We note that the analysed faults at this location (inactive fault trace) may have also been tilted east by up to 16° as a result of synformal deformation on the western limb of the rider block similar to the calcite vein samples PNG16-17E and PNG14-15 (**Figure 4.8C, 8G**). A backward rotation of the inactive fault surface to the horizontal (rotation axis is parallel to the strike of the inactive Mai'iu fault) together with the fault-slip data would not result in a major change of the σ_1 and σ_3 -directions, except σ_1 would plunge horizontally towards the WNW.

Our largest, and thus perhaps most representative, single dataset of fault-slip data is from location PNG16-1BW south of the active trace of the Mai'iu fault (N=26 fault-

slip couplets, **Figure 4.9D**; note, fault-slip data from this location are not included in **Figure 4.9B** to avoid repetition in the dataset). Because the Ma'iu fault, which is known to have back-rotated (i.e., shallowed in dip) by a rolling-hinge process during exhumation of the mylonitic footwall rocks that host the analysed brittle faults—we forward-rotated the fault slip data at this location about the strike of the Mai'iu fault (103°) in an attempt to reconstruct possible original attitudes of the faults, and thus also the principal directions of stress causing slip on them. We did this in two ways: 1) by assuming that the Mai'iu fault (which today dips $\sim 22^\circ$ NNE at the surface at this locality) originally dipped 30° when the faults formed (**Figure 4.9E**); and 2) that it originally dipped 40° (**Figure 4.9F**). Regardless of the chosen rotation, the data indicate that σ_3 was arranged $\sim 11^\circ$ to 17° more shallow than the fault plane; however, with increasing inferred original dip of the Mai'iu fault at the time of brittle fault formation, the reconstructed plunge of σ_3 increases correspondingly. In all cases, mean σ_1 plunges subhorizontally to the WNW or ENE (**Figure 4.9D, 9F**)—or it is subvertical (**Figure 4.9E**). Such “flipping” of σ_1 between subhorizontal and subvertical is not unexpected given the high stress ratios of $\Phi = 0.83\text{--}0.94$ ($\sigma_1 \approx \sigma_2$).

As a final exercise, we reconstructed paleo-principal stress directions for the unmetamorphosed hangingwall of the Mai'iu fault. This was done by inversion of fault-slip data collected in the Gwoira rider block—which was deposited in the former hangingwall. The analysed faults are almost entirely normal faults dipping at a moderate to steep angle relative to bedding, and that have both synthetic (down-to-the-north) and antithetic senses of slip. Using the MIM technique, inversion of the fault-slip data in their present orientations yields estimates for σ_1 that vary between subvertical to subhorizontal, (E-W trending, **Figure 4.9G**). The corresponding σ_3 axes plunge gently to the N or S. The global average of this dataset ($N=30$) yields a subvertical σ_1 , a N-trending, subhorizontal σ_3 and a stress ratio of $\Phi=0.66$ ($\text{MASD}=44^\circ$) and is thus almost “ideally” Andersonian. A more accurate result can be obtained, we believe, by restoring local bedding attitudes back to horizontal in an attempt to reconstruct the original attitudes of the adjacent faults (and striae) cutting those beds. The beds have been back-tilted so that today they typically dip at $15\text{--}35^\circ$ to the SW, and locally they have been folded to even steeper dips. Despite a diversity of measured bedding and fault dips in the data set, local bedding-fault angles everywhere remain $55\text{--}78^\circ$ —a relationship that suggests that faulting predated most

of the stratal tilting. For this reason, we rotated every fault-slip measurement about the local strike of bedding to reconstruct its original attitude before inverting the data for stress (**Figure 4.9H**). Such “unrotation” of the fault-slip data results in stress solutions that are less scattered and more homogenous (mean angular stress distance reduced from 44 to 29°). They also calculate a mean trend of σ_3 that is NNE (rather than NS)—a result that is more accordant with the known extension direction of the Mai’iu fault and Woodlark Rift.

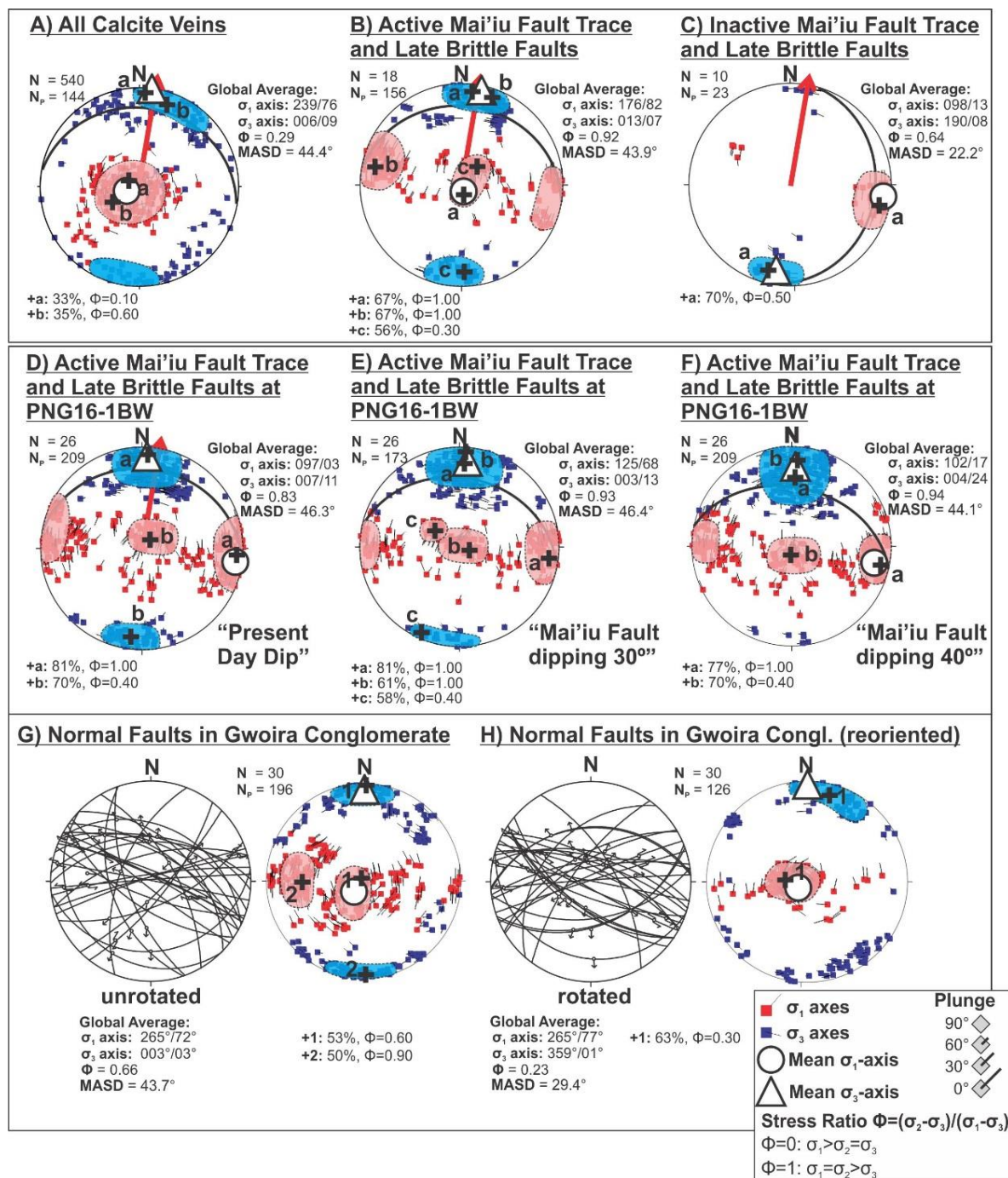


Figure 4.9 (previous page). A) Global mean of paleo-principal stress axis solutions (σ_1 and σ_3) plotted in lower hemisphere, equal-area stereograms based on application of the MIM technique to an aggregation of all calcite twin-pair data collected in the footwall of the Mai'iu fault (this pools together all locations and fault rock units, except for samples PNG14-15 and PNG16-17 on the east-tilted synformal limb beneath the rider block). Same symbology as in Figure 4.8. B) Paleo-principal stress axis solutions based on MIM analysis of fault-slip data for all brittle faults that cross-cut the exhumed footwall of the Mai'iu fault near the active range front (the analysed fault-slip data are shown in Figure 4.3B, 3C, and 3D). C) Solutions for paleo-principal stress axes at site PNG16-17 beneath the east-tilted western limb of the rider block (the analysed fault-slip data are shown on Figure 4.3E). D) Solutions for paleo-principal stress axes based on fault-slip data of brittle faults that cross-cut the Mai'iu fault footwall at sample location PNG16-1BW (Biniguni Falls—a subset of the data in Figure 4.3B, 3C, and 3D). E) Same as (D), but, prior to the stress inversion, the fault-slip was rotated about the 103° strike of the Mai'iu fault to simulate a case where the Mai'iu fault (now dipping 22° NE at the surface) originally dipped 30° at the time of footwall faulting (i.e., the data in Figure 4.9C has been subject to an 8° anticlockwise rotation about the fault strike). F) Same as (D), but the fault-slip data, prior to inversion, was rotated 18° anticlockwise about the strike of the Mai'iu fault. G) Solutions for paleo-principal stress axes based on MIM analysis of fault-slip data (high-angle normal faults) cutting Pliocene strata (Gwoira Conglomerate) in the rider block. H) Same as G, but, prior to the stress inversion, the normal faults were reoriented to an assumed original attitude by restoring the dip of adjacent strata to horizontal by a rotation about their strike.

4.5 DISCUSSION

4.5.1 Uncertainties in Calcite Paleopiezometry and its Applicability to Fault Rocks

Our differential stress estimates derived from the density of mechanical e-twinning in calcite accords with the predictions of Rowe and Rutter (1990) and Rybacki et al. (2011), who argue that the relationship between twin density and differential stress is independent of grain size. Based on our data, calculated differential stress magnitudes in fault rocks vary widely, reflecting differences between the e-twin paleopiezometer equations of Rowe and Rutter (1990), Rybacki et al., (2011, 2013) and Ferrill (1998), (**Table C.2** in Appendix C.2). These inconsistencies in calculated differential stresses are related to differences in experimental setups used to calibrate each of these paleopiezometers (Rybacki et al., 2013). The calcite-twin paleopiezometer equation by Rybacki et al. (2013), presented in our studies, was calibrated using both conventional triaxial and torsion (simple shear) loading experiments at strain rates $\sim 10^{-4}$ – 10^{-6} s $^{-1}$ and confining pressures of 50–400 MPa—conditions applicable to semi-brittle deformation. The classical piezometer

by Rowe and Rutter (1990) was calibrated in low-strain, axial-compression experiments on dense samples of Carrara and Taiwan marble at $400^{\circ}\text{C} < T < 800^{\circ}\text{C}$ and confining pressure of 100 MPa—conditions promoting ductile deformation. Calculated differential stresses based on this latter paleopiezometer were the highest in our studies relative to the others (**Table C.2** in Appendix C.2). As shown by previous studies on calcite-twin paleopiezometry (e.g., Ferrill, 1998; Brandstaetter et al., 2017), the Rowe and Rutter (1990) paleopiezometer is very sensitive to small changes in twin density. The relatively high differential stresses (and standard errors) that are typically calculated using this paleopiezometer might be explained by its application to natural rocks that were deformed at low temperatures and/or high shear strains. We agree with the concerns by Burkhard (1993) that the laboratory conditions used by Rowe and Rutter (1990) may not be appropriately extrapolated to all naturally deformed rocks. The paleopiezometric calibration by Rybacki et al. (2011, 2013), on the other hand, employs conditions relevant to medium to lower greenschist-facies rocks that have been deformed to high strains, and thus seems best-suited to our study. Of the three, the Ferrill (1998) paleopiezometer consistently returns the lowest estimates for differential stress. This calibration is based on laboratory deformation of the porous Indiana limestone deformed to strains at 6% at room temperature and confining pressure of 100 MPa, conditions that seem less suitable to our fault rocks.

Most “classic” paleopiezometers based on recrystallized calcite grain size have not yet been adequately calibrated for EBSD acquisition of grain-size data (e.g., Schmid et al., 1980; Rutter, 1995; Barnhoorn et al., 2004). The calibration by Valcke et al. (2015), based on EBSD grain-size acquisition, is known to underestimate differential stresses in comparison with other paleopiezometers (e.g., Barnhoorn et al., 2004; Platt & De Bresser, 2017). Platt and De Bresser (2017) suggested that the relatively small differential stresses returned by the Valcke et al. (2015) paleopiezometer may relate to a systematic bias in that method towards the smallest new grains imposed by the criteria used by Valcke et al. (2015); for example, Valcke et al. (2015) used the $<1^{\circ}$ average internal misorientation angle in calcite grains as an objective criterion to distinguish recrystallized grains. Platt and De Bresser (2017) used microstructural criteria (proximity and similarity in size of recrystallized grains to subgrains and grain-boundary bulges in adjacent relict grains) for their calibrations. The Cross et al. (2017) approach (that was applied in our studies) uses a threshold

value for average internal misorientation angle that is estimated from a cumulative plot of the number of grains versus the GOS (trade-off curves) for each EBSD-map to distinguish between recrystallized and relict grains. In our studies of the calcite veins, these threshold GOS values range from 1.15–2.15 (**Table C.1** in Appendix C.1). We found that the grain-size of grains coded as “recrystallized” closely matched that of grain-boundary bulges in the adjacent parent (unrecrystallized) grains—a feature that is consistent with the microscopic calibrations by Platt and De Bresser (2017; **Figure 4.5C** and **Figure 4.6B**). We therefore suggest that the Valcke et al. (2015) paleopiezometer provides a lower boundary for differential stresses and the estimated values with the Platt and De Bresser (2017) paleopiezometer are preferred.

4.5.2 Peak Metamorphic Conditions of Mylonites, Calcite Deformation Temperatures and Temperature-Depth Distribution

Based on microstructural observations, we assigned approximate deformation temperatures to our analysed calcite veins using the microstructures in calcite (e.g., Ferrill, 1991; Burkhard, 1993) and the calcite-twin geothermometer of Ferrill et al. (2004; **Figure 4.7A**). According to this scheme, calcite veins in our samples that contain recrystallized grains and Type III and Type IV e-twins are assigned deformational temperatures of >200–400°C. These are our Group 1 and Group 2 veins, found in the mylonite zone and subjacent schist. Samples exhibiting a dominance of Type II and Type I e-twins are assigned deformation temperatures <200°C. These are our Group 3 and Group 4 veins, found in the foliated cataclasite and ultracataclasite units (**Figure 4.7A**). Further constraints on deformation temperature are provided by chlorite geothermometry determinations for 10 calcite veins (see chlorite geothermometry data from Chapter 3 and ‘Chlorite_EPMA_data.xlsx’ in the Digital Appendix). The deformation temperatures were based on the composition of chlorite grains occupying syntectonic microstructural sites in the rock, such as shear bands, strain shadows, and extensional gashes. The chosen sites have cross-cutting or syntectonic relationships with respect to the calcite veins. Based on the particulars of these, we are able to use these data to bracket the emplacement temperature of calcite veins. These are listed in **Table C.5** in Appendix C.4.

The geothermal gradient near the Mai’iu fault is unknown; however, geological data and thermomechanical modelling allow us to place constraints on the temperature-depth distribution along this detachment fault (**Figure 4.10**). Based on

pseudosection modelling of peak mineral assemblages (Daczko et al., 2009), the mafic mylonitic rocks exposed just updip of the Mai'iu fault trace have been exhumed from $\sim 425 \pm 50^\circ\text{C}$ and 5.9–7.2 kbar (i.e., 25 ± 5 km depth, **Figure 4.10**). $^{40}\text{Ar}/^{39}\text{Ar}$ ages of the glassy melt phase in pseudotachylite veins intruding the foliated cataclasites are as young as ca. 2.2 Ma (Little et al., 2018). Using the measured dip-slip rate of ~ 10 mm/yr (Webber et al., 2018) and assuming a mean fault dip in the subsurface of $\sim 30^\circ$, we infer from this result that pseudotachylite veins formed at ~ 11 km depth. Chlorite geothermometry of the foliated cataclasite unit that hosts the dated pseudotachylite veins indicates temperatures of $253 \pm 50^\circ\text{C}$ (PNG16-17H, 'Chlorite_EPMA_data.xlsx' in the Digital Appendix). Some calcite veins that cross-cut pseudotachylite veins in that unit indicate deformation temperatures as low as $\sim 170^\circ\text{C}$ based on the Ferrill et al. (2004) geothermometer (**Figure 4.7A**). We interpret these temperatures as maximum and minimum estimates, respectively, for the foliated cataclasite unit that hosts the pseudotachylites. Thermomechanical models of the Mai'iu fault by Biemiller et al. (2019) are constrained by velocity boundary conditions that are tuned to the Mai'iu fault. These models assume a pre-extensional (post-subduction) geothermal gradient of $15^\circ\text{C}/\text{km}$, yield slip on the Mai'iu fault at a cm/year rate, and generate a convex upward exhumed fault of similar dimensions and shape and dip as the SDM. Between 2.0 Ma to 3.4 Ma of slip on the Mai'iu fault, the models predict an increasing geothermal gradient along the detachment fault as a result of progressive footwall advection (see Supplementary Information of Biemiller et al., 2019, for evolving isotherms and the temperature-depth paths of particles along the detachment fault). At 3.4 Ma, the geothermal gradient in the upper 10 km on the detachment fault is as high as $\sim 24^\circ\text{C}/\text{km}$, decreasing at >20 km depth to ~ 14 – $16^\circ\text{C}/\text{km}$. While acknowledging that a steady state thermal structure may not have been attained in the model (e.g., Ketcham, 1996), we use the modelled temperature structure at 2.0 Ma together with the above geological constraints on geothermal gradient—which agree with that model—to construct a temperature-depth profile for the Mai'iu fault (**Figure 4.10**).

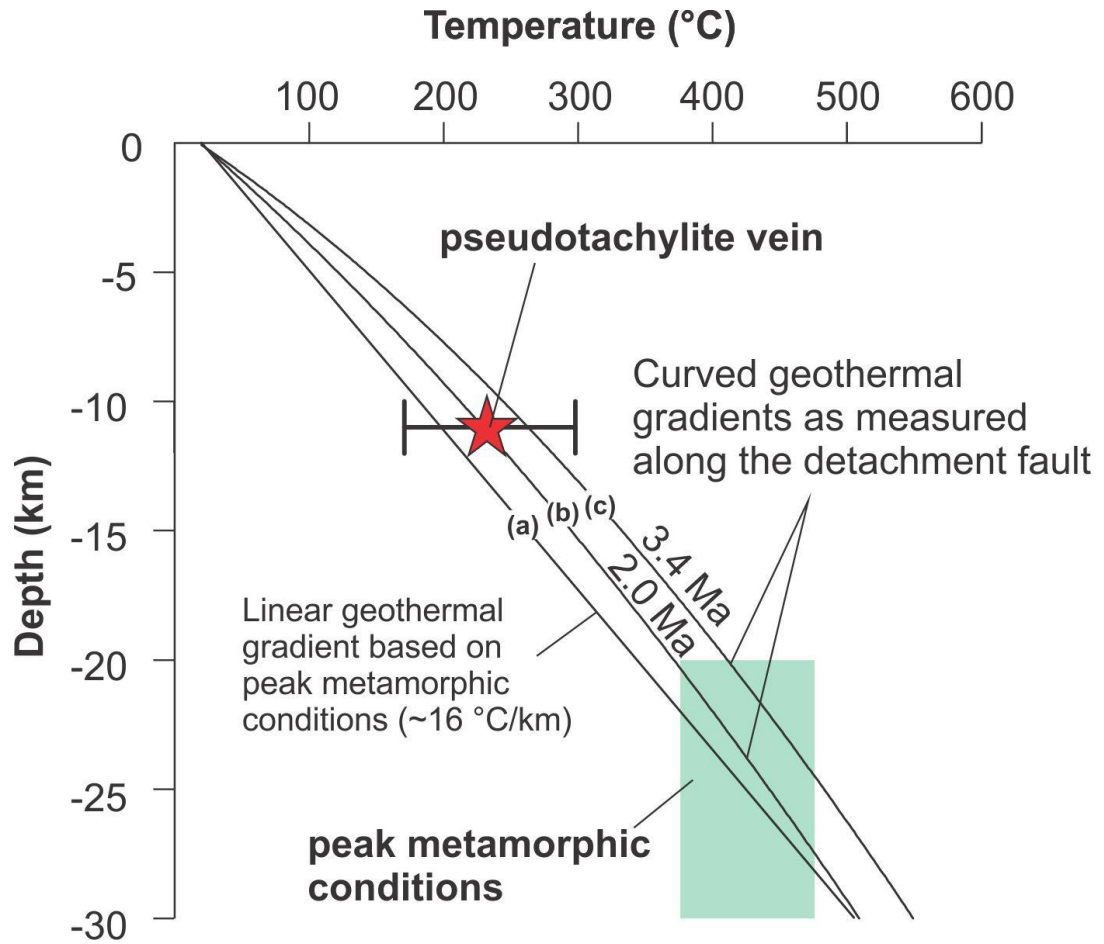


Figure 4.10. Depth versus temperature plot of the Mai'iu fault. Peak metamorphic conditions observed in the mafic mylonites are indicated by a green box (based on pseudosection modelling of the mafic mineral assemblage by Daczko et al., 2009). Red star indicates the inferred depth of dated pseudotachylite veins (see text; based on Little et al., 2019). Error bars on the red star indicate the inferred temperature range of the foliated cataclasites that host the pseudotachylite veins (see text). The temperature-depth curves are derived as follows: a) linear geothermal gradient based on peak metamorphic conditions (~ 16 °C/km); b) and c) curved geothermal gradients based on thermomechanical modelling of the SDM evolution by Biemiller et al. (2019) after a model run of 2 Ma (b), and 3.4 Ma (c). Initial conditions of the thermomechanical model are stated in the contribution by Biemiller et al. (2019).

4.5.3 Strength-Depth Profile of the Mai'iu fault

Figure 4.11A is a schematic profile across the SDM showing the inferred depth distribution of key fault rock units in the footwall of the Mai'iu fault and their estimated temperatures (modified from Little et al., 2019). The depicted dip of the Mai'iu fault at the ground surface (21°) is that seen in outcrop along the profile in **Figure 4.2C** (Mizera et al., 2019). Dip angles in the subsurface are constrained by microseismicity foci at ~ 12 – 25 km depth that are colinear with the trace of the Mai'iu

fault (based on a projection of the microseismicity data ~40 km farther east of this profile as located by Abers et al., 2016). The inferred depth at which the dated pseudotachylite veins formed (~10–12 km depth; Little et al., 2019) is indicated by a red star. In **Figure 4.11B**, we plot differential stresses versus depth based on our calcite paleopiezometric studies (**Figure 4.7B, 7C**), and the estimated deformation temperatures based on chlorite thermometry and calcite microstructures, with these temperatures being converted to depths using the thermal structure in **Figure 4.10 (Figure 4.7A)**. The error bars on each differential stress data point accommodates: a) the standard deviation (1σ) of the mean twin density in the analysed calcite grains; b) the deviation between the Valcke et al. (2015) and Platt and De Bresser (2017) recrystallized grain-size paleopiezometer; c) the uncertainties in deformation temperatures (vertical bars; **Table C.5** in Appendix C.4); and d) the uncertainties in geothermal gradient (**Figure 4.10**). In **Figure 4.11B** several brittle failure curves are depicted in the strength-depth profile assuming Andersonian stresses (σ_1 is vertical) and a hydrostatic pore fluid pressure ratio ($\lambda=0.4$). The thick black failure curve represents failure of an intact basaltic crust for which a linear Coulomb Failure criteria (CF) limits differential stress (cohesion, $C_0=28$ MPa, Schultz, 1993; coefficient of friction, $\mu_i=0.75$), and for which faults are ideally oriented. The several dotted curves represent reshear conditions for non-optimally oriented, cohesionless faults at dips (α) of 21 or 35°; and at static coefficients of friction (μ_d) of 0.15, 0.32, or 0.6. The equations for the brittle failure curves and material parameters used in this plot are presented in Appendix C.6.

According to our differential stress versus depth profile of the Mai'iu fault (**Figure 4.11B**), the mylonites formed at depths of 20–12 km depth, and experienced differential stresses of 25–135 MPa, with the average stress magnitude increasing with reduced temperature and depth. A peak in differential stress at ~8–12 km depth was measured in rocks from the foliated cataclasite unit, which hosts ultracataclasite bands and pseudotachylite veins. There, we measured some differential stresses >150 MPa—a value that exceeds the theoretical brittle strength curve for intact basaltic rocks (CF). This is in accordance with our observation that newly formed brittle faults cut the metabasaltic footwall of the Mai'iu fault (e.g., **Figure 4.3F**). Despite this localized yielding in the footwall, the Mai'iu fault as a whole remained viable—and its continued slip eventually led to exhumation of its (mesoscopically faulted) footwall.

Given the large differential stresses near the stress peak at 8–12 km depth, such reshear would have been possible for any coefficient of friction <0.6 if the mean dip of the fault at this depth is $\sim 35^\circ$ (**Figure 4.11B**). At shallower depths of <7 km, where the fault dips $\sim 21^\circ$, the fault strength was controlled by the frictional properties of the clay-rich fault gouge. There, we consider reshear criteria appropriate to a saponite- or smectite-rich fault gouge ($\mu_{\text{sap}} \approx 0.15$, $\mu_{\text{sme}} \approx 0.32$; Saffer & Marone, 2003; Lockner et al., 2011; Saffer et al., 2012). **Figure 4.11B** shows that the differential stresses required for the fault to slip at this shallower and more misoriented dip angle depend on the fault friction coefficient. The maximum allowable friction coefficient on the Mai'iu fault would be that corresponding to a differential stress (for reshearing) that is equal in magnitude to that required for intact fracture of the footwall by ideally oriented faults (CF failure line). For a Mai'iu fault dip of 21° , this friction coefficient is ~ 0.38 . For an active fault dip that is locally as low as 16° the maximum allowable coefficient of friction would be ~ 0.28 . In agreement with these predictions, abundant saponite and corrensite were identified in Mai'iu fault gouges by XRD-analysis on parts of the fault, both active and inactive, that dip $<21^\circ$ (sites PNG16-142 and PNG16-17, Little et al., 2019). We infer from the known stability range of saponite ($T < \sim 150^\circ\text{C}$; e.g., Lockner et al., 2011; Richard et al., 2014 and references therein), that the saponitic gouges formed at shallow depths by pervasive alteration of the mafic footwall, thus forming a frictionally weak rock that might also be prone to aseismic frictional sliding (velocity-strengthening behaviour). We note that the brittle failure curves presented here assume Andersonian stresses; however, our results suggest that the principal stress axes may not be strictly Andersonian in the footwall of the Mai'iu fault. This disposition of the principal stress axes and the consequences for fault strength are discussed in further detail in the next section.

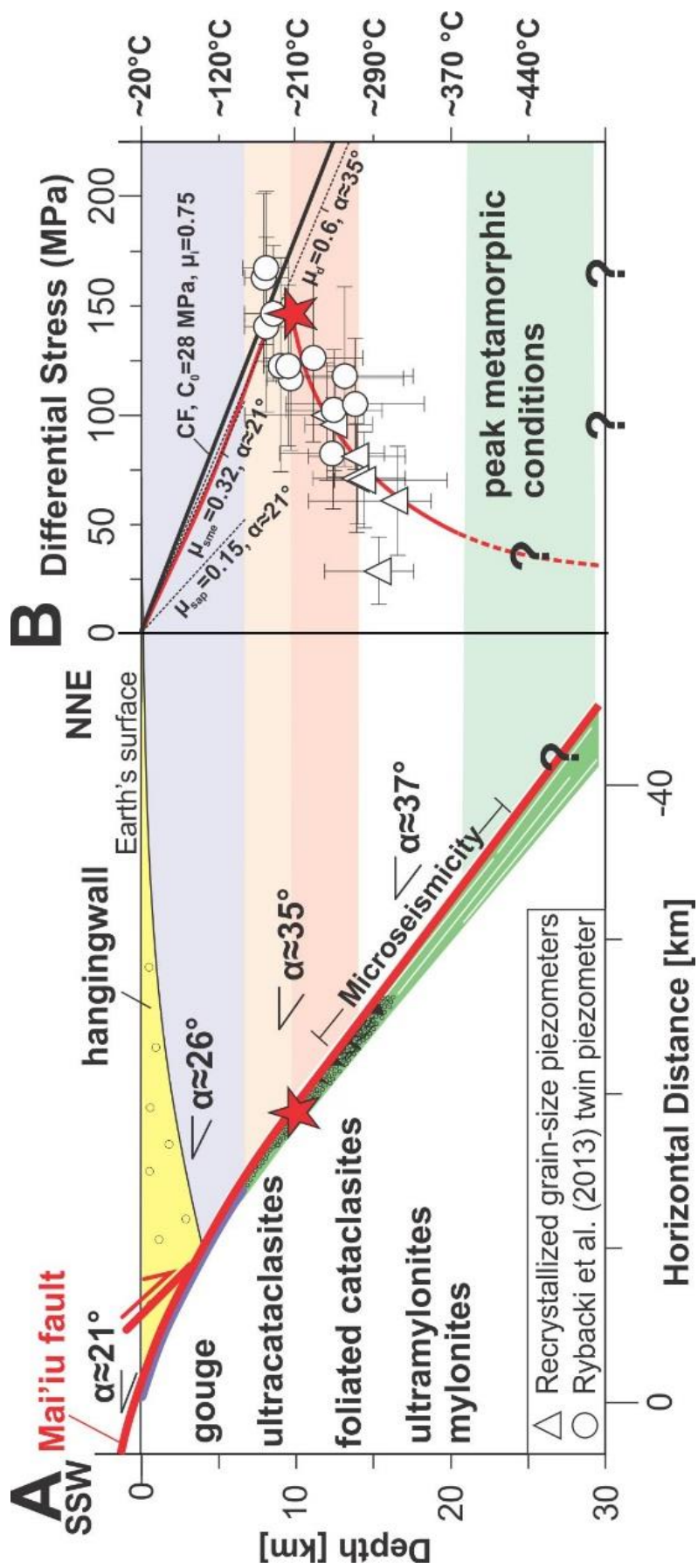


Figure 4.11 (previous page). Strength profile of the Mai'iu fault. A) Left: Profile of the Mai'iu fault (modified after Little et al., 2019; Mizera et al., 2019). Microseismicity based on Abers et al. (2016) projected from ~40 km farther east (see also Mizera et al., 2019). α —dip angle of the Mai'iu fault; Red Star—depth of dated pseudotachylite veins. B) Right: differential stress versus depth-temperature profile with calculated differential stresses (Figure 4.7). The temperature-depth relation is based on curve (b) in Figure 4.10 (non-steady state). Brittle failure curves for intact basaltic crust for which a linear Coulomb criteria (CF) limits differential stress (cohesion, $C_0=28$ MPa, Schultz, 1993; coefficient of friction, $\mu_i=0.75$) and a non-optimal oriented, cohesionless fault with varying dip angles (α) and coefficient of frictions, for which reshear criteria limits differential stress ($\mu_{\text{sap,sme,d}}=0.15\text{--}0.6$; dip angle of the fault, $\alpha=21\text{--}35^\circ$). μ_{sap} —coefficient of friction for saponite (e.g., Lockner et al., 2011); μ_{sme} —coefficient of friction for smectite (e.g., Saffer & Marone, 2003; Saffer et al., 2012); μ_d —“Byerlee” friction (Byerlee, 1978); red line—*inferred change in strength of the Mai'iu fault with depth and temperature.*

4.5.4 Disposition of Principal Stress Axes

Solutions for paleo-principal stress axes causing twinning of calcite veins in mylonites and non-mylonitic schists (Group 1 and Group 2 veins; **Figure 4.8A–8F**), and causing outcrop-scale late brittle faulting of the exhumed mylonites (**Figure 4.9B–9F**) similarly indicate a stress state in the footwall of the Mai'iu fault for which $\sigma_1 \approx \sigma_2 > \sigma_3$ (a constrictional state of stress), and for which σ_3 plunges subhorizontally to the ~NNE or SSW (i.e., subparallel to the regional extension direction). In these solutions, σ_1 either plunges subhorizontally in an ESE-WNW direction (subparallel to the strike of the Mai'iu fault), or it is subvertical (classic Andersonian extensional state of stress). The latter situation agrees with several previous field studies constraining stress orientations near ancient detachment faults, where it has been inferred that σ_1 is subvertical and arranged at a high angle ($55^\circ\text{--}80^\circ$) to the highly misoriented, low-angle detachmant fault (e.g., Axen & Selverstone, 1994; Hayman et al., 2003; Axen, 2004, and references therein). In these studies, principal stress orientations were inferred from the attitude of mixed-mode extensional and shear fractures in the footwall and/or hangingwall of the detachment.

In the footwall of a high-slip detachment fault, a constrictional state of stress characterized by $\sigma_1 \approx \sigma_2$ may reflect reduction of subvertical stresses coupled with an increase in strike-parallel horizontal stress that took place during back-flexure of the exhuming footwall (Fletscher et al., 1995; Singleton, 2013). The reduction of vertical stress might be related to progressive unloading of the footwall as a result of fault slip and/or thinning of the hangingwall during prolonged normal faulting (e.g., Singleton,

2013). During rolling-hinge-style flexural unbending of an exhumed footwall, the outer surface of this footwall contracts in the dip direction. At the same time, the layer thickens according to Poisson's ratio, and the strike direction of the layer also attempts to expand, again according to Poisson's ratio. For a case of lateral confinement where the footwall cannot expand parallel to strike (i.e., it is restricted by the surrounding rocks), this situation may lead to a progressive increase in strike-parallel horizontal stress (σ_2) during fault slip, and thus to an increase in the magnitude of σ_2 at the same time that tectonic denudation is reducing σ_1 . Such a constrictional state of stress can explain the common observation of extension-perpendicular shortening (and associated folding) as documented in the Buckskin-Rawhide MCC, west central Arizona, (e.g., Singleton, 2013); and indeed along the Mai'iu fault, where slip-parallel megacorrugations are inferred to have been amplified as folds (**Figure 4.12A, 12B**; Little et al., 2019). The observations are consistent with a high Φ -ratio ($\sigma_1 \approx \sigma_2$) and a ~E–W trending maximum principal stress direction. In agreement with this, a 2.5 dimensional geodynamical model for the SDM that was presented in Mizera et al. (2019) predicted the generation of E–W, strike-parallel (out of the model plane) compressive stresses in the shallow parts of the metabasaltic footwall and the underlying continental crust, as well as in the shallowest portion of the hangingwall.

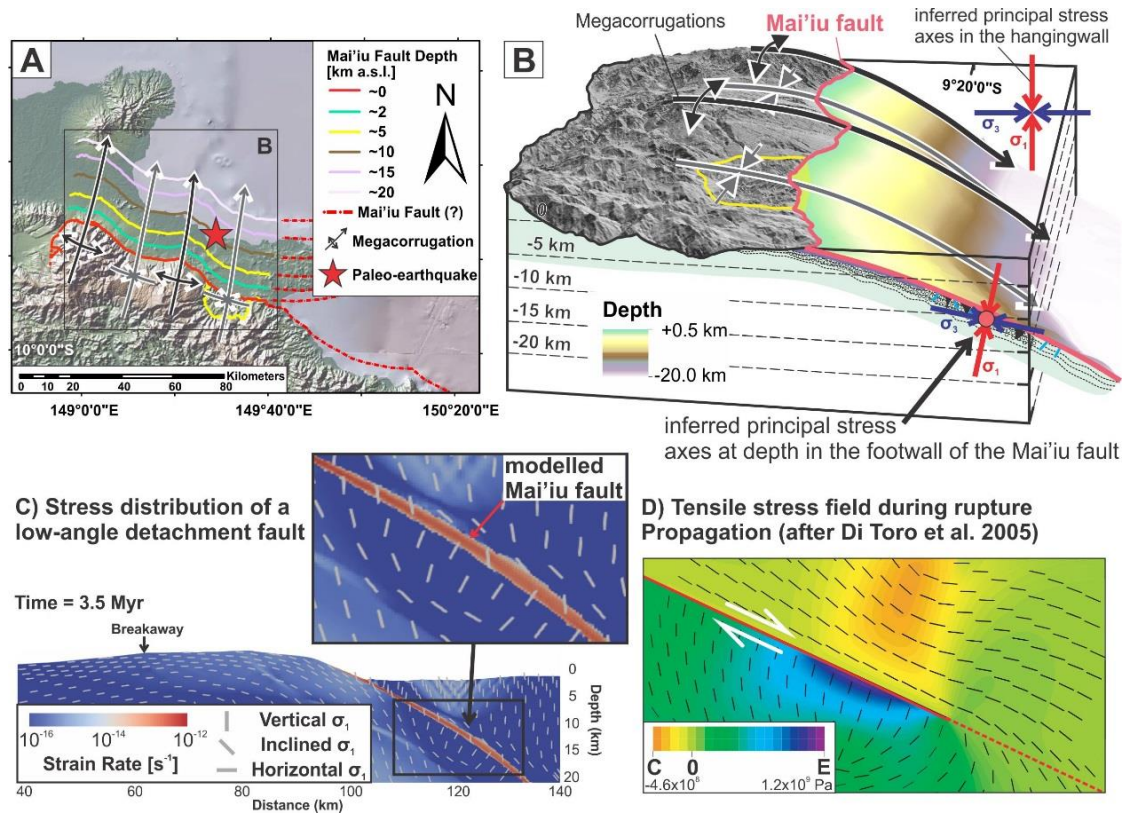


Figure 4.12. Evolution of paleo-principal stress axes in the footwall and hangingwall of the Mai'iu fault. A) Landsat image (30 m cell size) draped over Shuttle Radar Topography Mission digital elevation model (~30 m cell size) showing the SDM and megacorrugations (black arrows). Red line—trace of the Mai'iu fault at the surface. Coloured lines—inferred subsurface continuation of the Mai'iu fault after Abers et al. (2016). Red star—inferred depth of dated pseudotachylite veins. B) Perspective view illustrating the corrugated fault surface of the Mai'iu fault and its subsurface continuation. Principal stress axes σ_1 (red arrows) and σ_3 (blue arrows) are based on Figure 4.9E (footwall) and Figure 4.9H (hangingwall). The red dot in the middle of the stress axes indicate that σ_1 and σ_2 are of subequal magnitude in the footwall. C) Thermomechanical model by Biemiller et al. (2019) showing the development of a detachment fault that accommodates rolling-hinge style deformation. White glyphs— σ_1 -orientations accommodating slip on this fault (see text). D) Tensile stress field on a $>25^\circ$ dipping plane during rupture propagation in the vicinity of a fracture dip (i.e., pseudotachylite vein) after Di Toro et al. (2005). Colour shows stress magnitude, where orange is negative (compression [C], hangingwall) and blue positive (tension [E], footwall). The maximum principal stress σ_1 in the footwall of the propagating rupture front is oriented almost orthogonal to the fault plane in this example.

The Mai'iu fault dips $\sim 20^\circ$ NNE at the surface. Most of our fault-slip data-based solutions for the orientation of σ_3 either trend to the NNE and are subhorizontal; or they plunge at an angle that is less steep than the Mai'iu fault by $10\text{--}20^\circ$ —whereas σ_1 is vertical to subvertical (**Figure 4.9B–9F**). Poles to extension gashes that can be interpreted as σ_3 -directions are at an angle of $\sim 18\text{--}22^\circ$ to the Mai'iu fault surface

(**Figure 4.3A**). Such Andersonian to “near-Andersonian” (i.e., slightly inclined) stress directions are unfavourable for slip on the shallow-dipping Mai’iu fault. If the apparent non-zero plunge of σ_3 is real (see, for example, **Figure 4.9F**, which rotates and restores the stress direction solution to reflect a case where the measured structures formed at depth along a part of the Mai’iu fault that originally dipped 40°) then the stresses were not exactly Andersonian at depth, a situation that would make slip on the shallow-dipping fault even more mechanically unfavorable (**Figure 4.12B**). Such a stress obliquity is also implied by some of our calcite-twinning based solutions for stress orientation (e.g., **Figure 4.8E, 8H**). A possible local cause for departures from Andersonian stress orientation might be stress concentrations around geometric irregularities or asperities in the fault zone (Chester & Fletcher, 1997; Chester & Chester, 2000; Rutter et al., 2007); however, near the Mai’iu fault the pattern seems to be manifested across our entire data set.

Figure 4.12C shows stress trajectories calculated as part of a geodynamic model exploring reactivation of subduction thrusts as extensional detachments (see Mizera et al., 2019 and Biemiller et al., 2019 for a detailed explanation of the model). The finite element model imposes extensional velocity boundary conditions across a pre-weakened subduction zone, with the white glyphs depicting trajectories of σ_1 . The model reproduces a rolling-hinge evolution of the detachment fault, the exhumed portion that becomes convex upward in shape. The model is of interest here, because it predicts spatial changes in stress orientation. In the hangingwall of the detachment, σ_1 is mostly vertical, but it deflects slightly anticlockwise in proximity to the weak fault zone to become more nearly parallel to it. By contrast, in the immediate footwall of the detachment, σ_1 deflects from the vertical in the opposite sense to become nearly perpendicular to the fault—with σ_3 arranged nearly parallel to it. At structurally higher levels, near the fault itself, σ_1 deflects anticlockwise to become more nearly Andersonian. The above-mentioned stress refractions in the footwall of the model reflect flexural stresses there, and they depend on the relative strengths of the footwall, the fault zone and the hangingwall materials. In the Biemiller et al. (2019) model, the fault was made weak to begin with, and was weakened further by strain softening. Although some shear stresses are transmitted across the fault, the magnitude of these may be less than that of internal elastic stresses accumulating in the beam as the result of active bending. In short, the model shows that, as a result of flexure, the principal

stress directions in the footwall of convex up, rolling-hinge style detachment faults may deflect away from “Andersonian”—with σ_3 aligning at a small angle to the fault. To what extent bending stresses affected the observed orientation of stress axes in our study cannot be answered confidently due to the large uncertainties in the calculated stress orientations; however, the stress states ($\sigma_1 \approx \sigma_2$; σ_1 is subvertical and σ_3 is subhorizontal parallel to the extension direction) are kinematically compatible with rolling-hinge style flexure of an exhuming detachment fault as described and predicted in other MCCs (e.g., Fletcher et al., 1995; Singleton, 2013).

The calculated stress ratios (Φ) and principal stress directions inferred from twinning of calcite veins in the foliated cataclasite and ultracataclasite units (these are the Group 3 and Group 4 veins) indicate subvertical σ_1 , and σ_3 axes that trend and plunge variably (**Figure 4.8G–8L**). The high differential stresses estimated from twin densities in some of these veins, as well as “pulverization” of one example (**Figure 4.6F–6H**), and the occurrence of pseudotachylite veins in these fault rocks suggest that the locally high inferred differential stresses and variable stress orientations may reflect dynamic stress conditions during propagation of earthquake ruptures through the rocks. Dynamic rupture processes might be controlled by earthquake rupture directivity, rupture velocity and fracture energy (e.g., Di Toro et al., 2005). Di Toro et al. (2005) and Mello et al. (2010) modelled the principal stress orientations during rupture propagation for different rupture velocities. One example from Di Toro et al. (2005) is shown in **Figure 4.12D**. The colours in this figure represent stress magnitudes from orange (negative, compressional) to blue (positive, tensile). Note that the maximum principal stresses (σ_1 , black glyphs) in the footwall of the rupture front propagating downdip are oriented nearly orthogonal to the fault surface. The subvertical σ_1 -orientation of Group 3 and Group 4 calcite veins (**Figure 4.8G–8L**) and their relations to pseudotachylite veins (**Figure 4.4C**) indicate that these calcite veins may have similarly been influenced by earthquake ruptures and their propagating rupture front.

4.5.5 Mohr Construction for Slip on the Mai’iu Fault

Twinning-based differential stress estimates in the foliated cataclasite and ultracataclasite units (which formed at temperatures ~ 150 – 275°C) can be interpreted as recording those at our inferred mid-crustal peak in strength at 8–12 km depth (Little et al., 2019). The degree to which these stress estimates may reflect interseismic

stresses rather than short-lived, dynamic ones during earthquakes is uncertain. The occurrence of shattered calcite grains (**Figure 4.6F–6H**), pseudotachlyite veins injected into the unit (**Figure 4.3C, Figure 4.4H**), and solutions for stress orientations that are complex and heterogeneous (**Figure 4.8G–8K**) suggest that at least some of our differential stress estimates—presumably the highest ones—may reflect dynamic stresses that existed during (or soon after) earthquakes. Indeed, a few differential stress estimates in this unit exceed 200 MPa. If we exclude these highest (>200 MPa) estimates, this yields a mean differential stress estimate (σ_{Diff}) for the foliated cataclasite and ultracataclasite unit of ~164 MPa (**Figure 4.7B**). Assuming that this mean value is representative of the long-term, interseismic peak strength on the Mai’iu fault at ~10 km depth, we can construct a Mohr circle diagram to depict this situation (**Figure 4.13**). To do so, we allow σ_1 to range between vertical (ideal Andersonian stress state, σ_1 at a 55° angle to the 35°-dipping fault) to slightly inclined (i.e., non-Andersonian, with σ_1 disposed at ~75° to the 35°-dipping fault). We note that calcite veins in the fault rocks may indicate high fluid pressures at times to induce local hydrofracturing (i.e., $P_f > \sigma_3$), but overall there is little evidence for sustained fluid flow or high pore fluid pressure in the foliated cataclasite unit, which contains ductilely sheared calcite veins (e.g., **Figure 4.6A**; Chapter 3; Little et al., 2019). Thus we assign pore fluid pressure ratio of $\lambda=0.4$ (hydrostatic). Assuming a 35° dipping Mai’iu fault in the subsurface, our paleo-differential stress measurements indicate that to drive slip on such a fault the mean coefficient of static friction must have been ~0.24–0.60 in the foliated cataclasites. At the same time, the differential stresses in the foliated cataclasites would have been high enough (>150 MPa) to cause new brittle yielding of formerly intact, strong mafic footwall rocks, as is expressed by small faults cutting the exhumed fault surface (**Figure 4.3G, 3H**).

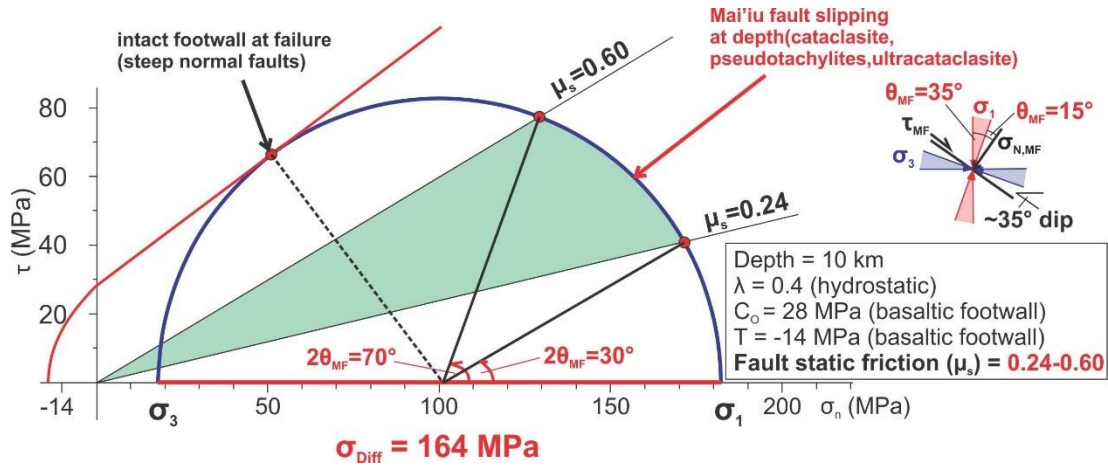


Figure 4.13. Mohr construction for peak differential stress conditions (~164 MPa) as observed in the foliated cataclasites and ultracataclasites of the SDM. The Mai'iu fault's static friction (μ_s) was calculated for a 35° dipping fault segment at 10 km depth and hydrostatic pore fluid pressures ($\lambda=0.4$) in a variably Andersonian and non-Andersonian stress regime (based on calcite veins and late brittle faults in the footwall of the Mai'iu fault). To allow slip on this fault segment, a coefficient of friction between 0.6 (bottom end of “Byerlee” friction; Byerlee, 1978) and 0.24 (smectite-rich coefficient of friction; Saffer & Marone, 2003) might be required. Differential stresses are high enough to cause brittle yielding of the metabasaltic footwall (intact failure strength for basalt from Schultz et al., 1993).

4.6 CONCLUSION

Our study documents differential stresses and principal stress orientations occurring near an active low-angle normal fault in SE Papua New Guinea, the abandoned surface of which is exposed, and which has self-exhumed a sequence of fault rocks that formed as the footwall was exhumed from the mid crust to the surface. We applied structural field work, paleostress analysis and microstructural geothermometry on exhumed metabasaltic footwall rocks of the Mai'iu fault to reconstruct a strength-profile through the middle crust in this region. With regard to this strength profile our results show that:

- Differential stresses in the deepest-formed mylonites and non-mylonitic schists in the footwall of the Mai'iu fault ranged from >25 MPa at ~18 km depth up to 135 MPa at ~12 km depth. These differential stresses increased upwards with decreasing depth and temperature as recorded by deformation twinning in the shallower formed, brittle fault rocks.
- In the foliated cataclasite and ultracataclasite units, peak differential stresses reached ~140–185 MPa (mean 164.3 ± 37.8 MPa) at 8–12 km depth. Such high differential stresses are consistent with the occurrence of pseudotachylite veins

in that fault rock, whereas the depth range agrees with the $^{40}\text{Ar}/^{39}\text{Ar}$ age of the melt phase and the known slip-rate of the Mai'iu fault. Some calcite veins in the foliated cataclasites recorded very high differential stresses (>200 MPa) that we suggest have formed as a result of dynamic stresses during earthquake ruptures (or as transiently high stresses soon thereafter).

- The differential stresses in the mid-crustal foliated cataclasite unit were overall high enough (>150 MPa) to cause new brittle yielding of strong, formerly intact mafic footwall rocks, at least locally, and to drive slip on a part of the Mai'iu fault that dipped moderately and that was relatively strong. The foliated cataclasite formed in a zone of mixed-mode seismic/aseismic behaviour (thesis Chapter 3).
- At the shallowest crustal levels (<8 km; $T < 150^\circ\text{C}$), the Mai'iu fault is a true low-angle normal fault, dipping $\sim 20^\circ$, and is highly misoriented. Here, clay-rich gouges contain abundant saponite and are inferred to have a low coefficient of friction of $\mu < 0.28$.
- The results emphasise that the Mai'iu fault is frictionally weak near the surface, but stronger in the middle crust ($\mu > 0.24\text{--}0.6$).

Some solutions for the orientation of σ_1 , and mostly high stress ratios (Φ) of >0.8 reflect σ_1 and σ_2 that were subequal in magnitude, and compression subparallel to the strike of the Mai'iu fault. We attribute this to a combination of vertical unloading as a result of finite dip-slip on the fault together with 3-D bending stresses related to rolling-hinge style flexure of the footwall.

Chapter 5: Conclusion—A Synthesis of Detachment Fault Evolution

This chapter forms the concluding part of my thesis and summarizes the deformational processes that accommodate slip on the Mai'iu fault. The Introduction of my thesis outlines fundamental questions concerning the mechanical paradox of LANFs—do LANFs initiate at moderate to steep angles then back rotate? are LANFs intrinsically weak? do LANFs generate large earthquakes albeit infrequently or do they generally creep aseismically? Below I present the major conclusions based on previous discussions and contributions from my research Chapters 2–4. An outline of directions for future research is provided at the end of this chapter.

5.1 QUESTIONS AND CONCLUSIONS

Q: *“How do continental detachment faults achieve low dips at the Earth's surface: do they originate as low-angle normal faults, or does the footwall of an originally steeper fault deform in response to a ‘rolling-hinge’ unloading process?”*

To answer this question, I delineated near-surface patterns of translation and tilting affecting the exhumed fault surface of the now-domal Mai'iu fault using structural field data together with geomorphic data interpreted from GeoSAR-derived digital terrain models (DTMs) and aerial photography (Chapter 2). Based on a detailed tectono-geomorphic dataset, the following can be shown (**Figure 5.1A**):

- Windgaps perched on the crest of the SDM, and nearby south-tilted fluvial terraces that were deposited by north-flowing streams provide direct evidence of updip tectonic advection of the exhumed footwall together with progressive back-tilting of the fault surface of the Mai'iu fault.
- Updip tectonic transport of the footwall was accompanied by progressive back-warping of both the exhumed surface of the Mai'iu fault and an underlying foliation (subparallel to it) through $>26^\circ$. In agreement with this, bedding-fault cutoff angles in a stranded rider

block of former hangingwall rocks indicate that the Mai'iu fault had an initial surface dip of $\geq 40^\circ$.

- Microseismicity suggests that today deeper parts of the Mai'iu fault (~10–25 km depth) dip at $30\text{--}40^\circ$ (Abers et al., 2016).

These lines of evidence indicate that the Mai'iu fault evolved by the rolling-hinge mechanism from a fault having an original surface dip of at least 40°N to one that is now highly exhumed (>28 km wide) and domal in shape. On the strongly back-warped, southern flank of the Suckling-Dayman Metamorphic Core Complex, the exhumed fault surface dips south at $\sim 12^\circ$, requiring a total angular rotation in the footwall of $42\text{--}52^\circ$.

Q: *“How was this back-rotation of the exhuming footwall accommodated?”*

- Antithetic-sense (i.e., northside up) dip-slip motion on a widespread set of steep faults in the exhumed footwall that strike parallel to the Mai'iu fault accommodated some of the exhumation-related, inelastic footwall bending that caused the SDM to deform into a domal shape (**Figure 5.1A**). These late-stage faults have scarps (mean throw of ~ 20 m) that offset and deflect stream channels, and are therefore inferred to have been recently active. These mapped faults also reveal that the footwall plastically yields in a distributed type of flexural failure (i.e., “crunching” mode; Buck, 1997).

Finally, a late-stage, exhumation-related increment of shortening in the exhumed footwall that was subparallel to slip is indicated by (a) a pervasive, upright postmetamorphic crenulation foliation with hingelines that trend parallel to the Mai'iu fault trace, (b) folds of Pliocene and younger strata in the stranded rider block that have hingelines trending parallel to the Mai'iu fault trace, and (c) fault-strike parallel warps that deform the exhumed fault surface into an undulatory shape. This late-stage phenomenon is an expected response to footwall unbending at the rolling hinge (e.g., Manning & Bartley, 1994), confirmed by thermomechanical modelling.

Q: *“What micro-scale deformation mechanisms accommodate slip on LANFs in a metabasaltic protolith, and how do they vary with depth; are low-angle normal faults prone to aseismic creep, or earthquakes, or both?”*

Exposures of the Mai'iu fault along the active and inactive fault trace contain a full suite of ductile (mylonite) to brittle fault rocks (foliated cataclasite, ultracataclasite, gouge). Microstructural observations of these fault rocks in the Mai'iu fault zone (Chapter 3) document the space-time evolution of fault rock development in a fine-grained mafic protolith that led to a reduction of long-term (steady state) strength of the Mai'iu fault allowing it to slip at dips of only $\sim 15\text{--}22^\circ$ in the near surface. The evolution of fault rocks and the changing deformation mechanisms accommodating slip on this rapidly slipping, active detachment fault are as follows (**Figure 5.1B**):

- Mylonitic deformation at >15 km depth where the Mai'iu fault dips $\sim 40^\circ$ was mainly controlled by rotation and sliding of a pre-existing fine-grained ($6\text{--}33\ \mu\text{m}$ diameter) mafic mineral assemblage comprising epidote, titanite, actinolite, chlorite, albite and quartz. Slip was accomplished by grain-boundary sliding accommodated by diffusion-creep at temperatures of $\sim 270\text{--}370^\circ\text{C}$ and strain-rates of 5.3×10^{-12} to $2.1 \times 10^{-10}\ \text{s}^{-1}$.
- At shallower levels on the fault ($T \geq 150\text{--}300^\circ\text{C}$, $\sim 8\text{--}15$ km depth, dipping $30\text{--}40^\circ$), fluid-assisted mass transfer of albite, quartz and calcite during dissolution-precipitation creep led to mineral transformation reactions with continuous chlorite growth, creating a $1.5\text{--}3$ m thick zone of foliated cataclasite that deformed in part aseismically at a maximum strain rate of 1.1×10^{-10} to $2.1 \times 10^{-10}\ \text{s}^{-1}$.
- During the above creep process, precipitation of albite, calcite, chlorite and quartz caused sealing of fractures and pores in the cataclasite. This increased cohesion and decreased the mean diffusion distance, reducing creep rates, while also hardening the rock and promoting an increase in frictional strength and differential stress. Build-up of elastic-strain in albite-rich folia may have led to the nucleation of earthquakes as evidenced by multiple generations of pseudotachylite veins that cross-cut the foliated cataclasites within a frictionally strong, high stress ramp at $10\text{--}12$ km depth.

- Creep in the ultracataclasite unit (~150–225°C) was at least in part accomplished by a distributed granular flow of the ultrafine-grained mafic minerals as inferred by the formation of clast cortex aggregates and from plastically deformed calcite veinlets embedded in the ultracataclasites.
- At the shallowest crustal levels ($T < 150^{\circ}\text{C}$), clay-rich gouges contain abundant saponite, a weak phase that might allow slip on the shallowest dipping most poorly oriented part of the Mai'iu fault (dipping ~15–22°), and that is velocity-strengthening, possibly promoting aseismic creep.

Q: *“What is the evidence for seismic slip on the Mai'iu fault?”*

Several lines of evidence indicate that slip on the Mai'iu fault was in part seismic (Chapter 3). These include: (1) pseudotachylite veins in mylonites and foliated cataclasites; (2) nm-sized magnetite \pm maghemite grains in veins cross-cutting the ultracataclasite matrix, and in (or around) older ultracataclasite clasts; and (3) mirror-like surfaces on hangingwall cobbles truncated by the fault.

Taken together, the field and microstructural data (Chapter 3) support geodetic, seismological, and geomorphic evidence for mixed-mode, seismic-to-aseismic slip behaviour on the Mai'iu fault.

Q: *“What stresses (principal stress orientations, differential stresses, stress ratios) drive slip on an active low-angle normal fault, and how do they vary with depth?”*

I have collected stress-depth points in terms of differential stress and temperature estimates to construct a strength-profile through the middle crust in the region of the Mai'iu fault based on structural field work, paleostress analysis and microstructural geothermometry on the exhumed metabasaltic footwall rocks of the Mai'iu fault (Chapter 4). From this I infer that (**Figure 5.1C**):

- Differential stresses in the deepest-formed mylonites and non-mylonitic schists in the footwall of the Mai'iu fault ranged from >25 MPa at ~18 km depth up to 135 MPa at ~12 km depth. The estimated differential stresses increased upwards with decreasing depth and temperature as recorded by deformation twinning in the shallower brittle fault rocks.

- In the foliated cataclasite and ultracataclasite units, peak differential stresses reached ~140–185 MPa (mean 164.3 ± 37.8 MPa) at 8–12 km depth, where the Mai'iu fault is inferred to dip at 30–40°. Such high differential stresses are consistent with the occurrence of pseudotachylite veins in the foliated cataclasite.
- The differential stresses in the mid-crustal foliated cataclasite unit were overall high enough (>150 MPa) to cause new brittle yielding of strong, formerly intact mafic footwall rocks, at least locally, and to drive slip on that part of the Mai'iu fault that dipped moderately and was relatively strong.
- High stress ratios (Φ) of >0.8 (i.e., $\sigma_1 \approx \sigma_2$) at this depth (middle crust), with subvertical σ_1 and significant compression (typically σ_2) arranged subparallel to the strike of the Mai'iu fault, might be attributed to a combination of vertical unloading as a result of slip on the fault, together with three-dimensional bending stresses related to rolling-hinge style flexure of the exhuming footwall.

At the shallowest crustal levels (<8 km; $T < 150^\circ\text{C}$), the clay-rich gouge is inferred to have a low coefficient of friction of $\mu < 0.28$. Thus, the Mai'iu fault is frictionally weak near the surface, but stronger in the middle crust ($\mu > 0.24$ – 0.6).

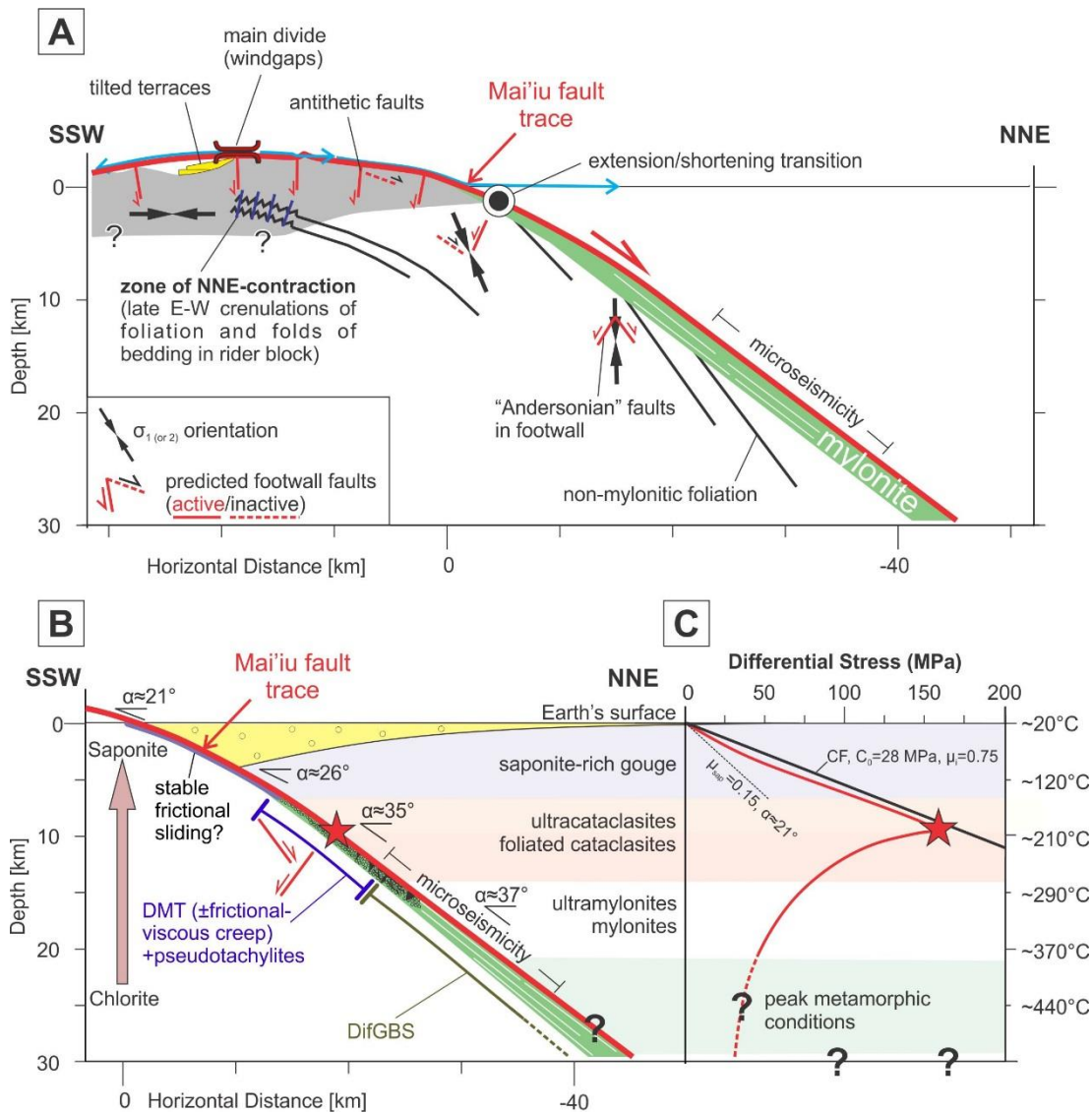


Figure 5.1. Schematic profiles and strength profile across the Mai'iu fault. A) Key structural and geomorphic observations of footwall deformation in the exhuming slab of the Mai'iu fault with superimposed stress trajectories. B) Spatiotemporal changes of deformation mechanisms in the different fault rock units of the Mai'iu fault. Surface fault dip of $\sim 21^\circ$ is taken from dip slopes on section line. Dip angles in the subsurface are inferred from microseismicity data between 12 and 25 km (Abers et al., 2016). Arrow with chlorite and saponite: stability and change of these minerals as a function of depth. DifGBS—diffusion accommodated grain-boundary sliding; DMT—fluid-assisted diffusive mass transfer. C) Differential stress versus depth-temperature profile. Red line—inferred change in strength of the Mai'iu fault with temperature and depth based on calcite paleopiezometry; black, thick line—brittle failure curve for intact basaltic crust for which a linear Coulomb criteria (CF) limits differential stress (cohesion, $C_0=28$ MPa, Schultz, 1993; coefficient of friction, $\mu_i=0.75$); dashed line—brittle failure curve for a non-optimal oriented (21°), cohesionless, saponite-rich ($\mu_{sap}=0.15$) fault for which reshear criteria limits differential stress; μ_{sap} —coefficient of friction for saponite.

5.2 THE LOW-ANGLE NORMAL FAULT MECHANICAL PARADOX

Classical Anderson-Byerlee frictional fault mechanics theory (the maximum principal compressive stress is vertical and friction coefficients of $0.6 < \mu_s < 0.85$) predicts no initiation and active slip on normal faults that dip less than 30° . The rarity of moderate and large dip-slip earthquakes on LANFs ($M > 5.5$; i.e., Jackson, 1987; Jackson & White, 1989; Collettini et al., 2019) supports the conventional notion that normal faults frictionally “lock-up” at dips $< 30^\circ$ (Axen, 2004). In this thesis, I have shown that the Mai’iu fault had indeed an initial surface dip of at least 40° . Abundant structural and geomorphic evidence indicate that the Mai’iu fault has evolved by the “rolling-hinge” mechanism involving progressive flexural back-tilting during exhumation of an originally moderate dipping fault. Today, the Mai’iu fault is only poorly oriented for slip (a true LANF) in the uppermost crust (< 7 km depth) dipping at $\sim 15\text{--}22^\circ$. In agreement with rolling hinge-style bending, aligned microseismicity 12–25 km downdip of the Mai’iu fault trace delineates a convex upward fault zone that steepens downward to a $30\text{--}40^\circ$ dip (Abers et al., 2016). Fault rocks in the shallowest part of the Mai’iu fault are clay-rich gouges containing abundant saponite, a frictionally weak (non-Byerlee) clay mineral ($\mu_{\text{Sap}} < 0.28$). These gouges are thus probably weak enough to slip in an unfavourable orientation in an Andersonian stress regime. It is inferred from microstructural data of the different fault rocks that slip on the Mai’iu fault was accommodated in part by aseismic creep; however, several lines of evidence indicate that slip on the Mai’iu fault was also in part seismic. In conclusion, LANFs are not a mechanical paradox if a pre-existing, weak fault zone is reactivated at a moderate to steep dip angle, the fault zone is governed by non Byerlee’s friction and most of the fault is creeping aseismically.

5.3 FUTURE RESEARCH: UNANSWERED QUESTIONS AND DIRECTIONS

- The association of slip- or spreading-parallel corrugations and megacorrugations with continental and oceanic MCCs suggests that these geometric features are fundamentally related to the evolution of detachment faults (e.g., Singleton, 2013) and therefore important for the understanding of the three-dimensional processes occurring during exhumation along a detachment fault. The origin and evolution of corrugations are, however, not well-understood. Key questions that remain to be solved are: The origin of extension-parallel detachment fault corrugations; When and at what depth (time and space) do corrugations form? What is amplifying the corrugation formation—variable melt production? Heterogeneous vertical stress field? Along-strike variability in the magnitude of tectonic erosion? The Mai'iu fault is an ideal setting to tackle these questions by applying tectonic-geomorphic analysis and three-dimensional thermomechanical models. Initial work, but not reported in this thesis, has revealed megacorrugation growth in the near surface of the Mai'iu fault as indicated by formerly NNE draining streams on the west and east limb of a near summit antiformal culmination that have been pirated by more westerly and easterly draining streams that are still active today.
- One major question that arises from Chapter 4 is whether an increase in σ_2 is necessary, or if a decrease in σ_1 with constant strike-parallel σ_2 would be sufficient to cause the warping, corrugations and paleostresses measured. Furthermore, what effect do the difference in lithologies between dense, strong metabasaltic footwall rocks and weaker, less-dense hangingwall rocks have on the predicted interaction between overburden and Poisson's ratio-style σ_2 increase? Three-dimensional thermomechanical modelling of detachment fault evolution would further improve our understanding of the processes and the stress conditions that lead to a constrictive stress field (as discussed in Chapter 2 and Chapter 4 of this thesis).

- What are the stresses (differential stresses, paleo-principal stress directions) in the upper crust of the SDM? Calcite that cemented the Gwoira conglomerate might be a potential candidate to determine any differential stresses and paleo-principal stress directions within the upper crust of the SDM and may provide the missing link to the strength of the inactive Mai'iu fault. Preliminary results from a calcite cement sample in the Gwoira conglomerate exhumed from ~2–3 km depth just south of the Gwoira fault trace suggest differential stresses of 46.5 ± 25.8 MPa (1σ). Further measurements of both differential stresses and paleo-principal stress directions may be conducted at different structural levels of the Gwoira conglomerate.
- The uncertainties determined on the strength-depth profile presented in Chapter 4 are currently large, particularly the related temperature measurements of individual calcite veins. The formation temperature of the calcite veins might be better derived and refined using “clumped”-isotope geochemistry (i.e. $^{13}\text{C}^{16}\text{O}_2^{18}\text{O}^{2-}$, Δ_{47} ; e.g., Schauble et al., 2006; Ghosh et al., 2006; Zaarur et al., 2013).



Appendix A

Appendix A is related to Chapter 2 of this thesis. It contains further explanations and descriptions regarding: A.1) stream modelling, fault surface model, and the fault-surface roughness analysis (+python-code) in Chapter 2.3.2 (*“Fault Surface Modeling”*); A.2) unpublished structural data from the southern flank of the Dayman Dome in Chapter 2.4 (*“Morphology of the Exhumed Mai’iu Fault Surface”*); A.3) tilting of fluvial terraces across the Agaun main divide in Chapter 2.5 (*“Drainage Network and Fluvial Geomorphology”*); A.4) the interpretation of measured crenulation foliation orientations in Chapter 2.6.3 (*“Late-Stage Footwall Deformation Structures”*); A.5) vertical faults causing rotation of the main fault in Chapter 2.7.2 (*“Kinematics of the ‘Rolling-Hinge’ Mechanism”*); A.6) the equations by Buck (1997) and variables to determine the flexing mechanisms accommodating flexural failure of the Mai’iu fault as described in Chapter 2.7.2; A.7) the numerical methods and model setups used in Chapter 2.7.3 (*“Geodynamic Modeling”*); and A.8) the effect of topographic stresses and density contrasts on the stress field.

A.1 Stream Modelling, Fault Surface Model and Fault Surface Roughness Analysis

Stream channels (**Figure 2.7A**) and the three-dimensional fault surface model of the Mai’iu fault (**Figure 2.5A**, **Figure A.1**) were constructed in ArcGIS 10.1 from the 30 meter-spaced, GeoSAR-derived digital terrain model processed by FUGRO, LTD. The following steps were performed in ArcGIS:

- 1. Convert DTM-Raster to points:** The 30 m DTM rasterfile was converted to a point cloud ([DTM_pts.shp], every pixel of the DTM is represented by a point), which was done by the “Raster to Point” tool.
- 2. Delete all Points not part of the remnant fault surface:** The “fault surface remnant” shapefile ([fault_remnants.shp], **Figure 2.4A**) was used to select points from the point cloud that are part of the Mai’iu fault surface (i.e. exclude all points that are to the north of the Mai’iu fault trace or sit in deep river valleys).

> Select By Location → Select features from [DTM_pts.shp] → Source layer [fault_remnants.shp] → Spatial selection method for target layer feature(s): are within the source layer feature.

The selected points are exported to a separated file [DTM_pts-fr].

3. **Delete all remaining points with slopes >24°:** Most slopes >24° were excluded from the model because these are clearly the result of channel incision. Exceptions to this along the range front were the steep scarp of the Gwoira fault and (farther south) dip slopes of the inactive Mai'iu fault, which are inferred to have been tilted. A shapefile was produced from each cell of the DTM by using the “Slope” tool. By using the “Reclassify” tool, a new rasterfile was created with two new categories: (1) slope 0–24° = NoData and (2) slope >24°. This rasterfile was converted to a polygon-file [Slope24.shp] in order to exclude points from the shapefile [DTM_pts-fr]:

> Select By Location → Select features from [DTM_pts-fr.shp] → Source layer [Slope24.shp] → Spatial selection method for target layer feature(s): are within the source layer feature.

It is important to invert the selection as only the points with a slope >24° were selected at this stage. After the inversion, the selected points were exported as a separate shapefile [DTM_pts-frsl24].

4. **Delete all points at the bottom of channels and river valleys:** In order to remove points sitting in the creeks of the eroded surface a stream model was produced. The following procedures were executed:
 - a. **Fill sinks:** This tool removes sinks in the DTM areas. Sinks are depressions in the topography, where cells with higher elevations surround cells with low elevation. In a river channel, water would be trapped in these so called sinks. The “Sink” tool was used to distinguish imperfections in the DTM and natural depressions such as lakes, but was not used for further stream modelling. Imperfections were removed with the “Fill” tool. The input file was the DTM raster. The output file produced a new DTM raster with filled sinks [DTM_fill].

- b. Flow direction: The “Flow Direction” tool uses the eight direction pour point method (the direction of steepest descent from a cell to its neighbouring cells) to calculate a flow direction for every cell in the DTM. The input surface raster was [DTM_fill]. A flow direction grid [DTM_flow] was generated with this tool.
- c. Flow accumulation: This tool was used to compute the accumulated number of cells draining to any particular cell in the DTM by using the [DTM_flow] rasterfile. This process produces a new flow accumulation grid (here, [DTM_Acc]) that was used to create stream network shapefiles (next step).
- d. Stream network: The flow accumulation grid [DTM_Acc] contains the number of cells that drain to any particular cell. The assumption is that a stream channel is formed when flow accumulation exceeds a threshold value. The lower this threshold the more extensive the stream network. Here, the drainage network was defined as any pixel with an accumulation value of a) >10, b) >80, c) >100, d) >200, e) >500 and f) >1000 using the following expression in the “Raster Calculator” tool:

> Stream_1000 = SetNull ([DTM_Acc] < 100, 1)

In this example, all cells in the output file [Flow_Acc_100] with an accumulation value <100 are excluded from the raster (set to “no data”) all other cells have a value of 1 representing the streams. A couple of flow accumulation files were produced that were compared with topographic maps and aerial photographs.

5. In order to delete the points at the bottom of channels and river valleys, the shapefiles produced in the four steps above were used: by using the “Buffer” tool the stream-shapefiles were turned into polygons—a buffer of 200 m (100 m radius) was used for streams with width of ~200–300 m ([Stream_1000] → [Stream1000Buff200]) and for the smaller streams a buffer of 100 m (50 m radius; [Stream_100] → [Stream100Buff100]). All points that intersect the newly produced buffer-files were deleted:

> Select By Location → Select features from [DTM_pts-frsl24] → Source layer [Stream1000Buff200] → Spatial selection method for target layer feature(s): are within the source layer feature. Inverse selection and export to [DTM_pts-frsl24_BufferS1000200]

> Select By Location → Select features from [DTM_pts-frsl24_BufferS1000200] → Source layer [Stream100Buff100] → Spatial selection method for target layer feature(s): are within the source layer feature. Inverse selection and export to [DTM_pts-frsl24_BufferS1000200100100].

The residual of this subtractive process selects the generally smooth interfluves on the exhumed footwall (**Figure A.1A**). The fault surface model was built from the nondeleted point set by using a natural-neighbor interpolator algorithm in ArcGIS 10.1.

Figure A.1B is the final fault surface model. The morphology of this fault surface can be characterized by its topographic roughness over a wide range of spatial scales (e.g., Candela et al., 2012). Fault-surface roughness can be quantified in cross-section by measuring the average asperity height (H) divided by the profile length (L), also known as the aspect ratio (e.g., Brodsky et al., 2016). Fourier analysis is an effective tool to determine the scale-dependent roughness, as the resulting spectra fit a power law function of wavelength. We studied the Mai'iu fault's spatial change of topographic roughness with a particular goal to determine if the fault is a single, continuously exhumed surface or if it might be a composite one, potentially incorporating more than one fault segment. We performed the following steps: (1) generating a smoothed fault reference surface in form of a 4th-order polynomial surface with respect to the fault surface model (**Figure A.1C**); (2) creating a new surface map—here, we call it the “fault surface relief” map (**Figure A.1D** and **Figure 2.5G**)—by subtracting the smooth reference surface from the highly corrugated fault surface model; (3) extracting profiles from this new surface (**Figure A.2A**), comprising slip-perpendicular profiles close to the fault trace and the summit (see Chapter 2 and **Figure 2.6A**, and **Figure A.2B**), as well as slip-parallel profiles chosen to coincide with synformal and antiformal culminations (**Figure A.2C**); (4) analyzing the scale-dependent roughness by calculating the discrete Fourier transform for each profile, whereas the power spectrum is equal to the square of the amplitudes of the coefficients

(Brodsky et al., 2016); (5) the power spectral density (PSD) is derived from the wavelength-normalized power spectrum (see python-code below for the fourier transform and power spectral density calculations from the extracted topographic profiles); and (6) the resulting spectra have been averaged in a last step using the “plotAverage” toolbox for MATLAB by Jonas Dorn (2010). The scaling behavior of the spectra in the power-spectral density (PSD)-plot is expressed by the Hurst (roughness) exponent ζ (**Figure A.2D**; e.g., Candela et al. 2009).

The results of the Fourier analysis and the power spectral density curves of the individual profiles can be seen in the PSD-plot of **Figure A.2D**. As described in the main text (Chapter 2.4), the averaged Fourier power spectra of the below-slope-break (orange) and above-slope-break (red) profiles line up at a wavelength of ~ 0.3 km and show an identical scaling-behavior at higher wavelength expressed by the same Hurst exponent of $\zeta = 0.68 \pm 0.04$ ($\pm 2SD$, **Figure A.2D**). A Hurst exponent of $\zeta < 1$ means that the topography of the fault surface is rougher at smaller wavelengths (Brodsky et al., 2016). Note, the calculated Fourier power spectra derived from farther up the scarp appear to be smoother in the PSD-plot at wavelength < 0.3 km than the ones downdip. This is an artefact of the “removal” of the more deeply incised stream channels during the fault modeling process and the stream-spacing.

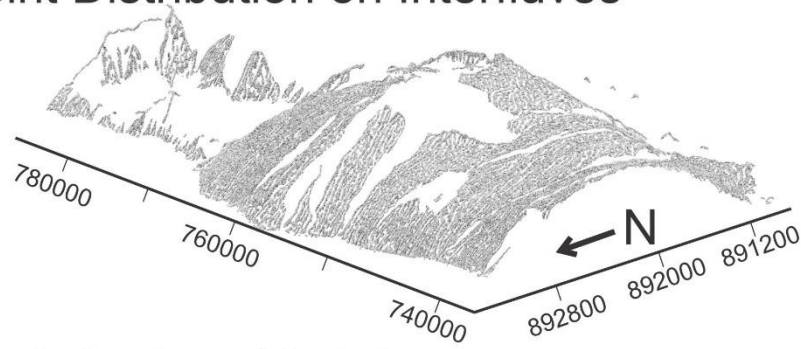
Slip-parallel profiles have been taken from the “fault surface relief” map along the NNE trending antiformal and synformal megacorrugations ($N=40$). The synformal surface relief profiles (**Figure A.2C**, brown) show two corrugations with an amplitude and wavelength of 90 ± 60 m ($\pm 2SD$) and 10.0–13.6 km, respectively. These minor corrugations are related to the concave-up embayment of the fault surface in this area (see Curvature Map in **Figure 2.5C**). The antiformal surface profiles are in general smooth, but rougher at lower wavelength as evident in the PSD-plot of the calculated Fourier spectra (**Figure A.2D**). The Hurst exponents of the averaged Fourier power spectra of the slip-parallel profiles range from 0.45 ± 0.04 to 0.48 ± 0.04 ($\pm 2SD$).

Figure A.2D not only shows the calculated Fourier spectra of slip-parallel fault-surface profiles from our analysis (m-to-km scale), but also from faults at much lower wavelengths (nm-to-m scale) by Brodsky et al. (2011), Candela et al. (2012) and Kirkpatrick and Brodsky (2014). This comparison highlights that the scaling relationships for the different slip-parallel profiles measured over a wide spatial range do not deviate too strongly from each other. The Mai’iu fault exposes the same scaling

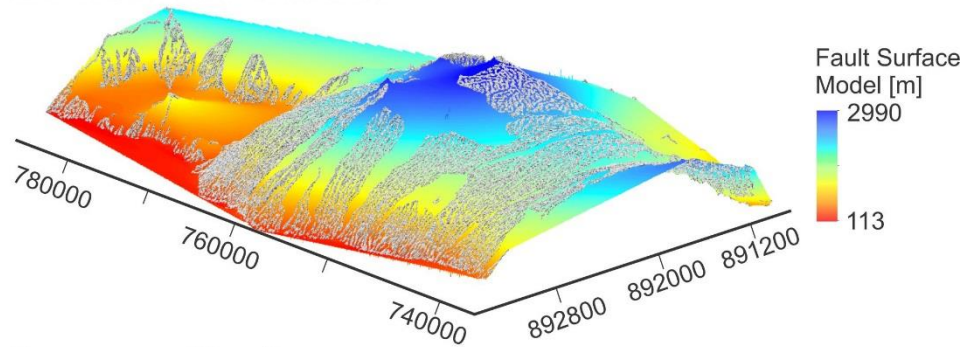
behavior as smaller scale normal faults. This may suggest that all normal faults evolve by the same mechanical principles. The Hurst exponents calculated for the slip-parallel profiles from the Mai'iu fault are slightly lower than those measured on smaller-scale other normal faults ($\zeta < 0.6$); a difference that might be related to the large magnitudes of dip-slip on the Mai'iu fault (> 30 km). Renard et al. (2013) showed that slip-perpendicular profiles from the scale of micro-fractures to the scale of continents share a power-law exponent of $\zeta = 0.77 \pm 0.23$. Our estimate of slip-perpendicular profiles from the Mai'iu fault falls within this range indicating that faulting processes across a wide range of scales may share common characteristics shaping the fault surface (Renard et al., 2013).

Figure A.1 (next page). A) Three-dimensional distribution of remnant points on the interfluvial which is also shown in B-D. B) Fault surface model. C) 4th-order polynomial reference surface. D) Fault surface relief, that is the 4th-order polynomial surface (Surf_{Ref}) subtracted from the fault surface model ($\text{Surf}_{\text{Model}}$).

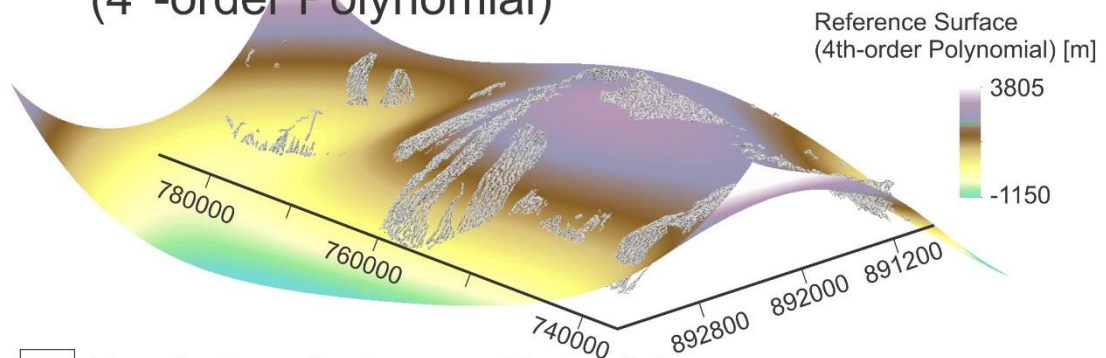
A Point Distribution on Interfluves



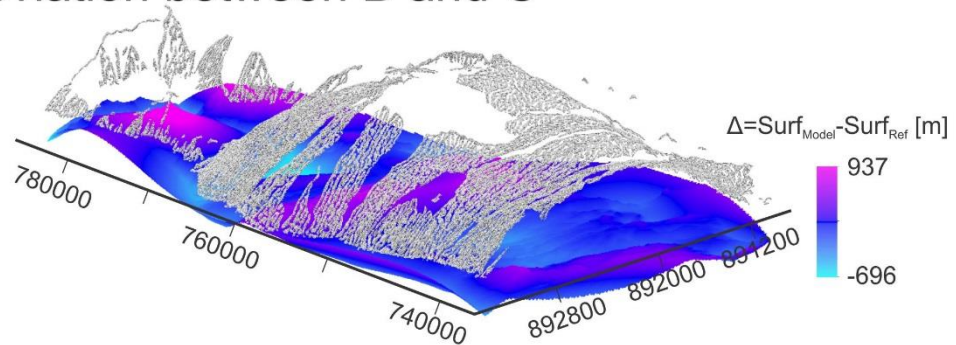
B Fault-Surface Model



C Reference Surface (4th-order Polynomial)



D Deviation between B and C



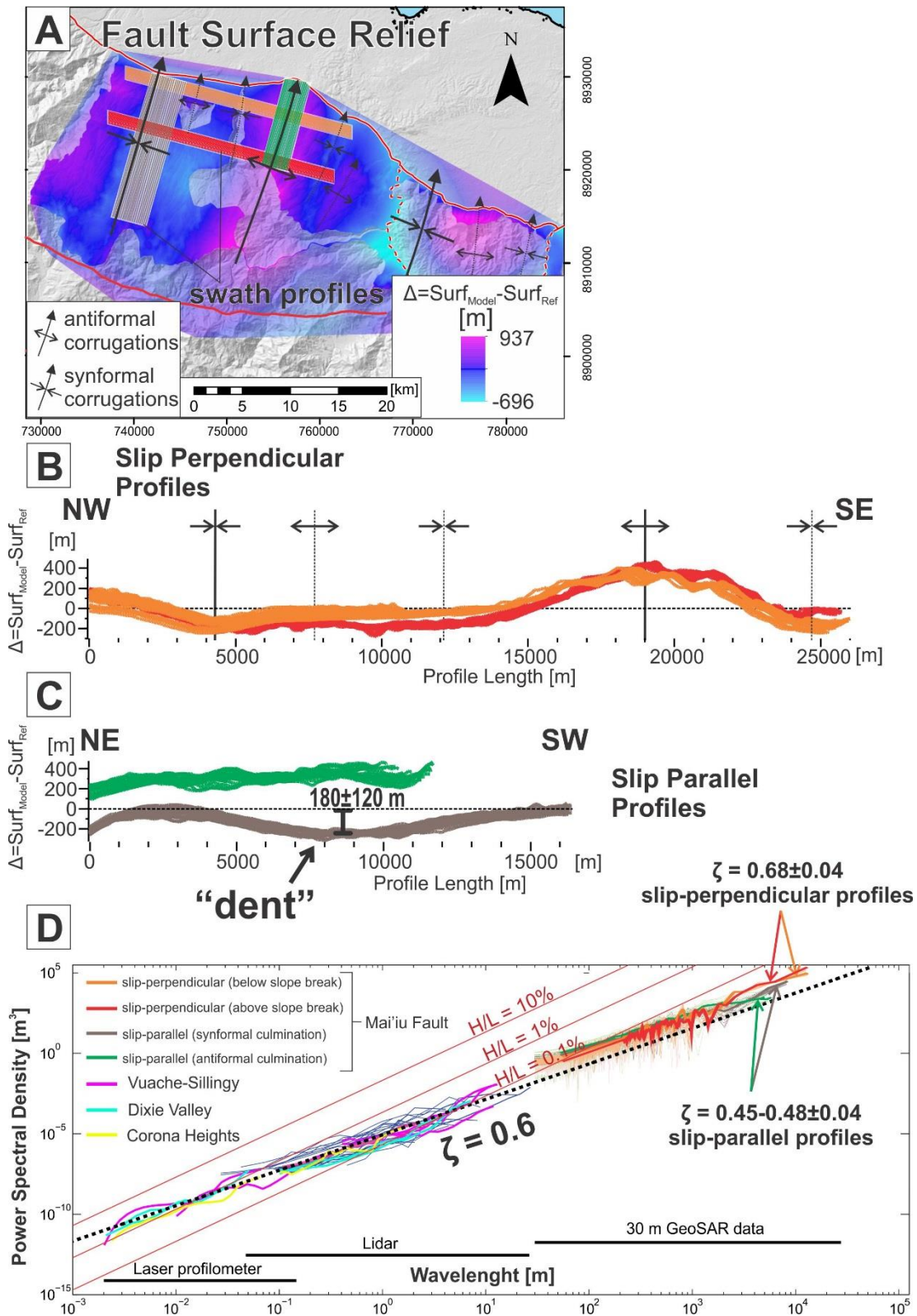


Figure A.2 (previous page). A) “Fault surface relief” map. Black arrows—trend of megacorrugations; orange swath—slip-perpendicular profiles below slope-break (N=20); red swath—slip-perpendicular profiles above slope-break (N=20); brown swath—slip-parallel profiles along synformal corrugation; green swath—slip-parallel along antiformal corrugation. B) Slip-perpendicular and C) slip-parallel relief profiles derived from the “fault surface relief” map in (A) are stacked together for comparison. Note, profiles in B and C are exaggerated in elevation relative to profile length. D) Power spectra density (PSD)-plot with a compilation of roughness data: H/L —roughness aspect ratio; ζ —Hurst exponent; Light colored lines—stacked roughness spectra; Dark colored lines—averaged spectra.

Python-code for fault-roughness analysis (created with Python 3.5):

```
import numpy as np
import matplotlib.pyplot as plt
import scipy.fftpack
# import topographic profile i.e. from arcgis
filename = "Roughness_perpendicular_to_slip.csv"
# in order to calculate dx
previousX = 0.0
# constant for fourier trafo
# will be calculated later
dx = 0.0
yValues = []
with open(filename) as infile:
    lines = infile.readlines()
    for l in lines:
        values = l.strip("\n").strip("\r").split("\t")
        if len(values) > 1:
            x = float(values[0])
            y = float(values[1])
            yValues.append(y)
            if x != 0.0:
                dx = x - previousX
                previousX = x
        print("Found in %s:    x = %f    y = %f    (dx = %f)" % (l, x, y, dx))
numberOfPoints = len(yValues)
totalLength = float(numberOfPoints) * dx
# create numpy array for fft
yArray = np.array(yValues)
xf = np.linspace(0.0, numberOfPoints/totalLength, numberOfPoints/2)
yf = scipy.fftpack.fft(yArray)

#write to file
with open("Roughness_perpendicular_to_slip.dat", "w") as outfile:
    for i in range(int(numberOfPoints/2)):
        if xf[i] != 0.0:
            waveLength = 1.0 / xf[i]
            outfile.write(str(waveLength) + " " + str(1.0/(2*totalLength) * np.abs(yf[i]) * np.abs(yf[i])) + "\n")
```

A.2 Unpublished Structural Data

For the cross-section in **Figure 2.4B**, we incorporated foliation data close to the drawn profile. Foliation data on the southern flank of the Dayman Dome (south of Mt Dayman) derived from unpublished field books (1968) and field sheets (Australian Geological Survey Organization) are shown in **Table A.1**. Outcrop locations were derived from orthorectified aerial photographs in ArcGIS.

Table A.1. Unpublished structural data used in Figure 2.4.

Geologist	Year	Aerial Photograph	Measured Dominant Foliation (Schistosity)			Elevation (SRTM) [m.a.s.l.]	X	Y
			Strike	Dip Dir.	Dip			
P.E. Pieters	1968	Gwoira Run 4/16 5059	165	255	26	482	752867	8900150
P.E. Pieters	1968	Gwoira Run 4/16 5059	170	260	28	491	752763	8900050
P.E. Pieters	1968	Gwoira Run 4/16 5059	180	270	25	499	752636	8899940
P.E. Pieters	1968	Gwoira Run 4/16 5059	175	265	20	363	749882	8898720
P.D. Hohnen	1968	Gwoira Run 4/16 5060	160	250	80	679	754142	8903230
P.D. Hohnen	1968	Gwoira Run 4/16 5060	310	40	35	662	754168	8902850
H.L. Davies	1968	Gwoira Run 4/16 5060	340	70	30	954	754930	8905080
H.L. Davies	1968	Gwoira Run 4/16 5060	220	310	25	767	754446	8904320
H.L. Davies	1968	Gwoira Run 4/16 5060	120	210	20	855	754076	8903930
H.L. Davies	1968	Gwoira Run 4/16 5060	270	0	45	946	754915	8905280
I. Smith	1968	Mt Orian Run 2/185 5151	60	150	15	769	745024	8907080
I. Smith	1968	Mt Orian Run 2/185 5151	160	250	25	523	752384	8899870

A.3 Tilted Terraces

We extracted surface slope information from a 5-meter DTM of the terrace flight to measure tilt on five terraces and the Agaun Valley floor, namely (**Figure A.3**; from the oldest to the youngest): T1, T2_A, T2_B, T2_C, T3 and Valley Floor. The mapped terraces were represented by point clouds with a 5-meter spacing (**Figure A.3B**) in order to calculate the average elevation and dip-direction/dip (aspect/slope) of the terraces (see **Table A.2**). Postformational gullying locally incises the terraces. We therefore assume that the lowest slope-values on these fluvial terraces are the representative ones. We reduced noise by excluding all data points yielding a slope greater than the average slope within one estimated standard deviation. In this way, we fit a 1st-order polynomial surface to the remnant point clouds representing dip-direction/dip of five terraces. Errors were calculated by comparing these results with the raw data (without noise reduction) and also by using another method that calculates the spatial average of every point-cloud representing a single terrace (Openstereo Statistics; **Table A.2**). These yield an estimated elevation error of <2 m and a dip-error of <0.5° for the slope-angle and <8° for the dip-direction.

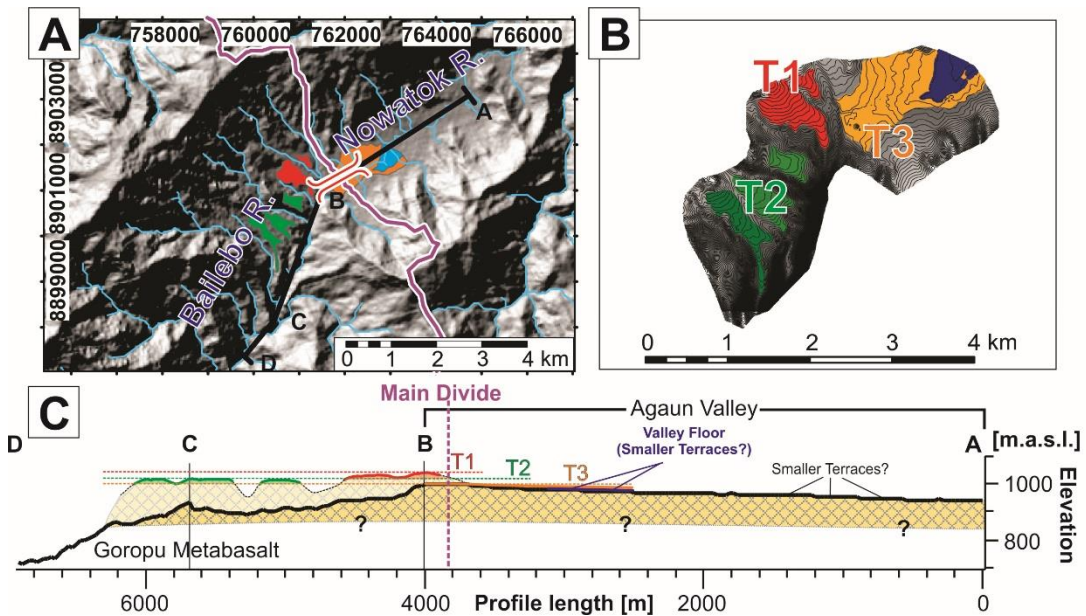


Figure A.3. A) Map of Agaun Valley hosting several fluvial terraces. Note, the Nowatok River is also called Agaun River in Smith and Davies (1976) and the Bailebo River is described as a tributary of the Tavane River in the same contribution. B) 5-meter DTM showing fluvial terraces and 5-meter contour lines. C). Cross-section (profile line is shown in A) through the Nowatok and Bailebo River. Terraces are plotted “on top” of this cross-section.

Table A.2. Surface slope information of tilted fluvial terraces (**Figure A.3**) from a 5-meter DTM. Spatial average of points (Openstereo statistic) were calculated with the software OpenStereo (Grohmann & Campanha, 2010). Green highlighted dip-direction/dip measurements are cited in the main text.

Terrace ID	Agaun River Valley (Smaller Terraces)	Agaun T3	Agaun T2 C	Agaun T2 B	Agaun T2 A	Agaun T1
Number of Points RAW	7925	43536	4004	6676	8243	13097
Mean Elevation RAW	967.14	982.37	1003.00	1010.40	1012.53	1026.54
Std-Dev Elevation RAW	2.18	11.38	7.82	12.28	20.20	17.73
Mean Slope RAW	2.22	3.14	6.20	5.12	5.92	6.33
Std-Dev Slope RAW	1.31	2.29	3.17	2.91	2.78	2.08
Number of Points	6643	39586	3338	5681	7094	11461
Mean Elevation	967.00	982.05	1004.06	1012.08	1013.70	1026.56
Std-Dev Elevation	2.18	11.46	6.89	11.04	18.76	17.31
Mean Slope	1.78	2.65	5.13	4.18	5.11	5.77
Std-Dev Slope	0.77	1.18	2.14	1.72	1.88	1.41
Openstereo Statistics						
Number of Points	6643	39586	3338	5681	7094	11461
Mean Plane	60.2/0.8	78.0/1.1	99.1/3.5	126.6/3.0	140.5/3.6	150.3/4.6
Normal to Plane	240.2/89.2	258.0/88.9	279.1/86.5	306.6/87.0	320.5/86.4	330.3/85.4
Radius of Confidence at 5% (degrees)	0.04 degrees	0.02 degrees	0.13 degrees	0.08 degrees	0.08 degrees	0.06 degrees
Fitted 1st-order Polynomial to Points						
Plane dip direction	58	85	106	132	135	144
Plane dip	0.44	1.38	3.05	3.4	3.48	4.42

A.4 Strike-Distribution of Crenulation Foliation

A pervasive postmetamorphic crenulation fabric has developed in the non-mylonitic and mylonitic footwall during exhumation and records extension-parallel contraction (see also Little et al. 2019). Folding in the Gwoira rider block, that records most recent increments of extension-parallel contraction, suggests that these folds may have formed as a result of unbending of the once steeper, but now unloaded and uplifting footwall of the Mai'iu fault (e.g., see Chapter 2.7.3 Geodynamic Modeling). Close to the Gwoira embayment the strike of the crenulation foliation is parallel to the now inactive part of the Mai'iu fault and shows E-W compression rather than N-S compression. **Figure A.4** shows an interpretation of the strike orientation of measured crenulation foliation that mimics the dome's curvature: From time t_0 to t_2 the hangingwall is progressively withdrawn leading to exhumation of the footwall. Shortening of the non-mylonitic and mylonitic foliations in the subsurface is accommodated by folding (crenulation) of the foliation about axes that are orthogonal to the direction of maximum exhumation gradient in the fault footwall (exhumation gradient is depicted with red cross-hatching in snapshot t_1). On most of the SDM, fault strike is E-W, and the direction of this gradient is downdip to the north, leading to N-S shortening and E-W fold hinges. Close to the Gwoira embayment farther to the east, the Mai'iu fault strikes nearly N-S. There, the direction of maximum exhumation gradient is not N-S but more easterly. At t_2 , the Mai'iu fault bounding the shallow-dipping Gwoira Embayment is not able to accommodate further slip, which leads to its abandonment. Initiation of the Gwoira fault in the former hangingwall leads to N-S shortening in the uplifted footwall of this fault as revealed by E-W folding of the south-tilted beds in the captured Gwoira rider block.

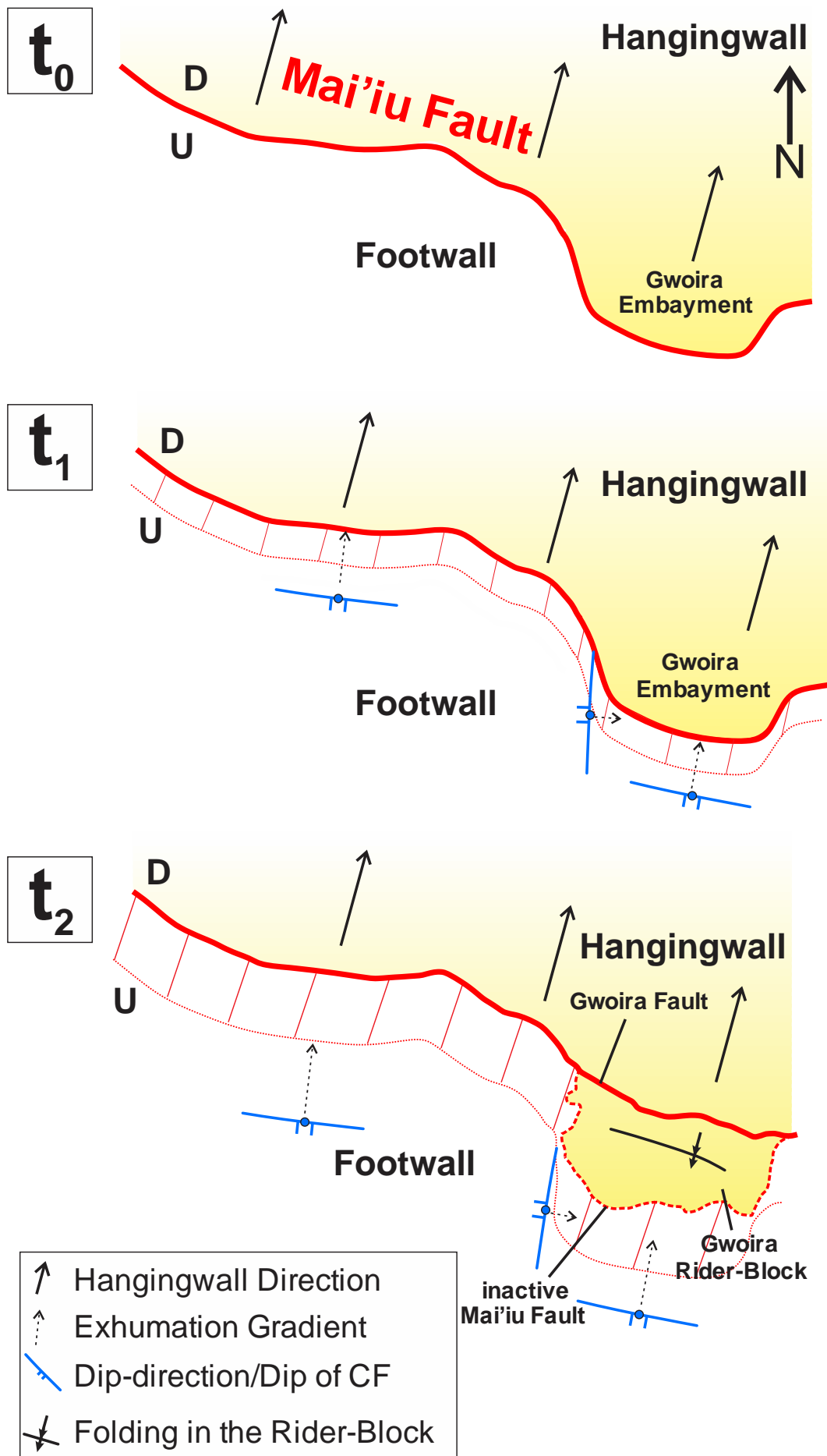


Figure A.4 (previous page). Schematic evolution of the strike orientation of measured crenulation foliation. t_0 : Onset of hangingwall removal. t_1 : Crenulation foliation, possibly formed in the subsurface during exhumation, follows the exhumation gradient of the footwall. Corrugations may amplify during slip (Little et al., 2019). t_2 : Initiation of the Gwoira fault and folding of sedimentary beds.

A.5 Rotation of the Mai'iu Fault Accommodated by Vertical Footwall Faults

We infer that the steep northside up faults formed in response to “rolling-hinge” style flexure of the exhuming fault surface and note that slip on such antithetic faults kinematically will contribute to back-rotation of the footwall (Spencer, 1984; Wernicke & Axen, 1988; Wdowinski & Axen, 1992). In order to evaluate the possible kinematic contribution of such faulting we calculated the shear strain ($\gamma = \tan(\psi)$, where ψ is the angular shear strain) that would be required in such fault array to accommodate all of the back-rotation of the footwall, between an initial 40° northward downdip from the fault trace to a horizontal dip at the crest of the dome (**Figure A.5**). Assuming an average throw of 15 m and a spacing of 1.5 km between the faults, the estimated shear strain is $\gamma = 0.01$. By contrast, rotation from 40° to horizontal with 1.5 km spacing would require a shear strain of $\gamma = 0.84$. This magnitude of finite shear strain in turn would require a throw of at least 1.35 km on every mapped fault or a spacing of <17 m if each fault has a throw of 15 m. The serial fault slip would also shorten the footwall and its sub-parallel foliation by -23%—a prediction that exceeds our minimum shortening estimates in the exhumed footwall of -4.0% to -9.6% (see Chapter 2.6.3). We note that the foliation between individual faults require distributed shearing in order to rotate.

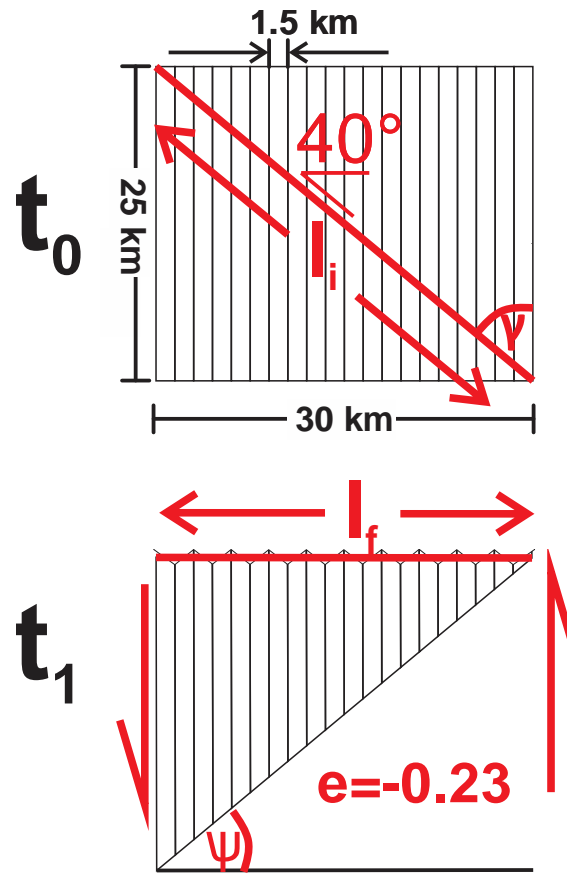


Figure A.5. Sketch of an array of vertical faults causing rotation of the main fault (red line); l_i : initial length of fault; l_f : length of fault after 40° of rotation; γ : shear strain along fault; ψ : angular shear strain; e : longitudinal shortening parallel to the fault surface (23%). t_0 : time before footwall unloading; t_1 : rotation of the footwall accommodated by slip along subvertical faults.

A.6 Flexing Mechanisms Accommodating Flexural Failure

This section follows the approach by Buck (1997) to determine whether a thin lithospheric beam, in our case the thin Goropu Metabasalt layer of ~5 km thickness, bends in a distributed manner (“crunching”) or in a localized way (“snapping”).

According to Buck (1997), the flexing mechanism depends on how the bending moment (M) changes with curvature (w''), where the moment-curvature relation depends on the strength of the lithosphere. For calculating the yield stress—the difference between the maximum and minimum principal stress (σ_D) needed to satisfy the Mohr-Coulomb failure criterion for faulting on an optimally oriented fault—we assume that one of the principal stresses is vertical (Anderson, 1951) and equals the overburden, $\rho'gz$, where ρ' is the effective density of the Goropu Metabasalt (1860 kgm^{-3} ; see **Table A.3**), g is the acceleration of gravity and z the depth. For a given coefficient of friction (μ) and cohesion (τ_0), the yield stress (onset of faulting) is then:

$$\sigma_Y = Cz + S \quad (\text{Eq. A.1})$$

where

$$C = \frac{-2\mu\rho'g}{(1+\mu^2)^{\frac{1}{2}} \pm \mu}$$

and

$$S = \frac{-2\tau_0}{(1+\mu^2)^{\frac{1}{2}} \pm \mu}$$

The signs on top and bottom indicate extensional and compressional failure, respectively; C and S will be denoted by the subscripts e and c for extension and compression, respectively. For our calculation we used a coefficient of friction of 0.6 (Byerlee, 1978) and a cohesion of 5 MPa (representing a minimal strength; see **Figure 2.10A**, inset: green lines). If the flexed lithospheric beam is below the yield stress at any depth (z) then the deformation is accommodated by elastic strain. Buck (1997) assumes that the elastic bending stresses vary linearly with depth through the elastic part of the flexed plate (Bodine et al., 1981). The elastic fiber bending stress within the elastic part of the plate is then:

$$\sigma_E = \frac{Ew''(z-z_0)}{(1-\nu^2)} \quad (\text{Eq. A.2})$$

where E is Young's Modulus, z_0 is the depth of the neutral surface, and ν is the Poisson's Ratio (see **Table A.3**). Here, we assume that the neutral surface is at depth of 2500 m, a Young's Modulus for basalt/schist of 4.1×10^{10} Pa and a Poisson's Ratio for basalt/schist of 0.14 (Shah & Shroff, 2003). The limiting curvature (w''_0), where the entire 5 km-thick basalt beam deforms in a purely elastic way (see **Figure 2.10C**, inset: orange line), can be calculated by the following equation:

$$w''_0 = \frac{2(S_C + \sigma_P)(1 - \nu^2)}{Eh} \quad (\text{Eq. A.3})$$

where σ_P is the average applied horizontal stress and h the beam thickness. Assuming an average horizontal stress σ_P of 0 MPa and a beam thickness of 5 km, the maximum curvature is $1.69 \times 10^{-7} \text{ m}^{-1}$. **Figure 2.10A** shows that the elastic bending stresses exceeds the yield stress for our calculated curvature of $1.68 \times 10^{-5} \text{ m}^{-1}$ (w''_{MIN}) meaning that the flexed Goropu Metabasalt layer will fail plastically.

After Buck (1997) the maximum brittle layer thickness that should fail as the beam bends can be estimated by calculating the maximum plastic bending moment, ($M_{P_{\text{max}}}$):

$$M_{P_{\text{max}}} = C_e \frac{z_0^3}{6} + C_c (z_0 - h)^2 \left(\frac{z_0^3}{6} + \frac{h}{3} \right) - \sigma_P \left(z_0 h - \frac{h^2}{2} \right) \quad (\text{Eq. A.4})$$

$M_{P_{\text{max}}}$ is the bending moment as the curvature of the beam approaches an infinite value. Snapping is predicted when $M_{P_{\text{max}}}$ is less than the maximum elastic moment M_0 , where:

$$M_0 = \frac{(S_C + \sigma_P)h^2}{6} \quad (\text{Eq. A.5})$$

Using the values given in **Table A.3** $M_{P_{\text{max}}} = 5.4 \times 10^{14}$ Nm and exceeds $M_0 = 7.4 \times 10^{13}$ Nm, predicting a “crunching” deformation. The maximum critical layer thickness, where a transition between “snapping” and “crunching” is expected when no horizontal stress is applied, is about $1.5 \times S/C$. According to this, “snapping” is expected for a layer thickness of ≤ 685 m (see main text). This maximum layer thickness for “snapping” increases with applied average horizontal stress (**Figure A.6**); for example, adding 90 MPa of average compression to the unbending beam would increase the critical layer thickness that should snap to ≤ 4186 m assuming the neutral surface is half this thickness. An increase in cohesion would also increase the

critical layer thickness (see **Figure A.6**) showing that a thin, more cohesive beam should bend by “snapping” (Buck, 1997).

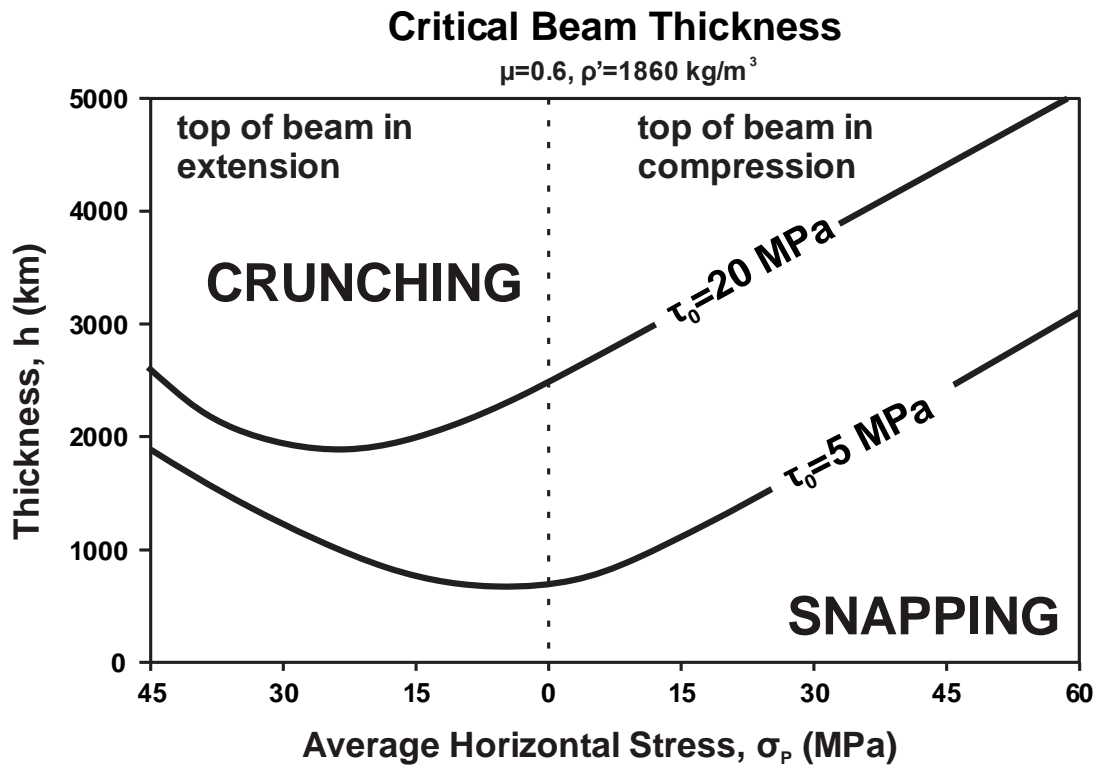


Figure A.6. Critical beam thickness that allows distributed crunching or localized snapping flexural failure as a function of the average horizontal stress, σ_p , when a beam is bent so as to put the top in compression. This thickness is calculated for a cohesion of either 5 MPa or 20 MPa.

Table A.3. Overview of variables used for equations.

Symbol	Quantity	Assumed Values	Units
σ_Y	Yield Stress		Pa
σ_E	Elastic Bending Stress		Pa
σ_P	Average Horizontal Stress	0	Pa
μ	Coefficient of Friction	0.6	
λ	Pore Fluid Factor	0.4	
ρ	Rock Density	3100	kgm ⁻³
ρ'	Effective Rock Density. $\rho' = \rho - \lambda \times \rho$	1860	kgm ⁻³
g	Acceleration due to Earth Gravity	9.81	ms ⁻²
τ_0	Cohesion	5×10^6	Pa
E	Young's Modulus (Basalt/Schist)	4.1×10^{10}	Pa
ν	Poisson's Ratio (Basalt/Schist)	0.14	
h	Beam Thickness	5000	m
z	Depth below Fault Surface		m
z_0	Depth of Neutral Surface	2500	m
M	Bending Moment		Nm
M_0	Maximum Elastic Moment		Nm
M_{Pmax}	Maximum Plastic Bending Moment (when plate curvature approaches infinite value)		Nm
w''	Plate Curvature		m ⁻¹
w''_0	Limiting Value of Curvature w'' for $M=M_0$		m ⁻¹

A.7 Geodynamic Model

Our numerical model was constructed using the thermomechanical finite-element geodynamic code SULEC, developed by Susan Ellis and Susanne Buiter (Ellis et al., 2011; Buiter & Ellis, 2012). SULEC solves the momentum equation for incompressible temperature-dependent power-law flows. Brittle-plastic behavior is considered using the pressure-dependent frictional Mohr-Coulomb yield criterion, and elasticity is approximated as an effective elastic viscosity using the method described in Moresi et al (2003). Strain and strain rate are calculated at each time step for each element where deformation responds to the minimum of the viscous flow stress and the plastic yield stress. Temperature is advected on tracer particles and calculated for each element by solving the two-dimensional unsteady thermal conduction equation. Upper layers have constant rock density, while in the asthenosphere, temperature-dependent density is given by the Boussinesq approximation to account for the thermal expansivity of rocks. See Tetreault and Buiter (2012) for details of these calculations.

The initial model setup is shown in **Figure 2.11A** of Chapter 2.7.4 and model parameters are given in **Table A.4A** and **Table A.5B**. Extension is applied at left and right boundaries to give a total extension rate of 1 cm yr^{-1} , where outflow of material in the upper 60 km of each boundary is compensated by inflow in the lower 100 km so that mass is conserved. The total extension rate is based on modern extension rates inferred from campaign GPS data (Wallace et al., 2014). The initial thermal state is calculated from the steady state solution of the heat equation for boundary temperatures of 1300°C at 160 km depth and 20°C at the surface with no lateral heat flow at the left and right boundaries. This solution yields an average initial crustal geothermal gradient of about 18°C/km which agrees with previous estimates of the geothermal gradient in the Trobriand Basin and Goodenough Bay ranging from 14.4°C/km (Garside, 1973) to 22.5°C/km (Martinez et al., 2001), respectively. Simple erosion and sedimentation functions are applied where rates depend on the height above or below the initial surface elevation. The sedimentation rate is $0.3 \text{ mm yr}^{-1} \text{ km}^{-1}$ and erosion rate is $0.2 \text{ mm yr}^{-1} \text{ km}^{-1}$ and $1 \text{ mm yr}^{-1} \text{ km}^{-1}$ for continental crust and PUB, respectively.

The entire two-dimensional model domain is 230 km wide by 160 km deep. Our model only simulates a time period of 3.5 Myr; hence, the initial conditions for the model reflect inferred conditions immediately prior to extension and exhumation. The

modeled footwall simulates a ~6-km-thick slab of metabasaltic oceanic crust atop a ~35-km-thick region of continental crust, representing the obducted Goropu Metabasalt / Kutu Volcanics slab that was emplaced onto Australian continental crust (e.g., Davies, 1978; **Figure 2.11A**). The modelled metabasalt slab has a composite flow law whose strength is controlled by the lower yield stress of the calculated diffusion and dislocation creep stresses of synthetic wet anorthite-diopside aggregates (An₇₅Di₃₅W) by Dimanov and Dresen (2005), and incorporates grain-size dependence using the grain-size piezometer for experimentally deformed plagioclase aggregates by Post and Tullis (1999). Continental crust uses a strong end-member dislocation creep flow law for wet quartzite from Gleason and Tullis (1995). The contact between these units is modeled as a 1-km-thick layer with the same ductile properties as the crust but with a lower frictional cohesion to represent a shear zone weakened by enhanced strain during emplacement. Initial hanging wall material (PUB) is modeled with an olivine-pyroxene dislocation creep power-law rheology (Hirth & Kohlstedt, 1995) to represent the Papuan Ultramafic Belt unit and underlying upper mantle lithosphere, with densities from Finlayson et al (1977). We model the Mai'iu fault zone as a frictionally and ductilely-weak shear zone (**Table A.4A**, **Table A.5B**)—a reactivation of the Owen-Stanley thrust which emplaced the PUB onto the Kutu-Goropu metabasalt. At depth, an initial dip angle of 45° for the Mai'iu fault and underlying footwall units beneath the hangingwall was chosen based on the evolution of cutoff angles between the Mai'iu fault and sedimentary bedding within the Gwoira Conglomerate (Webber, 2017). Because mantle lithosphere is assumed to deform by dislocation creep in olivine (e.g., Savage, 1999; Tetreault & Buiter, 2012), a diffusion creep flow stress is not computed in the mantle lithosphere and no grain-size dependence is considered for this material. The lower 100 km in the model consists of asthenospheric mantle, which uses a composite dislocation/diffusion-creep flow law for wet olivine aggregates of Hirth and Kohlstedt (2004).

Examination of **Figure 2.11B** shows that the in-plane principal compressive stress σ_1 is close to horizontal or vertical over most of the model domain. In plane-strain (2D) models, the intermediate principal stress σ_2 is out-of-plane (OOP: perpendicular to the modelled section) and equal to the mean of the maximum and minimum in-plane principal compressive stresses $(\sigma_1 + \sigma_3)/2$. This means that—in locations where these principal stresses converge on the mean stress and change in

relative magnitude—there is a rapid “flip” from in-plane horizontal contraction to extension (**Figure 2.11B**), i.e. from:

$$\sigma_1 \sim \sigma_v > \sigma_{OOP} > \sigma_h \text{ [in-plane extension by normal faulting]} \quad (\text{Eq. A.6})$$

to

$$\sigma_1 \sim \sigma_h > \sigma_{OOP} > \sigma_v \text{ [in-plane contraction by reverse faulting]} \quad (\text{Eq. A.7})$$

where h represents horizontal and v vertical principal stress.

In a fully three-dimensional model undergoing net extension, the OOP stress is unlikely to correspond to the mean in-plane stress, since the mean stress includes tectonic extensional stress and will therefore be lower than overburden stress. In **Figure 2.11C** we estimate the effect of assuming that out-of-plane stress is equal to overburden stress rather than being constrained as the mean stress as in the plane-strain approximation. This adds to the range of possible stress states as follows:

$$\sigma_1 \sim \sigma_v > \sigma_h > \sigma_{OOP} \text{ [out-of-plane extension by normal faulting]} \quad (\text{Eq. A.8})$$

$$\sigma_1 \sim \sigma_h > \sigma_v > \sigma_{OOP} \text{ [out-of-plane extension by strike-slip faulting]} \quad (\text{Eq. A.9})$$

$$\sigma_1 \sim \sigma_{OOP} > \sigma_h > \sigma_v \text{ [out-of-plane contraction by reverse faulting]} \quad (\text{Eq. A.10})$$

$$\sigma_1 \sim \sigma_{OOP} > \sigma_v > \sigma_h \text{ [out-of-plane contraction by strike-slip faulting]} \quad (\text{Eq. A.11})$$

At each model step we compute the overburden stress and use it to replace the mean stress as the OOP stress component. While stress states (Eq. A.6) and (Eq. A.7) predominate—with a switch from in-plane extension by normal faulting in the distal and deeper parts of the hangingwall to in-plane compression in the exhumed footwall—there are regions where out-of-plane contraction is likely (states (Eq. A.10) and (Eq. A.11))—particularly in the shallow hangingwall near the location where in-plane extension switched to in-plane compression (**Figure 2.11B, 2.11C**).

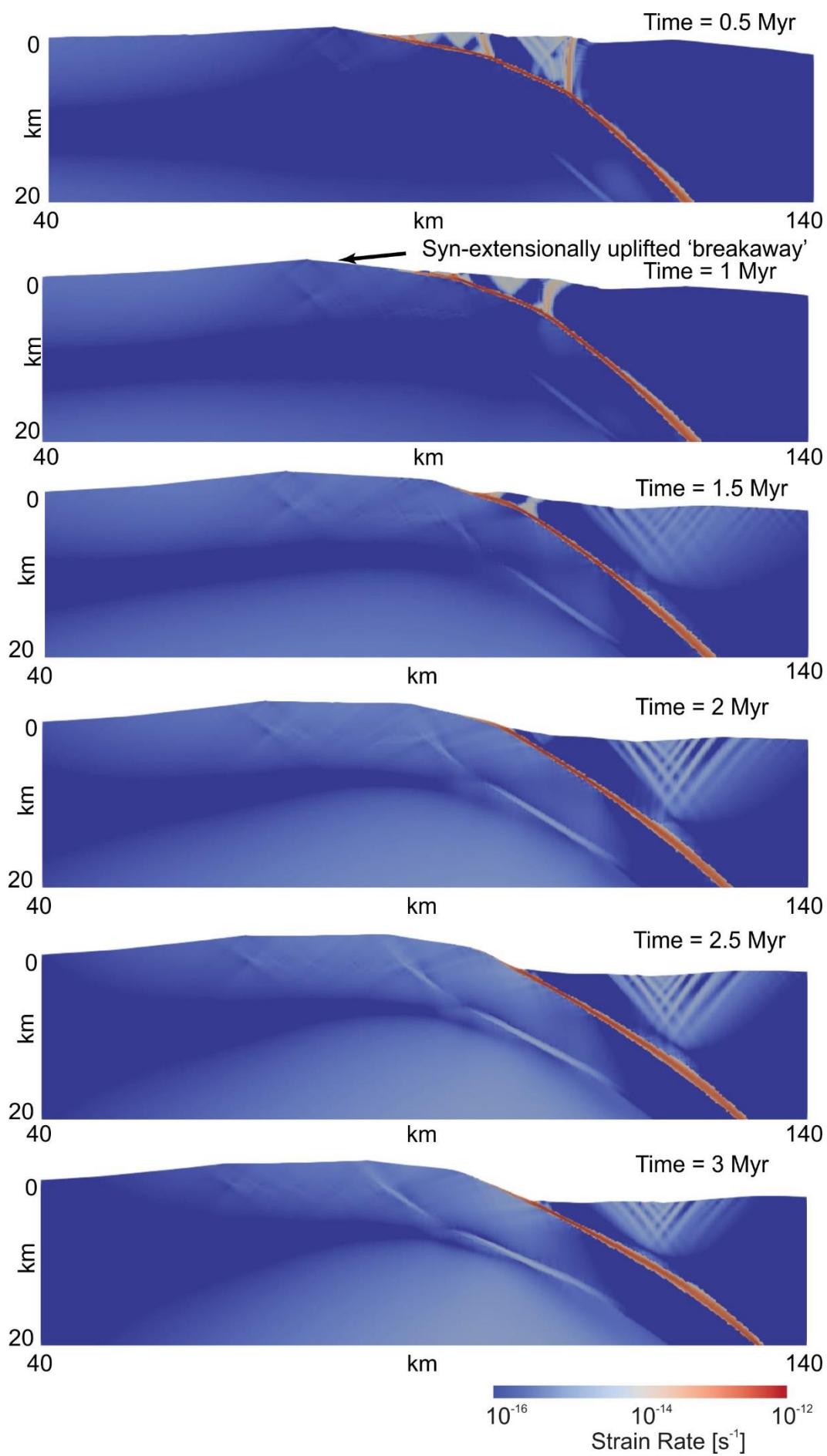


Figure A.7 (previous page). Strain-rate (the second invariant of the strain-rate tensor) at 0.5 My snapshots for the model shown in Figure 2.11.

Table A.4A. Frictional and thermal properties of modeled materials.

Material	Cohesion: Initial, Final (MPa)	Friction Angle: Initial, Final (°)	Linear strain- softening limits	Density (kg m ⁻³) ^a	Shear modulus (GPa)	Reference temperature (K)	Thermal expansion coefficient (K ⁻¹), compressibility coefficient (Pa ⁻¹)	Thermal conductivity (W m ⁻¹ K ⁻¹)
Continental crust	20, 0.5	37, 33	0.2, 0.5	2750	30	-	-, -	2.48
Metabasalt	20, 1	37, 33	0.2, 0.5	2900	30	-	-, -	2.50
Mai'iu Fault	0.001	7, 7	-	3000	30	-	-, -	2.48
Continent - metabasalt interface	1, 0.1	37, 33	0.2, 0.5	2750	30	-	-, -	2.48
Oceanic Lithosphere (PUB)	20, 20	37, 33	0.2, 0.5	2900	30	-	-, -	3.0
Mantle lithosphere	20, 20	37, 33	0.2, 0.5	3330	30	-	-, -	3.0
Mantle asthenosphere	1, 0.1	37, 33	0.2, 0.5	3330	30	273	2.65x10 ⁻⁵ , 10 ⁻¹¹	20.0 ^b

^aFor materials with nonzero thermal expansivity, density is the reference density at listed reference temperature. ^bHigh thermal conductivity used to incorporate effects from small-scale convective heat transfer in the asthenosphere.

Table A.5B. Ductile rheological properties of modeled materials. For materials with a composite diffusion and dislocation creep flow law, diffusion creep parameters are listed first.

Material	Pre-exponential constant (Pa ⁿ m ^{-P} s ⁻¹)	Flow-law exponent	Activation energy (kJ mol ⁻¹)	Activation volume (m ³ mol ⁻¹)	Grain size (μm)	Grain size exponent (P)
Continental crust	8.57 x 10 ⁻²⁸	4.0	310	0	-	-
Metabasalt	8.50 x 10 ⁻²⁷ , 3.16 x 10 ⁻²⁸	1.0, 5.0	310, 533	0	10, -	3.0, -
Mai'iu Fault	8.57 x 10 ⁻²⁸	4.0	210	0	-	-
Continent - ophiolite interface	8.50 x 10 ⁻²⁷ , 3.16 x 10 ⁻²⁸	1.0, 5.0	310, 533	0	10, -	3.0, -
Oceanic Lithosphere (PUB)	5.33 x 10 ⁻¹⁹	3.5	480	11 x 10 ⁻⁶	-	-
Mantle lithosphere	5.33 x 10 ⁻¹⁹	3.5	480	11 x 10 ⁻⁶	-	-
Mantle asthenosphere	1.5 x 10 ⁻¹⁸ , 5.33 x 10 ⁻¹⁹	1.0, 3.5	335, 480	4 x 10 ⁻⁶ , 11 x 10 ⁻⁶	10, -	3.0, -

A.8 The effect of topographic stresses and density contrasts on the stress field

Figure A.8 shows a closeup of the model result after 3.5 My of extension at 1 cm/yr, where the background colors show differential stress magnitude and the white glyphs indicate the direction of maximum principal compressive stress. This stress field is created by a combination of (1) far-field tectonic extension (at 1 cm/yr); (2) topography; (3) density contrasts between crust, mantle lithosphere, and asthenosphere; and (4) internal deformation and material strength contrasts (e.g., across the LANF). To check which of these is most important for stress magnitudes and directions we took the model temperature, topography and material properties at 3.5 My and turned off far-field extension. Comparison between **Figure A.8A** and **Figure A.8B** shows that stress magnitudes below the crust are reduced significantly when extension is turned off; however, stress orientations and magnitudes near the surface are similar, showing that topography and density changes—interacting with material contrasts—control near-surface stress patterns.

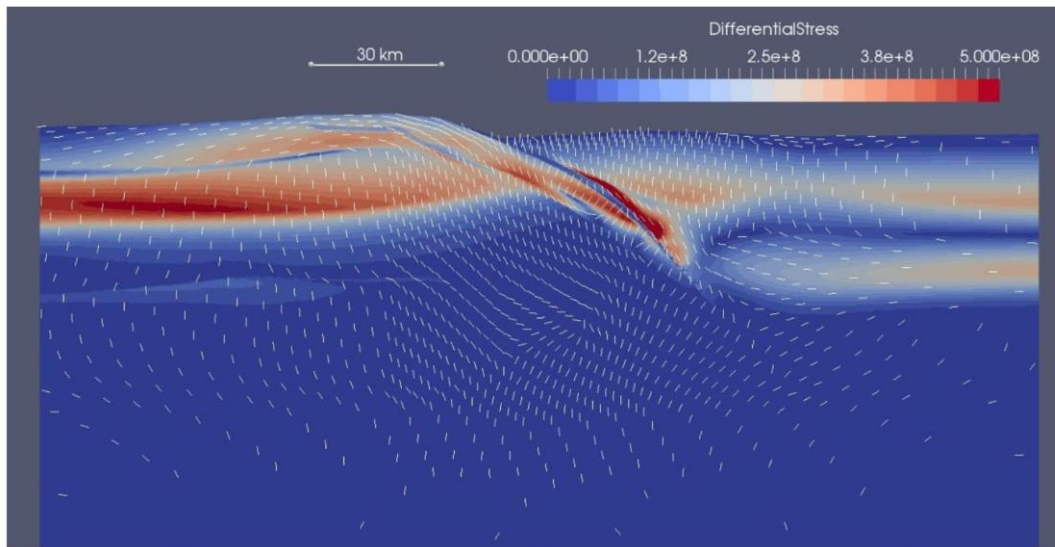


Figure A.8A. Differential stress magnitude (color contours) and maximum principal compressive stress direction (white glyphs) for a close-up of the model used in the main paper, after 3.5 My of extension.

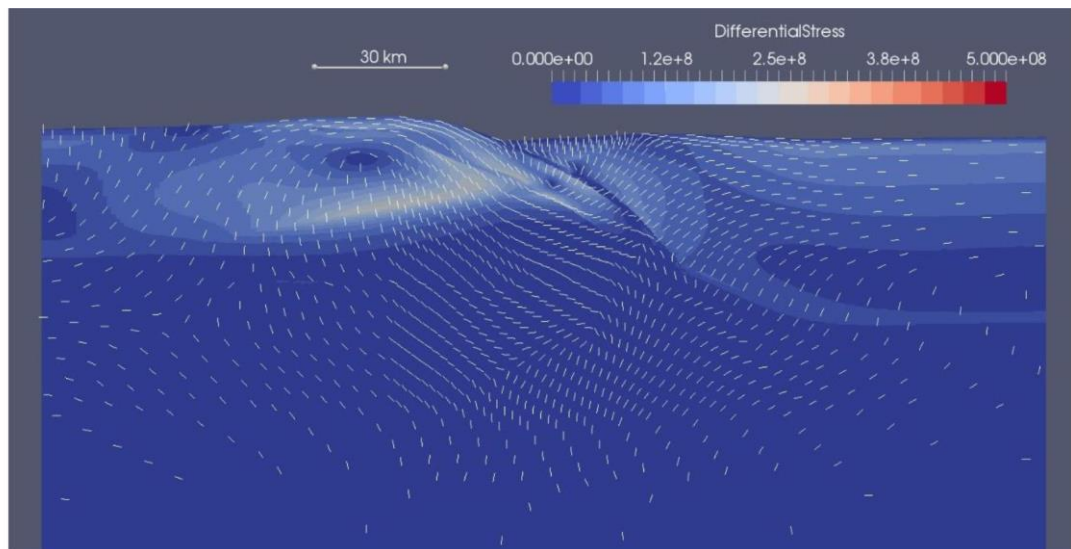


Figure A.8B. Same as Figure A.8A but with extensional boundary conditions at the right and left-hand sides of the model turned off.

Appendix B

This appendix provides compositional and microstructural data on metabasaltic fault rocks associated with Chapter 3. The present microstructural and compositional dataset was derived from multiple analytical techniques, including: (1) field emission gun scanning electron microscope (FEG-SEM) equipped with energy dispersive spectroscopy (EDS) and electron backscatter diffraction (EBSD) detectors; (2) temperature-dependent magnetic susceptibility experiment; (3) transmission electron microscope (TEM); (4) Raman spectroscopy; (5) X-Ray fluorescence (XRF); (6) X-Ray Diffraction (XRD); and (6) electron probe micro-analyzer (EPMA). The spatiotemporal evolution of the metabasaltic protolith that has been exhumed in the footwall of the rapidly slipping, active Mai'iu fault is herein documented in a collection of photomicrographs, element and phase maps, compositional data on the fault rocks and especially on chlorite and albite, grain size statistics, and pole figures of the main mineral assemblage (actinolite, epidote, titanite and albite).

B.1 EDS-based Elemental Compositions of Mafic Fault Rocks

Elemental compositions of whole thin section (~2x1 cm) are shown in **Table B.1**. Elemental compositions of polyphase clasts in gouge samples are shown in **Table B.2** and **Table B.3**. The elemental data shown in **Table B.1** of the different fault rock units indicate a decrease in Na and an increase in K in the ultracataclasites relative to the mylonite and foliated cataclasite samples. EDS-based elemental compositions of polyphase clasts in the gouges indicate that these clasts are similar in composition to the structurally underlying fault rocks (mylonite, cataclasite and ultracataclasite).

Table B.1. EDS-based elemental compositions (wt%) of the different fault rock units (collected just south of the active Mai'iu fault trace at PNG16-142). Highlighted fields in the ultracataclasites show a strong elemental decrease (red) of Na and Ca and a strong increase (green) of K.

Spectrum Label	Mylonite	Cataclasite	UCAT-D2	UCAT-D1	Green Gouge	Grey Gouge
	PNG16-142C	PNG16-142E	PNG16-142D2	PNG16-142D1	PNG16-142A	PNG16-142B
O	42.65	41.99	37.68	41.61	36.35	29.28
Na	2.23	2.71	0.47	0.52	2.08	0.72
Mg	4.57	3.23	4.38	4.36	3.41	3.41
Al	8.04	6.87	6.49	6.97	6.77	5.09
Si	22.55	21.14	20.26	21.31	19.13	14.68
K	0.18	0.23	4.62	5.39	0.2	1.29
Ca	8.46	9.6	4.96	5.44	6.15	7.59
Ti	0.64	0.84	1	1.04	1	0.61
Mn	0.15	0.17	0.12	0.12	0.14	0.13
Fe	7.35	7.18	7.44	7.36	8.12	6.19
Zn	0.13	0.16	0.04	0.03	0.13	0.05
Total	96.95	94.17	87.48	94.16	83.65	69.27

Table B.2. EDS-based elemental composition (wt%) of polyphase clasts in a gouge sample (PNG16-142A) just south of the active Mai'iu fault trace. Analysed clasts are shown in the EDS maps of Figure B.1 (see below).

Green Gouge (PNG16-142A)

Spectrum Label	Clast-Chemistry 1	Clast-Chemistry 2	Clast-Chemistry 3	Clast-Chemistry 4	Clast-Chemistry 5	Clast-Chemistry 6
O	42.26	45.8	41.92	42.5	41.14	42.03
Na	1.58	5.57	2.56	1.58	1.57	2.01
Mg	3.71	1.69	3.73	3.49	3.03	3.58
Al	8.2	10.39	7.61	8.42	4.59	7.71
Si	19.27	26.14	21.18	19.43	27.25	21.34
K	0.14	0.13	0.29	0.16	0.2	0.3
Ca	8.47	3.94	6.49	8.84	4.42	7.43
Ti	1.3	0.17	1.21	1.37	0.53	1.04
Mn	0.16			0.12	0.13	0.14
Fe	10.4	5.6	8.35	9.92	6.25	8.63
Total	96.08	99.42	93.35	95.84	89.19	94.19

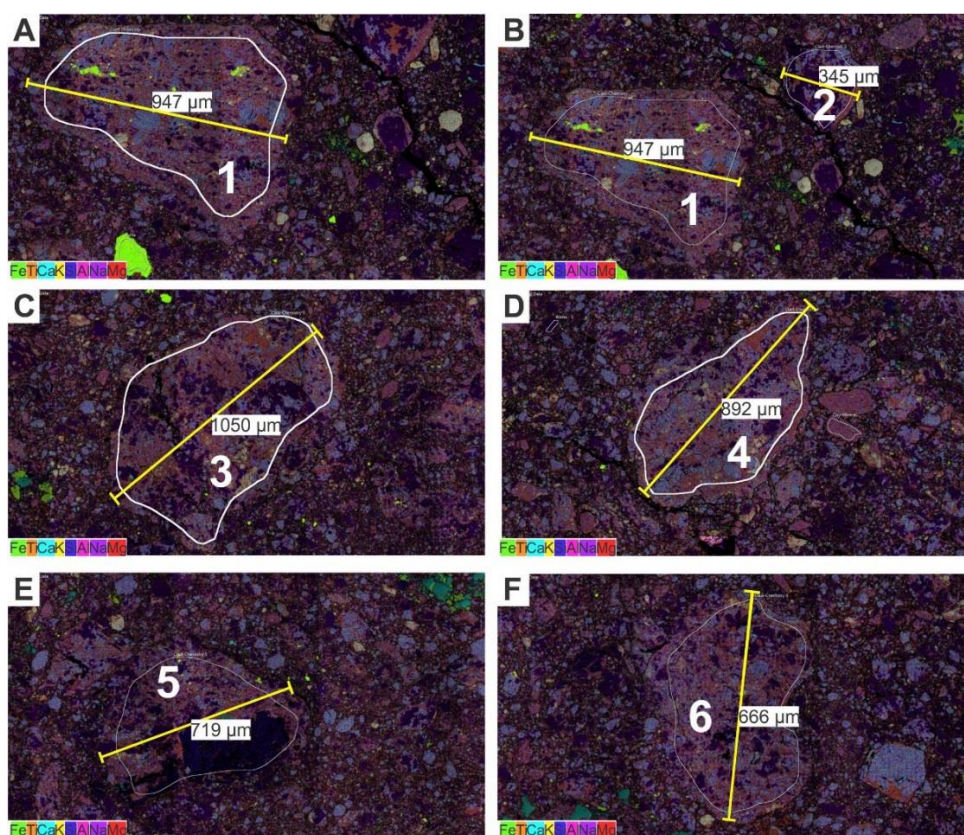


Figure B.1. Layered elemental images of polyphase clasts embedded in fault gouge (PNG16-142A). EDS-based elemental compositions are shown in **Table B.2**. A-F) Different sized polyphase clasts. Elemental composition of these clasts are similar to mylonites and foliated cataclasites.

Table B.3. EDS-based elemental compositions (wt%) of polyphase clasts in a gouge sample (PNG16-142B) just south of the active Mai'iu fault trace. Analysed clasts are shown in the EDS map and SEM back-scatter image of **Figure B.2** (see below).

Grey Gouge (PNG16-142B)						
Spectrum Label	Clast Chemistry 1	Clast Chemistry 2	Clast Chemistry 3	Clast Chemistry 4	Clast Chemistry 5	Clast Chemistry 6
O	43.53	36.6	36.16	42.3	40.18	40.45
Na	3.73	1.13	2.73	1.31	0.66	0
Mg	3.54	3.71	3.87	1.75	4.41	6.8
Al	10.07	7.88	7.11	7.37	7.91	7.34
Si	22.52	16.69	20.66	23.45	21.74	19.65
K	0.08	0	1.49	6.19	5.66	3.88
Ca	2.39	7.38	2.1	8.07	2.01	2.59
Ti	1.02	1.33	1.21	0.57	1.06	0.74
Mn	0.16	0	0	0	0	0
Fe	7.8	7.54	5.68	3.03	9	8.67
Total	94.84	82.43	81.22	94.04	92.63	90.12

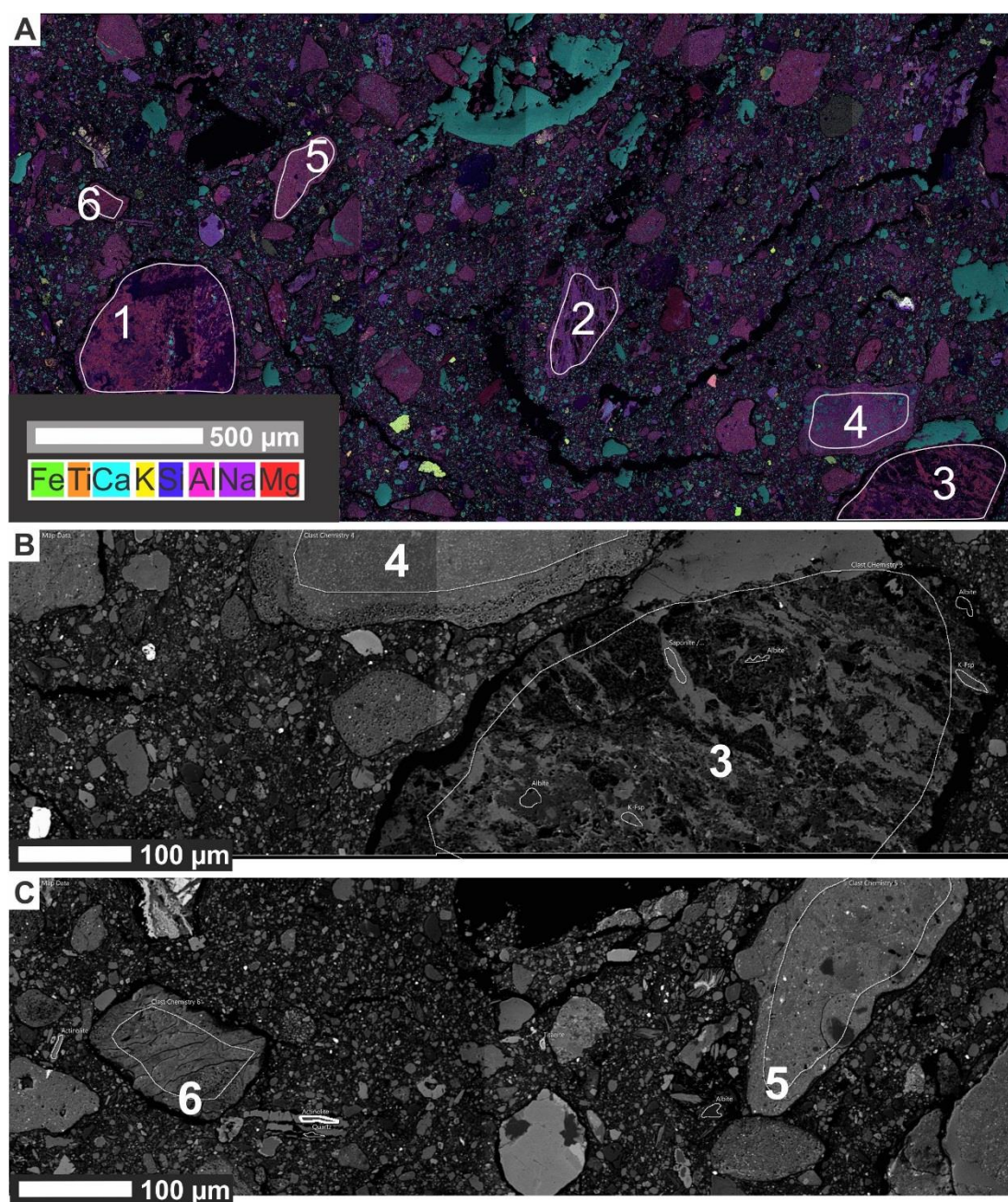


Figure B.2. Layered elemental image and SEM back-scatter images of polyphase clasts embedded in fault gouge (PNG16-142B). EDS-based elemental compositions of the analysed clasts are shown in **Table B.3**. Clasts 1-3 are similar to mylonites and foliated cataclasites in elemental composition; Clasts 4-6 are similar to ultracataclasites in elemental composition. B) SEM back-scatter image of clast 3 and 4 (A). C) SEM back-scatter image of clast 5 and 6 (A). Both clasts resemble the ultracataclasite in texture and composition.

B.2 Additional SEM Back-Scatter Images and EDS Maps of Mafic Fault Rocks

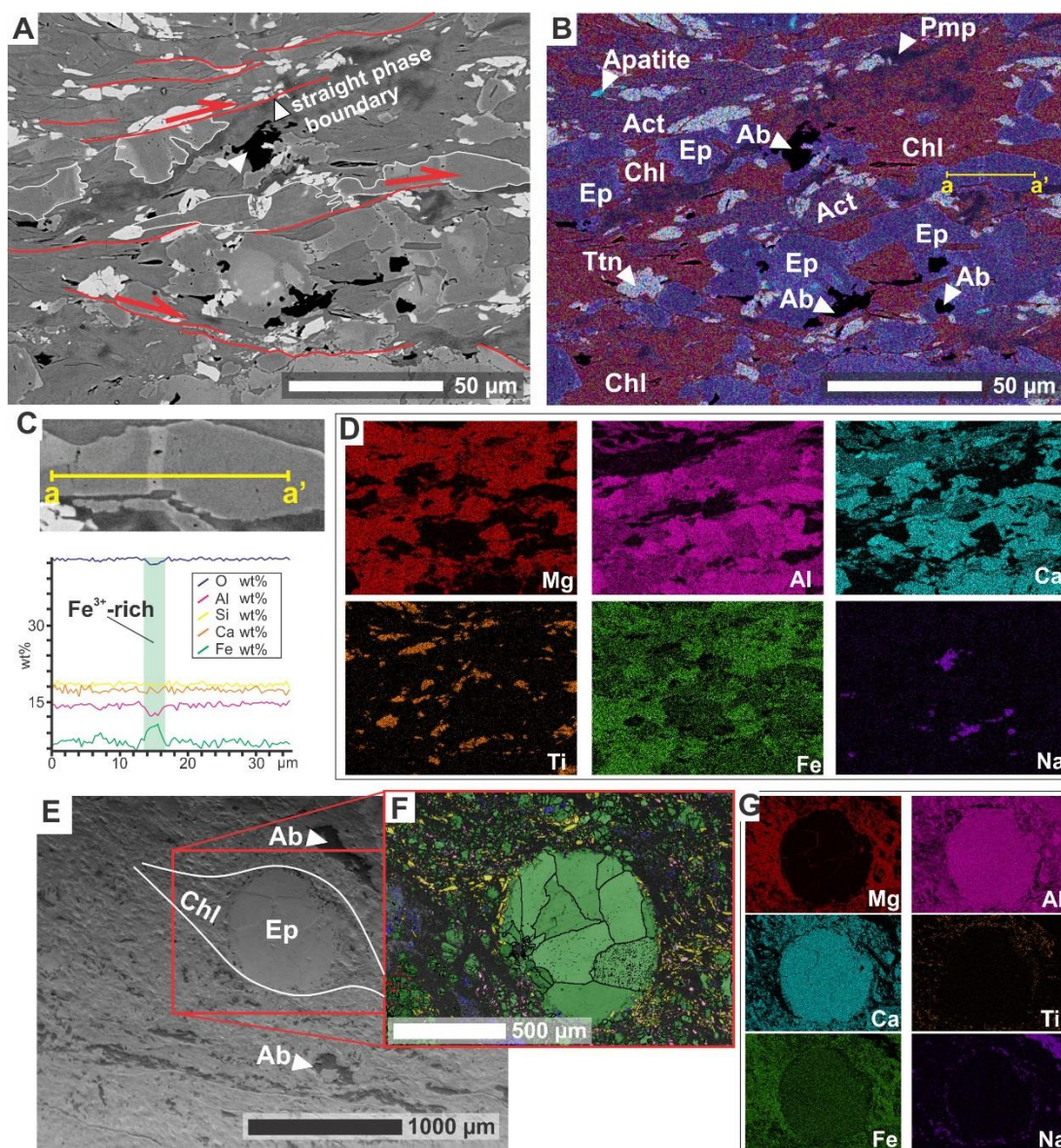


Figure B.3. Mafic mylonite (PNG15-59A). Figures are arranged with the normal slip sense of the Mai'iu fault shown top-to-the-right. A) SEM back-scatter image of the fine-grained mylonitic matrix. Epidotes are zoned and have Fe-rich rims. B) Layered elemental image (element maps in D). Dark red colours highlights chlorite. Albite (dark “inkspots”) appears in relation with epidote. C). Elemental-profile through epidote-clast. D) Element maps. E) SEM back-scatter image of epidote amygdale in fine-grained mafic matrix. F) EBSD phase map. Green—epidote; yellow—actinolite; blue—albite; pink—titanite. G) Element maps of F. Dark red areas in the Magnesium map indicate growth of chlorite.

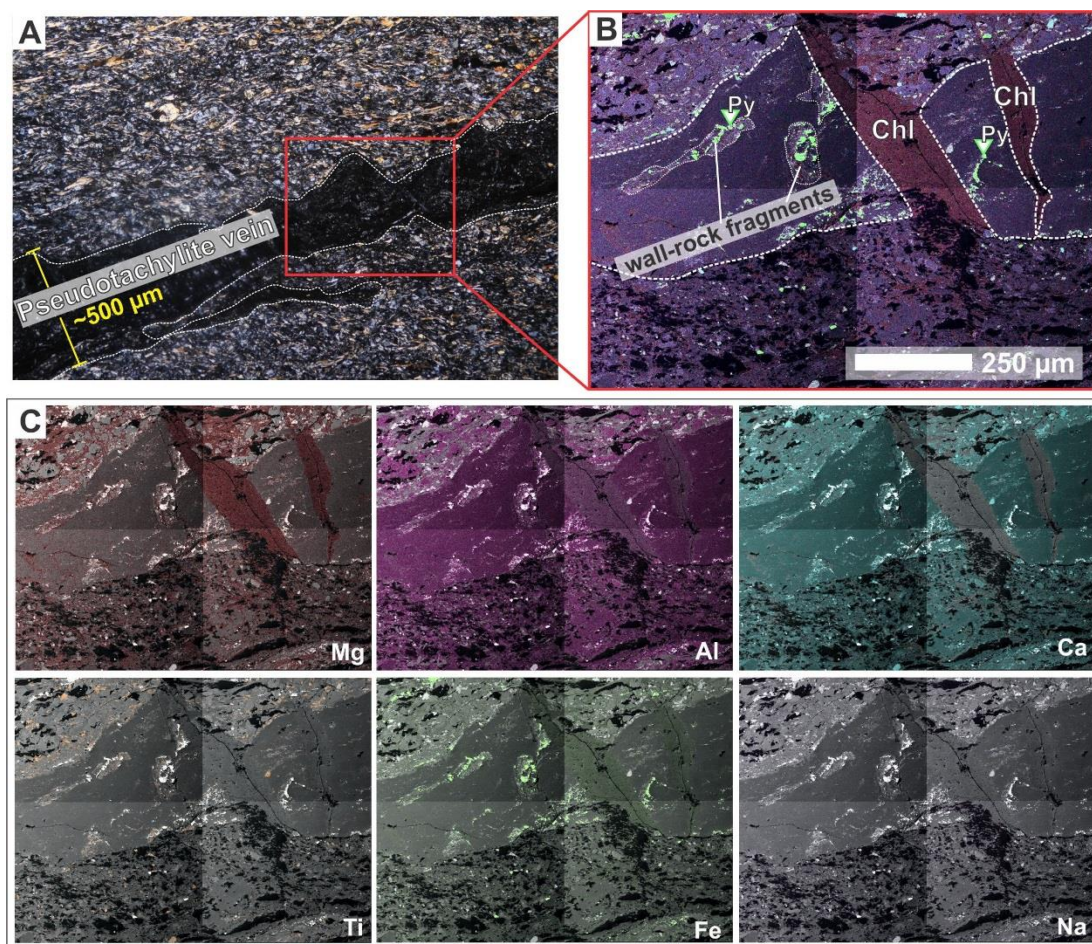


Figure B.4. Pseudotachylite vein in mylonite sample (PNG16-142C). A) Optical photomicrograph (XPOL). B) Layered elemental image of pseudotachylite vein with abundant pyrite grains and wall-rock fragments. C) Element maps. Dark red areas in the Magnesium map highlights chlorite growth.

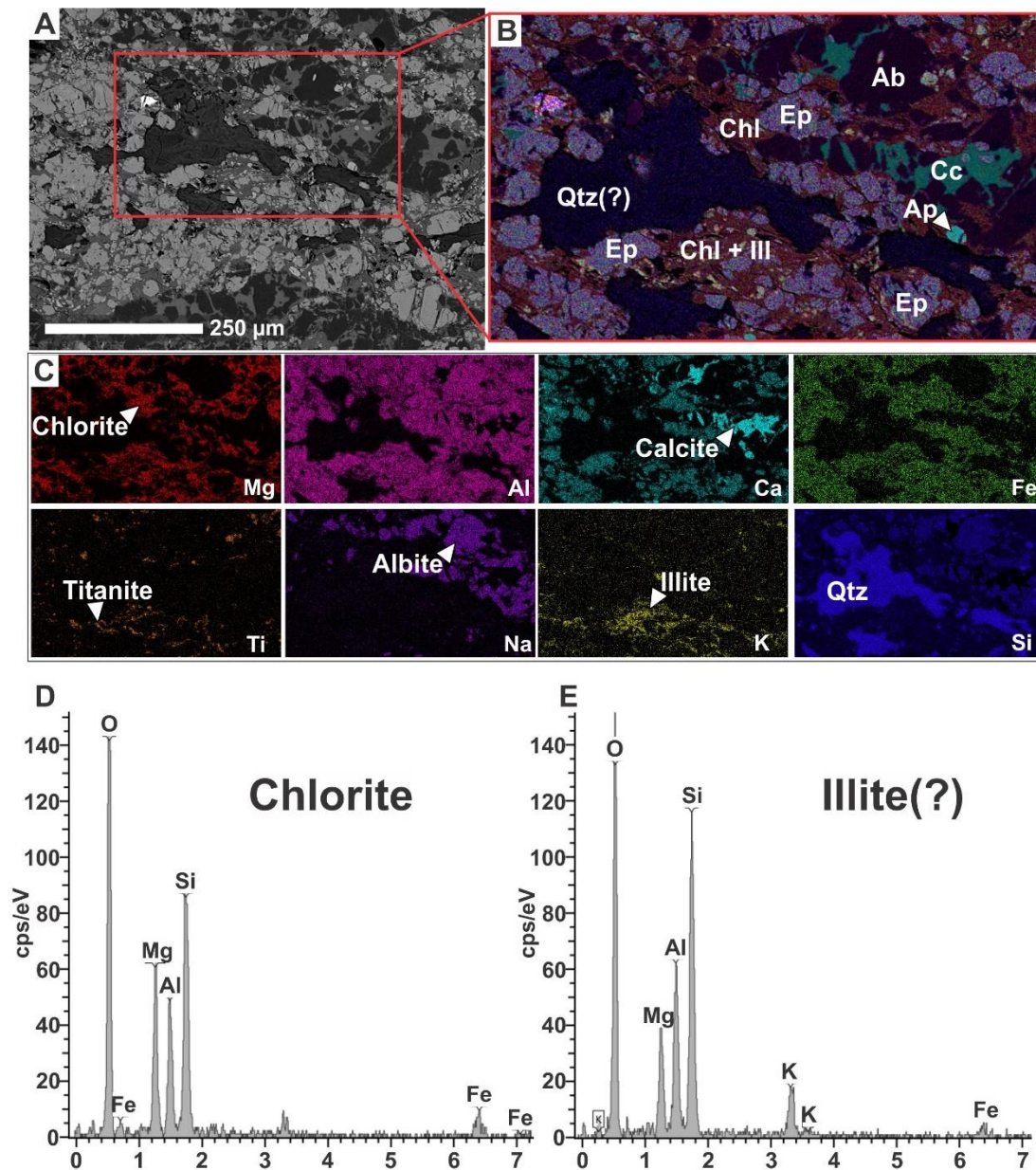


Figure B.5. Foliated cataclasite (PNG16-17H). Figures are arranged with the normal slip sense of the Mai'iu fault shown top-to-the-right. A) SEM back-scatter image of dark folia in the cataclasite. B) Layered elemental image based on EDS analysis of the dark folia. Dark, brick red colours indicate chlorite. We infer that chlorite grew and was passively concentrated during a reaction that consumed epidote (purple colour) and actinolite (purple-red colour). C) Elemental maps. D) and E) EDS spectra of chlorite and presumably Illite. 1Md and 2M1 illites are verified by XRD analyses (see Little et al., 2019).

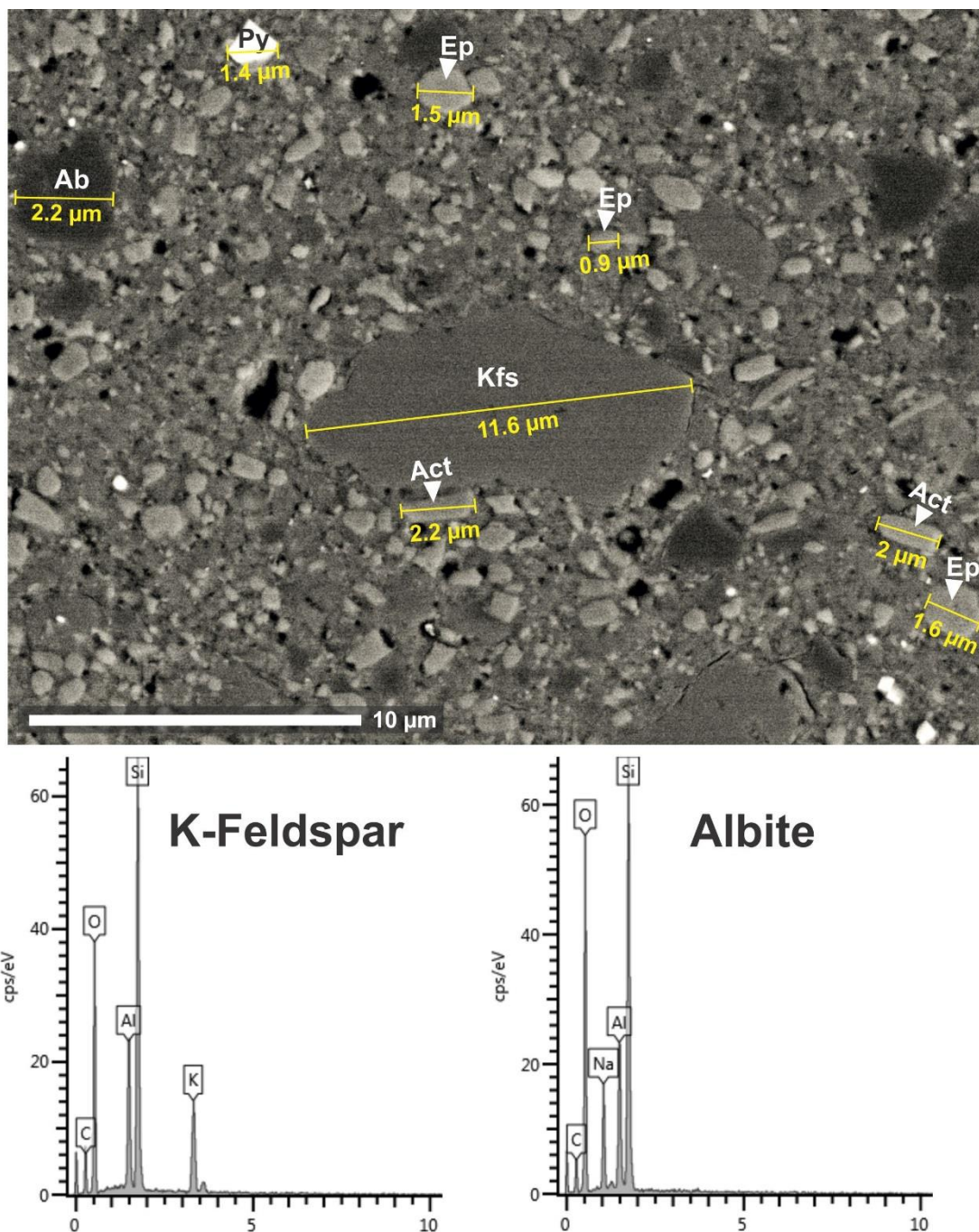


Figure B.6. SEM back-scatter images of ultracataclasite and EDS spectra of albite and K-feldspar grains in the matrix (sample PNG15-50DR). The back-scatter image also shows sizes (diameter) of relict mafic grains and K-feldspar.

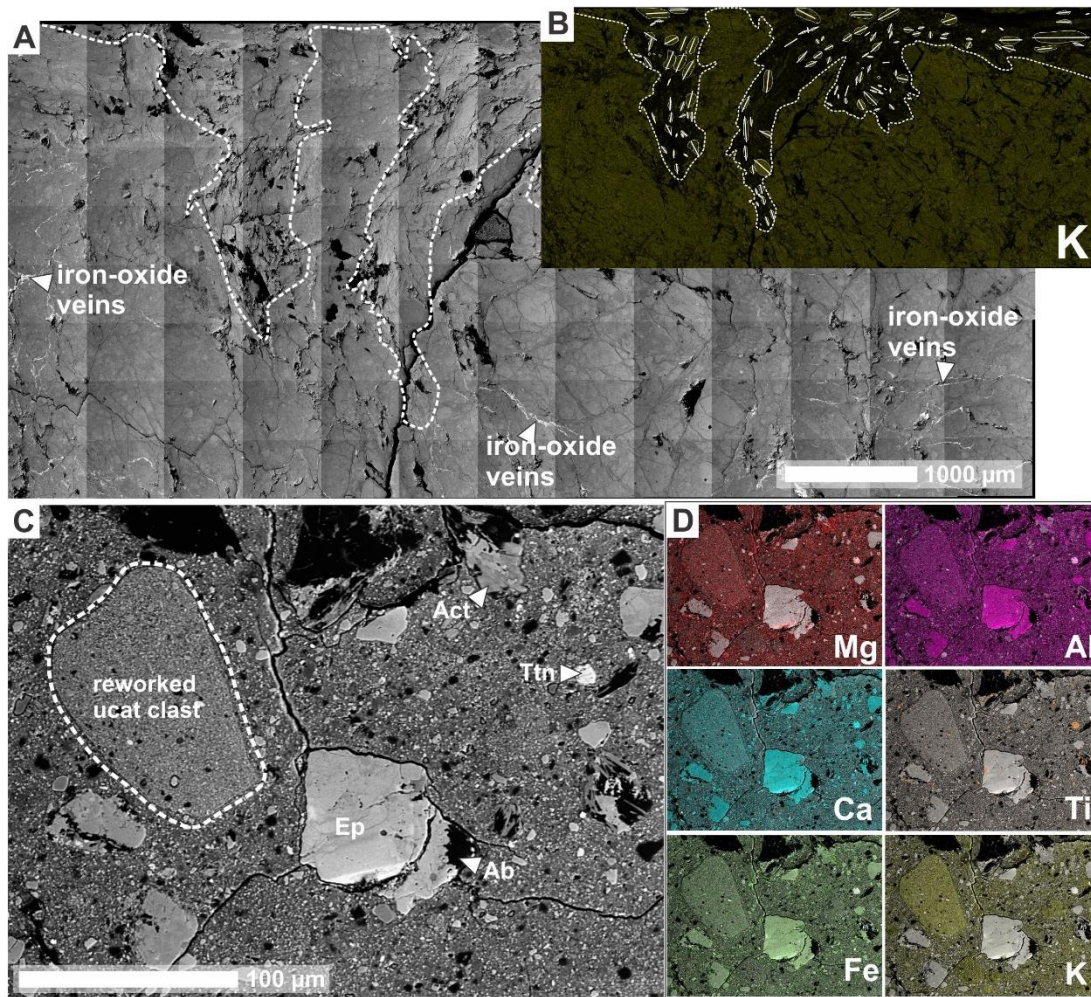


Figure B.7. SEM back-scatter images and EDS maps (PNG16-142D2, ultracataclasite). A) Electron image of the whole thin section. Note, light veins are iron-oxide veins. Elemental zonation (white-dashed line shows boundary) is highlighted in the potassium (K)-map in (B). B) Potassium map indicates elemental zonation (a K enriched domain and K depleted domain). White glyphs indicate orientation of long-axis of K-rich fragments in the overall K-depleted domain. C) Back-scatter image of ultracataclasite matrix. Older ultracataclasite-clasts are reworked in the matrix and show an apparent higher concentration of potassium relative to the surrounding matrix. D) Elemental maps of C.

B.3 EBSD Data Processing

Raw EBSD data were processed with the MTEX toolbox for MATLAB (Bachmann et al., 2010) after the approach of Cross (2015). In MTEX, raw EBSD data of indexed pixels are converted to grains based on a Voronoi decomposition method (Voronoi, 1907). The script is populating the whole map with grains (defined as areas encompassed by boundaries of $>10^\circ$ misorientation), whereas non-indexed phases are removed in a later step. Identified “grains” smaller than 2×2 pixels in size were removed from the acquired EBSD map as they are likely the result of misindexing. A

smoothing factor of 2 was applied to the mapped grains. Furthermore, poorly constrained grains were removed based on the fraction of their area covered by raw data (f_i), (Cross, 2015):

$$f_i = \frac{n_i \cdot d_{step}^2}{A_{grain}}, \quad (\text{Eq. B.1})$$

where n_i is the number of indexed pixels in a grain, d_{step} is the step size (width of each pixel), and A_{grain} is the area a grain covers based on the Voronoi decomposition. Because some fault rocks were poorly indexed (especially ultracataclasites, fault gouge, and weathered schists), a critical threshold value for f_i was estimated for every sample based on trade-off curves for the indexed fraction of grains versus the cumulative number of grains. The knee of this curve represents the threshold value between poorly constrained and well constrained grains (Cross, 2015). The grains that fall under the category “poorly constrained grains” were removed from the EBSD map. Step sizes and threshold values for f_i are given for each sample in **Table B.4** to **Table B.7** of Appendix B.4. Fabric strength is herein quantified by calculating both the J-index of Bunge (2013) and the M-index of Skemer et al. (2005) and are given in the aforementioned **Table B.4** to **Table B.7**. All MTEX scripts for the data processing can be found in the Digital Appendix under the folder ‘MTEX’.

B.4 EBSD-based Fabric Strength and Grain-Size Estimates of Mafic Fault Rocks

The following tables and figures summarize the results of the processed EBSD data from the different mafic fault rocks. The results presented in the following tables include mean grain size estimates and fabric strength of actinolite, epidote, albite and titanite in the different fault rock units. The tables are followed by figures of all analysed and processed EBSD maps starting with mafic mylonite samples and continuing with foliated cataclasite, ultracataclasite, gouge and non-mylonitic mafic schist. All pole plots shown in these figures are Schmidt lower hemisphere equal-area projections.

Table B.4. Grain-size statistics, J-index, S-index and M-index for actinolite based on EBSD analysis. N_O—number of orientation; N_P—number of pixels; N_G—number of grains; Mean GS—mean grain size; 1 σ —standard deviation; Min, Max—minimum, maximum estimated grain size.

Sample#	Rock Type	Domain	Tradeoff-Curve	Step Size (μm)	N _O	N _P	N _G	Mean GS				All Grains				1 point per Grain			
								GS	(1 σ)	Min	Max	J (ODF)	J (MDF)	S	M	J (ODF)	J (MDF)	S	M
15-43	Mylonite	Mafic Matrix	0.4	2.0	80860	57671	523	25.0	± 16	4.1	103.8	3.707	1.260	-0.851	0.105	2.762	1.179	0.700	0.080
16-142C	Mylonite	Montaged Mafic Matrix	0.5	2.0	364636	303953	8140	13.4	± 8.6	3.3	117.9	5.317	1.856	-1.097	0.225	4.796	1.708	0.995	0.204
15-52A	Mylonite	Mafic Matrix	0.3	2.0	44740	29633	433	22.2	± 14	5.3	96.9	8.628	2.649	-1.547	0.300	8.013	2.537	1.498	0.291
16-17E	Mylonite	Mafic Matrix Whole	0.4	1.0	61041	27372	587	9.1	± 5	2.3	38.2	1.768	1.058	-0.325	0.041	1.812	1.056	0.349	0.038
15-73A	Mylonite	Sample Actinolite	0.5	1.0	275101	163625	2359	10.2	± 5.7	2.0	64.5	8.172	2.785	-1.514	0.317	7.838	2.769	1.508	0.291
15-73A	Mylonite	Layer Fine Grained	0.5	1.0	208327	153596	1916	10.7	± 6	2.2	64.9	9.217	3.127	-1.649	0.346	8.558	3.092	1.628	0.316
15-73A	Mylonite	Matrix	0.5	1.0	77930	37409	763	8.7	± 4.7	2.0	35.7	6.438	2.132	-1.257	0.261	6.575	2.096	1.263	0.246
15-59A	Mylonite	Mafic Matrix	0.5	2.0	625853	532722	14657	12.7	± 8.7	3.3	162.2	2.479	1.181	-0.515	0.087	2.184	1.122	0.421	0.072
15-59A	Mylonite	Mafic Matrix	0.4	5.0	34121	19267	1606	23.3	± 11	10.0	120.4	3.546	1.430	-0.800	0.149	3.656	1.452	0.822	0.151
15-59A	Mylonite	Mafic Matrix	0.3	5.0	21434	16443	1335	23.3	± 9.6	10.0	97.4	4.320	1.656	-0.984	0.181	4.487	1.687	1.001	0.185
15-59A	Mylonite	Dark Matrix	0.3	5.0	5681	3585	281	25.0	± 9.8	9.2	65.1	3.492	1.335	-0.779	0.139	3.543	1.317	0.813	0.142
16-125B	Cataclasite	Mafic Matrix	0.3	1.0	25779	17011	262	10.3	± 7.4	2.0	70.1	6.814	1.590	-1.050	0.194	4.214	1.280	0.846	0.144
16-125B	Cataclasite	Mafic Matrix	0.2	0.5	8798	6471	89	7.3	± 4.8	1.0	18.4								
16-142E	Cataclasite	Montaged Mafic Matrix	0.5	2.0	239868	189670	5296	12.7	± 8.7	3.6	107.8	1.621	1.034	-0.272	0.051	1.523	1.028	0.233	0.045
16-142E	Ultramylonite	Layer	0.5	2.0	2900	2227	119	9.1	± 4.4	3.3	29.7	2.508	1.021	-0.498	0.022	2.070	1.014	0.478	0.021
15-50E	Cataclasite	Mafic Matrix	0.3	1.0	15082	9090	149	11.5	± 5.8	2.4	37.7	3.551	1.313	-0.783	0.145	3.014	1.157	0.702	0.093
16-50RD	Cataclasite	Mafic Matrix	0.3	2.0	24298	12356	236	22.1	± 11	5.5	61.2	2.152	1.056	-0.410	0.062	2.117	1.043	0.441	0.051
16-151E	Cataclasite	Dark Matrix	0.4	1.0	71118	54041	1465	7.4	± 4.2	1.8	48.5	4.792	1.615	-0.957	0.212	4.653	1.615	0.935	0.200
16-151E	Cataclasite	Dark Matrix	0.4	2.0	20381	12054	373	13.3	± 8.8	4.2	95.7	4.686	1.382	-0.961	0.157	5.017	1.560	0.988	0.196

Table B.4 (continued).

Sample#	Rock Type	Domain	Tradeoff-Curve	Step Size (μm)	N _o	N _p	N _G	Mean GS	(1σ)	Min	Max	All Grains				1 point per Grain			
												J (ODF)	J (MDF)	S	M	J (ODF)	J (MDF)	S	M
16-125A	Ultracataclasite	UCAT matrix	0.1	0.5	136359	1715	141	2.3	±0.9	1.3	12.8	1.102	1.000	-0.049	0.003	1.798	1.007	0.378	0.016
16-142D	Ultracataclasite	UCAT matrix	0.2	0.6	600	148	6	6.3	±2.8	1.8	10.0	4.019	1.053	-0.738	0.034	14.575	2.477	2.477	0.212
16-142B	Gouge	Matrix	0.3	0.6	28686	8103	250	3.5	±2.5	1.2	22.9	1.256	1.001	-0.098	0.005	1.641	1.013	0.300	0.018
16-142A	Gouge	Matrix	0.4	0.5	156216	77242	1368	3.8	±2.8	1.0	39.9	1.234	1.001	-0.094	0.006	1.121	1.001	0.058	0.004
16-126A	Schist/Mylonite?	Mafic Matrix	0.3	0.8	190428	120029	726	12.9	±8.1	1.4	68.6	3.276	1.300	-0.725	0.115	2.747	1.222	0.625	0.093
16-126B	Schist	Mafic Matrix	0.35	1.5	45274	21704	754	11.3	±5.9	3.2	52.3	2.257	1.127	-0.469	0.071	2.313	1.128	0.487	0.076
16-169	Schist	Mafic Matrix	0.3	1.5	98667	79461	1918	11.9	±7.9	2.9	80.6	3.305	1.382	-0.771	0.108	3.188	1.358	0.742	0.114
16-176	Schist	Mafic Matrix	0.3	2.0	40561	12060	288	19.3	±11	4.6	81.5	4.394	1.661	-0.978	0.163	4.849	1.792	1.116	0.165
16-182	Schist/Mylonite?	Mafic Matrix	0.3	2.0	150845	109770	1042	25.7	±19	3.6	157.5	3.544	1.418	-0.829	0.127	3.939	1.650	0.923	0.151

Table B.5. Grain-size statistics, J-index, S-index and M-index for epidote based on EBSD analysis. N_O—number of orientation; N_P—number of pixels; N_G—number of grains; Mean GS—mean grain size; 1 σ —standard deviation; Min, Max—minimum, maximum estimated grain size.

Sample#	Rock Type	Domain	Tradeoff-Curve	Step Size (μm)	N _O	N _P	N _G	Mean GS	(1 σ)	Min	Max	All Grains				1 point per Grain			
												J (ODF)	J (MDF)	S	M	J (ODF)	J (MDF)	S	M
15-43	Mylonite	Mafic Matrix Montaged	0.4	2.0	36874	15459	320	19.0	± 8.8	3.7	48.5	1.388	1.009	-0.171	0.030	1.555	1.009	-0.247	0.032
16-142C	Mylonite	Mafic Matrix	0.5	2.0	400404	380064	2770	22.8	± 18	3.6	135.8	2.376	1.183	-0.546	0.136	2.062	1.126	-0.424	0.118
15-52A	Mylonite	Mafic Matrix	0.3	2.0	52085	30822	549	23.2	± 10	4.1	61.7	2.157	1.122	-0.447	0.114	2.301	1.167	-0.520	0.136
16-17E	Mylonite	Mafic Matrix	0.4	1.0	667540	512312	5383	12.0	± 7.1	1.7	87.5	1.093	1.000	-0.045	0.007	1.079	1.000	-0.040	0.007
15-73A	Mylonite	Whole Sample	0.5	1.0	102747	60270	327	13.8	± 9.4	2.2	77.1	2.193	1.025	-0.376	0.048	1.586	1.016	-0.284	0.041
15-73A	Mylonite	Actinolite Layer Fine Grained	0.5	1.0	24870	18773	66	15.1	± 11	2.8	78.4	6.067	1.143	-0.950	0.071	2.702	1.036	-0.696	0.049
15-73A	Mylonite	Mafic Matrix	0.5	1.0	80935	47727	305	13.4	± 7.9	2.2	74.7	2.437	1.032	-0.395	0.052	1.581	1.015	-0.286	0.040
15-59A	Mylonite	Mafic Matrix	0.5	2.0	623947	598470	4035	21.8	± 20	3.3	223.8	1.204	1.001	-0.091	0.008	1.057	1.000	-0.029	0.004
15-59A	Mylonite	Mafic Matrix	0.4	5.0	50459	38023	1472	31.2	± 19	10.4	170.6	1.283	1.004	-0.128	0.019	1.202	1.004	-0.096	0.020
15-59A	Mylonite	Mafic Matrix	0.3	5.0	18985	17722	682	30.1	± 17	11.3	172.7	1.655	1.004	-0.249	0.014	1.295	1.004	-0.140	0.021
15-59A	Mylonite	Mafic Matrix Montaged	0.3	5.0	24119	20831	776	33.2	± 18	12.2	170.8	1.660	1.016	-0.276	0.036	1.429	1.014	-0.192	0.038
16-142E	Cataclasite	Mafic Matrix	0.5	2.0	190620	153614	3254	14.8	± 9.6	3.6	115.1	1.160	1.001	-0.075	0.010	1.109	1.001	-0.053	0.008
15-50E	Cataclasite	Mafic Matrix	0.3	1.0	32839	29326	134	18.7	± 10	3.7	60.4	2.589	1.019	-0.569	0.031	1.925	1.013	-0.422	0.039
16-50RD	Cataclasite	Mafic Matrix	0.3	2.0	29596	19683	277	26.2	± 11	5.8	63.9	1.324	1.001	-0.148	0.007	1.399	1.002	-0.188	0.013
16-151E	Cataclasite	Dark Matrix	0.4	2.0	65694	35518	821	17.1	± 9	4.5	76.4	1.197	1.001	-0.094	0.009	1.229	1.002	-0.110	0.012

Table B.5 (continued).

Sample#	Rock Type	Domain	Tradeoff-Curve	Step Size (μm)	N _o	N _p	N _G	Mean GS	(1σ)	Min	Max	All Grains				1 point per Grain			
												J (ODF)	J (MDF)	S	M	J (ODF)	J (MDF)	S	M
16-125A	Ultracataclasite	UCAT Matrix	0.1	0.5	100167	237	37	1.6	±0.5	1.0	3.0	1.415	1.007	-0.168	0.021	6.282	1.159	-1.279	0.056
16-142D	Ultracataclasite	UCAT Matrix	0.2	0.6	24865	4116	164	3.0	±2.1	1.2	14.0	1.260	1.002	-0.116	0.005	1.503	1.002	-0.242	0.006
16-142B	Gouge	Matrix	0.3	0.6	30410	12664	244	3.7	±3	1.1	18.7	1.441	1.002	-0.169	0.006	1.586	1.004	-0.264	0.013
16-142A	Gouge	Matrix	0.4	0.5	221658	151589	2351	3.9	±3.1	0.7	56.6	1.275	1.001	-0.099	0.003	1.201	1.001	-0.096	0.006
16-126B	Schist	Mafic Matrix	0.4	1.5	213165	189910	1116	20.3	±14	2.7	148.7	3.953	1.065	-0.499	0.066	1.478	1.008	-0.176	0.029
16-182	Schist/Mylonite?	Mafic Matrix	0.3	2.0	164960	121725	1188	27.1	±16	3.9	180.0	1.372	1.006	-0.165	0.024	1.319	1.008	-0.149	0.029
15-72A	Schist	Mafic Matrix	0.5	2.0	119483	109578	1733	16.2	±12	3.7	109.8	1.832	1.045	-0.340	0.067	1.721	1.052	-0.305	0.068

Table B.6. Grain-size statistics, J-index, S-index and M-index for albite based on EBSD analysis. N_O—number of orientation; N_P—number of pixels; N_G—number of grains; Mean GS—mean grain size; 1 σ —standard deviation; Min, Max—minimum, maximum estimated grain size.

Sample#	Rock Type	Domain	Tradeoff-Curve	Step Size (μm)	N _O	N _P	N _G	Mean GS				All Grains				1 point per Grain			
												J (ODF)	J (MDF)	S	M	J (ODF)	J (MDF)	S	M
15-43	Schist	Mafic Matrix	0.4	2.0	170016	120357	2415	16.7	± 11.0	3.6	99.8	1.814	1.023	-0.323	0.031	1.745	1.017	-0.309	0.027
16-142C	Mylonite	Montaged Mafic Matrix	0.5	2.0	108869	87195	2368	13.0	± 8.6	3.3	66.6	1.443	1.008	-0.206	0.017	1.340	1.004	-0.171	0.013
15-52A	Mylonite	Mafic Matrix	0.3	2.0	22353	16053	227	21.7	± 14.0	3.6	83.8	3.138	1.040	-0.675	0.036	2.520	1.029	-0.622	0.030
16-17E	Mylonite	Matrix	0.4	1.0	454765	222597	5336	8.5	± 4.6	1.8	61.5	1.418	1.013	-0.219	0.022	1.539	1.022	-0.277	0.028
15-59A	Mylonite	Mafic Matrix	0.5	2.0	5753	4914	118	12.5	± 9.3	3.6	56.8	21.897	3.987	-2.102	0.326	13.885	2.237	-1.812	0.211
15-59A	Mylonite	Mafic Matrix	0.4	5.0	8296	5187	256	28.5	± 19.0	9.7	99.9	2.470	1.015	-0.515	0.019	2.178	1.017	-0.517	0.025
15-59A	Mylonite	Mafic Matrix	0.3	5.0	4670	3956	190	25.9	± 14.0	11.2	85.4	4.961	1.081	-0.909	0.035	2.721	1.026	-0.667	0.027
16-125B	Cataclasite/Ultramylonite	Mafic Matrix	0.3	1.0	50774	38749	732	8.7	± 6.5	1.8	46.7	1.984	1.009	-0.369	0.019	1.712	1.007	-0.319	0.017
16-125B	Cataclasite/Ultramylonite	Mafic Matrix	0.2	0.5	272017	213089	1770	6.8	± 6.9	0.8	55.8	1.781	1.007	-0.300	0.017	1.656	1.006	-0.273	0.013
16-142E	Cataclasite	Montaged Mafic Matrix	0.5	2.0	238202	172818	3692	14.4	± 11.0	3.3	106.1	1.491	1.011	-0.226	0.023	1.370	1.007	-0.191	0.018
16-142E	Ultramylonite	Ultramylonite Layer	0.5	2.0	1967	1241	84	9.9	± 3.9	4.4	22.4	3.115	1.030	-0.722	0.027	3.651	1.042	-0.954	0.026
15-50E	Cataclasite	Mafic Matrix	0.3	1.0	69721	58896	360	13.1	± 12.0	1.8	67.7	3.599	1.069	-0.764	0.041	2.520	1.023	-0.562	0.028
16-50RD	Cataclasite	Mafic Matrix	0.3	2.0	22338	15439	295	18.9	± 13.0	3.6	65.5	2.594	1.028	-0.539	0.031	3.198	1.029	-0.653	0.024
16-151E	Cataclasite	Dark Matrix	0.4	1.0	268945	232190	2483	10.4	± 7.8	1.8	56.9	1.429	1.005	-0.204	0.015	1.318	1.003	-0.164	0.011
16-151E	Cataclasite	Dark Matrix	0.4	2.0	89562	63191	1428	16.6	± 9.4	3.3	74.9	1.550	1.009	-0.255	0.022	1.453	1.008	-0.230	0.020
16-125A	Ultracataclasite	UCAT Matrix	0.3	0.5	6412	3044	163	2.5	± 1.5	1.0	10.3	2.114	1.008	-0.340	0.014	2.846	1.023	-0.711	0.028

Table B.6 (continued).

Sample#	Rock Type	Domain	Tradeoff- Curve	Step Size (μm)	N _O	N _P	N _G	Mean GS	(1 σ)	Min	Max	All Grains				1 point per Grain			
												J (ODF)	J (MDF)	S	M	J (ODF)	J (MDF)	S	M
16-142D	Ultracataclasite	UCAT Matrix	0.2	0.6	2497	944	114	2.1	± 0.8	1.1	5.6	1.929	1.007	-0.324	0.012	3.608	1.046	-0.886	0.026
16-142B	Gouge	Matrix	0.3	0.6	17292	13270	508	2.9	± 2.4	1.1	16.8	3.595	1.040	-0.682	0.024	2.416	1.011	-0.493	0.012
16-142A	Gouge	Matrix	0.4	0.5	47391	35808	1081	2.8	± 2.3	0.9	20.0	2.412	1.021	-0.464	0.025	2.065	1.007	-0.385	0.009
16-126A	Schist/Mylonite?	Mafic Matrix	0.3	0.8	166814	114747	1312	8.7	± 6.6	1.3	68.6	1.736	1.012	-0.284	0.021	1.633	1.011	-0.284	0.019
16-126B	Schist	Mafic Matrix	0.4	1.5	39122	22449	623	11.5	± 7.2	2.5	41.4	1.645	1.008	-0.285	0.016	1.728	1.011	-0.334	0.019
16-169	Schist	Mafic Matrix	0.3	1.5	110051	78042	2168	12.2	± 7.0	2.7	65.6	1.510	1.004	-0.226	0.012	1.408	1.004	-0.200	0.014
16-176	Schist	Mafic Matrix	0.3	2.0	11691	4851	130	17.8	± 9.0	4.8	49.4	2.197	1.013	-0.441	0.017	3.107	1.033	-0.801	0.024
16-182	Schist/Mylonite?	Mafic Matrix	0.3	2.0	50956	25171	367	24.5	± 14.0	4.0	94.2	2.229	1.061	-0.515	0.050	2.673	1.105	-0.691	0.065
15-72A	Schist	Mafic Matrix	0.5	2.0	96519	75656	2593	12.3	± 7.0	3.3	57.9	1.503	1.010	-0.230	0.021	1.413	1.007	-0.203	0.019

Table B.7. Grain-size statistics, J-index, S-index and M-index for titanite based on EBSD analysis. N_O—number of orientation; N_P—number of pixels; N_G—number of grains; Mean GS—mean grain size; 1 σ —standard deviation; Min, Max—minimum, maximum estimated grain size.

Sample#	Rock Type	Domain	Tradeoff-Curve	Step Size (μm)								All Grains				1 point per Grain			
					N _O	N _P	N _G	Mean GS	(1 σ)	Min	Max	J (ODF)	J (MDF)	S	M	J (ODF)	J (MDF)	S	M
16-142C	Mylonite	Montaged Mafic Matrix	0.5	2.0	43512	35236	1211	12.2	7.0	3.3	56.9	2.318	1.171	-0.507	0.096	2.044	1.133	-0.429	0.085
15-52A	Mylonite	Mafic Matrix	0.3	2.0	4023	1233	73	13.1	5.1	4.7	30.9	2.357	1.129	-0.591	0.087	3.366	1.179	-0.914	0.114
15-73A	Mylonite	Mafic Matrix	0.5	1.0	182312	73344	2114	7.8	3.4	2.0	30.2	2.023	1.144	-0.412	0.080	2.141	1.165	-0.453	0.085
15-73A	Mylonite	Mafic Matrix	0.5	1.0	36330	18659	447	8.3	3.4	2.4	22.7	2.787	1.340	-0.658	0.118	3.576	1.570	-0.873	0.151
15-73A	Mylonite	Fine Grained Matrix	0.5	1.0	148002	60466	1791	7.6	3.3	2.0	30.4	1.892	1.112	-0.371	0.071	1.959	1.123	-0.399	0.074
16-17E	Mylonite	Mafic Matrix	0.4	1.0	24395	5565	336	5.8	2.5	1.9	15.0	1.157	1.002	-0.075	0.010	1.373	1.002	-0.179	0.011
15-59A	Mylonite	Mafic Matrix	0.5	2.0	85909	62208	3350	10.5	4.8	3.3	43.5	1.473	1.033	-0.209	0.038	1.404	1.024	-0.181	0.032
15-59A	Mylonite	Mafic Matrix	0.4	5.0	2488	177	34	16.4	2.8	12.0	23.8	1.380	1.013	-0.179	0.025	4.372	1.200	-1.149	0.091
15-59A	Mylonite	Mafic Matrix	0.3	5.0	723	96	19	17.0	3.3	12.0	25.5	1.723	1.031	-0.338	0.043	5.582	1.282	-1.366	0.109
15-59A	Ultramylonite?	Mafic Matrix	0.3	5.0	1028	81	16	18.8	3.7	13.7	25.6	1.485	1.009	-0.219	0.021	7.436	1.620	-1.645	0.194
16-142E	Cataclasite	Montaged Mafic Matrix	0.5	2.0	17517	9227	642	9.1	4.3	3.3	44.4	1.279	1.004	-0.123	0.010	1.314	1.006	-0.158	0.011
16-142E	Ultramylonite	Ultramylonite Layer	0.5	2.0	460	230	22	8.0	3.2	4.5	15.6	3.301	1.053	-0.756	0.035	5.334	1.171	-1.299	0.057
15-50E	Cataclasite	Mafic Matrix	0.3	1.0	1961	1051	30	9.2	4.5	2.4	18.4	3.194	1.056	-0.672	0.041	3.557	1.034	-0.922	0.021
16-50RD	Cataclasite	Mafic Matrix	0.3	2.0	3161	781	39	13.8	6.4	5.6	34.0	1.594	1.003	-0.263	0.009	3.415	1.060	-0.935	0.060
16-151E	Cataclasite	Mafic Matrix	0.4	1.0	6824	3288	169	5.9	2.5	1.9	16.2	1.746	1.027	-0.310	0.037	1.832	1.028	-0.377	0.037
16-151E	Cataclasite	Mafic Matrix	0.4	2.0	1776	356	36	9.2	3.2	4.8	17.8	1.887	1.024	-0.351	0.038	3.747	1.076	-0.991	0.045

Table B.7 (continued).

Sample#	Rock Type	Domain	Tradeoff-Curve	Step Size (μm)	N ₀	N _P	N _G	Mean GS	(1σ)	Min	Max	All Grains				1 point per Grain			
												J (ODF)	J (MDF)	S	M	J (ODF)	J (MDF)	S	M
16-125A	Ultracataclasite	UCAT Matrix	0.3	0.5	57747	463	49	2.1	0.6	1.1	3.5	1.191	1.002	-0.089	0.006	2.649	1.022	-0.698	0.022
16-142D	Ultracataclasite	UCAT Matrix	0.2	0.6	12604	932	109	2.2	0.8	1.2	4.9	1.199	1.002	-0.091	0.009	1.809	1.005	-0.383	0.016
16-142B	Gouge	Matrix	0.3	0.6	10744	1889	118	2.7	1.4	1.2	8.3	1.215	1.002	-0.099	0.008	1.796	1.007	-0.364	0.016
16-142A	Gouge	Matrix	0.4	0.5	59202	26103	1266	2.6	1.5	0.9	16.6	1.140	1.000	-0.064	0.005	1.095	1.000	-0.047	0.002
16-126A	Schist/Mylonite?	Mafic Matrix	0.3	0.8	40846	12956	321	7.6	3.7	1.8	25.5	1.309	1.009	-0.145	0.021	1.455	1.011	-0.219	0.027
16-126B	Schist	Mafic Matrix	0.4	1.5	20265	6685	389	9.3	4.2	3.2	31.9	1.445	1.022	-0.201	0.039	1.538	1.019	-0.256	0.036
PNG16-169	Schist	Mafic Matrix	0.3	1.5	4948	1236	114	7.5	2.8	3.5	14.6	1.249	1.001	-0.116	0.007	1.890	1.014	-0.420	0.030
16-182	Schist/Mylonite?	Mafic Matrix	0.3	2.0	10012	2115	118	13.5	5.5	5.0	32.7	1.475	1.016	-0.227	0.029	2.148	1.022	-0.493	0.032
15-72A	Schist	Mafic Matrix	0.5	2.0	5904	1401	168	7.1	3.3	3.7	37.8	1.427	1.011	-0.186	0.029	1.838	1.024	-0.385	0.045

Mafic Mylonites:

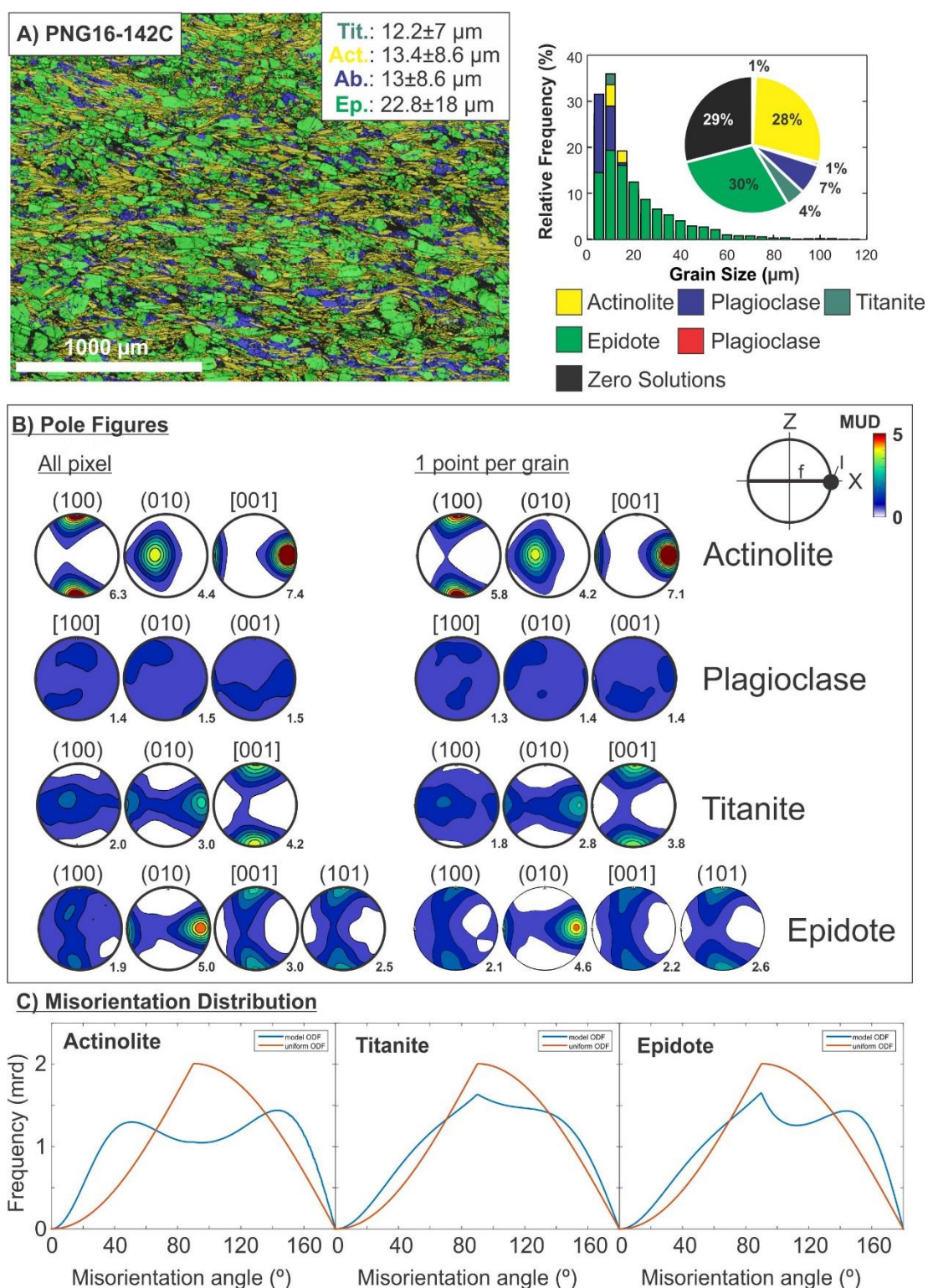


Figure B.8. EBSD analysis of mylonite sample PNG16-142C (active Mai'iu fault trace). A) Phase map, grain size distributions and phase fraction (%). B) Contoured pole figures; left—based on all pixels; right—based on one point per grain. C) Misorientation distribution plots. MUD—Multiples of uniform distribution; ODF—Orientation density functions.

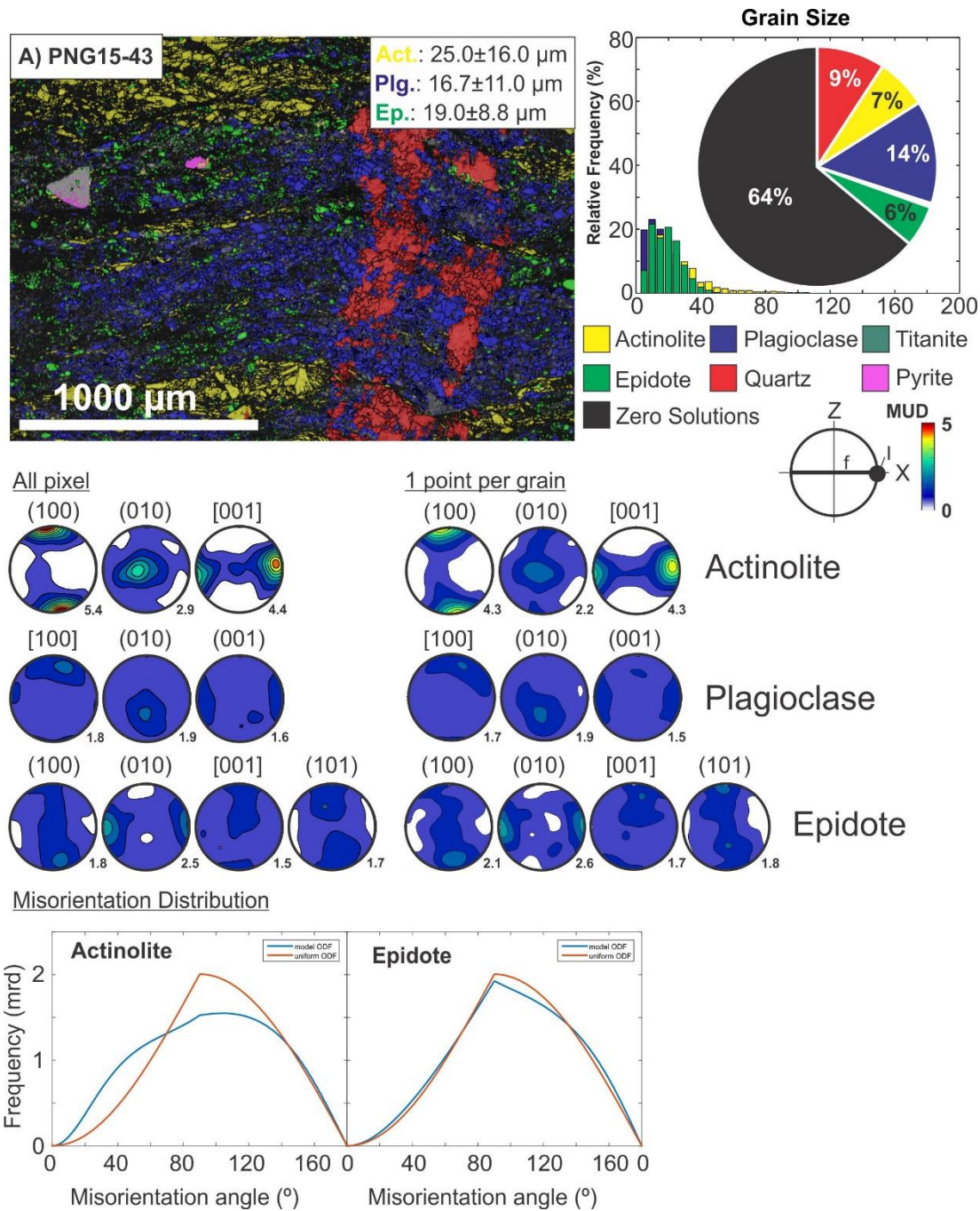


Figure B.9. EBSD analysis of mylonite sample PNG15-43 (~700 m south of the active Mai'iu fault trace). A) Phase map, grain size distributions and phase fraction (%). B) Contoured pole figures; left—based on all pixels; right—based on one point per grain. C) Misorientation distribution plots. MUD—Multiples of uniform distribution; ODF—Orientation density functions.

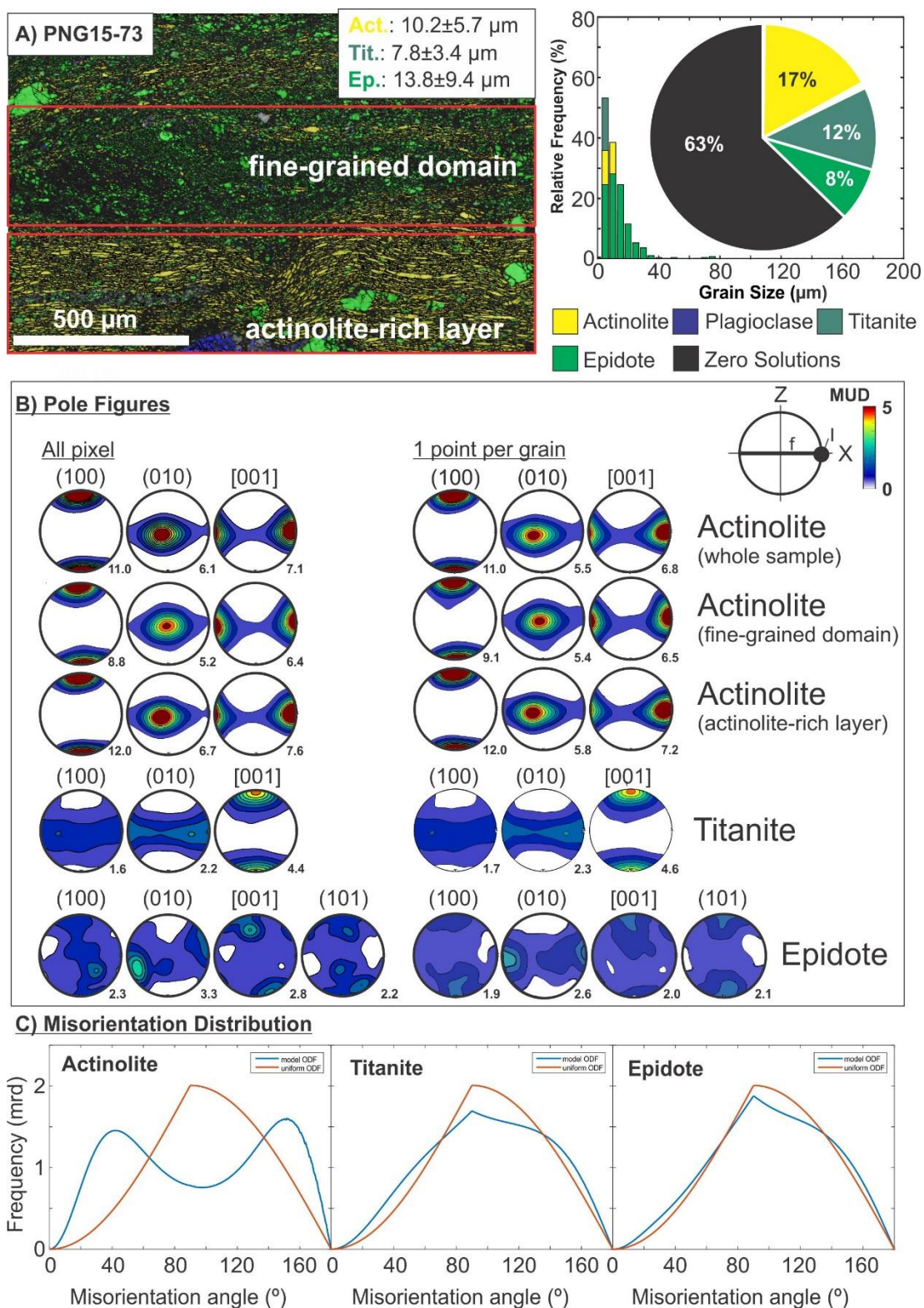


Figure B.10. EBSD analysis of mylonite sample PNG15-73 (close to active Mai'iu fault trace). A) Phase map, grain size distributions and phase fraction (%). B) Contoured pole figures; left—based on all pixels; right—based on one point per grain. C) Misorientation distribution plots. MUD—Multiples of uniform distribution; ODF—Orientation density functions.

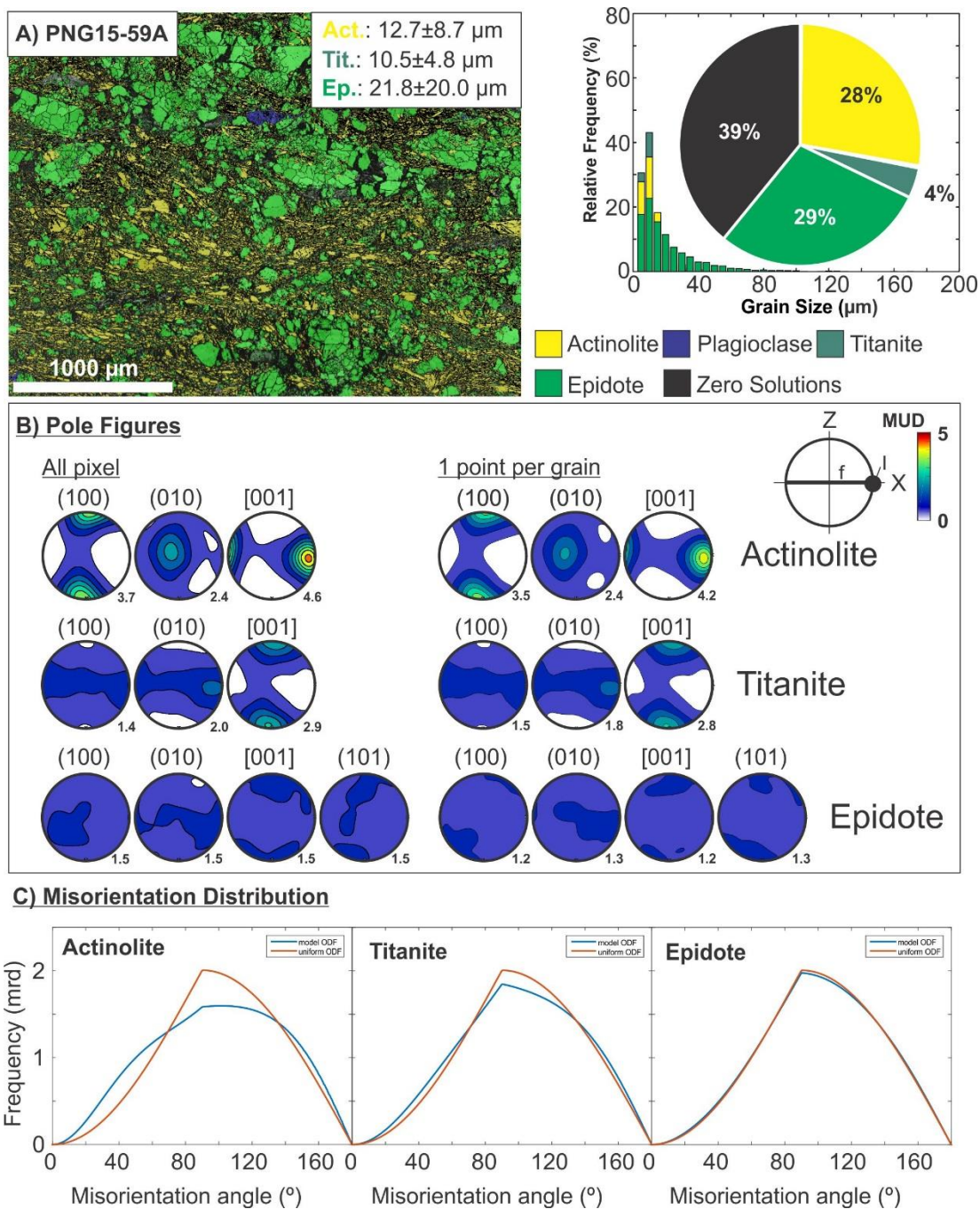


Figure B.11. EBSD analysis of an epidote-rich domain of mylonite sample PNG15-59A (close to active fault trace). A) Phase map, grain size distributions and phase fraction (%). B) Contoured pole figures; left—based on all pixels; right—based on one point per grain. C) Misorientation distribution plots. MUD—Multiples of uniform distribution; ODF—Orientation density functions.

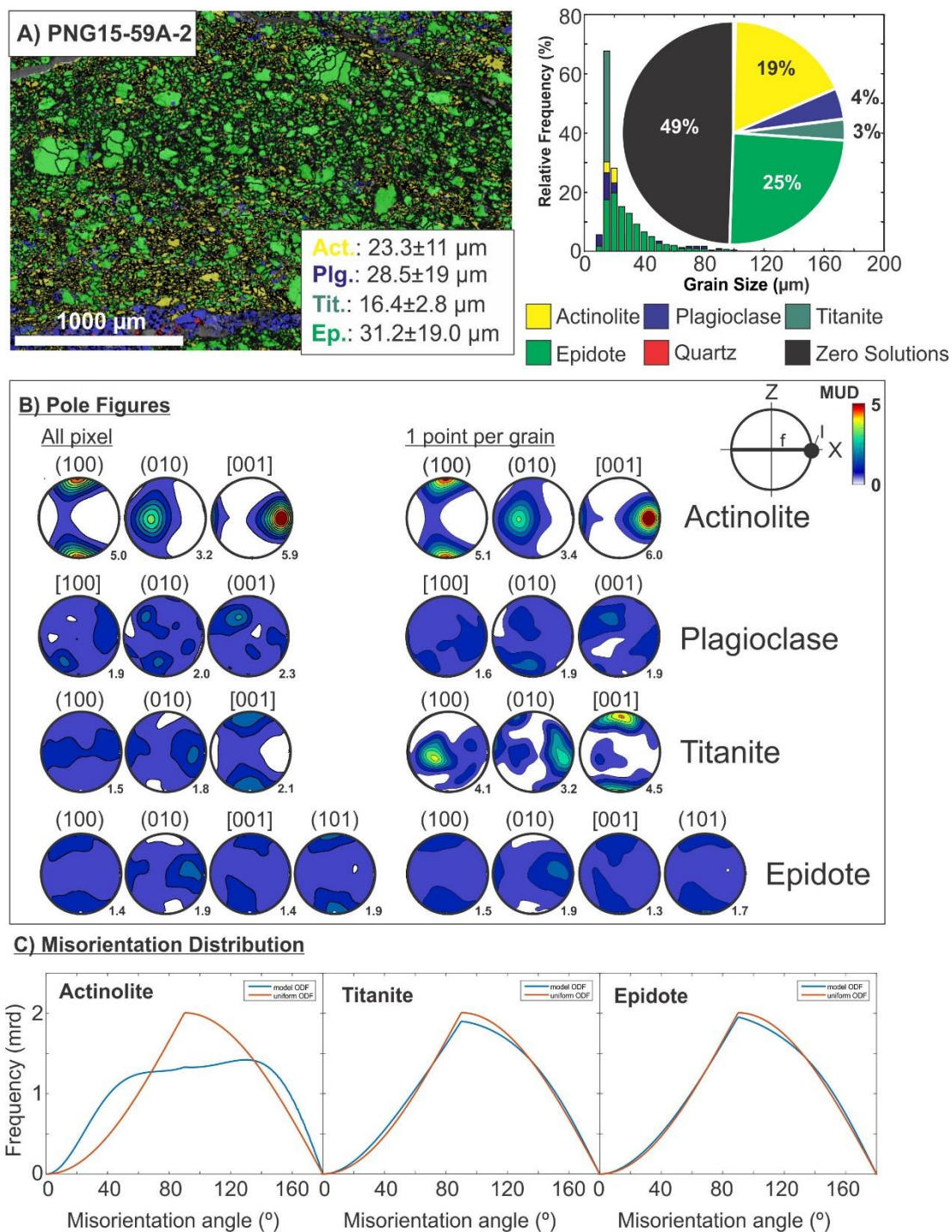


Figure B.12. EBSD analysis of mylonite sample PNG15-59A-2 (close to active fault trace). A) Phase map, grain size distributions and phase fraction (%). B) Contoured pole figures; left—based on all pixels; right—based on one point per grain. C) Misorientation distribution plots. MUD—Multiples of uniform distribution; ODF—Orientation density functions.

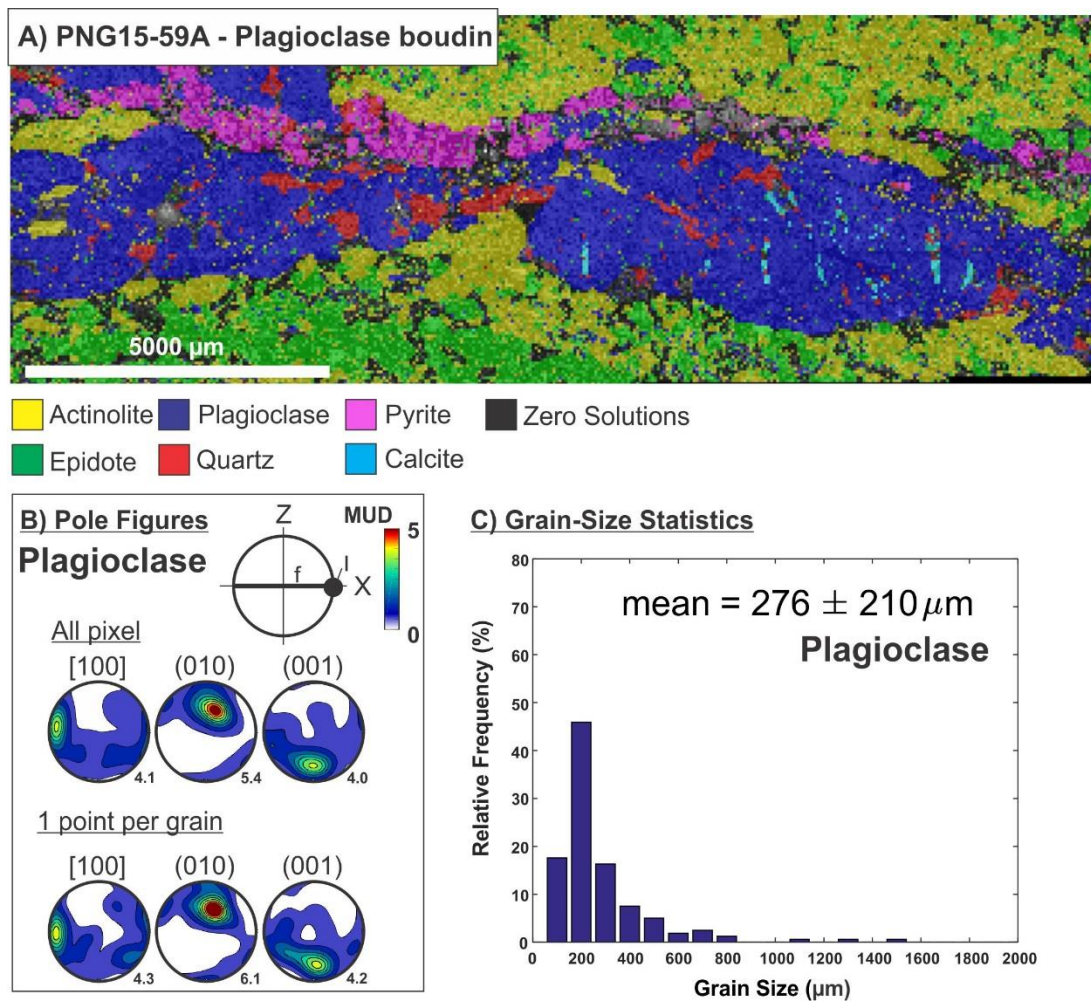


Figure B.13. EBSD analysis of albitic boudin in mylonite sample PNG15-59A (albite only; close to active fault trace). A) Phase map. B) Contoured pole figures of albite based on all pixels and based on one point per grain. C) Albite grain size statistics.

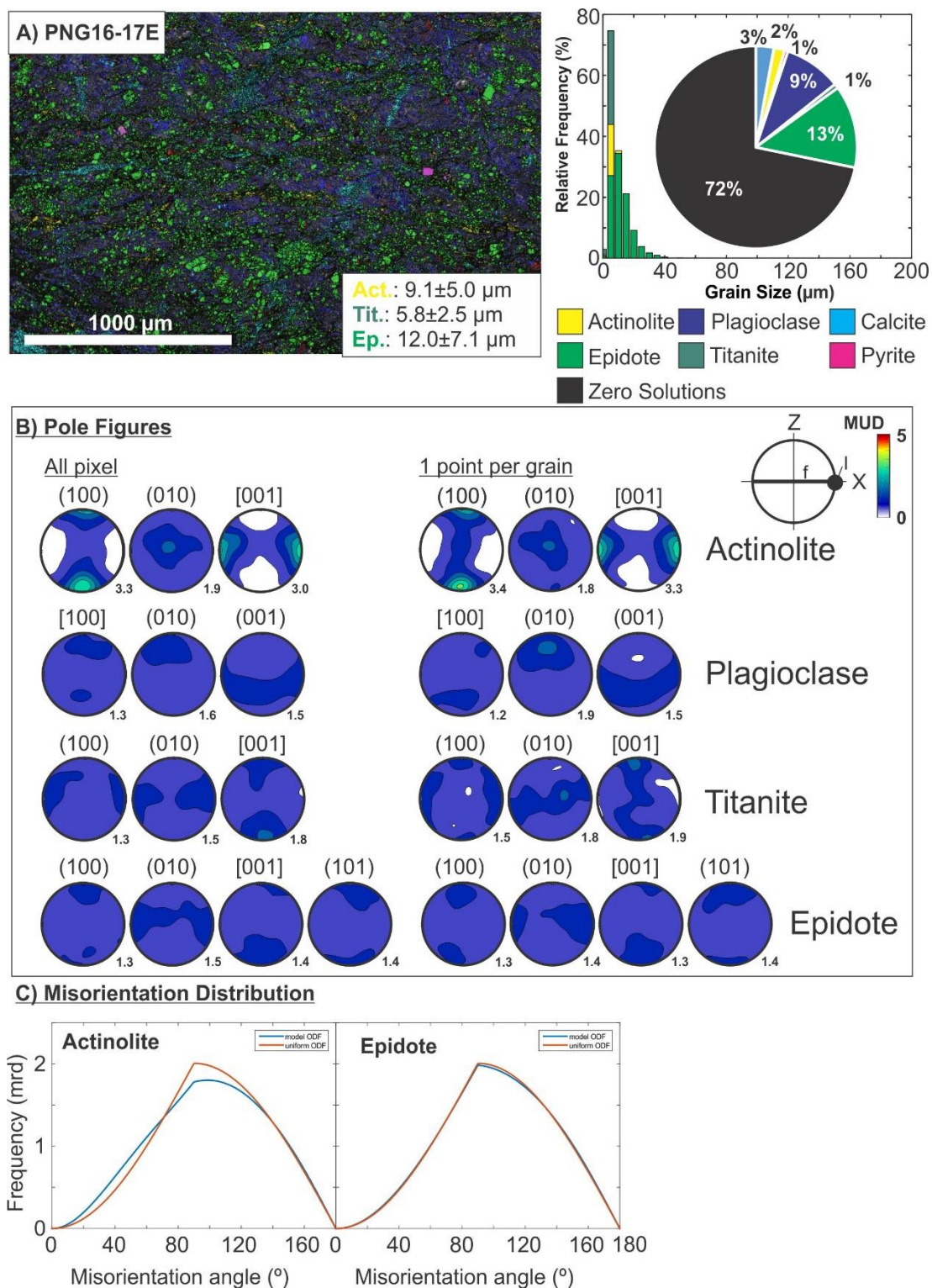


Figure B.14. EBSD analysis of (ultra?)mylonite sample PNG16-17E (close to the inactive Mai'iu fault trace). A) Phase map, grain size distributions and phase fraction (%). B) Contoured pole figures; left—based on all pixels; right—based on one point per grain. C) Misorientation distribution plots. MUD—Multiples of uniform distribution; ODF—Orientation density functions.

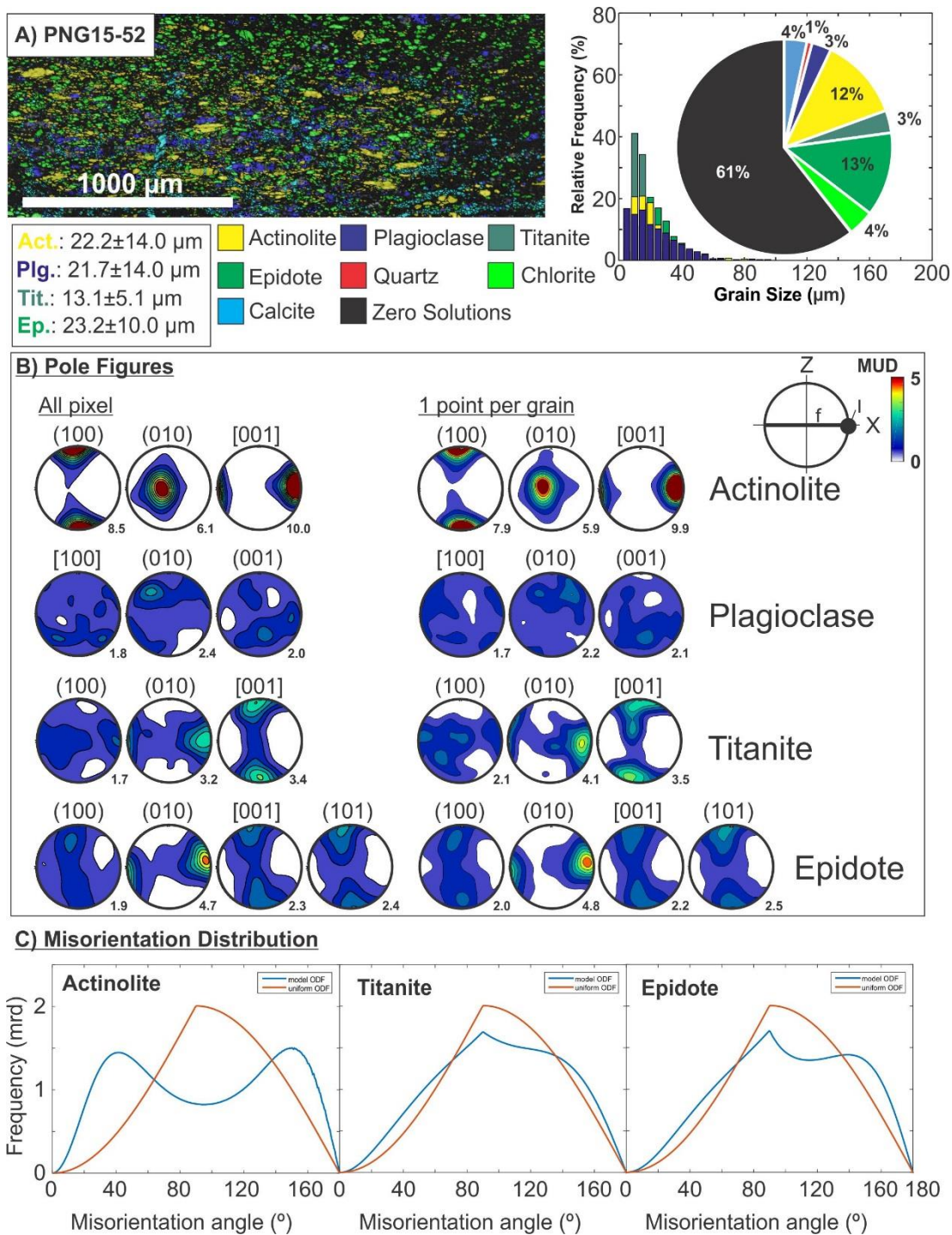


Figure B.15. EBSD analysis of mylonite sample PNG15-52 (just south of active Mai'iu fault trace). A) Phase map, grain size distributions and phase fraction (%). B) Contoured pole figures; left—based on all pixels; right—based on one point per grain. C) Misorientation distribution plots. MUD—Multiples of uniform distribution; ODF—Orientation density functions.

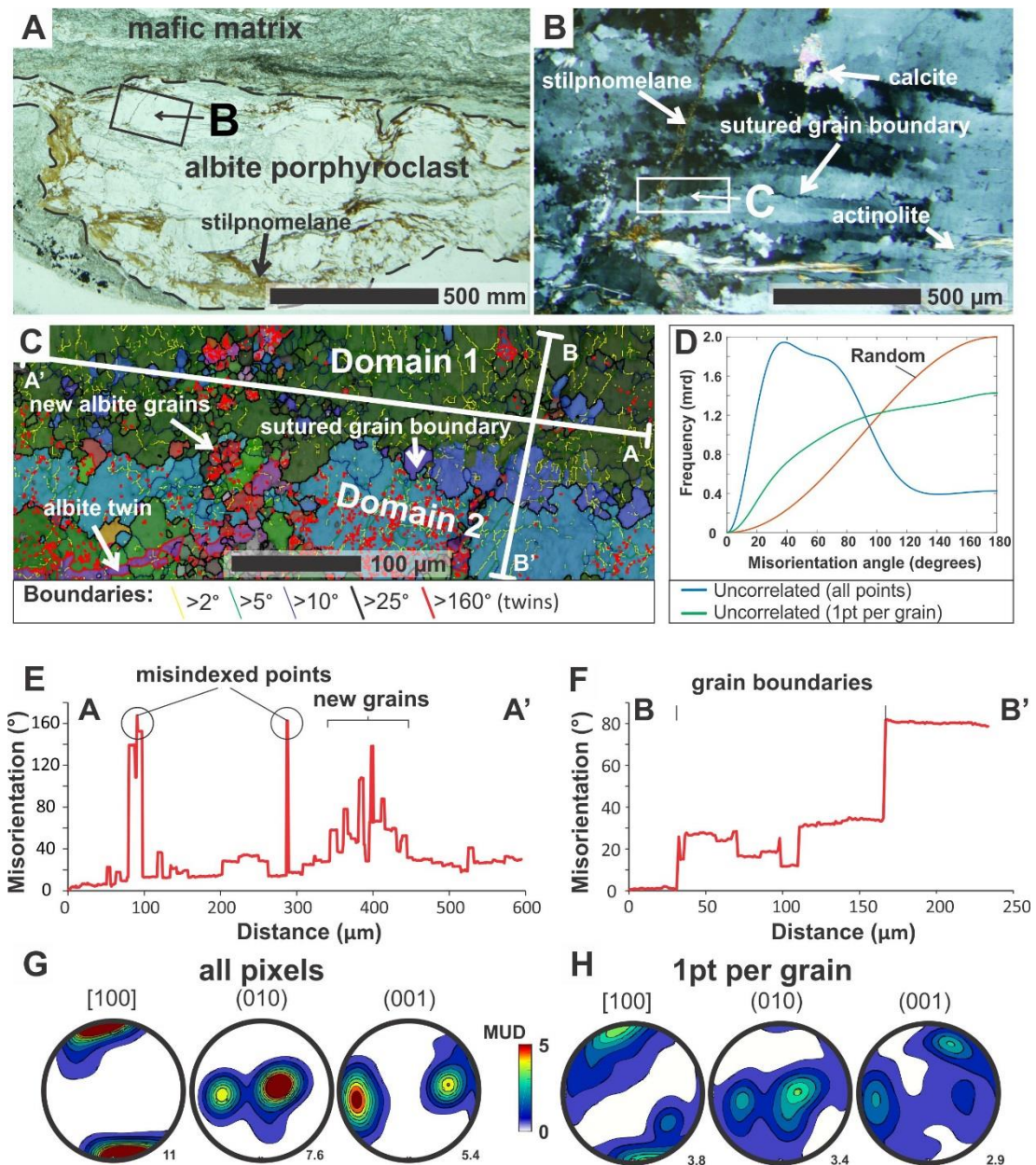


Figure B.16. Microstructural analysis of an albite porphyroblast in the mafic mylonite sample PNG15-73. A) Optical photomicrograph of an albite porphyroblast (up to 2 cm in diameter). Stilpnomelane grew at the outer rim and along fractures of this porphyroblast. B) Optical photomicrograph (XPOL) of the deformed albite porphyroblast showing strong internal lattice distortion, intergrown actinolite fibres, and stilpnomelane \pm calcite in fractures. C) EBSD (all Euler colors) map of the host albite grain (Domain 1), a large, new albite grain with bulged and sutured grain boundaries (Domain 2), and smaller albite aggregates (step size: 1 μ m). D) Misorientation distribution plot (misorientation angle versus frequency [mrd=multiples of random density]) for all collected points and one point per grain (uncorrelated), and a theoretical random distribution. Note, misindexed points were excluded from this analysis. E) and F) misorientation profiles (misorientation angle relative to the starting point) across the different albite domains. G) and H) Lower-hemisphere, equal-area pole plots (Schmidt projection) of all collected points (pixels; highlights the orientation of the parent albite grain) and one point per grain (highlights the orientation of all grains in the analyzed section).

Mafic Foliated Cataclasites:

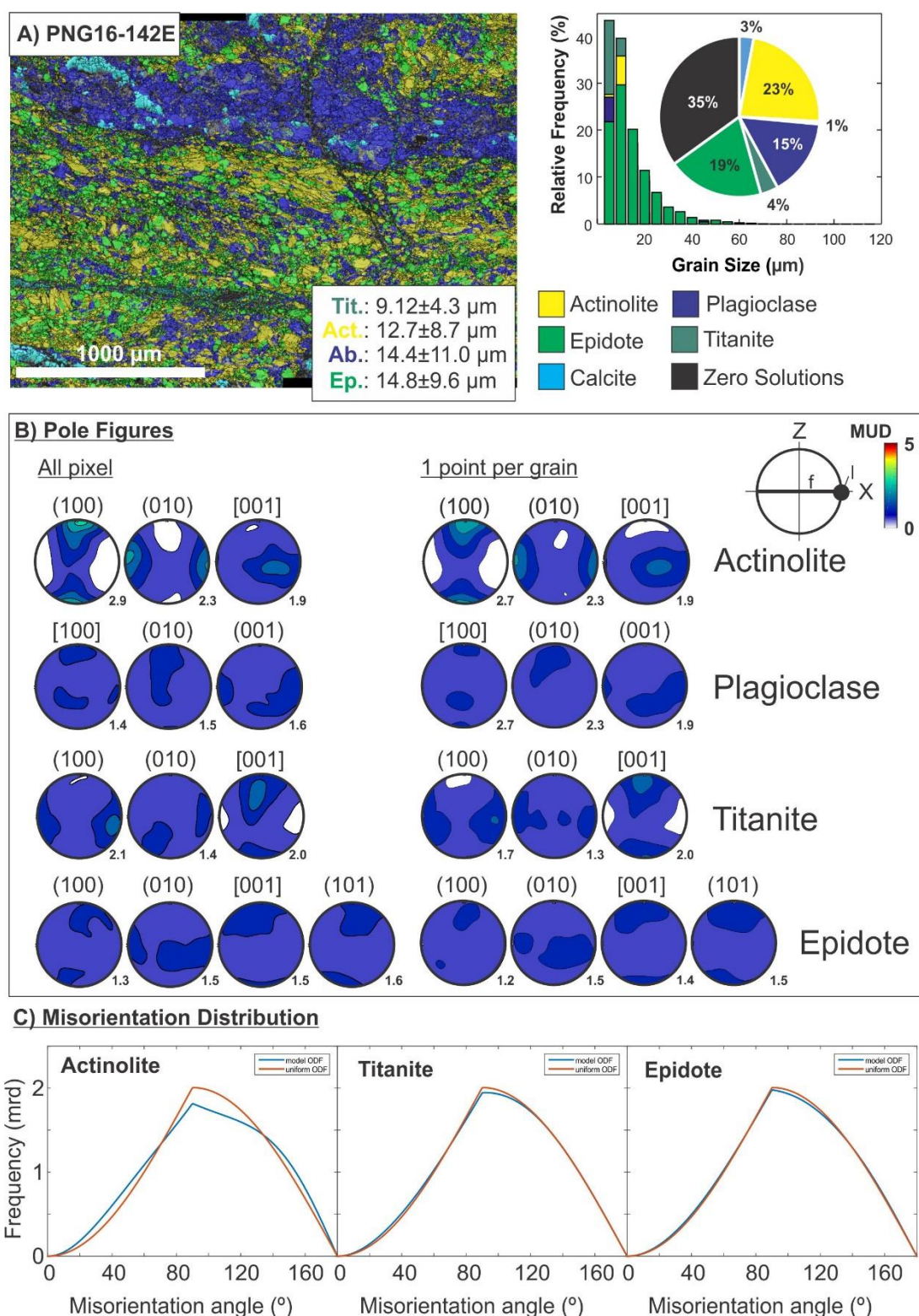


Figure B.17. EBSD analysis of foliated cataclasite sample PNG16-142E (at active Mai'iu fault trace). A) Phase map, grain size distributions and phase fraction (%). B) Contoured pole figures; left—based on all pixels; right—based on one point per grain. C) Misorientation distribution plots. MUD—Multiples of uniform distribution; ODF—Orientation density functions.

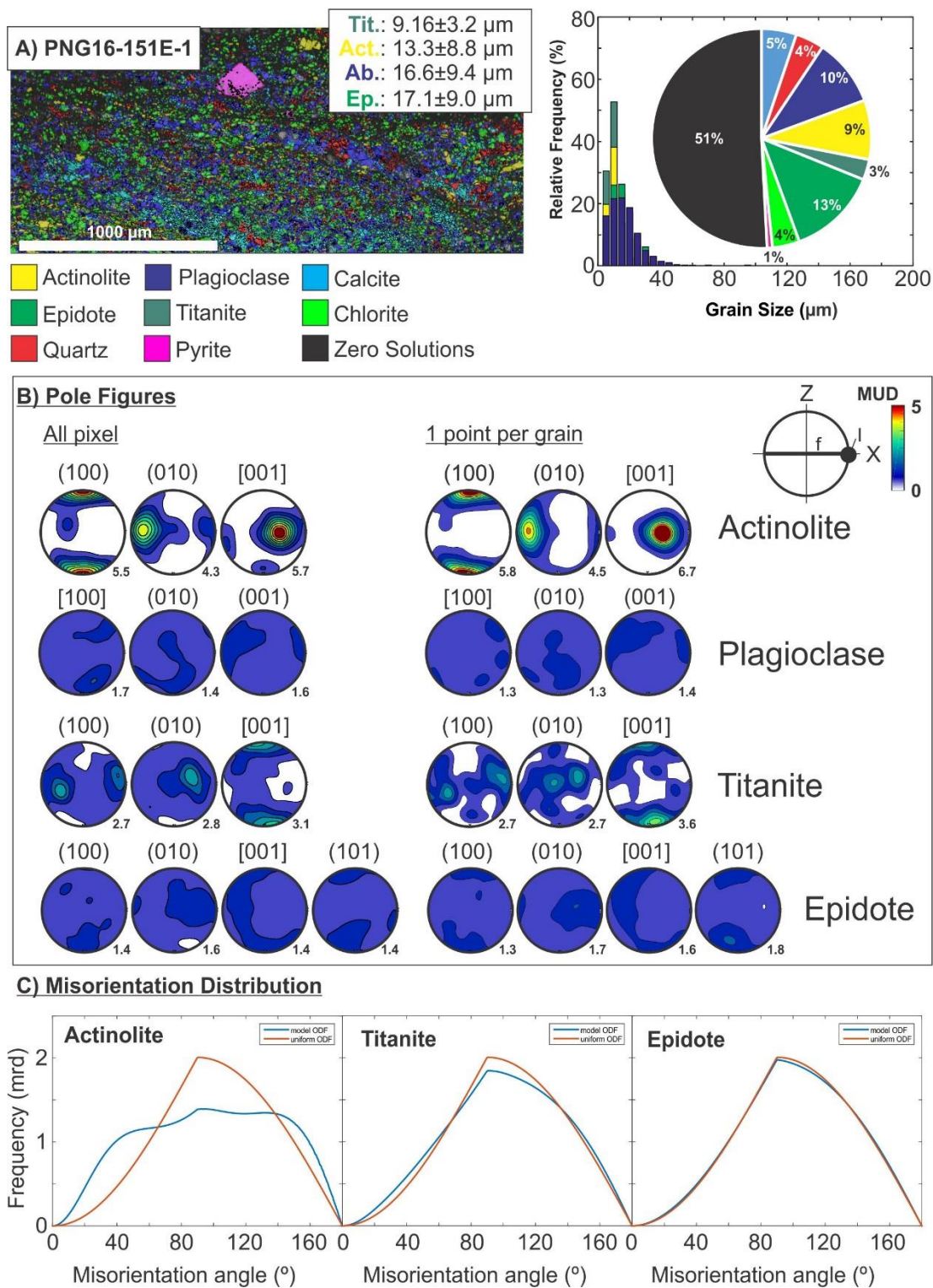


Figure B.18. EBSD analysis of foliated cataclasite sample PNG16-151E-1 (just south of active Mai'iu fault trace). A) Phase map, grain size distributions and phase fraction (%). B) Contoured pole figures; left—based on all pixels; right—based on one point per grain. C) Misorientation distribution plots. MUD—Multiples of uniform distribution; ODF—Orientation density functions.

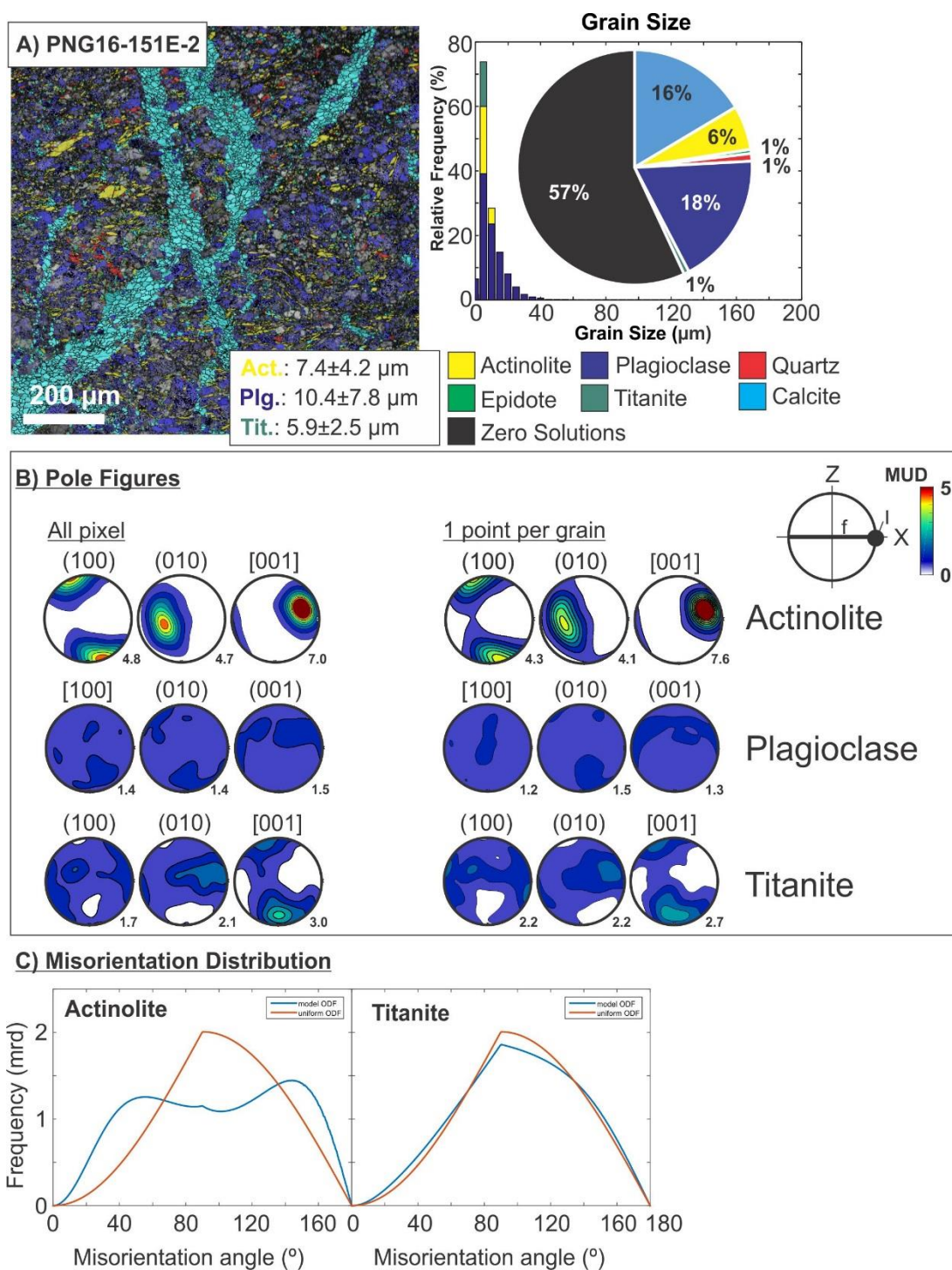


Figure B.19. EBSD analysis of foliated cataclasite sample PNG16-151E-2 (just south of active Mai'iu fault trace). A) Phase map, grain size distributions and phase fraction (%). B) Contoured pole figures; left—based on all pixels; right—based on one point per grain. C) Misorientation distribution plots. MUD—Multiples of uniform distribution; ODF—Orientation density functions.

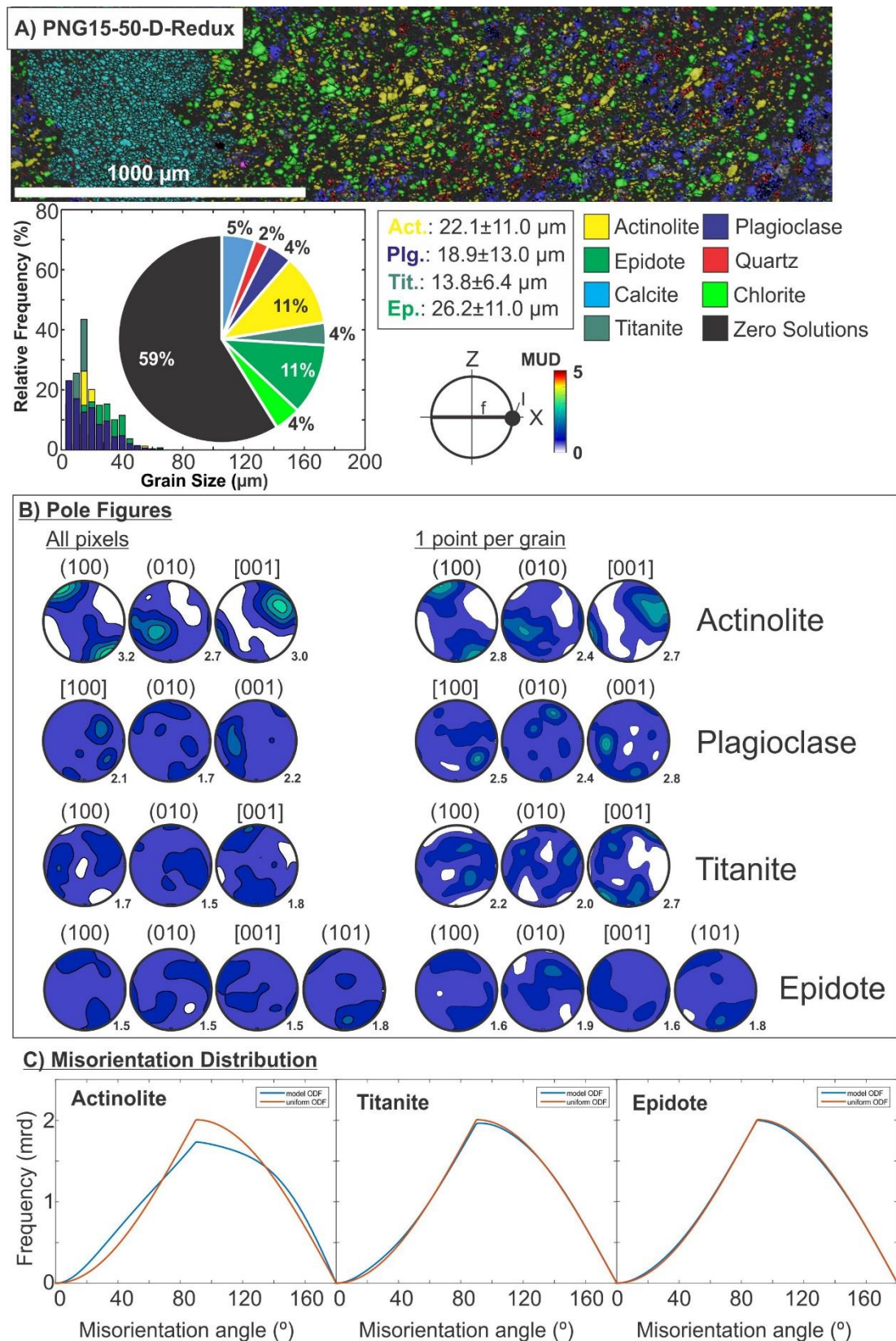


Figure B.20. EBSD analysis of foliated cataclasite sample PNG15-50D-Redux (active Mai'iu fault trace). A) Phase map, grain size distributions and phase fraction (%). B) Contoured pole figures; left—based on all pixels; right—based on one point per grain. C) Misorientation distribution plots. MUD—Multiples of uniform distribution; ODF—Orientation density functions.

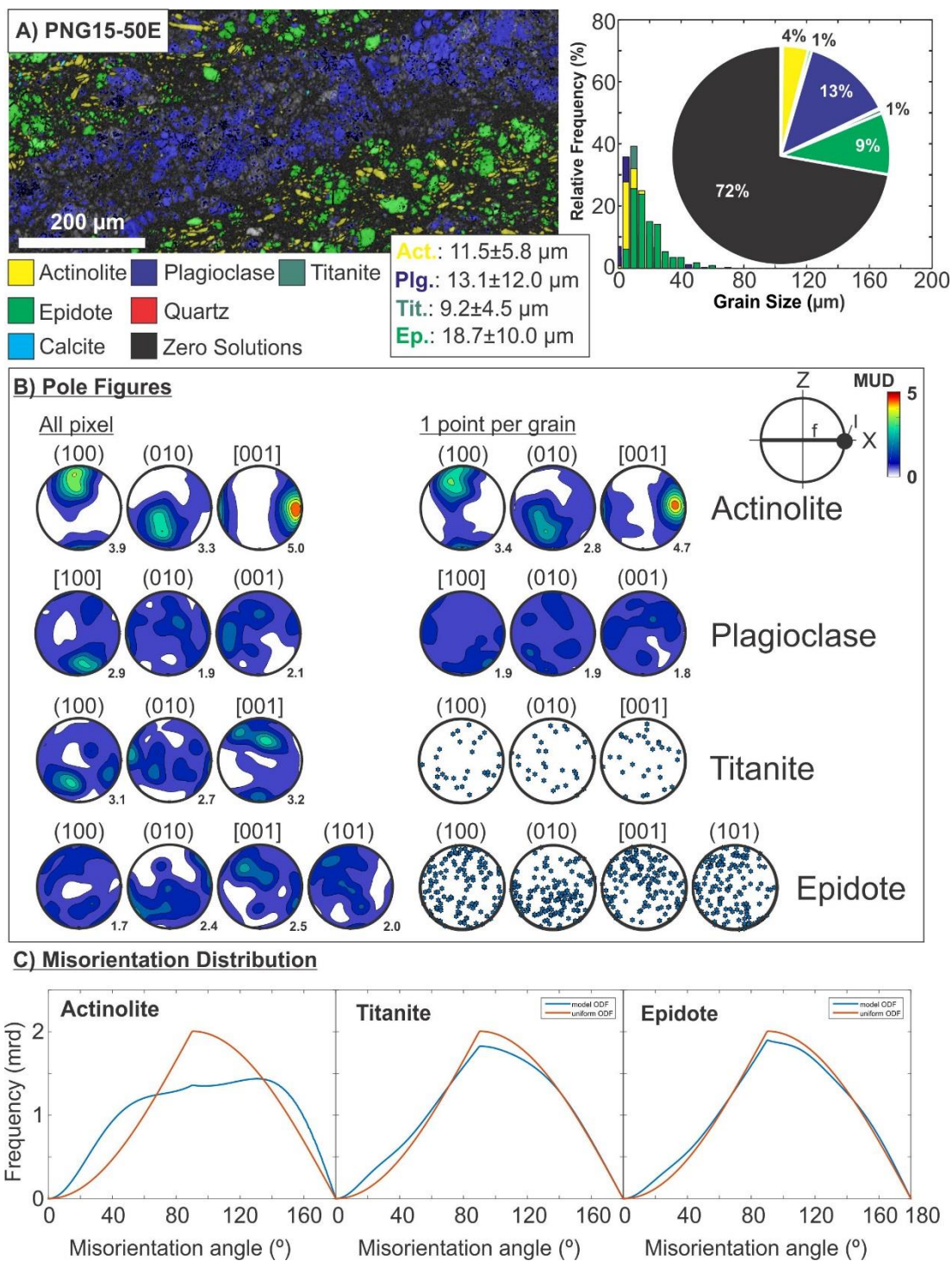


Figure B.21. EBSD analysis of foliated cataclasite sample PNG15-50E (active Mai'iu fault trace). A) Phase map, grain size distributions and phase fraction (%). B) Contoured pole figures; left—based on all pixels; right—based on one point per grain. C) Misorientation distribution plots. MUD—Multiples of uniform distribution; ODF—Orientation density functions.

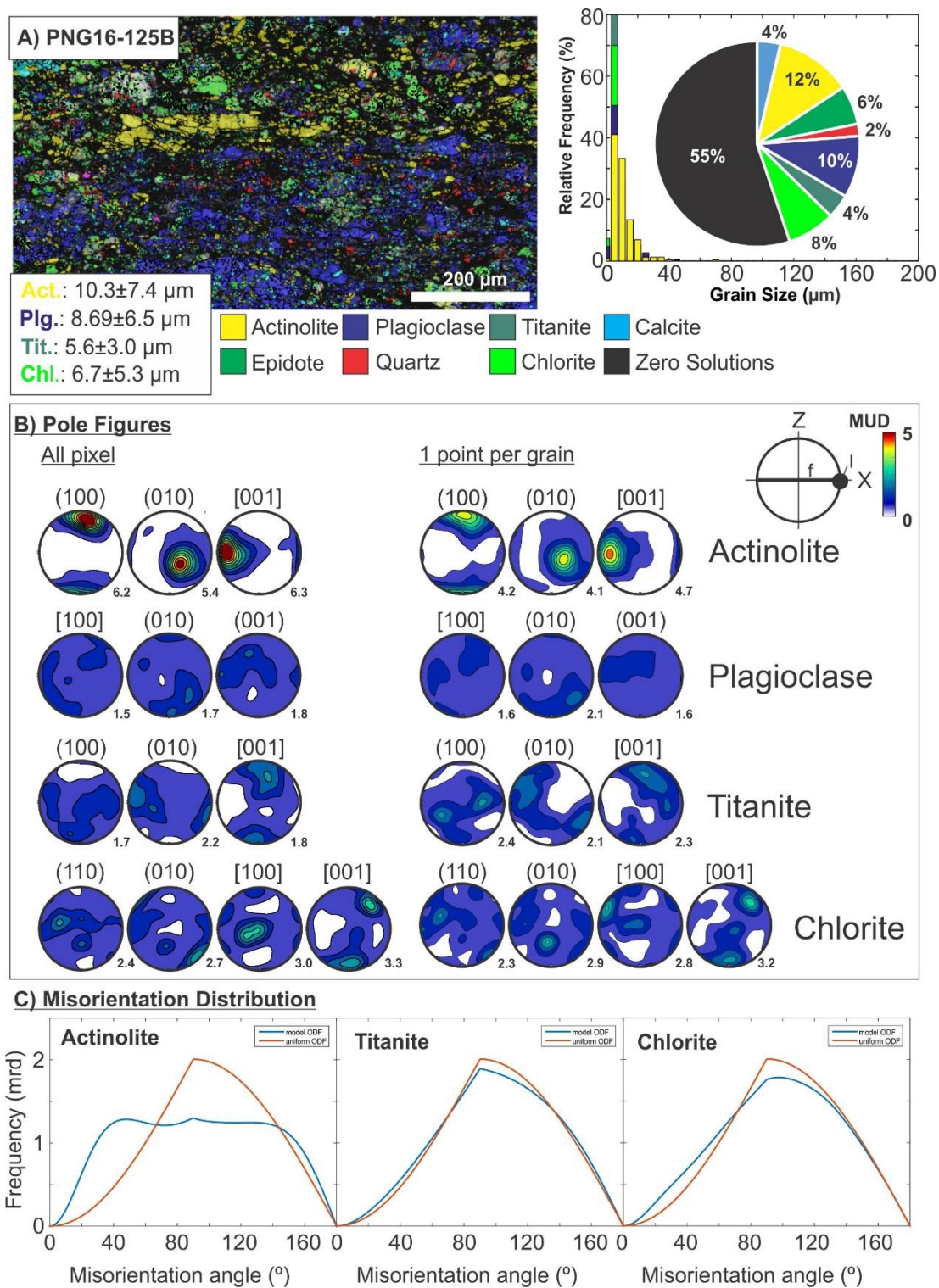


Figure B.22. EBSD analysis of cataclasite sample PNG16-125B (just south of active(?) Mai'iu fault trace, close to Gwoira fault). A) Phase map, grain size distributions and phase fraction (%). B) Contoured pole figures; left—based on all pixels; right—based on one point per grain. C) Misorientation distribution plots. MUD—Multiples of uniform distribution; ODF—Orientation density functions.

Mafic Ultracataclasites:

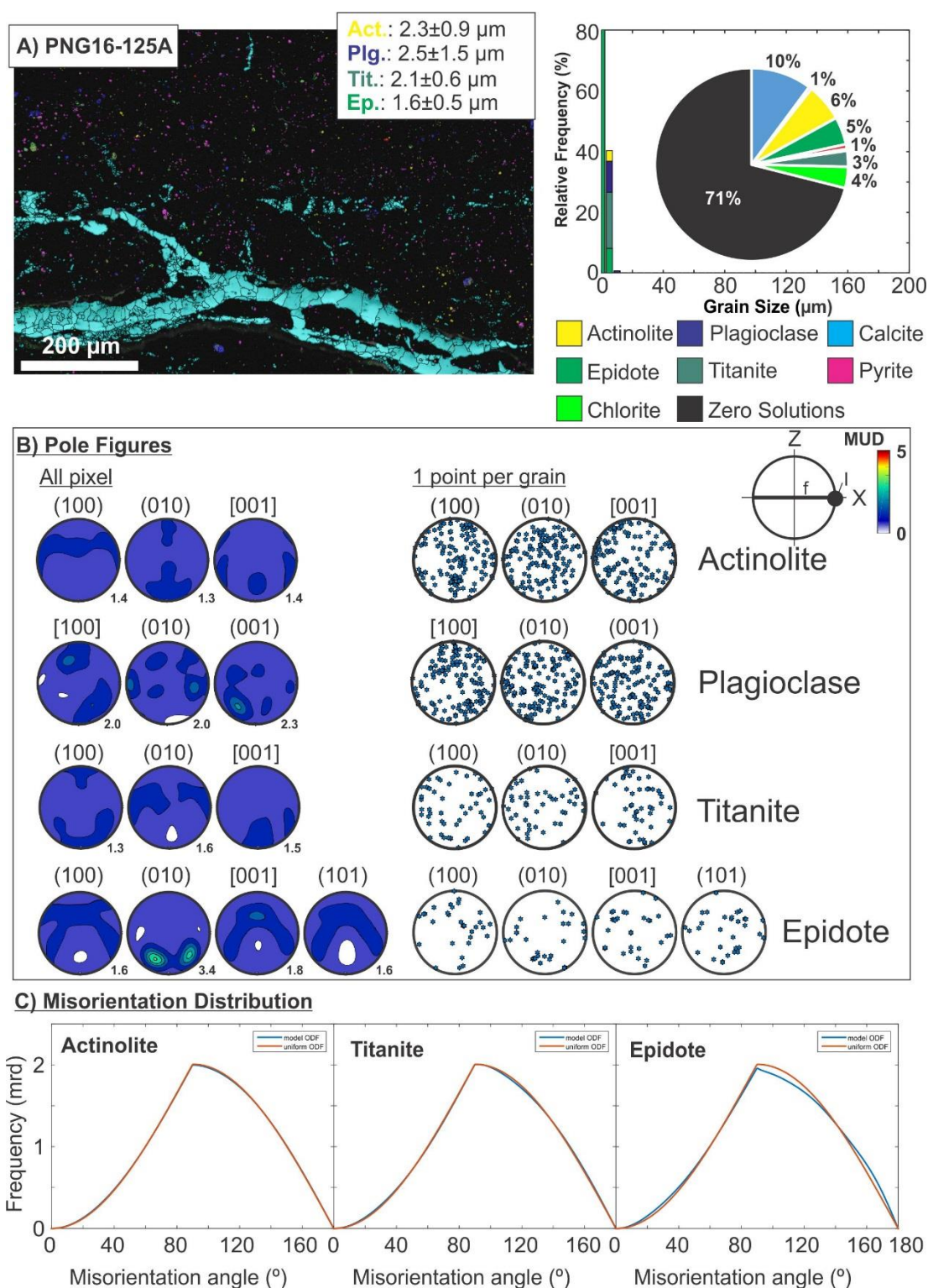


Figure B.23. EBSD analysis of ultracataclasite sample PNG16-125A. A) Phase map, grain size distributions and phase fraction (%). B) Pole figures; left—contoured, based on all pixels; right—based on one point per grain. C) Misorientation distribution plots. MUD—Multiples of uniform distribution; ODF—Orientation density functions.

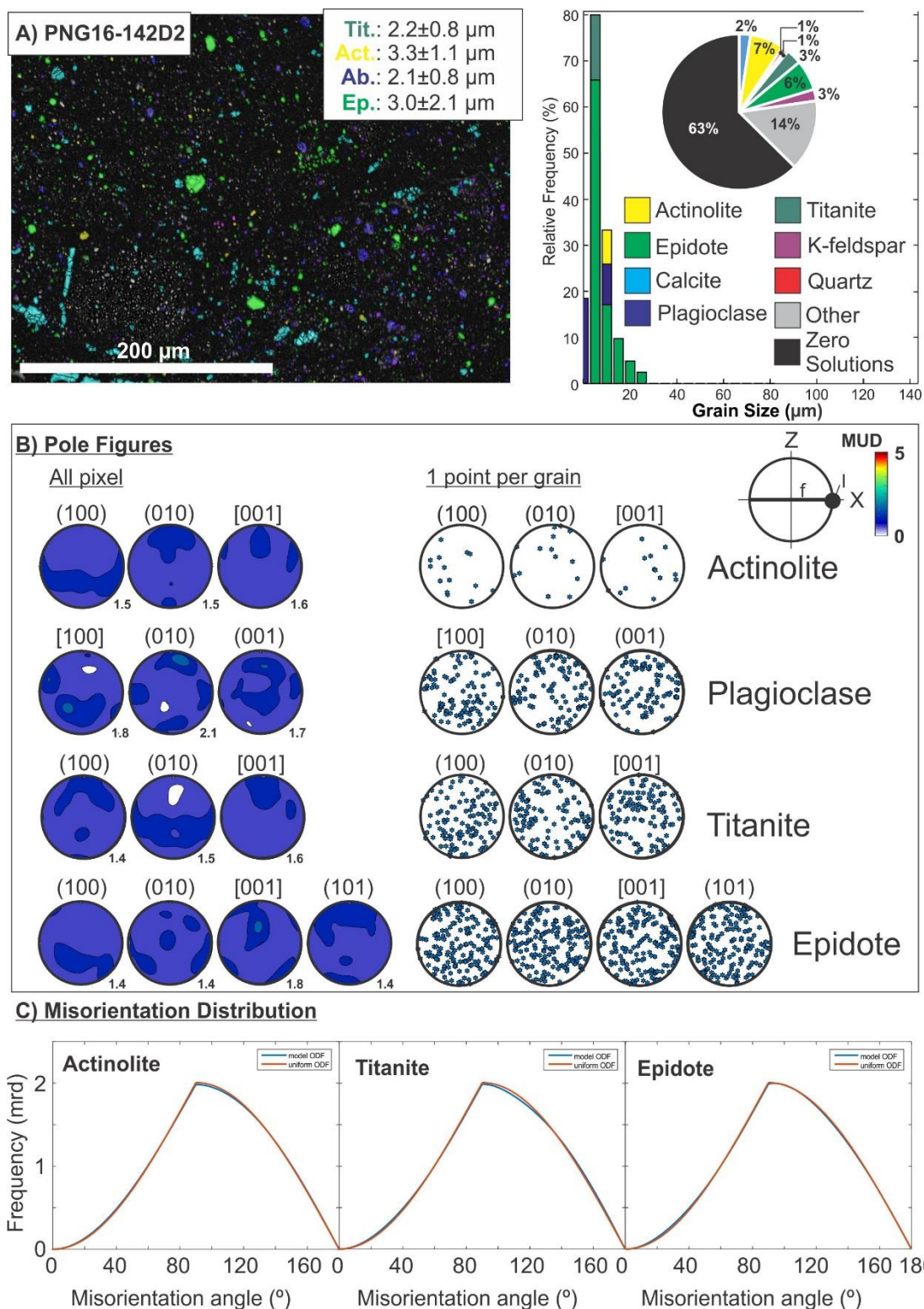


Figure B.24. EBSD analysis of ultracataclasite sample PNG16-142D2. A) Phase map, grain size distributions and phase fraction (%). B) Pole figures; left—contoured, based on all pixels; right—based on one point per grain. C) Misorientation distribution plots. MUD—Multiples of uniform distribution; ODF—Orientation density functions.

Mafic Gouges:

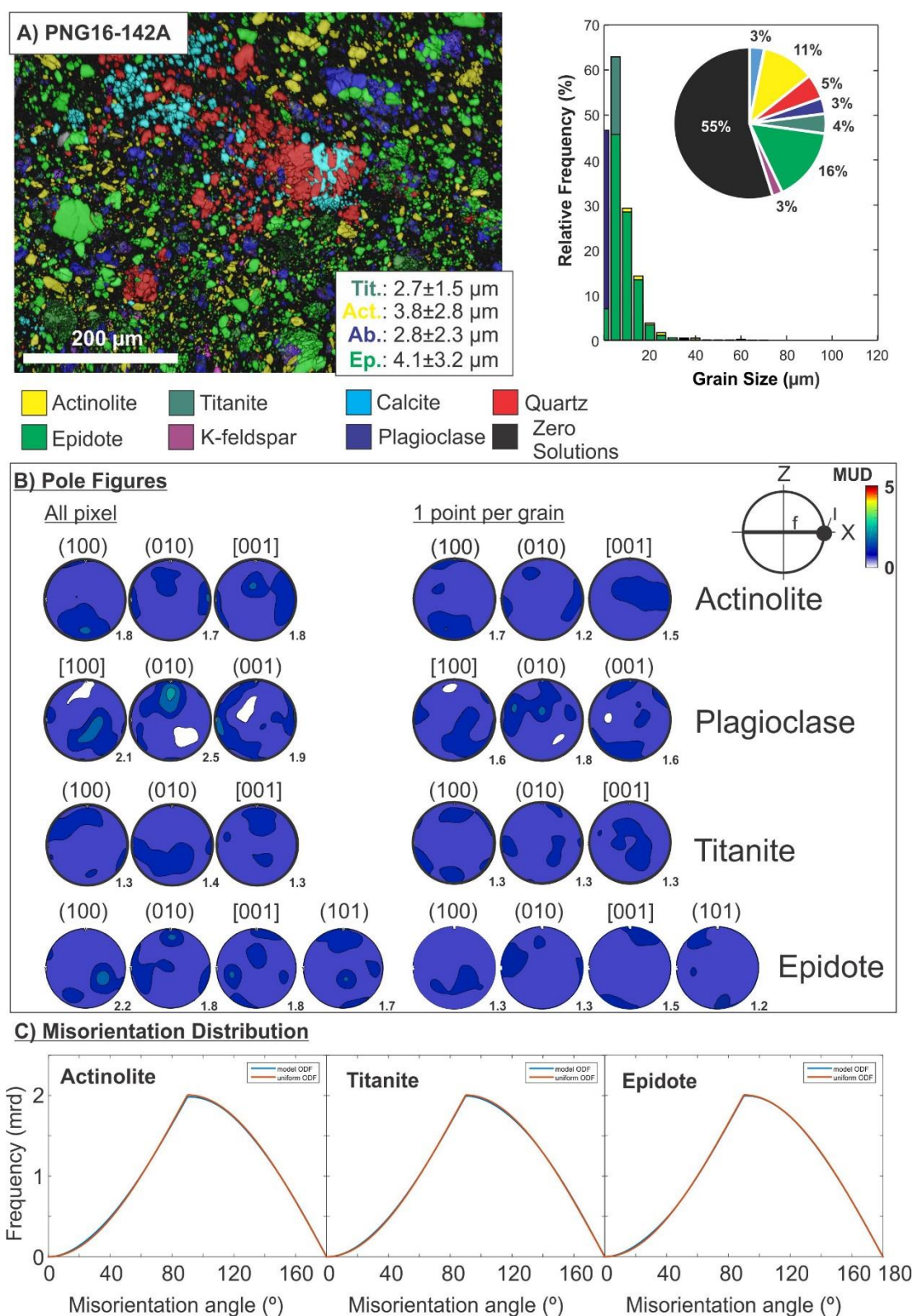


Figure B.25. EBSD analysis of gouge sample PNG16-142A (active Mai'iu fault trace). A) Phase map, grain size distributions and phase fraction (%). B) Contoured pole figures; left—based on all pixels; right—based on one point per grain. C) Misorientation distribution plots. MUD—Multiples of uniform distribution; ODF—Orientation density functions.

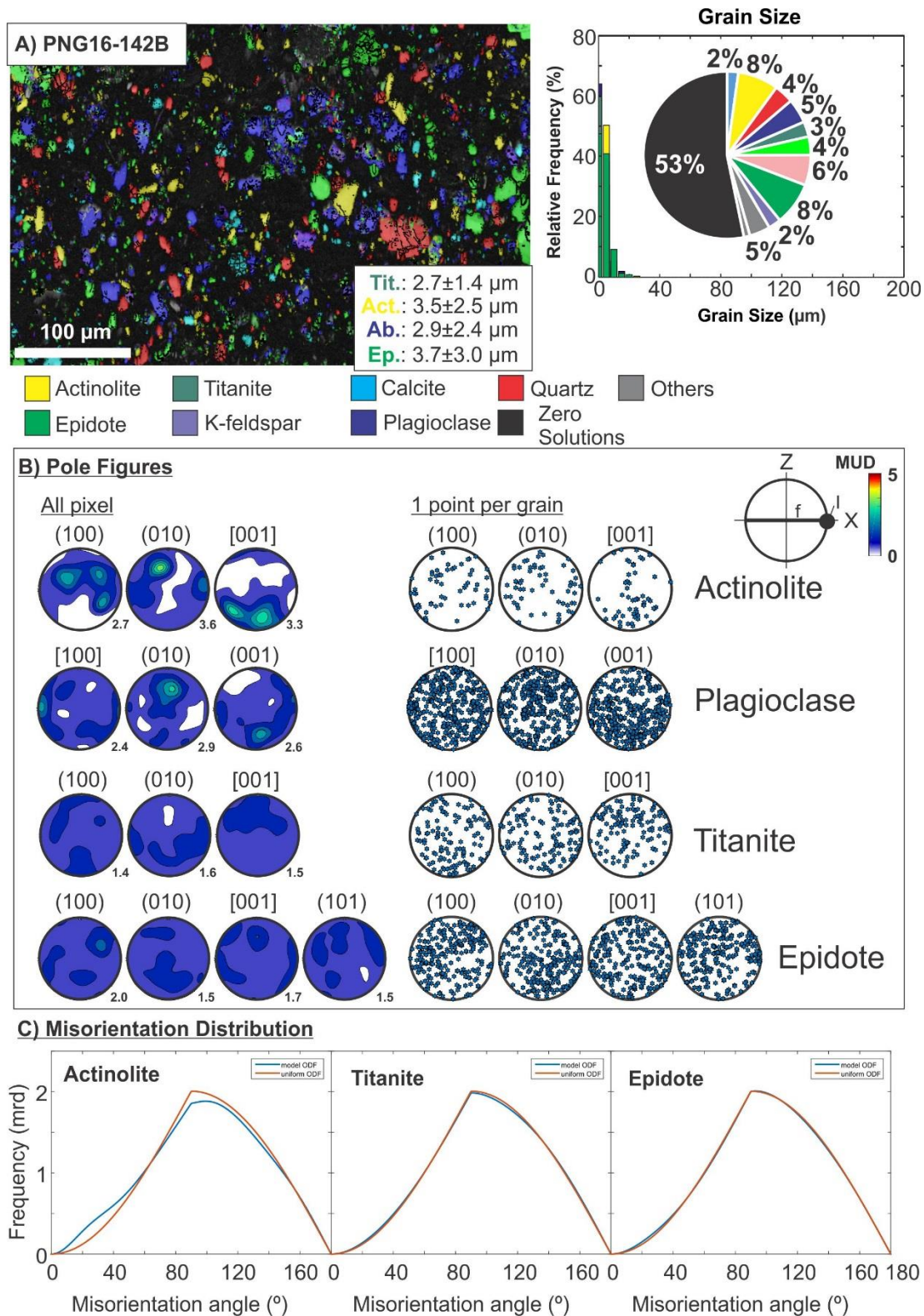


Figure B.26. EBSD analysis of gouge sample PNG16-142B (active Mai'iu fault trace). A) Phase map, grain size distributions and phase fraction (%). B) Pole figures; left—contoured, based on all pixels; right—based on one point per grain. C) Misorientation distribution plots. MUD—Multiples of uniform distribution; ODF—Orientation density functions.

Non-mylonitic mafic schists:

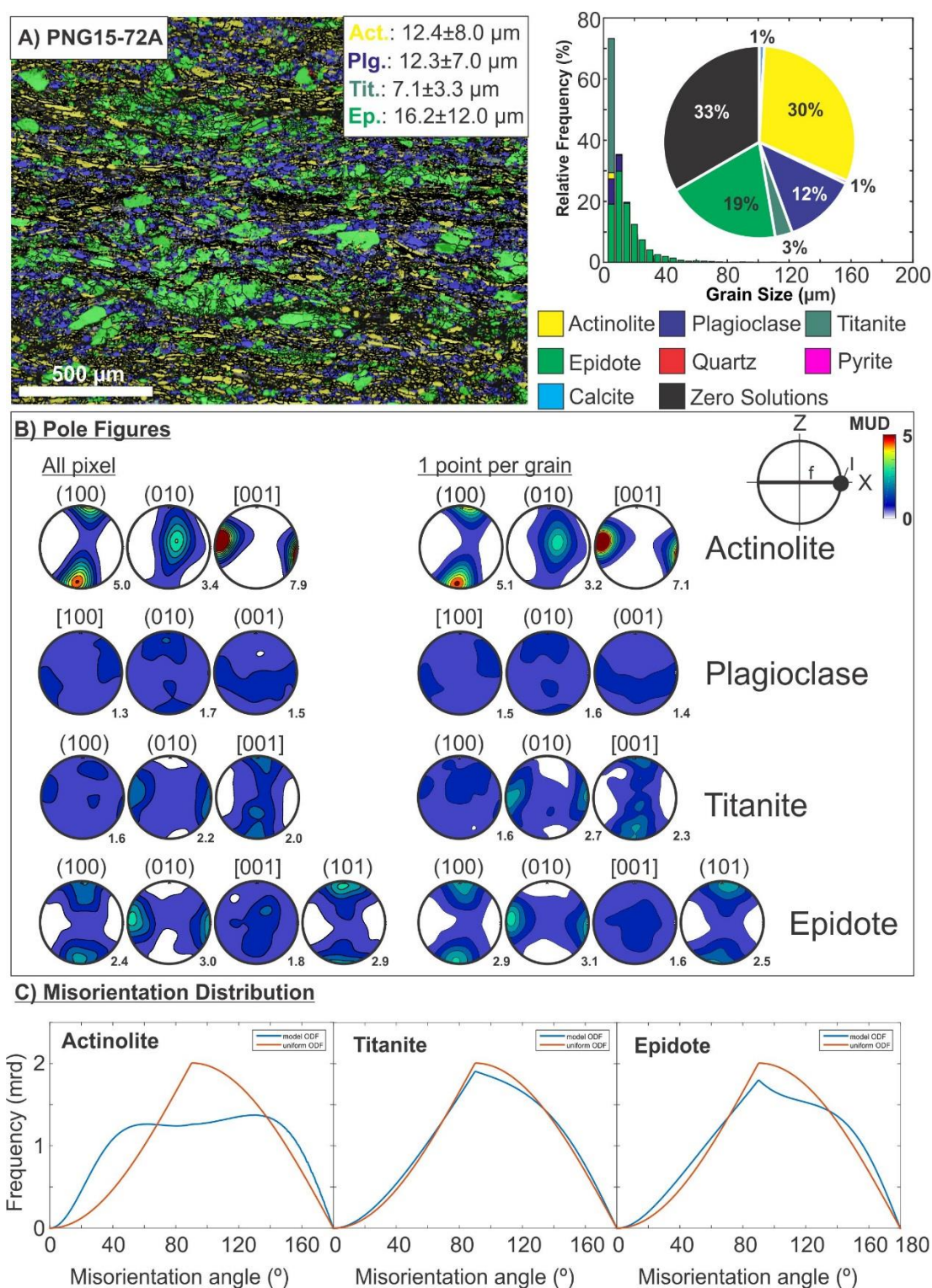


Figure B.27. EBSD analysis of a non-mylonitic schist (PNG15-72A). A) Phase map, grain size distributions and phase fraction (%). B) Contoured pole figures; left—based on all pixels; right—based on one point per grain. C) Misorientation distribution plots. MUD—Multiples of uniform distribution; ODF—Orientation density functions.

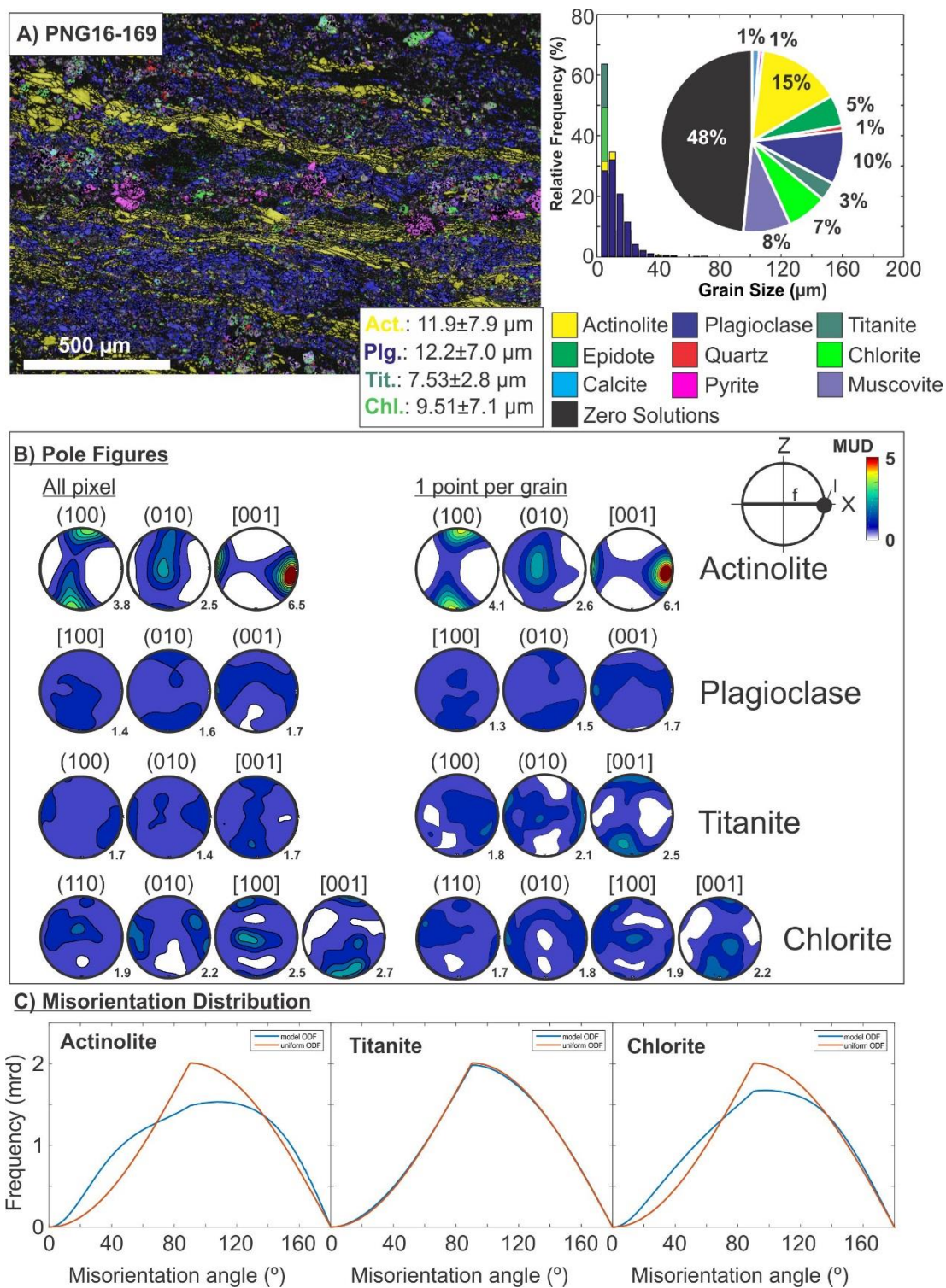


Figure B.28. EBSD analysis of a non-mylonitic schist (~5.7 km south of the active Mai'iu fault trace; PNG16-169). A) Phase map, grain size distributions and phase fraction (%). B) Contoured pole figures; left—based on all pixels; right—based on one point per grain. C) Misorientation distribution plots. MUD—Multiples of uniform distribution; ODF—Orientation density functions.

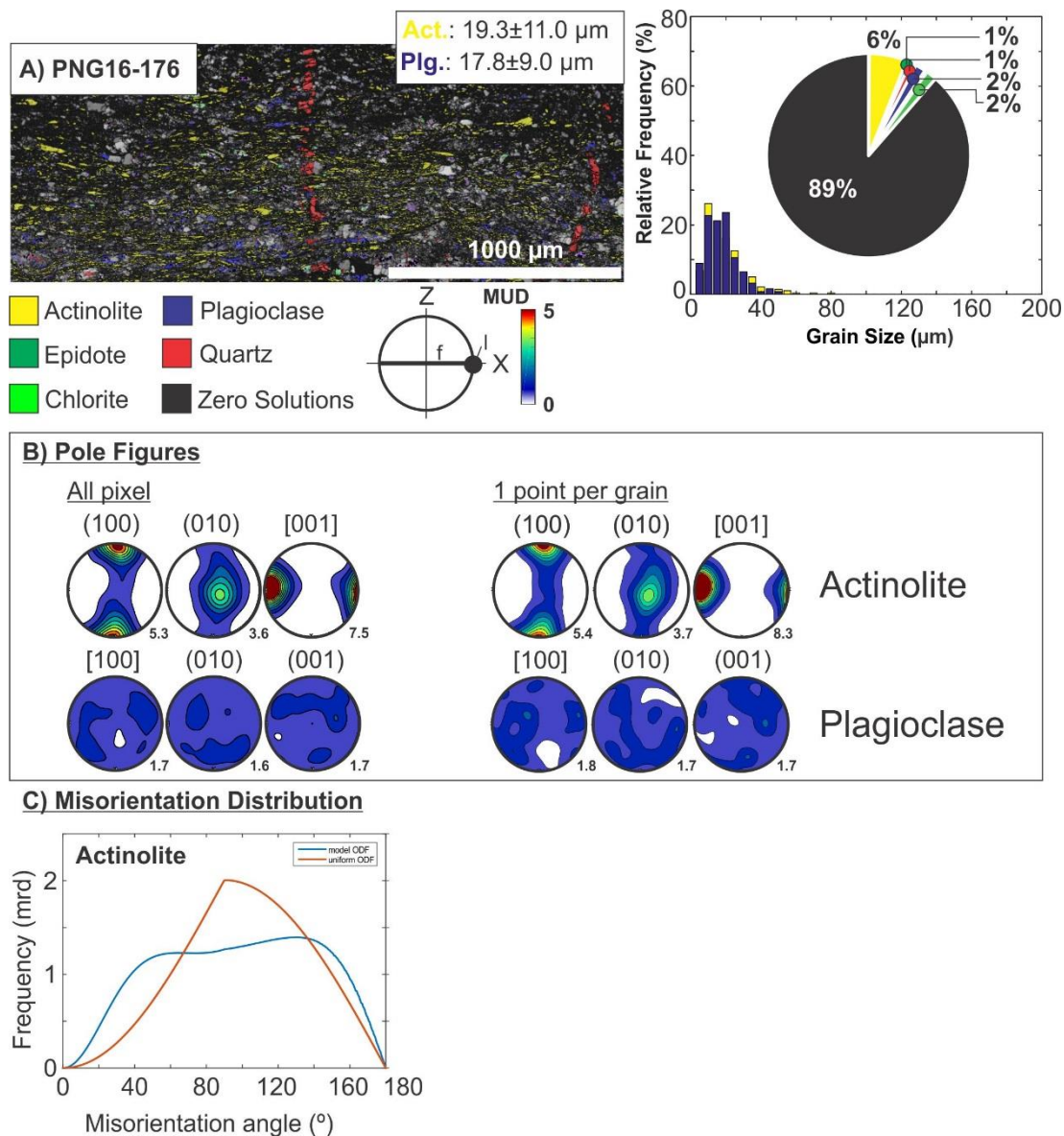


Figure B.29. EBSD analysis of a non-mylonitic schist (~4.5 km south of the active Mai'iu fault trace; PNG16-176). A) Phase map, grain size distributions and phase fraction (%). B) Contoured pole figures; left—based on all pixels; right—based on one point per grain. C) Misorientation distribution plots. MUD—Multiples of uniform distribution; ODF—Orientation density functions.

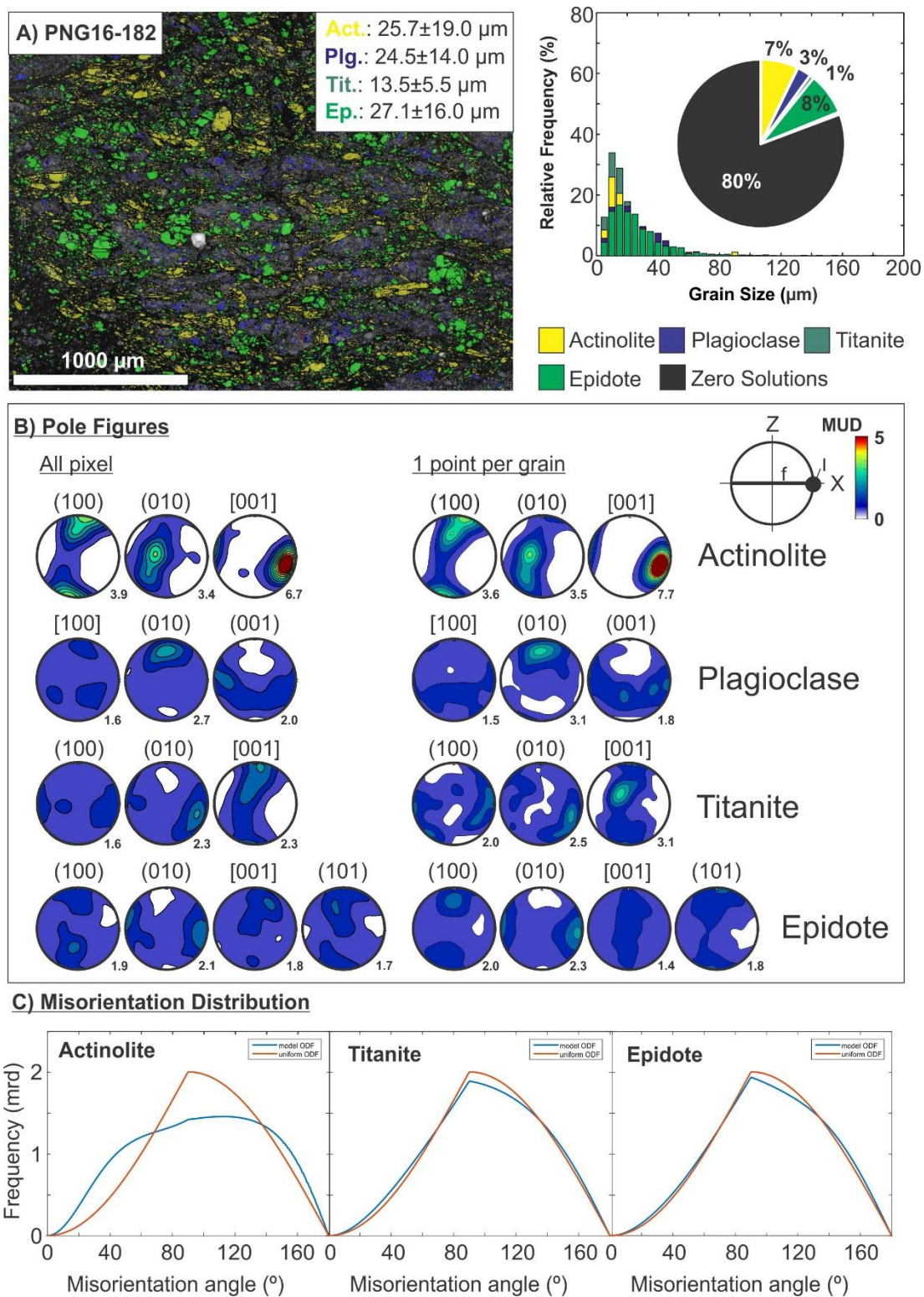


Figure B.30. EBSD analysis of a non-mylonitic schist (~1.8 km south of the active Mai'iu fault trace; PNG16-182). A) Phase map, grain size distributions and phase fraction (%). B) Contoured pole figures; left—based on all pixels; right—based on one point per grain. C) Misorientation distribution plots. MUD—Multiples of uniform distribution; ODF—Orientation density functions.

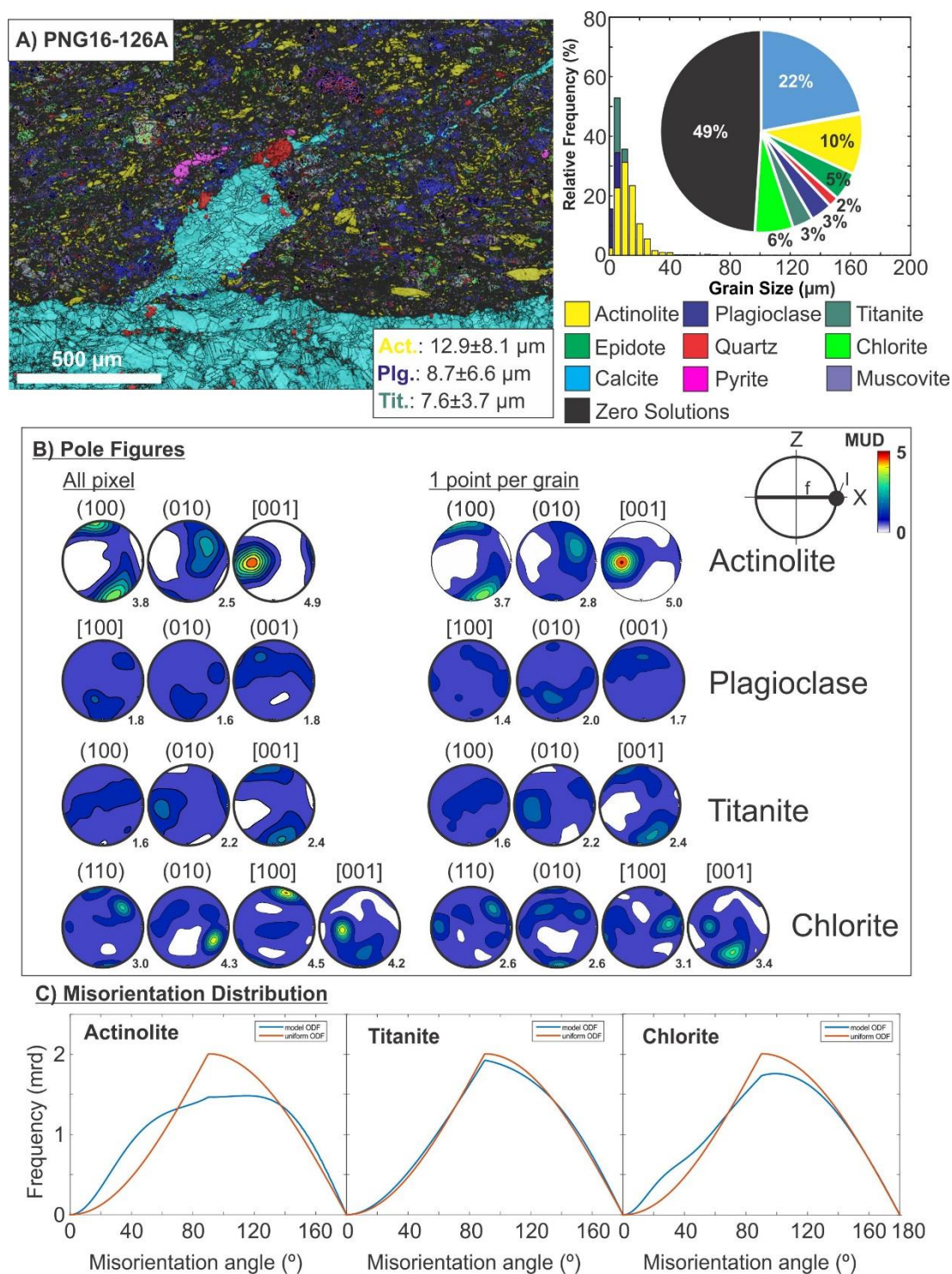


Figure B.31. EBSD analysis of a non-mylonitic schist (just south of active(?) Mai'iu fault trace, close to Gwoira fault; PNG16-126A). A) Phase map, grain size distributions and phase fraction (%). B) Contoured pole figures; left—based on all pixels; right—based on one point per grain. C) Misorientation distribution plots. MUD—Multiples of uniform distribution; ODF—Orientation density functions.

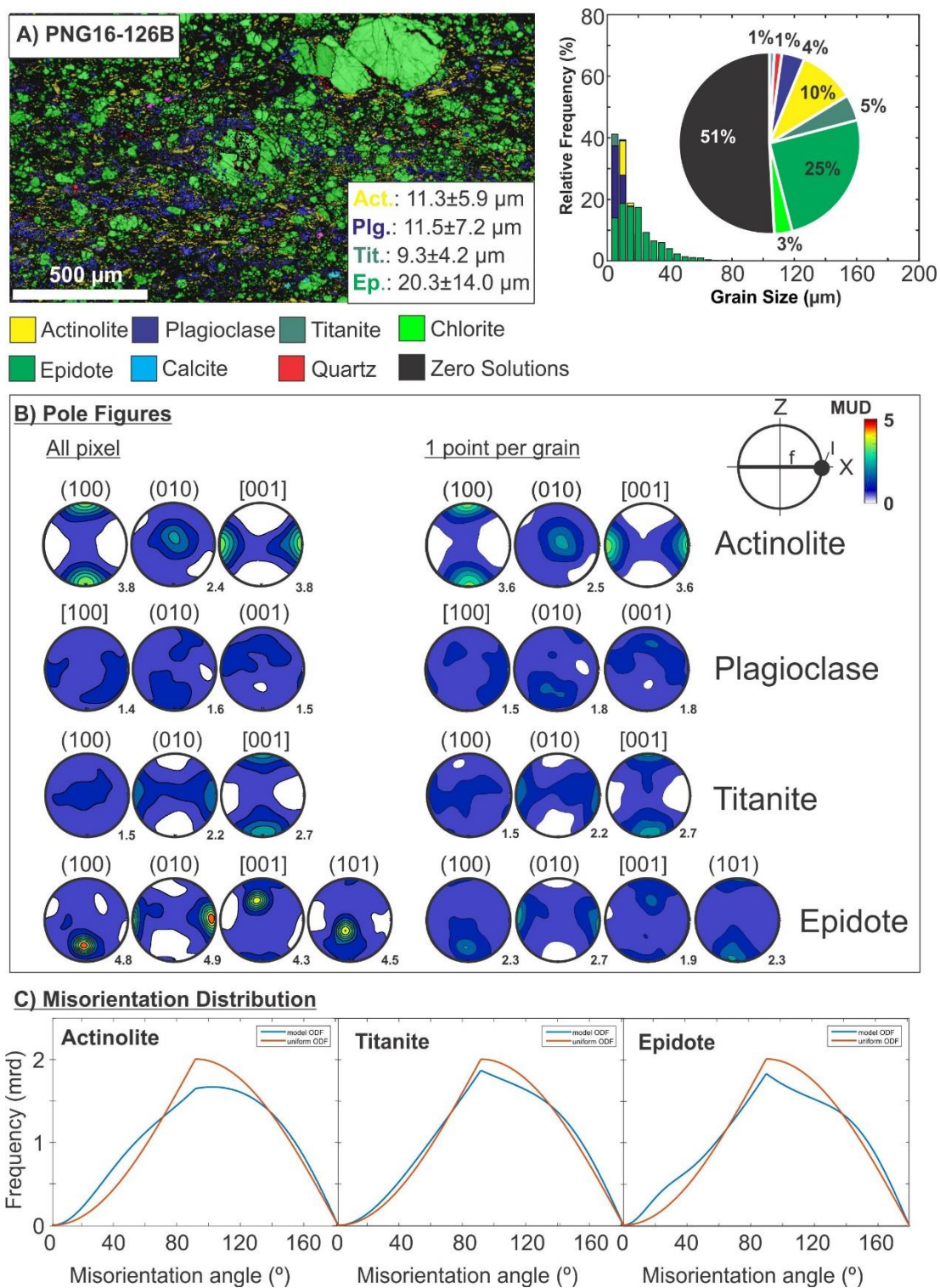


Figure B.32. EBSD analysis of a non-mylonitic schist (just south of active(?) Mai'iu fault trace, close to Gwoira fault; PNG16-126B). A) Phase map, grain size distributions and phase fraction (%). B) Contoured pole figures; left—based on all pixels; right—based on one point per grain. C) Misorientation distribution plots. MUD—Multiples of uniform distribution; ODF—Orientation density functions.

B.5 Recrystallized Quartz Grain Size Paleopiezometry

The recrystallized grain size of a mineral is a function of differential stress and can be quantified from EBSD maps (e.g., Halfpenny et al., 2006; Valcke et al. 2014; Cross et al., 2017). We followed the recommendation by Cross et al. (2017) to quantify grain-sizes and define recrystallized grains: (1) the step-size of collected EBSD maps is smaller than one fifth the diameter of the smallest recrystallized grains; (2) the grain orientation spread (GOS) was used to separate relict and recrystallized grains in both quartz and calcite veins; (3) a threshold GOS value that separates relict from recrystallized grains was calculated from trade-off curves for the cumulative number of grains versus the GOS; and (4) the two-dimensional recrystallized grain size (diameter of a circle with equivalent area) was calculated for every grain by applying the MTEX script “RexRelict.m” by Cross et al. (2017). Input values for the outlined data-processing method is given for each EBSD map in **Table B.8**.

Cross et al. (2017) calibrated the “original” recrystallized grain size piezometer for quartz by Stipp and Tullis (2003) for EBSD data acquisition. Differential stresses (σ_{Diff}) were calculated with the “sliding resolution” piezometer relationship by Cross et al. (2017) that combines 1 μm step-size data at coarser grain sizes with 200 nm step-size data at finer grain sizes:

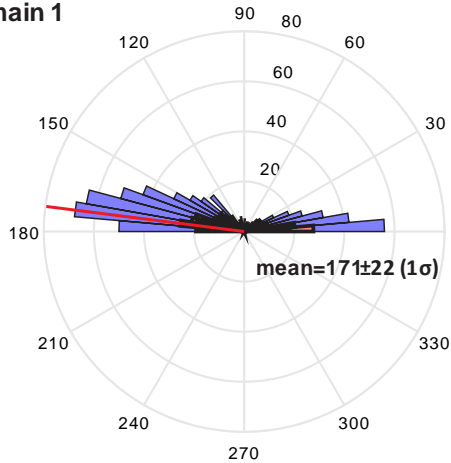
$$D_{RMS} = 10^{4.22 \pm 0.51} \cdot \sigma_{Diff}^{-1.59 \pm 0.26}, \quad (\text{Eq. B.2})$$

where D_{RMS} is the root-mean-square (RMS) mean diameter of recrystallized quartz grains. Results are shown in **Table B.8**. MTEX scripts can be found in the Digital Appendix under the folder ‘MTEX’.

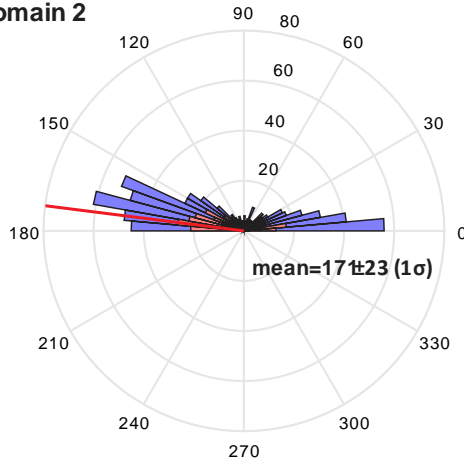
Table B.8. Calculated differential stresses based on the recrystallized grain-size of quartz using the paleopiezometer equation Eq. B.2. All samples were collected from outcrops just couple of meters south of the active Mai'iu fault trace. The grain orientation spread (GOS)—the average degree of intracrystalline lattice distortion proportional to dislocation density in each grain—was used to separate relict and recrystallized (ReX) grains in the quartz veins (see Cross et al., 2017). The data was collected with EBSD and processed with a modified version of the MTEX script “RexRelict.m”. D_{RMS} — root-mean-square mean diameter of recrystallized quartz grains.

Sample# PNG	Subset (Domain)	GOS Threshold	Step Size	Total No. of grains	No. of relict Grains	No of ReX Grains	D_{RMS} (μm)	σ_{Diff} (MPa)
16-140CJS	1.1	2.05	0.5	950	245	705	8.4 \pm 3.4	119 \pm 10
16-140CJS	1.2	2.2	0.5	918	234	684	9.7 \pm 4.6	108 \pm 6
16-140CJS	1.3	1.7	0.5	698	205	493	8.7 \pm 3.6	116 \pm 9
16-1BW-E	1.1	1.45	0.5	1209	352	857	6.7 \pm 4.2	136 \pm 19
16-1BW-E	1.2	1.55	0.5	1017	322	695	8.0 \pm 4.6	122 \pm 12
15-76C	1	1.8	0.5	1645	270	1375	9.8 \pm 6.3	108 \pm 6

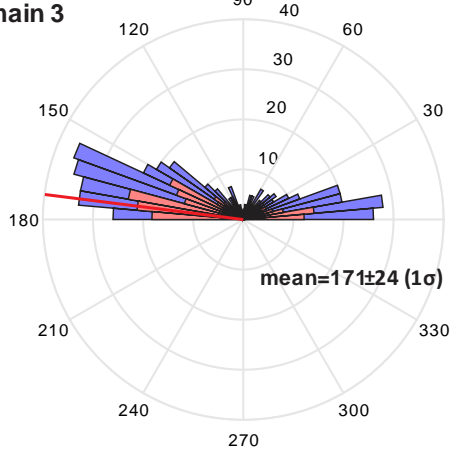
**A) PNG16-140C-JS
Domain 1**



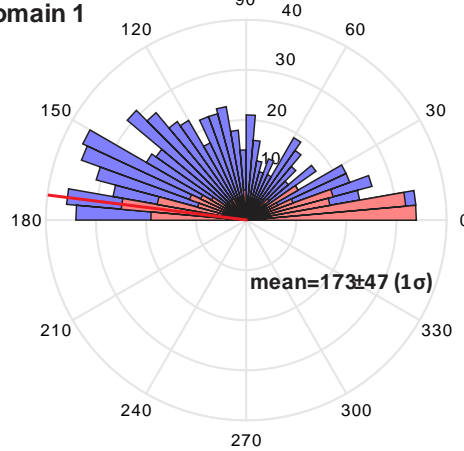
**B) PNG16-140C-JS
Domain 2**



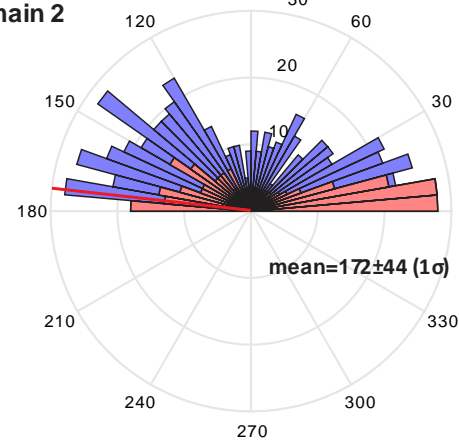
**C) PNG16-140C-JS
Domain 3**



**D) PNG16-1BW-E
Domain 1**



**E) PNG16-1BW-E
Domain 2**



F) PNG15-76C

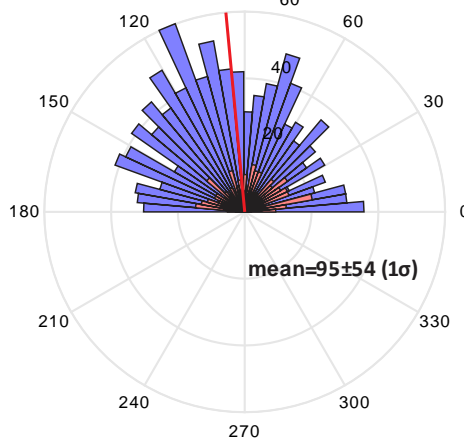


Figure B.33. Shape preferred orientation (SPO) analysis of recrystallized (blue) and relict (red) quartz grains using MTEX. The numbers around the rose diagrams can be interpreted as follows: 0: parallel to the (normal-sense) stretching lineation of the mafic mylonites (parallel to the kinematic X-direction); 90: orthogonal to the stretching lineation (kinematic Z-direction). Bin width is 5°. A-C) Sample PNG16-140C-JS shows a sharp SPO that is consistent with top-to-the-south sense of shear (thrust sense). Relict grains in this samples are variably folded. D-E) Sample PNG16-1BW-E shows a SPO that is consistent with top-to-the-south sense of shear (thrust sense). F) Sample PNG15-76C is an albite- and quartz-rich vein. A SPO is not evident.

B.6 Temperature-Dependent Magnetic Susceptibility Experiment on Ultracataclasite

Temperature-dependent magnetic susceptibility experiments were conducted on the ultracataclasite sample PNG16-142D on a Bartington MS2 furnace system at the paleomagnetic laboratory at the School of Chemical and Physical Sciences, Victoria University of Wellington, in order to determine the Curie temperature(s) of the constituent ferromagnetic/ferrimagnetic phase(s) and therefore the magnetic mineralogy of this sample. We crushed the sample to a fine powder with mortar and pestle and extracted ~3.5 g of material for the sample holder. The extracted material was heated and cooled and its magnetic susceptibility was monitored throughout this process. The magnetic susceptibility was measured once the material in the sample holder reached 40°C, with measurements taken every 10°C. A peak temperature of 700°C was set for the experiment, before cooling back to 40°C. The results of this experiment are shown in **Figure B.34** and additional SEM back-scatter images and EDS analyses of the ultracataclasite (PNG16-142D) and magnetite-bearing veins and clasts in **Figure B.35**, **Figure B.36**, **Figure B.37** and **Figure B.38**.

The thermomagnetic curves of the ultracataclasite sample are nearly reversible suggesting that no alteration has occurred to the magnetic mineralogy and none of the paramagnetic phases have altered into ferromagnetic/ferromagnetic ones during the course of the experiment to temperatures of 700°C and pressures at 1 atm (**Figure B.34**). During heating we observe an almost linear increase in magnetic susceptibility up to 380°C, above where the magnetic susceptibility shows a sharp linear increase up to 480°C. A peak with little variation of magnetic susceptibility is evident between 490 and 520°C just below the magnetite Curie point (Hopkinson peak). The susceptibility curve shows a strong drop from ~540°C down to 580°C and shallows to a Curie temperature of ~620–640°C close to the one of maghemite ($T_C \approx 645^\circ\text{C}$; Özdemir, 1990; Dunlop & Özdemir, 1997). The cooling run is below the heating run and shows a sharp increase in magnetic susceptibility from ~600°C to 500°C and reaches a plateau at ~480°C. The susceptibility drops again at ~450°C and the curve starts to flatten around ~300°C. We infer from this experiment that the principal magnetic mineral in the ultracataclasite is a stable (reversible heating and cooling curves), single domain (fine grained) magnetite. The observed Curie temperature

above 580°C and below 645°C indicates cation deficient magnetite, slightly oxidized to maghemite (Özdemir & Banerjee, 1984; Dunlop & Özdemir, 1997).

Temperature-dependent magnetic susceptibility

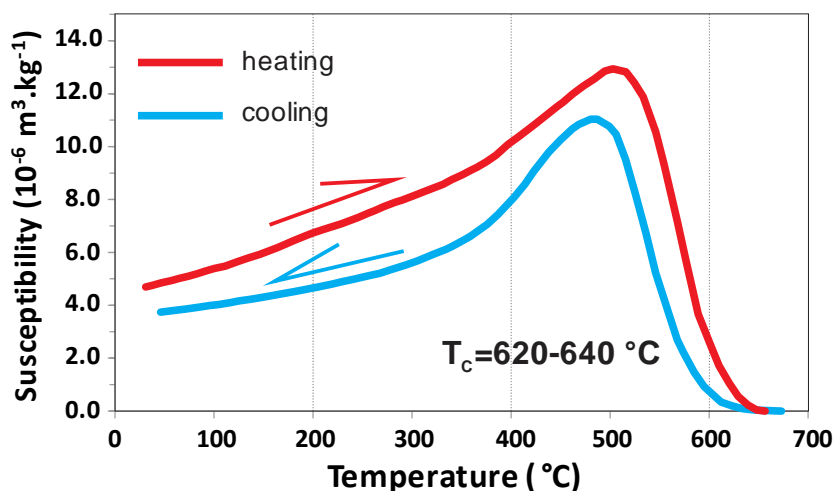


Figure B.34. Curves of temperature dependant magnetic susceptibility for sample PNG16-142D (ultracataclasite). The red and blue lines denote heating and cooling, respectively, from 40°C to 700°C and vice versa. T_C refers to the Curie temperature.

SEM-EDS analyses show that magnetite can be found in veins in association with fractured ultracataclasite, veins within the non-fractured ultracataclasite, and coating of and/or swirled into rounded fragments of ultracataclasite (**Figure B.35**). Single, μm -sized magnetite grains are rare in the ultracataclasites; if preserved they show alteration towards maghemite with Ti-rich rims. Elemental analyses of the fine-grained magnetite-bearing veins are ambiguous; all analysed veins show high concentrations of Fe and small amounts of Ti, Si, K, Al and Mg (**Figure B.36**, **Figure B.37**). We infer that the magnetite in the veins is too small ($<1\ \mu\text{m}$), in part altered and intermingled with the smectitic ultracataclasite matrix to be unambiguously identified with EDS.

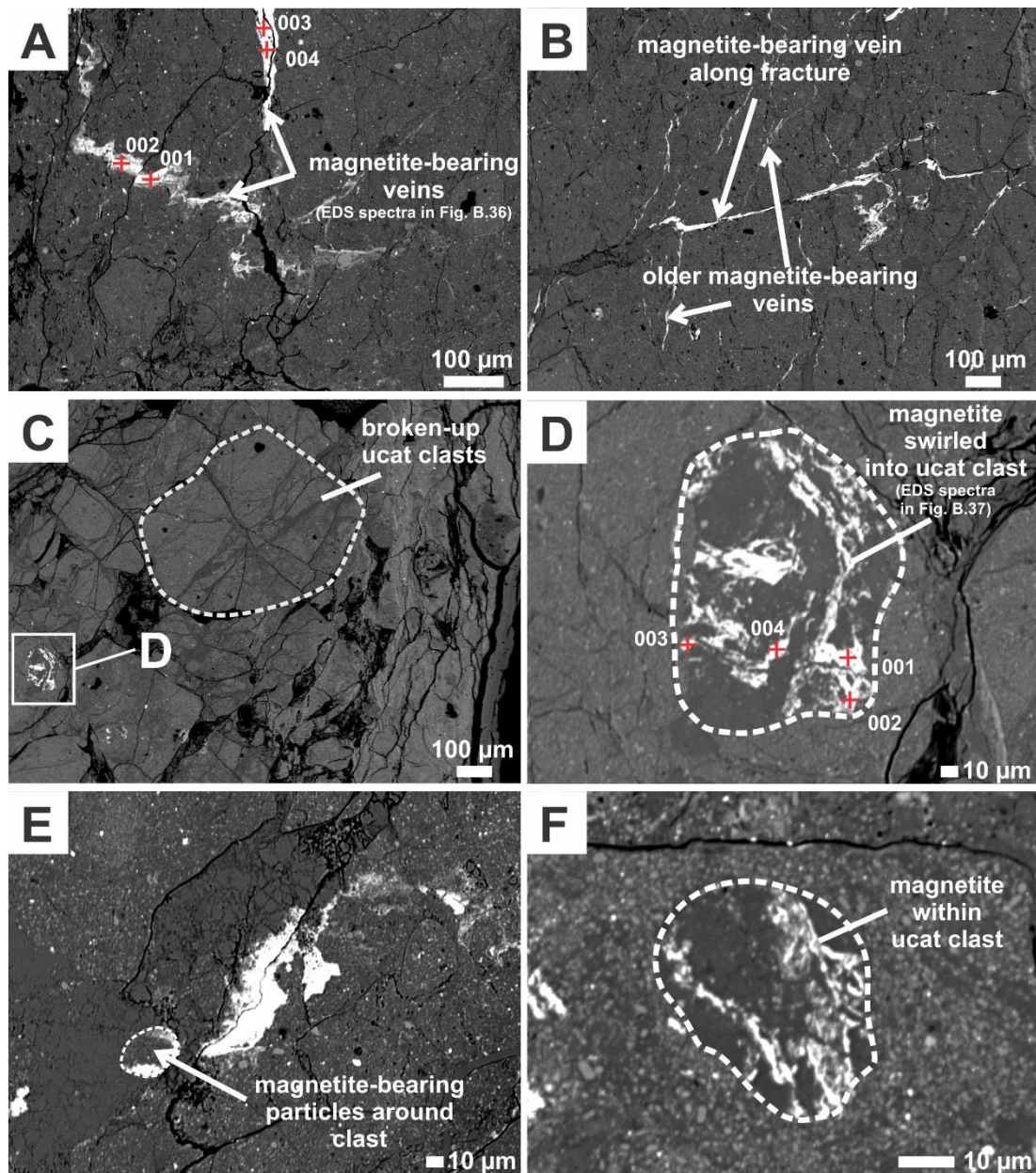


Figure B.35. Back-scatter images of magnetite-bearing veins and clasts in ultracataclasite (PNG16-142D). A) Magnetite in veins in association with fractured ultracataclasite and within the non-fractured ultracataclasite. Sample spots for the EDS analysis are indicated by red crosses. The spectra can be seen in **Figure B.36**. B) Magnetite-bearing veins along fractures in the ultracataclasite. C) Broken ultracataclasites clast and an older, reworked clast with magnetite-bearing veins. D) Close up of C. This close-up shows the magnetite-bearing veins are in somewhat 'swirled' within the clast. Sample spots for the EDS analysis in **Figure B.38** are indicated by red crosses. E) Magnetite-bearing particles surround a small clast. F) Magnetite within a ucat clast.

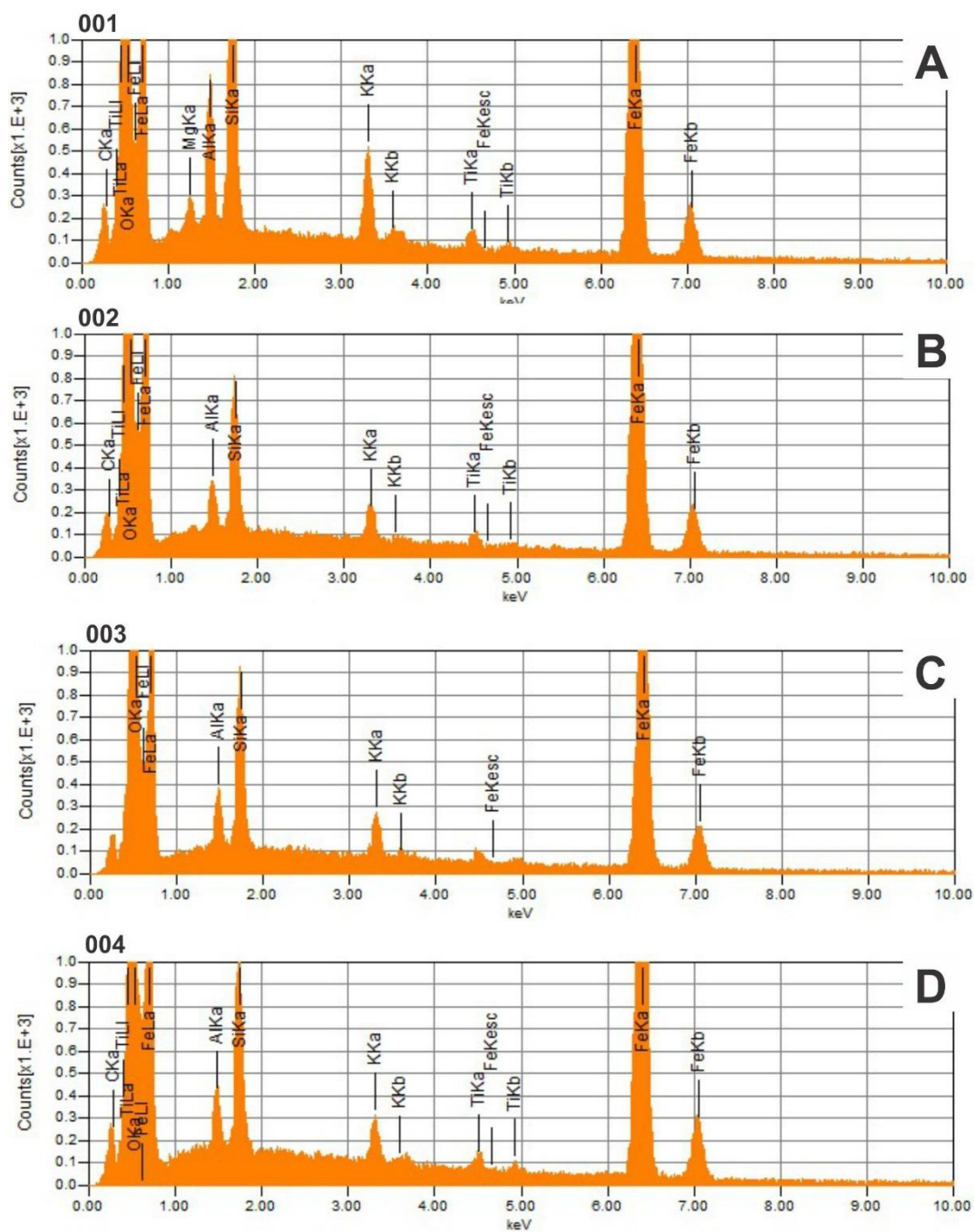


Figure B.36. A-D) EDS-spectra of magnetite-bearing veins in **Figure B.35A** (PNG16-142D).

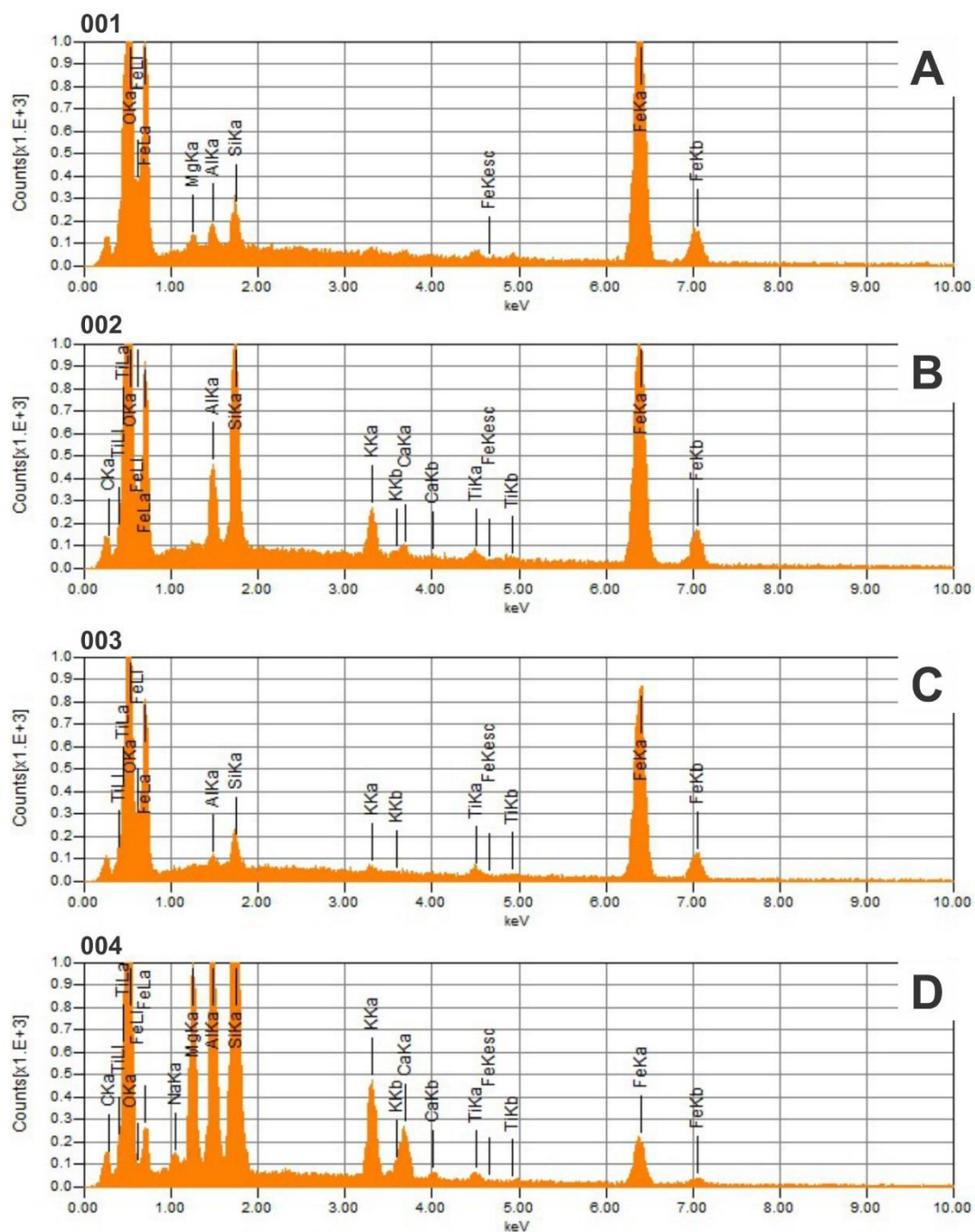


Figure B.37. EDS-spectra of a magnetite-bearing clast in **Figure B.35D** (PNG16-142D).

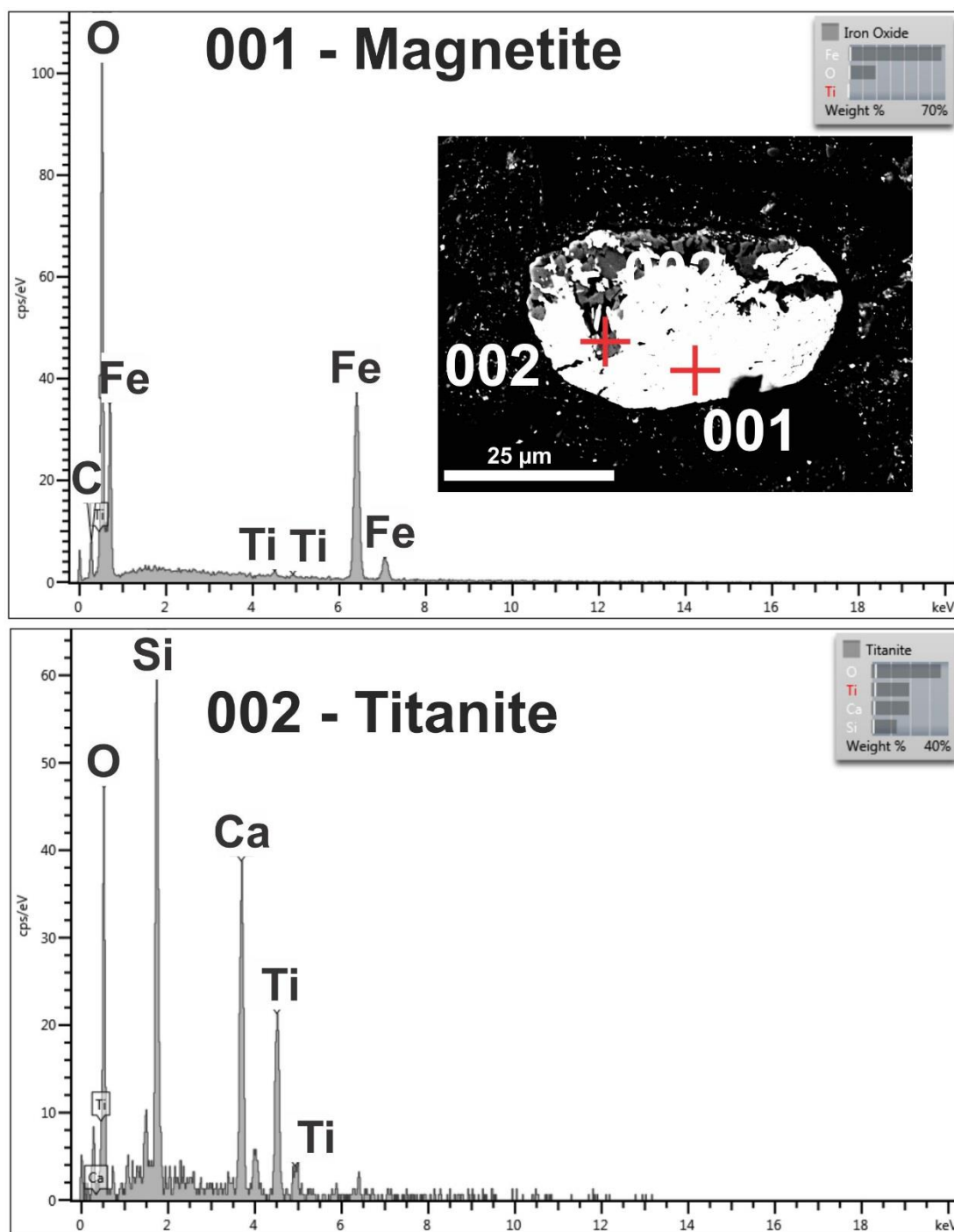


Figure B.38. EDS analysis of a single magnetite grain in the ultracataclasite matrix (PNG16-142D).

B.7 TEM Analysis of a Mirror-like Facet on Gabbroic Clast

The hangingwall contact atop the Mai'iu fault truncates cm- to dm-sized pebbles and cobbles in the Gwoira Conglomerate. A suite of samples has been collected in the field, from which we have analyzed one dolerite with TEM (**Figure 3.10**) in order to describe the composition, thickness and grain-size of the shiny, fault-truncated surface, and the origin of striation on these surfaces. A TEM foil was cut perpendicular to the

shiny surface (**Figure 3.10D**) and was prepared using a FEI Quanta 3D FEG-SEM with focused ion beam (FIB) at University of Vienna, Department of Lithospheric Research. TEM used a JEOL 2011 STEM equipped with a double-tilt analytical holder and a Gatan MSC digital camera for imaging at the University of New Brunswick, Microscopy and Microanalysis Facility. The results of this method are presented in Chapter 3.4.2.

B.8 Raman spectroscopy

Raman mapping on sample PNG16-17G that contains suspicious silica patches was conducted with an Alpha 300R+ confocal Raman microscope (Witec GmbH, Ulm, Germany) using a 100x dry objective (Zeiss, Germany) and a 532 nm laser (Coherent, California) with a power of 5.0 mW at the University of Otago, Department of Chemistry. The Raman microscope was equipped with a piezoelectric and mechanical stage. The spatial resolution of this setup is ~370 nm as validated by Rooney et al. (2018). Calibration and optimisation of the microscope with a silicon wafer was carried out before mapping to verify the position and intensity of the Si band at 520.6 cm^{-1} . Raman spectra were acquired on a polished thin section slide of sample PNG16-17G (uncovered) in a square grid pattern using a step size of 360 nm and an acquisition time of 2 s per point. A map with a dimension of $25\text{ }\mu\text{m} \times 25\text{ }\mu\text{m}$ comprise 4,761 spectra (69×69 sample points). The beam focus was 1–2 μm below the surface to ensure only unadulterated grains were measured. The acquired spectra were processed and analysed with the Witec Project Plus software. A multi-linear baseline correction was performed on the collected spectra.

Figure B.39 shows the result of Raman spectra imaging on a silica-rich patch in the fault gouge sample PNG16-17G (close to the inactive fault trace of the Mai'iu fault). Background noise in the baseline corrected spectrum is caused by residual carbon coating that was removed with methanol. The analysed silica patch in **Figure B.39** shows a broad, asymmetric band located between 325 cm^{-1} and 500 cm^{-1} . Raman bands on this broad feature are located at 383 cm^{-1} , 443 cm^{-1} and at on the shoulder at 485 cm^{-1} . Further bands are identified at 601 cm^{-1} , 800 cm^{-1} (broad peak), 970 cm^{-1} and 1076 cm^{-1} . A peak at 3731 cm^{-1} that is only evident in the raw spectrum might be related to O–H groups in these silica patches (Bertoluzza et al., 1982). The analysed silica-rich patch contains ~97% SiO_2 (**Figure B.39D**).

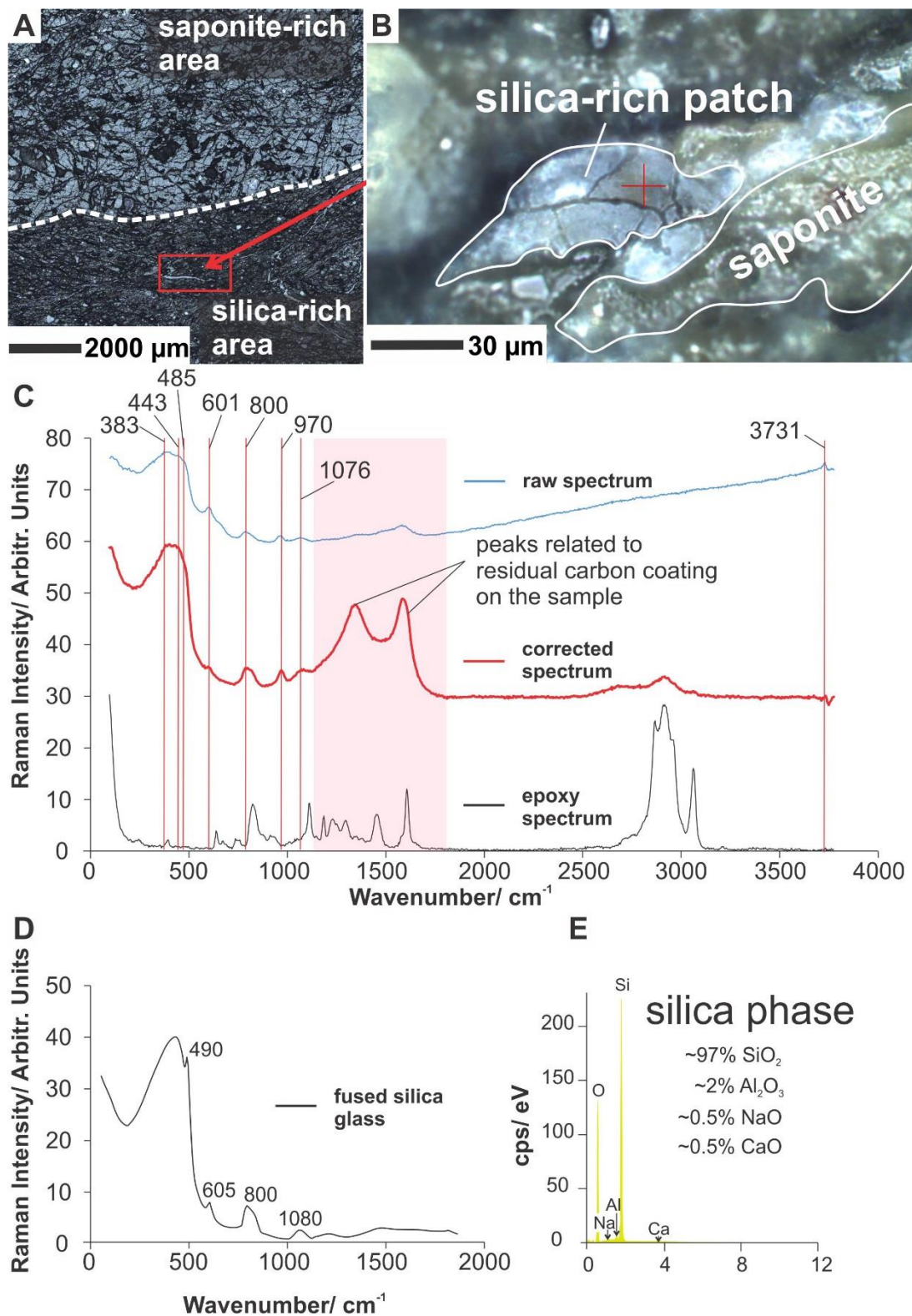


Figure B.39. A) Photomicrograph of sample PNG16-17G indicating two different domains (saponite-rich versus silica-rich domain). B) Close up of the silica-rich domain and area of collected Raman spectra. C) Collected Raman spectra including a raw spectrum, a baseline corrected spectrum and an epoxy spectrum. D) Raman spectrum of fused silica glass (here: wavelength: 780 nm; see also for comparison: Awazu & Kawazoe, 2003; Rossano & Mysen, 2012; Degioanni et al., 2015). E) EDS spectrum of the silica phase shown in **Figure 3.9D**.

B.9 XRD analysis on Mai'iu Fault Rocks

A collection of 15 fault rock samples comprising ultracataclasites, gouges and serpentinite were analysed with X-Ray Diffraction by Mark Raven at CSIRO Land and Water Flagship, Mineral Resources Flagship, at the Centre for Australian Forensic Soil Science (CAFSS), in Urrbrae, South Australia. For these, 1.5 g sub-samples were ground for 10 minutes in a McCrone micronizing mill under ethanol. The resulting slurries were oven dried at 60°C then thoroughly mixed in an agate mortar and pestle before being lightly pressed into aluminium sample holders for X-ray diffraction analysis. XRD patterns from the micronized materials showed variable hydration of the interlayer which causes problems with quantification. As the samples did not appear to contain any water soluble phases they were calcium saturated and the data re-analysed. XRD patterns were recorded with a PANalytical X'Pert Pro Multi-purpose Diffractometer using Fe filtered Co Ka radiation, auto divergence slit, 2° anti-scatter slit and fast X'Celerator Si strip detector. The diffraction patterns were recorded in steps of 0.016° 2 theta with a 0.4 second counting time per step, and logged to data files for analysis. **Table B.9** (below) lists the phases that were identified in each sample. These XRD-results are also published in Little et al. (2019), but are shown here as supporting information important for Chapter 3.

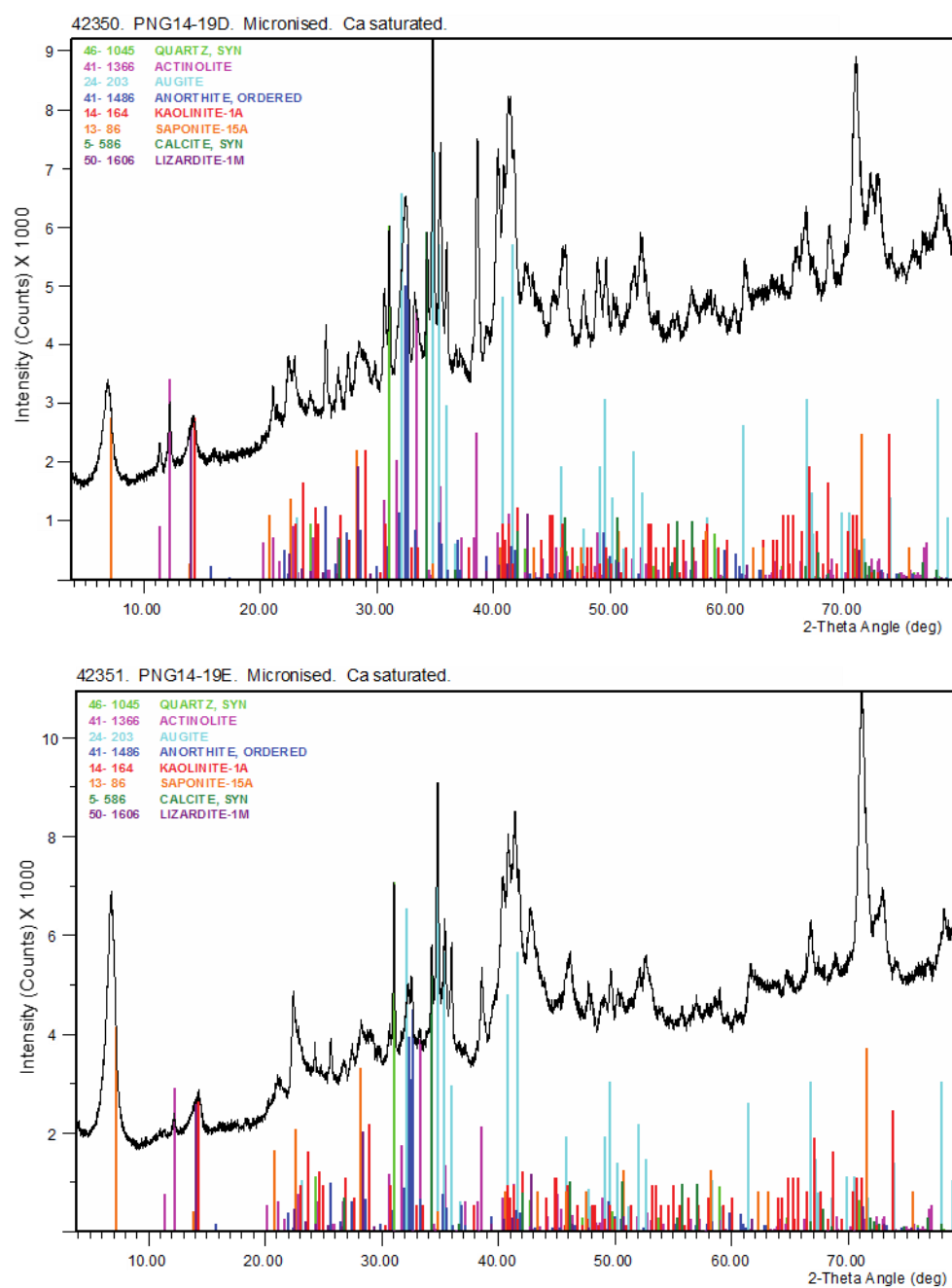
Table B.9. Mineral Phases in Mai'iu fault rocks determined by X-Ray Diffraction.

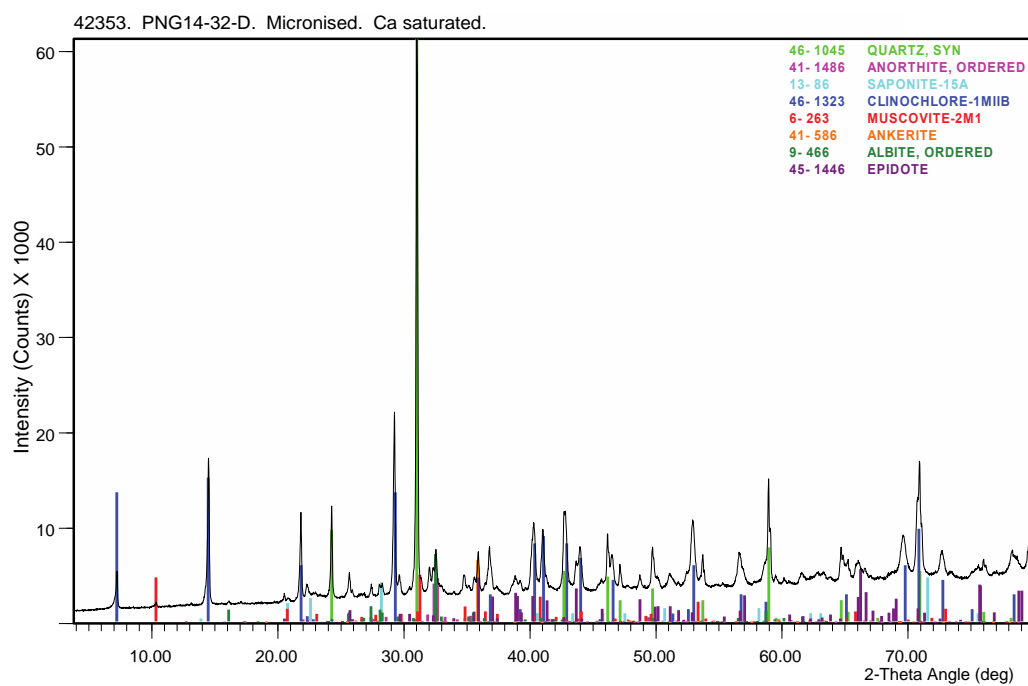
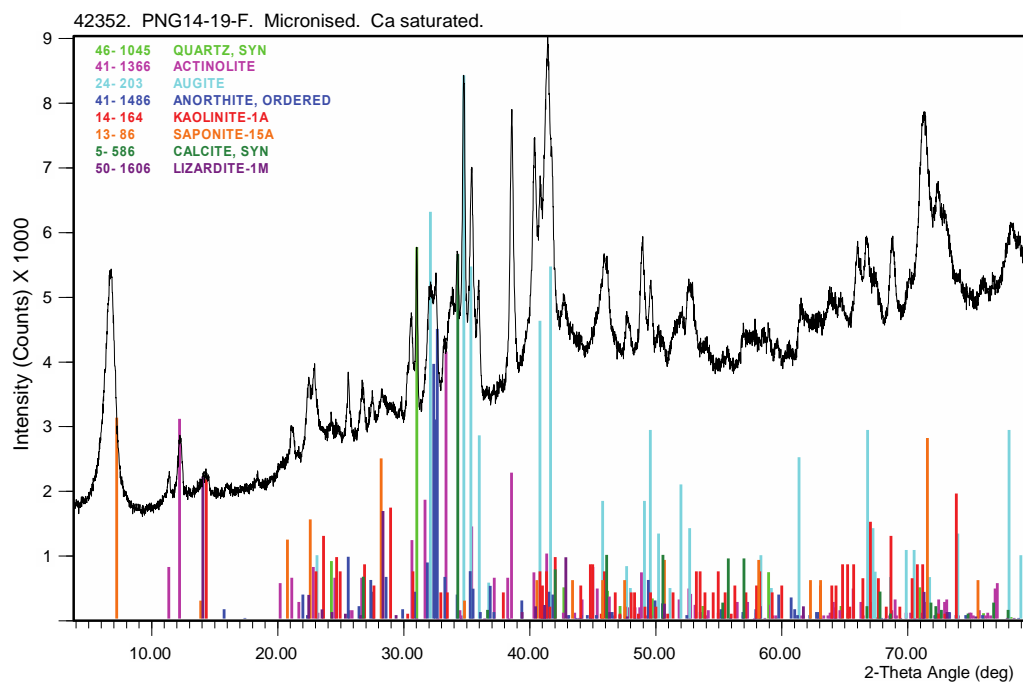
CSIRO ID	Field Sample No.	Fault Rock Unit	Fault	Degrees South (WGS84)	Degrees East (WGS84)
				Latitude	Longitude
42350	PNG-14-19-D	ultracataclasite	inactive Mai'iu F.	149.44082	-9.82862
42351	PNG14-19-E	gouge	inactive Mai'iu F.	149.44082	-9.82862
42352	PNG-14-19-F	gouge	inactive Mai'iu F.	149.44082	-9.82862
42353	PNG-14-32-D	gouge	Biniguni Splay F.	149.38230	-9.67883
42354	PNG-14-32-E-g	gouge	Biniguni Splay F.	149.38230	-9.67883
42355	PNG-14-32-E-r	gouge	Biniguni Splay F.	149.38230	-9.67883
42356	PNG-14-32-F	gouge	Biniguni Splay F.	149.38230	-9.67883
42357	PNG-14-33-A	gouge	active Mai'iu F.	149.35904	-9.67726
42358	PNG-14-33-B	gouge	active Mai'iu F.	149.35904	-9.67726
45070	PNG-15-50-B	ultracataclasite	active Mai'iu F.	149.28669	-9.67778
45071	PNG-15-70	serpentininite	active Mai'iu F.	149.61246	-9.82863
47041	PNG-16-17-C	ultracataclasite	inactive Mai'iu F.	149.44028	-9.82967
47042	PNG-16-30-B	gouge	inactive Mai'iu F.	149.44059	-9.82499
47043	PNG-16-108-G	gouge	active Gwoira F.	149.46712	-9.77150
47044	PNG-16-142-B	gouge	active Mai'iu F.	149.35913	-9.67729

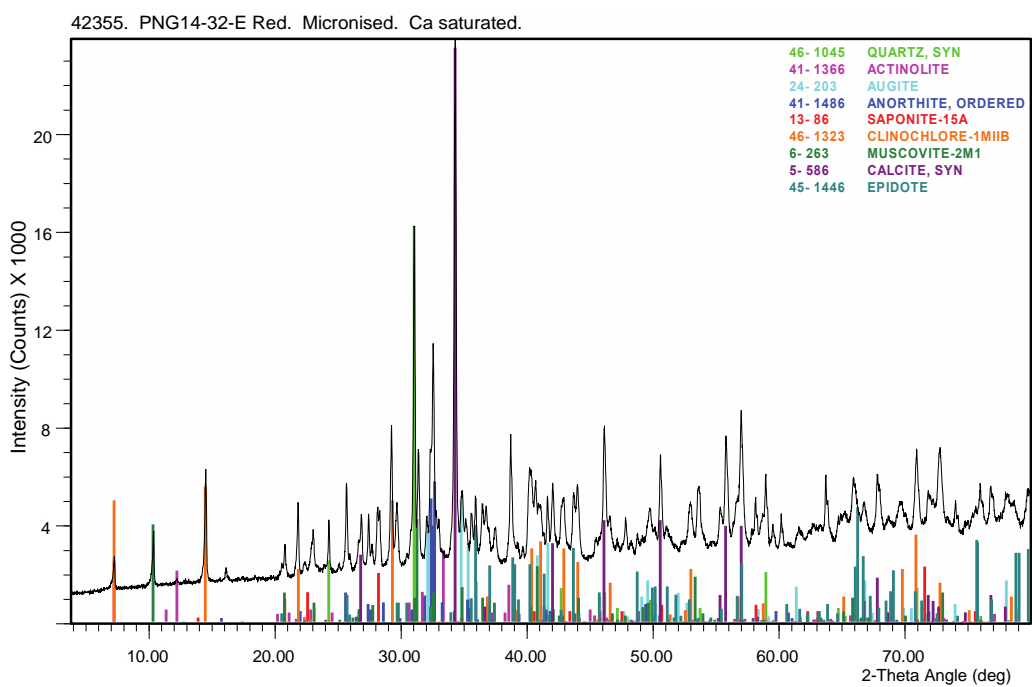
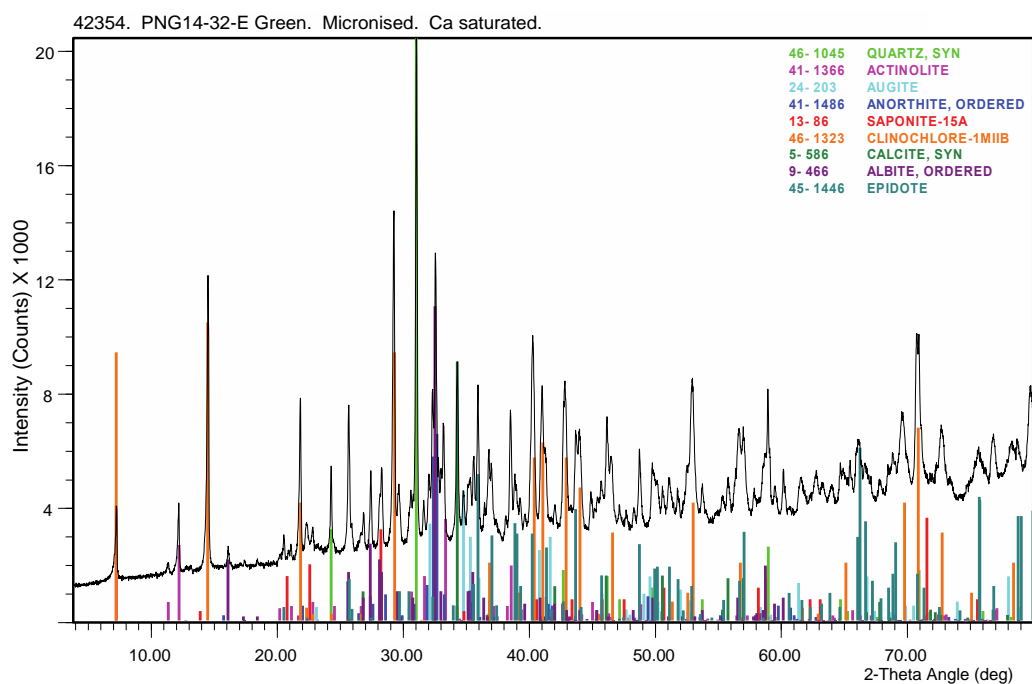
CSIRO ID	Notes
42350	Near lower transition into foliated cataclasite unit
42351	Upper of two gouge layers. Light grey, 1.5 cm thick
42352	Lower of of two gouge layers. Dark grey, 17 cm thick
42353	Porphyroclastic gouge layer 1m thick. Greenish grey.
42354	Green-colored gouge in variegated gouge layer >1 m thick
42355	Maroon-colored gouge in variegated gouge layer >1 m thick
42356	White-colored gouge in variegated gouge layer >1 m thick
42357	Lower of two gouge layers. Green, 10 cm thick.
42358	Upper of two gouge layers. Grey, 5 cm thick.
45070	Exhumed pavement surface at base of scarp
45071	Serpentinite fault slice structurally atop exhumed Mai'iu fault near Mt Masasoru
47041	Same fault outcrop as location PNG-14-19
47042	Upper gouge layer. Grey, 2 cm thick.
47043	Collected 21 cm below PDS
47044	Upper of two gouge layers. Purple-grey, 5 cm thick. Same as PNG-14-33-B

CSIRO ID	Whole Rock Mineralogy
42350	Corrensite/Saponite, Augite, Amphibole, Plagioclase, Kaolin, Calcite, Quartz
42351	Corrensite/Saponite, Augite, Amphibole, Plagioclase, Kaolin, Calcite, Quartz
42352	Corrensite/Saponite, Augite, Amphibole, Plagioclase, Kaolin, Calcite, Quartz
42353	Chlorite, Quartz, Epidote, Plagioclase, Mica, Titanite
42354	Chlorite, Plagioclase, Amphibole, Epidote, Quartz, Calcite, Titanite
42355	Calcite, Mica, Plagioclase, Epidote, Chlorite, Quartz, Titanite, Hematite, Amphibole
42356	Quartz, Chlorite, Mica, Plagioclase, Calcite, Epidote, Titanite, Amphibole, Hematite
42357	Plagioclase, Epidote, Amphibole, Corrensite/Saponite, Chlorite, Stilpnomelane, Titanite, Calcite, Quartz, K-feldspar
42358	Corrensite/Saponite, Calcite, Montmorillonite, Plagioclase, Epidote, K-feldspar, Amphibole, Quartz, Dolomite/Ankerite, Chlorite, Mica
45070	Corrensite, K-feldspar, Plagioclase, Amphibole, Augite, Chlorite, Calcite, Quartz
45071	Serpentine (Lizardite), Magnesite, Saponite, Quartz, Calcite, Dolomite/Ankerite, Maghemite
47041	Saponite, Amphibole, Plagioclase, Augite, Calcite, Chlorite, Quartz
47042	Saponite, Amphibole, Plagioclase, Augite, Calcite, Chlorite, Quartz
47043	Saponite, Amphibole, Plagioclase, Augite, Quartz, Chlorite, K-feldspar, Laumontite, Calcite, Magnesite
47044	Saponite, Plagioclase, Augite, Amphibole, Chlorite/Corrensite, Dolomite/Ankerite, Quartz, Calcite, Mica, Magnesite

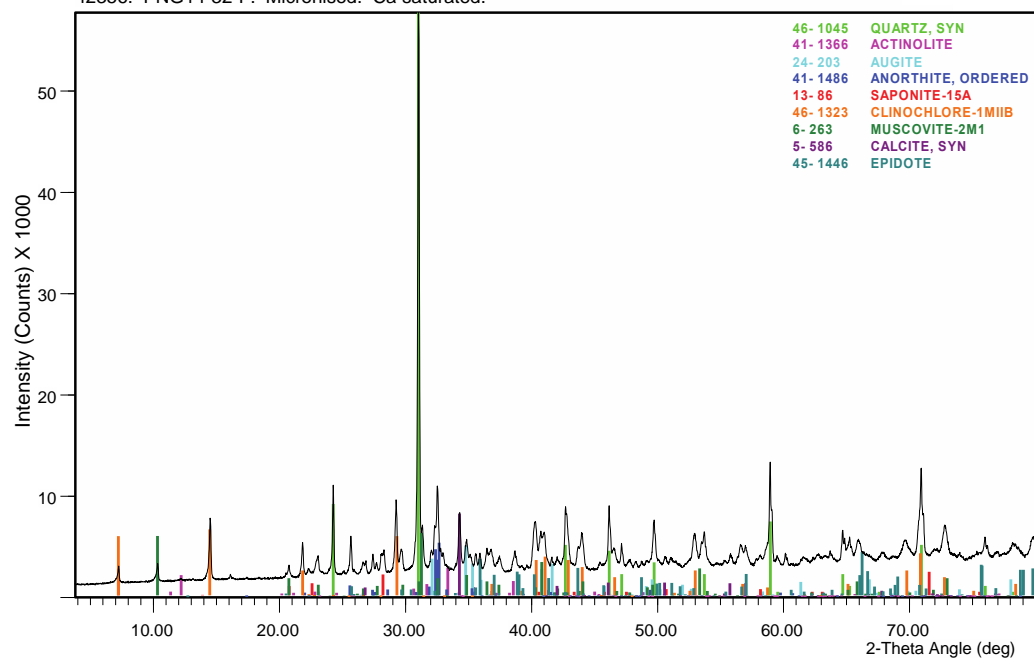
Figure B.40. Whole rock, Ca-saturated X-ray diffraction patterns.



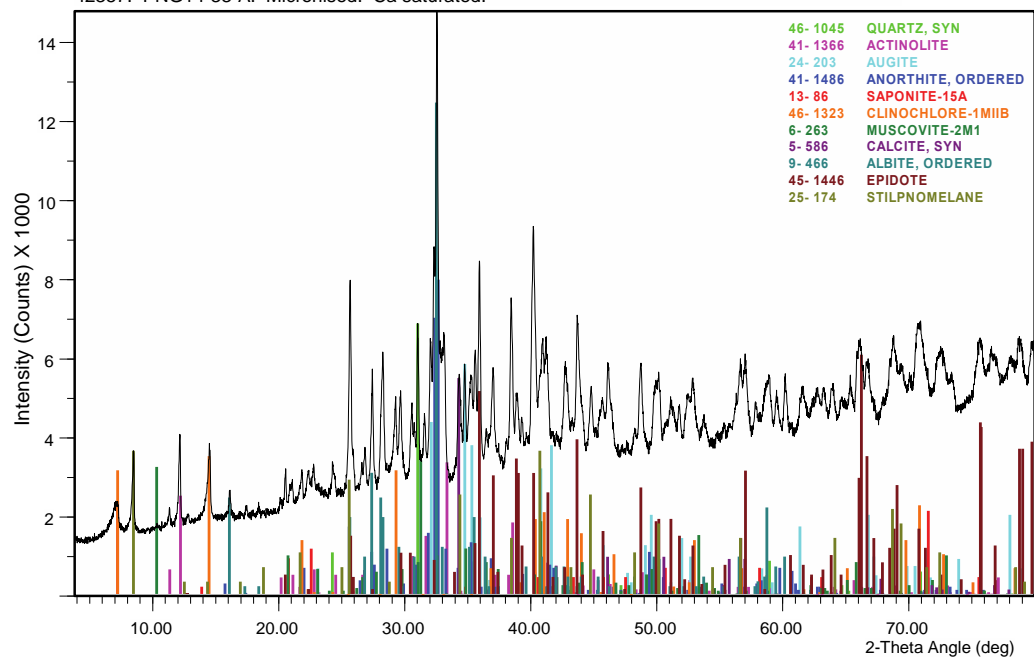




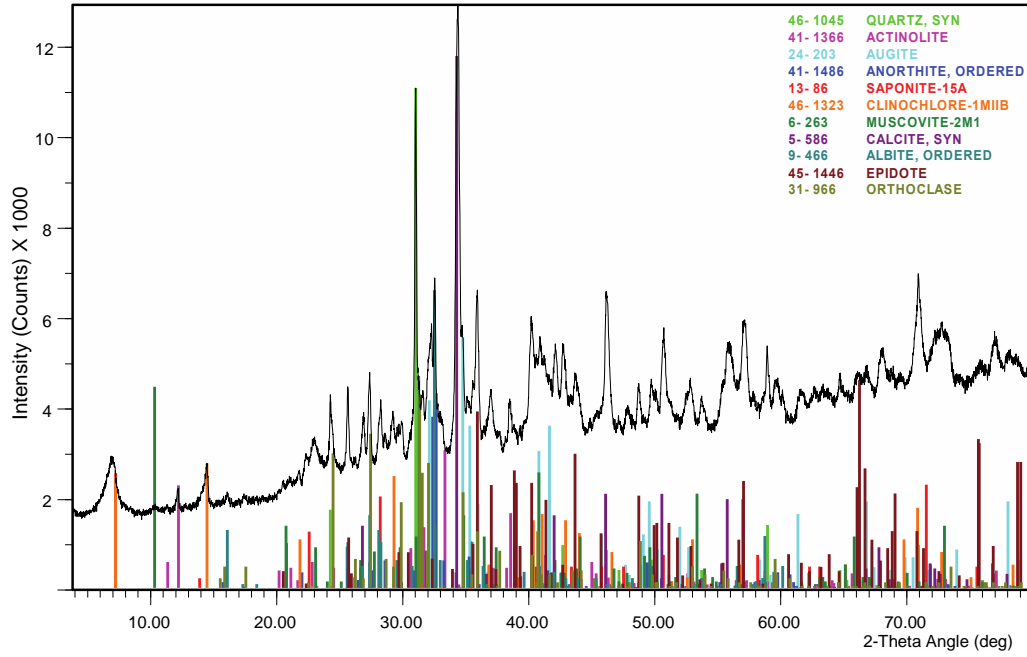
42356. PNG14-32-F. Micronised. Ca saturated.



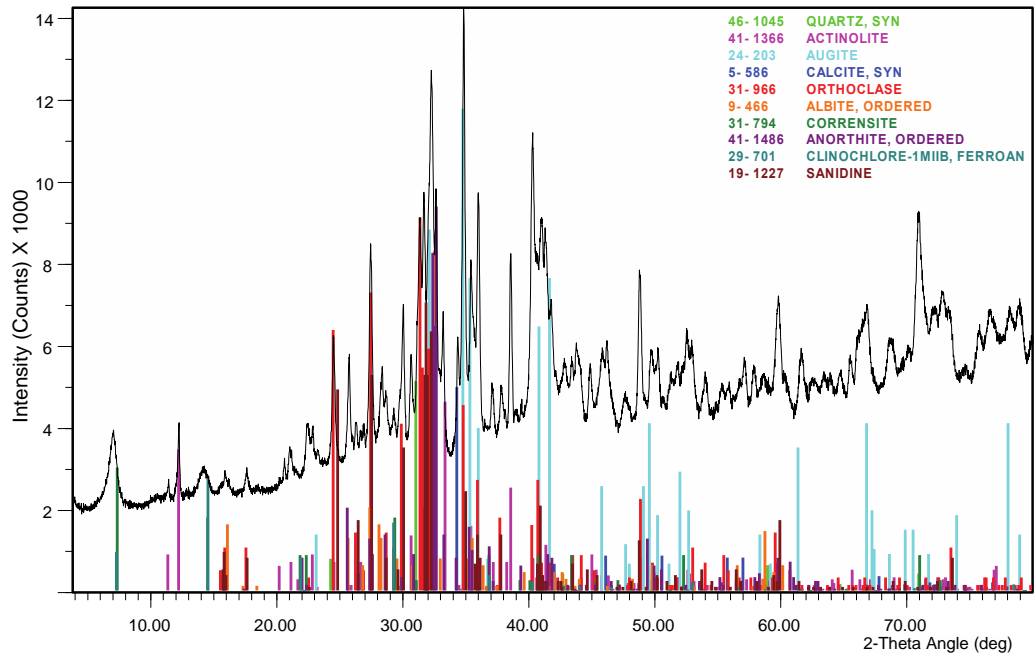
42357. PNG14-33-A. Micronised. Ca saturated.

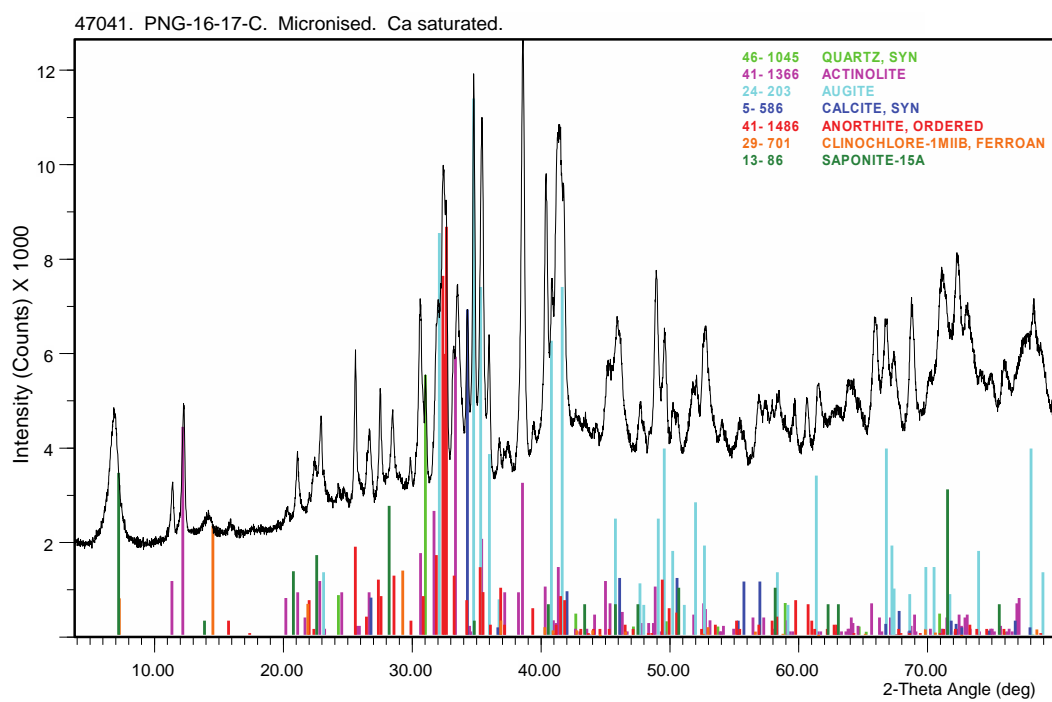
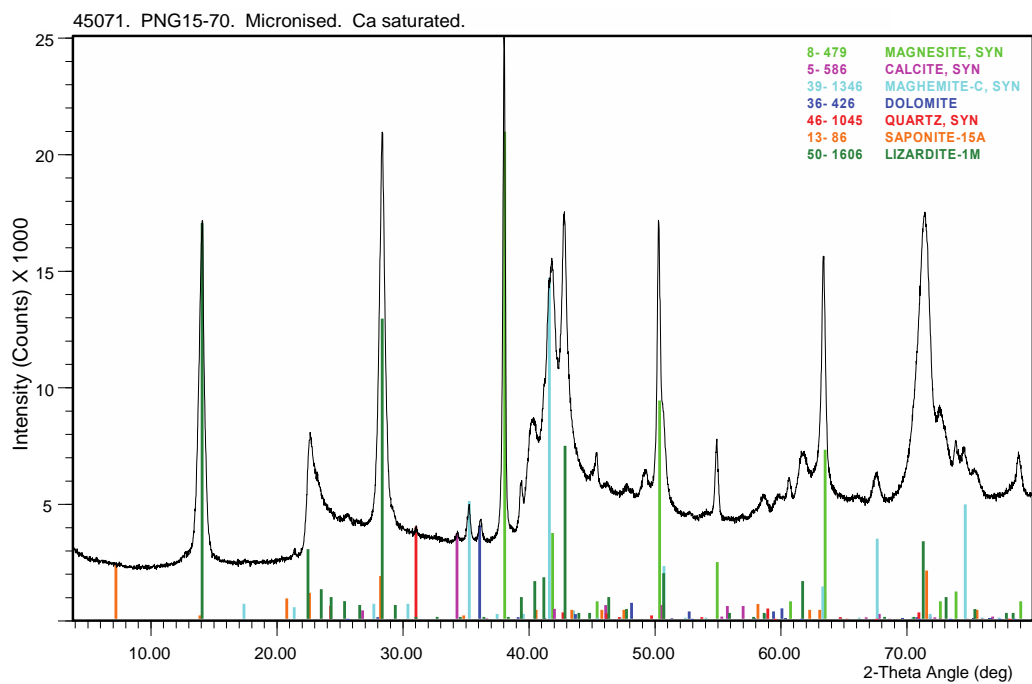


42358. PNG14-33-B. Micronised. Ca saturated.

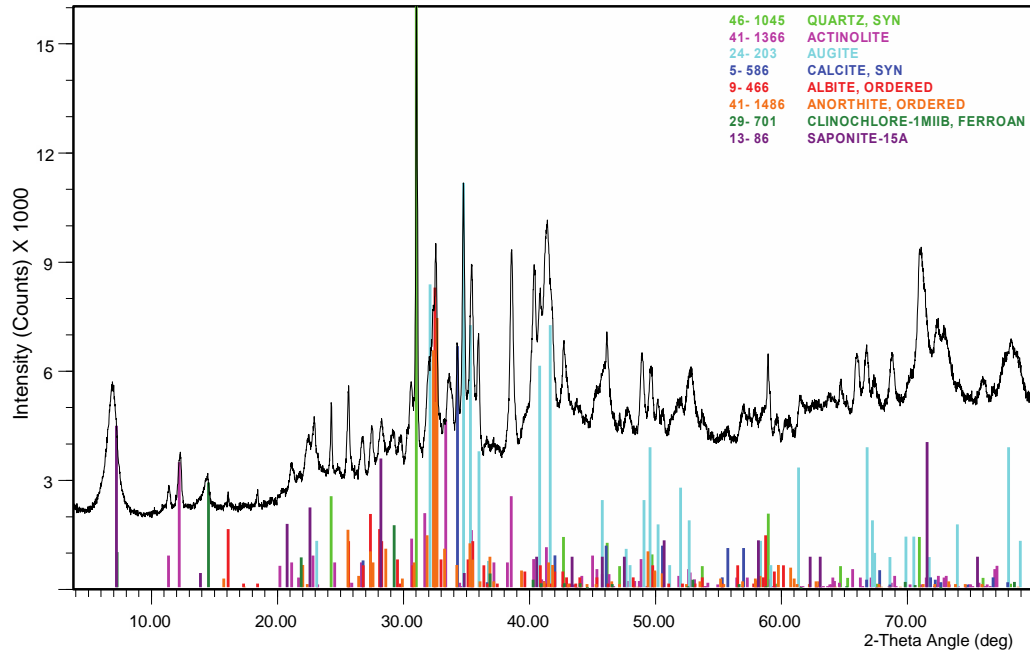


45070. PNG15-15B. Micronised. Ca saturated.

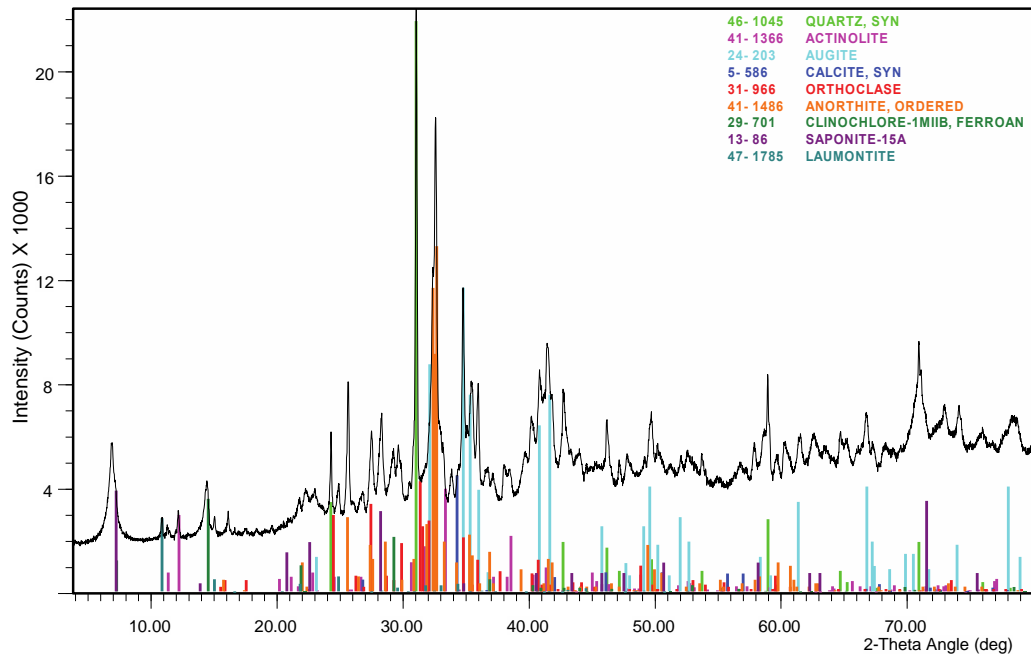


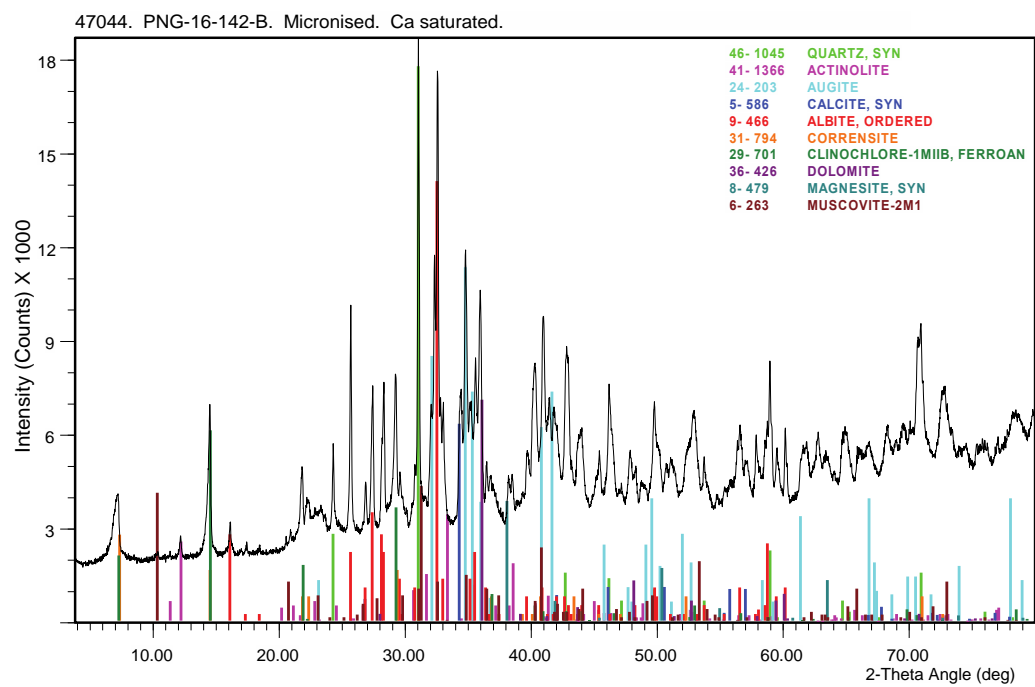


47042. PNG-16-30-B. Micronised. Ca saturated.



47043. PNG-16-108-G. Micronised. Ca saturated.





B.10 XRF Chemical Data of Bulk Mafic Fault Rocks

Whole rock major element concentrations were determined based on X-ray fluorescence (XRF) spectrometry with a SPECTRO X-LAB 2000 at the Department of Earth & Ocean Sciences, University of Waikato, on fused glass disks cast using a 10:1 flux ratio in lithium borate flux. Trace element concentrations were measured with a Thermo-Scientific Element2 sector-field inductively coupled plasma mass spectrometry (ICP-MS) at the School of Geography, Environment and Earth Sciences, Victoria University Wellington. A gravimetric multi-element synthetic mixture was employed to calibrate the unknowns and to monitor for drift. The accuracy of the unknowns were determined with a secondary reference material (AGV-2).

Table B.10. Chemical analyses of Mai'iu fault rock samples comprising a non-mylonitic, almost undeformed Goropu Metabasalt, a mylonite and two gouge samples. Note, the increase in Cr and Ni in the gouge sample relative to the other samples (highlighted in yellow). Also compare with Smith (2013).

Sample# Formation Sequence	PNG-16-17_2D Goropu Metabasalt Non-Mylonitic	PNG-16-17z Goropu Metabasalt Mafic Mylonite	PNG-14-19e Goropu Metabasalt Gouge	PNG-14-19F Goropu Metabasalt Gouge
wt.%				
SiO ₂	45.56	48.84	42.93	43.80
TiO ₂	1.33	1.63	0.86	0.81
Al ₂ O ₃	14.74	12.32	11.45	11.16
Fe ₂ O ₃	11.45	11.95	11.23	10.84
MnO	0.19	0.22	0.22	0.23
MgO	7.60	6.75	16.80	16.58
CaO	11.49	9.37	7.54	8.40
Na ₂ O	2.08	2.96	0.94	0.90
K ₂ O	0.14	0.04	0.08	0.03
P ₂ O ₅	0.14	0.19	0.11	0.11
SO ₃	0.07	0.17	0.07	0.13
SrO (Sr - PPM)	82.00	271.00	53.00	71.00
BaO (Ba - PPM)	94.00	81.00	42.00	45.00
CO ₂ (%)	4.24	4.91	7.04	6.27
Total (%)	99.04	99.38	99.28	99.26
ppm				
Cr	309.38	200.54	1303.54	1346.79
Ni	67.49	51.19	709.16	758.27
Cs	0.05	0.03	0.17	0.10
Ba	17.30	21.11	23.80	16.47
Rb	2.86	0.27	1.69	0.48
Sr	140.70	267.79	96.00	112.01
Pb	0.28	1.01	2.08	2.28
Th	0.21	0.56	0.79	0.75
U	0.10	0.18	0.21	0.20
Zr	162.60	103.73	127.05	123.87
Nb	4.80	6.65	2.35	2.27
Hf	2.16	2.81	1.72	1.67
Ta	0.45	0.63	0.28	0.26
Y	22.08	23.65	17.23	17.11
V	308.84	290.29	207.72	197.23
Sc	41.95	33.89	29.47	29.54
Co	51.98	36.24	72.64	74.47
Cu	107.17	99.43	93.24	95.15
Zn	92.07	172.19	74.86	76.38
Ga	19.17	16.57	13.00	12.10
La	4.67	6.19	4.64	4.54
Ce	11.89	15.77	10.93	10.66
Pr	1.79	2.34	1.54	1.51
Nd	9.34	11.42	7.71	7.50
Sm	3.04	3.36	2.28	2.32
Eu	2.29	1.26	1.59	1.57
Gd	3.66	4.03	2.75	2.77
Tb	0.68	0.79	0.52	0.52
Dy	4.41	4.89	3.42	3.38
Ho	0.91	1.02	0.72	0.71
Er	2.67	2.98	2.12	2.14
Tm	0.38	0.42	0.31	0.31
Yb	2.34	2.67	1.93	1.94
Lu	0.37	0.41	0.29	0.30
Au	0.22	0.36	0.13	0.16

B.11 EPMA

Wavelength dispersive analysis of chlorite and albite was carried out on a JEOL electron microprobe at the School of Geography, Environmental and Earth Science, Victoria University of Wellington. We used an acceleration voltage of 15 kV and a sample current of 12 nA. Synthetic and natural mineral standards were used for calibration comprising the elements Si, Al, Mg, Mn, Fe, Zn, Ni, Cr, Na, K and Ca for chlorite and Si, Al, Mg, Mn, Fe, Ni, Ti, Na, K and Ca for plagioclase (albite). Errors in the raw data were reduced by ZAF correction. The results from this analysis can be found in the 'EPMA Data' folder of the Digital Appendix. 'Albite_EPMA_Data.xlsx' shows the results for albite; and 'Chlorite_EPMA_data.xlsx' shows the results of all analysed chlorite grains in the mafic mylonites, foliated cataclasites and chlorite veins. The folder also contains additional SEM backscatter images of chlorite domains.

Appendix C

C.1 Estimated Recrystallized Calcite Grain Sizes and Differential Stresses

Table C.1. Calculated differential stresses based on the recrystallized grain-size of calcite using the paleopiezometer equations by Valcke et al. (2015) and Platt and De Bresser (2017). The grain orientation spread (GOS)—the average degree of intracrystalline lattice distortion proportional to dislocation density in each grain—was used to separate relict and recrystallized (ReX) grains in calcite veins (see Cross et al., 2017). The data was collected with EBSD and processed with a modified version of the MTEX script “RexRelict.m” (see below). Images of the processed calcite data including grain maps (relict versus recrystallized calcite grains), GOS maps and grain-size distribution plots (relict versus recrystallized calcite) of all analysed calcite samples can be found in the subfolder ‘Calcite Grain-Size Piezometer’ of ‘Calcite Paleopiezometry’ in the Digital Appendix. D_{AVG} —average grain size of recrystallized calcite grains; D_{RMS} — root-mean-square mean diameter of recrystallized calcite grains.

Sample PNG#	Host Rock	Subset	Step Size	GOS Threshold	Number of Calcite Grains						Paleopiezometer σ_{Diff} (MPa)	
					All	Relict	ReX	D_{AVG}	D_{RMS}	1σ	Valcke et al. (2015)	Platt and De Bresser (2017)
16-125Di	Mylonite	1	0.5	1.95	393	147	246	16.8	20.0	± 10.8	13.3	44.2
16-125Di	Mylonite	1	0.5	2.15	402	114	288	16.2	21.2	± 13.7	14.2	41.9
16-1BW-B	Mylonite	1.1	0.75	1.35	1243	211	1032	10.0	11.2	± 4.9	31.4	75.2
16-1BW-B	Mylonite	2.1	1.5	1.75	3811	649	3162	8.7	10.4	± 5.7	40.0	80.5
16-1BW-B	Mylonite	2.2	1.5	2.05	2946	489	2457	8.5	9.9	± 5.1	41.2	84.0
16-1BW-B	Mylonite	3.1	0.5	1.65	1098	195	903	8.3	10.4	± 6.2	43.0	80.5
16-1BW-B	Mylonite	3.2	0.5	1.95	767	152	615	8.2	9.8	± 5.3	44.3	85.4
16-142C	Mylonite	1	0.5	1.15	4075	610	3465	7.7	9.1	± 4.9	48.9	90.7
15-52A	Ultramylonite	1.1	0.2	1.55	1303	303	1000	6.7	7.3	± 3.0	62.3	111.7
15-52A	Ultramylonite	1.2	0.2	1.35	1397	483	914	5.6	6.2	± 2.6	83.6	130.0
15-52A	Ultramylonite	1.3	0.2	1.4	1532	519	1013	6.1	6.7	± 2.8	72.4	120.5
16-17E	Myl/Cat	1	0.5	1.85	1985	427	1558	5.1	6.5	± 4.0	96.4	123.9
16-17E	Myl/Cat	2	0.5	2.05	2923	662	2261	6.2	7.4	± 4.0	70.3	110.3
16-151C	Cataclasite	1.1	0.5	1.65	1373	1002	905	7.8	8.7	± 3.9	47.9	94.6
16-151C	Cataclasite	1.2	0.5	1.45	1188	394	794	7.7	8.7	± 4.1	48.6	94.6
16-151C	Cataclasite	1.3	0.5	1.95	1188	296	892	8.1	9.1	± 4.2	45.0	91.0
16-151E	Cataclasite	1.1	0.75	1.45	1406	429	977	7.6	8.7	± 4.3	50.5	94.9
16-151E	Cataclasite	1.2	0.75	1.85	1665	385	1280	7.6	8.8	± 4.4	49.5	93.7
16-151E	Cataclasite	2	0.2	1.15	795	194	601	6.2	7.7	± 4.5	69.4	106.1

C.2 Estimated Mean Twin Width, Mean Twin Density and Differential Stress of Twinned Calcite Grains

Table C.2. Calculated differential stresses based on the twin density of calcite grains using the paleopiezometer equations by Rybacki et al. (2013), Rowe and Rutter (1990), and Ferrill (1998). EBSD maps of analysed calcite grains and twins as well as orientation data (given in Euler angles) and coordinate system transformation of analysed samples given as Excel spreadsheets can be found in the Digital Appendix in the subfolder ‘Calcite E-Twin Analysis’.

Sample PNG#	Host Rock	#Grains	#Twins	Mean Twin Width (μm)	1σ	Mean Twin Density (#/mm)	1σ	Paleopiezometer (MPa)					
								Rybacki et al. (2013)	1σ	Rowe & Rutter (1990)	1σ	Ferrill (1998)	1σ
16-125Di	Mylonite	75	339	2.8	±1.7	40.8	±27.9	117.4	±41.5	205.1	±54.7	83.1	±49.3
15-76C	Mylonite	26	95	2.3	±1.6	29.9	±18.7	102.3	±28.1	189.3	±37.8	63.8	±33.1
16-176	Schist	22	36	3.3	±2.1	19.9	±12.5	83.1	±25.8	156.4	±45.6	45.1	±24.2
14-15_PV	Schist/Mylonite	49	209	2.4	±2.2	48.0	±22.9	131.2	±32.1	226.6	±38.7	96.9	±39.9
14-15_OV	Schist/Mylonite	52	481	2.3	±1.9	38.4	±30.0	113.6	±44.6	199.7	±56.5	78.9	±52.9
16-126A	Schist/Mylonite	37	152	2.8	±2.0	38.9	±20.9	116.1	±33.7	205.5	±47.8	80.3	±37.8
16-142C	Mylonite	30	102	3.7	±2.6	45.8	±36.8	122.6	±48.6	210.3	±56.6	91.1	±63.0
16-18W-C1	Mylonite	24	276	4.3	±2.6	42.0	±26.2	120.3	±39.3	210.1	±50.7	85.8	±46.6
16-18W-C2	Mylonite	8	83	5.7	±3.3	25.5	±10.0	96.3	±20.2	181.8	±32.9	56.4	±19.5
16-18W-C3	Mylonite	12	140	4.6	±1.4	27.5	±15.0	98.6	±27.0	183.2	±41.3	59.8	±28.0
16-17E_V1	Myl/Cat	25	120	2.8	±1.3	39.9	±17.5	119.9	±28.3	213.2	±39.5	82.8	±31.8
16-17E_V2	Myl/Cat	41	153	2.1	±1.1	53.5	±31.6	137.2	±39.2	232.1	±41.8	106.0	±53.2
16-17E_H1	Myl/Cat	29	42	1.6	±1.1	42.4	±21.4	122.8	±30.7	216.9	±36.6	86.5	±37.7
16-151E-V1	Cataclasite	55	103	1.7	±1.5	95.4	±39.2	185.1	±36.1	281.2	±28.0	172.9	±60.4
16-151E-V2	Cataclasite	50	88	1.9	±0.9	63.9	±28.1	152.2	±33.4	249.8	±33.0	124.2	±47.0
16-151E-V3	Cataclasite	50	63	1.9	±1.0	76.4	±34.8	166.9	±34.4	264.1	±29.2	145.0	±55.0
15-50RD	Cataclasite	53	71	0.9	±0.4	161.0	±61.0	229.5	±47.4	311.3	±30.6	250.8	±90.3
16-151C	Cataclasite	51	80	2.1	±0.9	58.7	±24.6	146.0	±31.5	243.6	±33.7	115.6	±41.9
16-125B	Ucat/Cat	48	214	1.2	±0.8	75.5	±37.2	164.3	±41.5	259.6	±40.3	143.0	±60.8
15-125A	Ultracataclasite	15	18	1.3	±1.2	56.6	±31.4	141.1	±40.1	236.2	±42.0	111.2	±53.5

C.3 Paleo-principal Stress Axes Based on Calcite Twin-Pairs

Table C.3. Results of the calcite strain-gage technique based on Groshong (1972, 1974). Calculated principal strains, eigenvalues and eigenvectors are based on this technique and were determined by using an Excel-script by Tielke (2010). The Excel spreadsheets with the processed orientation data and the strain-gage technique can be found in the subfolder ‘Calcite E-Twin Analysis’ in the Digital Appendix.

Sample PNG#	Principal Strains			Shear Strain	Eigenvalues			Strain Gage Technique - Eigenvectors		
	e1	e2	e3	SQRT(J2)	e1(%)	e2(%)	e3(%)	e1(°)	e2(°)	e3(°)
15-76C	0.020	-0.011	-0.009	0.017	-0.140	-0.058	0.198	133/05	231/57	040/32
16-176	0.035	-0.027	-0.008	0.032	-0.551	-0.088	0.639	243/89	078/01	348/00
14-15_PV	-0.057	0.031	0.026	0.049	-0.536	0.225	0.311	289/35	166/38	046/33
14-15_OV	-0.075	0.052	0.023	0.067	-0.333	0.008	0.325	275/42	109/47	011/07
16-126A	-0.048	0.044	0.004	0.046	-0.205	0.033	0.172	206/84	094/02	003/06
16-142C	-0.038	0.031	0.008	0.035	-0.135	-0.030	0.164	199/20	109/00	017/70
16-1BW-C1	-0.062	0.051	0.011	0.057	-0.217	0.038	0.179	353/32	260/04	163/58
16-1BW-C2	-0.050	0.035	0.015	0.044	-0.296	0.028	0.268	284/65	059/18	154/17
16-1BW-C3										

Table C.4. Reconstructed orientations of paleo-principal stress axes based on the Multiple Inverse Method by Yamaji (2000), P-, B- and T-axes calculations after Turner (1953) and dihedral calculation after Angelier and Mechler (1977).

Sample PNG#	Multiple Inverse Method after Yamaji (2000)				P-, B- and T-axes after Turner (1953)				Dihedral Calculation after Angelier & Mechler (1977)		
	σ_1	σ_3	Phi (Φ)	MASD($^\circ$)	Theta angle($^\circ$)	P($^\circ$)	B($^\circ$)	T($^\circ$)	σ_1	σ_2	σ_3
15-76C	306/31	049/15	0.83	53	48	140/63	225/19	349/26	131/01	222/45	040/44
16-176	054/72	163/06	0.80	43	30	311/81	080/07	172/10	229/89	077/01	347/00
14-15_PV	291/45	028/07	0.35	33	50	286/43	155/16	056/42	289/30	194/07	092/59
14-15_OV	275/49	019/12	0.59	57	44	280/65	116/15	027/17	280/33	137/51	023/18
16-126A	285/74	021/01	0.44	57	30	248/35	123/66	356/11	208/82	092/04	002/07
16-142C	234/04	351/81	0.86	69	55	090/01	202/51	296/56	209/07	299/02	047/82
16-1BW-C1	340/38	143/51	0.57	55	50	324/48	031/04	108/22	355/24	263/04	165/66
16-1BW-C2	270/60	160/11	0.38	26	36	315/71	088/16	166/13	279/58	056/24	155/19
16-1BW-C3	024/48	293/01	0.16	52	18	011/22	266/04	282/42	023/40	155/39	268/26
16-17E_V1	109/20	001/41	0.73	34	40	170/62	240/05	353/33	099/01	190/55	009/35
16-17E_V2	283/11	032/59	0.82	57	55	285/16	190/37	032/57	274/11	183/08	059/76
16-17E_H1	231/27	341/34	0.60	40	30	198/54	059/01	333/30	257/06	157/56	351/33
16-151E-V1	247/22	350/30	0.79	28	45	245/29	091/42	342/33	250/15	143/48	352/38
16-151E-V2	222/49	001/34	0.68	32	66	273/22	166/48	012/35	256/22	139/48	002/34
16-151E-V3	234/69	031/19	0.75	44	50	151/53	273/24	031/21	128/15	260/68	033/15
15-50RD	243/50	128/20	0.40	26	45	241/51	009/29	111/24	239/51	010/28	114/24
16-151C	299/42	109/47	0.25	40	70	286/63	046/07	145/12	282/33	058/48	176/23
16-125B	177/78	080/02	0.63	61	30	303/67	023/17	245/55	317/08	210/65	050/23
15-125A	130/41	254/33	0.40	16	55	006/46	152/33	270/37	131/46	359/33	251/25

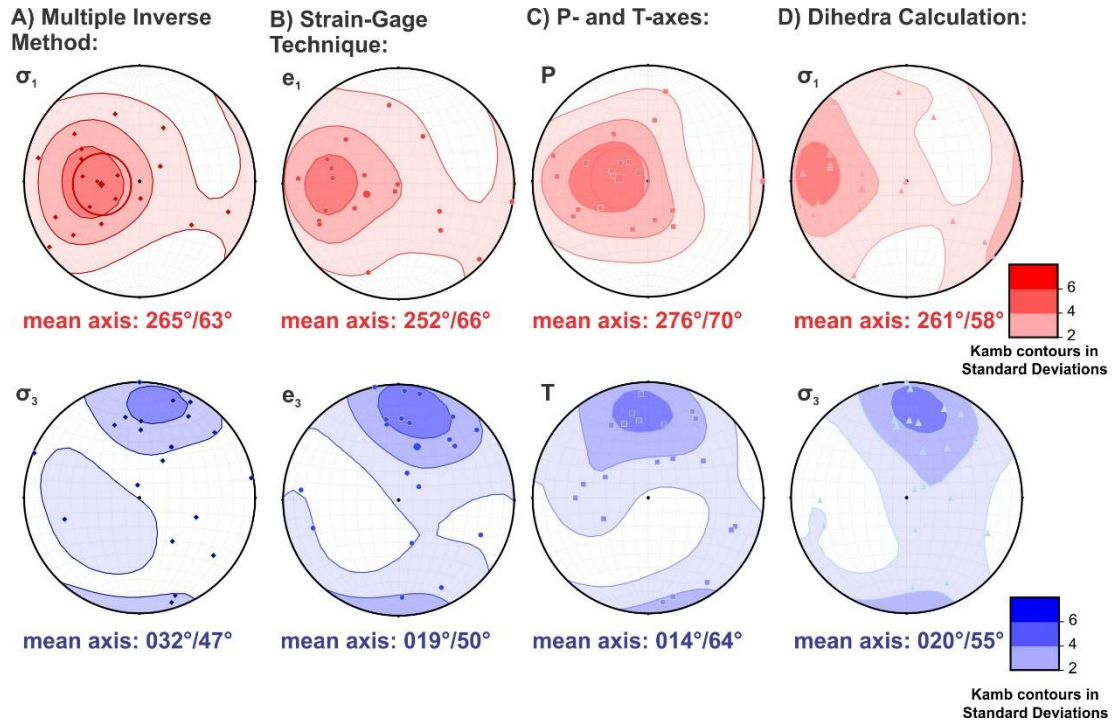


Figure C.1. Mean principal axes distribution in lower hemisphere, equal area stereonet from all calcite veins and the mean distribution of all samples derived from different stress inversion techniques. Red data points and contours indicate the trend and plunge of the maximum principal stress axes. Blue data points and contours indicate the trend and plunge of the minimum principal stress axes. A) Multiple Inverse Method by Yamaji (2000). B) Strain-gage techniques by Groshong (1972, 1974) calculated with an Excel script by Tielke (2010). C) Calculated P- and T-axes after Turner (1953). D) Dihedra calculation based on Angelier and Mechler (1977).

C.4 Temperature Constraints On Calcite Veins

Table C.5. Temperature constrains on the formation and deformation of calcite veins. ReX—dynamic recrystallization of calcite; Twin—twinning of calcite grains. σ_{Diff} —estimated differential stresses.

Sample PNG#	Twin/ReX	Average σ_{Diff} (MPa)	Minimum σ_{Diff} (MPa)	Maximum σ_{Diff} (MPa)	T (°C) based on twin morphology (Ferrill et al., 2004)	avg. Chlorite T (°C)	min. Chlorite T (°C)	max Chlorite T (°C)	Comments
16-17E	ReX	100.3	70.3	110.3		230	146	280	
16-125D	ReX	28.4	13.3	44.2		293	240	330	
16-1BW-B	ReX	60.6	31.4	85.0		309	220	346	Used the Temperatu res from PNG16-59A
16-142C	ReX	69.8	48.9	90.7		279	140	366	
15-52A	ReX	96.8	72.4	120.5		253	223	286	
16-151C	ReX	70.3	45.0	94.7		273	227	319	Used mean for fol. Cataclasite
16-151E	ReX	77.4	49.5	106.1		273	227	319	Used mean for fol. Cataclasite
16-125D	Twin	117.4	75.9	158.9	~200				
16-76C	Twin	102.3	74.3	130.3	>200				No ReX grains; T=200-300 °C
16-176	Twin	83.1	57.3	108.9	>200				No ReX grains; T=200-300 °C
14-15	Twin	122.4	84.4	160.4	~190			262	
16-126A	Twin	116.1	82.4	149.8	~190-200	252	169	320	
16-142C	Twin	122.6	74.0	171.2	~190				
16-17E	Twin	126.6	86.6	166.6	~180	230	146	280	
16-1BW-B	Twin	105.1	75.1	135.1	>200	292	220	346	
16-151E	Twin	168.1	134.1	202.1	~170				
16-151C	Twin	146.0	114.5	177.5	170-180				
16-125B	Twin	164.3	122.8	205.8	~170	272	159	305	
16-125A	Twin	141.1	101.0	181.2	~170				

C.5 Calcite E-twin Boundary Removal for Grain-Size Analysis in MTEX

Major changes of the “RexRelict.m” MTEX-script were related to the removal of e-twin boundaries and the merging of calcite grains separated by these twins prior to grain size analysis. We used a critical misorientation of 10° to construct grains (e.g., Cross et al., 2017). Here, twin boundaries are defined as all boundaries with rotations of 77° to the crystallographic planes (1,-1,0,-4) and (0,-1,1,4). The code to remove twin boundaries is as follows:

```
%% Remove twin boundaries

% Find all calcite-calcite grain boundaries
gb_cc = grains.boundary('Calcite','Calcite');

% Find all boundaries with rotations of 77 degree to the axis
defined
% below, based on the MTEX Google forum. This is the old unit cell
setting
% - these are e-twins:
rot = rotation('axis',Miller(1,-1,0,-4,CS{2}),Miller(0,-
1,1,4,CS{2}),'angle',77*degree);
ind = angle(gb_cc.misorientation,rot)<5*degree;
twinBoundary = gb_cc(ind);

% Merge grains separated by twin boundaries
% - this is computationally expensive
[mergedGrains,grains.prop.parentId] = merge(grains,twinBoundary);
```


C.6 Differential Stress Limited by Coulomb Failure

The brittle failure curves presented in **Figure 4.1** and **Figure 4.11** have been calculated after the approach by Sibson (1998) and Axen (2004) in which differential stresses are limited by a linear Coulomb failure criterion:

$$\tau_i = \mu_i \sigma_{ni} + C \quad (\text{Eq. C.1})$$

where τ_i is the resolved shear traction and σ_{ni} the effective normal traction on the newly formed fracture, μ_i is the coefficient of friction and C is cohesion (~28 MPa for metabasalt, Karaman et al., 2013). Using trigonometric relations in Mohr-Coulomb space (**Figure C.2**), the differential stress is obtained (Labuz & Zang, 2012):

$$\sigma_D = 2(\mu_i \sigma_1 + C) \tan \theta_i \quad (\text{Eq. C.2})$$

where σ_1 is the maximum principal effective stress and θ_i is the angle between σ_1 and the newly formed ideal fault plane (see **Figure C.2**). In the example of **Figure C.2** it is assumed that σ_1 equals the vertical effective stress σ_v with hydrostatic fluid pressure ($\lambda=0.4$) and can be calculated as follows:

$$\sigma_1 = \sigma_v = (\rho_r - \rho_w)gz \quad (\text{Eq. C.3})$$

where ρ_r is density of metabasaltic rock (~2900 kgm⁻³), ρ_w is the density of water (~1000 kgm⁻³), g is gravitational acceleration (9.81 ms⁻²), and z is the depth (Anderson, 1951). For intact metabasaltic rock with typical “Byerlee” coefficient of static friction ($\mu=0.6-0.85$) values, the change in differential stress with depth to cut intact metabasaltic crust (σ_{Di}) can be calculated by substituting equation (C.3) into (C.2).

Using the trigonometric relations in Mohr-Coulomb space, the coefficient of friction on a detachment can be calculated as follows:

$$\mu_d = \frac{\sin 2\theta_d}{\frac{\sigma_1}{(\mu_i \sigma_1 + C) \tan \theta_i} - 2 \cos^2 \theta_d} \quad (\text{Eq. C.4})$$

where θ_d is the angle between σ_1 and the detachment fault. Note that in Chapter 4, θ_{MF} is defined as the observed angle between the maximum principal effective stress and the effective normal traction (normal to the fault surface of the Mai’iu fault). By substituting equation (C.2) into (C.4), it possible to calculate the differential stress that is required for slip on a detachment fault (σ_{Dd} ; see also Choi & Buck, 2012):

$$\sigma_{Dd} = \frac{2\mu_d \sigma_1}{\sin 2\theta_d + 2\mu_d \cos^2 \theta_d} \quad (\text{Eq. C.5})$$

Both slip on the detachment fault and cutting of intact crust occurs when $\sigma_{Dd} = \sigma_{Di}$.

Table C.6. Material parameters and variables to calculate differential stresses limited by a linear Coulomb failure criterion as described above.

Symbol	Quantity	Assumed Values	Units
μ_i	Coefficient of Friction (“Byerlee”)	0.75	
μ_d	Coefficient of Friction on the Detachment Fault		
λ	Pore Fluid Factor	0.4	
ρ_r	Rock Density	2900	kgm^{-3}
ρ_w	Density of Water	1000	kgm^{-3}
g	Gravitational Acceleration	9.81	ms^{-2}
C	Cohesion of Intact Metabasalt	28×10^6	Pa
z	Depth		m
σ_1	Maximum Principal Effective Stress		Pa
θ_i	Angle between σ_1 and ideal Fault Plane	30	degrees

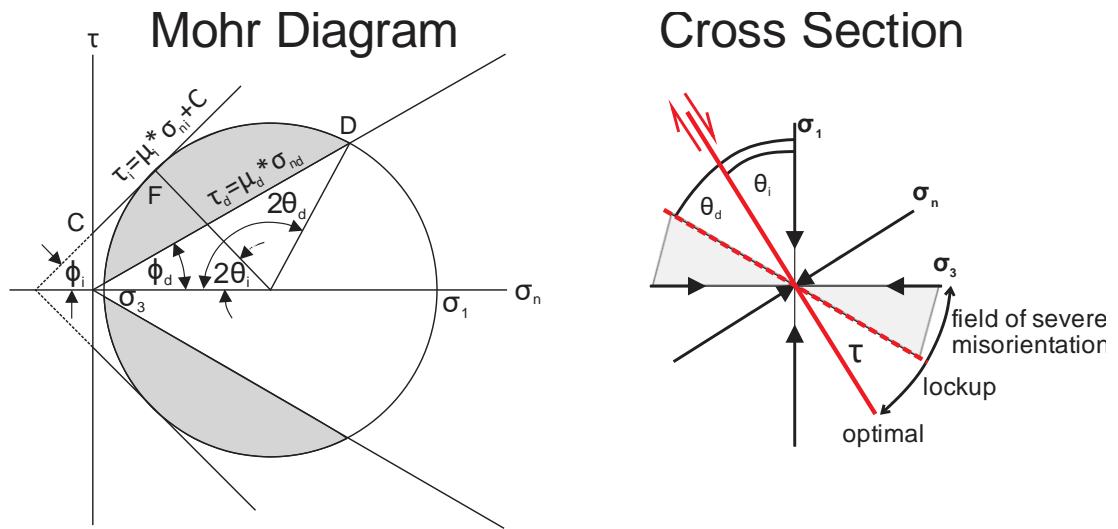


Figure C.2. Mohr diagram in which Coulomb failure limits differential stress (Axen, 2004). The shaded area in the Mohr diagram indicates permissible shear and effective normal tractions for faults to slip.

Bibliography

- Abers, G. A., Mutter, C. Z., & Fang, J. (1997). Shallow dips of normal faults during rapid extension: Earthquakes in the Woodlark-D'Entrecasteaux rift system, Papua New Guinea. *Journal of Geophysical Research: Solid Earth*, 102(B7), 15301-15317.
- Abers, G. A., Ferris, A., Craig, M., Davies, H., Lerner-Lam, A. L., Mutter, J. C., & Taylor, B. (2002). Mantle compensation of active metamorphic core complexes at Woodlark rift in Papua New Guinea. *Nature*, 418(6900), 862.
- Abers, G. A., Eilon, Z., Gaherty, J. B., Jin, G., Kim, Y. H., Obrebski, M., & Dieck, C. (2016). Southeast Papuan crustal tectonics: Imaging extension and buoyancy of an active rift. *Journal of Geophysical Research: Solid Earth*, 121(2), 951-971.
- Anderson, E. M. (1951). The dynamics of faulting.
- Anderson, T. A. (1972). Paleogene nonmarine Gualanday Group, Neiva basin, Colombia, and regional development of the Colombian Andes. *Geological Society of America Bulletin*, 83(8), 2423-2438.
- Angelier, J. T., & Mechler, P. (1977). Sur une methode graphique de recherche des contraintes principales egalement utilisables en tectonique et en seismologie: la methode des diedres droits. *Bulletin de la Société géologique de France*, 7(6), 1309-1318.
- Angelier, J. (1979). Determination of the mean principal directions of stresses for a given fault population. *Tectonophysics*, 56(3-4), T17-T26.
- Armstrong, R. L. (1982). Cordilleran metamorphic core complexes--From Arizona to southern Canada. *Annual review of earth and planetary sciences*, 10(1), 129-154.
- Aspiroz, M. D., Lloyd, G. E., & Fernández, C. (2007). Development of lattice preferred orientation in clinoamphiboles deformed under low-pressure metamorphic conditions. A SEM/EBSD study of metabasites from the Aracena metamorphic belt (SW Spain). *Journal of Structural Geology*, 29(4), 629-645.
- Awazu, K., & Kawazoe, H. (2003). Strained Si–O–Si bonds in amorphous SiO₂ materials: a family member of active centers in radio, photo, and chemical responses. *Journal of Applied physics*, 94(10), 6243-6262.
- Axen, G. J., & Wernicke, B. P. (1991). Comment on “Tertiary extension and contraction of lower-plate rocks in the central Mojave Metamorphic Core Complex, southern California” by John M. Bartley, John M. Fletcher, and Allen F. Glazner. *Tectonics*, 10(5), 1084-1086.
- Axen, G. J., & Selverstone, J. (1994). Stress state and fluid-pressure level along the Whipple detachment fault, California. *Geology*, 22(9), 835-838.
- Axen, G. J., Bartley, J. M., & Selverstone, J. (1995). Structural expression of a rolling hinge in the footwall of the Brenner Line normal fault, eastern Alps. *Tectonics*, 14(6), 1380-1392.

- Axen, G. J., & Bartley, J. M. (1997). Field tests of rolling hinges: Existence, mechanical types, and implications for extensional tectonics. *Journal of Geophysical Research: Solid Earth*, 102(B9), 20515-20537.
- Axen, G. J. (2004). Mechanics of low-angle normal faults. *Rheology and Deformation of the Lithosphere at Continental Margins*, 46-91.
- Axen, G. J. (2007). Research Focus: Significance of large-displacement, low-angle normal faults. *Geology*, 35(3), 287-288.
- Bachmann, F., Hielscher, R., & Schaeben, H. (2010). Texture analysis with MTEX—free and open source software toolbox. In *Solid State Phenomena* (Vol. 160, pp. 63-68). Trans Tech Publications.
- Bachmann, F., Hielscher, R., & Schaeben, H. (2011). Grain detection from 2d and 3d EBSD data—Specification of the MTEX algorithm. *Ultramicroscopy*, 111(12), 1720-1733.
- Baines, A. G., Cheadle, M. J., John, B. E., & Schwartz, J. J. (2008). The rate of oceanic detachment faulting at Atlantis Bank, SW Indian Ridge. *Earth and Planetary Science Letters*, 273(1-2), 105-114.
- Baldwin, S. L., Monteleone, B. D., Webb, L. E., Fitzgerald, P. G., Grove, M., & Hill, E. J. (2004). Pliocene eclogite exhumation at plate tectonic rates in eastern Papua New Guinea. *Nature*, 431(7006), 263.
- Baldwin, S. L., Webb, L. E., & Monteleone, B. D. (2008). Late Miocene coesite-eclogite exhumed in the Woodlark Rift. *Geology*, 36(9), 735-738.
- Baldwin, S. L., Fitzgerald, P. G., & Webb, L. E. (2012). Tectonics of the New Guinea region. *Annual Review of Earth and Planetary Sciences*, 40, 495-520.
- Barber, D. J., & Wenk, H. R. (1979). Deformation twinning in calcite, dolomite, and other rhombohedral carbonates. *Physics and Chemistry of Minerals*, 5(2), 141-165.
- Barnhoorn, A., Bystricky, M., Burlini, L., & Kunze, K. (2004). The role of recrystallisation on the deformation behaviour of calcite rocks: large strain torsion experiments on Carrara marble. *Journal of Structural Geology*, 26(5), 885-903.
- Bartley, J. M., Fletcher, J. M., & Glazner, A. F. (1990). Tertiary extension and contraction of lower-plate rocks in the Central Mojave Metamorphic Core Complex, southern California. *Tectonics*, 9(3), 521-534.
- Behnsen, J., & Faulkner, D. R. (2012). The effect of mineralogy and effective normal stress on frictional strength of sheet silicates. *Journal of Structural Geology*, 42, 49-61.
- Behr, W. M., & Platt, J. P. (2011). A naturally constrained stress profile through the middle crust in an extensional terrane. *Earth and Planetary Science Letters*, 303(3-4), 181-192.
- Behr, W. M., & Platt, J. P. (2013). Rheological evolution of a Mediterranean subduction complex. *Journal of Structural Geology*, 54, 136-155.
- Behr, W. M., & Platt, J. P. (2014). Brittle faults are weak, yet the ductile middle crust is strong: Implications for lithospheric mechanics. *Geophysical Research Letters*, 41(22), 8067-8075.

- Behrmann, J. H. (1985). Crystal plasticity and superplasticity in quartzite; a natural example. *Tectonophysics*, 115(1), 101-129.
- Beiersdorfer, R. E., & Day, H. W. (1995). Mineral paragenesis of pumpellyite in lowgrade mafic rocks. *Low-Grade Metamorphism of Mafic Rocks: Boulder, Colorado*, Geological Society of America. Special Paper, 296, 5-27.
- Bertoluzza, A., Fagnano, C., Morelli, M. A., Gottardi, V., & Guglielmi, M. (1982). Raman and infrared spectra on silica gel evolving toward glass. *Journal of Non-Crystalline Solids*, 48(1), 117-128.
- Bettison, L. A., & Schiffman, P. (1988). Compositional and structural variations of phyllosilicates from the Point Sal ophiolite, California. *American Mineralogist*, 73(1-2), 62-76.
- Bevins, R. E., Robinson, D., & Rowbotham, G. (1991). Compositional variations in mafic phyllosilicates from regional low-grade metabasites and application of the chlorite geothermometer. *Journal of Metamorphic Geology*, 9(6), 711-721.
- Biemiller, J., Ellis, S. M., Little, T., Mizera, M., Wallace, L. M., & Lavier, L. (2017, December). The influence of tectonic inheritance on crustal extension style following failed subduction of continental crust: applications to metamorphic core complexes in Papua New Guinea. In *AGU Fall Meeting Abstracts*.
- Biemiller, J., Wallace, L. M., Ellis, S. M., Little, T. A., Lavier, L., Mizera, M., & Webber, S. M. (2018, December). Short-and Long-term Deformation Styles on an Active Low-angle Normal Fault: Mai'iu Fault, Papua New Guinea. In *AGU Fall Meeting Abstracts*.
- Biemiller, J., Ellis, S., Mizera, M., Little, T., Wallace, L., & Lavier, L. (2019). Tectonic inheritance following failed continental subduction: a model for core complex formation in cold, strong lithosphere. *Tectonics*.
- Bistacchi, A., Griffith, W. A., Smith, S. A., Di Toro, G., Jones, R., & Nielsen, S. (2011). Fault roughness at seismogenic depths from LIDAR and photogrammetric analysis. *Pure and Applied Geophysics*, 168(12), 2345-2363.
- Blackman, D. K., Cann, J. R., Janssen, B., & Smith, D. K. (1998). Origin of extensional core complexes: Evidence from the Mid-Atlantic Ridge at Atlantis fracture zone. *Journal of Geophysical Research: Solid Earth*, 103(B9), 21315-21333.
- Bodine, J. H., Steckler, M. S., & Watts, A. B. (1981). Observations of flexure and the rheology of the oceanic lithosphere. *Journal of Geophysical Research: Solid Earth*, 86(B5), 3695-3707.
- Bos, B., & Spiers, C. J. (2002). Frictional-viscous flow of phyllosilicate-bearing fault rock: Microphysical model and implications for crustal strength profiles. *Journal of Geophysical Research: Solid Earth* (1978–2012), 107(B2), ECV-1.
- Boschi, C., Früh-Green, G. L., Delacour, A., Karson, J. A., & Kelley, D. S. (2006). Mass transfer and fluid flow during detachment faulting and development of an oceanic core complex, Atlantis Massif (MAR 30 N). *Geochemistry, Geophysics, Geosystems*, 7(1).

- Boulton, C., Yao, L., Faulkner, D. R., Townend, J., Toy, V. G., Sutherland, R., ... & Shimamoto, T. (2017). High-velocity frictional properties of Alpine Fault rocks: Mechanical data, microstructural analysis, and implications for rupture propagation. *Journal of Structural Geology*, 97, 71-92.
- Boulton, C., Barth, N. C., Moore, D. E., Lockner, D. A., Townend, J., & Faulkner, D. R. (2018). Frictional properties and 3-D stress analysis of the southern Alpine Fault, New Zealand. *Journal of Structural Geology*.
- Bourdelle, F., & Cathelineau, M. (2015). Low-temperature chlorite geothermometry: a graphical representation based on a T–R₂–Si diagram. *European Journal of Mineralogy*, 27(5), 617-626.
- Boutareaud, S., Calugaru, D. G., Han, R., Fabbri, O., Mizoguchi, K., Tsutsumi, A., & Shimamoto, T. (2008). Clay-clast aggregates: A new textural evidence for seismic fault sliding?. *Geophysical Research Letters*, 35(5).
- Boutareaud, S., Boullier, A. M., Andreani, M., Calugaru, D. G., Beck, P., Song, S. R., & Shimamoto, T. (2010). Clay clast aggregates in gouges: New textural evidence for seismic faulting. *Journal of Geophysical Research: Solid Earth*, 115(B2).
- Brace, W. F., & Kohlstedt, D. L. (1980). Limits on lithospheric stress imposed by laboratory experiments. *Journal of Geophysical Research: Solid Earth*, 85(B11), 6248-6252.
- Brandstätter, J., Kurz, W., & Rogowitz, A. (2017). Microstructural analysis and calcite piezometry on hydrothermal veins: Insights into the deformation history of the Cocos Plate at Site U1414 (IODP Expedition 344). *Tectonics*, 36(8), 1562-1579.
- Britton, T. B., Jiang, J., Guo, Y., Vilalta-Clemente, A., Wallis, D., Hansen, L. N., ... & Wilkinson, A. J. (2016). Tutorial: Crystal orientations and EBSD—Or which way is up?. *Materials Characterization*, 117, 113-126.
- Brodsky, E. E., Gilchrist, J. J., Sagy, A., & Collettini, C. (2011). Faults smooth gradually as a function of slip. *Earth and Planetary Science Letters*, 302(1-2), 185-193.
- Brodsky, E. E., Kirkpatrick, J. D., & Candela, T. (2016). Constraints from fault roughness on the scale-dependent strength of rocks. *Geology*, 44(1), 19-22.
- Brun, J. P., Sokoutis, D., Tirel, C., Gueydan, F., Van den Driessche, J., & Beslier, M. O. (2018). Crustal versus mantle core complexes. *Tectonophysics*, 746, 22-45.
- Buck, W. R. (1988). Flexural rotation of normal faults. *Tectonics*, 7(5), 959-973.
- Buck, W. R. (1990). Comment on “Origin of regional, rooted low-angle normal faults: A mechanical model and its tectonic implications” by An Yin, *Tectonics*, 9(3), 545–546, doi: 10.1029/TC009i003p00545.
- Buck, W. R. (1997). Bending thin lithosphere causes localized “snapping” and not distributed “crunching”: Implications for abyssal hill formation. *Geophysical research letters*, 24(20), 2531-2534.

- Buiter, S., & Ellis, S. (2012, April). SULEC: Benchmarking a new ALE finite-element code. In EGU General Assembly Conference Abstracts (Vol. 14, p. 7528).
- Bunge, H. J. (2013). *Texture analysis in materials science: mathematical methods*. Elsevier.
- Burkhard, M. (1993). Calcite twins, their geometry, appearance and significance as stress-strain markers and indicators of tectonic regime: a review. *Journal of structural geology*, 15(3-5), 351-368.
- Burov, E. B., & Guillou-Frottier, L. (1999). Thermomechanical behavior of large ash flow calderas. *Journal of Geophysical Research: Solid Earth*, 104(B10), 23081-23109.
- Byerlee, J. (1978). Friction of rocks. In *Rock friction and earthquake prediction* (pp. 615-626). Birkhäuser, Basel.
- Cai, Y., Pei, J., Wang, H., Sheng, M., & Si, J. (2019). Paleo-earthquakes revealed by rock magnetic evidence from the Anxian-Guanxian Fault, Sichuan Province, China. *Tectonophysics*, 752, 68-80.
- Cairns, E. A., Little, T. A., Turner, G. M., Wallace, L. M., & Ellis, S. (2015). Paleomagnetic evidence for vertical-axis rotations of crustal blocks in the Woodlark Rift, SE Papua New Guinea: Miocene to present-day kinematics in one of the world's most rapidly extending plate boundary zones. *Geochemistry, Geophysics, Geosystems*, 16(7), 2058-2081.
- Caffi, P., 2008, *Evolution of an Active Metamorphic Core Complex, Suckling-Dayman Massif, Eastern Papua New Guinea* [B.Sc. (Honor's) thesis]: Sydney, Australia: Macquarie University, 113 p.
- Candela, T., Renard, F., Bouchon, M., Brouste, A., Marsan, D., Schmittbuhl, J., & Voisin, C. (2009). Characterization of fault roughness at various scales: Implications of three-dimensional high resolution topography measurements. In *Mechanics, Structure and Evolution of Fault Zones* (pp. 1817-1851). Birkhäuser Basel.
- Candela, T., Renard, F., Klinger, Y., Mair, K., Schmittbuhl, J., & Brodsky, E. E. (2012). Roughness of fault surfaces over nine decades of length scales. *Journal of Geophysical Research: Solid Earth*, 117(B8).
- Cann, J. R., Blackman, D. K., Smith, D. K., McAllister, E., Janssen, B., Mello, S., ... & Escartin, J. (1997). Corrugated slip surfaces formed at ridge-transform intersections on the Mid-Atlantic Ridge. *Nature*, 385(6614), 329.
- Carpenter, B. M., Saffer, D. M., & Marone, C. (2012). Frictional properties and sliding stability of the San Andreas fault from deep drill core. *Geology*, 40(8), 759-762.
- Cathelineau, M., & Nieva, D. (1985). A chlorite solid solution geothermometer the Los Azufres (Mexico) geothermal system. *Contributions to Mineralogy and Petrology*, 91(3), 235-244.
- Cathelineau, M. (1988). Cation site occupancy in chlorites and illites as function of temperature. *Clay minerals*, 23(4), 471-85.

- Chauvet, A., & Séranne, M. (1994). Extension-parallel folding in the Scandinavian Caledonides: implications for late-orogenic processes. *Tectonophysics*, 238(1-4), 31-54.
- Chester, J. S., & Fletcher, R. C. (1997). Stress distribution and failure in anisotropic rock near a bend on a weak fault. *Journal of Geophysical Research: Solid Earth*, 102(B1), 693-708.
- Chester, F. M., & Chester, J. S. (2000). Stress and deformation along wavy frictional faults. *Journal of Geophysical Research: Solid Earth*, 105(B10), 23421-23430.
- Chiaralucente, L., Chiarabba, C., Collettini, C., Piccinini, D., & Cocco, M. (2007). Architecture and mechanics of an active low-angle normal fault: Alto Tiberina fault, northern Apennines, Italy. *Journal of Geophysical Research: Solid Earth*, 112(B10).
- Chiaralucente, L., Amato, A., Carannante, S., Castelli, V., Cattaneo, M., Cocco, M., ... & Marzorati, S. (2014). The Alto Tiberina Near Fault Observatory (northern Apennines, Italy). *Annals of Geophysics*, 57(3).
- Choi, E., & Buck, W. R. (2012). Constraints on the strength of faults from the geometry of rider-blocks in continental and oceanic core complexes. *Journal of Geophysical Research: Solid Earth*, 117(B4).
- Collettini, C., & Sibson, R. H. (2001). Normal faults, normal friction?. *Geology*, 29(10), 927-930.
- Collettini, C., & Holdsworth, R. E. (2004). Fault zone weakening and character of slip along low-angle normal faults: insights from the Zuccale fault, Elba, Italy. *Journal of the Geological Society*, 161(6), 1039-1051.
- Collettini, C., Niemeijer, A., Viti, C., & Marone, C. (2009a). Fault zone fabric and fault weakness. *Nature*, 462(7275), 907-910.
- Collettini, C., Viti, C., Smith, S. A., & Holdsworth, R. E. (2009b). Development of interconnected talc networks and weakening of continental low-angle normal faults. *Geology*, 37(6), 567-570.
- Collettini, C. (2011). The mechanical paradox of low-angle normal faults: Current understanding and open questions. *Tectonophysics*, 510(3), 253-268.
- Collettini, C., Niemeijer, A., Viti, C., Smith, S. A., & Marone, C. (2011). Fault structure, frictional properties and mixed-mode fault slip behavior. *Earth and Planetary Science Letters*, 311(3-4), 316-327.
- Collettini, C., Tesei, T., Scuderi, M. M., Carpenter, B. M., & Viti, C. (2019). Beyond Byerlee friction, weak faults and implications for slip behavior. *Earth and Planetary Science Letters*, 519, 245-263.
- Coney, P. J. (1974). Structural analysis of the Snake Range 'Décollement,' east-central Nevada. *Geological Society of America Bulletin*, 85(6), 973-978.
- Coney, P. J. (1980). Cordilleran metamorphic core complexes: An overview. *Geological Society of America Memoirs*, 153, 7-31.
- Cooper, F. J., Platt, J. P., & Behr, W. M. (2017). Rheological transitions in the middle crust: insights from Cordilleran metamorphic core complexes. *Solid Earth*, 8(1), 199.

- Cowan, D. S., Cladouhos, T. T., & Morgan, J. K. (2003). Structural geology and kinematic history of rocks formed along low-angle normal faults, Death Valley, California. *Geological Society of America Bulletin*, 115(10), 1230-1248.
- Craddock, J. P., & Magloughlin, J. F. (2005). Calcite strains, kinematic indicators, and magnetic flow fabric of a Proterozoic pseudotachylyte swarm, Minnesota River valley, USA. *Tectonophysics*, 402(1-4), 153-168.
- Cross, A. J. (2015). Microstructural evolution under non-steady state deformation in mid-crustal ductile shear zones (Doctoral dissertation, University of Otago).
- Cross, A. J., Prior, D. J., Stipp, M., & Kidder, S. (2017). The recrystallized grain size piezometer for quartz: An EBSD-based calibration. *Geophysical Research Letters*, 44(13), 6667-6674.
- Daczko, N. R., Caffi, P., Halpin, J. A., & Mann, P. (2009). Exhumation of the Dayman dome metamorphic core complex, eastern Papua New Guinea. *Journal of Metamorphic Geology*, 27(6), 405-422.
- Daczko, N. R., Caffi, P., & Mann, P. (2011). Structural evolution of the Dayman dome metamorphic core complex, eastern Papua New Guinea. *Geological Society of America Bulletin*, 123(11-12), 2335-2351.
- Davies, H. L., & Smith, I. E. (1971). Geology of eastern Papua. *Geological Society of America Bulletin*, 82(12), 3299-3312.
- Davies, H. L., & Smith, I. E. (1974). Tufi-Cape Nelson, Papua New Guinea, Sheets SC/55-8 and SC55-4, Geological Series and Explanatory Notes: Bureau of Mineral Resources, Geology and Geophysics, Department of Minerals and Energy in co-operation with the Geological Survey of Papua New Guinea, scale 1:250,000.
- Davies, H. L. (1978). Folded thrust fault and associated metamorphism in the Suckling-Dayman massif, Papua New Guinea. *Geological Survey of Papua New Guinea*.
- Davies, H. L., & Jaques, A. L. (1984). Emplacement of ophiolite in Papua New Guinea. *Geological Society, London, Special Publications*, 13(1), 341-349.
- Davies, H. L., & Warren, R. G. (1988). Origin of eclogite-bearing, domed, layered metamorphic complexes ("core complexes") in the D'entrecasteaux Islands, Papua New Guinea. *Tectonics*, 7(1), 1-21.
- Davis, G. A., Anderson, J. L., Frost, E. G., & Shackelford, T. J. (1980). Cordilleran metamorphic core complexes. *Geological Society of America Memoir*, 153, 7-31.
- Davis, G. H. (1983). Shear-zone model for the origin of metamorphic core complexes. *Geology*, 11(6), 342-347.
- Davis, G. A., & Lister, G. S. (1988). Detachment faulting in continental extension: Perspectives from the southwestern US Cordillera. *Processes in continental lithospheric deformation: Geological Society of America Special Paper*, 218, 133-159.

- Davis, G. H. (2013). Localization control for chlorite breccia deformation beneath Catalina detachment fault, Rincon Mountains, Tucson, Arizona. *Journal of Structural Geology*, 50, 237-253.
- De Bresser, J. H. P., & Spiers, C. J. (1997). Strength characteristics of the r, f, and c slip systems in calcite. *Tectonophysics*, 272(1), 1-23.
- De Bresser, J. H. P., Evans, B., & Renner, J. (2002). On estimating the strength of calcite rocks under natural conditions. *Geological Society, London, Special Publications*, 200(1), 309-329.
- De Bresser, J. H. P., Urai, J. L., & Olgaard, D. L. (2005). Effect of water on the strength and microstructure of Carrara marble axially compressed at high temperature. *Journal of Structural Geology*, 27(2), 265-281.
- De Paola, N., Holdsworth, R. E., Viti, C., Collettini, C., & Bullock, R. (2015). Can grain size sensitive flow lubricate faults during the initial stages of earthquake propagation?. *Earth and Planetary Science Letters*, 431, 48-58.
- Degioanni, S., Jurdyc, A. M., Cheap, A., Champagnon, B., Bessueille, F., Coulm, J., ... & Vouagner, D. (2015). Surface-enhanced Raman scattering of amorphous silica gel adsorbed on gold substrates for optical fiber sensors. *Journal of Applied Physics*, 118(15), 153103.
- Dick, H. J., Natland, J. H., Alt, J. C., Bach, W., Bideau, D., Gee, J. S., ... & Ildefonse, B. (2000). A long in situ section of the lower ocean crust: results of ODP Leg 176 drilling at the Southwest Indian Ridge. *Earth and planetary science letters*, 179(1), 31-51.
- Dick, H. J., Tivey, M. A., & Tucholke, B. E. (2008). Plutonic foundation of a slow-spreading ridge segment: Oceanic core complex at Kane Megamullion, 23 30' N, 45 20' W. *Geochemistry, Geophysics, Geosystems*, 9(5).
- Dimanov, A., & Dresen, G. (2005). Rheology of synthetic anorthite-diopside aggregates: Implications for ductile shear zones. *Journal of Geophysical Research: Solid Earth*, 110(B7).
- Di Toro, G., Nielsen, S., & Pennacchioni, G. (2005). Earthquake rupture dynamics frozen in exhumed ancient faults. *Nature*, 436(7053), 1009.
- Di Toro, G., Han, R., Hirose, T., De Paola, N., Nielsen, S., Mizoguchi, K., ... & Shimamoto, T. (2011). Fault lubrication during earthquakes. *Nature*, 471(7339), 494.
- Duebendorfer, E. M., Faulds, J. E., Fryxell, J. E., Umhoefer, P. J., Beard, L. S., & Lamb, M. A. (2010). The South Virgin–White Hills detachment fault, southeastern Nevada and northwestern Arizona: Significance, displacement gradient, and corrugation formation. Miocene tectonics of the Lake Mead region, central Basin and Range: *Geological Society of America Special Paper*, 463, 275-287.
- Dunlop, D. J., Özdemir, Ö., & Schmidt, P. W. (1997). Paleomagnetism and paleothermometry of the Sydney Basin 2. Origin of anomalously high unblocking temperatures. *Journal of Geophysical Research: Solid Earth*, 102(B12), 27285-27295.

- Eilon, Z., Abers, G. A., Gaherty, J. B., & Jin, G. (2015). Imaging continental breakup using teleseismic body waves: the Woodlark Rift, Papua New Guinea. *Geochemistry, Geophysics, Geosystems*, 16(8), 2529-2548.
- Ellis, S. M., Little, T. A., Wallace, L. M., Hacker, B. R., & Buiter, S. J. H. (2011). Feedback between rifting and diapirism can exhume ultrahigh-pressure rocks. *Earth and Planetary Science Letters*, 311(3-4), 427-438.
- Engelder, T. (1979). Mechanisms for strain within the Upper Devonian clastic sequence of the Appalachian Plateau, western New York. *American Journal of Science*, 279(5), 527-542.
- England, P. C., & Thompson, A. B. (1984). Pressure—temperature—time paths of regional metamorphism I. Heat transfer during the evolution of regions of thickened continental crust. *Journal of Petrology*, 25(4), 894-928.
- Escartín, J., Mével, C., MacLeod, C. J., & McCaig, A. M. (2003). Constraints on deformation conditions and the origin of oceanic detachments: The Mid-Atlantic Ridge core complex at 15°45' N. *Geochemistry, Geophysics, Geosystems*, 4(8).
- Etchecopar, A., Vasseur, G., & Daignieres, M. (1981). An inverse problem in microtectonics for the determination of stress tensors from fault striation analysis. *Journal of Structural Geology*, 3(1), 51-65.
- Etheridge, M. A., Wall, V. J., Cox, S. F., & Vernon, R. H. (1984). High fluid pressures during regional metamorphism and deformation: implications for mass transport and deformation mechanisms. *Journal of Geophysical Research: Solid Earth* (1978–2012), 89(B6), 4344-4358.
- Evans, M. A., & Dunne, W. M. (1991). Strain factorization and partitioning in the North Mountain thrust sheet, central Appalachians, USA. *Journal of Structural Geology*, 13(1), 21-35.
- Faulkner, D. R., Mitchell, T. M., Healy, D., & Heap, M. J. (2006). Slip on 'weak' faults by the rotation of regional stress in the fracture damage zone. *Nature*, 444(7121), 922.
- Faulkner, D. R., Mitchell, T. M., Behnsen, J., Hirose, T., & Shimamoto, T. (2011). Stuck in the mud? Earthquake nucleation and propagation through accretionary forearcs. *Geophysical Research Letters*, 38(18).
- Ferrill, D. A. (1991). Calcite twin widths and intensities as metamorphic indicators in natural low-temperature deformation of limestone. *Journal of Structural Geology*, 13(6), 667-675.
- Ferrill, D. A. (1998). Critical re-evaluation of differential stress estimates from calcite twins in coarse-grained limestone. *Tectonophysics*, 285(1-2), 77-86.
- Ferrill, D. A., Stamatakis, J. A., & Sims, D. (1999). Normal fault corrugation: Implications for growth and seismicity of active normal faults. *Journal of Structural Geology*, 21(8-9), 1027-1038.
- Ferrill, D. A., Morris, A. P., Evans, M. A., Burkhard, M., Groshong Jr, R. H., & Onasch, C. M. (2004). Calcite twin morphology: a low-temperature deformation geothermometer. *Journal of structural Geology*, 26(8), 1521-1529.

- Ferris, A., Abers, G. A., Zelt, B., Taylor, B., & Roecker, S. (2006). Crustal structure across the transition from rifting to spreading: the Woodlark rift system of Papua New Guinea. *Geophysical Journal International*, 166(2), 622-634.
- Finlayson, D. M., Drummond, B. J., Collins, C. D. M., & Connelly, J. B. (1977). Crustal structures in the region of the Papuan Ultramafic Belt. *Physics of the Earth and Planetary Interiors*, 14(1), 13-29.
- Fitz, G., & Mann, P. (2013). Tectonic uplift mechanism of the Goodenough and Fergusson Island gneiss domes, eastern Papua New Guinea: Constraints from seismic reflection and well data. *Geochemistry, Geophysics, Geosystems*, 14(10), 3969-3995.
- Fletcher, J. M., & Bartley, J. M. (1994). Constrictional strain in a non-coaxial shear zone: implications for fold and rock fabric development, central Mojave metamorphic core complex, California. *Journal of Structural Geology*, 16(4), 555-570.
- Fletcher, J. M., Bartley, J. M., Martin, M. W., Glazner, A. F., & Walker, J. D. (1995). Large-magnitude continental extension: An example from the central Mojave metamorphic core complex. *Geological Society of America Bulletin*, 107(12), 1468-1483.
- Fletcher, J. M., & Spelz, R. M. (2009). Patterns of Quaternary deformation and rupture propagation associated with an active low-angle normal fault, Laguna Salada, Mexico: Evidence of a rolling hinge?. *Geosphere*, 5(4), 385-407.
- Floyd, J. S., Mutter, J. C., Goodliffe, A. M., & Taylor, B. (2001). Evidence for fault weakness and fluid flow within an active low-angle normal fault. *Nature*, 411(6839), 779.
- Fynn, G. W., & Powell, W. J. A. (1979). The cutting and polishing of electro-optic materials.
- Gans, P. B., & Miller, E. L. (1983). Style of mid-Tertiary extension in east-central Nevada. Geological excursions in the overthrust belt and metamorphic core complexes of the Intermountain region: Utah Geological and Mineral Survey Special Studies, 59, 107-139.
- Gans, P. B., & Gentry, B. J. (2016). Dike emplacement, footwall rotation, and the transition from magmatic to tectonic extension in the Whipple Mountains metamorphic core complex, southeastern California. *Tectonics*, 35(11), 2564-2608.
- Garcés, M., & Gee, J. S. (2007). Paleomagnetic evidence of large footwall rotations associated with low-angle faults at the Mid-Atlantic Ridge. *Geology*, 35(3), 279-282.
- Garside I.E., S. J. D. (1973). Goodenough No. 1 well completion report: Amoco Australia Exploration Company.
- Getsinger, A. J., Hirth, G., Stünitz, H., & Goergen, E. T. (2013). Influence of water on rheology and strain localization in the lower continental crust. *Geochemistry, Geophysics, Geosystems*, 14(7), 2247-2264.
- Getsinger, A. J., & Hirth, G. (2014). Amphibole fabric formation during diffusion creep and the rheology of shear zones. *Geology*, 42(6), 535-538.

- Gleason, G. C., & Tullis, J. (1995). A flow law for dislocation creep of quartz aggregates determined with the molten salt cell. *Tectonophysics*, 247(1-4), 1-23.
- Goodwin, L. B. (1999). Controls on pseudotachylyte formation during tectonic exhumation in the South Mountains metamorphic core complex, Arizona. Geological Society, London, Special Publications, 154(1), 325-342.
- Gordon, S. M., Luffi, P., Hacker, B., Valley, J., Spicuzza, M., Kozdon, R., ... & Minaev, V. (2012). The thermal structure of continental crust in active orogens: insight from Miocene eclogite and granulite xenoliths of the Pamir Mountains. *Journal of Metamorphic Geology*, 30(4), 413-434.
- Ghosh, P., Garzione, C. N., & Eiler, J. M. (2006). Rapid uplift of the Altiplano revealed through ^{13}C - ^{18}O bonds in paleosol carbonates. *Science*, 311(5760), 511-515.
- Gratier, J. P. (2011). Fault permeability and strength evolution related to fracturing and healing episodic processes (years to millennia): the role of pressure solution. *Oil & Gas Science and Technology—Revue d'IFP Energies nouvelles*, 66(3), 491-506.
- Gratier, J. P., Dysthe, D. K., & Renard, F. (2013). The role of pressure solution creep in the ductility of the Earth's upper crust. In *Advances in Geophysics* (Vol. 54, pp. 47-179). Elsevier.
- Grohmann, C. H., & Campanha, G. A. (2010, December). OpenStereo: open source, cross-platform software for structural geology analysis. In *AGU Fall Meeting abstracts*.
- Groshong Jr, R. H. (1972). Strain calculated from twinning in calcite. *Geological Society of America Bulletin*, 83(7), 2025-2038.
- Groshong Jr, R. H. (1974). Experimental test of least-squares strain gage calculation using twinned calcite. *Geological Society of America Bulletin*, 85(12), 1855-1864.
- Groshong Jr, R. H. (1975). Strain, fractures, and pressure solution in natural single-layer folds. *Geological Society of America Bulletin*, 86(10), 1363-1376.
- Groshong Jr, R. H., Teufel, L. W., & Gasteiger, C. (1984). Precision and accuracy of the calcite strain-gage technique. *Geological Society of America Bulletin*, 95(3), 357-363.
- Groshong Jr, R. H. (1988). Low-temperature deformation mechanisms and their interpretation. *Geological Society of America Bulletin*, 100(9), 1329-1360.
- Gueydan, F., Mehl, C., & Parra, T. (2005). Stress-strain rate history of a midcrustal shear zone and the onset of brittle deformation inferred from quartz recrystallized grain size. Geological Society, London, Special Publications, 243(1), 127-142.
- Haines, S. H., & van der Pluijm, B. A. (2012). Patterns of mineral transformations in clay gouge, with examples from low-angle normal fault rocks in the western USA. *Journal of Structural Geology*, 43, 2-32.

- Halfpenny, A., Prior, D. J., & Wheeler, J. (2006). Analysis of dynamic recrystallization and nucleation in a quartzite mylonite. *Tectonophysics*, 427(1-4), 3-14.
- Hamilton, W. B. (1988). Laramide crustal shortening. *Geological Society of America Memoirs*, 171, 27-40.
- Han, R., & Hirose, T. (2012). Clay-clast aggregates in fault gouge: An unequivocal indicator of seismic faulting at shallow depths?. *Journal of Structural Geology*, 43, 92-99.
- Hashimoto, M. (1972). Reactions producing actinolite in basic metamorphic rocks. *Lithos*, 5(1), 19-31.
- Hayman, N. W., Knott, J. R., Cowan, D. S., Nemser, E., & Sarna-Wojcicki, A. M. (2003). Quaternary low-angle slip on detachment faults in Death Valley, California. *Geology*, 31(4), 343-346.
- Hayman, N. W. (2006). Shallow crustal fault rocks from the Black Mountain detachments, Death Valley, CA. *Journal of Structural Geology*, 28(10), 1767-1784.
- Hayman, N. W., Grindlay, N. R., Perfit, M. R., Mann, P., Leroy, S., & de Lépinay, B. M. (2011). Oceanic core complex development at the ultraslow spreading Mid-Cayman Spreading Center. *Geochemistry, Geophysics, Geosystems*, 12(3).
- Healy, D. (2008). Damage patterns, stress rotations and pore fluid pressures in strike-slip fault zones. *Journal of Geophysical Research: Solid Earth*, 113(B12).
- Herwegh, M., Linckens, J., Ebert, A., Berger, A., & Brodhag, S. H. (2011). The role of second phases for controlling microstructural evolution in polyminerale rocks: A review. *Journal of Structural Geology*, 33(12), 1728-1750.
- Hickman, S., & Zoback, M. (2004). Stress orientations and magnitudes in the SAFOD pilot hole. *Geophysical Research Letters*, 31(15).
- Hill, E. J., Baldwin, S. L., & Lister, G. S. (1992). Unroofing of active metamorphic core complexes in the D'Entrecasteaux Islands, Papua New Guinea. *Geology*, 20(10), 907-910.
- Hirono, T., Lin, W., Yeh, E. C., Soh, W., Hashimoto, Y., Sone, H., ... & Murayama, M. (2006). High magnetic susceptibility of fault gouge within Taiwan Chelungpu fault: Nondestructive continuous measurements of physical and chemical properties in fault rocks recovered from Hole B, TCDP. *Geophysical Research Letters*, 33(15).
- Hirose, T., & Hayman, N. W. (2008). Structure, permeability, and strength of a fault zone in the footwall of an oceanic core complex, the Central Dome of the Atlantis Massif, Mid-Atlantic Ridge, 30 N. *Journal of Structural Geology*, 30(8), 1060-1071.
- Hirth, G., & Kohlstedt, D. L. (1995). Experimental constraints on the dynamics of the partially molten upper mantle: Deformation in the diffusion creep regime. *Journal of Geophysical Research: Solid Earth*, 100(B2), 1981-2001.

- Hirth, G., Teyssier, C., & Dunlap, J. W. (2001). An evaluation of quartzite flow laws based on comparisons between experimentally and naturally deformed rocks. *International Journal of Earth Sciences*, 90(1), 77-87.
- Hirth, G., & Kohlstedt, D. (2004). Rheology of the upper mantle and the mantle wedge: A view from the experimentalists. *Inside the subduction Factory*, Geophys. Monogr. 138, 83-105.
- Holdsworth, R. E. (2004). Weak faults--rotten cores. *Science*, 303(5655), 181-182.
- Holdsworth, R. E., Van Diggelen, E. W. E., Spiers, C. J., De Bresser, J. H. P., Walker, R. J., & Bowen, L. (2011). Fault rocks from the SAFOD core samples: Implications for weakening at shallow depths along the San Andreas Fault, California. *Journal of Structural Geology*, 33(2), 132-144.
- Holm, D. K., Fleck, R. J., & Lux, D. R. (1994). The Death Valley turtlebacks reinterpreted as Miocene-Pliocene folds of a major detachment surface. *The Journal of Geology*, 102(6), 718-727.
- Hreinsdóttir, S., & Bennett, R. A. (2009). Active aseismic creep on the Alto Tiberina low-angle normal fault, Italy. *Geology*, 37(8), 683-686.
- Ikari, M. J., Saffer, D. M., & Marone, C. (2009). Frictional and hydrologic properties of clay-rich fault gouge. *Journal of Geophysical Research: Solid Earth* (1978–2012), 114(B5).
- Ildefonse, B., Blackman, D. K., John, B. E., Ohara, Y., Miller, D. J., & MacLeod, C. J. (2007). Oceanic core complexes and crustal accretion at slow-spreading ridges. *Geology*, 35(7), 623-626.
- Imber, J., Holdsworth, R. E., Butler, C. A., & Strachan, R. A. (2001). A reappraisal of the Sibson-Scholz fault zone model: The nature of the frictional to viscous ("brittle-ductile") transition along a long-lived, crustal-scale fault, Outer Hebrides, Scotland. *Tectonics*, 20(5), 601-624.
- Işık, V., Seyitoğlu, G., & Cemen, I. (2003). Ductile–brittle transition along the Alaşehir detachment fault and its structural relationship with the Simav detachment fault, Menderes Massif, Western Turkey. *Tectonophysics*, 374(1-2), 1-18.
- Jackson, J. A. (1987). Active normal faulting and crustal extension. *Geological Society, London, Special Publications*, 28(1), 3-17.
- Jackson, J. A., & White, N. J. (1989). Normal faulting in the upper continental crust: observations from regions of active extension. *Journal of Structural Geology*, 11(1-2), 15-36.
- Jamison, W. R., & Spang, J. H. (1976). Use of calcite twin lamellae to infer differential stress. *Geological Society of America Bulletin*, 87(6), 868-872.
- Jaques, A. L., & Chappell, B. W. (1980). Petrology and trace element geochemistry of the Papuan ultramafic belt. *Contributions to Mineralogy and Petrology*, 75(1), 55-70.
- Jaya, A., & Nishikawa, O. (2013). Paleostress reconstruction from calcite twin and fault–slip data using the multiple inverse method in the East Walanae fault zone: Implications for the Neogene contraction in South Sulawesi, Indonesia. *Journal of Structural Geology*, 55, 34-49.

- Jefferies, S. P., Holdsworth, R. E., Shimamoto, T., Takagi, H., Lloyd, G. E., & Spiers, C. J. (2006). Origin and mechanical significance of foliated cataclastic rocks in the cores of crustal-scale faults: Examples from the Median Tectonic Line, Japan. *Journal of Geophysical Research: Solid Earth*, 111(B12).
- Jiang, Z., Prior, D. J., & Wheeler, J. (2000). Albite crystallographic preferred orientation and grain misorientation distribution in a low-grade mylonite: implications for granular flow. *Journal of Structural Geology*, 22(11-12), 1663-1674.
- Jiasheng, Z., Dirks, P. H., & Passchier, C. W. (1994). Extensional collapse and uplift in a polymetamorphic granulite terrain in the Archaean and Palaeoproterozoic of north China. *Precambrian Research*, 67(1-2), 37-57.
- Jin, G., Gaherty, J. B., Abers, G. A., Kim, Y., Eilon, Z., & Buck, W. R. (2015). Crust and upper mantle structure associated with extension in the Woodlark Rift, Papua New Guinea from Rayleigh-wave tomography. *Geochemistry, Geophysics, Geosystems*, 16(11), 3808-3824.
- John, B. E. (1987). Geometry and evolution of a mid-crustal extensional fault system: Chemehuevi Mountains, southeastern California. *Geological Society, London, Special Publications*, 28(1), 313-335.
- John, B. E., & Cheadle, M. J. (2010). Deformation and alteration associated with oceanic and continental detachment fault systems: Are they similar. *Diversity of Hydrothermal Systems on Slow Spreading Ocean Ridges*, *Geophys. Monogr. Ser.*, 188, 175-206.
- Johnson, S. E., & Williams, M. L. (1998). Determining finite longitudinal strains from oppositely-concave microfolds in and around porphyroblasts: a new quantitative method. *Journal of Structural Geology*, 20(11), 1521-1530.
- Kanai, T., & Takagi, H. (2016). Determination of the stress conditions of the ductile-to-brittle regime along the Auke Shear Zone, SW Japan. *Journal of Structural Geology*, 85, 154-167.
- Karaman, K., Cihangir, F., & Kesimal, A. Kaya Malzemesinin Kohezyon ve İçsel Sürtünme Açısının Dolaylı Yöntemlerle İrdelenmesi. *Mehmet Akif Ersoy Üniversitesi Fen Bilimleri Enstitüsü Dergisi*, 4(2), 13-19.
- Karato, S. I. (2012). *Deformation of earth materials: an introduction to the rheology of solid earth*. Cambridge University Press.
- Karson, J. A., & Dick, H. J. B. (1983). Tectonics of ridge-transform intersections at the Kane fracture zone. *Marine Geophysical Researches*, 6(1), 51-98.
- Karson, J. A., Früh-Green, G. L., Kelley, D. S., Williams, E. A., Yoerger, D. R., & Jakuba, M. (2006). Detachment shear zone of the Atlantis Massif core complex, Mid-Atlantic Ridge, 30 N. *Geochemistry, Geophysics, Geosystems*, 7(6).
- Karson, J. A., Früh-Green, G. L., Kelley, D. S., Williams, E. A., Yoerger, D. R., & Jakuba, M. (2006). Detachment shear zone of the Atlantis Massif core complex, Mid-Atlantic Ridge, 30 N. *Geochemistry, Geophysics, Geosystems*, 7(6).

- Kennedy, L. A., & White, J. C. (2001). Low-temperature recrystallization in calcite: Mechanisms and consequences. *Geology*, 29(11), 1027-1030.
- Ketcham, R. A. (1996). Thermal models of core-complex evolution in Arizona and New Guinea: Implications for ancient cooling paths and present-day heat flow. *Tectonics*, 15(5), 933-951.
- Kilsdonk, B., & Wiltschko, D. V. (1988). Deformation mechanisms in the southeastern ramp region of the Pine Mountain block, Tennessee. *Geological Society of America Bulletin*, 100(5), 653-664.
- Kirby, E., Snyder, N., Whipple, K., Walker, J. D., & Andrew, J. (2003, December). Neotectonics of the Panamint Valley fault zone: Active slip on a low-angle normal fault system. In AGU Fall Meeting Abstracts.
- Kirkpatrick, J. D., & Rowe, C. D. (2013). Disappearing ink: How pseudotachylytes are lost from the rock record. *Journal of Structural Geology*, 52, 183-198.
- Kirkpatrick, J. D., & Brodsky, E. E. (2014). Slickenside orientations as a record of fault rock rheology. *Earth and Planetary Science Letters*, 408, 24-34.
- Knipe, R. J. (1989). Deformation mechanisms—recognition from natural tectonites. *Journal of Structural Geology*, 11(1-2), 127-146.
- Kuo, L. W., Song, S. R., Suppe, J., & Yeh, E. C. (2016). Fault mirrors in seismically active fault zones: A fossil of small earthquakes at shallow depths. *Geophysical Research Letters*, 43(5), 1950-1959.
- Labuz, J. F., & Zang, A. (2012). Mohr–Coulomb failure criterion. *Rock mechanics and rock engineering*, 45(6), 975-979.
- Lacombe, O., & Laurent, P. (1996). Determination of deviatoric stress tensors based on inversion of calcite twin data from experimentally deformed monophase samples: preliminary results. *Tectonophysics*, 255(3-4), 189-202.
- Lapworth, T., Wheeler, J., & Prior, D. J. (2002). The deformation of plagioclase investigated using electron backscatter diffraction crystallographic preferred orientation data. *Journal of Structural Geology*, 24(2), 387-399.
- Laurent, P., Kern, H., & Lacombe, O. (2000). Determination of deviatoric stress tensors based on inversion of calcite twin data from experimentally deformed monophase samples. Part II. Axial and triaxial stress experiments. *Tectonophysics*, 327(1-2), 131-148.
- Lavier, L. L., Roger Buck, W., & Poliakov, A. N. (1999). Self-consistent rolling-hinge model for the evolution of large-offset low-angle normal faults. *Geology*, 27(12), 1127-1130.
- Lindley, I. D. (2014). Suckling Dome and the Australian–Woodlark plate boundary in eastern Papua: the geology of the Keveri and Ada'u Valleys. *Australian Journal of Earth Sciences*, 61(8), 1125-1147.
- Lister, G. S., Banga, G., & Feenstra, A. (1984). Metamorphic core complexes of Cordilleran type in the Cyclades, Aegean Sea, Greece. *Geology*, 12(4), 221-225.
- Lister, G. S., & Davis, G. A. (1989). The origin of metamorphic core complexes and detachment faults formed during Tertiary continental extension in the

- northern Colorado River region, USA. *Journal of Structural Geology*, 11(1-2), 65-94.
- Little, T. A., Baldwin, S. L., Fitzgerald, P. G., & Monteleone, B. (2007). Continental rifting and metamorphic core complex formation ahead of the Woodlark spreading ridge, D'Entrecasteaux Islands, Papua New Guinea. *Tectonics*, 26(1).
- Little, T. A., Hacker, B. R., Gordon, S. M., Baldwin, S. L., Fitzgerald, P. G., Ellis, S., & Korchinski, M. (2011). Diapiric exhumation of Earth's youngest (UHP) eclogites in the gneiss domes of the D'Entrecasteaux Islands, Papua New Guinea. *Tectonophysics*, 510(1), 39-68.
- Little, T. A., Webber, S. M., Mizera, M., Boulton, C., Oesterle, J., Ellis, S., ... & Biemiller, J. (2019). Evolution of a rapidly slipping, active low-angle normal fault, Suckling-Dayman metamorphic core complex, SE Papua New Guinea. *Geological Society of America Bulletin*.
- Lockner, D. A., Morrow, C., Moore, D., & Hickman, S. (2011). Low strength of deep San Andreas fault gouge from SAFOD core. *Nature*, 472(7341), 82.
- Lus, W. Y., McDougall, I., & Davies, H. L. (2004). Age of the metamorphic sole of the Papuan Ultramafic Belt ophiolite, Papua New Guinea. *Tectonophysics*, 392(1-4), 85-101.
- Magloughlin, J. F. (1992). Microstructural and chemical changes associated with cataclasis and frictional melting at shallow crustal levels: the cataclasite-pseudotachylyte connection. *Tectonophysics*, 204(3-4), 243-260.
- Magloughlin, J. F. (2005). Immiscible sulfide droplets in pseudotachylyte: Evidence for high temperature (> 1200 C) melts. *Tectonophysics*, 402(1-4), 81-91.
- Mainprice, D., Bouchez, J. L., Blumenfeld, P., & Tubià, J. M. (1986). Dominant c slip in naturally deformed quartz: Implications for dramatic plastic softening at high temperature. *Geology*, 14(10), 819-822.
- Mainprice, D., Bachmann, F., Hielscher, R., & Schaebe, H. (2015). Descriptive tools for the analysis of texture projects with large datasets using MTEX: strength, symmetry and components. *Geological Society, London, Special Publications*, 409(1), 251-271.
- Maitland, T., & Sitzman, S. (2006). Backscattering detector and EBSD in nanomaterials characterization. In *Scanning Microscopy for Nanotechnology* (pp. 41-75). Springer, New York, NY.
- Malvoisin, B., Carlut, J., & Brunet, F. (2012). Serpentinization of oceanic peridotites: 1. A high-sensitivity method to monitor magnetite production in hydrothermal experiments. *Journal of Geophysical Research: Solid Earth*, 117(B1).
- Mancktelow, N. S., & Pavlis, T. L. (1994). Fold-fault relationships in low-angle detachment systems. *Tectonics*, 13(3), 668-685.
- Manning, A. H., & Bartley, J. M. (1994). Postmylonitic deformation in the Raft River metamorphic core complex, northwestern Utah: Evidence of a rolling hinge. *Tectonics*, 13(3), 596-612.

- Marotta, A. M., Spalla, M. I., & Gosso, G. (2009). Upper and lower crustal evolution during lithospheric extension: numerical modelling and natural footprints from the European Alps. Geological Society, London, Special Publications, 321(1), 33-72.
- Martinez, F., Goodliffe, A. M., & Taylor, B. (2001). Metamorphic core complex formation by density inversion and lower-crust extrusion. *Nature*, 411(6840), 930.
- McCaig, A. M., Delacour, A., Fallick, A. E., Castelain, T., & Früh-Green, G. L. (2010). Detachment fault control on hydrothermal circulation systems: Interpreting the subsurface beneath the TAG hydrothermal field using the isotopic and geological evolution of oceanic core complexes in the Atlantic. *Diversity of Hydrothermal Systems on Slow Spreading Ocean Ridges*, Geophys. Monogr. Ser, 188, 207-240.
- Mehl, L., & Hirth, G. (2008). Plagioclase preferred orientation in layered mylonites: Evaluation of flow laws for the lower crust. *Journal of Geophysical Research: Solid Earth*, 113(B5).
- Mello, M., Bhat, H. S., Rosakis, A. J., & Kanamori, H. (2010). Identifying the unique ground motion signatures of supershear earthquakes: Theory and experiments. *Tectonophysics*, 493(3-4), 297-326.
- Miller, E. L., Gans, P. B., & Garing, J. (1983). The Snake Range decollement: An exhumed mid-Tertiary ductile-brittle transition. *Tectonics*, 2(3), 239-263.
- Miller, S. R., Baldwin, S. L., & Fitzgerald, P. G. (2012). Transient fluvial incision and active surface uplift in the Woodlark Rift of eastern Papua New Guinea. *Lithosphere*, 4(2), 131-149.
- Miranda, E. A. (2006). Structural development of the Atlantis Bank oceanic detachment fault system, Southwest Indian Ridge (Doctoral dissertation, University of Wyoming).
- Miranda, E. A., & John, B. E. (2010). Strain localization along the Atlantis Bank oceanic detachment fault system, Southwest Indian Ridge. *Geochemistry, Geophysics, Geosystems*, 11(4).
- Miranda, E. A., Hirth, G., & John, B. E. (2016). Microstructural evidence for the transition from dislocation creep to dislocation-accommodated grain boundary sliding in naturally deformed plagioclase. *Journal of Structural Geology*, 92, 30-45.
- Mishima, T., Hirono, T., Soh, W., & Song, S. R. (2006). Thermal history estimation of the Taiwan Chelungpu fault using rock-magnetic methods. *Geophysical research letters*, 33(23).
- Mishima, T., Hirono, T., Nakamura, N., Tanikawa, W., Soh, W., & Song, S. R. (2009). Changes to magnetic minerals caused by frictional heating during the 1999 Taiwan Chi-Chi earthquake. *Earth, planets and space*, 61(6), 797-801.
- Mizera, M., Little, T. A., Biemiller, J., Ellis, S., Webber, S., & Norton, K. P. (2019). Structural and Geomorphic Evidence for Rolling-Hinge Style Deformation of an Active Continental Low-Angle Normal Fault, SE Papua New Guinea. *Tectonics*.

- Montone, P., Mariucci, M. T., Pondrelli, S., & Amato, A. (2004). An improved stress map for Italy and surrounding regions (central Mediterranean). *Journal of Geophysical Research: Solid Earth*, 109(B10).
- Moore, D. E., & Lockner, D. A. (2004). Crystallographic controls on the frictional behavior of dry and water-saturated sheet structure minerals. *Journal of Geophysical Research: Solid Earth*, 109(B3).
- Moore, D. E., & Rymer, M. J. (2012). Correlation of clayey gouge in a surface exposure of serpentinite in the San Andreas Fault with gouge from the San Andreas Fault Observatory at Depth (SAFOD). *Journal of Structural Geology*, 38, 51-60.
- Moore, D. E. (2014). Comparative mineral chemistry and textures of SAFOD fault gouge and damage-zone rocks. *Journal of Structural Geology*, 68, 82-96.
- Moore, D. E., Lockner, D. A., & Hickman, S. (2016). Hydrothermal frictional strengths of rock and mineral samples relevant to the creeping section of the San Andreas Fault. *Journal of Structural Geology*, 89, 153-167.
- Moresi, L., Dufour, F., & Mühlhaus, H. B. (2003). A Lagrangian integration point finite element method for large deformation modeling of viscoelastic geomaterials. *Journal of Computational Physics*, 184(2), 476-497.
- Morris, A., Gee, J. S., Pressling, N., John, B. E., MacLeod, C. J., Grimes, C. B., & Searle, R. C. (2009). Footwall rotation in an oceanic core complex quantified using reoriented Integrated Ocean Drilling Program core samples. *Earth and Planetary Science Letters*, 287(1), 217-228.
- Niemeijer, A. R., & Spiers, C. J. (2005). Influence of phyllosilicates on fault strength in the brittle-ductile transition: Insights from rock analogue experiments. *Geological Society, London, Special Publications*, 245(1), 303-327.
- Oesterle, J., Seward, D., Little, T. & Stockli, D. (2018). The evolution of an actively exhuming metamorphic core complex, the Suckling-Dayman massif in Papua New Guinea. 16th International Conference on Thermochronology, Thermo 2018 Conference Abstracts, 16.09.-21.09.2018, Quedlinburg, Germany.
- Offerhaus, L. J., Wirth, R., & Dresen, G. (2001). High-temperature creep of polycrystalline albite. *Deformation Mechanisms, Rheology and Tectonics*, 124, 107-131.
- Özdemir, Ö., & Banerjee, S. K. (1984). High temperature stability of maghemite (γ -Fe₂O₃). *Geophysical research letters*, 11(3), 161-164.
- Özdemir, Ö. (1990). High-temperature hysteresis and thermoremanence of single-domain maghemite. *Physics of the Earth and planetary interiors*, 65(1-2), 125-136.
- Okudaira, T., Takeshita, T., Hara, I., & Ando, J. I. (1995). A new estimate of the conditions for transition from basal $\langle a \rangle$ to prism $\langle c \rangle$ slip in naturally deformed quartz. *Tectonophysics*, 250(1-3), 31-46.
- Oldow, J. S., Elias, E. A., Ferranti, L., McClelland, W. C., McIntosh, W. C., & Cashman, P. H. (2009). Late Miocene to Pliocene synextensional deposition in fault-bounded basins within the upper plate of the western Silver Peak–Lone Mountain extensional complex, west-central Nevada. *Late Cenozoic*

Structure and Evolution of the Great Basin–Sierra Nevada Transition:
Geological Society of America Special Paper, 447, 275-312.

- Ollier, C. D., & Pain, C. F. (1980). Actively rising surficial gneiss domes in Papua New Guinea. *Journal of the Geological Society of Australia*, 27(1-2), 33-44.
- Oohashi, K., Hirose, T., & Shimamoto, T. (2011). Shear-induced graphitization of carbonaceous materials during seismic fault motion: Experiments and possible implications for fault mechanics. *Journal of Structural Geology*, 33(6), 1122-1134.
- Otsubo, M., & Yamaji, A. (2006). Improved resolution of the multiple inverse method by eliminating erroneous solutions. *Computers & geosciences*, 32(8), 1221-1227. Otsubo, M., Yamaji, A., & Kubo, A. (2008). Determination of stresses from heterogeneous focal mechanism data: An adaptation of the multiple inverse method. *Tectonophysics*, 457(3-4), 150-160.
- Parsons, T., & Thompson, G. A. (1993). Does magmatism influence low-angle normal faulting?. *Geology*, 21(3), 247-250.
- Parnell-Turner, R., Sohn, R. A., Peirce, C., Reston, T. J., MacLeod, C. J., Searle, R. C., & Simão, N. M. (2017). Oceanic detachment faults generate compression in extension. *Geology*, 45(10), 923-926.
- Parnell-Turner, R., Escartin, J., Olive, J. A., Smith, D. K., & Petersen, S. (2018). Genesis of corrugated fault surfaces by strain localization recorded at oceanic detachments. *Earth and Planetary Science Letters*, 498, 116-128.
- Passchier, C. W., & Trouw, R. A. (2005). *Microtectonics*. Springer Science & Business Media.
- Pearce, M. A., Wheeler, J., & Prior, D. J. (2011). Relative strength of mafic and felsic rocks during amphibolite facies metamorphism and deformation. *Journal of Structural Geology*, 33(4), 662-675.
- Petersen, K. D., & Buck, W. R. (2015). Eduction, extension, and exhumation of ultrahigh-pressure rocks in metamorphic core complexes due to subduction initiation. *Geochemistry, Geophysics, Geosystems*, 16(8), 2564-2581.
- Pigram, C. J., & Symonds, P. A. (1993). Eastern Papuan Basin—A new model for the tectonic development, and implications for petroleum prospectivity. Papua New Guinea (PNG) Petroleum Convention Proceedings.
- Platt, J. P., Behr, W. M., & Cooper, F. J. (2015). Metamorphic core complexes: windows into the mechanics and rheology of the crust. *Journal of the Geological Society*, 172(1), 9-27.
- Platt, J. P., & De Bresser, J. H. P. (2017). Stress dependence of microstructures in experimentally deformed calcite. *Journal of Structural Geology*, 105, 80-87.
- Poirier, J. P. (1985). *Creep of crystals: high-temperature deformation processes in metals, ceramics and minerals*. Cambridge University Press.
- Post, A., & Tullis, J. (1999). A recrystallized grain size piezometer for experimentally deformed feldspar aggregates. *Tectonophysics*, 303(1-4), 159-173.
- Prante, M. R., Evans, J. P., Janecke, S. U., & Steely, A. (2014). Evidence for paleoseismic slip on a continental low-angle normal fault: Tectonic

- pseudotachylyte from the West Salton detachment fault, CA, USA. *Earth and Planetary Science Letters*, 387, 170-183.
- Proffett Jr, J. M. (1977). Cenozoic geology of the Yerington district, Nevada, and implications for the nature and origin of Basin and Range faulting. *Geological Society of America Bulletin*, 88(2), 247-266.
- Putnis, A., Hinrichs, R., Putnis, C. V., Golla-Schindler, U., & Collins, L. G. (2007). Hematite in porous red-clouded feldspars: evidence of large-scale crustal fluid-rock interaction. *Lithos*, 95(1-2), 10-18.
- Raj, R., & Ashby, M. F. (1971). On grain boundary sliding and diffusional creep. *Metallurgical transactions*, 2(4), 1113-1127.
- Ranero, C. R., & Reston, T. J. (1999). Detachment faulting at ocean core complexes. *Geology*, 27(11), 983-986.
- Rempe, M., Smith, S. A., Ferri, F., Mitchell, T. M., & Di Toro, G. (2014). Clast-cortex aggregates in experimental and natural calcite-bearing fault zones. *Journal of Structural Geology*, 68, 142-157.
- Renard, F., Candela, T., & Bouchaud, E. (2013). Constant dimensionality of fault roughness from the scale of micro-fractures to the scale of continents. *Geophysical Research Letters*, 40(1), 83-87.
- Renner, J., Evans, B., & Siddiqi, G. (2002). Dislocation creep of calcite. *Journal of Geophysical Research: Solid Earth*, 107(B12).
- Reston, T. J., & Ranero, C. R. (2011). The 3-D geometry of detachment faulting at mid-ocean ridges. *Geochemistry, Geophysics, Geosystems*, 12(7).
- Reynolds, S. J., & Lister, G. S. (1987). Structural aspects of fluid-rock interactions in detachment zones. *Geology*, 15(4), 362-366.
- Rice, J. R. (1992). Fault stress states, pore pressure distributions, and the weakness of the San Andreas fault. *International Geophysics*, 51, 475-503.
- Richard, S. M., Smith, C. H., Kimbrough, D. L., Fitzgerald, P. G., Luyendyk, B. P., & McWilliams, M. O. (1994). Cooling history of the northern Ford Ranges, Marie Byrd Land, West Antarctica. *Tectonics*, 13(4), 837-857.
- Richard, J., Gratier, J. P., Doan, M. L., Boullier, A. M., & Renard, F. (2014). Rock and mineral transformations in a fault zone leading to permanent creep: Interactions between brittle and viscous mechanisms in the San Andreas Fault. *Journal of Geophysical Research: Solid Earth*, 119(11), 8132-8153.
- Rigo, A., Lyon-Caen, H., Armijo, R., Deschamps, A., Hatzfeld, D., Makropoulos, K., ... & Kassaras, I. (1996). A microseismic study in the western part of the Gulf of Corinth (Greece): implications for large-scale normal faulting mechanisms. *Geophysical Journal International*, 126(3), 663-688.
- Robinson, D., Schmidt, S. T., & De Zamora, A. S. (2002). Reaction pathways and reaction progress for the smectite-to-chlorite transformation: evidence from hydrothermally altered metabasites. *Journal of metamorphic Geology*, 20(1), 167-174.
- Rong, J., & Wang, F. (2016). *Metasomatic Textures in Granites*. Springer. Mineral, 22, 143-144.

- Rooney, J. S., Tarling, M. S., Smith, S. A., & Gordon, K. C. (2018). Submicron Raman spectroscopy mapping of serpentinite fault rocks. *Journal of Raman Spectroscopy*, 49(2), 279-286.
- Rossano, S., & Mysen, B. O. (2012). Raman spectroscopy of silicate glasses and melts in geological systems. *EMU Notes in Mineralogy*, 12(1), 319-364.
- Rowe, K. J., & Rutter, E. H. (1990). Palaeostress estimation using calcite twinning: experimental calibration and application to nature. *Journal of Structural Geology*, 12(1), 1-17.
- Rowe, C. D., Meneghini, F., & Moore, J. C. (2011). Textural record of the seismic cycle: Strain-rate variation in an ancient subduction thrust. *Geological Society, London, Special Publications*, 359(1), 77-95.
- Rowe, C. D., Fagereng, Å., Miller, J. A., & Mapani, B. (2012). Signature of coseismic decarbonation in dolomitic fault rocks of the Naukluft Thrust, Namibia. *Earth and Planetary Science Letters*, 333, 200-210.
- Rowe, C. D., & Griffith, W. A. (2015). Do faults preserve a record of seismic slip: A second opinion. *Journal of Structural Geology*, 78, 1-26.
- Rutter, E. H., & Mainprice, D. H. (1979). On the possibility of slow fault slip controlled by a diffusive mass transfer process. *Gerlands Beitrage zur Geophysik*, 88(2), 154-162.
- Rutter, E. H. (1983). Pressure solution in nature, theory and experiment. *Journal of the Geological Society*, 140(5), 725-740.
- Rutter, E. H. (1995). Experimental study of the influence of stress, temperature, and strain on the dynamic recrystallization of Carrara marble. *Journal of Geophysical Research: Solid Earth*, 100(B12), 24651-24663.
- Rutter, E. H., Faulkner, D. R., Brodie, K. H., Phillips, R. J., & Searle, M. P. (2007). Rock deformation processes in the Karakoram fault zone, Eastern Karakoram, Ladakh, NW India. *Journal of Structural Geology*, 29(8), 1315-1326.
- Rybacki, E., Janssen, C., Wirth, R., Chen, K., Wenk, H. R., Stromeyer, D., & Dresen, G. (2011). Low-temperature deformation in calcite veins of SAFOD core samples (San Andreas Fault)—microstructural analysis and implications for fault rheology. *Tectonophysics*, 509(1-2), 107-119.
- Rybacki, E., Evans, B., Janssen, C., Wirth, R., & Dresen, G. (2013). Influence of stress, temperature, and strain on calcite twins constrained by deformation experiments. *Tectonophysics*, 601, 20-36.
- Saffer, D. M., & Marone, C. (2003). Comparison of smectite-and illite-rich gouge frictional properties: application to the updip limit of the seismogenic zone along subduction megathrusts. *Earth and Planetary Science Letters*, 215(1-2), 219-235.
- Saffer, D. M., Lockner, D. A., & McKiernan, A. (2012). Effects of smectite to illite transformation on the frictional strength and sliding stability of intact marine mudstones. *Geophysical Research Letters*, 39(11).
- Sammis, C. G., & Ben-Zion, Y. (2008). Mechanics of grain-size reduction in fault zones. *Journal of Geophysical Research: Solid Earth*, 113(B2).

- Savage, M. K. (1999). Seismic anisotropy and mantle deformation: what have we learned from shear wave splitting?. *Reviews of Geophysics*, 37(1), 65-106.
- Schauble, E. A., Ghosh, P., & Eiler, J. M. (2006). Preferential formation of ^{13}C – ^{18}O bonds in carbonate minerals, estimated using first-principles lattice dynamics. *Geochimica et Cosmochimica Acta*, 70(10), 2510-2529.
- Schmid, S. M., Paterson, M. S., & Boland, J. N. (1980). High temperature flow and dynamic recrystallization in Carrara marble. *Tectonophysics*, 65(3-4), 245-280.
- Schmid, S. M., & Casey, M. (1986). Complete fabric analysis of some commonly observed quartz c-axis patterns. *Mineral and rock deformation: Laboratory studies*, 36, 263-286.
- Schouten, H., Smith, D. K., Cann, J. R., & Escartín, J. (2010). Tectonic versus magmatic extension in the presence of core complexes at slow-spreading ridges from a visualization of faulted seafloor topography. *Geology*, 38(7), 615-618.
- Schroeder, T., & John, B. E. (2004). Strain localization on an oceanic detachment fault system, Atlantis Massif, 30 N, Mid-Atlantic Ridge. *Geochemistry, Geophysics, Geosystems*, 5(11).
- Schultz, R. A. (1993). Brittle strength of basaltic rock masses with applications to Venus. *Journal of Geophysical Research: Planets*, 98(E6), 10883-10895.
- Scott, R. J., & Lister, G. S. (1992). Detachment faults: Evidence for a low-angle origin. *Geology*, 20(9), 833-836.
- Seiler, C., Fletcher, J. M., Quigley, M. C., Gleadow, A. J., & Kohn, B. P. (2010). Neogene structural evolution of the Sierra San Felipe, Baja California: Evidence for proto-gulf transtension in the Gulf Extensional Province?. *Tectonophysics*, 488(1-4), 87-109.
- Shah, D. L., & Shroff, A. V. (2003). *Soil mechanics and geotechnical engineering*. CRC Press.
- Sibson, R. H. (1977). Fault rocks and fault mechanisms. *Journal of the Geological Society*, 133(3), 191-213.
- Sibson, R. H. (1985). A note on fault reactivation. *Journal of Structural Geology*, 7(6), 751-754.
- Sibson, R. H. (1990). Conditions for fault-valve behaviour. *Geological Society, London, Special Publications*, 54(1), 15-28.
- Sibson, R. H. (1998). Brittle failure mode plots for compressional and extensional tectonic regimes. *Journal of Structural Geology*, 20(5), 655-660.
- Sibson, R. H., Toy, V. G., Abercrombie, R., McGarr, A., Di Toro, G., & Kanamori, H. (2006). The habitat of fault-generated pseudotachylyte: Presence vs. absence of friction-melt. *GEOPHYSICAL MONOGRAPH-AMERICAN GEOPHYSICAL UNION*, 170, 153.
- Sibson, R. H. (2009). Rupturing in overpressured crust during compressional inversion—the case from NE Honshu, Japan. *Tectonophysics*, 473(3-4), 404-416.

- Simpson, R. W. (1997). Quantifying Anderson's fault types. *Journal of Geophysical Research: Solid Earth*, 102(B8), 17909-17919.
- Singleton, J. S., & Mosher, S. (2012). Mylonitization in the lower plate of the Buckskin-Rawhide detachment fault, west-central Arizona: Implications for the geometric evolution of metamorphic core complexes. *Journal of Structural Geology*, 39, 180-198.
- Singleton, J. S. (2013). Development of extension-parallel corrugations in the Buckskin-Rawhide metamorphic core complex, west-central Arizona. *Geological Society of America Bulletin*, 125(3-4), 453-472.
- Singleton, J. S., Wong, M. S., & Johnston, S. M. (2018). The role of calcite-rich metasedimentary mylonites in localizing detachment fault strain and influencing the structural evolution of the Buckskin-Rawhide metamorphic core complex, west-central Arizona. *Lithosphere*, 10(2), 172-193.
- Skelton, A. D. L., Valley, J. W., Graham, C. M., Bickle, M. J., & Fallick, A. E. (2000). The correlation of reaction and isotope fronts and the mechanism of metamorphic fluid flow. *Contributions to Mineralogy and Petrology*, 138(4), 364-375.
- Sleep, N. H., & Blanpied, M. L. (1992). Creep, compaction and the weak rheology of major faults. *Nature*, 359(6397), 687-692.
- Skemer, P., Katayama, I., Jiang, Z., & Karato, S. I. (2005). The misorientation index: Development of a new method for calculating the strength of lattice-preferred orientation. *Tectonophysics*, 411(1-4), 157-167.
- Smith, I. E., & Davies, H. L. (1976). *Geology of the southeast Papuan mainland* (Vol. 11). Australian Government Pub. Service.
- Smith, I. E. (2013). The chemical characterization and tectonic significance of ophiolite terrains in southeastern Papua New Guinea. *Tectonics*, 32(2), 159-170.
- Smith, S. A. F., Holdsworth, R. E., Collettini, C., & Imber, J. (2007). Using footwall structures to constrain the evolution of low-angle normal faults. *Journal of the Geological Society*, 164(6), 1187-1191.
- Smith, S. A. F., Holdsworth, R. E., & Collettini, C. (2011a). Interactions between low-angle normal faults and plutonism in the upper crust: Insights from the Island of Elba, Italy. *Bulletin*, 123(1-2), 329-346.
- Smith, S. A. F., Holdsworth, R. E., Collettini, C., & Pearce, M. A. (2011b). The microstructural character and mechanical significance of fault rocks associated with a continental low-angle normal fault: the Zuccale Fault, Elba Island, Italy. *Geological Society, London, Special Publications*, 359(1), 97-113.
- Smith, S. A. F., Di Toro, G., Kim, S., Ree, J. H., Nielsen, S., Billi, A., & Spiess, R. (2013). Coseismic recrystallization during shallow earthquake slip. *Geology*, 41(1), 63-66.
- Sorel, D. (2000). A Pleistocene and still-active detachment fault and the origin of the Corinth-Patras rift, Greece. *Geology*, 28(1), 83-86.

- Speckbacher, R., Behrmann, J. H., Nagel, T. J., Stipp, M., & Mahlke, J. (2012). Fluid flow and metasomatic fault weakening in the Moresby Seamount detachment, Woodlark Basin, offshore Papua New Guinea. *Geochemistry, Geophysics, Geosystems*, 13(11).
- Speckbacher, R., Stipp, M., Behrmann, J. H., & Heidelbach, F. (2013). Fluid-assisted fracturing, cataclasis, and resulting plastic flow in mylonites from the Moresby Seamount detachment, Woodlark Basin. *Journal of Structural Geology*, 56, 156-171.
- Spencer, J. E. (1984). Role of tectonic denudation in warping and uplift of low-angle normal faults. *Geology*, 12(2), 95-98.
- Spencer, J. E. (1985). Miocene low-angle normal faulting and dike emplacement, Homer Mountain and surrounding areas, southeastern California and southernmost Nevada. *Geological Society of America Bulletin*, 96(9), 1140-1155.
- Spencer, J. E., & Chase, C. G. (1989). Role of crustal flexure in initiation of low-angle normal faults and implications for structural evolution of the Basin and Range province. *Journal of Geophysical Research: Solid Earth*, 94(B2), 1765-1775.
- Spencer, J. E. (1999). Geologic continuous casting below continental and deep-sea detachment faults and at the striated extrusion of Sacsayhuaman, Peru. *Geology*, 27(4), 327-330.
- Spencer, J. E. (2010). Structural analysis of three extensional detachment faults with data from the 2000 Space-Shuttle Radar Topography Mission. *GSA Today*, 20(8), 4-10.
- Spencer, J. E. (2011). Gently dipping normal faults identified with Space Shuttle radar topography data in central Sulawesi, Indonesia, and some implications for fault mechanics. *Earth and Planetary Science Letters*, 308(3), 267-276.
- Spencer, J. E., Reynolds, S. J., Scott, R. J., & Richard, S. M. (2016). Shortening in the upper plate of the Buckskin-Rawhide extensional detachment fault, southwestern US, and implications for stress conditions during extension. *Tectonics*, 35(12), 3119-3136.
- Steltenpohl, M. G., Hames, W. E., & Andresen, A. (2004). The Silurian to Permian history of a metamorphic core complex in Lofoten, northern Scandinavian Caledonides. *Tectonics*, 23(1).
- Stewart, M., Holdsworth, R. E., & Strachan, R. A. (2000). Deformation processes and weakening mechanisms within the frictional–viscous transition zone of major crustal-scale faults: insights from the Great Glen Fault Zone, Scotland. *Journal of Structural Geology*, 22(5), 543-560.
- Stipp, M., Stünitz, H., Heilbronner, R., & Schmid, S. M. (2002). Dynamic recrystallization of quartz: correlation between natural and experimental conditions. *Geological Society, London, Special Publications*, 200(1), 171-190.
- Stipp, M., & Tullis, J. (2003). The recrystallized grain size piezometer for quartz. *Geophysical Research Letters*, 30(21).

- Stünitz, H., & Tullis, J. (2001). Weakening and strain localization produced by syn-deformational reaction of plagioclase. *International Journal of Earth Sciences*, 90(1), 136-148.
- Surace, I. R., Clauer, N., Thélín, P., & Pfeifer, H. R. (2011). Structural analysis, clay mineralogy and K–Ar dating of fault gouges from Centovalli Line (Central Alps) for reconstruction of their recent activity. *Tectonophysics*, 510(1-2), 80-93.
- Tanikawa, W., Mishima, T., Hirono, T., Lin, W., Shimamoto, T., Soh, W., & Song, S. R. (2007). High magnetic susceptibility produced in high-velocity frictional tests on core samples from the Chelungpu fault in Taiwan. *Geophysical Research Letters*, 34(15).
- Tanikawa, W., Mishima, T., Hirono, T., Soh, W., & Song, S. R. (2008). High magnetic susceptibility produced by thermal decomposition of core samples from the Chelungpu fault in Taiwan. *Earth and Planetary Science Letters*, 272(1-2), 372-381.
- Taylor, B., Goodliffe, A. M., & Martinez, F. (1999). How continents break up: insights from Papua New Guinea. *Journal of Geophysical Research: Solid Earth*, 104(B4), 7497-7512.
- Taylor, B., & Huchon, P. (2002). Active continental extension in the western Woodlark Basin: A synthesis of Leg 180 results. In *Proceedings of the Ocean Drilling Program, Scientific Results* (Vol. 180, pp. 1-36). P. Huchon, B. Taylor, and A. Klaus.
- Ter Heege, J. H., De Bresser, J. H. P., & Spiers, C. J. (2002). The influence of dynamic recrystallization on the grain size distribution and rheological behaviour of Carrara marble deformed in axial compression. *Geological Society, London, Special Publications*, 200(1), 331-353.
- Tetreault, J. Á., & Buiter, S. J. H. (2012). Geodynamic models of terrane accretion: Testing the fate of island arcs, oceanic plateaus, and continental fragments in subduction zones. *Journal of Geophysical Research: Solid Earth*, 117(B8).
- Tielke, J. A., 2010, Development and application of a method for determining paleostress from calcite deformation twins using electron backscatter diffraction: M.s. thesis, South Dakota School of Mines and Technology, 133 p.
- Tjhin, K. T. (1976). Trobriand Basin exploration, Papua New Guinea. *The APPEA Journal*, 16(1), 81-90.
- Tregoning, P., Lambeck, K., Stolz, A., Morgan, P., McClusky, S. C., Beek, P., ... & Murphy, B. (1998). Estimation of current plate motions in Papua New Guinea from Global Positioning System observations. *Journal of Geophysical Research: Solid Earth*, 103(B6), 12181-12203.
- Tucholke, B. E., Lin, J., & Kleinrock, M. C. (1998). Megamullions and mullion structure defining oceanic metamorphic core complexes on the Mid-Atlantic Ridge. *Journal of Geophysical Research: Solid Earth*, 103(B5), 9857-9866.
- Tucholke, B. E., Fujioka, K., Ishihara, T., Hirth, G., & Kinoshita, M. (2001). Submersible study of an oceanic megamullion in the central North Atlantic. *Journal of Geophysical Research: Solid Earth*, 106(B8), 16145-16161.

- Tucholke, B. E., Behn, M. D., Buck, W. R., & Lin, J. (2008). Role of melt supply in oceanic detachment faulting and formation of megamullions. *Geology*, 36(6), 455-458.
- Tulloch, A. J., & Kimbrough, D. L. (1989). The Paparoa metamorphic core complex, New Zealand: cretaceous extension associated with fragmentation of the Pacific margin of Gondwana. *Tectonics*, 8(6), 1217-1234.
- Tullis, T. E. (1980). The use of mechanical twinning in minerals as a measure of shear stress magnitudes. *Journal of Geophysical Research: Solid Earth*, 85(B11), 6263-6268.
- Turner, F. J. (1953). Nature and dynamic interpretation of deformation lamellae in calcite of three marbles. *American Journal of Science*, 251(4), 276-298.
- Turner, F. J., Griggs, D. T., & Heard, H. (1954). Experimental deformation of calcite crystals. *Geological Society of America Bulletin*, 65(9), 883-934.
- Turner, F. J. (1962, January). Compression and tension axes deduced from (0112) Twinning in Calcite. In *Journal of Geophysical Research* (Vol. 67, No. 4, p. 1660). 2000 FLORIDA AVE NW, WASHINGTON, DC 20009: AMER GEOPHYSICAL UNION.
- Urai, J. L., Means, W. D., & Lister, G. S. (1986). Dynamic recrystallization of minerals. *Mineral and rock deformation*, 161-199.
- Vadacca, L., Casarotti, E., Chiaraluce, L., & Cocco, M. (2016). On the mechanical behaviour of a low-angle normal fault: the Alto Tiberina fault (Northern Apennines, Italy) system case study. *Solid Earth*, 7(6), 1537-1549.
- Valcke, S. L. A., De Bresser, J. H. P., Pennock, G. M., & Drury, M. R. (2015). Influence of deformation conditions on the development of heterogeneous recrystallization microstructures in experimentally deformed Carrara marble. *Geological Society, London, Special Publications*, 409(1), 175-200.
- Verberne, B. A., Plümper, O., de Winter, D. M., & Spiers, C. J. (2014). Superplastic nanofibrous slip zones control seismogenic fault friction. *Science*, 346(6215), 1342-1344.
- Wallace, L. M., Stevens, C., Silver, E., McCaffrey, R., Lortung, W., Hasiata, S., ... & Taugaloidi, J. (2004). GPS and seismological constraints on active tectonics and arc-continent collision in Papua New Guinea: Implications for mechanics of microplate rotations in a plate boundary zone. *Journal of Geophysical Research: Solid Earth*, 109(B5).
- Wallace, L. M., Ellis, S., Little, T., Tregoning, P., Palmer, N., Rosa, R., ... & Kwazi, J. (2014). Continental breakup and UHP rock exhumation in action: GPS results from the Woodlark Rift, Papua New Guinea. *Geochemistry, Geophysics, Geosystems*, 15(11), 4267-4290.
- Walker, A. N., Rutter, E. H., & Brodie, K. H. (1990). Experimental study of grain-size sensitive flow of synthetic, hot-pressed calcite rocks. *Geological Society, London, Special Publications*, 54(1), 259-284.
- Wdowinski, S., & Axen, G. J. (1992). Isostatic rebound due to tectonic denudation: A viscous flow model of a layered lithosphere. *Tectonics*, 11(2), 303-315.

- Webb, L. E., Baldwin, S. L., Little, T. A., & Fitzgerald, P. G. (2008). Can microplate rotation drive subduction inversion?. *Geology*, 36(10), 823-826.
- Webber, S. (2017). Using Structural Geology and Cosmogenic Nuclide Dating to Infer the Slip Rate and Frictional Strength of the Active Mai'iu Low-Angle Normal Fault, Eastern Papua New Guinea.
- Webber, S., Norton, K. P., Little, T. A., Wallace, L. M., & Ellis, S. (2018). How fast can low-angle normal faults slip? Insights from cosmogenic exposure dating of the active Mai'iu fault, Papua New Guinea. *Geology*.
- Webber, S., Little, T., Norton, K., Österle, J., Mizera, M., Seward, D., & Holden, G. (2019). Progressive back-warping of a rider block atop an actively exhuming, continental low-angle normal fault. *Journal of Structural Geology*, 103906.
- Weissel, J. K., Taylor, B., & Karner, G. D. (1982). The opening of the Woodlark Basin, subduction of the Woodlark spreading system, and the evolution of northern Melanesia since mid-Pliocene time. *Tectonophysics*, 87(1-4), 253-277.
- Wenk, H. R. (1985). Carbonates. In *Preferred Orientation in Deformed Metal and Rocks* (pp. 361-384).
- Wernicke, B. (1981). Insights from Basin and Range surface geology for the process of large-scale divergence of the continental lithosphere. In *Processes of Planetary Rifting* (Vol. 457, p. 90).
- Wernicke, B., & Axen, G. J. (1988). On the role of isostasy in the evolution of normal fault systems. *Geology*, 16(9), 848-851.
- Westaway, R. (2005). Active low-angle normal faulting in the Woodlark extensional province, Papua New Guinea: A physical model. *Tectonics*, 24(6).
- Whitney, D. L., Teyssier, C., Rey, P., & Buck, W. R. (2013). Continental and oceanic core complexes. *Geological Society of America Bulletin*, 125(3-4), 273-298.
- Wintsch, R. P., & Yeh, M. W. (2013). Oscillating brittle and viscous behavior through the earthquake cycle in the Red River Shear Zone: Monitoring flips between reaction and textural softening and hardening. *Tectonophysics*, 587, 46-62.
- Wong, M. S., & Gans, P. B. (2008). Geologic, structural, and thermochronologic constraints on the tectonic evolution of the Sierra Mazatán core complex, Sonora, Mexico: New insights into metamorphic core complex formation. *Tectonics*, 27(4).
- Yamaji, A. (2000). The multiple inverse method: a new technique to separate stresses from heterogeneous fault-slip data. *Journal of Structural Geology*, 22(4), 441-452.
- Yamaji, A., & Sato, K. (2006). Distances for the solutions of stress tensor inversion in relation to misfit angles that accompany the solutions. *Geophysical Journal International*, 167(2), 933-942.
- Yamaji, A. (2015). How tightly does calcite e-twin constrain stress?. *Journal of Structural Geology*, 72, 83-95.

- Yavuz, F., Kumral, M., Karakaya, N., Karakaya, M. Ç., & Yıldırım, D. K. (2015). A Windows program for chlorite calculation and classification. *Computers & Geosciences*, 81, 101-113.
- Yin, A. (1989). Origin of regional, rooted low-angle normal faults: A mechanical model and its tectonic implications. *Tectonics*, 8(3), 469-482.
- Zaarur, S., Affek, H. P., & Brandon, M. T. (2013). A revised calibration of the clumped isotope thermometer. *Earth and Planetary Science Letters*, 382, 47-57.
- Zhao, X., & Tominaga, M. (2009). Paleomagnetic and rock magnetic results from lower crustal rocks of IODP Site U1309: Implication for thermal and accretion history of the Atlantis Massif. *Tectonophysics*, 474(3-4), 435-448.
- Zoback, M. D., & Harjes, H. P. (1997). Injection-induced earthquakes and crustal stress at 9 km depth at the KTB deep drilling site, Germany. *Journal of Geophysical Research: Solid Earth*, 102(B8), 18477-18491.